

# ICCESEN-2018

5<sup>th</sup> International Conference on Computational and Experimental Science and Engineering

Limak-Limra Hotel and Resort Kemer-Antalya-TURKEY

12-16 October 2018

## Proceedings of ICCESEN-2018

EDITORS

**Prof.Dr. İskender AKKURT**

**Dr. Kadir GÜNOĞLU**

**Dr. Hakan AKYILDIRIM**

**ISBN : 978-605-68728-0-8**

2018.iccesen.org iccesen2018@gmail.com

# ICCESSEN-2018

5<sup>th</sup> International Conference on Computational and Experimental Science and Engineering

**Limak-Limra Hotel and Resort Kemer-Antalya-TURKEY**  
**12-16 October 2018**

# Proceedings of ICCESSEN-2018

## Editors:

**Prof.Dr. İskender AKKURT**

**Dr. Kadir GÜNOĞLU**

**Dr. Hakan AKYILDIRIM**

**ISBN:978-605-68728-0-8**

## **Proceedings of ICCESSEN-2018**

5<sup>th</sup> International Conference on Computational and Experimental Science and Engineering (**ICCESSEN-2018**)

12-16 October 2018, Kemer-Antalya-TURKEY

### **Editors:**

Prof. Dr. İskender AKKURT  
Dr. Kadir GÜNOĞLU  
Dr. Hakan AKYILDIRIM

**Published :** 28 December 2018  
**ISBN:** 978-605-68728-0-8

This work is subject to copyright. All rights are reserved, whether the whole or part of the material is concerned. Nothing from this publication may be translated, reproduced, stored in a computerized system or published in any form or in any manner, including, but not limited to electronic, mechanical, reprographic or photographic, without prior written permission from the Publisher [2018.iccesen.org](http://2018.iccesen.org) . Pls contact at [iccesen2018@gmail.com](mailto:iccesen2018@gmail.com).

The individual contributions in this publication and any liabilities arising from them remain the responsibility of the authors. The publisher is not responsible for possible damages, which could be a result of content derived from this publication.

# TABLE OF CONTENTS

TABLE OF CONTENTS	iii
FOREWORD	vii
ORGANISATION COMMITTEE	viii
SCIENTIFIC COMMITTEE	ix
INVITED SPEAKERS	xi
<b>Razika Zamoum Boushaki , Farida Kessal and Feriel Abahri</b> “Control of a MIMO aircraft system by LQG controller”	1 -4
<b>Razika Zamoum Boushaki , Feriel Aahri and Farida Kessal</b> “Control of a MIMO aircraft system by $H_{\infty}$ controller”	5-11
<b>Xun Sun, Shicheng Zhang, Xinfang Ma and Kai Lia</b> “Experimental study on the influence of structure anisotropy on mechanical property of coal”	12-17
<b>Ziyao Zhong, Xiaodong Wu, Guoqing Han, Lei Zheng, Shuzhe Shi, Zhan Meng</b> “Numerical Study on Coal Particle Transport Under Air-Water Multiphase Flow in V-Shaped Elbow”	18-25
<b>Y. Aribi, R. Zamoum Boushaki</b> “Sliding-Mode Enhancement for a Class of Fuzzy-based Controllers for surge control in Compression Systems”	26-31
<b>Li zhun , XiaoDong Wu and Guoqing Han</b> “Performance of multiple-fracture horizontal wells with consideration of the long-term fracture conductivity”	32-41
<b>Şemsettin Kılınçarslan, Metin Davraz and Mehmet Ali Akbulut</b> “Determination of Engineering Properties of Ready Thermal Insulation Plaster and Acceptability Assessment”	42-45
<b>Şemsettin Kılınçarslan, Metin Davraz, Nuri Işıldar</b> “Investigation of the Effect of Fly Ash And Perlite on Foam Concrete Properties”	46-53
<b>Yang zhang, Wei Feng, Zhongnan Jiang, Chen Yang, Wentong Fan, Lufeng Zhang, Jin Wang, Yuechun Wang</b> “Experimental Investigation on Perforation Temporary Plugging by Degradable Materials in Multi-Fracturing”	54-61
<b>Kun Qian, Shenglai Yang, Hongen Dou and Yu Huang</b> “Experimental Investigation on Interfacial and Swelling Behavior of CO <sub>2</sub> -light Crude Oil System”	62-68
<b>Qian Wang, Sheng Lai Yang, Hai Shui Han, Kun Qian, Jia jun Li</b> “Experimental study on the changes in the physical properties of low permeability sandstone reservoirs after injection of CO <sub>2</sub> in different methods”	69-76
<b>Assia Boukezzata, Sihem Bouanik, Samira Kaci, Ammar Manseri, Hamid Menari, Lakhder Guerbous<sup>2</sup>, Aissa Keffous</b> “Elaboration and characterization of nanowire hydrogenated amorphous silicon carbide (a-SiC:H) thin films for energy conversion”	77-81



<b>Şemsettin Kılınçarslan, Bilgin İçel and Yasemin Şimşek</b> “Determination of Modulus of Elasticity for Ash ( <i>Fraxinus</i> spp.) Grown in Turkey Using Ultrasound”	82-86
<b>Jiangshuai Wang, Gonghui Liu, Jun Li, Xueting Wu, Hongwei Yang, Kuidong Luo</b> “Study on Temperature Distribution in Wellbore during Drilling”	87-92
<b>Debin Kong, Yiqiang Li, Shanzhi Xu, Hu Guo and Yingfeng Peng</b> “Stable Isotope Analysis of Soil Carbon Dioxide for Monitoring CO <sub>2</sub> -EOR and Sequestration in Yanchang Oilfield”	93-98
<b>Katerina Horackova, Lenka Škaroupková and Michaela Kalčíková Hisemová</b> “Precautionary measures of ventilator-associated pneumonia”	99-102
<b>Jana Wichsova, Katerina Horackova and Barbora Lidakova</b> “Hygiene and Epidemiology Nursing - Student Grant Competition”	103-107
<b>Kai Liao, Shicheng Zhang, Xinfang Ma and Xun Sun</b> “Numerical investigation of thermal fluid fracturing in low-mobility tight oil reservoirs”	108-117
<b>Mingda Dong, Xiang'an Yue</b> “Effect of Surfactant Emulsification on High Water-cut Reservoir in Shengli Oilfield”	118-122
<b>Güldem ÜRER</b> “Energy Levels of Hydrogen Like Mendelevium”	123-125
<b>Rongrong Qi, Zhengfu Ning, Qing Wang, Shuang Zhang, Xiaojun Wu, Zhilin Cheng</b> “CO <sub>2</sub> Adsorption Capacity of Shale with the Consideration of Adsorption-induced Swelling”	126-130
<b>Wang Jin, Zhou Fujian, Yang Chen, Zhang Lufeng, Feng Wei, Wang Yuechu</b> “Numerical simulation on plugging efficiency of degradable particle based on Fluent software”	131-138
<b>Yamani Dalila, Mouhouche Ali and Ait El Djoudi Amel</b> “Training on educational uses of ICTs: the disciplinary dimension of learners in the training contents”	139-146
<b>Elif Deniz Yelmenoglu, Numan Celebi and Tugrul Taşçı</b> “Saliency Detection with Hybrid Artificial Bee Colony- Firefly Optimization Method”	147-151
<b>Murat Kiyak, Orhan Cakır and Ibrahim Sahin</b> “Cutting Fluids in Machining and Environmental Issues -A Review”	152-159
<b>Ming Chen, Shicheng Zhang, Yun Xu, Xinfang Ma, Yushi Zou</b> “Experimental and theoretical investigation on proppant embedment of hydraulic fracturing in shales”	160-163
<b>Arslan Say, Demet Çakır, Arif Ayar</b> “Effects of Socio-demographic Factors on Psychological Conditions of Vocational School Students”	164-166
<b>Salim Djezairi, Boushaki Zamoum Razika, Bouzouia Brahim, Abahri Ferial</b> “Task Planning for Mobile Manipulators Using Backward Climbing”	167-171

<b>Burak Kurt</b> “A Note on the Symmetric Relation for Degenerate Genocchi Polynomials”	172-174
<b>Zouani Amina, Guerfi bahdja, Mezroud Fouzia, Kermout Imene, Talailef Assma</b> “Evaluation Of The Water Fluoride Exposure In Urban Areas In The Province Of Blida, Algeria”	175-183
<b>Hongwei Yang, Jun Li and Gonghui Liu</b> “Why the Variable Gradient Drilling Approach Can Better Fit the Complex and Narrow Pressure Window in Ultra-deep Water Drilling?”	184-190
<b>Arslan Say</b> “Investigation of Antiproliferative Effects of AHCC”	191-193
<b>Chao Wang, Gonghui Liu, Jun Li, Tao Zhang, Hailong Jiang, Kai Ren</b> “Downhole WOB Measurement Error Owing to Temperature Variation”	194-200
<b>Dali-Youcef Zohra</b> “Use of titanium oxide in phenol degradation of paper”	201-206
<b>Xiaosong Wen, Gonghui Liu, Jun Li, Chunqing Zha and Xueli Guo</b> “A Comprehensive Analysis of Compound Impactor Based on Mixed Flow Impeller Drive”	207-214
<b>Saliha Boutora, Dhia Elhak Messaoud, Hamid Bentarzi</b> “Power Quality Improvement in Grid-Tied PV System”	215-228
<b>Atilla Evcin, Nalan Çiçek Bezir, Iskender Akkurt, Yonca Yahşi Çelen, Kadir Günoğlu and Bahri Ersoy</b> “Usability of Bentonite and Boron Waste as a Radiation Shielding Materials”	229-232
<b>Nilay Duman, Reşat Duman, Atilla Evcin</b> “Effect of Topical Pumpkin Seed Oil Exposure on Morphological Analysis of Hair Fibers on Scanning Electron Microscopy”	233-236
<b>Houssem Menhour and Süleyman Eken</b> “Is Video from a Security Footage or Not?”	237-240
<b>Amer A. G. Al Abdel Hamid</b> “A Selective Chemosensor for Lead Divalent Based on Ruthenium-[(E)-2-(((4-(ethoxycarbonyl)phenyl)iminio)-methyl)phenolate] Complex”	241-246
<b>Sameer Al-Obaidi, Kadir Günoğlu, Hakan Akyıldırım, Iskender Akkurt</b> “An Experimental Test for neutron shielding”	247-251
<b>Gül Bahar Bülbül, Vilda Purutçuoğlu</b> “Model Selection in MARS-Constructed Biological Networks”	252-254
<b>Wang Deqiang, Cheng Linsong*, Cao Renyi, Yin Fuguo</b> “Evaluation of asynchronous injection alternating production considering boundary layer effect in tight oil with complex fracture networks”	255-259

<b>Suran Wang*, Linsong Cheng, Shijun Huang, Yongchao Xue, Yonghui Wu, Pin Jia and Deqiang Wang</b> “A Novel Approach for Production Data Analysis of Fractured Carbonate Wells during Transient Flow Regime”	260-264
<b>Pin Jia, Linsong Cheng, Yongchao Xue, Deqiang Wang and Suran Wang</b> <sup>1</sup> “Laboratory Investigation of High-speed and High-efficiency Development Mechanism of Sandstone Reservoir”	265-269
<b>Dansen Shang, Jirui Hou</b> “Effect of Descending Viscosity Injection Pattern for Alkali-surfactant-polymer (ASP) Flooding on Enhanced oil Recovery”	270-274
<b>Jiuzhu Wu, Deqiang Wang, Changchao Chen, Jing Zhu, Guangtao Chang and Huixian Zhang</b> “A Novel Characterization of Fluid Viscosity in Micro Sized Throats - Based On Micro Flow Experiments”	275-279
<b>Xiang Rao, Linsong Cheng , Renyi Cao, Pin Jia, Yonghui Wu</b> “A novel embedded discrete fracture model based on GEM of two-set nodes”	280-284
<b>Tingting Cheng, Jirui Hou, Yulong Yang, Xiaoyu Feng, Haoya Zhai, Ajiao Jiang</b> “Study on the Feasibility and Oil-displacement Mechanisms of Nano-TiO <sub>2</sub> in Low-permeability Reservoirs”	285-289
<b>Faez Waheed, Kadir Günoğlu, Hakan Akyıldırım, İskender Akkurt</b> “Variation of Detector Resolution with the Source-Detector Distance”	290-297
<b>Faez Waheed, Hakan Akyıldırım, Kadir Günoğlu, İskender Akkurt</b> “The Importance of Buildup Factor for NaI(Tl) Detector System”	298-300
<b>Hüseyin Eriş, Feray Kabalcıoğlu Bucak</b> “Hastanelerde Çalışan Ebe Ve Hemşirelerin Hepatit A Ve B Hakkında Bilgi Düzeyleri Ve Aldıkları Önlemlerin Belirlenmesi”	301-306
<b>Susan Shukur Noori, İskender Akkurt, Nurdan Karpuz Demir</b> “Calculations of Cross Sections of Zinc Nucleus Induced by Proton to Produce Gallium-66”	307-310
<b>Sameer Al-Obaidi, Hakan Akyıldırım, Kadir Günoğlu, İskender Akkurt</b> “FLUKA calculation for neutron shielding from <sup>252</sup> Cf source”	311-313
<b>Abdlhamed Abdlhamed, Zeynep Parlar, İskender Akkurt</b> “Investigation of Shielding Properties of Recycled Rubber Composites for Gamma Radiation”	314-316
<b>Zuhal Er</b> “Application of Analytic Hierarchy Method for Solar Artificial Intelligence Systems”	317-321
<b>Vildan Girişta, İsmail Kaya and Zeynep Parlar</b> “The Effect of Interference Force on the Lifecycle of Lip Seals”	322-323
<b>Umut Serdar Çivici, Zeynep Parlar</b> “Locomotion Control of Soft Robot with Surface Texture”	324-327
<b>Hüseyin ERİŞ, Ayça KARAHAN</b> “Hastanelerde Algılanan Değer ile Hasta Sadakati Arasındaki ilişki: Bir Üniversite Hastanesi Örneği”	328-335

## **FOREWORD**



Dear Colleagues,

It is a great honor for me to host you all in “**5<sup>th</sup> International Conference on Computational and Experimental Science and Engineering (ICCESSEN-2018)**” taken place at Limak-Limra Hotel and Resort, Kemer-Antalya-Turkey) in the period of 12-16 October 2018.

We are also happy to publish the proceeding of ICCESSEN-2018. All papers have been reviewed by two reviewers.

I am hoping to meet you all in ICCESSEN-2019.

Prof. Dr. İskender AKKURT

Chair for ICCESSEN-2018

Editor for Proceedings of ICCESSEN-2018

## ORGANISATION COMMITTEE

<b>Prof.Dr. Iskender AKKURT (Chair)</b>	Suleyman Demirel University, Isparta -Turkey
Dr. Kadir GÜNOĞLU (secretary)	Isparta Uygulamalı Bilimler University, Isparta -Turkey
Dr. Hakan AKYILDIRIM	Suleyman Demirel University, Isparta -Turkey
Dr. Ahmet BEYÇİOĞLU	Düzce University, Düzce -Turkey
Dr. Nilgün DEMİR	Uludag University, Bursa -Turkey
Dr. Ümit KARA	Suleyman Demirel University, Isparta -Turkey
Dr. Hüseyin Ozan TEKİN	Üsküdar University, Istanbul-Turkey
Dr. Nurdan KARPUZ DEMİR	Amasya Demirel University, Amasya -Turkey
Dr. Feride KULALI	Üsküdar University, Istanbul-Turkey
Dr. Zehra Nur KULUÖZTÜRK	Bitliseren University, Bitlis-Turkey
Dr. M. Fatih KULUÖZTÜRK	Bitliseren University, Bitlis-Turkey
Dr. Özge Kozguş GÜLDÜ	Ege University, İzmir-Turkey

## SCIENTIFIC COMMITTEE




Prof.Dr. Iskender AKKURT (Chair)	Suleyman Demirel University, Isparta –Turkey
Prof.Dr. Majid ABBASPOUR	Sharif University of Technology-Iran
Prof.Dr. Zahid Hussain ABRA	Quadi-E-Awam University, Sindh-Pakistan
Prof.Dr. Abdullah ALAMRI	King Saud University, Saudi Arabia
Prof.Dr. Nezam Mahdavi-AMIRI	Sharif University Iran
Dr. John R.M.ANNAND	Glasgow University, Glasgow-Scotland (UK)
Dr. Majda AOUITITEN	Abdelmalek Essaadi University-Morocco
Prof.Dr. Mohamed Kheireddine AROUA	University of Malaya-Malaysia
Dr. Rachid BELKADA	CRSTSE -Algeria
Dr. Radhey S BENIWAL	CSIR-NISCAIR, New Delhi 110012, India
Dr. Mahmoud Abdullah BENNASER	Kuwait University-Kuwait
Dr. Djoudi BOUHAFS	Centre de Recherche en Technologie -Algeria
Prof. Oleg BURDAKOV	Linköping University Linköping, Sweden
Prof.Dr. Lotfi CHOUCANE	Weill Cornell MEDical College-Qatar
Prof.Dr. Alpaslan DAYANGAÇ	Osmaniye Korkutata University, Osmaniye –Turkey
Dr. Nermin DEMİRKOL	Kocaeli University, Kocaeli –Turkey
Prof.Dr. İbrahim DİNÇER	University of Ontario Institute of Technology (UOIT)-Canada
Prof. Dr. Mitra DJAMAL	Institute Teknologi Bandung-Indonesia
Prof.Dr.Witold DOBROWOLSKI	Fizyki, PolskaAkademia Nauk-Poland
Prof.Dr. Mahmut DOĞRU	Bitlis Eren University, Bitlis-Turkey
Prof.Dr. Mohammed Mostafa EL TOKHI	United Arab Emirates University-UAE
Dr. Zuhale ER	Istanbul Technical University, Istanbul-Turkey
Prof.Dr. Mustafa EROL	Dokuz Eylul University, İzmir-Turkey
Prof.Dr. Ümran ERTÜRK	Uludağ University, Bursa-Turkey
Prof.Dr. Madjid FATHI	Dept. of EECS University of Siegen- Germany
Prof.Dr. Jan FELBA	Wroclaw University of Technology-Poland
Prof.Dr. S. Mostafa GHIAASIAAN	Mechanical/Nuclear Engineering, Georgia Tech USA
Prof.Dr. Mustafa GÜNAL	Gaziantep University, Gaziantep-Turkey
Prof. Dr. Amir HUSSAIN	University of Stirling- Scotland(UK)
Dr. Nabi IBADOV	Warsaw University of Technology-Poland
Dr. Sibel KAÇMAZ	Giresun University, Giresun-Turkey

Prof.Dr. Fatma KARİPCİN	Nevşehir Hacı Bektaş Veli University-Turkey
Prof.Dr. Hamdi Ş. KILIÇ	Selcuk University, Konya-Turkey
Prof. Dr. İsmail KOYUNCU	Istanbul Technical University, Istanbul-Turkey
Dr. Irida MARKJA	Polytechnic University,Tirana-Albania
Dr. F Zümrüt Biber MÜFTÜLER	Ege University, Izmir-Turkey
Prof.Dr. Ravindra NUGGEHALI	New Jersey Institute of Technology-USA
Prof.Dr. İbrahim ÖRÜN	Aksaray University, Aksaray-Turkey
Prof.Dr. Necati ÖZDEMİR	Balıkesir University, Balıkesir-Turkey
Dr. Zehra Kamışlı ÖZTÜRK	Anadolu University, Eskişehir-Turkey
Dr. Zeynep PARLAR	Istanbul Technical University, Istanbul-Turkey
Dr. Tomasz PIOTROWSKI	Warsaw University of Technology, Warsaw-Poland
Prof.Dr. Javad RAHIGHI	AEOI, Tehran-Iran.
Dr. Abdelmadjid RECIOUI	University of Bumerdes-Algeria
Prof.Dr. Miljko SATARIC	Faculty of Technical Sciences Novi Sad-Serbia
Prof.Dr. Saleh SULTANSOY	TOBB University, Ankara-Turkey
Dr. Naim SYLA	University of Prishtina-Kosova
Dr. Huseyin TOROS	Istanbul Technical University, Istanbul-Turkey
Prof.Dr. Ahmad UMAR	Najran University-Saudi Arabia
Prof.Dr. Abolhassan VAFAI	Sharif University Tehran-Iran
Prof.Dr. Gerhard-Wilhelm WEBER	Middle East Technical University Ankara-Turkey



## INVITED SPEAKERS

	<p><b>Prof.Dr. Numan AKDOGAN</b></p> <p>Gebze Technical University Institute of Nanotechnology Kocaeli-TURKEY</p> <p><b>Title:</b> <i>Recent Advances in Nanotechnology and Shapeable Magneto-electronics</i></p>
	<p><b>Prof.Dr. Oleg BURDAKOV</b></p> <p>Linköping University Department of Mathematics Linköping- SWEDEN</p> <p><b>Title:</b> <i>Regularized Monotonic Regression</i></p>
	<p><b>Prof.Dr. Madjid FATHI</b></p> <p>Dept. of EECS University of Siegen, GERMANY</p> <p><b>Title:</b> <i>A Knowledge based Concept for Mechanical Therapy instead of Chemical Therapy</i></p>
	<p><b>Prof.Dr. Amir HUSSAIN</b></p> <p>Edinburg Napier University, UK</p> <p><b>Title:</b> <i>Cognitive Big Data Analytics for Cybersecurity Applications</i></p>
	<p><b>Prof.Dr. Sushil Kumar KANSAL</b></p> <p>Pajcab University INDIA</p> <p><b>Title:</b> <i>Visible Light Photo catalysts: Preparation, Characterization and Application for the Treatment of Organic Pollutants in Aqueous Phase</i></p>

	<p style="text-align: center;"><b>Prof.Dr. Ravindra NUGGEHALLI</b></p> <p style="text-align: center;">New Jersey Institute of Technology-USA</p> <p><b>Title:</b> <i>Research Opportunities and Challenges in Materials Science &amp; Engineering – An Overview</i></p>
	<p style="text-align: center;"><b>Prof.Dr. Ahmad UMAR</b></p> <p style="text-align: center;">Najran University, Kingdom of Saudi Arabia</p> <p><b>Title:</b> <i>Semiconductor nanomaterials for Sensors and environmental remediation applications</i></p>
	<p style="text-align: center;"><b>Prof.Dr. Gerhard-Wilhelm WEBER</b></p> <p style="text-align: center;">Poznan University of Technology-POLAND</p> <p><b>Title:</b> <i>Voxel-MARS and CMARS: Early Warning of Alzheimer's Disease by Classification of Structural Brain MRI</i></p>

## Control of a MIMO aircraft system by LQG controller

**Razika Zamoum Boushaki \***, Farida Kessal and Ferial Abahri

University of M'hamed Bougara of Boumerdes Institute of Electrical and Electronic Engineering,  
Boumerdes, ALGERIA

\*boushakiraz@yahoo.fr

### ABSTRACT

This paper presents an application of the LQG technique on a MIMO aircraft system. LQG deals with linear systems having uncertainties and lacking state information's. Robustness and stability margins were attested and the results showed the dependence of the robustness margins on the weighting matrices.

**KEYWORDS-LQG;** Aircraft control; loop shaping

### 1. INTRODUCTION

The study of aircraft dynamics leading to the development of the aircraft equations of motion, we will present basic equations of motions in this work then in the second we will linearize them in order to apply linear control methods to enhance the performance and robustness of the studied model. The main purpose of every feedback loop is to reduce the effect of uncertainty on vital system functions. The feedback can be used for stabilization but the design involves certain risks by reducing the regions of stability of the nonlinear system. The equations are developed to describe the motion of a flight vehicle, subject to the prescribed aerodynamic forces and moments.

### 2. MODELING OF THE AIRCRAFT

The normal flight situations correspond to relatively small variations in the state variables which can lead to significant accelerations. Thus, we will consider

The linearization of the fundamental equations of longitudinal motion is formulated in the state space as  $\dot{\mathbf{X}} = \mathbf{A}\mathbf{X} + \mathbf{B}\mathbf{U}$ ; where  $\mathbf{X} = [\Delta u, \Delta w, \Delta q, \Delta \theta]^T$  Are the state vectors and  $\mathbf{U} = [\Delta \delta_e, \Delta \delta_T]^T$  Is the control vector [2].

Longitudinal mode :

$$\begin{bmatrix} \Delta \dot{u} \\ \Delta \dot{w} \\ \Delta \dot{q} \\ \Delta \dot{\theta} \end{bmatrix} = \begin{bmatrix} X_u & X_w & 0 & -g \\ Z_u & Z_w & u_0 & 0 \\ M_u + M_w Z_u & M_w + M_w Z_w & M_q + M_w u_0 & 0 \\ 0 & 0 & 1 & 0 \end{bmatrix} \begin{bmatrix} \Delta u \\ \Delta w \\ \Delta q \\ \Delta \theta \end{bmatrix} + \begin{bmatrix} X_{\delta_e} X_{\delta_T} & \\ Z_{\delta_e} & Z_{\delta_T} \\ M_{\delta_e} + M_w Z_{\delta_e} & M_{\delta_T} + M_w Z_{\delta_T} \\ 0 & 0 \end{bmatrix} \begin{bmatrix} \Delta \delta_e \\ \Delta \delta_T \end{bmatrix} \quad (1)$$

Lateral mode:

$$\dot{\mathbf{X}} = \mathbf{A}\mathbf{X} + \mathbf{B}\mathbf{U}, \quad \begin{bmatrix} \Delta \dot{v} \\ \Delta \dot{p} \\ \Delta \dot{r} \\ \Delta \dot{\phi} \end{bmatrix} = \begin{bmatrix} Y_v & Y_p & -(u_0 - Y_r) & g \cos \theta_0 \\ L_v & L_p & L_r & 0 \\ N_v & N_p & N_r & 0 \\ 0 & 1 & 0 & 0 \end{bmatrix} \begin{bmatrix} \Delta v \\ \Delta p \\ \Delta r \\ \Delta \phi \end{bmatrix} + \begin{bmatrix} 0 & Y_{\delta_r} \\ L_{\delta_a} & L_{\delta_r} \\ N_{\delta_a} & N_{\delta_r} \\ 0 & 0 \end{bmatrix} \begin{bmatrix} \Delta \delta_a \\ \Delta \delta_r \end{bmatrix} \quad (4)$$

As an experimental platform, the "Zagi Flying Wing" is chosen. For the demonstration of the previously developed equations, the dynamics and the characteristics of this UAV are used [4].

In this last step, the previously calculated stability derivatives and the developed equations are substituted in linearized lateral and longitudinal equations of motion by adding the height of the

drone "h" and replacing the velocity component "v" by the skid angle  $\beta$ . The complete model in the state space form, [2]

$$\begin{bmatrix} \Delta \dot{u} \\ \Delta \dot{w} \\ \Delta \dot{q} \\ \Delta \dot{\theta} \\ \Delta \dot{h} \\ \Delta \dot{\beta} \\ \Delta \dot{p} \\ \Delta \dot{r} \\ \Delta \dot{\phi} \end{bmatrix} = \begin{bmatrix} -0.33 & 1.31 & 0.00 & -9.80 & 0.00 & 0.00 & 0.00 & 0.00 & 0.00 \\ -1.79 & -3.90 & 9.82 & 0.00 & 0.00 & 0.00 & 0.00 & 0.00 & 0.00 \\ 0.70 & -3.53 & -11.39 & 0.00 & 0.00 & 0.00 & 0.00 & 0.00 & 0.00 \\ 0.000 & 0.00 & 1.00 & 0.00 & 0.00 & 0.00 & 0.00 & 0.00 & 0.00 \\ 0.00 & -1.00 & 9.82 & 0.00 & 0.00 & 0.00 & 0.00 & 0.00 & 0.00 \\ 0.00 & 0.00 & 0.00 & 0.00 & 0.00 & -0.10 & 0.19 & -1.00 & 0.99 \\ 0.00 & 0.00 & 0.00 & 0.00 & 0.00 & -1.22 & -1.91 & 1.00 & 0.00 \\ 0.00 & 0.00 & 0.00 & 0.00 & 0.00 & 1.72 & 0.09 & -1.71 & 0.00 \\ 0.00 & 0.00 & 0.00 & 0.00 & 0.00 & 0.00 & 1.00 & 0.00 & 0.00 \end{bmatrix} \begin{bmatrix} \Delta u \\ \Delta w \\ \Delta q \\ \Delta \theta \\ \Delta h \\ \Delta \beta \\ \Delta p \\ \Delta r \\ \Delta \phi \end{bmatrix} + \begin{bmatrix} -0.7436 & 6.8728 & 0.0000 & 0.0000 \\ 3.7855 & 0.0000 & 0.0000 & 0.0000 \\ 47.917 & 0.0000 & 0.0000 & 0.0000 \\ 0.0000 & 0.0000 & 0.0000 & 0.0000 \\ 0.0000 & 0.0000 & 0.0000 & 0.0000 \\ 0.0000 & 0.0000 & 0.0000 & -1.1855 \\ 0.0000 & 0.0000 & 8.3480 & 0.0000 \\ 0.0000 & 0.0000 & 4.2400 & -2.1272 \\ 0.0000 & 0.0000 & 0.0000 & 0.0000 \end{bmatrix} \begin{bmatrix} \Delta \delta_e \\ \Delta \delta_T \\ \Delta \delta_a \\ \Delta \delta_r \end{bmatrix} \quad (11)$$

### 3. LINEAR-QUADRATIC-GAUSSIAN CONTROL

The linear-quadratic-Gaussian (LQG) control is a control method applicable to uncertain linear systems disturbed by additive white Gaussian noise, with state information that is incomplete state. The LQG controller is the combination of a Kalman filter with a linear-quadratic regulator (LQR). The application to linear time-varying systems enables the design of linear feedback controllers for non-linear uncertain systems [5]. Consider the continuous-time linear dynamic system:

$$\begin{cases} \dot{x} = Ax + Bu + v \\ y = Cx + w \end{cases} \quad (12)$$

Where: Q and R are two weighting matrices. The linear quadratic Gaussian control theory is now applied to the model.

$$Q_{Long} = \begin{bmatrix} 12.00 & 0.000 & 0.000 & 0.000 & 0.000 \\ 0.000 & 60.00 & 0.000 & 0.000 & 0.000 \\ 0.000 & 0.000 & 60.00 & 0.000 & 0.000 \\ 0.000 & 0.000 & 0.000 & 1200 & 0.000 \\ 0.000 & 0.000 & 0.000 & 0.000 & 120.0 \end{bmatrix}; \quad Q_{Lat} = \begin{bmatrix} 12.00 & 0.000 & 0.000 & 0.000 & 0.000 \\ 0.000 & 60.00 & 0.000 & 0.000 & 0.000 \\ 0.000 & 0.000 & 60.00 & 0.000 & 0.000 \\ 0.000 & 0.000 & 0.000 & 1200 & 0.000 \\ 0.000 & 0.000 & 0.000 & 0.000 & 120.0 \end{bmatrix}$$

#### 3.1. Longitudinal mode

The response of the different states of the system is now more flexible, an evolution Fig.1, almost without oscillations towards the final values. Settling times are more reasonable. All the poles of the system are stable, so the internal stability of the system is thus guaranteed. The designed controller to be robust, the closed loop system must meet the stability and performance requirements for any uncertain value.

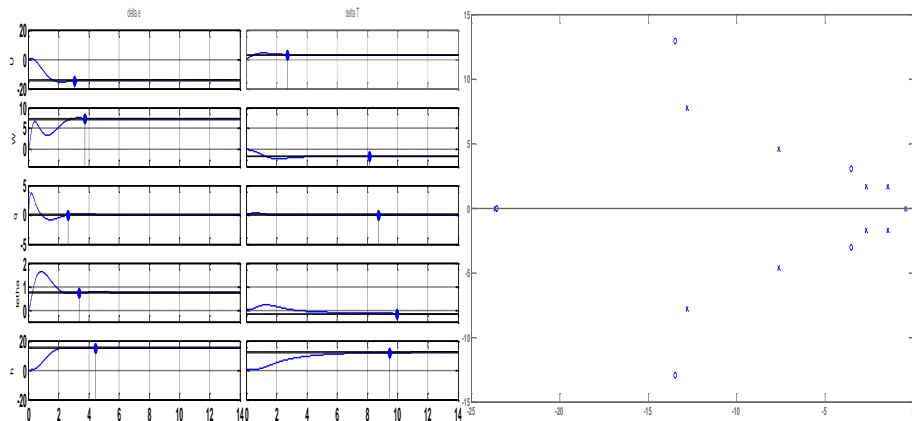


**Figure1.** Longitudinal mode response with LQG regulator

The upper and lower performance limits are calculated in the case of uncertainty on the system. The uncertainty parameter " $1 \pm 25\%$ ." must be added to the nominal system (without controller). The system is robust for all variation in the range  $\pm 25\%$  and the smallest value destabilizing the system is somewhere between 250% and 400%.

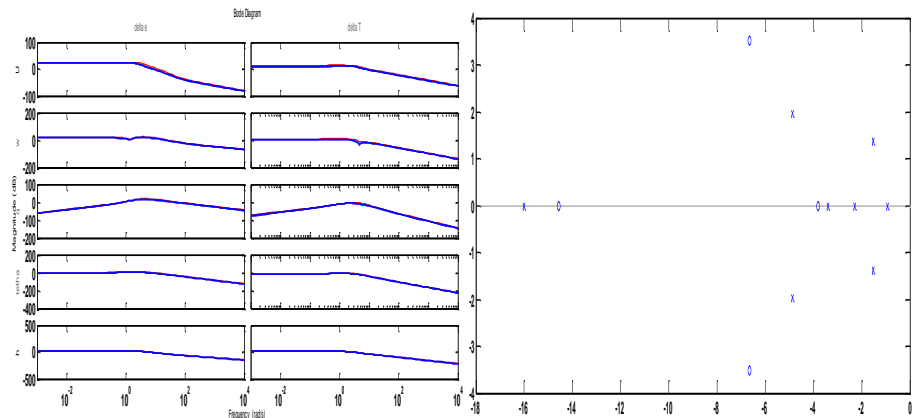


**Figure2.** Poles and Comparison between « worst case » and random samples of the uncertain system

At small frequencies, the main maximum gain is far from the minimum main gain. On the other hand, the controlled system has maximum and minimum singular values very close, especially at small frequencies. We Notice in this figure that the gains of the random samples are always lower than that of the worst case. The gain of uncertain system depends on the value of its uncertainty element. Here the word 'gain' refers to the maximum singular value of the frequency response matrix. The "worst case" analysis returns to the determination of the maximum gain among all the permissible values of the uncertain element.

### 3.2. Lateral Mode:

The responses of the different states of the system are now more flexible: an evolution almost without oscillations towards the final values. Settling times are more reasonable. The new eigenvalues of the closed loop system are stable. The system is robust for any variation in the  $\pm$

25% range and the smallest value destabilizing the system is somewhere between 356% and 400% . The parameter variation inducing destabilization at 400% is of an amplitude of -4.0000.

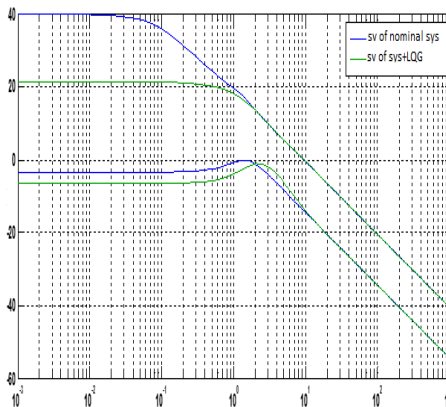


Figure5. nominal & the controlled systems

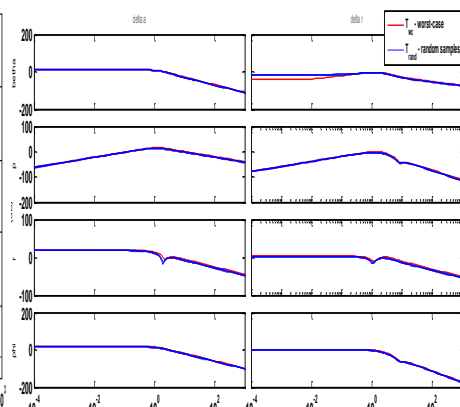


Figure6. worst and random samples of the uncertain system

At small frequencies, the maximum gain is far from the minimum main gain. On the other hand, the controlled system has maximum and minimum singular values close at small frequencies. It can be seen in this figure that the gains of the random samples are almost less than the worst case.

#### 4. CONCLUSION

In this paper our objective was providing a good performance and robustness of the aircraft system obtained in the model of the aircraft. The LQG controller provides good robustness margins and this robustness depends on a good choice of the weighting matrices.

#### REFERENCES

- [1].CAUGHEY D. A.. Introduction to Aircraft stability and control course Notes for M&AE5070.Cornell University .Ithaca, New York 14853-7501 2011.
- [2].DUPREZ J. Automatisation du pilotage au sol pour la navigation aéroportuaire. Automatique / Robotique. Université Paul Sabatier - Toulouse III, 2004.
- [3].BEARD, R. W., AND MCLAIN, T. W. Small Unmanned Aircraft: Theory and Practice. Princeton University Press. 2011
- [4].MONTARNAL P.. Non linear Aircraft dynamics and PIO, Hamburg university of applied sciences, 8 july 2009.
- [5].PITTET C.and ARZELIER D.. «DEMETER : a benchmark for robust analysisand control of the attitude of flexible micro satellites». Dans «IFACSymposium on Robust Control Design (ROCOND)», Toulouse, France,2006.
- [6].STEIN G. and ATHANS M.. «The LQG/LTR Procedure for MultivariableFeedback Control Design». IEEE Trans. Autom. Control, tome 32, no2,1987.

# Control of a MIMO aircraft system by $H^\infty$ controller

**Razika Zamoum Boushaki<sup>\*</sup>, Feriel Abahri and Farida Kessal**

University of M'hamed Bougara of Boumerdes, Institut of Electrical and Electronic Engineering, Boumerdes,  
ALGERIA

<sup>\*</sup>boushakiraz@yahoo.fr

## ABSTRACT

In this paper the robust controller for a MIMO aircraft system is designed in order to achieve robust stability margins and good performance in step response of the system.  $H^\infty$  controller guarantee a good robust stability margins and this robustness depend on the choice of the weighting functions.

**KEYWORDS**— $H^\infty$ ; Aircraft control; loop shaping

## 1. INTRODUCTION

The study of aircraft dynamics leading to the development of the aircraft equations of motion, we will present basic equations of motions in this work then in the second we will linearize them in order to apply linear control methods to enhance the performance and robustness of the studied model.

The main purpose of every feedback loop is to reduce the effect of uncertainty on vital system functions. The feedback can be used for stabilization but the design involves certain risks by reducing the regions of stability of the nonlinear system. The equations are developed to describe the motion of a flight vehicle, subject to the prescribed aerodynamic forces and moments.

## 2. MODELING OF THE AIRCRAFT

### 2.1. Lineaze of equation of motion

The normal flight situations correspond to relatively small variations in the state variables which can lead to significant accelerations. The linearization of the fundamental equations of longitudinal motion is formulated in the state space as  $\dot{X} = AX + BU$ ; where  $X = [\Delta u, \Delta w, \Delta q, \Delta \theta]^T$  Are the state vectors and  $U = [\Delta \delta_e, \Delta \delta_T]^T$  Is the control vector [2].

**Longitudinal mode :**

$$\begin{bmatrix} \Delta \dot{u} \\ \Delta \dot{w} \\ \Delta \dot{q} \\ \Delta \dot{\theta} \end{bmatrix} = \begin{bmatrix} X_u & X_w & 0 & -g \\ Z_u & Z_w & u_0 & 0 \\ M_u + M_w Z_u & M_w + M_w Z_w & M_q + M_w u_0 & 0 \\ 0 & 0 & 1 & 0 \end{bmatrix} \begin{bmatrix} \Delta u \\ \Delta w \\ \Delta q \\ \Delta \theta \end{bmatrix} + \begin{bmatrix} X_{\delta_e} X_{\delta_T} & \\ Z_{\delta_e} & Z_{\delta_T} \\ M_{\delta_e} + M_w Z_{\delta_e} & M_{\delta_T} + M_w Z_{\delta_T} \\ 0 & 0 \end{bmatrix} \begin{bmatrix} \Delta \delta_e \\ \Delta \delta_T \end{bmatrix} \quad (1)$$

**Lateral mode:**

The fundamental equations of directional lateral motion are formulated in the state space; where  $X = [\Delta \beta, \Delta p, \Delta r, \Delta \phi]^T$  are the state vectors and  $U = [\Delta \delta_a, \Delta \delta_r]^T$  are the control vectors [2].

$$\dot{X} = AX + BU$$

$$\begin{bmatrix} \Delta \dot{\beta} \\ \Delta \dot{p} \\ \Delta \dot{r} \\ \Delta \dot{\phi} \end{bmatrix} = \begin{bmatrix} \frac{Y_\beta}{u_0} & \frac{Y_p}{u_0} & -\left(1 - \frac{Y_r}{u_0}\right) \frac{g \cos \theta_0}{u_0} & 0 \\ L_\beta & L_p & 0 & 0 \\ N_\beta & N_p & N_r & 0 \\ 0 & 1 & 0 & 0 \end{bmatrix} \begin{bmatrix} \Delta \beta \\ \Delta p \\ \Delta r \\ \Delta \phi \end{bmatrix} + \begin{bmatrix} 0 & \frac{Y_{\delta_r}}{u_0} \\ L_{\delta_a} & L_{\delta_r} \\ N_{\delta_a} & N_{\delta_r} \\ 0 & 0 \end{bmatrix} \begin{bmatrix} \Delta \delta_a \\ \Delta \delta_r \end{bmatrix} \quad (6)$$



In this last step, the previously calculated stability derivatives and the developed equations are substituted in linearized lateral and longitudinal equations of motion ( Zagi) by adding the height of the drone "h" and replacing the velocity component "v" by the skid angle  $\beta$ .

**For longitudinal mode:**

$$\begin{bmatrix} \Delta \dot{u} \\ \Delta \dot{\alpha} \\ \Delta \dot{q} \\ \Delta \dot{\theta} \\ \Delta \dot{h} \end{bmatrix} = \begin{bmatrix} X_u & X_w & 0 & -g & 0 \\ Z_u/u_0 & Z_\alpha & 1 & 0 & 0 \\ M_u + M_w Z_u & M_w + M_w Z_w & M_q + M_w u_0 & 0 & 0 \\ 0 & 0 & 0 & 0 & 0 \\ 0 & -1 & 0 & u_0 & 0 \end{bmatrix} \begin{bmatrix} \Delta u \\ \Delta \alpha \\ \Delta q \\ \Delta \theta \\ \Delta h \end{bmatrix} + \begin{bmatrix} X_{\delta_e} X_{\delta_T} & \\ Z_{\delta_e} & Z_{\delta_T} \\ M_{\delta_e} + M_w Z_{\delta_e} & M_{\delta_T} + M_w Z_{\delta_T} \\ 0 & 0 \end{bmatrix} \begin{bmatrix} \Delta \delta_e \\ \Delta \delta_T \end{bmatrix} \quad (7)$$

**For lateral mode :**

$$\begin{bmatrix} \Delta \dot{v} \\ \Delta \dot{p} \\ \Delta \dot{r} \\ \Delta \dot{\phi} \end{bmatrix} = \begin{bmatrix} Y_v & Y_p - (u_0 - Y_r) & g \cos \theta_0 & \\ L_v & L_p & L_r & 0 \\ N_v & N_p & N_r & 0 \\ 0 & 1 & 0 & 0 \end{bmatrix} \begin{bmatrix} \Delta v \\ \Delta p \\ \Delta r \\ \Delta \phi \end{bmatrix} + \begin{bmatrix} 0 & Y_{\delta_r} \\ L_{\delta_a} & L_{\delta_r} \\ N_{\delta_a} & N_{\delta_r} \\ 0 & 0 \end{bmatrix} \begin{bmatrix} \Delta \delta_a \\ \Delta \delta_r \end{bmatrix} \quad (8)$$

Where:  $\Delta \delta_e, \Delta \delta_a$  and  $\Delta \delta_r$  are the deflections of: elevator, aileron, and rudder, respectively.  $\Delta \delta_T$  Is of the pushing force, and  $X_u, X_w \dots L_p N_p \dots$  are derivatives of stability.

The complete model in the state space form, [2]

$$\begin{bmatrix} \Delta \dot{u} \\ \Delta \dot{w} \\ \Delta \dot{q} \\ \Delta \dot{\theta} \\ \Delta \dot{h} \\ \Delta \dot{\beta} \\ \Delta \dot{p} \\ \Delta \dot{r} \\ \Delta \dot{\phi} \end{bmatrix} = \begin{bmatrix} -0.3356 & 1.3181 & 0.0000 & -9.8066 & 0.0000 & 0.0000 & 0.0000 & 0.0000 & 0.0000 \\ -1.7916 & -3.9003 & 9.8215 & 0.0000 & 0.0000 & 0.0000 & 0.0000 & 0.0000 & 0.0000 \\ 0.7020 & -3.5375 & -11.392 & 0.0000 & 0.0000 & 0.0000 & 0.0000 & 0.0000 & 0.0000 \\ 0.00000 & 0.0000 & 1.0000 & 0.0000 & 0.0000 & 0.0000 & 0.0000 & 0.0000 & 0.0000 \\ 0.0000 & -1.0000 & 9.8215 & 0.0000 & 0.0000 & 0.0000 & 0.0000 & 0.0000 & 0.0000 \\ 0.0000 & 0.0000 & 0.0000 & 0.0000 & 0.0000 & -0.1069 & 0.1962 & -1.0000 & 0.9998 \\ 0.0000 & 0.0000 & 0.0000 & 0.0000 & 0.0000 & -1.2213 & -1.9155 & 1.0096 & 0.0000 \\ 0.0000 & 0.0000 & 0.0000 & 0.0000 & 0.0000 & 1.7255 & 0.0919 & -1.7198 & 0.0000 \\ 0.0000 & 0.0000 & 0.0000 & 0.0000 & 0.0000 & 0.0000 & 1.0000 & 0.0000 & 0.0000 \end{bmatrix} \begin{bmatrix} \Delta u \\ \Delta w \\ \Delta q \\ \Delta \theta \\ \Delta h \\ \Delta \beta \\ \Delta p \\ \Delta r \\ \Delta \phi \end{bmatrix} + \begin{bmatrix} -0.7436 & 6.8728 & 0.0000 & 0.0000 \\ 3.7855 & 0.0000 & 0.0000 & 0.0000 \\ 47.917 & 0.0000 & 0.0000 & 0.0000 \\ 0.0000 & 0.0000 & 0.0000 & 0.0000 \\ 0.0000 & 0.0000 & 0.0000 & 0.0000 \\ 0.0000 & 0.0000 & 0.0000 & -1.1855 \\ 0.0000 & 0.0000 & 8.3480 & 0.0000 \\ 0.0000 & 0.0000 & 4.2400 & -2.1272 \\ 0.0000 & 0.0000 & 0.0000 & 0.0000 \end{bmatrix} \begin{bmatrix} \Delta \delta_e \\ \Delta \delta_T \\ \Delta \delta_a \\ \Delta \delta_r \end{bmatrix} \quad (11)$$

### 3. CONTROL OF THE AIRCRAFT BY $H_\infty$

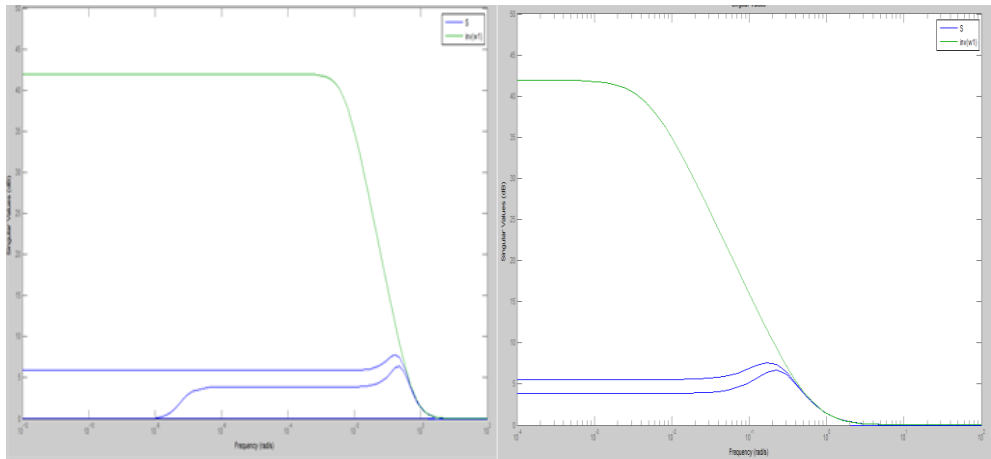
The two matrices  $S(s)$  and  $T(s)$  are respectively "sensitivity function" and "complementary sensitivity function", they are defined as follows:

$$S(s) \stackrel{\text{def}}{=} (I + L(s))^{-1} \quad \text{and} \quad T(s) \stackrel{\text{def}}{=} L(s)(I + L(s))^{-1} = I - S(s)$$

Where is the matrix of transfer functions of the loop  $L(s)=G(s)*K(s)$  [ $G(s)$  is the representation of the system and  $K(s)$  is that of the controller].The Bode diagram of the singular values of these functions plays an important role in modeling the robust commands of multivariable systems. The singular values of the matrix of the closed loop transfer functions  $L(s)$  are important because  $L(s)$  determine the matrices  $S(s)$  and  $T(s)$ .

The Bode diagram of singular values of  $T(s)$  is used to measure the stability margins of modeling of a multivariate system controller in the presence of multiplicative disturbances. A consequence of the robustness theorem makes it possible to specify the stability of the control system through the following inequality:

$$\bar{\sigma}(T\{j\omega\}) \leq |W_3^{-1}(j\omega)|$$



a)Longitudinal mode

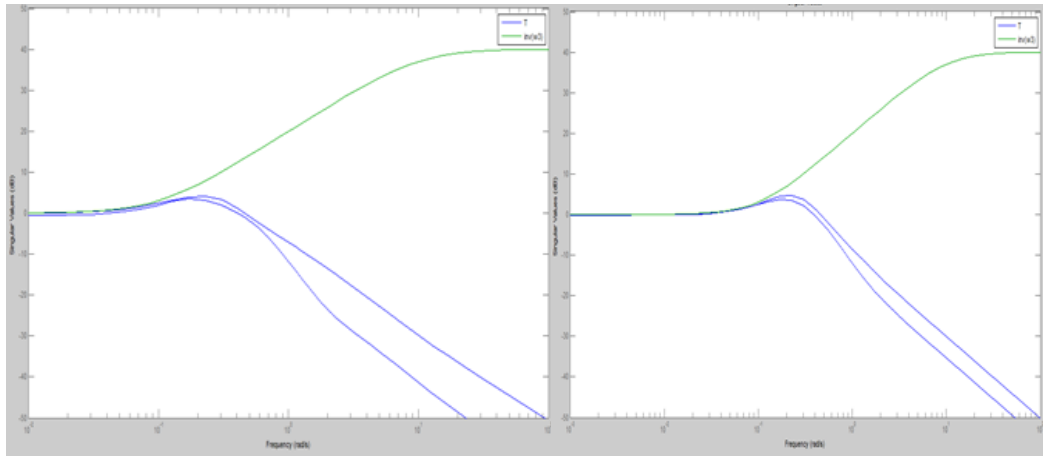
b) Lateral mode

**Figure 24:**  $S(s)$  and  $W_1^{-1}$  comparison (singular values bode plot)

This is clearly verified by the choices of the weighting functions, which is shown in Figure 24. The chosen weighting functions are :

$$W_1(s) = \frac{s+0.005}{s+0.625} \quad \text{and} \quad W_3(s) = \frac{0.01(s+10)}{(s+0.1)}$$

Which are a low pass and high pass respectively as shown in Figure 4.18. By this choice we obtain  $\gamma = 1.010$ .



a)Longitudinal mode

b) Lateral mode

**Figure 25:**  $T(s)$  and  $W_3^{-1}$  comparison (singular values bode plot)

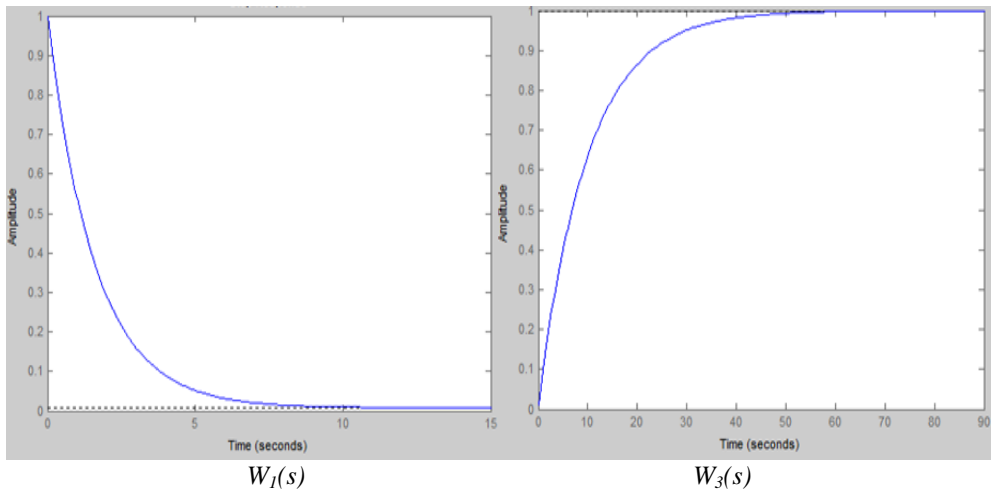


**Figure 26 :** Weighting functions response

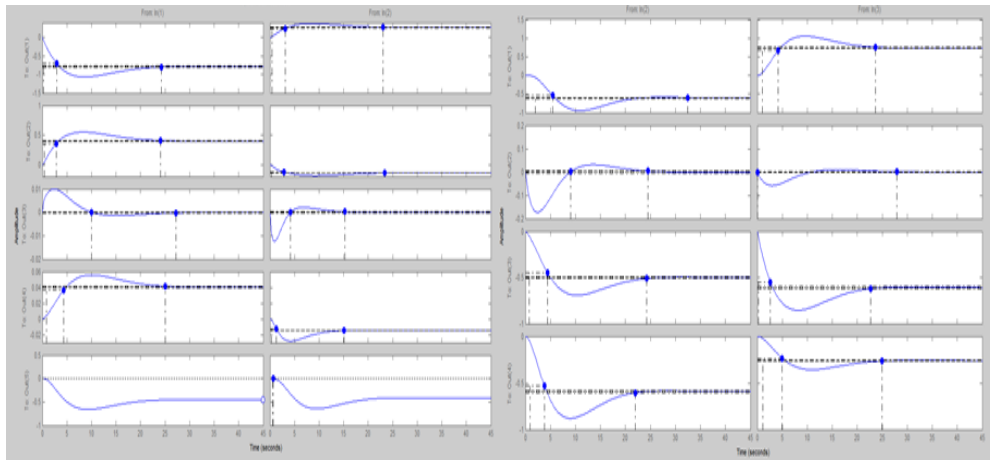
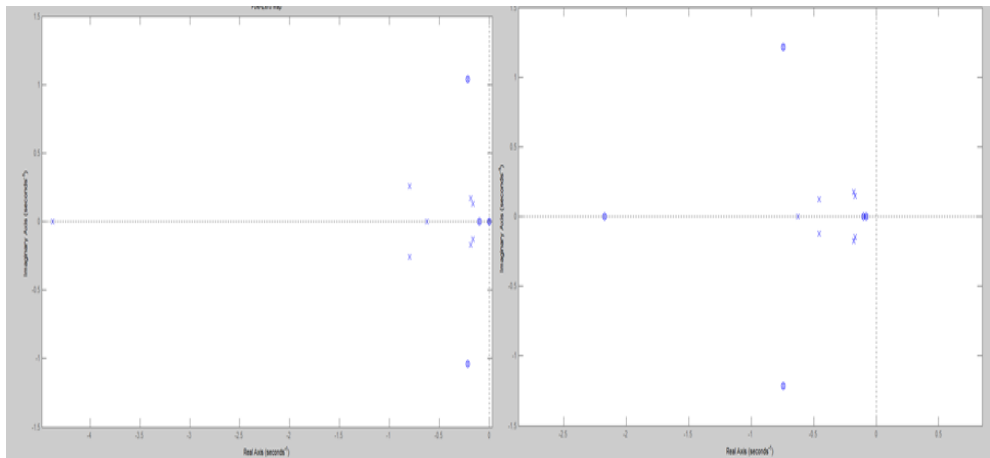


**Figure. 27:** System response with  $H_\infty$  controller

It can be seen in this figure that the response of the various states of the system is almost without oscillations towards the steady state

The closed loop eigenvalues are all negative real parts. The poles of the system are all negative real parts which confirms its internal stability. Longitudinal mode: The robust stability of the system is guaranteed for any variation in the range  $\pm 25\%$  and the system can tolerate up to 388% of the tolerated uncertainty. The upper bound is infinite, which means that there is no uncertainty in this range that can cause the system to destabilize. The sensitivity of the system with respect to the uncertain element already introduced is 15%.increasing this parameter by 25% causes the stability margin to decrease by 4%..

Lateral mode: The system is robust for any variation in the range  $\pm 25\%$  and the smallest value destabilizing the system is somewhere between 240% and 400% greater than  $\pm 25\%$  which means between  $\pm 60\%$  and  $\pm 100\%$ .

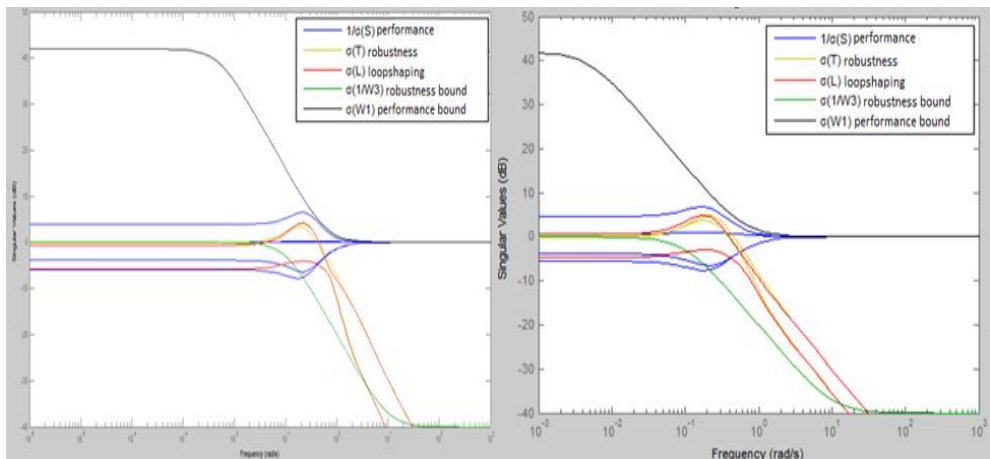


a) Longitudinal mode

b) Lateral mode

**Figure.28 :** The poles of the controlled system ( $H_\infty$ )

An estimate of the parameter variation inducing destabilization at 400% is of an amplitude - 4.0000. The sensitivity of the system with respect to the uncertain element already introduced is 14%. Increasing this parameter by 25% causes the stability margin to decrease by 4%. The system has a comfortable safety margin before it becomes unstable.



a) Longitudinal mode

b) Lateral mode

**Figure. 29:** Singular values of  $S, T, L, W1$  and  $1/W3$

#### 4. CONCLUSION

Our objective was providing a good performance and robustness of the aircraft system obtained in the model of the aircraft; the  $H_\infty$  controller is used allowing robust stabilization of the system. Studying and analyzing the controlled system leads us to the conclusion that the  $H_\infty$  controller provides robustness margins and this robustness depends on a good choice of the weighting functions.

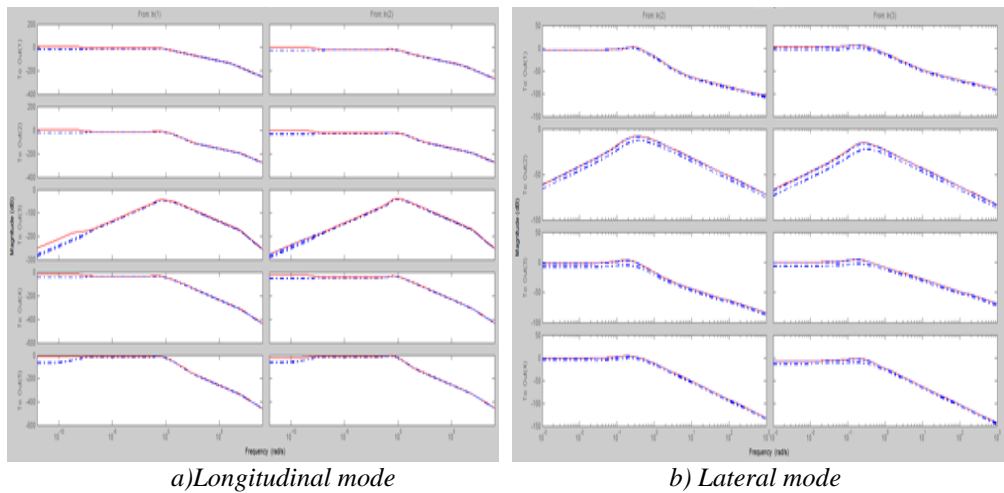


**Figure 30:** Comparison between « worst case » and four random samples of the uncertain system

## REFERENCES

- [1]. DAVID A.CAUGHEY. Introduction to Aircraft stability and control course Notes for M&AE5070.Cornell University .Ithaca, New York 14853-7501 2011.
- [2]. JEAN DUPREZ. Automatisation du pilotage au sol pour la navigation aéroportuaire. Automatique / Robotique. Université Paul Sabatier - Toulouse III, 2004.
- [3]. BEARD, R. W., AND MCLAIN, T. W. Small Unmanned Aircraft: Theory and Practice. Princeton University Press. 2011
- [4]. MONTARNAL PHILIPPE. Non linear Aircraft dynamics and PIO, Hamburg university of applied sciences, 8 july 2009.
- [5]. Edouard LAROCHE, cours « Commande Optimale », année académique 2009/2010
- [6]. J. C. DOYLE and G. STEIN, “Multivariable feedback design : Concepts for classical/modern synthesis”, IEEE Trans. Autom. Control, vol. 26,no. 1, 1981.
- [7]. S. GARG and P. OUZTS. «Integrated flight/propulsion control design for a STOLV aircraft using H-infinity control design techniques». Dans«American Control Conference (ACC)», 1982.
- [8]. C. PITTET and D. ARZELIER. «DEMETER : a benchmark for robust analysis and control of the attitude of flexible micro satellites». Dans «IFAC Symposium on Robust Control Design (ROCOND)», Toulouse, France, 2006.
- [9]. [D. ARZELIER AND D. PEAUCELLE. «Multiobjective H2/H $\infty$  impulse-to-peaks synthesis: application to the control of an aerospace launcher». Dans «IFAC Symp. Automatic Control in Aerospace (ACA)», Saint-Petersbourg, Russie, 2004.
- [10]. J. DOYLE. «Synthesis of robust controllers and filters». Dans «IEEE Conf. Dec. Control», San-Antonio, Texas, USA, dec 1983.
- [11]. K. GLOVER and J. DOYLE. «State-space formulae for all stabilizing controllers that satisfy an Hnorm bound and relations to risk sensitivity». Systems and Control letters, tome 11, pages 167–172, 1988.

- [12]. G. STEIN and M. ATHANS. «The LQG/LTR Procedure for Multivariable Feedback Control Design». IEEE Trans. Autom. Control, tome 32, no2, 1987.
- A. PACKARD, J. DOYLE, AND G. BALAS. «Linear, multivariable robust control with a  $\mu$  perspective». ASME J. Dynamic Systems, Measurement and Control, tome 115, no2, pages 310–319, 1993.
- [13]. D. C. MCFARLANE AND K. GLOVER. «A loop shaping design procedure using  $H_\infty$  synthesis». IEEE Trans. Autom. Control, tome 37, no6, pages 759–769, 1992.

## Experimental study on the influence of structure anisotropy on mechanical property of coal

Xun Sun<sup>1\*</sup>, Shicheng Zhang<sup>1</sup>, Xinfang Ma<sup>1</sup> and Kai Liao<sup>1</sup>

<sup>1</sup> China University of Petroleum (Beijing), College of Petroleum Engineering, Beijing-CHINA

\* wsxsx8888@163.com

### ABSTRACT

Hydraulic fracturing can create complex fractures in coal reservoir and is widely used. However, the mechanical properties of coal are quite different from those of others due to the large amount of cleats, and this makes its mechanism of fracture initiation and propagation different from conventional reservoir. In this study, triaxial compression test and Brazilian splitting test were conducted on three drilling directions of coal. The morphology of internal structure of coal was described and analyzed by scanning electron microscope. The stress-displacement curves, elastic modulus and tensile strength were obtained. The results showed that there was obvious dispersion for compressive and tensile strength in the orientation of perpendicular and parallel to bedding. The compressive strength of coal drilled vertically to bedding was 1.2 times those of vertical to face cleats, and 1.3 times those of vertical to butt cleats, similar result was also concluded in tensile strength, which indicated the non-uniform distribution of coal composition and directionality of cleats had a great influence on the anisotropy of coal mechanical properties. The stress-displacement curves of coal drilled vertical to bedding were more stable than that of parallel to bedding, and the sample photographs demonstrated the former deformation feature was shear failure and the latter was splitting failure. This study showed coal had the characters of low strength, easily broken and significant anisotropy, the result would provide important parameters for fracturing design and a theoretical basis for the study of hydraulic fracturing mechanism under complex cleats and fractures in coalbed reservoir.

**KEYWORDS** - Coal, Cleats, Mechanical behavior, Anisotropy

### 1. INTRODUCTION

China has abundant coalbed methane resources. According to the recent research, the total amount of CBM resource which buried within 1500 m is 10.87 Tcm, the total amount of CBM resource which buried within 2000 m is 36.81 Tcm, this means CBM resource in China has high exploitation potential compared with the geological resource of natural gas (35 Tcm) (Liu, Zhu, Che, Yang, & Fan, 2009) [1]. But the total commercial production of CBM still fail to meet the target set in 12th Five-Year Plan (China, 2015) [2] due to the low single well production. Hydraulic fracturing can effectively increase production and is widely used in coal seams. However, cleats, the extensive discontinuities in coal, make a strong directional influence on mechanical properties (Li, Zhang, Liu, & Engineering, 2016) [3-5]. Meanwhile, coal has extremely low permeability and strong stress sensitivity (Peng & Li, 2018) [6], these characteristics will complicate the hydraulic fracture propagation mechanism [7][Zhou, 2013 #15]. In this paper, we aimed to study the influence of structure anisotropy on mechanical property of coal, the scanning electron microscopy, triaxial compression test and Brazilian splitting test were conducted. The elastic modulus, Poisson ratio, compressive strength and tensile strength were obtained. The results will provide important parameters for fracturing design and a theoretical basis for the study of hydraulic fracturing mechanism under complex cleats and fractures in coalbed reservoir.

### 2. METHODS AND MATERIALS

The coal samples were taken from Qinshui Basin, Southeast of Shanxi Province. In order to take the directionality effect of bedding and cleats into consideration, the coals were drilled in three



directions: perpendicular to bedding, perpendicular to face cleat and perpendicular to butt cleat (Fig. 1).



**Figure 1.** Three groups of coals in different drilling directions.

According to the method for determining physical and mechanical properties of coal and rock [8], the process of cutting and polishing were applied on coals after drilling, and coals were processed as standard samples finally. The sample size for triaxial compression test is  $25\text{mm} \times 50\text{mm}$  and the sample size for Brazilian splitting test is  $25\text{mm} \times 5\text{mm}$ .

### 3. RESULTS AND DISCUSSION

#### 3.1. Scanning electron microscopy of coals experiment

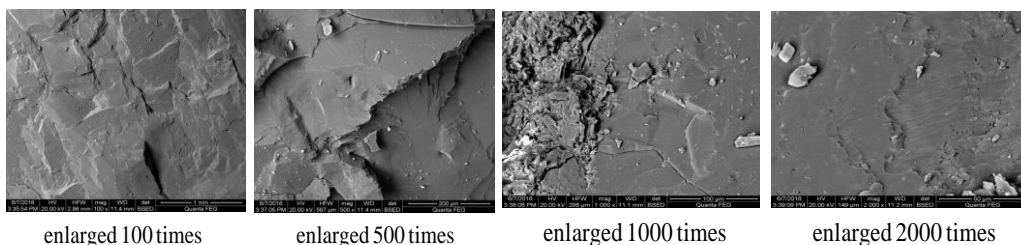


**Figure 2.** Internal structure of coal

The morphology of internal structure of coal was described and analyzed by scanning electron microscope. Because of the uneven bulk compaction, the internal stress of coal is larger than the strength of coal, then the micropores and fractures gradually develop in coal, which indicates coal has high heterogeneity.

#### 3.2. Triaxial compression test

From the test results we can see the deformation parameters of each coal sample are discreteness, the compressive strength of coal drilled vertically to bedding was 1.2 times those of vertical to face cleats, and 1.3 times those of vertical to butt cleats. The difference of the deformation parameters between the 3 sets of coal samples reflects the high anisotropy of mechanical characteristics under three axial compression condition, that is to say, from a statistical mechanics point of view, there are obvious differences in elastic modulus, Poisson's ratio and compressive strength between these coal samples.

The mechanical properties of coal under three axial compression condition have a certain degree of discreteness, the variation coefficient of height, diameter, quality and density of the 3 groups is very small, but in the test results, the variation coefficient of elastic modulus, Poisson's ratio and compressive strength is large. The mechanical properties of three groups show obvious dispersion, but the first set, which was drilled along the vertical bedding direction, is more prominent.

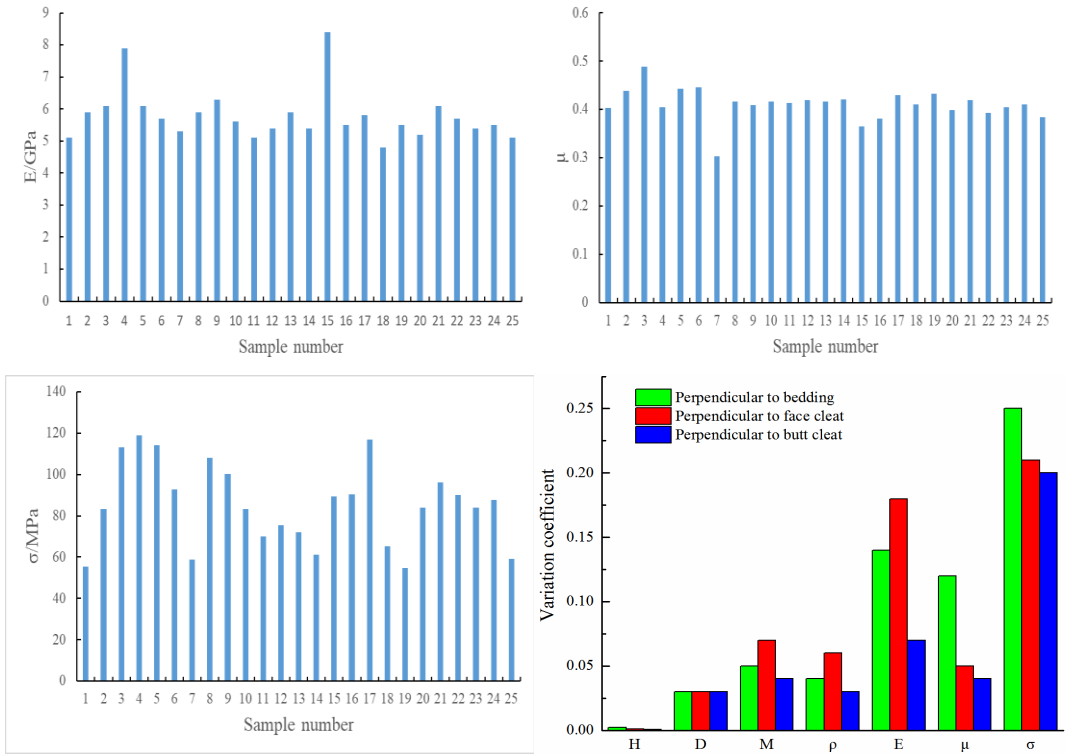


**Figure 3.** Results of triaxial compression test for all samples and basic parameters of coal samples and histograms of variation coefficient

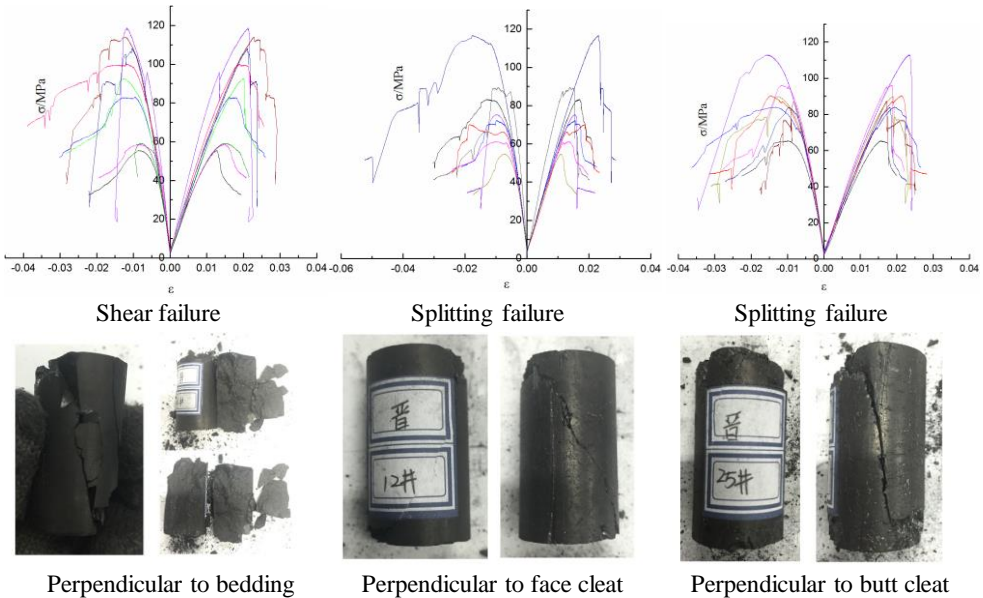


**Figure 4.** Mechanism of deformation characteristics and failure mode

Triaxial stress-strain curves of coal samples in different directions to the bedding plane is shown in Fig. 4. The compaction stage does not exist in the compression test because the confining pressure is applied, but they all experienced 3 stages: linear deformation stage, nonlinear deformation stage of crack propagation and crack accelerated to propagate until the rock burst. The deformation characteristics of the three groups of coal samples are quite different before and after the peak value, and the mechanical behavior is obviously discrete on the whole.

In the failure mode, the failure mode of coal samples perpendicular to bedding plane under triaxial compression is mainly shear failure, and easy to burst into fragments; However, the failure mode of other groups, perpendicular to face cleat and perpendicular to butt cleat, are mainly splitting failure, and the coal sample is cracked in the middle and becomes flaky.

### 3.3. Brazilian splitting test

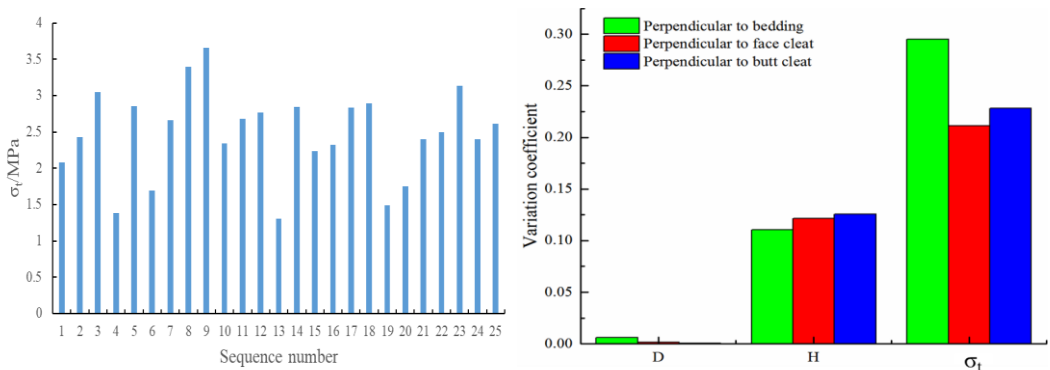


**Figure 5.** Results of Brazilian splitting test for all samples and basic parameters of coal samples and histograms of variation coefficient

From a statistical point of view, the tensile strength of coal in different loading directions all have certain discreteness, but the degree of dispersion is different, The variation coefficient of perpendicular to bedding plane is 0.3, the variation coefficient of perpendicular to face cleat is 0.21, the variation coefficient of perpendicular to butt cleat is 0.23. Obviously, the former group is more discrete. At the same time, the tensile strength measured in three directions is different, which fully reflects the anisotropy of mechanical properties of coal.

Tensile strength and lateral strain curves of coal sample in different directions are shown above.

(1) The deformation characteristics of stress and strain curves in vertical direction are similar, showing a relatively stable mechanical state; stress drops rapidly after peak value, the graded drop platform is very short, the duration of residual stress is short and the drop speed is generally fast.

(2). The deformation characteristics of stress and strain curves in the other 2 directions are different before peak value, some deformation characteristics are the same as the first group, showing a stable state, but some of them are obviously different from the former; There are also many kinds of stress drop after the peak, some of them fall rapidly, some of them fall in stages, and the mechanical behavior is dispersed remarkably in general.

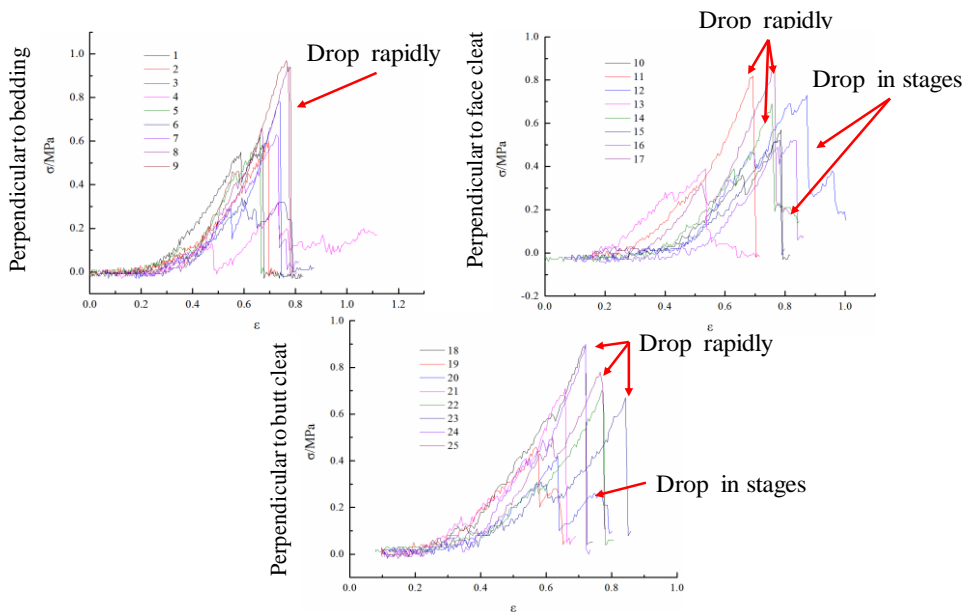


**Figure 6.** Tensile strength and lateral strain curves of coal sample in different directions

#### 4. CONCLUSION

In this research, Scanning electron microscopy, triaxial compression test and Brazilian splitting test were conducted on three drilling directions of coal, the main conclusions are as follows:

- (1) The triaxial compression strength, tensile strength and deformation parameters in three directions are obviously different, which indicates the high anisotropy of coal.
- (2) The triaxial compression characteristics and tensile strength in three directions are both discrete ; but the discreteness of group which direction is perpendicular to bedding is much more obvious.
- (3) Directionality of coal cleat system is the internal causes to decide the anisotropy of coal mechanical properties.

#### REFERENCES

- [1].Liu, C. L., Zhu, J., Che, C. B., Yang, H. L., and Fan, M. Z, Methodologies and results of the latest assessment of coalbed methane resources in China, Natural Gas Industry, 29(11), 130-132.
- [2].China, G. O, Ministry of Land and Resources, 2015.
- [3].Li, Yu Wei, J. Zhang, and Y. Liu. Effects of Loading Direction on Failure Load Test Results for Brazilian Tests on Coal Rock. Rock Mechanics & Rock Engineering 49.6(2016):1-8. DOI:10.1007/s00603-015-0841-8
- [4].M. Avcar. International Conference on Computational and Experimental Science and Engineering (ICCESN 2015), 14-19 October, 2015 Antalya-Turkey
- [5].Hao, Xianjie, et al. Influence of bedding and cleats on the mechanical properties of a hard coal. Arabian Journal of Geosciences 11.9(2018):200. DOI: 10.1007/s12517-018-3541-3

- [6].Peng, Zeyang, and X. Li. Improvements of the permeability experiment in coalbed methane. *Arabian Journal of Geosciences* 11.11(2018):259. DOI: 10.1007/s12517-018-3608-1
- [7].Zhou, Wu, Li, Ren and Xin. International Conference on Computational and Experimental Science and Engineering (ICCESSEN 2015), 14-19 October, 2015 Antalya-Turkey
- [8].General Administration of Quality Supervision, Inspection and Quarantine of the Peoples Republic of China; Standardization Administration of the Peoples Republic of China. Methods for determining the physical and mechanical properties of coal and rock [S]. Beijing: China National Coal Association, 2010. (in Chinese)

# Numerical Study on Coal Particle Transport Under Air-Water Multiphase Flow in V-Shaped Elbow

Ziyao Zhong<sup>1\*</sup>, Xiaodong Wu<sup>1</sup>, Guoqing Han<sup>1</sup>, Lei Zheng<sup>1</sup>, Shuzhe Shi<sup>1</sup>, Zhan Meng<sup>1</sup>

<sup>1</sup> College of Petroleum Engineering, China University of Petroleum, Beijing, 18 Fuxue Road, Changping, Beijing, CHINA

\* zzy\_shiyou@163.com

## ABSTRACT

The coal fine output from coalbed methane(CBM) formation during the production of CBM wells seems to be a common occurrence. The aggregation of coal fine particles exists at the lower section of wellbore. The researches on coal particle transport in terrain-induced slug flow were little. In present study, the Computational Fluid Dynamics (CFD) model was adopted to simulated the process of slug generation at the bottom of the lower elbow with an inner diameter of 50 mm, and the process of slug dissipation along the upward flow. Moreover, particle transport was examined under slug/pseudo-slug flow regimes by the use of particle tracking method. It was noticed that the particles would move forward with the liquid slug body, but move backward due to the backflow of the liquid film. The average concentration of coal particles in the elbow section of the pipeline increased with time under of low velocity conditions. A critical velocity condition is defined as the lower limits of gas and liquid velocities to avoid coal particles left in the elbow. The CFD results of the critical velocities was assessed using experimental data in a visual V-shaped pipe. The comparison result illustrates that the CFD model can be used to investigate the transport mechanism of coal particles in actual CBM wellbores with the multiphase flow conditions.

**KEYWORDS** -Multiphase flow, Numerical investigation, Coal particle, Terrain slug, Coalbed methane.

## 1. INTRODUCTION

Horizontal wells have been used to develop CBM reservoirs in the last twenty years. The actual tracks of the wellbores are not absolute horizontal, and the lower elbow section of undulating down-hole pipe provides favourable condition for particle aggregation. When the concentration of coal fines reaches a certain range, it will affect the normal work of the down-hole equipment, and lead to the sedimentation and aggregation of coal fines in the wellbore, which could reduce the cross area of flow and increase pressure drop and fluctuation.

The theoretical and experimental studies, some researchers adopted numerical method to study the multiphase flow of gas-liquid and gas-liquid-solid. The Computational fluid dynamics (CFD) method can simulate the complicated flow of gas and liquid in the pipeline, and obtain the real-time distribution of gas and liquid phase for determining the local flow pattern. Volume of fluid (VOF) model is a widely utilized CFD model for simulation of gas-liquid multiphase flow. The VOF model has been proved to be very accurate in the simulation of the slug flow or churn flow by the previous studies (Ratkovich, Stefano [4, 5]).

The Euler method was widely used to deal with the interaction between particles and fluid, and the movement of particles in the flow is simulated. The particles were treated as a discrete phase, and their movement was governed by Newton's second law. Numerical simulation has been widely used to study mechanism of erosion under single phase and multiphase flow conditions (Peng, Parsi [6-7]). While these studies rarely paid attention to the retention of particles at a lower elbow at the low flow velocity. In the present study, the treatment of the particle dynamics in multiphase flow was presented in Section 2. The main objective of the present study was to evaluate this coupled model for simulation of churn flow or slug flow at the gas and liquid flow rates in the

CBM wellbore and present the velocity requirement to discharge the coal particles from the V-shaped lower elbow.

## 2. CFD MODELING

### 2.1. Computational Domain

Air-water-coal particle multiphase flow was investigated in the geometry shown in Fig. 1. A pipe with internal diameter  $D=50\text{mm}$  was used in the simulations. The whole pipe consisted of three sections: downward straight section, V-shaped section and upward straight section. The incline angles of two straight sections were  $15^\circ$ . Both uphill section and downhill section length is  $2\text{m}$  ( $40D$ ), and the length of bending section is  $0.75\text{m}$  ( $15D$ ). The elbow radius of curvature was  $0.5\text{m}$ . The structured grids were used in the simulations. Fig. 1(b) shows the mesh grids of inlet cross-sectional slice which has 1425 cells.

At the specific cross-section, the time-series of cross-sectional average liquid holdup and average pressure was recorded both in the experiments and numerical simulations. And the results of experiments and CFD were compared with each other in the following section of this paper.

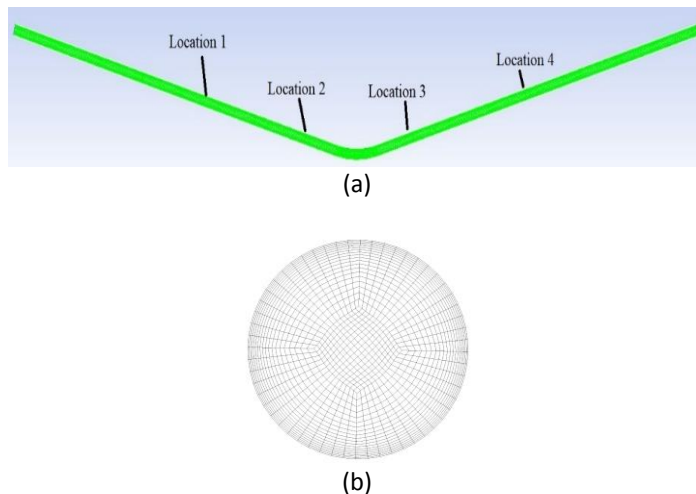


**Figure 1.** Computational Domain. (a) the V-shaped Elbow Used in Present Simulations; (b) the CFD Mesh on Pipe Cross-section.

### 2.2. Simulation Model for Air-Water Flow

The simulations were performed using three-dimensional transient model, and the effect of gravity was considered. The properties of the fluid (air and water) were known and set up in advance to the computing system. The RNG- $k\epsilon$  turbulence model was used to obtain a solution in the turbulent flows. The pressure-velocity coupling method for the simulations was semi-implicit method for pressure-linked equations (SIMPLE) method. The second order upwind method was adopted for momentum equation, while first order upwind method for the two turbulence equations (turbulent kinetic energy and turbulent dissipation rate).

The MultiFluid VOF model was used to separately solve for mass and momentum equations of each phase. This is a hybrid model combining the Eulerian-Eulerian approach with the VOF interface tracking model. In all simulation cases, the time-step, and maximum number of iterations per time-step were set to  $0.001\text{ s}$  and  $30$ , respectively. The maximum residual was set to  $1\text{e-}3$  for all parameters.

### 2.3. Particle Tracking in Air-Water Multiphase Flow



In the pipeline transportation process, the coal particle is forced by other particles, slurry and pipe wall, which can be described by Newton's second law of motion using the discrete element method.

$$\frac{du_p}{dt} = F_D + F_L + F_P + F_{VM} + F_B \quad (1)$$

where  $u_p$  is particle velocity;  $F_D$ ,  $F_L$ ,  $F_P$ ,  $F_{VM}$  and  $F_B$  are drag force, Saffman lift force, pressure gradient force, virtual mass force and buoyancy force respectively. In addition, particles are all simplified to spherical particles of a certain diameter and injected from the inlet of the pipe with a certain volumetric concentration.

#### 2.4. Boundary Conditions and Initiation Conditions

The fluid flows from the left end of the pipeline to the right, as shown in Fig. 1(a). The inlet zone was divided into two top and bottom sections, which were used to inject air(top) and water(down) respectively. The velocity boundary condition was imposed at each half-section of the inlet zone, and the turbulence intensity was set to 5% at the inlet. To ensure that the flow rates in the simulations were identical to specified values, the phase velocities at the inlet were obtained from the following equations:

$$u_{gi} = 2 \frac{Q_g}{A} \quad (2)$$

$$u_{Li} = 2 \frac{Q_L}{A} \quad (3)$$

where  $u_{gi}$  and  $u_{Li}$  are the gas and liquid velocities imposed at the inlet, respectively.  $Q_g$  and  $Q_L$  are the gas and liquid flow rate, respectively.  $A$  is the pipe cross-sectional area.

Coal particles were injected through liquid phase. The injection direction of the particles was perpendicular to the inlet cross-sectional area with the same velocity as liquid phase. And the particle diameter and volume concentrations were 0.66mm and 2%.

#### 2.5. Simulation Program

The simulations were executed on the computing workstation platform with the Intel Xeon(R) CPU (E5 2690v3, 2.90GHz, 12 cores), Memory (16 GB, 2133GHz) and OS (Windows 7). For each case, about 3 days consumed for the simulation of the flow in 25s. The flow velocity used in each case is given in Table 1.

**Table 1.** The Flow Parameters for the Numerical Settings of Each Case.

Case NO.	Multiphase flow condition	
	Gas superficial velocity m/s	Liquid superficial velocity m/s
1	0.2	0.1
2	0.8	0.1
3	1.5	0.1
4	0.8	0.05
5	0.8	0.15
6	0.2	0.15

### 3. RESULTS AND DISCUSSIONS

### 3.1. CFD Simulation Results

Simultaneous consideration of time series of liquid hold-up and particle volume concentration at a specific cross-section can reveal the particles' behaviour relative to flow behaviour. Fig. 2 are the simulation result of gas and liquid phase distribution along the axial plane of the pipe at different instants of time. The charts show the formation process of liquid slug in the pipeline with the inclination angle of  $\theta_2 = \theta_2 = 15^\circ$ .

The inlet gas velocities are 0.2, 0.8 and 1.5 m/s respectively for the cases in the graphs. The phase fraction distribution at different moments ( $t$ ) is described in the contours. The blue region represents the gas phase, while the red one represents the liquid phase.

The slug structure would be different under different flow conditions, as shown in Fig. 2(a), (b) and (c). At low gas velocity, the bubbles had a relatively regular shape with a short length. At higher gas velocity, the length difference between the bubbles increases. When  $u_{sL}=0.1\text{m/s}$ ,  $u_{sg}=0.8\text{m/s}$ , the shape of the bubbles changes from the bullet shape to that has characteristics of the Taylor bubble, and the thickness of the liquid film under the bubble decreases. At the interface between the tail of a large bubble and the front of liquid slug, a part of the gas is involved in the liquid phase due to the flow eddy. When the mixture flow velocity increases, the volume of the small bubbles in the liquid slug will increase. As shown in Fig. 2, when the flow time is 20s, the flow field basically has entered a stable stage. That is to say, the flow parameters fluctuate in a certain range, while the flow characteristics, such as flow pattern and pressure, have time similarity, and no fundamental change. Therefore, the flow time-period for the simulations which is set to 25s, can satisfy the analysis requirements for multiphase flow.

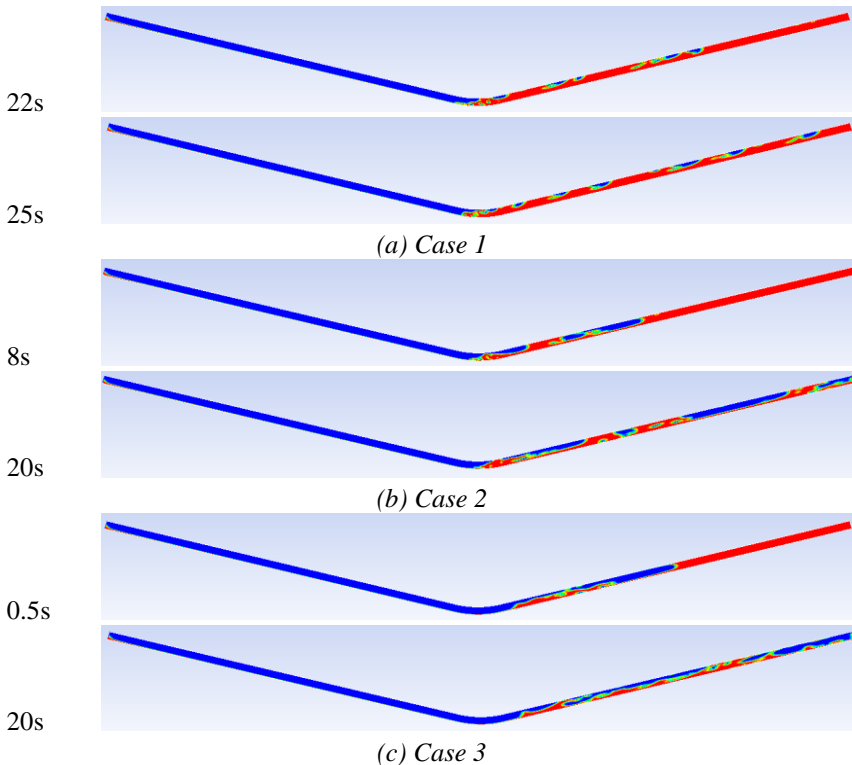


**Figure 2.** Liquid and Gas Phase Distribution Change with Time Under Different Flow Conditions (Blue Region was Gas Phase and Red Region was Liquid Phase).

Fig. 3 illustrates the cross-sectional averaged liquid holdup time series of the resulting from CFD for Case 1 to Case 3. In each subplot, there are four lines which are the averaged liquid holdup data of the cross sections at the Location 1 ~ 4 as shown in Fig. 1, respectively. The time series of Location 3 and Location 4 display high amplitude waves that can be linked to the passages of periodic liquid and gas structure (e.g. slug and bubble) through the cross-sections. The other two time-series are relatively steady. Under the action of gravity, the stratified flow is developed in the downward straight pipe, as shown in Fig. 2. As the gas velocity increases, the liquid holdup at Location 3 and 4 decreases, and the fluctuation is more intense. This result is in agreement with the experimental observation and the measured data.

During the upward movement of the slug structure, the slugs dissipated, and the small bubbles formed at the bottom of the elbow gradually merged into large bubbles. In Fig. 3(a) and (b), the averaged liquid holdup at Location 4 is lower and the vibration frequency is less than that at Location 3. In Fig. 3 (c), the averaged time-series of liquid holdup at Location 3 do not fluctuate because the scouring effect of gas on the liquid phase at high air flow velocity caused no reflux and accumulation of water in the elbow section before Location 3.

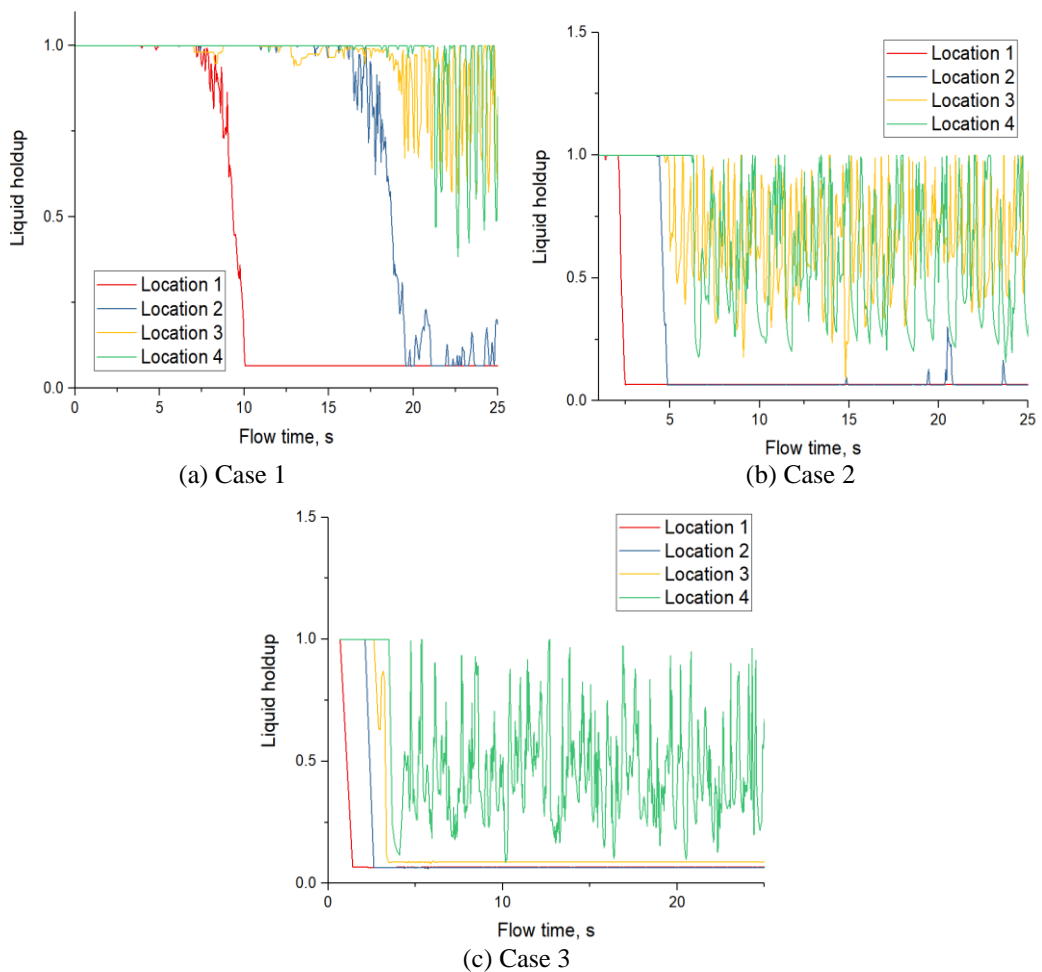


**Figure 3.** Cross-Sectional Averaged Liquid Holdup Time Series

The experiments were carried out in an air-water flow loop system, mentioned above. In this paper, the experimental data are employed to validate our numerical method. The conductivity method was used to measure the slug liquid holdup. The results of the comparison between the experimental and numerical data of case 2 are shown in Fig. 4.

Note that these periodic waves a range of amplitudes both exist in the curve of CFD simulation and experiments. It can be seen that the two real time curves of the liquid holdup fluctuate in the same range, and the fluctuation frequencies of the two curves are not very different. Therefore, the numerical results are in good agreement with the experimental data.

The value of the liquid holdup affects the flow pressure drop in the pipe. Fig. 5 shows the mean value of the pressure difference between the Location 3 and 4 within a certain time period (2s) after the flow in the simulation has stabilized. It can be seen from the chart that the pressure drop of CFD method are greater than the experimental results. But the relative errors at all the gas velocity point are about 5%, and the maximum is 8.32%, which is still in the acceptable range. In this way, the results can be used to verify the reasonableness of the numerical model.

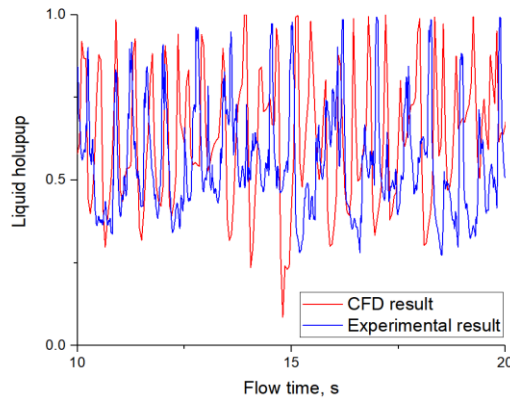


**Figure 4.** Comparison of liquid holdup data of CFD simulations and experiments

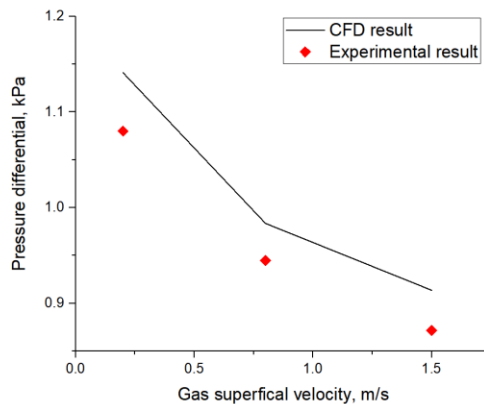


**Figure 5.** The Mean Pressure Drops Between Location 3 and Location 4 Resulting from CFD Simulations and Experiments

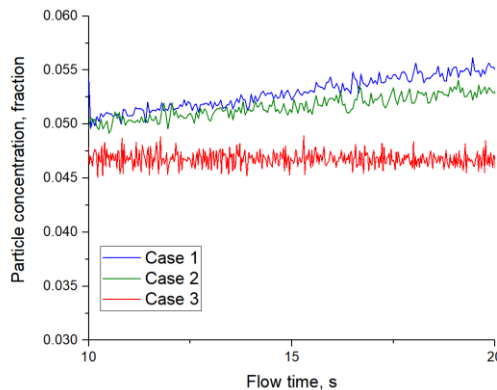
### 3.2. Critical Mixture Velocity for Discharge Coal Particles

In previous studies, the calculation models of critical flow velocity for particle movement were built on the basis of the correlation between gas-liquid velocity and the particle movement. In the undulating pipeline, due to the existence of terrain slugs, the characteristic parameters of the slug,

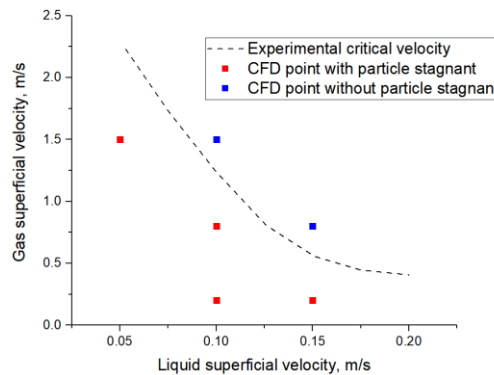
such as length and translational velocity of each section, have a decisive influence on the movement of particles. In this study, we experimentally obtained the gas and liquid velocity conditions for coal fine particles to be fully removed from the test V-shaped pipe.

Fig. 6 shows the time series of the particle concentration resulting from CFD in the lower elbow which is the pipe section between the Location 1 and Location 4. When  $u_{sg}=0.2\text{m/s}$  and  $0.8\text{m/s}$ , the concentration of coal particles in the bend section rises continuously, while the concentration of particles varies little with time when  $u_{sg}=1.5$ . In this way, it can be explained that the particles cannot be discharged from the upward pipe due to the small rising translational velocity of the liquid slug when  $u_{sg}=0.2$  and  $0.8$ , that leads to the rising of the particle concentration at the bottom of the elbow. And  $u_{sg}=1.5$  reached the flow rate required for pulverized coal discharge.

Fig. 7 illustrates if the velocity of each cases meets the coal particle removal condition. The black dotted line in the figure gives the critical mixture velocity obtained by the experiments, that is, the gas and liquid velocity distributed at the region on the left side of the curve do not satisfy the pulverized coal discharge condition. As shown in the figure, the red points represent that those gas and liquid velocities satisfy the discharge condition of the particle according the CFD simulation results, but the velocities at the blue points are not satisfied. The results show the agreement with the experimental results, that means all the red points are at the left side of the curve of the critical velocity, and blue points are at the right side. Therefore, the CFD method can be used to study the movement of coal particles in the complex flow of the bend pipe.



**Figure 6.** Coal Particle Concentration in the Lower Elbow vs Simulation Time



**Figure 7.** Critical Discharge Velocity and the Velocity Distribution of Each Case

#### 4. CONCLUSION

A CFD model was adopted to study air-water-coal particle multiphase flow in a geometry including two straight pipes connected by a V-shaped elbow with a diameter of 50 mm.

1. The VOF model was used to simulate air-water flow with different superficial gas and liquid velocities, respectively. Important data such as time series of cross-sectionally averaged liquid holdup at different locations, phase distributions, and pressure were obtained.
2. It is proved that the numerical model can simulate the real gas-liquid multiphase flow accurately by comparing the results of the numerical simulations and the experiments.
3. Discharging the coal particles from the lower elbow needs a certain gas and liquid flow velocity. If the flow condition satisfies the particle discharge requirement, the concentration of the particles in the pipe will not rise all the time. The numerical simulation results show that the ability of gas-liquid flow to discharge coal particles from the elbow is in agreement with the experimental results.

#### REFERENCES

- [1].B. Stefano,E. Riva, D. Col, Condensation in a Square Minichannel: Application of the VOF Method, *Heat Transfer Engineering* 35 (2014) 193-203. DOI: 10.1080/01457632.2013.812493
- [2].J. Fan, K. Luo, X. Zhang, K. Cen, Large Eddy Simulation of the Anti-Erosion Characteristics of the Ribbed-Bend in Gas-Solid Flows, *Journal of Engineering for Gas Turbines & Power* 126 (2004) 672-679. DOI: 10.1115/1.1760523
- [3].W. Peng, X. Cao, Numerical simulation of solid particle erosion in pipe bends for liquid–solid flow, *Powder Technology* 294 (2016) 266-279. DOI: 10.1016/j.powtec.2016.02.030
- [4].M. Parsi, M. Kara, M. Agrawal, N. Kesana, A. Jatale, P. Sharma, S. Shirazi, CFD simulation of sand particle erosion under multiphase flow conditions, *Wear* 376-377 (2016). DOI: 10.1016/j.wear.2016.12.021
- [5].M. Parsi, M. Agrawal, V. Srinivasan, R. Vieira, C. Torres, B. Mclaury, S. Shirazi, CFD simulation of sand particle erosion in gas-dominant multiphase flow, *Journal of Natural Gas Science & Engineering* 27 (2015) 706-718. DOI: 10.1016/j.jngse.2015.09.003
- [6].C. Zhou, X. Wu, H. Li, Z. Ren, Y. Xin, Influence of in-situ stress distribution on selection of fracturing fluid backflow technology, *Acta Physica Polonica A* 130 (2016) 347-351. DOI: 10.12693/APhysPolA.130.347
- [7].Y. Meng, X. Li, M. Jiang, D. Feng, T. Zhang, Z. Zhang, Experimental research on three dimensional flow characteristics of multiple horizontal fractures utilizing an innovative experiment apparatus, *Arabian Journal of Geosciences* 11 (2018) 243. DOI: 10.1007/s12517-018-3589-0
- [8].M. Günal, A. Ismael, Experimental investigation of turbulent flow field at downstream-facing round nosed pier, *Acta Physica Polonica A* 130 (2016) 126-127. DOI: 10.12693/APhysPolA.130.126

# Sliding-Mode Enhancement for a Class of Fuzzy-based Controllers for surge control in Compression Systems

Y. Aribi<sup>1\*</sup>, R. Zamoum Boushaki<sup>1</sup>

<sup>1</sup> Signals and Systems Laboratory, Institute of Electrical and electronics engineering,  
M'hamed Bougara University- Boumerdes (UMBB), Avenue de l'indépendance, Boumerdes, Alegria.  
\*y.aribi@univ-boumerdes.dz / aribiyacine13@gmail.com

## ABSTRACT

In Major industries, Compression systems build based on Centrifugal and axial compressors are widely used. Practically, Centrifugal Compressors are known to be subjected to major oscillations and limit cycles during their operation known as Surge phenomenon. The previously mentioned instabilities impose huge challenges for compression systems in terms of efficiency, production cut, and maintenance cost. In this paper, a combined control strategy is proposed in order to actively control the compressor surge. A surge controller is proposed based on FIS to provide a real-time precise control for the recycle valve and a sliding mode controller is designed to enhance the main fuzzy block robustness and to reduce chattering phenomenon.

**Keywords:** Centrifugal Compressor, Recycle Valve, Surge, Fuzzy Controller, Multi-stage Fuzzy controller, Sliding Mode Control.

## 1. INTRODUCTION

Industrial Compression systems (CS) are subjected to falling into deep surge; a major instability that rises in terms of an uncontrolled vibration and flow reversal in the CS. Surge phenomenon rises when the intake flow to the CS decreases beyond the allowable limit. CS Surge can lead to catastrophic damages to the compressor's impeller, seals, drive, shaft ...etc. and imposes huge degradation in compression efficiency which leads to unwanted production cut and increases the CS maintenance cost. In this work, A Fuzzy Inference system (FIS) is combined with a second order sliding mode controller (2-SMC) to provide a model-free robust and precise control for the CS in order to decrease the vibrations while operating in high efficiency regions and prevent the system from falling into surge.

## 2. SYSTEM MODLING AND CONTROLLER STRUCTURE

One of the widely used models for centrifugal compressors has been provided in [1] and [2]. Eq. (1) to (4) has found a wide acceptance in academic papers.

$$\dot{P}_1 = \frac{a_p^2}{V_1} (Q_f + Q_r - Q) \quad (1)$$

$$\dot{P}_2 = \frac{a_p^2}{V_2} (Q - Q_t - Q_r) \quad (2)$$

$$\dot{Q} = \frac{A}{L} (\Psi_c(Q, \omega) P_1 - P_2) \quad (3)$$

$$\dot{\omega} = \frac{1}{J} (\tau_d - \tau_c) \quad (4)$$

The Compressor parameters are listed in Table 1. By assuming a constant angular speed and  $Q_r$  is zero, the system as described can be proven to be stable around the equilibrium point if the compressor is operating in the negative slope of  $\Psi - Q$  characteristics, or at most, at a small positive slope [3]. The rise in pressure, as a function of the mass flow and the drive speed, defines the compressor characteristic;  $\Psi_c(Q, \omega)$ . Fig.1, represents a recycle CS [4], the system is composed of two plenums, a centrifugal compressor (CC) defined by the compressor map

extracted based on a real process data, a feed flow valve for suction, throttle valve, bleed valve, and a recycle line with a recycle valve to be used as a main surge control actuator. The compressor characteristic shown in Fig.4 and Fig.7,  $\Psi_c(Q, \omega)$ , has an S-shape for a constant speed  $\omega_0$ . The error signal is calculated as the Euclidean distance between the operating point and its perpendicular projection into the surge limit line. The aim of the process is to keep the system operating as close as possible to the surge line without falling into deep surge.

#### a. Sliding Mode Controller

The sliding mode controller is designed to provide a precise and model-free control for the CS. A 2-SMC control is to be used with a super twisting algorithm (STA) in order to regulate the recycle valve. The 2-SMC with STA is defined by Eq. (5) to (7) where  $\sigma$  defines the sliding surface,  $u$  is the control signal, and  $W$  is a weighting parameter.

$$\sigma = e \quad (5)$$

$$u = -\sqrt{W \cdot |\sigma|} \cdot \text{sgn}(\sigma) - v \quad (6)$$

$$\dot{v} = -1.1W \cdot \text{sgn}(\sigma) \quad (7)$$

Changes in  $\text{sgn}(\sigma)$  value lead to oscillations in the control signal  $u(t)$  and therefore in the recycle valve Actuator. In order to reduce the oscillations, a proper tuning for  $W$  has to be achieved.

#### b. The design of the Fuzzy Inference System

Fuzzy based control has been addressed as one of the most effective model-free expert-knowledge based control [5,6]. The FIS is subjected to the designer's experience. However, a set of rules can be heuristically derived from the error and the change in error signals regardless of the controlled systems.

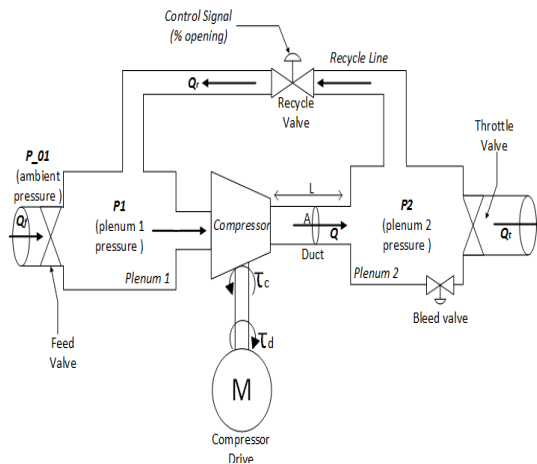


Figure 1. The compression system with recycle line



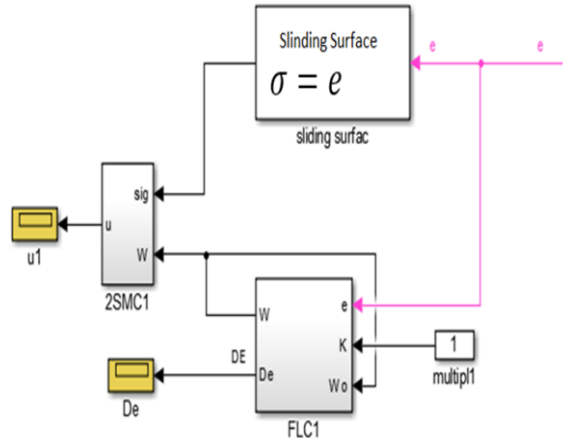


Figure 2. controller structure

Table 1. Different variables and parameters

Parameter	Meaning	Unit	Parameter	Meaning	Unit/Value
$\psi_c$	Pressure rise through the compressor	N/A	$P_{01}$	Ambient pressure	101325 (Pa)
$P_1, P_2$	Suction/ Discharge Plenum Pressure	Pa	$A$	Duct Cross-sectional Area	0.08 (m <sup>2</sup> )
$Q, Q_f, Q_t, Q_r$	Mass (Direct), Feed, Throttle, and recycle flows	kg/s	$L$	Duct Length	2.93 (m)
$\omega$	Rotational velocity	rad/s	$\tau_d, \tau_c$	Drive and Compressor torques	N.m

$E$  and  $\Delta E$  are the error and the chance in error signals, respectively. The FIS is designed using five Gaussian membership functions (GMF) for the Error signal, and three GMFs for the change in error, and five Gaussian membership functions for the output which is the increment in the SMC gain, with a total of 15 rules listed in Table 2. The linguistic variables are defined as: NL-Negative large, N-Negative, Z-Zero, P- Positive, and PL- Positive Large.

Table 2. Set of rules for the FIS

		$\Delta E$		
		N	Z	P
$E$	NL	PL	P	P
	N	PL	P	P
	Z	P	Z	Z
	P	P	Z	Z
	PL	Z	Z	N

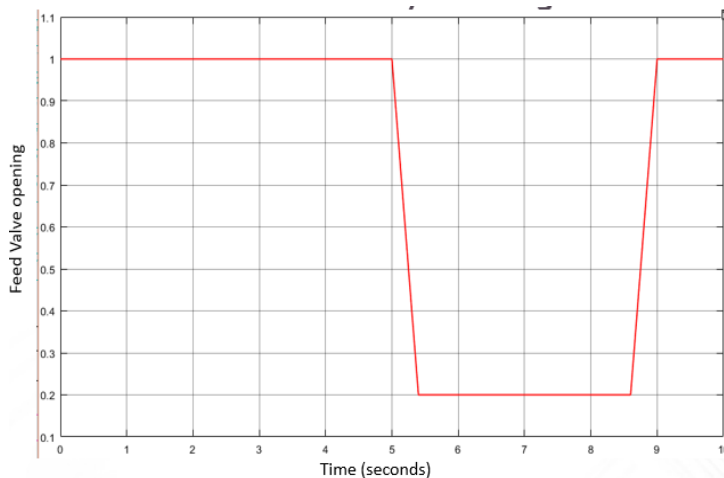


**Figure 3.** feed flow valve scheme

### 3. SIMULATION RESULTS

#### 3.1. Simulation of the uncontrolled system

The primary simulation is run without controller and with the recycle valve fully closed. When the feed flow valve in Fig.3 reaches 30% opening, oscillations observed in the different flows (Fig.5) and the operating point, Fig.4, starts moving along the trajectory in a cyclic behaviour. The pressure rise in Fig.6 increases above the initial values and starts oscillating as well.

#### 3.2. Simulation of the controlled system

The control scheme in Fig.2 has been implemented with a CC model build based on Eq. (1) to (4). As the feed flow decreases (Fig.3 and Fig.8), The operating point in Fig.7 deviates along a fixed speed line (43000rpm) near the SSOP region. The feed and throttle flow in Fig.8 decreased with the throttle valve closure while the recycle flow increased depicting the opening of the recycle valve and hence the activation of the controller. The mass flow (Q) kept a steady behaviour without any potential drop and/or flow reversal. The pressure rise in Fig.9 also shows a steady value with smaller oscillations. Some oscillations can be observed in both Fig.8 and Fig.9 due to the switching in the SMC. The proper auto-tuning for the weighting parameter successfully allowed the model-free controller to decrease the oscillations to an acceptable range and prevents flow reversal.

### 4. CONCLUSION

In this work, a real time tuning with FIS has been proposed and implemented for a 2-SMC controller. The model-free Sliding-Fuzzy controller prevented the compression system from falling into deep surge. The proper tuning decreased the oscillation to a level that prevents the undesirable limit cycle even with low feed flow.

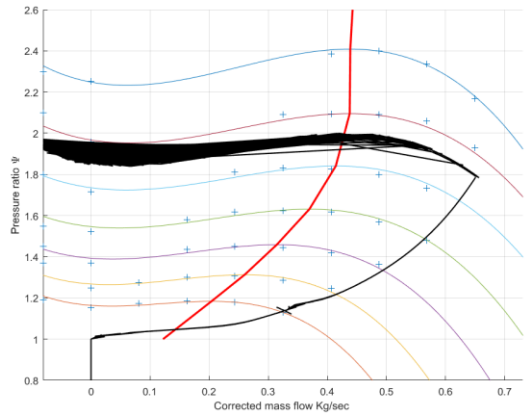


Figure 4. Compressor map and OP during surge

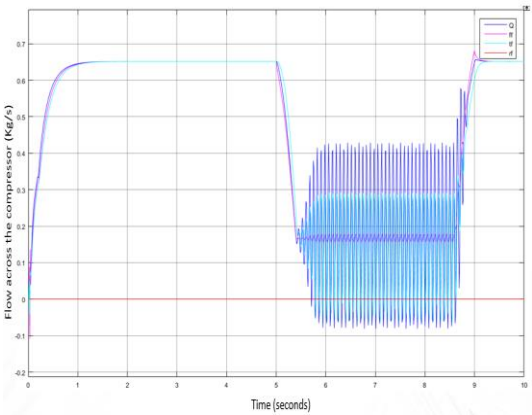


Figure 5. Fluid flow during surge

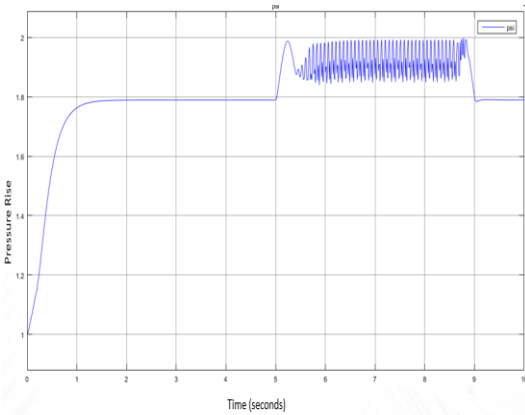


Figure 6. Pressure Rise during surge

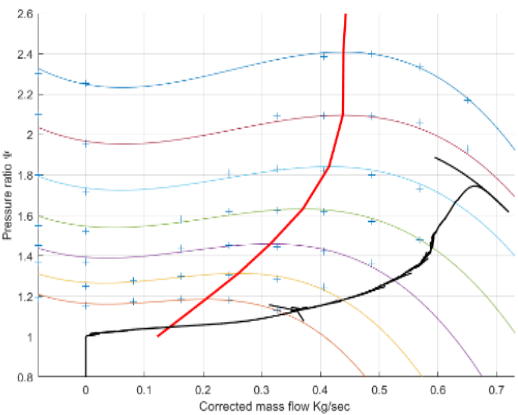


Figure 7. Compressor map and OP for the controlled system

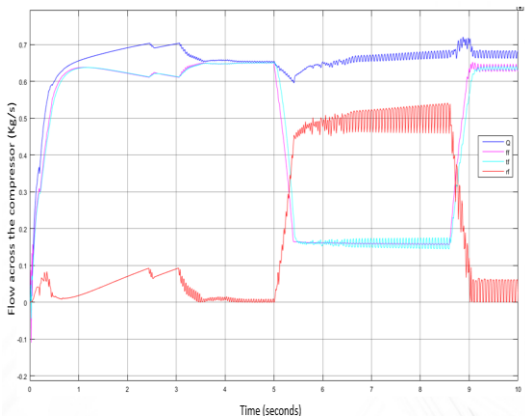


Figure 8. Fluid flow for the controlled system

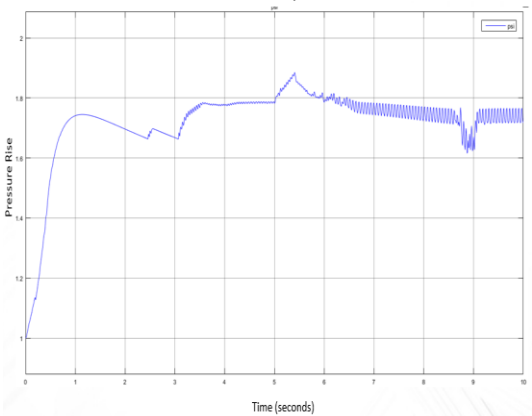


Figure 9. Pressure Rise for the controlled system

## REFERENCES

- [1].Greitzer, E. M., 1976, Surge and Rotating Stall in Axial Flow Compressors, Part I: Theoretical Compression System Model, *ASME J. of Eng. for Power*, Vol. 98, 190.
- [2].Gravdahl J.T, Egeland O., 1999, Compressor surge and rotating stall: modeling and control, Springer-Verlag.
- [3].Mohamed A. W, Ibrahim F. T, Ahmed M. E, 2014, Surge Detection System for Centrifugal Compressor, *INTERNATIONAL JOURNAL OF ENGINEERING SCIENCES & RESEARCH TECHNOLOGY*, Vol.3 No-2, pp.692-698.
- [4].Bjørn Ove Barstad, MSc, 2010, The Compressor Recycle System, Norwegian University of Science and Technology (NTNU).
- [5].Chetate B., Zamoum R., Fegriche A., Boumdin M., 2013, PID and Novel Approach of PI Fuzzy Logic Controllers for Active Surge in Centrifugal Compressor, *AJSE*, Springer 38, pp.1405-1414.
- [6].N.G. Adar, A. Egrisogut Tiryaki, R. Kozan, Real Time Visual Servoing of a 6-DOF Robotic Arm using Fuzzy-PID Controller, *ACTA PHYSICA POLONICA A*, 128 (2015), No-2. B-348-B-351.

# Performance of multiple-fracture horizontal wells with consideration of the long-term fracture conductivity

Li zhun<sup>1\*</sup>, XiaoDong Wu<sup>1</sup> and Guoqing Han<sup>1</sup>

<sup>1</sup> Key Laboratory of Education Ministry for Petroleum Engineering, China University of Petroleum, Beijing, CHINA

\*1058488311@qq.com

## ABSTRACT

A hybrid analytical/numerical method is proposed with consideration of the change of fracture conductivity over time. Results are compared to the previous production models that are based on a constant fracture conductivity. The hybrid analytical/numerical model proposed in this paper has the advantages of minor calculation and better calculating stability compared to the numerical method.

The flow model in the formations is established and solved by source function and Newman's product method. 1D linear flow in fractures with a time-varying conductivity is solved by the finite difference method. By coupling the flow model of the formation and the numerical model of the fractures dynamically via the continuity of pressure and flux on the surface of fracture segments, a complete set of linear equations to simulate the flow behavior of a well with time-varying conductivity fractures is obtained. The associated matrix equation to solve the pressure and flux of each fracture segment is also provided.

The most significant new finding is that the impact of conductivity variation over time on the well performance should not be neglected. The accuracy of yield prediction depends on a precise coefficient of fracture conductivity variation. There are big differences of the flow rate and pressure distribution in fractures between constant and time-varying conductivity. The reservoir seepage field will be changed and more fluid flows through the fracture segments near the wellbore into the well as the fracture conductivity decreases. The results and conclusions obtained by the hybrid analytical/numerical productivity model accord well with that of the published numerical methods.

**KEYWORDS** : Multiple fractured horizontal well; Hybrid analytical/numerical method, Long-Term Fracture conductivity; Performance

## 1. INTRODUCTION

Multi-stage fracturing horizontal well is a key technology for increasing production during the development of tight oil and gas fields at home and abroad. Accurately evaluating and predicting the performance of MFHW is of great significance to the actual production practices. Fracture conductivity is one of the key parameters affecting the yield increase of MFHW, previous production models always assumed that the fracture conductivity was a certain value, while laboratory experiments and field practices showed that the fracture conductivity was changing over time during actual production. For the relationship between fracture conductivity and time, many scholars have carried out a large number of laboratory experiments to determine the corresponding empirical relationship. Yu Shaocheng et al. (1987) gave an empirical relationship between long-term fracture conductivity and time on the base of experiments on long-term fracture conductivity of ceramsite proppant and Lanzhou fracturing sand [1]. Considering fracturing fluid damage under high temperature conditions, Jiang Tingxue, Wang Yongli et al. (2004) calculated long-term conductivity changes based on short-term conductivity [2]. Wen Qingzhi et al. 2007 studied the influence of embedment of 20/40 mesh proppant ceramsite on the long-term conductivity of fractures, and obtained the relationship between the conductivity and time under a certain closure pressure [3-5]. Gringarten(1973) and ozkan (1991) used the source functions in real

space and Laplace space to solve the reservoir seepage problems respectively, and gave the source function solution database of reservoir seepage problem under certain conditions. [6,7]. Lian Peiqing et al. used the Newman product and source function method to solve the production model coupling the flowing in reservoir, fractures and horizontal wellbore, and treated the flow in the fracture as a plane radial flow from the fracture to the wellbore, which did not meet the real flow pattern in fracture [8]. Scholars have also done a lot of research on the distribution of fracture conductivity and the effect of changes over time on well performance. Liu Yu, Xiong Jian, Yao Shanshan et al. calculated the pressure and rate change of MPFW with fracture conductivity varying with position, and analysed the variation regularity of the pressure inside the wellbore and the fractures under different conductivity distribution modes. However, the change of fracture conductivity with time has not been considered [9-16]. Jiao Chunyan, He Shunli et al. (2011) established a model of seepage flow in vertical fracturing wells considering the variation with time of fracture conductivity, and analysed the influence of the change of conductivity on the production and pressure, but the finite difference method is used in the solution of the model, there are problems such as slow calculation speed, meshing of the reservoir, and poor convergence [17]. Xie Lisha et al. (2013, 2016) used the semi-analytical method to build the performance model of MPFW based on the pressure drop formula in an infinite formation and the principle of potential superposition, taking the influence of the time-dependent fracture conductivity into account. The paper analysed the influence of the time-dependent fracture conductivity on the productivity and seepage field of the MPFW, but the flow in the fracture is treated as the plane radial flow from the end to the bottom-hole, accurate calculation model of flow in the fracture has not been provided. [18,19]. Jia Pin et al considered the flow inside the fracture as a one-dimensional linear flow along the fracture direction. The flow equation was processed by the finite difference method. The Laplace space source functions were used to solve the reservoir seepage, and then the two were coupled to each other. Pressure analysis and production calculation model of fractured wells under complex fracture conditions had been made, but they did not consider the time-varying of fracture conductivity [20]. Based on the previous research results, this paper uses the closed boundary slab source function, combines the Newman product with superposition principle to obtain the reservoir seepage analytical solution, and uses the finite difference method to solve the fracture seepage model with a various conductivity with time. Using the conditions of continuous flux and pressure on the fracture interface, and the numerical and analytical solution are coupled to solve. The hybrid analytical/numerical model of the multi-stage fracturing horizontal well considering the long-term conductivity of the fracture is obtained. The variation of the fracture conductivity and the impact of production are analysed, the research results of this paper definitely have certain guiding significance for production practice.

## 2. MODEL DESCRIPTION

### 2.1. Model hypothesis:

There is a homogeneous anisotropic reservoir with six outer boundaries closed. Reservoir fluids are single-phase and slightly compressible. At time  $t=0$ , the entire reservoir pressure is equal everywhere, which is the initial reservoir pressure. There is a horizontal well paralleling to the y-axis direction in the reservoir. The horizontal section is fractured, and  $n$  fractures perpendicular to the horizontal well are pressed out, and the fracture passes through the entire oil layer thickness. In the horizontal section, no holes are reperforated, and the fluid will flow from the formation into the fracture first, and then flow along the fracture into the wellbore. The fracture is a finite diversion fracture, and the conductivity is changed with time. The inside of the fracture is the one-dimensional Darcy flow of the vertical wellbore, and the flow of the fracture to the wellbore is a plane radial flow.

For homogeneous heterogeneous reservoirs, the diffusion equation is often written as:

$$\eta_x \frac{\partial^2 p}{\partial x^2} + \eta_y \frac{\partial^2 p}{\partial y^2} + \eta_z \frac{\partial^2 p}{\partial z^2} = \frac{\partial p}{\partial t} \quad (1.1)$$

The source function method can be used to solve the above equation. According to the conclusions of Grington, Lian Peiqing et al. [6,8], a fracture with a volume of  $x_f \times y_d \times h$  can be regarded as a superposition of closed boundary plate sources with thicknesses of  $x_f, y_d, h$  in  $x, y, z$  the direction separately, satisfying The Newman product law, the pressure drop produced by the source  $(x_0, y_0, z_0)$  at  $(x, y, z)$  with pressure drop can be calculated by:

$$A(t) = p_{ini} - p(x_i, y_i, z_i, t) = \frac{1}{\phi C_t} \int_0^t (S_1 S_2 S_3) d\tau$$

$$S_1(x, x_0, \tau) = \frac{x_f}{a} \left[ 1 + \frac{4a}{\pi x_f} \sum_{n=1}^{\infty} \frac{1}{n} \exp\left(-\frac{n^2 \pi^2 K_x t}{\alpha a^2}\right) \sin\left(\frac{n\pi x_f}{2a}\right) \cos\left(\frac{n\pi x_0}{a}\right) \cos\left(\frac{n\pi x}{a}\right) \right]$$

$$S_2(y, y_0, \tau) = \frac{y_d}{b} \left[ 1 + \frac{4b}{\pi y_d} \sum_{n=1}^{\infty} \frac{1}{n} \exp\left(-\frac{n^2 \pi^2 K_y t}{\alpha b^2}\right) \sin\left(\frac{n\pi y_d}{2b}\right) \cos\left(\frac{n\pi y_0}{b}\right) \cos\left(\frac{n\pi y}{b}\right) \right] \quad (1.2)$$

$$S_3(z, z_0, \tau) = 1 + \frac{4}{\pi} \sum_{n=1}^{\infty} \frac{1}{n} \exp\left(-\frac{n^2 \pi^2 K_z t}{\alpha h^2}\right) \sin\left(\frac{n\pi}{2}\right) \cos\left(\frac{n\pi z_0}{h}\right) \cos\left(\frac{n\pi z}{h}\right)$$

where  $\alpha = \phi \mu C_t$ ,  $S_1$ ,  $S_2$ ,  $S_3$  represents Green Function at  $(x_0, y_0, z_0)$  separately in 3 directions ; a, b, h is the length, width and thickness of the reservoirs separately.

## 2.2 The seepage model considering long-term conductivity in fracture

Since the height and width of the fracture are small relative to the length of the fracture, the seepage in the fracture can be regarded as the one-dimensional Darcy flow in the longitudinal direction of the fracture, regardless of the spatial distribution of the fracture conductivity, that is, the fracture conductivity is equal everywhere [21, 22].

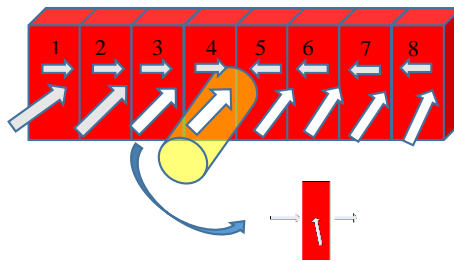


**Figure 1** Linear flow in the fractures

Cinco et al.(1991) pointed out that the compressibility of artificial fractures is negligible because the volume of fractures is small. Therefore the flow within the fracture can be considered incompressible [21, 22]. Under all the above assumptions, the flow equation of fractures can be simplified as :

$$\frac{\partial^2 p}{\partial x^2} + \frac{\mu}{k_F(t)} \times \frac{q_F(x, t)}{y_d h} = 0 \quad (1.3)$$

Using the central difference method, the one-dimensional Darcy flow in the fracture is discretized using a point-centred grid (Fig. 1), For isometric grids in Cartesian coordinates:

$\Delta x_{i+\frac{1}{2}} = \Delta x_{i-\frac{1}{2}} = \Delta x$ , the fully implicit difference format of Eq (1.3) is obtained as:

$$p_{i+1}^n - 2p_i^n + p_{i-1}^n + \frac{\mu \Delta x}{[k_F y_d]^n} \frac{q_{Fi}^n}{h} = 0 \quad (1.4)$$

Where  $q_F(x, t)$  is the volume of fluid flowing into the fractured grid block per unit time,  $m^3 / s$ ;  $[k_F y_d]^n$  is the fracture conductivity of the fracture at time  $n$ , and  $q_{Fi}^n$  is the flow velocity of the fluid flowing into the grid  $i$  at time  $n$ ,  $m^3 / s$ .

According to the research by Wen Qingzhi et al. [5], the calculation model of fracture conductivity with time is:

$$[k_F y_d]^n = k_{Fo} y_{do} [1 - \beta \lg (n / 86400 + 1)] \quad (1.5)$$

$\beta$  is the coefficient of variation of fracture conductivity, no dimension, the value is generally 0.2~0.3,  $k_{Fo} y_{do}$  is the initial fracture conductivity,  $m^2 D$ ;  $n$  is the time, s. Substituting equation (1.5) into equation (1.4), we can get the discrete form of fracture flow model that takes long-term fracture conductivity into account.

$$p_{i+1}^n - 2p_i^n + p_{i-1}^n + \frac{\mu \Delta x}{k_{Fo} y_{do} (1 - \beta \lg (n / 86400 + 1))} \frac{q_{Fi}^n}{h} = 0 \quad (1.6)$$

### 2.3 The couple model of the flow in reservoir and fracture

It is assumed that the reservoir node pressure at the interface between the reservoir and the fracture is  $p_1, p_2, \dots, p_N$  and the node pressure of the fracture is  $p_{F1}, p_{F2}, \dots, p_{FN}$ ; the flow from the reservoir node to the fracture node is  $q_{F1}, q_{F2}, \dots, q_{FN}$ . Due to the continuity of pressure and flux

at the interface, the reservoir joint pressure and the fracture joint pressure are equal:  $p_i = p_{Fi}$ .

Equation (1.2) gives the pressure drop of a single fracture block at any point in the reservoir. When multiple fractures are produced simultaneously, using the principle of spatial superposition, the

pressure drop at point  $(x_i, j_i, z_i)$  can be expressed as:

$$\Delta p_i = p_{ini} - \sum_{j=1}^n p((x_i, j_i, z_i); (x_j, j_j, z_j); t) = \sum_{j=1}^n A_{ij}(t) q_{Fj} \quad (1.7)$$



Where  $q_{Fj}$  is the flux of the  $j$ th fracture,  $m^3/s$ ;  $p((x_i, j_i, z_i); (x_j, j_j, z_j); t)$  is the pressure drop at the center of the fracture in the  $j$ th fracture at time  $t$ , MPa;  $A_{ij}$  is the pressure drop at point  $(x_i, j_i, z_i)$  when the  $j$ th fracture is produced in unit production. For variable mass flow, applying the Duhamel principle, the pressure drop anywhere in the formation can be obtained as:

$$\Delta p_i = \int_0^t \sum_{j=1}^N q_{Fj}(\tau) \left[ -\frac{dA_{ij}(t-\tau)}{d\tau} \right] d\tau \quad i=1, 2, \dots, N \quad (1.8)$$

Where  $N$  denotes the total number of fracture blocks, select the appropriate time step  $\Delta t$ , combine with the formula 1.7 and write the equation 1.8 as a numerical integral form for the time step [8]. For each fracture block  $i$ , there should be:

$$\sum_{j=1}^N q_{Fj}^k A_{ij}(\Delta t) + p_i(t^k) = p_{ini} - \sum_{m=1}^{k-1} \sum_{j=1}^N q_j(t^m) [A_{ij}((k-m+1)\Delta t) - A_{ij}((k-m)\Delta t)] \quad i=1, 2, \dots, N, \\ k=1, 2, 3, \dots, n \quad (1.9)$$

Where:  $A_{ij}(0) = 0$ ,  $A_{ij}(t^k - t^{k-1}) = A_{ij}(\Delta t)$ ,  $\Delta p_i = p_{ini} - p_i(t^k)$ ,  $t^k = k \times \Delta t$ .

#### 2.4. Discretization methods of inner boundary conditions

Equation 1.6 and Equation 1.9 give the expression of the linear flow inside the fracture. The flow from the fracture to the horizontal wellbore is regarded as a plane radial flow with a radius of  $h/2$  [11,12] (Fig. 2), and the production conditions of the epidermis are as follows considering the possible skin effects [20]

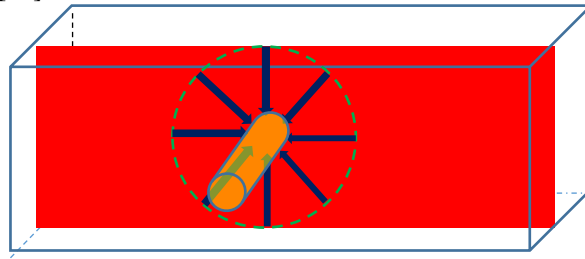


**Figure 2** The plane radial flow from the fracture to the wellbore

The flow rate of a single fracture grid to the wellbore is [20]:

$$\frac{2\pi^* [k_F y_d]^n (p_{Nw} - p_{wf})}{\mu \ln(h/2r_w + S)} = q_{Nw} \quad (1.10)$$

For multi-stage fracturing levels, the total flow is the sum of the individual fracture flows and is expressed by the following formula:

$$\sum_{N_w} \frac{2\pi^* [k_F y_d]^n (p_{N_w} - p_{wf})}{\mu \ln(h/2r_w + S)} = q \quad (1.11)$$

Where  $N_w$  is the number of the fracture grids connecting to the wellbore,  $p_{N_w}$  is the grid pressure of the fracture block connected to the wellbore, Pa;  $q_{N_w}$  is the flow of the grid node  $N_w$  to the wellbore,  $q$  is the total flow of the fractured well,  $m^3/s$ ; and  $p_{wf}$  is the bottom hole pressure, Pa; This paper assumes that the horizontal wellbore is of infinite conductivity, so it can be seen that the bottom hole pressure is the same everywhere.

Based on the above-mentioned reservoir seepage model, fracture seepage model, and discrete conditions of the solutions, the fracture is meshed according to the basic parameters of MFHW. Assuming that the total number of meshes is N, for each fracture block, the pressure response Eq(1.9) in the reservoir and the full implicit block-centered finite difference Eq(1.6) are used to establish the equations respectively, and 2N equations about  $q_{F1}, q_{F2}, \dots, q_{FN}$ ,

$p_{F1}, p_{F2}, \dots, p_{FN}$ , can be obtained, and then combine eq(1.11), 2N+1 equations about 2N+1 unknown variables are obtained. Finally, the equations about  $q_{F1}, q_{F2}, \dots, q_{FN}$ ,  $p_{F1}, p_{F2}, \dots, p_{FN}, q$ , can be quickly solved by the Gauss full principal elimination method.

### 3. ANALYSIS AND DISCUSSION

#### 3.1. Model validation and cases study

In order to verify the accuracy of the model, the relevant data in the literature [19], the actual data and the calculation results of the model in this paper are used for comparison. The basic data in the literature are shown in Table 1.

**Table 1** Basic parameters for model validation

Well name	A20
Original reservoir pressure/Mpa	30
Strata permeability/ $10^{-15} m^2$	30
Reservoir thickness/m	13.3
Oil viscosity/(Pa.s)	0.00125
Oil volume coefficient	1.3
Skin factor	8.7
Wellbore radius/m	0.054
Half fracture length /m	95
Original drawdown pressure/MPa	14
Original permeability of fracture/ $(10^{-12} m^2 \cdot m)$	1.250
Variation coefficient of flow permeability	0.31
Reservoir length/m	3000
Reservoir width/m	3000

It can be seen from the comparison results in Fig. 3 that the calculation results of the model are in good agreement with the actual data and the calculation results of the model in the previous literature, thus indicating the accuracy of the model.

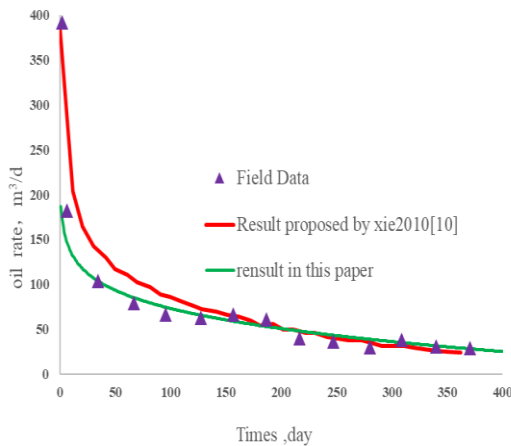


**Figure 3** The comparison chart of the model and production data

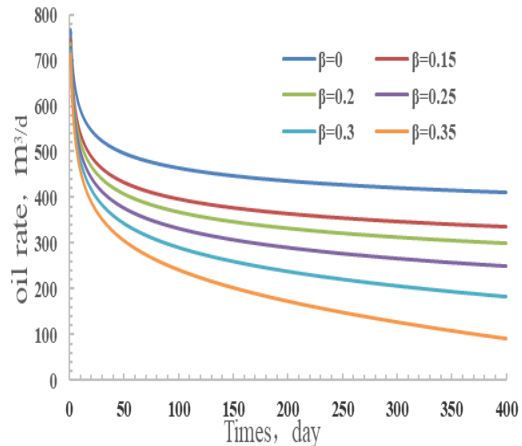


**Figure 4** The production curve under different fracture conductivity variation coefficient

### 3.2. Sensitivity Analysis for coefficient of conductivity variation

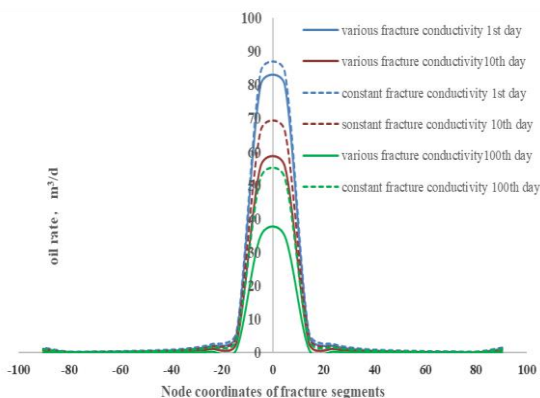
Sensitivity analysis of the fracture conductivity decline coefficient of a MFHW was carried out using the values of the reservoir parameters value method in [19]. The relevant values are shown in Table 1.

The production of MFHWs with a constant fracture conductivity and a time-dependent fracture conductivity was both calculated, the values of different fracture conductivity variation coefficient are considered for comparison and analysis. It can be seen from Fig. 4 that the rate is lower when considering the change of fracture conductivity with time, because as the fracture conductivity decreases, the seepage resistance of the fluid in the oil layer increases. When the producing differential pressure is constant, greater seepage resistance will result in lower production. We can conclude that, for the MFHW, the change of fracture conductivity has a great influence on the production. When the production prediction is carried out, the change of the fracture conductivity with time should be considered, so that the production can be predicted more accurately. Based on the production calculation results of different fracture conductivity variation coefficient, the change of the production is extremely sensitive to the fracture conductivity variation coefficient. Accurate determination of fracture conductivity variation coefficient is necessary for the performance of MFHW. In actual appliance, according to the literature [17], [19], the fracture conductivity decline coefficient can be obtained through the analysis of the experimental data of long-term fracture conductivity.

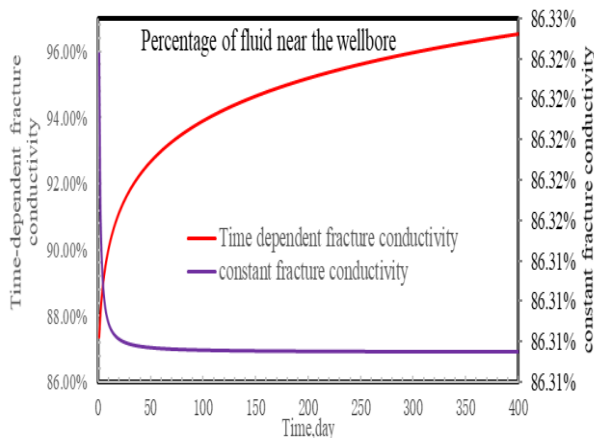
### 3.3. Study on the flux in the fractures

Figure 5 is the flux curve of a single fracture in different time, both the constant fracture conductivity and the time-dependent fracture conductivity are included. In both cases, the flow rate of the fracture in the near-well zone (-10~10m) and the fracture tip (90~100m, -90~-100m) are greater than the middle of the half fracture (30~60m, -30~-60m). The reason why the production in the near-wellbore is higher is that there is a great pressure loss in the fracture, the closer to the wellbore, the greater the production pressure difference, the higher the fracture flux. The

production of fractures at the distal end is higher than that of the middle because there is a larger drainage area, and the interference of the fracture nodes in the middle is stronger.



**Figure 5** Flux distribution of a single fracture



**Figure 6** The percentage of fluid near the wellbore

By comparing the proportion of near-well flux (-10~10m) to the total flux (Fig. 6), it can be found that under the condition of a certain flow pressure and a constant fracture conductivity, the change of the ratio over time is small (about 87%), and when considering the change of fracture conductivity with time, the ratio increases with time (finally more than 95%). This indicates that the loss of fracture conductivity leads to more fluid flowing into wellbore through the fracture in the near-well zone, which is in good agreement with the conclusion of literature [17].

#### 4. CONCLUSION

(1) The comparison of the model results shows that when considering the variation of fracture conductivity with time, the production of MFHW will be lower than that of the constant fracture conductivity. Considering the change of fracture conductivity with time, the predicted production is more consistent with the actual production data. The influence of time-dependent crack conductivity on capacity cannot be ignored.

(2) The calculation results of the production under different fracture conductivity decline coefficient indicate that the performance of MFHW is sensitive to the change of the variation

coefficient of the fracture conductivity. Therefore, the variation coefficient of the fracture conductivity should be accurately determined before the calculation of the fracture well production. In actual appliance, we can use the experimental data to get the variation coefficient of the fracture conductivity, on this basis, the production of MFHW is predicted more accurately.

(3) The calculation results of the model show that the flux of fracture reaches locally high peak near the wellbore, and the decrease of the fracture conductivity will seriously affect the distribution of the seepage field near the MFHW, the distribution of flow and pressure within the fractures, which will make the peak more obvious, finally will cause more fluid to flow into the the well through the fracture near the wellbore.

## ACKNOWLEDGEMENT

Authors thanks to the National Science and Technology Major Project (NSTMP) Program (grant number: 2017ZX05072006-002) and the National Science and Technology Major Project (NSTMP) Program (grant number: 2017ZX05009-003) in China. This paper was presented in “5rd International Conference on Computational and Experimental Science and Engineering (ICCES-2018)”

## REFERENCES

- [1]. SHAO Chengyu . Evaluation of long term fracture conductivity for ceramics proppant and fracturing sand from Lanzhou [J] [J]. Oil Drilling & Production Technology, 1987 (5) : 93–99. DOI:10.13639/j.odpt.1987.05.015
- [2]. JIANG tingxue, WANG yongli , DING yunhong et al Optimization seeking method of proppant in consideration of stress sensitivity and the long-term fracture conductivity[J] Drilling & Production Technology, 2004, 27 (5) : 75–76. DOI:10.3969/j.issn.1006-768X.2004.05.027.
- [3]. WEN qingzhi , WANG qiang , et al Analysis and Discussion on the factors influencing the long-term flow capacity of proppant [J]. Inner Mongolia Petrochemical Industry. 2003, 29 (3) : 101–104. DOI:10.3969/j.issn.1006-7981.2003.03.052.
- [4]. Wen Q, Zhang S, Wang L, et al. Influence of proppant embedment on fracture long-term flow conductivity [J] Natural Gas Industry .2005, 25 (5) : 65–68. DOI:10.3321/j.issn:1000-0976.2005.05.021.
- [5]. Wen Q, Zhang S, Wang L, et al. The effect of proppant embedment upon the long-term conductivity of fractures[J]. Journal of Petroleum Science & Engineering, 2007, 55(3):221–227. DOI:10.1016/j.petrol.2006.08.010
- [6]. Gringarten, A.C. and Ramey, H.J. (1973) The Use of Source and Green's Function in Solving Unsteady-Flow Problem in Reservoir. SPE Journal, 13, 285–296. <https://doi.org/10.2118/3818-PA>
- [7]. Ozkan, E., 1988. Performance of Horizontal Wells. PhD dissertation. U. of Tulsa, Tulsa, Oklahoma
- [8]. LIAN Peiqing, CHENG Linsong, CAO Renyi, HUANG Shijun A Coupling Model of Low Permeability Reservoir and Fractured Horizontal Wellbore in Nonsteady State [J] Computational physics 2010, 27(2):203–210. DOI:10.3969/j.issn.1001-246X.2010.02.007.
- [9]. Liu Yu. Study of Pressure Behavior and Productivity for vertical Fracture Well in Complex Conditions [D] Daqing Petroleum Institute ,2006.
- [10]. Xiong Jian, Ma Zhenchang, Ma Hua, Wang Shaoping . Study on production of vertical fracture oil well under the condition of variable conductivity[J] Complex Hydrocarbon Reservoirs ,2013,(04):52–54. DOI:10.16181/j.cnki.fzyqc.2013.04.025

- [11]. XIONG Jian, ZENG Shan, WANG Shaoping A Productivity Model of Vertically Fractured Well with Varying Conductivity for Low Permeability Reservoirs [J] Lithologic Reservoirs , 2013,(06):122-126.DOI:10.3969/j.issn.1673-8926.2013.06.023.
- [12]. Xiong Jian Deliverability analysis on the variable conductivity vertical fracture well of low permeability gas reservoirs[J] Reservoir Evaluation and Development. ,2013,(03):23-26. DOI:10.3969/j.issn.2095-1426.2013.03.006.
- [13]. XIONG Jian, MA Qiang , XIAO Feng, MA Qian. Study on Production of Vertical Fracture Gas Well under the Condition of Variable Conductivity Science Technology and Engineering , 2013,(11):2948-2952. DOI:10.3969/j.issn.1671-1815.2013.11.007.
- [14]. GAO yang ,ZHAO chao , ZHANG yun , WANG qi Transient Flow Model of the Fracture Horizontal Well with the Variable Conductivity Fractures in Tight Gas Reservoir [J] Petroleum Geology & Oilfield Development in Daqing. , 2015, (06): 141-147. DOI:10.3969/J.ISSN.1000-3754.2015.06.026.
- [15]. ZHAO chao ,XIAO jie , XU zhengdong et al .Dynamical pressure characteristics of multi-stage fractured horizontal well [J] Fault-Block Oil & Gas Field.2015,(06):798-802. DOI:10.6056/dkyqt201506026.
- [16]. The transient Flow Mathematical Model for Vertically Fractured Well in Circular closed reservoir [J] Petroleum Geology and Recovery Efficiency,2006,(06):66-69. DOI:10.3969/j.issn.1009-9603.2006.06.020.
- [17]. JIAO Chunyan, He Shunli, Zhang Haijie, et al. Research on Fractured Well Production Performance Under Variable Flow Conductivity [J]. Journal of Southwest Petroleum University (Science&Technology Edition), 2011, 33 ( 4):107—110. DOI:10.3863/j.issn.1674-5086.2011.04.019.
- [18]. XIE Li-sha , ZHANG Xiao, XU Jian-chun Productivity Performance of Multi-stage Fracturing Horizontal Well with Changing Conductivity Capacity[J] Science Technology and Engineering ,2012,(20):4888-4891. DOI:10.3969/j.issn.1671-1815.2012.20.007.
- [19]. Xie Lisha, Hu Yong, He Yifan, Wang Quanlin, Zhang Chi Research on Fracturing Well Productivity of Low Permeability Reservoir at Sea Considering Fracture Conductivity Varying Over Time [J] Natural Gas and Oil,2016,34(05):50-55. DOI:10.3969/j.issn.1006-5539.2016.05.011.
- [20]. Jia P, Cheng L, Huang S, et al. Transient behavior of complex fracture networks[J]. Journal of Petroleum Science & Engineering, 2015, 132:1-17. <https://doi.org/10.1016/j.petrol.2015.04.041>
- [21]. Cinco-ley, H., and Samaniego-V., F., Transient Pressure Analysis for Fractured Wells; JPT (Sept. 1981), 1749-66. <https://doi.org/10.2118/7490-PA>
- [22]. Cinco-Ley H, Meng H Z. Pressure Transient Analysis of Wells With Finite Conductivity Vertical Fractures in Double Porosity Reservoirs[J]. 1988. <https://doi.org/10.2118/18172-MS>
- [23]. Zhang F, Yao Y, Huang S, et al. Analytical method for performance evaluation of fractured horizontal wells in tight reservoirs[J]. Journal of Natural Gas Science & Engineering, 2016, 33:419-426. <https://doi.org/10.1016/j.jngse.2016.05.013>

## Determination of Engineering Properties of Ready Thermal Insulation Plaster and Acceptability Assessment

Şemsettin Kılınçarslan<sup>1\*</sup>, Metin Davrz<sup>2</sup> and Mehmet Ali Akbulut<sup>1</sup>

<sup>1,2</sup> Suleyman Demirel University/Natural and Industrial Building Materials Research Application Center, Isparta, TURKEY

\*semsettinkilincarslan@sdu.edu.tr

### ABSTRACT

Thermal insulation is all the measures taken in order to keep indoor temperatures at desired levels, to save energy in heating-cooling processes against external climatic conditions, to solve environmental problems and to reduce air pollution. Thermal insulation; at the same time it protects against external influences and extends the life span and reduces the operating costs as the building physics conditions are fulfilled. Within the scope of this thesis, it is aimed to investigate the conformity of declared heat insulation mortars according to TS EN 998-1 standard to other criteria specified in this standard, especially heat conductivity coefficient and compressive strength, and to compare the findings with declared values. For this purpose, plaster mortar samples were produced from the heat insulation facilities belonging to five different domestic companies. Fresh unit consistency, fresh unit volume mass, air content determination and dry unit volume mass, pressure and bending strength, capillary water absorption and thermal conductivity coefficient values of fresh samples were obtained. In addition, energy loss calculations and savings rates of traditional and thermal insulation plants have been determined.

When the obtained data were evaluated, it was observed that a significant part of the isolation plants did not satisfy the firm declaration values. Therefore, more frequent checks should be made and audits should be increased when the firm is approved. In this way, the next generation of energy-saving products that will increase the quality of the products marketed by the companies will be delivered to the users.

**KEYWORDS** - Thermal insulation plaster, technical specifications, conformity assessment

### 1. INTRODUCTION

The protection and durability of the structure against external factors is basically related to the outer shell of the structure [1]. One of the oldest applications to protect the structure from external factors is the plastering of the walls [2]. Plaster material is a mortar material applied to the interior and exterior wall surfaces in structures [3]. The use of materials that are not suitable as plaster in the buildings leads to a decrease in the expected efficiency, the increase of the weight of the structure and the increase of heat losses, thus resulting in savings in energy costs. In addition, it is known that suitable plaster mortar imparts high strength and strength properties [4,5]. In order to form walls with high resistance and thermal insulation, studies on the point of thermal insulation plasters are progressing rapidly [6-8].

In our country, there are concerns about whether the prefabricated thermal insulation plasters, which are very important for the protection of structures from external factors and for thermal insulation, provide the given properties. In this study, the heat conductivity coefficient and compressive strength of the thermal insulation mortars produced in accordance with the TS EN 998-1 standard in our country are compared with the other criteria mentioned in this standard and the findings are compared with the declared values.

### 2. MATERIAL AND METHODS

In this study, samples of five different companies which are the most preferred in the market have been provided from T1 class heat insulation plasters. The coding of the plasters of the companies was done as follows:

- AFYS= A Firm Insulation Plaster
- BFYS=B Firm Insulation Plaster
- CFYS=C Firm Insulation Plaster
- DFYS=D Firm Insulation Plaster
- EFYS=E Firm Insulation Plaster

Plaster samples production SDU Natural and Industrial Building Materials Research Center (DEYMAM) was made. Insulation plaster and water were prepared by weighing the amount of mixture proposed by the companies and mixed with a mixer. The mixing water amounts recommended by each company are different and therefore the mixture amounts cannot be given to the firms. A total of 5 serial plaster mortars were produced and placed in sample molds. Samples were left in the mold for 24 hours and removed from the mold at the end of this period. The plaster mortar samples produced are shown in Figure 1. During the study, the freshness of the plaster mortar samples was determined and the fresh air content was determined. In the study, dry unit volume mass, capillary water absorption, flexural and compressive strength, heat conductivity tests were performed and the findings obtained with the firm declaration values of heat insulation plasters were compared. In addition, energy loss values of wall sections and saving rates according to traditional plastered walls were determined.



**Figure 1.** Samples of plaster mortar produced.

Unit mass, air, spreading diameter, dry unit volume, capillary water absorption, flexural, pressure and thermal conductivity values of the plaster samples prepared within the scope of the study were obtained. Unit mass, air, spreading diameter, dry unit volume, capillary water absorption, flexural, pressure and thermal conductivity values given in Table 1.

The firm declaration values of AFYS, BFYS, CFYS, DFYS, EFYS plaster type and the findings obtained in the study are given in Table 2. The energy loss values of the wall sections and the saving rates according to the traditional plastered walls are given in Table 3. Measured and declared values of energy loss and saving (%) values are given in Table 4.



**Table 1.** Unit mass, air, spreading diameter, dry unit volume, capillary water absorption, flexural, pressure and thermal conductivity values.

Insulating plaster	Unit volume of mass (kg/m <sup>3</sup> )	Air (%)	Spreading diameter (mm)	Dry Unit volume of mass (kg/m <sup>3</sup> )	Capillary water absorption coefficient (kg/m <sup>2</sup> dak <sup>0.5</sup> )	fcf-28g (Flexure) (MPa)	fc-28g (Compressive) (MPa)	Thermal conductivity coefficient (W/m.K)
AFYS	657	6	13.9	369	0.48	0.53	1.77	0.0780
BFYS	763	8.5	14.5	615	0.261	0.97	3.25	0.1250
CFYS	687	4	14.0	373	1.22	0.35	0.66	0.0720
DFYS	739	9	18.0	434	1.66	0.63	2.20	0.0940
EFYS	973	4	14.3	604	1.69	1.52	3.77	0.1080

**Table 2.** The firm declaration values of AFYS, BFYS, CFYS, DFYS, EFYS plaster type and the findings obtained in the study.

Insulating plaster	Plaster Type	$\lambda_{10}$ -dry (W/m.K)	fc (MPa)	C (kg/m2dak0.5)
AFYS	Declaration Value	$\leq 0.040$	0.4-2.5	$\leq 0.40$
	Measurement findings	0.078	1.77	0.48
BFYS	Declaration Value	$\leq 0.10$	0.4-2.5	$\leq 0.40$
	Measurement findings	0.125	3.25	0.261
CFYS	Declaration Value	$\leq 0.067$	0.4-2.5	$\leq 0.40$
	Measurement findings	0.072	0.66	1.22
DFYS	Declaration Value	$\leq 0.10$	1.5-5	$\leq 0.40$
	Measurement findings	0.094	2.20	1.66
EFYS	Declaration Value	$\leq 0.10$	0.4-2.5	$\leq 0.40$
	Measurement findings	0.108	3.77	1.69

**Table 3.** The energy loss values of the wall sections and the saving rates according to the traditional plastered walls.

Plaster Type	Energy loss (W/m <sup>2</sup> )	Saving (%)
Traditional plaster	24.31	-
EPS	8.07	48
AFYS	9.42	61
BFYS	12.83	47
CFYS	8.76	64
DFYS	11.03	55
EFYS	11.68	52

### 3. CONCLUSION

When the results were evaluated, it was determined that the thermal conductivity coefficient, compressive strength and flexure strength increased in proportion to the unit mass. In addition, it has been determined that the compressive strength value increases with the flexure strength value. When the obtained data were evaluated, it was observed that a significant portion of the insulating plasters did not meet the firm declaration values.

**Tablo 4.** Measured and declared values of energy loss and saving (%) values

Plaster Type	Energy loss (W/m <sup>2</sup> )	Saving (%)
A Company	9.42	61
A Company(Declaration Value)	5.78	76
B Company	12.83	47
B Company (Declaration Value)	11.03	55
C Company	8.76	64
C Company (Declaration Value)	8.49	65
D Company	11.03	55
D Company (Declaration Value)	11.03	55
E Company	11.68	52

For this reason, more frequent checks should be done and audits should be increased when issuing certificates of approval to firms. In this way, the quality of the products marketed by the companies will be increased, the new generation of energy-saving environmental products will be delivered to the user.

In recent years, the increase in heat insulation awareness, energy saving, environmental pollution has brought mobility to the insulation sector. This mobility led to the emergence of new insulation materials and application techniques. In our country where perlite reserve is abundant, thermal insulation products should be intensified by AR-GE studies and contribution should be made to the development of alternative products which are more environmentally friendly and energy saving. More sustainable building insulation can be made with the use of these environmental friendly thermal insulation products that provide energy saving close to EPS jacketing.

## REFERENCES

- [1] A.N., Sürmeli, Energy Audit - Insulation Congress and Exhibition for Sustainable Environment, İstanbul, October, Proceedings Book, p.187, 2004.
- [2] F. N., Değirmenci, Preservation of Adobe By A Pozzalanite Plaster, PhD Thesis, Dokuz Eylül University, İzmir, 1998.
- [3] H., Akgöz, Thermal and Economical Analysis of Wall Elements for Thermal Insulation in Reinforced Concrete Buildings. Namık Kemal University, Department of Civil Engineering, MSc Thesis, 129s, Tekirdağ, 2009.
- [4] A. Çolakoğlu, Investigation of Thermal Insulation External Plaster Feasibility in Buildings, M.Sc. Thesis, Süleyman Demirel University, Isparta, 2004.
- [5] M., Davraz, Ş., Kılınçarslan, The Effect of Perlite Aggregated Plasters on Energy Saving in Buildings, II. International Davraz Symposium, 29-31 May 2014, Isparta, 2014.
- [6] Y. Erbil, Analyzing water and heat isolation problems in mass housing which is produced by tunnel shuttering, M.Sc. Thesis, Uludağ University, 2003.
- [7] K., Çomaklı, B., Yüksel, Optimizing Insulation Thickness of External Walls for Energy Saving. Applied Thermal Engineering, 23, 473-479, 2003.
- [8] A., Hasan, Optimizing Insulation Thickness for Buildings Using Life Cycle Cost". Applied Energy; (63): 115-124, 1999.

# Investigation of the Effect of Fly Ash And Perlite on Foam Concrete Properties

<sup>1</sup>Şemsettin Kılınçarslan, <sup>1</sup>Metin Davraz, <sup>2</sup>Nuri Işıldar

<sup>1</sup> Suleyman Demirel University/Natural And Industrial Building Materials Research Application Center, Isparta, TURKEY

<sup>2</sup> Suleyman Demirel University/Graduate School of Natural and Applied Sciences, Isparta, TURKEY

\*semsettinkilincarslan@sdu.edu.tr

## ABSTRACT

While the demand for building for the use of housing, workplace and other purposes caused by the increasing population all over the world increased day by day, studies for improving some of these qualities continue. Among these, the first order, especially in cold climates, is due to the fact that the energy cost and the usage prices are quite high, thus increasing the importance of heat insulation.

Foam concrete, its component types and combinations show great variability, especially the development of strength and thermal insulation properties will continue to occupy the agenda of today and near future. The aim of this study is; perlite applications on concrete drying shrinkage and some mechanical properties under conditions of constant water-binder ratio (0.45) and different levels of foam agent (350, 500 and 650 kg/m<sup>3</sup>). It is determined that the perlite is the most effective component in terms of the expansion rates of 28 days and that the smallest percent shrinkage obtained on the 151st day is specific to this component. The level of foam agent played the main determinant role on the pressure and splitting tensile strengths along with the dry density.

**KEYWORDS:** *lightweight concrete, foam concrete, perlite, fly ash, foam agent*

## 1. INTRODUCTION

Worldwide, there is an increasing demand for qualified buildings developed for different uses. High thermal insulation, depression resistance, light weight and low cost are among the required features for such buildings. As a matter of fact, efforts are being made to ensure that the loads exposed to the buildings are low and the strength to the load is high. This and other similar structural and functional properties are tried to be shaped depending on the purpose of use, either by changing the contribution rates of existing materials or by experimenting with new types of materials continuously. One of the most studied concrete types in this context is foam concrete, which is included in lightweight concrete. Foam concretes developed at different densities are known to be used for filling bridges, roof insulation, underpass and wall construction and similar applications [1].

One of the most frequently studied of the foam concrete components is fly ash, a waste material. The friendliness of this material and its ability to reduce costs lead to [2], its attractiveness in research. Likewise, the reaction of fly ash with calcium hydroxide in an aqueous environment is end-binding, in other words, it exhibits pozzolanic properties. It can be used instead of cement at high levels. Another component of high potency from the other side is expanded perlite [3]. Chemical stability, filling material properties that reduce mixture density, heat and sound insulator functioning and burn-off delay make it more valuable among additive materials. It is estimated that for the expanded perlite, binders derived from sodium-silicate, sodium-hydroxide, potassium-silicate, potassium-hydroxide or mixtures thereof used in the range of 2.5-15% by volume should provide a relatively low value of the heat conductivity of the concrete and a relatively high mechanical strength value. The heat transfer coefficient of the material is lower than the value of 0.065 W mK<sup>-1</sup>, which should be in the context of the TS 825 Standard of Building Thermal Insulation Rules. Another issue which is very important for this material available perlite reserves

in Turkey, forming 74% of the entire world and says it can be converted to the added value of it [4].

Some studies on the use of expanded perlite instead of sand at the water-cement ratio stability in mortar mixtures; concrete strength and thermal conductivity [5]. Which uses expanded perlite as well as some other aggregates, examined the change of compressive strength when the binder ratio was kept constant at 200 kg m<sup>-3</sup> and silica fume and C-class fly ash were added at 10, 20 and 30% levels of cement. It has been reported that the use of perlite at 20, 40 and 60% instead of pumice increases the pressure strength of 28 days and also the pressure resistance is decreased for all fly ash fractions instead of pumice [6]. On the other hand, Yang et al. [7] stated that lightweight aggregate segregation has an important place in research on lightweight aggregate concrete, and that this problem can be solved with fly ash, high performance additives, pre-wetted expanded perlite addition and some other technical applications. At the same conditions, the porosity and permeability properties of pre-wetted and un-wetted aggregate concrete at light weight were compared and found to be 4.6 times as porous as those pre-wetted.

It is observed that in concrete mortars, the potential for different designs to be realized is very high, in terms of the applicability of many components, the maintenance of water-binding or dry density. Therefore, in this study, it was aimed to determine the effects of expanded perlite and fly ash, especially on drying rust and other concrete properties, when the water-binder ratio is kept constant.

## 2. MATERIALS AND METHOD

To determine the effect of foam usage at different levels ( 650, 500, 350 dm<sup>3</sup>/m<sup>3</sup>) in the study, the perlite (PLT), fly ash (FA), and control application (FC) component quantities required for unit volume (1 m<sup>3</sup>) mortar mixtures, with a constant water-binder ratio (0.45) are designed as shown in the Table 1. In this scope; Portland cement, a product of Turkey Isparta Göltaş Cement Company (EN 197-1 CEM I 42.5 R), and extremely fine-sized waste flue ash, a product of Turkey-Manisa Soma Thermal Power Plant, and perlite, a product of Türkiye- Mersin Perlite Mining Company, and a synthetic foam agent (Contopp, Foam Builder SFS3, Knopp GmbH) were also used. Suleyman Demirel University West Campus tap water was used for all other operations required with concrete mortars and foam preparation.

The components for the designed mortar mixtures were mixed by using a mixer for about 3-5 minutes, followed by addition of foam and stirring for another 2-3 minutes. The concrete

**Table 1.** Components of a unit volume (1 m<sup>3</sup>) mortar mixture at constant water-binder ratio and at different levels of foam use.

Water-Binder Ratio= 0.45					
Applications	Cement (kg)	Water (kg)	Perlite (kg)	Fly Ash (kg)	Foam (dm <sup>3</sup> )
PLT1	317	142.65	21	-	650
PLT2	317	142.65	51	-	500
PLT3	317	142.65	81	-	350
FA1	408	202.10	-	41.11	650
FA2	530	286.08	-	105.73	500
FA3	631	369	-	189.01	350
FC1	454	204.49	-	-	650
FC2	649	291.99	-	-	500
FC3	845	379.17	-	-	350

**Table 2. Properties of Portland cement for Isparta Göltaş Cement Company [8].**

Chemical Properties of Clinker (%)		Physical Properties of Cement	
SiO <sub>2</sub>	20.52	Volumetric expansion (mm)	≤1
Al <sub>2</sub> O <sub>3</sub>	4.00	Fine (90 μ, %)	0.10
Fe <sub>2</sub> O <sub>3</sub>	3.45	Fine (200 μ, %)	1.10
CaO	64.28	Specific Surface Area (cm <sup>2</sup> /g)	3340
MgO	1.63	Start of Outlet (min)	185
SO <sub>3</sub>	2.53	Outlet Finish (min)	240
Na <sub>2</sub> O+K <sub>2</sub> O	1.35	Density (g/cm <sup>3</sup> )	3.12
Mechanical Properties of Cement (MPa)			
7 day Flexural Strength		5.8	Compressive Strength
28 day Flexural Strength		7.2	Compressive Strength
			39.3
			51.0

test specimens were removed from the molds 24 hours after the prepared mixtures were placed in the sample molds. In this scope; for each concrete mortar mixture; Four specimens of 25x 25x 285 mm specimens were subjected to initial size measurements after removal from the molds and kept at 95% relative humidity until the 28th day.

Time-length change relations were obtained by using the length measurements made at intervals of 7 days to day 35th and of 14 days to day 91th, and later 1 months intervals. The test procedure was carried out according to the principles specified in the ASTM C-596-01 [9] standard. Dry densities, in accordance with the principles specified in the TS EN-678 [10] TSE standard; the mass determined by the sensitive scale is determined by the volume fraction found by measuring the sample size with the electronic caliper.

Determination of the splitting tensile strength at the beam was made on the basis of TS EN 12390-6 [11] standard on 3 cubic samples of 15x 15x 15 cm. Splitting tensile strength was determined using the following equation.

$$F_{ct} = \frac{2F}{\pi dh} \quad (1)$$

In equation; F<sub>ct</sub> is the maximum load (N), h is the contact length of the sample in mm (mm), d is the selected cross-sectional dimension (mm) of the samples, in MPa or N/mm<sup>2</sup>.

The compressive strength test on 6 cubic samples of 10x 10x 10 cm was carried out under the conditions specified in the TS EN 1354 [12] standard using a uniaxial pressure testing device at a loading speed of 2400 N/s. Compressive strength was determined using the following equation.

$$F_c = \frac{F}{A_c} \quad (2)$$

In equation: F<sub>c</sub> is the compressive strength (MPa), F is the fracture load (N), A<sub>c</sub> is the cross-sectional area (mm<sup>2</sup>) of the sample in the load direction.

### 3. RESULTS AND DISCUSSION

#### 3.1. Actual dry density, Compressive Strength and Splitting Tensile Strength

The results of the effects of PLT, FA and FC use on the actual dry density, compressive strength and splitting tensile strength in the shrinkage of the concrete mortar mixtures where the water-binder ratio is kept constant at 0.45 and the foam level is reduced are given in Table 3. As a result of the increase in PLT application level, it was evaluated that the actual level of foam density, which is very low compared to other FA and FC applications and which varies in the range of 382-979 kg/m<sup>3</sup>, is the main determining factor. It has been determined that this is caused by decreased porosity. Likewise, in FA practice it has been determined that the fly ash in approximate quantities

containing cement quantities in the FC application does not cause a significant change in the actual density.

The relationship between true dry density and compressive strength values is the polynomial character (Figure 1). For increased application levels of PLT, FA and FC, the reduction of the foam ratio increased the dry density and thus the pressure resistance. Visagie [13] also reported that the dry density of foam concrete is dependent on the percentage of added foam, and Kearsley [14] and Zakaria [15] stated that the dry density has an effect on the compressive strength.

**Table 3.** Concrete dry density, compressive strength and splitting tensile strength changes at different levels of mortar mixture components.

Applications	Dry Density (kg/m <sup>3</sup> )	Compressive Strength (MPa)	Splitting Tensile Strength (MPa)
PLT1	382	0.347	0.047
PLT2	425	0.396	0.048
PLT3	500	0.896	0.097
FA1	534	1.150	0.110
FA2	705	2.727	0.330
FA3	916	6.964	0.350
FC1	489	1.896	0.131
FC2	676	3.187	0.288
FC3	979	8.675	0.578

In this study, the reduction of the foam ratio from 650 dm<sup>3</sup> to 350 dm<sup>3</sup> caused the pressure resistance values to be clearly high, especially for PLT3, FA3 and FC3 applications. For FA applications, obtaining lower but nearer strength values than FC applications was supported by the finding that high amounts of ash in the foam concrete mortar mixture resulted in an increase in the time required to reach the final strength [2].

The splitting tensile strength values of the specimens were found to be 0.097 MPa for PLT applications, 0.350 MPa for FA applications and 0.578 MPa for FC applications. It has been determined that the changes in the splitting tensile strength values at the spandex are largely related to the foam ratio, similar to the compressive strength at PLT, FA and FC application levels. The most obvious example of this is the compressive strength values obtained for FC application levels.

Although it is accepted that lightweight concrete containing expanded perlite is influenced by the mixture density, especially compressive strength and modulus of elasticity, mechanical strength is decreased, it is also important to contribute to the absorption of external shocks with local breaks [16].

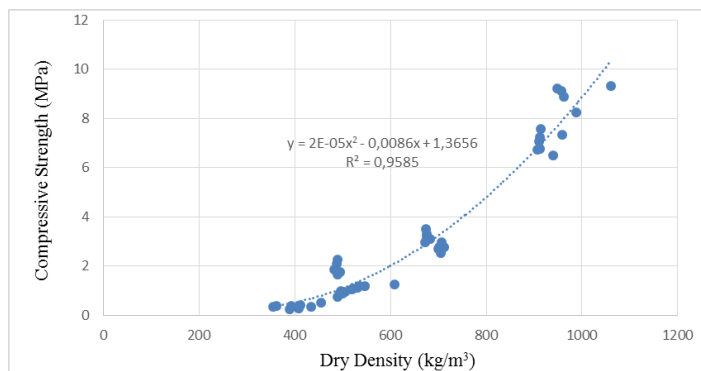


**Figure 1.** Relationship between true dry density and compressive strength.

### 3.2. Drying Shrinkage

In FC applications, the highest expansion rate caused by curing due to the first 28-day determinations is 0.038%. It has been determined that the expansion of the FC application to the 7th day and the subsequent change is very small (Figure 2).

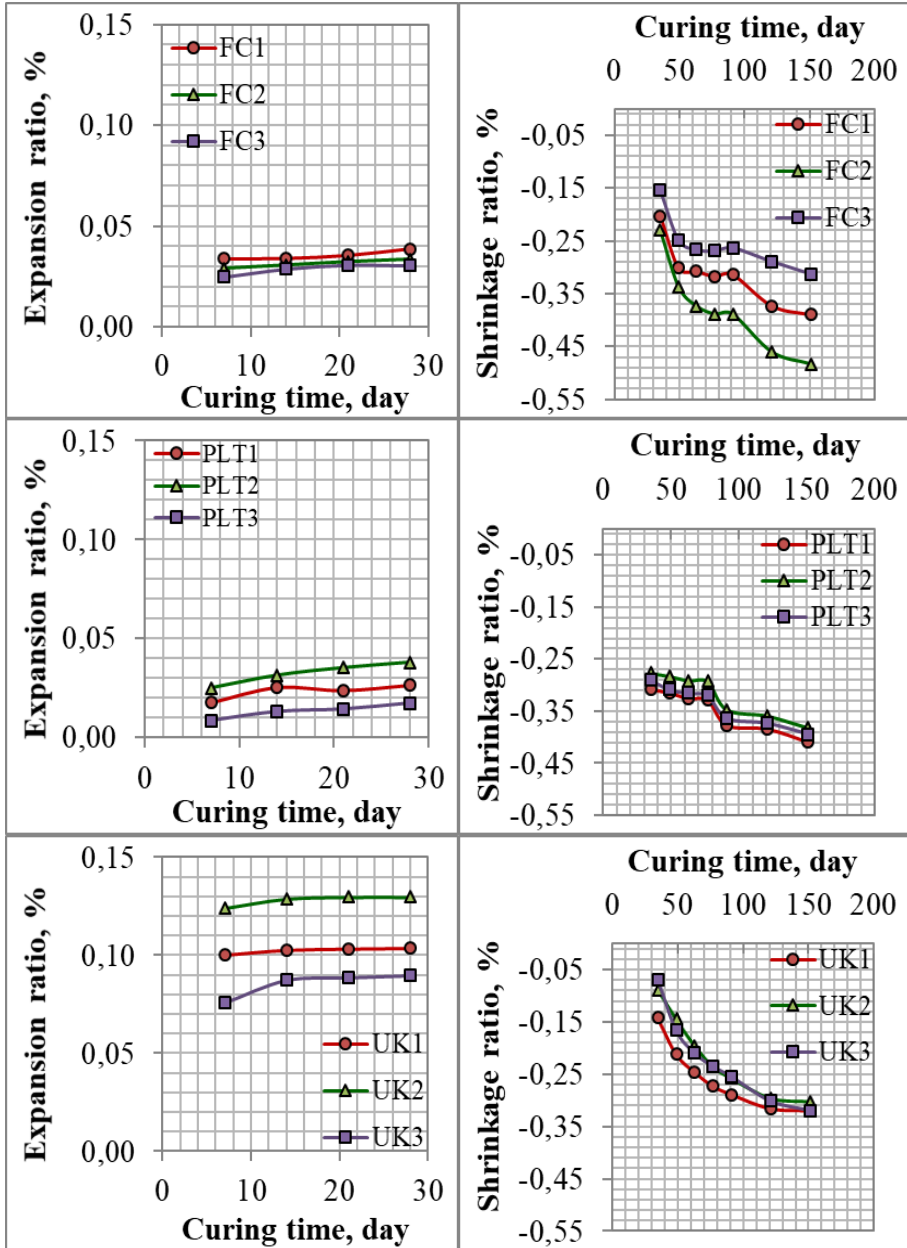


Figure 2. Effect of water-binder ratio of 0.45 and on the expansion and shrinkage ratios of PLT and FA use under reducing foam application conditions.

The relationship between PLT and FA application levels and the change in expansion (PLT2> PLT1> PLT3 and FA2> FA1> FA3), although similar, was found to vary in magnitude of expansion.

As of day 7 of curing, the amount of expansion in PLT applications ranged from 0.0085 to 0.025% and in FA applications ranged from 0.07 to 0.12%. As of the 28th day, the expansion ratios were 0.017 - 0.038% for PLT applications and 0.089 - 0.129% for FA applications. Fly ash has been found to cause more expansion in a shorter time than PLT and FC applications.

As a matter of fact, Kearsley and Wainwright [17] reported that the volume (kg/m<sup>3</sup>) of water absorbed by foamed concrete obtained by using ash at 75% of the cement in the mixture is about twice that of the same water-binding fraction containing no ash. The ash content used in this study is not so high but it is increasing the water absorption. Likewise, fly ash gave the highest expansion values for all three foam levels, with a 28-day expansion rate for PLT, FA and FC applications using the same level of foam.

The effect of the PLT and FA use on the 28 to 151 day shrinkage rate of the mortar mixture water-to-binder ratio is kept constant at 0.45 and under reduced foam application conditions is shown in Figure 3. For PLT, FA and FC applications, the changes in shrinkage rates from day 28 to day 151 differed. The final shrinkage ratios on day 151 were found to be the lowest in the FA for application levels of 650 and 350 dm<sup>3</sup> foam.

When the shrinkage ratios of 28 to 151 days in PLT, FA and FC applications using the same level of foam are examined, it has been assessed that FA applications for all levels of foam use give lower shrinkage values than the other PLT and FC applications and that the variation of the shrinkage ratios over time for that component may be explained by polynomial function.

#### 4. CONCLUSION

If the water-binder ratio is kept constant at 0.45 and the amount of foam is gradually reduced; While the PLT does not make a significant difference in FC compared to the 28-day expansion ratios in the samples used, the FA increases the expansion in the used samples to about 3 times. Most of the expansion in all applications occurred in the first 7 days. The shrinkage change ratios of 28 - 151 day intervals were determined as 0.13, 0.22 and 0.19 for PLT, FA and FC, respectively. For the 650 and 350 dm<sup>3</sup> foam application levels, the 151 day shrinkage ratios were obtained at the lowest values in FA-used samples.

#### REFERENCES

- [1] Jalal M.D., Tanveer, A., Jagdeesh, K and Ahmed, F. 2017. Foam Concrete. International Journal of Civil Engineering Research. Volume 8, Number 1, pp. 1-14.
- [2] Kearsley, E.P., Wainwright, P.J., 2001a. Porosity and Permeability of Foamed Concrete. Cement and Concrete Research 31: 805- 812.
- [3] Chen, X., Yan, Y., Liu, Y., Hu, Z., 2014. Utilization of Circulating Fluidized Bed Fly Ash for the Preparation of Foam Concrete. Construction and Building Materials. 54: 137-146.
- [4] Uluer, O., Karaağaç, İ., Aktaş, M., Durmuş, G., Ağbulut, Ü., Khanlari, A., Çelik, D. N., 2018. Genleştirilmiş perlitin ısı yalıtım teknolojilerinde kullanılabilirliğinin incelenmesi. Pamukkale University Journal of Engineering Sciences, 24(1).
- [5] Şengül, O., Azizi, S., Karaosmanoglu, F., & Tasdemir, M. A. (2011). Effect of expanded perlite on the mechanical properties and thermal conductivity of lightweight concrete. Energy and Buildings, 43(2-3), 671-676.



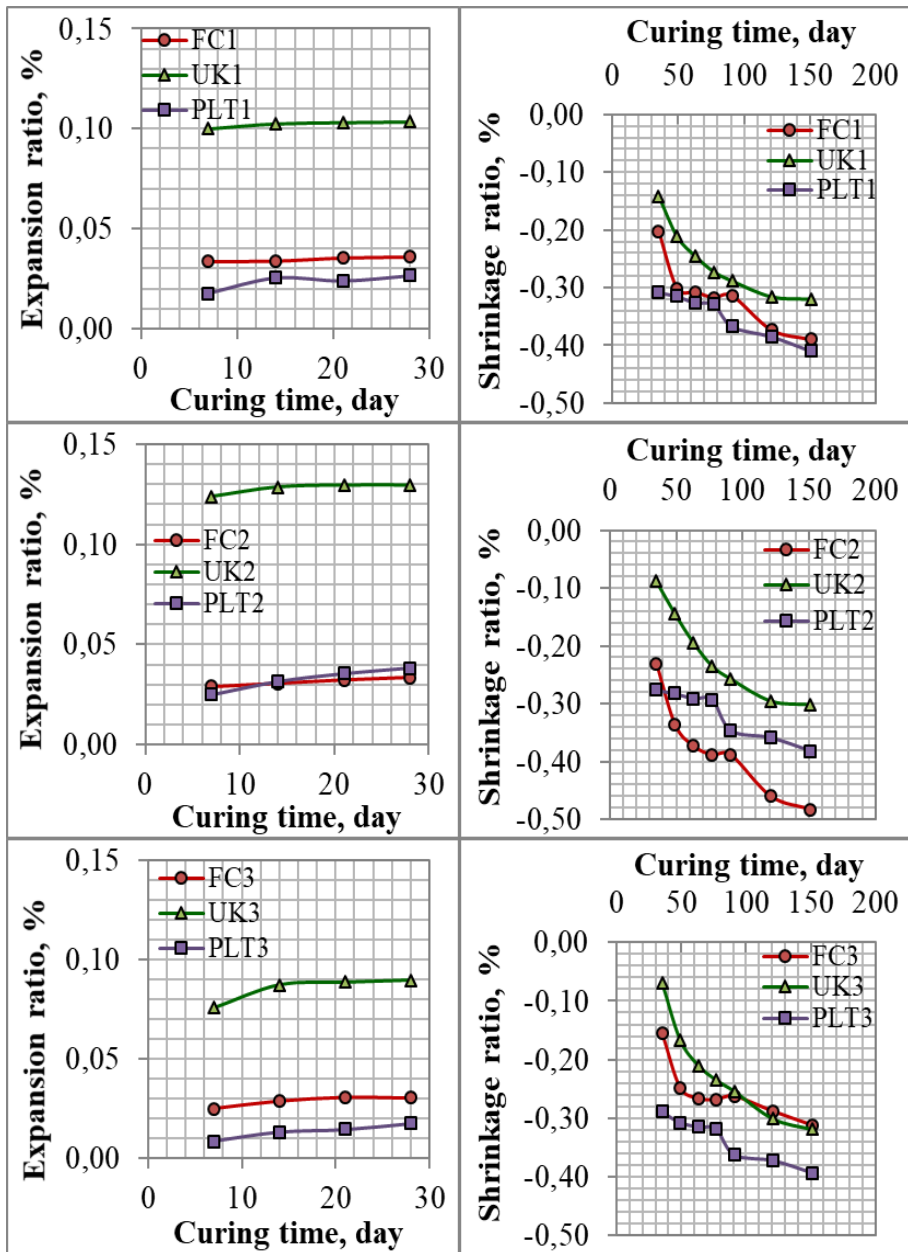


**Figure 3.** Expansion and shrinkage ratios of PLT, FA and FC applications using the same level of foam.

- [6] Demirboğa, R., Örüng, İ., Gül, R., 2001. Effects of expanded perlite aggregate and mineral admixtures on the compressive strength of low-density concretes. *Cement and Concrete Research*, 31(11), 1627-1632.
- [7] Yang, P., Zhao, W., Yang, J., Liu, L., Cao, M., 2014. Research on homogeneity of expanded perlite lightweight concrete, *Key Engineering Materials*, 99: 74- 77.
- [8] Göltaş, 2017. Isparta Göltaş Çimento A.Ş., Portland Cement Standard Pack.

- 
- [9] ASTM C596-01,2001. Standard Test Method for Drying Shrinkage of Mortar Containing Hydraulic Cement, ASTM International, West Conshohocken, PA, [www.astm.org](http://www.astm.org)
- [10] TSE, 1995. TS EN 678 Gaz ve Köpük Beton- Kuru Yoğunluk Tayini.
- [11] TSE, 2002, TS EN 12390-6 Beton-Sertleşmiş Beton Deneyleri- Bölüm 6: Deney Numunelerinin Yarmada Çekme Dayanımının Tayini.
- [12] TSE, 2007. TS EN 1354 Gözenekli Hafif Beton- Basınç Dayanımının Tayini.
- [13] Visagie, M., 2000. The Effect of Microstructure on the Properties of Foamed Concrete. Master Thesis. <https://repository.up.ac.za/dspace/bitstream/handle/2263/23075/dissertation.pdf?sequence=1>. Erişim Tarihi: 04.09.2017.
- [14] Kearsley, E.P., 1999. The Effect of High Volumes of Ungraded Fly Ash on the Properties of Foamed Concrete. PhD thesis. The University of Leeds. [http://etheses.whiterose.ac.uk/287/1/uk\\_bl\\_ethos\\_289789.pdf](http://etheses.whiterose.ac.uk/287/1/uk_bl_ethos_289789.pdf). Erişim Tarihi: 05.09.2017.
- [15] Zakaria, Z.Bin., 2010. Shrinkage Deformation of Different Shape of Foamed Concrete Specimen. Other thesis. [http://umpir.ump.edu.my/2610/1/ZUHAIRI\\_BIN\\_ZAKARIA](http://umpir.ump.edu.my/2610/1/ZUHAIRI_BIN_ZAKARIA). PDF. Erişim Tarihi: 06.09.2017.(Abstract).
- [16] Kramar, D., Bindiganavile, V., 2011. Mechanical properties and size effects in lightweight mortars containing expanded perlite aggregate. *Materials and Structures*, 44(4), 735-748.
- [17] Kearsley, E.P., Wainwright, P.J., 2001b. The Effect of High Fly Ash Content on the Compressive Strength of Foamed Concrete. *Cement and Concrete Research* 31: 105- 112.

## Experimental Investigation on Perforation Temporary Plugging by Degradable Materials in Multi-Fracturing

Yang zhang<sup>1</sup>, Wei Feng<sup>2\*</sup>, Zhongnan Jiang<sup>1</sup>, Chen Yang<sup>2</sup>, Wentong Fan<sup>1</sup>, Lufeng Zhang<sup>3</sup>, Jin Wang<sup>3</sup>, Yuechun Wang<sup>3</sup>

1. Tarim Oilfield PetroChina, Korla, Xinjiang, CHINA

2. College of Petroleum Engineering, China University of Petroleum (Beijing), CHINA

3. The Unconventional Natural Gas Institute, China University of Petroleum (Beijing), CHINA

\*fengw\_rsc\_cup@163.com

### ABSTRACT

Multi-fracturing is injecting treatment slurry from the same or new perforations to achieve enhanced and stable production in oil and gas reservoirs. Degradable fibers and particulates are common and effective in refracturing stimulations. The perforated clusters, not contributing to production, could be stimulated by temporary plugging effective perforation clusters. However, it is still unclear how the plugging is formed in perforation tunnel. In this paper, a simulation experiment system was built to observe the behavior of degradable materials in perforation tunnel. By a series of plugging experiments, it was found that by “bridging and plugging” the temporary plugging agents could effectively block the perforations. The plugging process is that temporary plugging ball firstly seals the perforation, then the particulates and fibers can further accumulate on the ball. And materials can form effective plugging because it is deformable and expandable. The plugging strength can be up to 4350psi. Besides, the injection sequence of particulates and fibers has little effect on the plugging time and pressure. However, the forming speed of temporary plugging increase with injection rate. The research results would provide a significant insight into the refracturing technology and the guideline for its successful application in unconventional reservoirs.

**KEYWORDS** – Multi-fracturing1, Perforation plugging2, Degradable materials3.

### 1. INTRODUCTION

Multi-fracturing in heterogeneous reservoir is an indispensable method to achieve enhanced production in unconventional reservoirs<sup>1-3</sup>. The core of this technology is efficiently plugging the high-permeability perforation, and applying diverters is regarded as a more promising approach because of its convenience and availability. Degradable fibers and particulates are common and effective as diverter materials, which can plug perforation and self-degrade at the formation temperature<sup>4-7</sup>.

To clarify the process that plugged zone formed in the perforation, an ocean of researches were conducted experimentally. Kastrop<sup>8</sup> first introduced that the seal ball can be used to well stimulation in petroleum engineering. Erbstoesser<sup>9</sup> performed a series of experiments using different density ball and found that high-density ball had better plugging efficiency in low speed flow. M.Nozaiki<sup>10</sup> set up lots of experiment using a device from BP and showed that the property of ball had more impact on plugging efficiency than injection rate. Li<sup>11</sup> built an experiment system that can simulate plugging process in three conditions, and evaluated the influence of injection rate and the number of balls. Wang<sup>12</sup> and Desai<sup>13</sup> confirmed the feasibility of plugging by field application.

In this paper, a simulation experiment system was established to observe the dynamic plugging performance of fibers and particulates in the perforation. Based on the experimental results, the synergic plugging mechanism by degradable materials in perforation was analyzed.

### 2. METHODOLOGY

## 2.1. Carrying fluid

The carrying fluid used for carrying the plugging materials contains approximately 0.3 wt% hydroxypropyl guar, 0.02% wt% citric acid, 0.15 wt% cross-linker regulator, 0.2 wt% cross-linker and other additives. In all laboratory tests of this study, the identical formulation as used in the field is applied to prepare the mimicked fracturing fluid for evaluating the degradable materials. Its viscosity is approximately 300 mPa·s at a shear rate of  $100 \text{ s}^{-1}$  at  $20^\circ\text{C}$ .

## 2.2. Degradable materials

The similar type of degradable materials composed of fibers, particulates and balls as used for plugging-diverting fracturing are chosen to reveal the plugging rule in the perforation in this study. These materials are a copolymer of lactic acid with glycolic acid and insoluble in water and oil. Depending on the reservoir temperature, its molecular weight can be tuned by the synthesis time, which in turn changes the degradability. The length and cross-section diameter of the fiber is 6mm and  $8\text{-}12\mu\text{m}$  separately, while the diameters of particulates and balls are 1-3mm and 10-12mm separately.



**Figure 1.** The degradable fibers (left) and particulates (right)

## 2.3. Equipment

In order to observe the behavior of degradable fibers and particulates in perforation tunnel, a simulation experiment system, composing of a mimicked perforation geometry model, a high-pressure holder, an ISCO pump, two differential pressure gauges, and a PC data acquisition system, was built as shown in Figure. Fibers and particulates are mixed with carrying fluid at certain concentration to form the treatment slurry. The slurry is injected into a mimicked perforation model by an ISCO pump. The electromagnetic flowmeters and pressure sensors are installed at the inlet and outlet of the perforation to record the flow rate and pressure. The effluent slurry flows into the recovery container, where the materials are filtered out for subsequent experiments. Relief valves are installed to ensure the safety.

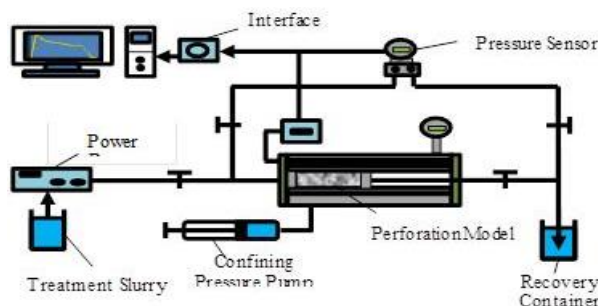


**Figure 2.** The flow diagram of experimental system

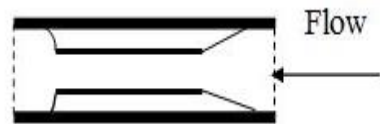


**Figure 3.** The diagrammatic sketch of perforation

Figure 2 shows the photo of experimental system. The volume of the treatment slurry is  $2\text{m}^3$  and the maximum pump rate of ISCO pump is 100 ml/min. The holder that the perforation model is

placed in is cylinder and its maximum pressure-bearing is 50MPa, the length and radius is 0.4m and 0.1m separately. The diagrammatic sketch of the perforation is shown in Figure 3, the width is designed corresponding experimental program, which can set to 6,8,10 and 12mm. The inlet shape of perforation is wedge-shaped, which would benefit the ball seal.

## 2.4. Evaluation indexes

To achieve the optimal effect of temporary plugging in perforation in deep reservoir, three key indexes for the temporary plugging technology are proposed in this paper. In order of importance degree, there are maximum plugging pressure, total slurry volume and total materials quantities.

## 3. RESULTS AND DISCUSSION

### 3.1. Selection standard for ball

Before evaluating the performance of ball on seating perforation, the selection standard for ball is firstly conducted to ensure the chosen size of ball can plugging the perforation and is the optimization. Considering a typical field case during perforating operations, the perforation width is regarded as 10 mm to research the selection standard. 13 groups of typical experiments are performed with parameters as detailed in Table 1. The plugged zones were not formed in the Group 1-7, and maximum pressure was below 1MPa (as shown in Figure 4). The pressure had a fluctuation during the plugging process, and the materials flowed out with the carrying fluid. In the process of plugged zone was formed, it is subject to the well pressure and flow pressure. Due to deformability and expandability, Internal extrusion between the plugging materials caused the failure of the formed zone.

**Table 1.** Different combinations and concentrations for 13 groups

Experiment Group No.	Ball Size (mm)	Ball Concentration	Imm Particulates Concentration	Fiber Concentration
1	6	1%	0	0.5%
2	6	2%	0	1%
3	6	3%	0	1.5%
4	8	1%	0	1%
5	8	2%	0	1.5%
6	8	3%	0	0.5%
7	10	single	0	1%
8	10	single	1%	1%
9	10	single	0.5%	1%
10	10	single	0.5%	0.5%
11	10	single	0.3%	0.5%
12	10	single	0.3%	0.3%
13	10	single	0.3%	0.4%

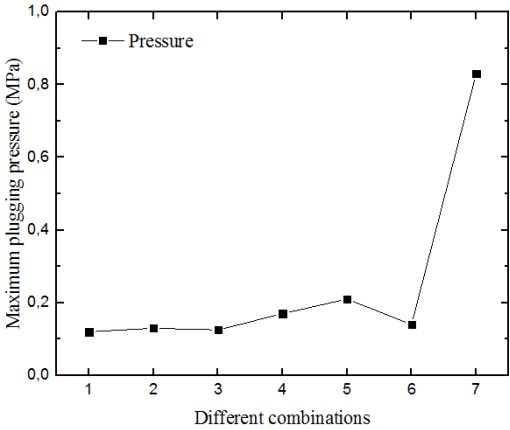


**Figure 4.** Pressure during the plugging process in Group 1-7

As shown in Figure 5 (a), the ball which diameter less than that of perforation was easier be swept under the lower pressure, and the particulates and fibers could not form the zone independent because of great width. After the equal-diameter ball sealed, if the margin of zone was unstable, it is easy to be discharged (b). In order that the plugged zone could be formed easier, the equal-diameter ball was used as the standard and the 1mm particulates and fiber were used as accessory materials.

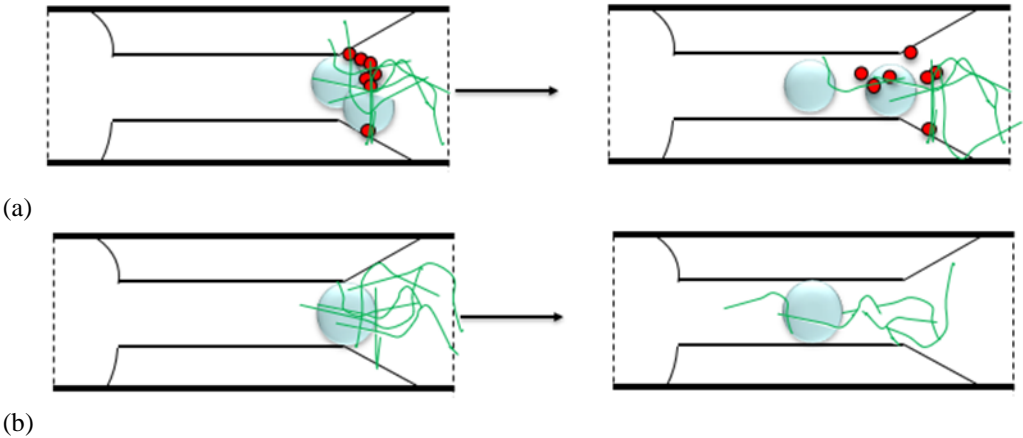


**Figure 5.** Schematic of failure of plugged zone

**3.2. Optimized combination of materials**

For economy maximization, the optimized combination experiments were carried out. The evaluation indexes were introduced in 2.4 and the combination detail of group 7-13 were shown in Table 1. Plugging strength reaching 4350psi was used as the standard for that the plugged zone was formed. The plugged zone were not formed in group 12 and 13 because of failure. Contrast the group 8-11, the time and materials (1mm particulates and fibers) quantities before plugged zone formed were shown in Figure 6. The combination of group 11 were selected as the optimal materials for plugging 10mm-diamater perforation by comprehensive consideration, though it spent the most time.

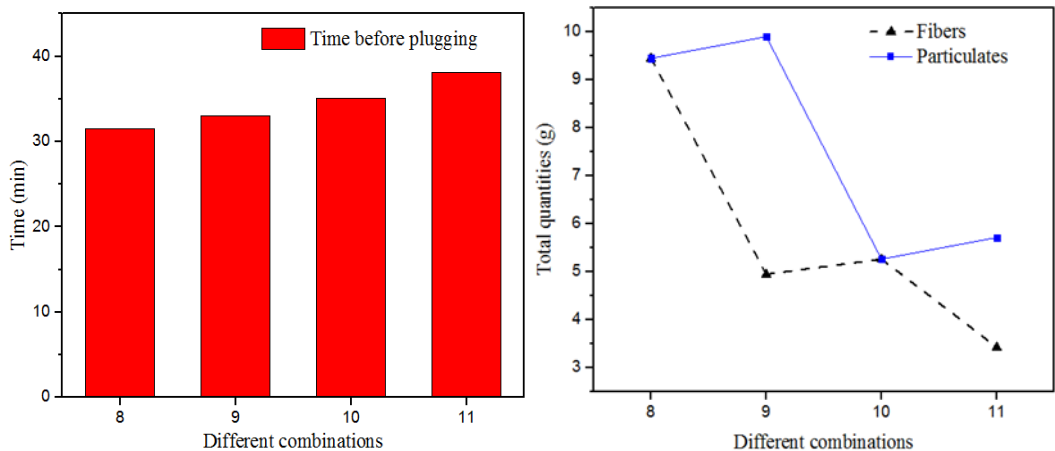


**Figure 6.** Time and quantities of different combinations before plugged zone formed

### 3.3. Plugging parameter analysis

#### a) Impact of injection rate in plugging

One of the main treatment parameters that could be adjusted to form plugged zone was injection rate. For the plugging process, the faster of injection rate, the more probable of contact between materials in the flow. On the other hand, the collision between materials was more intense with the increase of rate. With the limit of lab condition, displacement ranging from 20 to 30 ml/min (20, 25, 30) was set in the experimental group (1-3) are listed in Table 2, and the combination of group 11 was used as the experimental materials. Figure 7 (a) showed that the time of forming plugged zone changes with rates, and for a particular material combination, high-rate had greatly improved the efficiency of plugging.

*Table 2. Different rate for 3 groups*

Experiment Group No.	Experimental materials	Injection rate (ml/min)
1	optional combination	30
2	optional combination	25
3	optional combination	20

#### b) influence of perforation size on plugging

To figure out the size of the perforation on the plugging effect, three groups experiments were set up and the detail was listed in Table 3. The same injection flow rate (30 ml/min) was used in experiments, and the pressure was shown in Figure 8. It was found that the plugged zone was not formed in group 2 using the combination of group 1 that could plug the 10mm perforation. To plugging the 12mm perforation, the equal diameter ball was selected as the seal particulate, and the plugged zone was formed at approximately 31 mins.

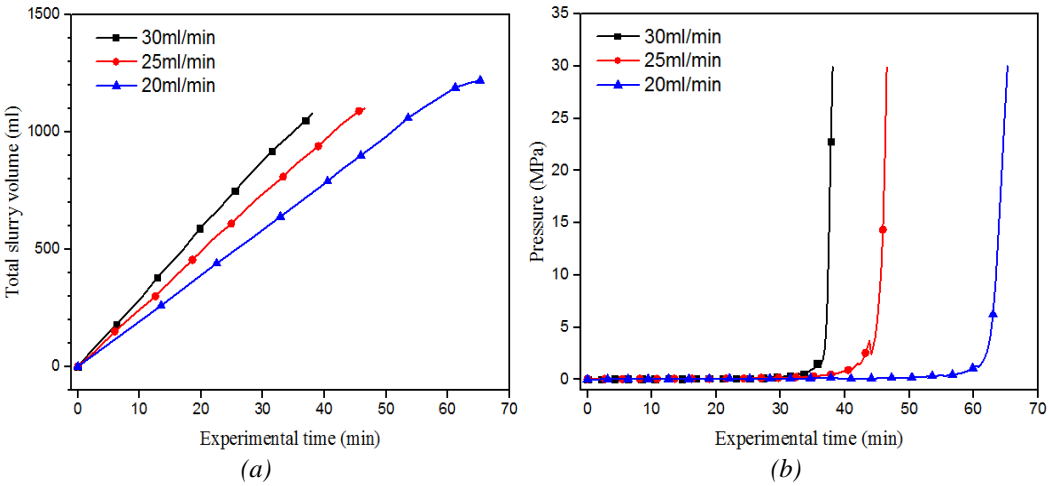


Figure 7. Slurry volume (a) and pressure (b) of different rate

Table 3. Different combination for 3 groups

Experiment Group No.	Perforation Size (mm)	Ball Size (mm)	1mm Particulates Concentration	Fiber Concentration
1	10	10	0.5%	0.5%
2	12	10	0.5%	0.5%
3	12	12	0.5%	0.5%

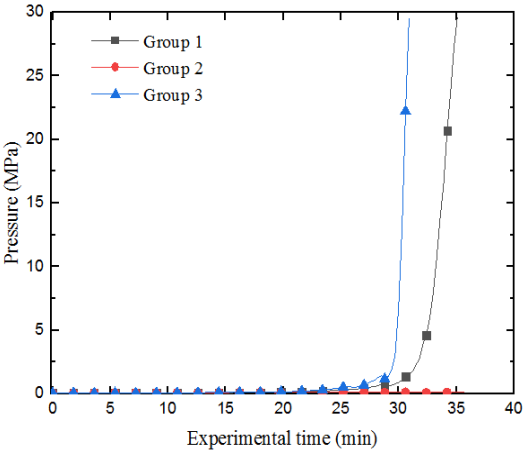


Figure 8. Pressure of different combination

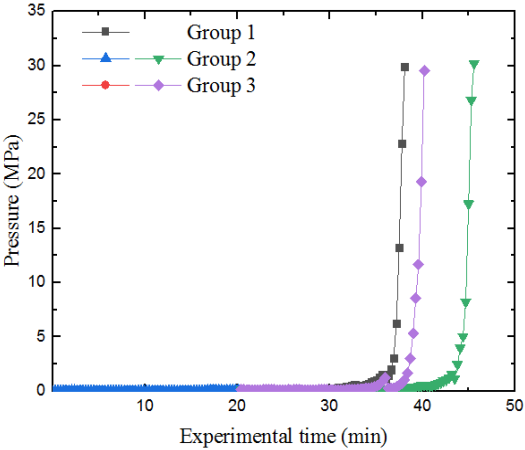


Figure 9. Pressure of different injection sequence

3.4. Plugging mechanism in perforation

To further clarify the roles which particulates and fibers played in the plugging process, the two extra experiments that the injection sequence of particulates and fibers was different were carried out and compared with mixed injection (Group 1). For the 10mm perforation, the optimal



combination was used and the injection rate was 30 ml/min unchanged. Group 2 was that the fibers were injected firstly about 20mins and then the particulates were injected until the plugged zone formed, while Group 3 was opposite. Figure 9 shows the pressure in the plugging process. In the first 20 mins, the pressure of different injection sequence almost kept constant, but when only the particulates or fibers as accessory materials were used, the pressure rose gently and reached the 4350psi later than mixture. Contrast the group 2 and 3, it is was found that the fibers were beneficial to improve the pressure strength.

From the experiments above, the plugging mechanism of fiber and particulate and ball in the perforation can be depicted by Figure 10. The equal diameter ball first entered the perforation with carrying fluid and other materials as Figure 10 (a) shown, and sealed at the perforation (b). The attached fibers captured the flowing particulates to fill the space caused by deformability and expandability (c), then plugged zone formed by the winding fibers to narrow the flow channel (d). Therefore, the plugging mechanism can be summed up as: temporary plugging ball firstly seals the perforation, then the particulates and fibers can further accumulate on the ball.

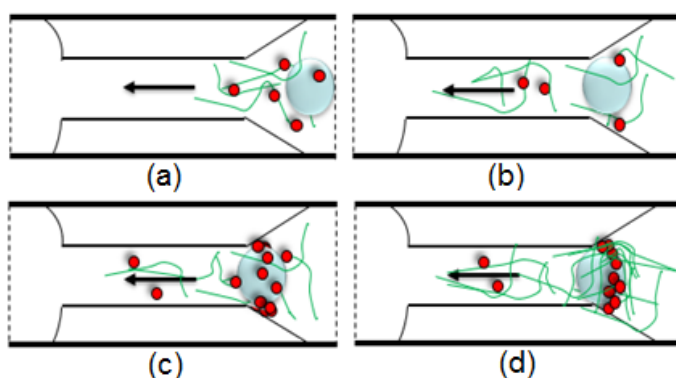


*Figure 10. Sketch map of the plugging process*

#### 4. CONCLUSION

The plugging mechanism of degradable materials in perforation was revealed in this paper. The following conclusions could be drawn from the experimental results:

- (1) The plugging process can be described in three stages: plugging ball seals the perforation, the small particulates help to bridge and the fibers gather to form plugged zone.
- (2) Failure is the main problem for forming plugged zone, and fibers and particulates can be used as accessory materials to improve the pressure strength.
- (3) The experimental results of injection rate and sequence would provide a significant insight into the refracturing technology and the guideline for its successful application in unconventional reservoirs.

#### ACKNOWLEDGEMENT

Supported by the National Science and Technology Major Project of China (No: 2016ZX05051) and Science Foundation of China University of Petroleum, Beijing (No: 2462017BJB02)

#### REFERENCES

- [1]. Dahi Taleghani, A., & Olson, J. E. (2014) How natural fractures could affect hydraulic-fracture geometry. SPE journal, 19(01), 161-171.

- [2]. ÖÖ. Karaçal. (2016) Computational material analysis of structural and hemodynamic model of coronary stent by cfd/fea in computer aided mechanical engineering approach. *Acta Physica Polonica*, 130(1), 249-251.
- [3]. Brown R W, Neill G H, Loper R G. (1963) Factors Influencing Optimum Ball Sealer Performance. *Journal of Petroleum Technology*, 15(4):450-454.
- [4]. Wang D.B., Zhou F.J., Ge H.K., et al. (2015) An experimental study on the mechanism of degradable fiber-assisted diverting fracturing and its influencing factors. *Journal of Natural Gas Science and Engineering*, 27: 260-273.
- [5]. Y. Özcanlı, Çavuş, F. K., & M. Beken. (2016) Comparison of mechanical properties and artificial neural networks modeling of pp/pet blends. *Acta Physica Polonica*, 130(1), 444-446.
- [6]. Wang B, Zhou F., et al. (2017) Fracture Interaction during Temporarily Plugging Staged Fracturing, *International Conference on Computational and Experimental Science and Engineering*, 8-13.
- [7]. Liang T., Zhou F., Shi Y., et al. (2018) Evaluation and optimization of degradable-fiber-assisted slurry for fracturing thick and tight formation with high stress. *Journal Petroleum Science and Engineering*. 165: 81–89.
- [8]. Mercado O, Ernesto C. (2012) Drill Cuttings-based Methodology to Optimize Multi-stage Hydraulic Fracturing in Horizontal Wells and Unconventional Gas Reservoirs. 410-420.
- [9]. Erbstoesser S R. (2013) Improved Ball Sealer Diversion. *Journal of Petroleum Technology*, 32(11):1903-1910.
- [10]. Nozaki M, Zhu D, Hill A. (2013) Experimental and Field Data Analyses of Ball Sealer Diversion. *Spe Production & Operations*, 28(3):286-295.
- [11]. Li S Y, Li Z M. (2012) Experimental Study on Ball Sealer Diversion for Lateral Well. *Advanced Materials Research*, 524-527: 1399-1407.
- [12]. Wang D, Wang X, Liu G, et al. (2012) A New Way of Staged Fracturing Using Ball Sealers. *Spe Production & Operations*, 27(3): 278-283.
- [13]. Desai K, Jajal H. (2014) Multi-zone stimulation technology. *Journal of Unconventional Oil & Gas Resources*, 6(2): 34-38.

## Experimental Investigation on Interfacial and Swelling Behavior of CO<sub>2</sub>-light Crude Oil System

Kun Qian<sup>1</sup>, Shenglai Yang<sup>1\*</sup>, Hongen Dou<sup>2</sup> and Yu Huang<sup>1</sup>

<sup>1</sup> China Universitu of Petroleum-Beijing, State Key Laboratory of Petroleum Resource and Engineering, Beijing, CHINA

<sup>2</sup> Research Institute of Petroleum Exploration and Development (RIPE), CNPC, Beijing, CHINA  
\*yangshenglai\_cupb@126.com

### ABSTRACT

CO<sub>2</sub> flooding is a dynamic process, in which the properties of the crude oil change with time and pressure due to the dissolution and extraction of CO<sub>2</sub>. In order to analysis the interaction and phase behavior of CO<sub>2</sub>-oil system and displacement mechanisms during CO<sub>2</sub> flooding, high-pressure visual apparatus was utilized to conduct swelling/extraction tests. The effect of oil components and temperature on the CO<sub>2</sub> solubility and oil swelling factor was investigated. The minimum extraction pressure was defined on the base of the oil swelling factor during CO<sub>2</sub> injection. The CO<sub>2</sub> solubility, oil swelling factor and interfacial tension (IFT) between the oil and CO<sub>2</sub> was simultaneously analyzed by combining swelling/extraction tests and IFT tests. Results revealed that the function of CO<sub>2</sub> to improve oil displacement efficiency could not be taken advantage of, because the CO<sub>2</sub> could only extract small amount of light components and dissolve in the crude oil to expand the oil. Moreover, gas channeling is easy to occur because of obvious gas-liquid interface, which is harmful to sweep efficiency. Therefore, in the process of conducting CO<sub>2</sub>-EOR technique, the reservoir pressure should be increased higher than minimum extraction pressure to take the advantage of CO<sub>2</sub> which could extract oil components and reduce the IFT.

**KEYWORDS** - CO<sub>2</sub>-oil system, Swelling/Extraction Test, Minimum Extraction Pressure, Interfacial Tension, Minimum Miscibility Pressure, Displacement Mechanism.

### 1. INTRODUCTION

CO<sub>2</sub> flooding has been proven to be an effective technique to enhance oil recovery through both laboratory experiments and field application for several decades[1-3]. The injected CO<sub>2</sub> could interact with crude oil in the reservoirs, leading to significant effects to enhance oil recovery (EOR). The main mechanisms to enhance oil recovery include oil swelling, viscosity reduction due to CO<sub>2</sub> dissolution in crude oil, hydrocarbon extraction and interfacial tension reduction, et al[1,4,5].

The CO<sub>2</sub>-oil system could be categorized into immiscible and miscible state, depending on whether the system pressure reaches minimum miscibility pressure (MMP)[6]. The dominant mechanisms contributing to oil recovery are different in each pressure stage[7,8]. Although miscibility is the most favorable state due to the high oil recovery factor, the miscibility may not be achieved in the reservoirs. Even so, other relevant mechanisms could also play an important role in CO<sub>2</sub>-EOR process[9].

Swelling/extraction tests are effective experiments to investigate the interaction and phase behaviors between the CO<sub>2</sub> and the crude, which could be utilized to analyze the CO<sub>2</sub>-EOR mechanisms due to CO<sub>2</sub>-oil interaction[10-13]. Following up these works, in order to analyze the interaction and phase behavior of CO<sub>2</sub>-oil system and displacement mechanisms during CO<sub>2</sub> flooding, the swelling/extraction tests and interfacial tension (IFT) tests were conducted. The effect of system temperature and oil composition on the oil swelling factor was investigated and the minimum extraction pressure was determined on the base of the oil swelling factor during CO<sub>2</sub> injection process. It is believed that the results derived from this work can provide some necessary clues for CO<sub>2</sub>-EOR project design.

### 2. EXPERIMENTAL SECTION

## 2.1. Materials

In this study, the oil sample A, B and C were collected from different oilfield. The molecular weight, density and viscosity of the oil sample A, B and C was shown in Table 1. The asphaltene content of the cleaned oil sample was measured to be 0.94wt% (n-pentane insoluble) with the standard ASTM D2007-03 method[14]. The purity of the CO<sub>2</sub> used in this study was equal to 99.95% supplied by Beijing Huayuan Gas Chemical Co. Ltd.

**Table 1.** Properties of crude oil sample A, B and C

Crude oil	A	B	C
Molecular weight/g/mol	229.7	278.6	343.5
Density/g/cm <sup>3</sup>	0.833	0.860	0.938
Reservoir temperature/°C	61	47	28
Viscosity at reservoir temperature/mPa•s	4.8	10.1	104.7
Asphaltene content/wt%	0.94	2.40	5.13

## 2.2. CO<sub>2</sub> solubility and oil swelling factor measurements

Figure 1 depicts the schematic diagram of the experimental apparatus used for CO<sub>2</sub> solubility and oil swelling factor measurements at various equilibrium pressures. The crude oil sample was injected into the visual cell to a specific volume of  $V_{o,i}=30\text{cm}^3$ . Then the cell was pressurized with CO<sub>2</sub> to a prespecified pressure  $P_i$ . When the pressure inside the cell reached a stable value ( $P_f$ ) and not changed, the CO<sub>2</sub>-oil system was considered to get equilibrium. The height of the oil sample inside the visual cell was measured by the cathetometer. In this study, the CO<sub>2</sub> solubility ( $\chi_{\text{CO}_2}$ ) is defined as the total moles of dissolved CO<sub>2</sub> in 1L of the original crude oil sample and was calculated using the mass balance equations as follows,

$$n_{\text{CO}_2} = n_{\text{CO}_2,i} - n_{\text{CO}_2,f} = \frac{P_i V_i}{Z_i RT} - \frac{P_f V_f}{Z_f RT} = \frac{1}{RT} \left( \frac{P_i V_i}{Z_i} - \frac{P_f V_f}{Z_f} \right) \quad (1)$$

$$\chi_{\text{CO}_2} = \frac{n_{\text{CO}_2}}{V_{o,i}} = \frac{1}{RT V_{o,i}} \left( \frac{P_i V_i}{Z_i} - \frac{P_f V_f}{Z_f} \right) \quad (2)$$

The swelling factor (SF) of the oil is determined by the ratio of the final volume of the oil to its initial value at the beginning of the experiment:

$$SF = \frac{V_{o,f}}{V_{o,i}} \quad (3)$$

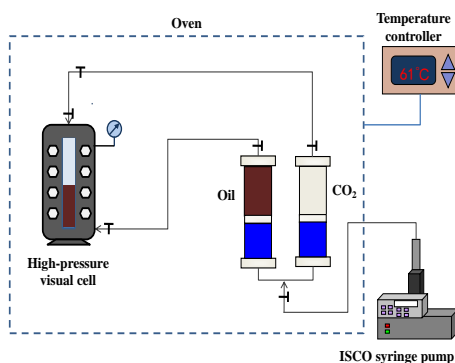


**Figure 1.** Schematic diagram of the experimental apparatus used for CO<sub>2</sub> solubility and oil swelling factor measurements at various equilibrium pressures.

### 2.3. CO<sub>2</sub>-oil interfacial tension measurements

The schematic diagram of the setup in this study to measure the dynamic interfacial tension between CO<sub>2</sub> and the live oil is shown in Figure 2. The core device of the set is the high-pressure IFT cell (IFT-10, Temco, USA) with maximum operating pressure and temperature of 69MPa and 177°C and the designed volume of the IFT cell is 49.5cm<sup>3</sup>.

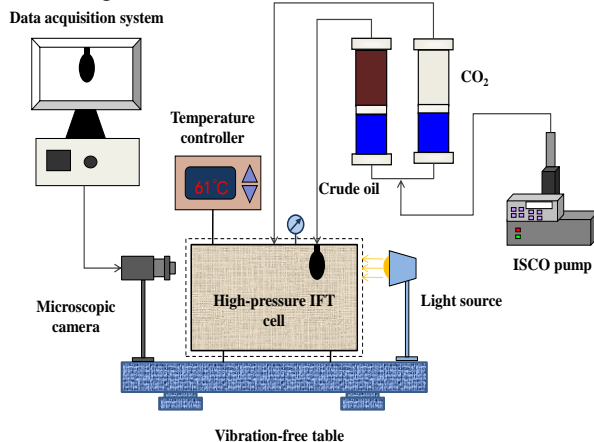


**Figure 2.** Schematic diagram of the experimental setup used for measuring the equilibrium interfacial tension.

## 3. RESULTS AND DISCUSSION

### 3.1. Phase behaviors of CO<sub>2</sub>-oil system

The swelling/extraction test of oil A was conducted at the reservoir temperature of 61°C. As shown in Figure 3, CO<sub>2</sub> solubility increases as the equilibrium increasing. At the same time, the oil swelling factor increases because of more dissolved CO<sub>2</sub> in the crude oil. However, the oil swelling factor doesn't monotonously increase in the throughout the experiment. When the equilibrium pressure is higher than 9.51MPa, the crude oil expand by 28% and the oil swelling factor begins to decrease. This is because increasing pressure compresses the liquid volume and makes the movement of CO<sub>2</sub> molecules more kinetic. As the pressure continuous to increase, the escaping rate of light component molecules begins to greater than the rate of CO<sub>2</sub> dissolved in the liquid phase[15]. When the equilibrium pressure reaches 14.83MPa, the oil swelling factor is only 0.61.

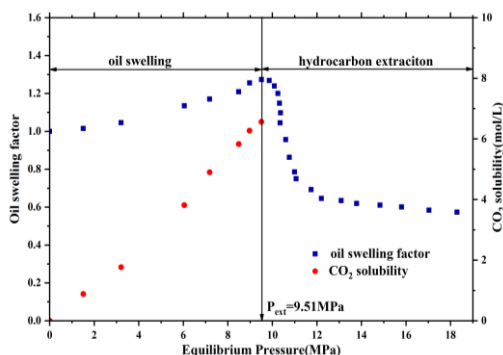


**Figure 3.** CO<sub>2</sub> solubility in the crude oil sample and oil swelling factor at various equilibrium pressures under the temperature of  $T = 61^{\circ}\text{C}$ .

### 3.2. The effect of oil composition

Figure 4 depicts the oil swelling factor of oil A, B and C at different equilibrium pressure in order to analyze the influence of oil composition on the phase behaviors of CO<sub>2</sub>-oil system. The MEP of the oil A, B and C is 9.51MPa, 8.59MPa and 7.75MPa and the MEP decreases with decrease of the light-component content of crude oil. When the pressure is lower than MEP, the light components in the crude oil continuously evaporates into the gas phase. The extraction capacity of CO<sub>2</sub> is certain under the same pressure[10]. The light-component content of the oil A is higher than that of oil B, so higher equilibrium pressure is necessary for oil A to enter the extraction stage. Furthermore, the MEP of oil C is the lowest due to the least light-component content.

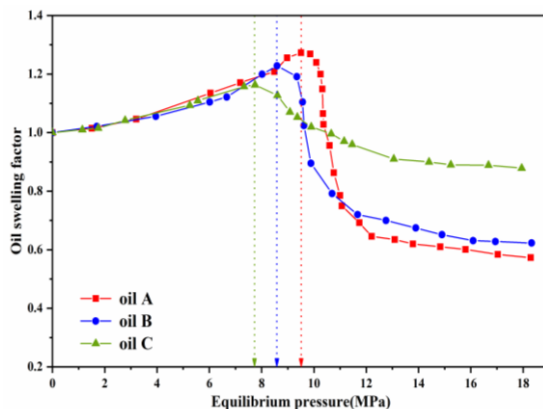


**Figure 4.** Oil swelling factors of different crude oil samples at various equilibrium pressures under the temperature of  $T = 61^{\circ}\text{C}$ .

### 3.3. The effect of temperature

Figure 5 depicts the oil swelling factor of oil A at different experimental temperature. When the pressure is lower than the MEP at the temperature of 50°C, the oil swelling factor is larger at lower temperature due higher CO<sub>2</sub> solubility. The MEP of oil A is 9.23MPa, 9.51MPa and 10.09MPa at the temperature of 50°C, 61°C and 70°C, respectively. The MEP of the crude oil increases with the increasing of temperature. Holm and Josendal thought the capacity of CO<sub>2</sub> extraction hydrocarbon is determined by the density of CO<sub>2</sub>. When the density of CO<sub>2</sub> reaches, the extraction effect of CO<sub>2</sub> begins playing a dominant role in the CO<sub>2</sub> injection process[10]. The density of the CO<sub>2</sub> under the MEP and temperature of 50°C, 61°C and 70°C is 0.30g/ml, 0.26 g/ml and 0.25 g/ml, which is all between range of 0.25-0.35g/ml. The swelling factor of oil A under the pressure of 14.5MPa and temperature of 50°C, 61°C and 70°C is 0.85, 0.61 and 0.52. The oil swelling factor changes relatively less at lower experimental temperature (Figure 5). This is because that the molecular motion is more intense at higher temperature and more light components could be extracted in the gas phase.

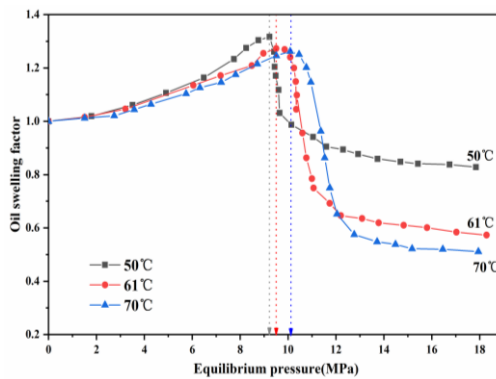


**Figure 5.** Oil swelling factors of crude oil A at various equilibrium pressures under the temperature of  $T = 50^{\circ}\text{C}$ ,  $61^{\circ}\text{C}$  and  $70^{\circ}\text{C}$ .

### 3.4. IFT tests

In this study, the axisymmetric drop shape analysis (ADSA) technique for the pendant drop case was applied to determine the IFT between the crude oil A and  $\text{CO}_2$ . Figure 6 depicts the measured IFT at different equilibrium pressure of oil. The IFT of  $\text{CO}_2$ -oil system decreases with the increasing of pressure and the  $\text{CO}_2$ -oil system is considered to get miscible when the IFT gets to be 0 [16]. The whole curve is divided into two sections to fit and extrapolate to intersect with X axis respectively (Figure 6). The two fitted straight lines intersect at 9.71 MPa, which is 0.2 MPa higher than MEP oil (9.51 MPa). Therefore, 9.71 MPa is the critical point where the interaction between the  $\text{CO}_2$  and crude oil changes from oil swelling effect to extraction effect.

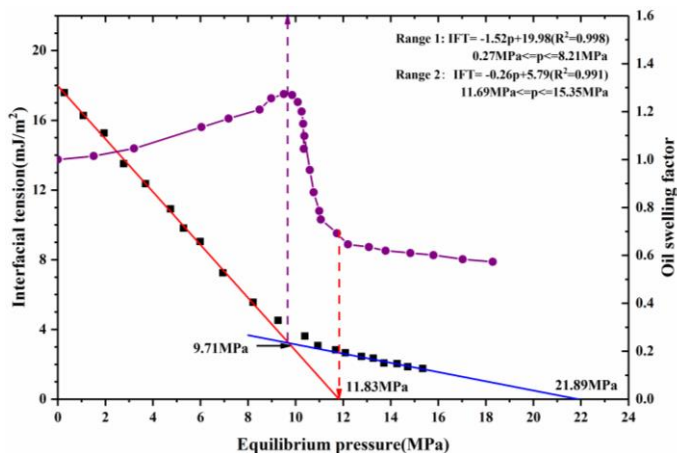


**Figure 6.** the interfacial tension of the  $\text{CO}_2$ -crude oil system at different equilibrium pressures under the temperature of  $61^{\circ}\text{C}$ .

## 4. CONCLUSION

In this work, swelling/extraction tests and interfacial tension tests were conducted. The influence of the system temperature and composition of the crude oil on the solubility of  $\text{CO}_2$  in crude oil, oil swelling factor and the interfacial tension between  $\text{CO}_2$  and oil was investigated. The specific conclusions can be drawn as follows.

The minimum extraction pressure (MEP) is related to the system temperature and composition of crude oil. The MEP of CO<sub>2</sub>-crude oil system increases as the system temperature increases. And, when the crude oil has higher content of the heavy components, the MEP and the volume change of the oil is smaller.

In CO<sub>2</sub> flooding process, when the injection is less than the MEP, only a small amount of CO<sub>2</sub> can be dissolved in crude oil and gas channelling is easier to occur due to the obvious gas-liquid phase, which is unfavourable for sweeping efficiency. The injection pressure should be maintained at least above the MEP. Moreover, for heavy oil reservoir, residual oil has more heavy components and higher viscosity after CO<sub>2</sub> flooding, which increases the difficulty and cost of the subsequent development. Thus, the CO<sub>2</sub>-EOR technique is more suitable for light oil reservoirs.

## REFERENCES

- [1] Huang L, Ning Z, Wang Q, et al. Enhanced gas recovery by CO<sub>2</sub> sequestration in marine shale: a molecular view based on realistic kerogen model[J]. *Arabian Journal of Geosciences*, 2018, 11(15): 404. doi: 10.1007/s12517-018-3762-5
- [2] Song L, Ning Z, Duan L. Research on reservoir characteristics of Chang7 tight oil based on nano-CT[J]. *Arabian Journal of Geosciences*, 2018, 11(16): 472. doi: 10.1007/s12517-018-3842-6
- [3] Tahroudi M N, Khalili K, Ahmadi F, et al. Development and application of a new index for analyzing temperature concentration for Iran's climate[J]. *International Journal of Environmental Science and Technology*, 2018: 1-14. doi: 10.1007/s13762-018-1739-2
- [4] Rudyk, Svetlana, Pavel Spirov, and Erik Sogaard. "Application of GC-MS chromatography for the analysis of the oil fractions extracted by supercritical CO<sub>2</sub> at high pressure." *Fuel* 106 (2013): 139-146. doi:10.1016/j.fuel.2012.12.004
- [5] Seyyedsar S M, Farzaneh S A, Sohrabi M. Experimental investigation of tertiary CO<sub>2</sub> injection for enhanced heavy oil recovery[J]. *Journal of Natural Gas Science and Engineering*, 2016, 34: 1205-1214. doi: 10.1016/j.jngse.2016.08.020
- [6] Zhang K, Gu Y. Two different technical criteria for determining the minimum miscibility pressures (MMPs) from the slim-tube and coreflood tests[J]. *Fuel*, 2015, 161: 146-156. doi:10.1016/j.fuel.2015.08.039
- [7] Abedini A, Torabi F. Oil recovery performance of immiscible and miscible CO<sub>2</sub> huff-and-puff processes[J]. *Energy & Fuels*, 2014, 28(2): 774-784. doi: 10.1021/ef401363b
- [8] Wei B, Gao H, Pu W, et al. Interactions and phase behaviors between oleic phase and CO<sub>2</sub> from swelling to miscibility in CO<sub>2</sub>-based enhanced oil recovery (EOR) process: A comprehensive visualization study[J]. *Journal of Molecular Liquids*, 2017, 232: 277-284. doi: 10.1016/j.molliq.2017.02.090
- [9] Torabi F, Firouz A Q, Kavousi A, et al. Comparative evaluation of immiscible, near miscible and miscible CO<sub>2</sub> huff-n-puff to enhance oil recovery from a single matrix-fracture system (experimental and simulation studies)[J]. *Fuel*, 2012, 93: 443-453. doi: 10.1016/j.fuel.2011.08.037
- [10] Holm L R W, Josendal V A. Effect of oil composition on miscible-type displacement by carbon dioxide[J]. *Society of Petroleum Engineers Journal*, 1982, 22(01): 87-98. doi: 10.2118/8814-PA
- [11] Hand J L, Pinczewski W V. Interpretation of swelling/extraction tests[J]. *SPE Reservoir Engineering*, 1990, 5(04): 595-600. doi: 10.2118/19471-PA
- [12] Tsau J S, Bui L H, Willhite G P. Swelling/extraction test of a small sample size for phase behavior study[C]//SPE improved oil recovery symposium. Society of Petroleum Engineers, 2010. doi: 10.2118/129728-MS



- [13] Lashkarbolooki M, Ayatollahi S. Experimental investigation on CO<sub>2</sub>-light crude oil interfacial and swelling behavior[J]. Chinese journal of chemical engineering, 2018, 26(2): 373-379. doi:10.1016/j.cjche.2017.07.010
- [14] ASTM D2007-03, Standard Test Method for Characteristic Groups in Rubber Extender and Processing Oils and Other Petroleum- Derived Oils by the Clay-Gel Absorption Chromatographic Method; ASTM International: West Conshohocken, PA, 2007.
- [15] Siagian U W R, Grigg R B. The extraction of hydrocarbons from crude oil by high pressure CO<sub>2</sub>[C]//SPE/DOE Improved Oil Recovery Symposium. Society of Petroleum Engineers, 1998. doi: 10.2118/39684-MS
- [16] Rao D N. A new technique of vanishing interfacial tension for miscibility determination[J]. Fluid Phase Equilibria, 1997, 139(1):311–324. doi:10.1016/S0378-3812(97)00180-5

# Experimental study on the changes in the physical properties of low permeability sandstone reservoirs after injection of CO<sub>2</sub> in different methods

Qian Wang<sup>1,2</sup> Sheng Lai Yang<sup>1,2✉</sup> Hai Shui Han<sup>3</sup> Kun Qian<sup>1,2</sup> Jia Jun Li<sup>1,2</sup>

<sup>1</sup> State Key Laboratory of Petroleum Resources and Engineering, China University of Petroleum-Beijing, 102249, CHINA

<sup>2</sup> School of Petroleum Engineering, China University of Petroleum-Beijing, 102249, CHINA

<sup>3</sup> State Key Laboratory of Enhanced Oil Recovery, Beijing 100083, CHINA  
yshenglai820@163.com

## ABSTRACT

In order to study the effect of different CO<sub>2</sub> injection methods on the physical property changes in low permeability sandstone reservoirs, CO<sub>2</sub>-formation water alternate (CO<sub>2</sub>-WAG) flooding and CO<sub>2</sub> flooding experiments were carried out on the cores with similar physical properties under formation conditions (78°C, 18MPa). The permeability, porosity, scanning electron microscopy (SEM) images, nuclear magnetic resonance (NMR) transversal relaxation time (T<sub>2</sub>) distribution and wettability before and after the flooding experiments showed that the core permeability decreased after CO<sub>2</sub> flooding was less than that of the core after CO<sub>2</sub>-WAG flooding, but the porosity remains unchanged. Parts of the pores were filled with kaolinite or attached by clastic particles and salt crystals. After the CO<sub>2</sub>-WAG flooding, the pore radius distribution of the core concentrated in the middle. In addition, the rocks become more hydrophilic after replacement. However, the change of range and amplitude of the pore radius distribution and wettability of the core after CO<sub>2</sub> flooding were less than those after CO<sub>2</sub>-WAG flooding. The reasons for the difference of changes in the physical properties of the core under different CO<sub>2</sub> injection methods were that the dissolution of minerals and the migration of the mineral particles mainly occurred in large pores during the CO<sub>2</sub> flooding, while CO<sub>2</sub>-WAG flooding could increase sweep area, the particles migration occurred in the large pores and the secondary pores, which eventually blocked the pores. The flooding experiment provided the evidence for analysing changes in reservoir physical properties during CO<sub>2</sub> injection for enhanced oil recovery (EOR).

**Keywords:** CO<sub>2</sub> flooding; CO<sub>2</sub>-water alternate flooding; low-permeability reservoirs; permeability; porosity; pore radius distribution

## 1. INTRODUCTION

CO<sub>2</sub> injection is the common method for EOR in oil fields, which also achieves the goal of CO<sub>2</sub> geological storage [1-4]. During in the long-term CO<sub>2</sub> injection process, CO<sub>2</sub>-brine-rock interactions occur in high water cut sandstone rocks near the injection well, which would cause changes in the pore structure of the rock and affect the subsequent injection capacity of CO<sub>2</sub> and brine [5-9]. In addition, different injection methods would also affect the changes of rock physical properties. Therefore, when the oilfields choose the displacement method, the effect of EOR and the changes in physical properties near the well are the focus of attention, deserving further research. In this paper, the changes in rock physical properties were by explored by the displacement experiments on high water cut cores, and the difference among these changes were compared after CO<sub>2</sub> flooding and CO<sub>2</sub>-WAG flooding, providing data support for numerical simulation.

## 2. EXPERIMENTAL SECTION

### 2.1. Experimental Materials and Analysis

The rock sample, H39 was taken from the Huang 3 formation (2137.65m depth) of the Chang Qing Oilfield, a typical low-permeability reservoir in the Ordos Basin in western China. The target oil reservoir Huang 3 in this study was one of the main production layers of the oilfield. The main minerals contained in the rocks of the reservoir are quartz, feldspar, rock debris, pore filler, classified as clastic. The porosity of the reservoir ranged from 11% to 14%, and the average permeability was  $1 \times 10^{-3} \mu\text{m}^2$ . The cores used in the experiment were taken from the area without CO<sub>2</sub>-EOR operation. High-purity CO<sub>2</sub> (99.99%) was used in this study. The brine used in the core-flooding experiments was prepared basing on data provided by the RIPED, which had a composition of 31.64 g/L CaCl<sub>2</sub>, 0.06 g/L MgCl<sub>2</sub>, 0.18 g/L Na<sub>2</sub>SO<sub>4</sub>, 19.13 g/L NaCl, and 0.19 g/L NaHCO<sub>3</sub>.

In order to make the comparison of the results of the flooding experiments meaningful, the homogeneous core sample H39 was cut equally into two sections, numbered H39-1, H39-2 (Table 1), these two cores were measured for porosity, permeability, wettability, pore radius distribution. A slice of 2 mm in thickness was cut from each core as sample to be measured by SEM and X-ray diffraction (XRD). These measurements were taken to ensure that the samples had the same initial physical properties before the experiments.

**Table 1** Basic parameters of the core samples

Core No.	Length cm	Diameter cm	Permeability mD	Porosity %
H39	6.26	2.51	0.856	9.18
H39-1	2.73	2.51	0.863	9.07
H39-2	2.64	2.51	0.849	9.11

**Table 2** Types and contents of mineral in the core samples

Core No.	Mineral types and content (wt.%)					
	Quartz	Feldspar	Debris	Carbonatite	Clay minerals	Others
H39-1	36.4	30.2	20.4	7.6	4.7	0.7
H39-2	37.1	30.9	19.1	7.2	4.9	0.8

wt.%—weight percent

## 2.2. Experimental procedure

The two core samples H39-1 and H39-2 were continuously evacuated for 24 hours and saturated with formation water for 24 hours, and the temperature of the constant temperature oven core system was set to 78°C and the outlet pressure of the core was steadily controlled at 18MPa according to the P-T conditions of the formation reservoir. After that, the core sample H39-1 was flooded by CO<sub>2</sub> and the injection flow rate of the was set to 3mL/h in order to avoid damage to the core due to velocity sensitivity. The experiment continued until the pressure at the outlet and inlet were stable and the total flooding time was 150h [10-11]. Then the core H39-2 was flooded by CO<sub>2</sub> and formation water in the way of WAG. The ratio of the volumes of water slug and CO<sub>2</sub> slug is 2: 1, the volume of the slug is 0.3 PV [12]. When the inlet pressure remained stable during gas drive in the three consecutive flooding cycles and the total flooding time was 150h, the core-flooding was completed.

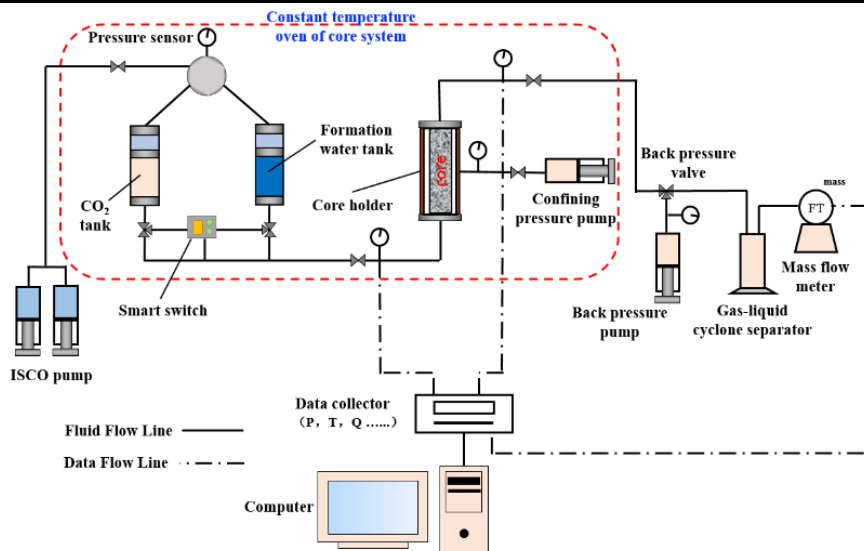


**Figure. 1** Schematic diagram of flooding experiment

After the flooding experiments, the cores were dried and measured for permeability and porosity values. Afterwards, the cores were evacuated to saturate the formation water for NMR and wettability measurements. Finally, samples from these cores after flooding were observed by SEM.

### 3. RESULTS

#### 3.1. Porosity and permeability

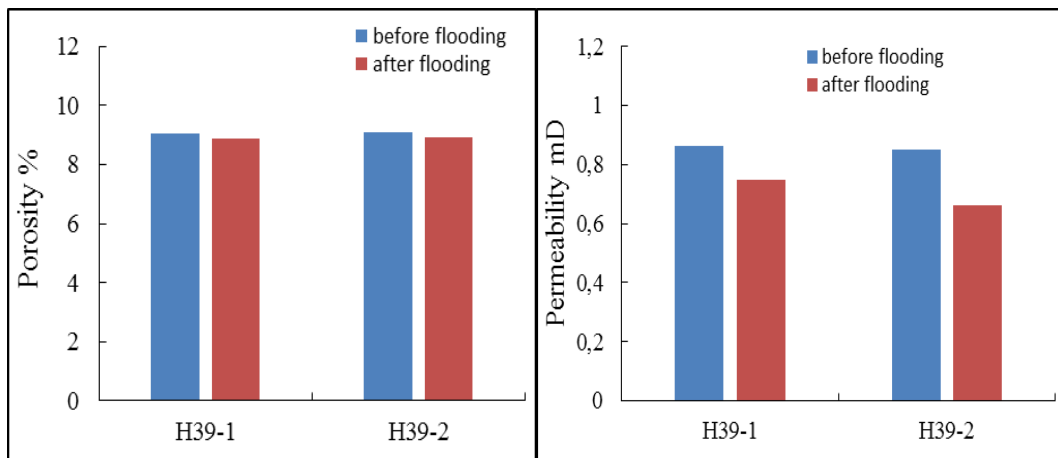


**Figure.2** Porosity and permeability of the core samples before and after the flooding experiments

The changes in porosity and permeability of the core samples before and after the displacement experiment were shown in the Fig.4. The core H39-1 showed decreases in porosity and permeability of 2% and 13.2%. The core H39-2 showed decrease in porosity and permeability of 2.2% and 22%.

### 3.2. Pore radius distribution

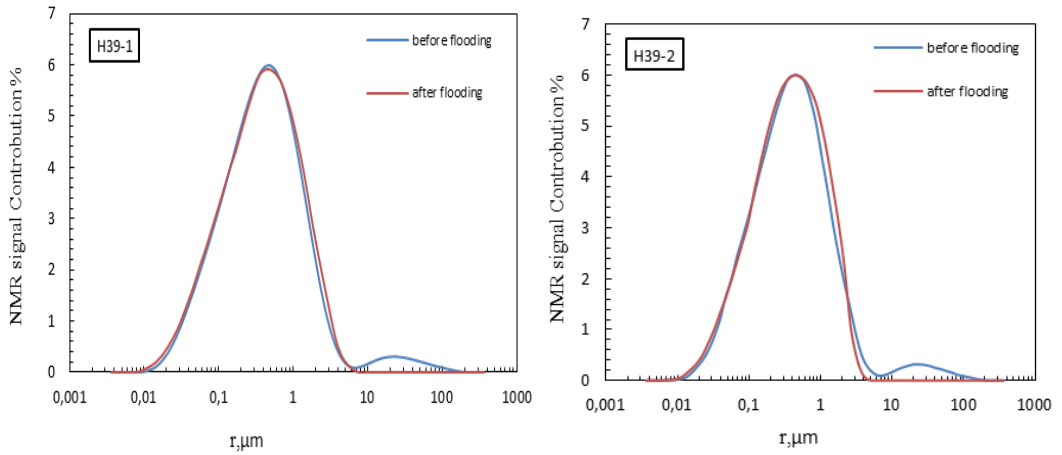


**Figure.3** Core pore radius distribution before and after the experiments

According to formula (1) [13], the relaxation time was converted into pore radius value, and the signal amplitude was normalized to obtain the pore radius distribution of the cores (Fig.3).

$$T_2 = Cr \quad (1)$$

in the formula:  $T_2$  relaxation time, ms;  $r$  pore radius,  $\mu\text{m}$ ;  $C$  conversion coefficient,  $27.52\text{ms}/\mu\text{m}$  in this paper. The Fig.3 showed that after injection of  $\text{CO}_2$  into the cores, the proportion of large pores decreased, the proportion of medium pores increased, while the proportion of small pores remained almost unchanged. However, the range and amplitude of the changes of pore radius distribution of the core H39-2 were larger than that of the core H39-1.

### 3.3. Wettability

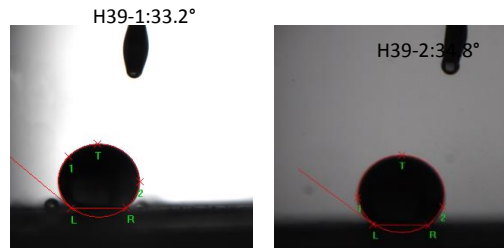


**Figure.4** Contact angle before the experiments

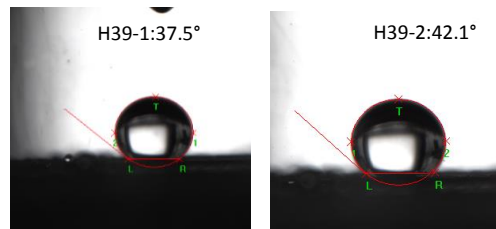


**Figure.5** Contact angle after the experiments

The Fig.4 and Fig.5 showed that after the experiment, the contact angle between the oil phase and the water phase becomes larger on the rock surface, indicating that the rock was more hydrophilic. In addition, the core H39-2 after CO<sub>2</sub>-WAG flooding showed a more hydrophilic tendency.

### 3.4. Microscopic morphology of pores

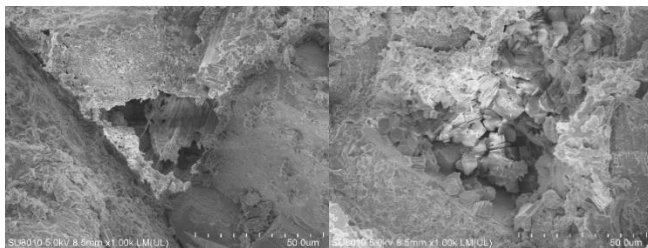


*Figure.6 SEM images of the pores before and after the flooding experiments*

After CO<sub>2</sub> injection, salt crystals formed bridging blockage in some pores of the cores, and some other pores were filled with loose flake kaolinite, which reduced the space volume of these pores or blocked their throats.

## 4. DISCUSSION

### 4.1. Physical property changes

Previous studies believed that CO<sub>2</sub> was injected into the core and dissolved into formation water to form carbonic acid, which triggered CO<sub>2</sub>-brine-rock interactions. During this process, the debris particles and clay mineral fragments were released and converted into movable particles. The migration of these particles and the precipitation of new minerals led to blockage in pores, eventually causing the rock permeability to decline. The migration of particles did not cause a significant reduction in the total pore volume of the cores, but the particles would accumulate at the pore throat and form blockages, which significantly reduced the fluidity of fluids in the flow channels in the rock.

In the CO<sub>2</sub> injection process, reactions occurring in sandstone rocks generally included dissolution of carbonate mineral, alkali feldspar, and clay mineral [9]. Under high temperature and high pressure, potassium feldspar would dissolve in the acidic environment, kaolinite was generated during the reaction and released from the rock matrix. But the carbonate minerals could react rapidly with carbonic acid [14], the stability of the surface of the rock particles would be destroyed, and the debris particles were released, then the particles migrated with the fluid in the pores and blocked the pores. On the other hand, the dissolution of carbonate minerals could also lead to an increase in the concentration of Ca<sup>2+</sup>, Mg<sup>2+</sup> and other ions in the fluid. Once the external conditions such as concentration, pH, temperature, or pressure changed, these ions were very likely to reprecipitate [15]. In addition, CO<sub>2</sub> could diffuse into the layers and change the charge between the clay mineral layers causing repulsive force, which destroyed the stability of the clay layer structure and finally resulted in the dispersion of clay minerals filled in the pores. Regarding the formation of salt crystals, when the NaCl solution was fully exposed to supercritical CO<sub>2</sub>, then NaCl crystals precipitated and adhered to the surface of minerals [16]. In the process of physical and chemical reactions of minerals, the wettability of the rock surface had also become more hydrophilic.

The pore radius distribution changed after experiments, while during the process there was no significant change in the total volume of the pores, which represented there were mutual transformations among the pores with different sizes in the core [17]. The changes in the

proportion of the pores with a certain radius value were caused by two factors: on the one hand, mineral dissolution, particle release (enlargement of pore space), particle migration, pore blockage (reduced pore space) occurred in the pores with the radius. These factors caused the pores of this radius to transform into pores of other sizes, which decreased the proportion of pores; on the other hand, pores of other sizes were also converted into pores of this radius for the same reasons. However, the probability of large pores transformation was large, the large pores were easy to transform into small pores. These were because large pores were the main flow space of fluids and were the main place for mineral dissolution and particle migration, so such pores were prone to conversion; in addition, the effect of particle migration and clogging pores is greater than that of mineral dissolution and expansion of pores in sandstone cores during the flooding.

#### 4.2. Difference in physical property changes

The comparison of the measured results of the core H39-1 and H39-2 showed that different flooding methods resulted in different physical property changes. There might be three reasons: when CO<sub>2</sub> was injected into the core, the formation water in the large pores would be displaced firstly, and the amount of carbonated water formed in the core was relatively small during CO<sub>2</sub> flooding, while the core was continuously replenished with CO<sub>2</sub> and formation water during WAG flooding. The contact between CO<sub>2</sub> and formation water was more sufficient, more minerals were dissolved in the rock, more debris particles and clay minerals migrated, finally causing more serious decline in permeability in the core H39-2. On the other hand, the low-speed flowing CO<sub>2</sub> had a weak ability to carry particles, which meant that the power of the particles migration during the CO<sub>2</sub> flooding was weaker than that during the WAG flooding. In addition, The WAG injection had the effect of expanding the sweep area of CO<sub>2</sub>. There were more pores in which mineral dissolution and particle migration occurred, and also more pores changed in size. During CO<sub>2</sub> flooding, the main flow channel of CO<sub>2</sub> as the non-wetting phase was large pore channel [18] (CO<sub>2</sub> was the continuous phase), so the pore size changes also occurred mainly in large pores. In general, the scales of mineral dissolution, particle migration and pore blockage in pores during CO<sub>2</sub> flooding were smaller than that during CO<sub>2</sub>-WAG flooding.

### 5. CONCLUSIONS

In this paper, the rock physical properties changes and the influences of CO<sub>2</sub> injection methods on these changes were investigated. The conclusions are as follows:

After the low-permeability sandstone cores were displaced by CO<sub>2</sub> in different ways, the core permeability decreased, but the porosity remained almost unchanged. And some pores of the rock were blocked by debris particles, clay minerals and salt crystals, rocks become more hydrophilic. The proportion of large pores decreased while the proportion of medium pores increased. Mineral dissolution, release of particles, particle migration and pore blockage caused by CO<sub>2</sub>-brine-rock interactions in cores were the cause of the changes in core physical properties.

The decrease of core permeability after CO<sub>2</sub>-WAG flooding was greater than that after CO<sub>2</sub> flooding, the variation of the pore radius distribution and wettability in the former was greater than that in the latter. The reasons for the differences in the changes might be that the reaction was more sufficient and more particles were released during the CO<sub>2</sub>-WAG flooding; the range of pores radii in which the fluid flowed was different, and particle migration and blockage occurred in more pores during the CO<sub>2</sub>-WAG flooding; CO<sub>2</sub> in the large pores was the continuous phase and the ability to carry particles was poor during CO<sub>2</sub> flooding.

### ACKNOWLEDGEMENT

This paper presented in "5<sup>th</sup> International Conference on Computational and Experimental Science and Engineering (ICCESN-2018)". And this study was supported by "Key technologies for CO<sub>2</sub> flooding and storage" of the 13th Five-Year National Major Science and Technology Project (2016ZX05016006-004).

## REFERENCES

- [1]. Khosrokhavar, R. Mechanisms for CO<sub>2</sub> Sequestration in Geological Formations and Enhanced Gas Recovery. Springer International Publishing, 2016. <https://doi.org/10.1007/978-3-319-23087-0>
- [2]. Jiao, Zunsheng, et al. A Feasibility Study of the Integration of Geologic CO<sub>2</sub> Storage with Enhanced Oil Recovery (CO<sub>2</sub> Flooding) in the Ordos Basin, China. Geological CO<sub>2</sub> Storage Characterization. Springer, New York, NY, 2013. 271-294. [https://doi.org/10.1007/978-1-4614-5788-6\\_13](https://doi.org/10.1007/978-1-4614-5788-6_13)
- [3]. Huang, Liang, et al. Enhanced gas recovery by CO<sub>2</sub> sequestration in marine shale: a molecular view based on realistic kerogen model. Arabian Journal of Geosciences 11.15 (2018): 404. <https://doi.org/10.1007/s12517-018-3762-5>
- [4]. Ganguli, Shib Sankar. Integrated Reservoir Studies for CO<sub>2</sub>-Enhanced Oil Recovery and Sequestration: Application to an Indian Mature Oil Field. Springer, 2017. <https://doi.org/10.1007/978-3-319-55843-1>
- [5]. Su, Wenbo, et al. Effect of water salinity and rock components on wettability alteration during low-salinity water flooding in carbonate rocks. Arabian Journal of Geosciences 11.11 (2018): 260. <https://doi.org/10.1007/s12517-018-3611-6>
- [6]. Saeedi, Ali. Experimental study of multiphase flow in porous media during CO<sub>2</sub> Geo-Sequestration processes. Springer Science & Business Media, 2012. <https://doi.org/10.1007/978-3-642-25041-5>
- [7]. Baines, S.J., Worden, R.H. The long-term fate of CO<sub>2</sub> in the subsurface: natural analogues for CO<sub>2</sub> storage. Geological Society 233, 59–85, 2004. <https://doi.org/10.1144/GSL.SP.2004.233.01.06>
- [8]. Fischer, S., Liebscher, A., Wandrey, M., the CO<sub>2</sub> SINK Group. CO<sub>2</sub>-brine-rock interaction—first results of long-term exposure experiments at in situ P–T conditions of the Ketzin CO<sub>2</sub> reservoir. Chemie der Erde 70, 155–164, 2010. <https://doi.org/10.1016/j.chemer.2010.06.001>
- [9]. Gaus, I. Role and impact of CO<sub>2</sub>–rock interactions during CO<sub>2</sub> storage in sedimentary rocks. International Journal of Greenhouse Gas Control 4, 73–89, 2010. <https://doi.org/10.1016/j.ijggc.2009.09.015>
- [10]. Yu, Z., Liu, L., Yang, S., Li, S., & Yang, Y., 2012. An experimental study of CO<sub>2</sub>–brine–rock interaction at in situ pressure–temperature reservoir conditions. Chemical Geology, 326, 88–101. <https://doi.org/10.1016/j.chemgeo.2012.07.030>
- [11]. Saeedi A, Delle Piane C, Esteban L. Flood characteristic and fluid rock interactions of a supercritical CO<sub>2</sub>, brine, rock system: South West Hub, Western Australia. International Journal of Greenhouse Gas Control, 54: 309-321, 2016. <https://doi.org/10.1016/j.ijggc.2016.09.017>
- [12]. Le Van S, Chon B H. Effects of salinity and slug size in miscible CO<sub>2</sub> water-alternating-gas core flooding experiments. Journal of Industrial and Engineering Chemistry, 52: 99-107, 2017. <https://doi.org/10.1016/j.jiec.2017.03.030>
- [13]. Fang T, Zhang L, Liu N. Quantitative characterization of pore structure of the Carboniferous–Permian tight sandstone gas reservoirs in eastern Linqing depression by using NMR technique. Petroleum Research, 2018. <https://doi.org/10.1016/j.ptlrs.2018.06.003>



- 
- [14]. Vialle, S., & Vanorio, T. Laboratory measurements of elastic properties of carbonate rocks during injection of reactive CO<sub>2</sub> - saturated water. *Geophysical Research Letters*, 38(1), 2011. <https://doi.org/10.1029/2010GL045606>
  - [15]. Pudlo, Dieter, Henkel, Steven, Reitenbach, Viktor. The chemical dissolution and physical migration of minerals induced during CO<sub>2</sub> laboratory experiments: their relevance for reservoir quality. *Environ. Earth Sci.* 73 (11), 7029–7042, 2015. <https://doi.org/10.1007/s12665-015-4411-x>
  - [16]. Pearce, J. M., Holloway, S., Wacker, H., Nelis, M. K., Rochelle, C. Natural occurrences as analogues for the geological disposal of carbon dioxide. *Energy Conversion and Management*, 37(6-8), 1123-1128, 1996. [https://doi.org/10.1016/0196-8904\(95\)00309-6](https://doi.org/10.1016/0196-8904(95)00309-6)
  - [17]. Xie Q, Saeedi A, Delle Piane C. Fines migration during CO<sub>2</sub> injection: Experimental results interpreted using surface forces. *International Journal of Greenhouse Gas Control*, 65: 32-39, 2017. <https://doi.org/10.1016/j.ijggc.2017.08.011>
  - [18]. Feng Q, Di L, Tang G. A visual micro-model study: The mechanism of water alternative gas displacement in porous media//*SPE/DOE Symposium on Improved Oil Recovery*. Society of Petroleum Engineers, 2004. <https://doi.org/10.2118/89362-MS>

## Elaboration and characterization of nanowire hydrogenated amorphous silicon carbide (a-SiC:H) thin films for energy conversion

Assia Boukezzata <sup>1\*</sup>, Sihem Bouanik <sup>2</sup>, Samira Kaci <sup>3</sup>, Ammar Manseri <sup>1</sup>, Hamid Menari <sup>1</sup>,  
Lakhder Guerbous <sup>2</sup>, Aissa Keffous <sup>1</sup>

<sup>1</sup> Centre de Recherche en Technologie des Semi-conducteurs pour l'Energétique (CRTSE), Couches Minces  
Surfaces et Interfaces (CMSI), Algiers, ALGERIA

<sup>2</sup> Centre de Recherche Nucléaire d'Alger (CRNA), B.P. 399 Alger-Gare, Algiers, ALGERIA

\*Corresponding Author Email: [assiab200@yahoo.fr](mailto:assiab200@yahoo.fr)

### ABSTRACT

In this work, we report the formation of nanowire amorphous SiC (NWASC) thin films for energy application. The NWASC was prepared by two steps: First, the formation of silicon nanowire on silicone type p by metal-assisted chemical etching. Second, deposited of hydrogenated amorphous SiC thin films on silicon nanowire by RF magnetron sputtering, with different thickness. The NWASC samples were analyzed using scanning electron microscopy (SEM), spectrophotometry UV and photoluminescence (PL). Results show the formation of NWASC nanostructured with high intensity of photoluminescence and low reflectance intensity. Because of the large surface areas and the high stability, the SiC nanowire was used as photoelectric device for energy conversion. Finally, it was found that such nanowire SiC structure exhibited an enhanced and extremely stable photoelectric performance and results obtained that could be promising for the construction of devices for energy conversion.

**KEYWORDS** - Amorphous SiC, Chemical etching, Nanowire SiC, Photoelectric, Energy conversion

### 1. INTRODUCTION

Silicon carbide (SiC) is an important semiconductor which can be operated at high powers, high temperatures, and high frequencies. Micrometer-sized whiskers of SiC have been widely used to strengthen ceramic composites which had brought dramatic revolution in mechanical and optoelectronic industries [1]. Furthermore, nanostructures of SiC [2] are of great interest because of their broad range of potential applications such as field electron emitter, light emitter other than their reinforcing use [3–8]. Considering these advantages of SiC, it is worthwhile to fabricate an efficient and stable photoelectrodes with favorable structures of SiC. Actually, such investigations have already been in progress. Bulk and film of the SiC have been employed as photocatalyst for water splitting [9–12]. It is known that the nano-structuration would greatly enlarge the specific surface areas of the SiC photocatalyst, and thus increase the reactive sites for photocatalysis. As a result, the efficiency of water splitting would be improved [13]. Results by Zhou et al. indicated that the SiC nanowires own a high photodegradation rate for acetaldehyde [14]. In particular, hydrogen amorphous silicon carbide (a-SiC:H) films have attracted much interest for their potential applications in many kinds of opto-electronic devices [15, 16]. By controlling the carbon content in a-Si<sub>0.72</sub>C<sub>0.28</sub>:H films, the optical band gap could be readily adjusted between 1.8 and 3.2 eV, which makes them become suitable candidates in application in full-color light emitting diodes (LED). In our previous work, we have studied the microstructures and optical properties of NWASC films prepared by two steps: First, the formation of silicon nanowire on silicone type p by metal-assisted chemical etching [17]. Second, deposited of hydrogenated amorphous SiC thin films on silicon nanowire by pulverization RF magnetron sputtering, with different thickness. The NWASC films elaborated are used to investigate devices for energy conversion.

### 2. EXPERIMENTAL

The formation of Nanowire Amorphous Silicon Carbide (NWASC) are prepared by two stapes: First, Elaborated silicon nanowires by metal-assisted chemical etching. Second, deposition of hydrogenated amorphous Silicon Carbide thin films on silicon nanowire, by RF magnetron sputtering of p-type 6H-SiC polycrystalline, with different thickness. Moreover, we have studied the morphology and optical properties of NASC with differences thickness of SiC thin films, using, scanning electron microscopy (SEM), UV Spectroscopy and photoluminescence (PL). After formation of the ohmic contact as aluminum, the samples were placed into a deposition chamber in order to evaporate a thin layer of gold (Au, with 99.9% purity) on the NWASC to form Schottky contact (Au/ NWASC /pSi/Al) to investigate devices for energy conversion.

### 3. RESULTS AND DISCUSSION

#### 3.1. Macrostructure of NWASC

The morphologies and structures of the Si and SiC nanowire arrays were further characterized by SEM, and the results are shown in Figure 1a, b, c and d. It can be observed from Figure 1b that the diameter and length of the Si nanowires are about 80 nm and 3  $\mu\text{m}$ , respectively. In Figure 1d demonstrates that the dimensions of the NWASC are similar to those of the Si nanowires.

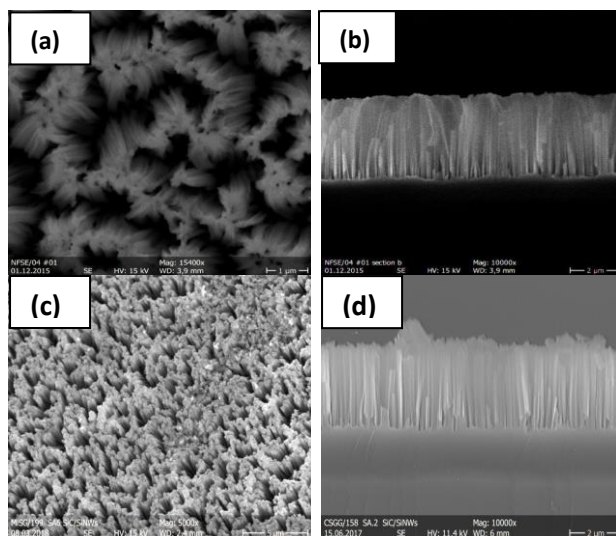


**Figure 1.** SEM micrographs of :*(a) Silicone nanowire (b) Cross sectional view Silicone nanowire (c) NWASC film grown on p-Si nanowire wafer (a) Cross sectional view of NWASC film grown on p-Si nanowire wafer*

#### 3.2. Photoluminescence measurements

The luminescence measurements were carried out at room temperature with a Perkin–Elmer LS-50B spectrometer and a Xenon lamp (150 W) with an excitation wavelength of 325 nm was used. Fig. 2 shows the PL spectra of NWASC exhibits a high PL intensity in bleu compared to the unetched a-SiC sample [18, 19]. Wang et al. found that the PL intensities are enhanced by UV irradiation 325 nm at room temperature and the luminescence center with peak energy 2.20 eV is induced by the UV light for the porous-like SiC samples, they suggested that UV irradiation may induce metastable states as luminescence centers in the sample [20, 21].

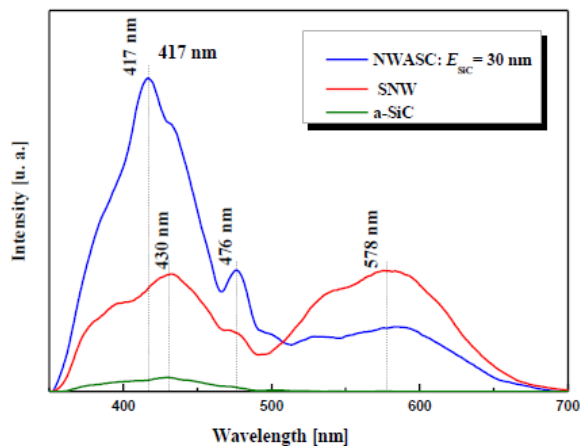


**Figure 2.** Photoluminescence spectra of a-SiC:H/p-Si, Si nanowire and NWASC films

### 3.3. Au-NASC Device

In order to study the electrical and optical performance of the formed NWASC layers a diode configuration has been realized. Figure 3 shows the top view of Au/NWASC/SNW/p-Si/Al Schottky diode structure.

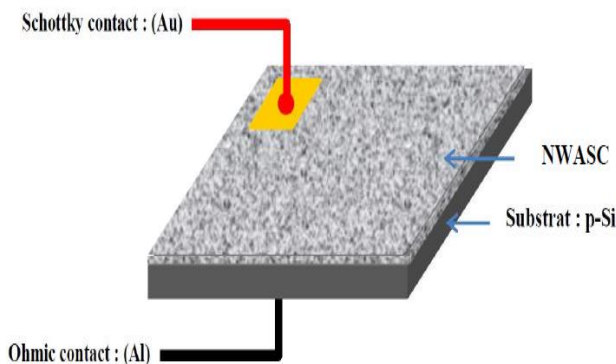


**Figure 3.** Top view of Au/NWASC/SNW/p-Si/Al Schottky diode structure

### 3.4. Device responses

Figure 4 shows the current–voltage characteristic of the Au/NWASC/SNW/p-Si/Al heterojunction measured in the dark and under illumination at room temperature. The I–V characteristics were measured under illumination by power white light (38 W) lamp, as shown in figure 4. Typical good rectifying and photoelectric behavior were observed for the device. The dark leakage current is small, whereas its photocurrent generated under illumination is higher. It is observed that the heterojunction exhibits a rectifying behavior in the presence of light too. Under reverse bias conditions photocurrent caused by the NWASC/SNW/p-Si heterojunction irradiated under illumination by white light lamp was evidently much larger than the dark current.

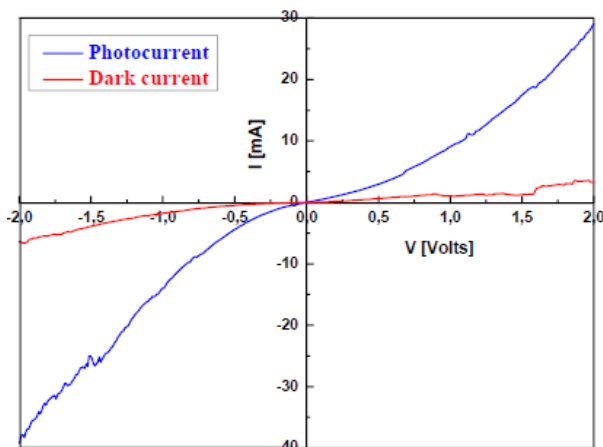


**Figure 4.** *I-V characteristics curves Au/NWASC/SNW/p-Si/Al heterojunction in dark and in light (light 38 W white lamp)*

#### 4. CONCLUSION

In this work, we have discussed the formation of NWASC. This obtained structure encouraged us to elaborate devices based on this substrate such as Au/NWASC/SNW/p-Si/Al Schottky diode. The obtained results indicated clearly the impact of the nanowires structure on the optical properties of the fabricated Au/NWASC/SNW/p-Si/Al Schottky diode, where an increase of the photocurrent was noticed. Finally, Schottky diodes realized with a nanowire thin SiC films (Au/NWASC/SNW/p-Si/Al) showed a good rectifying behavior which could allow the fabrication of Schottky diodes for energy conversion.

#### ACKNOWLEDGEMENTS

This work was supported by Funds National Research (DG-RSDT/MESRS, Algeria).

#### REFERENCES

- [1].T. Ishikawa, Y. Kohtoku, K. Kumagawa, T. Yamamura, T. Nagasawa, *Nature* 391 (1998) 773.
- [2].H. Dai, E.W. Wong, Y.Z. Lu, S. Fan, C.M. Lieber, *Nature* 375 (1995) 769.
- [3].K.W. Wong, T. Zhou, C.K. Au, H.L. Lai, C.S. Lee, S.T. Lee, *Appl. Phys. Lett.* 75 (1999) 2918.
- [4].J.W. Liu, D.Y. Zhong, F.Q. Xie, M. Sun, E.G. Wang, W.X. Liu, *Chem. Phys. Lett.* 348 (2001) 357.
- [5].Y.H. Gao, Y. Bando, K. Kurashima, T. Sato, *J. Electron Microsc.* 49 (2000) 641.
- [6].A. Kassiba, M. Tabellout, S. Charpentier, N. Herlin, J.R. Emery, *Solid State Commun.* 115 (2000) 389.
- [7].S. Kaci, R. Rahmoune, F. Kezzoula, Y. Boudiaf, A. Keffous, A. Manseri, H. Menari, H. Cheraga, L. Guerbous, Y. Belkacem, R. Chalal, I. Bozetine, A. Boukezzata, L. Talbi, K. Benfadel, M.-A. Ouadfel, Y. Ouadah *Optical Materials* 80 (2018) 225.
- [8].Y.H. Gao, Z. Zhang, L.S. Liao, X.M. Bao, *J. Mater. Res.* 12 (1997) 1640.
- [9].C. Schnabel, M. Worner, B. Gonzalez, I. Del Olmo, M. Braun, *Electrochim. Acta.* 47 (2001) 719.
- [10]. Larermann, R. Memming, D. Meissner, *J. Electrochem. Soc.* 144 (1997) 73.
- [11]. J. Akikusa, S.U.M. Khan, *Int. J. Hydrogen Energy* 27 (2002) 863.
- [12]. D.H. Van Dorp, N. Hijnen, M.D. Vece, J.J. Kelly, *Angew. Chem. Int. Ed.* 48 (2009) 6085.
- [13]. H. Liu, G. She, L. Mu, W. Shi, *Materials Research Bulletin* 47 (2012) 917.

- [14]. W.M. Zhou, L.J. Yan, Y. Wang, Y.F. Zhang, *Appl. Phys. Lett.* 89 (2006) 013105.
- [15]. Y. Hamakawa, D. Kruangam, T. Toyama, M. Yoshimi, S. Paasche, H. Okamoto, *Optoelectron. Dev. Technol.* 4 (1989) 281.
- [16]. Y. Tawada, M. Tsuge, H. Kondo, Y. Okamoto, J. Hamakawa, *J. Appl. Phys.* 53 (1982) 5273.
- [17]. N. Brahiti, T. Hadjersi, S. Amirouche, H. Menari, O. ElKechai, *International Journal of Hydrogen Energy*, 43, N° 24 (2018) 11411.
- [18]. A.M. Ouadfel, A. Keffous, A. Kheloufi, A. Cheriet, C. Yaddaden, N. Gabouze, M., Y. Belkacem, A. Boukezzata, S. Kaci, L. Talbi, Y. Ouadah, I. Bozetine, B. Rezgui, L. Guerbous, H. Menari, B. Mahmoudi, I. Menous. *Optical Materials* 65 (2017) 117-123
- [19]. Z. Enlei, W. Guosheng, L. Xiaozhu and W. Zhumin, *Bull. Mater. Sci.*, 37, N° 6 (2014) 1249.
- [20]. J.N. Wang, Z.M. Chen, P.W. Woo, W.K. Ge, Y.Q. Wang, M.B. Yu, *Appl. Phys. Lett.* 74 N° 7 (1999) 923.
- [21]. S. Kin, J.E. Spanier, I.P. Herman, *Jpn. J. Appl. Phys.* 39 (2000) 5875.

## Determination of Modulus of Elasticity for Ash (*Fraxinus spp.*) Grown in Turkey Using Ultrasound

Şemsettin Kılınçarslan<sup>1\*</sup>, Bilgin İçel<sup>2</sup> and Yasemin Şimşek<sup>1</sup>

<sup>1</sup> Suleyman Demirel University, Department of Civil Engineering, Isparta, TURKEY

<sup>2</sup> Çanakkale Onsekiz Mart University, Department of Material and Material Processing Technologies, Çanakkale, TURKEY

\*semsettinkilincarslan@sdu.edu.tr

### ABSTRACT

Non-destructive testing (NDT) is an effective method to test the mechanical and physical properties of the material. Ultrasound has been used in prediction for some important wood species grown in Turkey. The modulus of elasticity (MOE), is one of primary indexes in evaluating mechanical properties of wood. There are many studies in our country related to the modulus of elasticity (MOE) of wood. But, there is a lack of knowledge about dynamic modulus of elasticity values for hardwood species in Turkey. The primary objective of this study was to evaluate the effectiveness of a NDT device for MOE measurement depending on both literature and our results of standard testing.

In this study, three point bending test was performed for static modulus of elasticity on Ash (*Fraxinus ssp.*). EPOCH 650, works on the principle of sound waves velocity, was used for the dynamic modulus of elasticity. Specimens acclimatized 20 °C and 65% relative humidity conditions, until their moisture reach to 12% moisture content. 20 x 20 x 360 mm specimens were subjected to three point bending tests. Sound velocities of 20 x 20 x 20 mm specimens were determined using EPOCH 650 ultrasonic flaw detector with 2.25 MHz contact longitudinal transducers at constant moisture content. Densities of the samples were calculated according to TS 2472 (2005) using stereometric method.

Consequently, average dynamic modulus of elasticity ( $E_{dyn}$ ) values for the species tested varied from 10.506 to 13.458 GPa.  $E_{dyn}$  values obtained at the end of the study are higher than the calculated MOE values. As a result, results indicate that ultrasound can be used in determination of modulus of elasticity for Ash (*Fraxinus ssp.*). Ultrasonic wave technique may be considered as alternatives to destructive testing. The ultrasonic method is more rapid and offers an opportunity for much greater sampling.

**KEYWORDS** - Non-destructive testing, Ash, Modulus of elasticity,  $E_{dyn}$

### 1. INTRODUCTION

People have benefited from the tree as a building material from ancient times until today. From the time of use, the wood material has never lost its importance. The wood material used in a wide range of areas is the only natural raw material that does not harm the environment [1,2,3].

Wood as building material; it has been used for many years in the production of products such as passageways and bridges, berths, foundations, buildings' structural systems (billets, frames and panels), large span structures, roofs, walls, flooring and stair coverings, door and window joinery, molds and berths and furniture [4,5,6].

The conventional destructive tests used to determine the mechanical properties of wood materials, despite the precise results, damage the material. Since the material tested cannot be used for the same purpose, it can be said that economic loss has also occurred. In addition, destructive assessment methods are based on sampling. A number of samples should be taken to represent the whole of the material to be tested or a group of materials. Destructive traditional methods require a certain laboratory infrastructure and equipment for testing. These methods do not allow for on-site evaluation. These disadvantages of conventional destructive testing methods have led to the development of alternative methods. These methods are referred to as "non-destructive assessment

methods". In these methods, there is no damage to the material during and after the evaluation, or even though there is very little damage, the end use of the material does not have a significant effect on the properties and performance [7,8]. Therefore, the method of non-destructive testing is defined as the determination of the defects and condition of the material on the surface and internal structure without disturbing the integrity and usability of the material in any way [9].

Non-destructive testing (NDT) is an effective method to test the mechanical and physical properties of the material. Ultrasound has been used in prediction for some important wood species grown in Turkey. The modulus of elasticity (MOE), is one of primary indexes in evaluating mechanical properties of wood. There are many studies in our country related to the modulus of elasticity (MOE) of wood. But, there is a lack of knowledge about dynamic modulus of elasticity values for hardwood species in Turkey. The primary objective of this study was to evaluate the effectiveness of a NDT device for MOE measurement depending on both literature and our results of standard testing.

The main objective of this study is to evaluate the effectiveness of a non-destructive tester for the modulus of elasticity of hardwood. For this, uniaxial bending test was performed and dynamic elasticity module was determined by using static elasticity module and ultrasonic tester.

## 2. MATERIAL AND METHOD

In this study, three point bending test was performed for static modulus of elasticity on Ash (*Fraxinus* spp.). EPOCH 650, works on the principle of sound waves velocity, was used for the dynamic modulus of elasticity.

Ash timbers used in the study is supplied from Trabzon province. Samples from a trial area were studied to eliminate the impact of environmental conditions. Samples are given from nine different trees in one trial area. A tree was selected every ten meters. Thus, nine trees were selected. Nine samples were taken from these nine trees. Figure 1 shows images of ash timber used in the study.



*Figure 1. Images of Ash Timber Used For Modulus of Elasticity Measurement*

20x20x360 mm specimens were prepared bending tests. Specimens acclimatized 20 °C and 65% relative humidity conditions, until their moisture reach to 12% moisture content. 20 x 20 x 360 mm specimens were subjected to three point bending tests. Three point bending tests are given in Figure 2.



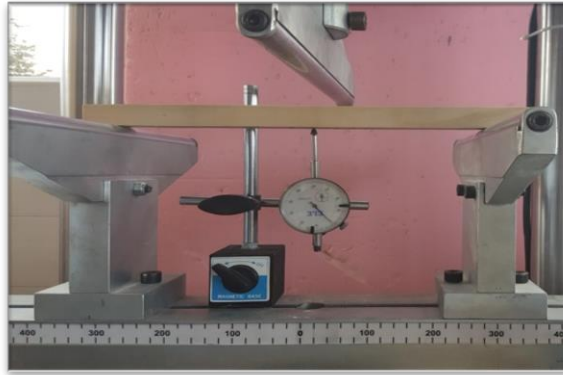


**Figure 2. Sample and Three Point Bending Test Configuration**

Static elastic modulus was calculated by using stress-strain values from the linear elastic region of these curves. Samples were obtained from the samples after the bending test for ultrasonic testing. Ultrasonic test samples sizes are 20x20x20 mm.

Sound velocities of 20 x 20 x 20 mm specimens were determined using ultrasonic flaw detector with 2.25 MHz contact longitudinal transducers at constant moisture content. Ultrasonic test is given in Figure 3.

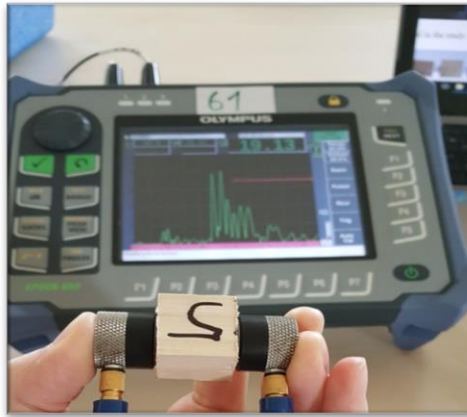


**Figure 3. Time of Flight Measurements of Samples**

Ultrasonic measurements were performed by using flaw detector (Olympus, USA). And, contact type transducer that propagates L direction waves at 2.25 MHz frequency were used to measure time of flight values. Direct method was used in ultrasonic measurements. Densities of the samples were calculated according to TS 2472 (2005) using stereometric method.

Ultrasonic wave velocities (UWV) were calculated by velocity and time relation using obtained time of flight values. Then,  $E_{dyn}$  calculated using Eq. 1.

$$E_{dyn} = \rho V^2 10^{-6} \quad (1)$$

$E_{dyn}$  is dynamic elasticity modulus (MPa)

$\rho$  is density ( $\text{kg/m}^3$ )

$V$  is ultrasonic wave velocity (m/s)

Dynamic and static modulus of elasticity values comparison are given in Table 1.

**Table 1.** *Dynamic and Static Modulus of Elasticity Values Comparison.*

Number of samples	Dynamic modulus of elasticity (GPa)	Static modulus of elasticity (GPa)
1	13.184	12.419
2	12.910	10.981
3	13.836	12.846
4	13.435	11.719
5	13.944	13.288
6	11.355	10.435
7	13.016	12.228
8	14.978	12.925
9	13.262	12.753
Average	13.324	12.177
Standard deviation	0.97	0.95

Results of three-point bending test show that the ash samples have static modulus of elasticity of about 12.177 GPa and standard deviation values of around 0.95. Results of EPOCH 650 measurement show that the ash samples have dynamic modulus of elasticity of about 13.324 GPa and standard deviation values of around 0.97.

Dynamic modulus of elasticity was higher than the values of the static modulus of elasticity. When the static and dynamic modulus of elasticity values of the samples were examined, the values of the elastic modulus were close to each other and the results were related to each other. Dynamic and static modulus of elasticity comparison graphic is given in Figure 4.

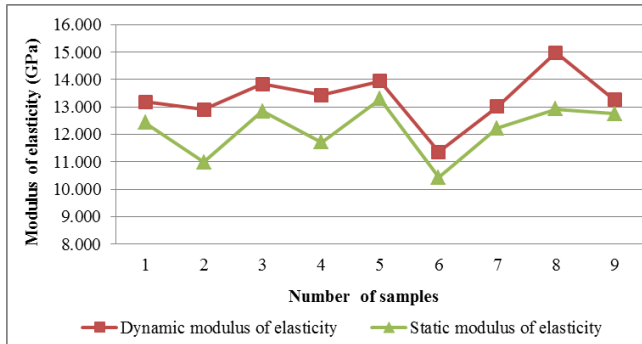


**Figure 4.** *Dynamic and Static Modulus of Elasticity Comparison.*

The values of the dynamic modulus of elasticity were higher than the values of the static modulus of elasticity. However, it is seen that the values are compatible with each other.

### 3. CONCLUSION

In the literature, it is stated that the dynamic modulus of elasticity is higher than the static modulus of elasticity. At the end of the study dynamic modulus of elasticity values obtained higher than the calculate static modulus of elasticity values.

When the static and dynamic modulus of elasticity values of the samples were examined, the values of the elastic modulus were close to each other and the results were related to each other. As a result, results indicate that ultrasound can be used in determination of modulus of elasticity for Ash (*Fraxinus spp.*). Ultrasonic wave technique may be considered as alternatives to destructive testing. The ultrasonic method is more rapid and offers an opportunity for much greater sampling.

## ACKNOWLEDGEMENTS

This study was supported by Suleyman Demirel University Scientific Research Projects. The authors would like to thank SDU-BAP for their support.

## REFERENCE

- [1] A.Y. Bozkurt, Wood technology. University of İstanbul, Stone Printing House, 220, 1986.
- [2] Y.A. Bozkurt, Y. Göker, Physical and mechanical wood technology. University of İstanbul, Faculty of Forestry Publications, İstanbul, 388 (1987), 345-348.
- [3] A.R. Uluata, Factors affecting the mechanical properties of wood materials. Atatürk University, Journal of Agriculture Faculty, 18 (1-4), Erzurum, 2011.
- [4] S. Cakır, Evaluation of traditional Black Sea wooden housing construction method in terms of contemporary technology. PhD Thesis, University of Mimar Sinan, Graduate School of Natural and Applied Sciences, s. 230, 2000.
- [5] E. Bostancıoğlu, E.D. Birir, Ecology and the future of the wood in wooden Turkey. University of Uludağ, Journal of Faculty of Engineering and Architecture, 37-44, 9-2, 2004.
- [6] H. Efe, A. Kasal, Determination of Some Physical and Mechanical Properties of Various Massive and Composite Wood Materials. Journal of Polytechnic, 10(3), 303-311, 2007.
- [7] H.F. Öktem, Examination of ultrasonic nondestructive examination technique with finite element method. PhD Thesis, University of Dokuz Eylül, Graduate School of Natural and Applied Sciences, 58, 2000.
- [8] H. Gür, Importance and Methods of Non-Destructive Testing, Ankara, 2004.
- [9] Anonim, İstanbul University Faculty of Forestry Non-Destructive Testing Methods Unpublished Lecture Notes, İstanbul, 2004.

## Study on Temperature Distribution in Wellbore during Drilling

Jiangshuai Wang<sup>1</sup>, Gonghui Liu<sup>1,2,\*</sup>, Jun Li<sup>1</sup>, Xueting Wu<sup>3</sup>, Hongwei Yang<sup>1</sup>, Kuidong Luo<sup>1</sup>

<sup>1</sup> China University of Petroleum (Beijing), College of Petroleum Engineering, Beijing, China

<sup>2</sup> Beijing University of Technology, Beijing, CHINA

<sup>3</sup> Xi'an Shiyou University, College of Earth Resource Sciences and Engineering, Xi'an, CHINA

\*Corresponding author Email: wjs125126@163.com

### ABSTRACT

Accurate prediction of wellbore temperature profile is significant for drilling. A simplified model is built in this study to predict the temperature distribution in wellbore during drilling. The simplified model takes the formation between the borehole and the position where the temperature is the original formation temperature as a heat-transfer unit. In addition, the Joule-Thomson cooling effect at the outlet of the nozzles is considered in this paper. The simplified model is validated by field measured data and the analytical model. The primary conclusions are as follows. (1) The calculated results are in good agreement with the measured temperature data. The maximum difference between calculated result and measured data does not exceed 2 °C when circulation is stable. In addition, the biggest error between the two does not exceed 7.3% during drilling. (2) The simplified model predictions are in good agreement with the analytical model results. It indicates that the simplified model is reliable.

**KEYWORDS**-Wellbore temperature profile, Simplified model, Heat-transfer, Joule-Thomson cooling effect, Measured data.

### 1. INTRODUCTION

The accurate calculation of wellbore temperature profile has a great influence on drilling engineering. It relates to drilling safety and wellbore pressure balance (Kabir et al. 1996; Cheng et al. 2011; Davraz et al. 2015; Koru and Serçe 2015; Kudaykulov and Zhumadillayeva 2015. Liu et al. 2018). Several models to predict the temperature distribution have been applied. In words, there are two methods for calculating the temperature profile in the wellbore. One is the numerical method (Raymond 1969; Wooley 1980; Wu et al. 2012); the other is analytic (Ramey 1962; Kabir et al. 1996; Shan et al. 2016). On numerical method aspect, Raymond (1969) developed the first numerical model. It can predict the temperature of circulating fluid for both pseudo-steady-state and transient conditions. Wooley (1980) developed a computer model for predicting wellbore temperatures for different flow options. The model is solved by applying the finite-difference method. Wu et al. (2012) developed a numerical model. It can calculate the heat transfer between the wellbore and reservoir during fluid circulation. On analytical method aspect, Ramey (1962) developed a model. It can predict the temperature profile for a single-phase fluid flowing through a single conduit in a line-source well. However, this solution is only limited to the ideal gas and incompressible fluid. Edwardson et al. (1962) developed an analytical model to determine the formation-temperature distribution caused by fluid circulation. Kabir et al. (1996) derived an analytical model to determine the temperature the temperature of the circulating fluid in drilling, workover, and well-control operations. Shan et al. (2016) derived a new analytical model. It can predict the temperature profiles in wellbore during drilling.

In this paper, a simplified model is developed to predict the temperature distribution in wellbore during drilling. First, the simplified model takes the formation between the borehole and the position where the temperature is the original formation temperature as a heat-transfer unit. Moreover, because of the Joule-Thomson cooling effect at the outlet of the nozzles, the fluid bottom-hole temperature is lower than that above the drill-bit nozzles. The Joule-Thomson cooling effect is ignored in most previous researches, but considered in this paper. In words, the simplified model established in this study is a numerical model, and easy to be solved with a high accuracy.

## 2. MODELING AND SOLVING

During normal drilling operation, drilling-fluid is injected into the drill string and then enters the annulus through the bit, eventually back to the ground (Figure 1). During circulation, the formation exchanges heat with the annulus drilling fluid. Meanwhile, the annulus drilling fluid exchanges heat with drilling fluid in the drill pipe.

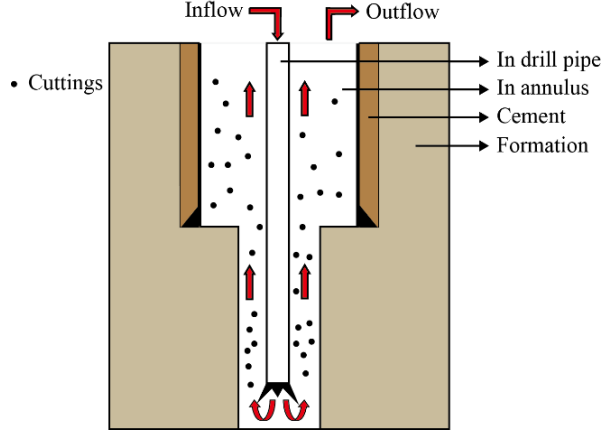


**Figure 1.** Schematic diagram of fluid flow during drilling

### 2.1. Mathematical model

Temperature distribution in drill pipe is shown in Eq. (1).

$$T_{p,L+\Delta L} = T_{p,L} + \frac{A_2 \Delta L \Delta t (T_{a,L} - T_{p,L})}{(A_1 \Delta t + A_3 \Delta L)} \quad (1)$$

$$\begin{cases} A_1 = C_p m_p \\ A_2 = \frac{\pi d_p k_p}{l_p} \\ A_3 = C_p \rho_p A_p \end{cases} \quad (2)$$

Where  $T_{p,L}$ ,  $T_{p,L+\Delta L}$ , is the fluid temperature of inflowing and outflowing microelement in pipe, °C;  $T_{a,L}$ , is the temperature of fluid in annulus, °C;  $C_p$  is the heat capacity of inflow fluid, J/(kg·°C);  $m_p$  is the mass flow of inflow fluid in drill pipe, kg/s;  $d_p$  is the outer diameter of drill pipe, m;  $k_p$  is the thermal conductivity of drill pipe, W/(m·°C);  $l_p$  is the pipe wall thickness, m;  $\rho_p$  is density of inflow fluid in pipe, kg/m<sup>3</sup>;  $A_p$  is flow area of fluid in drill pipe, m<sup>2</sup>;  $\Delta L$  is length of micro-body, m;  $\Delta t$  is time step, s.

Temperature distribution in annulus is shown in Eq. (3).

$$T_{a,L} = \frac{C_1 \Delta t T_{a,L+\Delta L} + C_2 \Delta L \Delta t T_{g,L+\Delta L} - C_2 \Delta L \Delta t T_{a,L+\Delta L}}{(C_1 \Delta t + C_4 \Delta L)} + \frac{C_3 \Delta L \Delta t T_{p,L+\Delta L} - C_3 \Delta L \Delta t T_{a,L+\Delta L} + C_4 \Delta L T_{a,L+\Delta L}}{(C_1 \Delta t + C_4 \Delta L)} \quad (3)$$

$$\begin{cases} C_1 = C_a m_a \\ C_2 = \frac{\pi d_c k_f}{l_{well}} \\ C_3 = \frac{\pi d_p k_p}{l_p} \\ C_4 = C_a \rho_a A_a \end{cases} \quad (4)$$

Where  $T_{a,L}$ ,  $T_{a,L+\Delta L}$  is the fluid temperature of inflowing and outflowing microelement in annulus, °C;  $C_a$  is the heat capacity of inflow fluid, J/(kg·°C);  $m_a$  is the mass flow of inflow fluid in annulus, kg/s;  $d_c$  is the outer diameter of the cylinder where temperature is initial formation temperature, m;  $k_f$  is the thermal conductivity of formation, W/(m·°C);  $T_{g,L+\Delta L}$  is the initial formation temperature at the  $L+\Delta L$ , °C;  $l_{well}$  is the distance between borehole and position where temperature is initial formation temperature (Holmes and Swift (1970) considers that the distance is 3.05m), m;  $\rho_a$  is density of inflow fluid in annulus, kg/m<sup>3</sup>;  $A_a$  is flow area of fluid in annulus, m<sup>2</sup>.

## 2.2. Solution

$T_a$  and  $T_p$  along the well trajectory can be solved by the following steps:

Step 1: Assume initial  $T_{a,L}^0 = T_{g,L}$  and use Eq. (1) to calculate  $T_{p,L}^i$  from surface to bottom.

Step 2: Use  $T_{p,L}^i$  and Eq. (3) to calculate  $T_{a,L}^i$  from bottom to surface.

Step 3: Use  $T_{a,L}^i$  and Eq. (1) to calculate  $T_{p,L}^{i+1}$  from surface to bottom.

Step 4: Use  $T_{p,L}^{i+1}$  and Eq. (3) to calculate  $T_{a,L}^{i+1}$  from bottom to surface.

Step 5: Repeat Step 3 and 4 until the follow convergence criterion is achieved:

$$\left| \frac{\sum_{j=1}^{H/\Delta L} T_{a,j}^{i+1}}{\sum_{j=1}^{H/\Delta L} T_{a,j}^i} - 1 \right| < 10^{-\varepsilon} \quad (5)$$

Where  $\varepsilon$  is a factor characterizing the accuracy of the simplified model.

## 3. CASE STUDY

To verify the reliability of the model, the simplified model is validated by field measured data and the Shan et al. (2016) analytical model.

### 3.1. Validation by field measured data

The simplified model is verified by use of the measured temperature data from a vertical well in JIDONG oilfield. The on-site operation process is “tripping out - installing measuring equipment - tripping in – drilling”. Well basic data and thermal properties parameters are provided in Table 1. In Figure 2, the calculated results of the annular bottom-hole temperature are basically consistent

with the measured data during drilling. The calculated maximum bottom-hole temperature is stable at 50~51 °C. The maximum error between calculated result and measured data does not exceed 2 °C when circulation is stable. In addition, the biggest error between the two does not exceed 7.3% during drilling. This phenomenon indicates that the simplified model can be applied in the oilfield.

**Table 1.** Basic data and thermo-physical parameters.

Depth (Vertical depth)/(m)	2050	Density of fluid/(kg/m <sup>3</sup> )	1150
Casing shoe depth /(m)	2010	Heat capacity of fluid/(J/kg•°C)	4180
Outer diameter of the drill pipe/(m)	0.127	Density of rock/(kg/m <sup>3</sup> )	2650
Inner diameter of the drill pipe/(m)	0.0889	Heat capacity of rock/ (J/kg•°C)	920
Diameter of bit/(m)	0.2159	Temperature of injected fluid/(°C)	20
Outer diameter of the casing/(m)	0.2445	Thermal conductivity of drill pipe/(W/m•°C)	43
Inner diameter of the casing/(m)	0.2245	Thermal conductivity of casing/(W/m•°C)	43
Rate of penetration/(m/h)	2	Pump rate/(L/s)	28
Thermal conductivity of formation/(W/m•°C)	2.25	Temperature drop in drill bit (the Joule-Thomson cooling effect) /(°C)	2

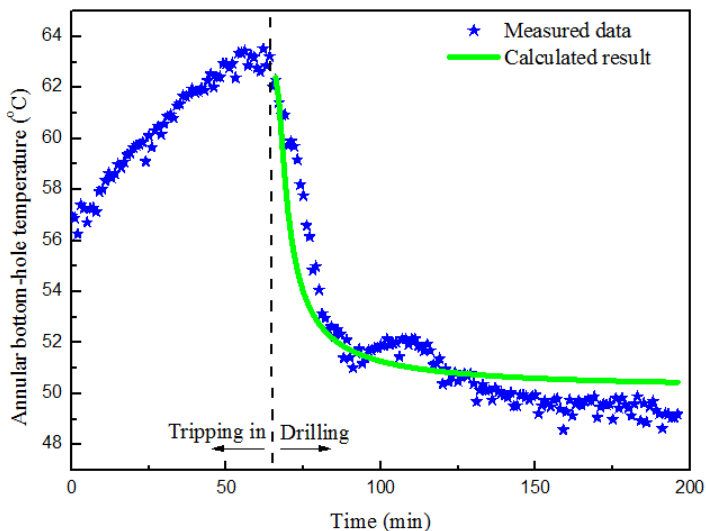


**Figure 2.** The comparison of simplified model with the measured data during drilling (JIDONG Well).

### 3.2. Validation by analytical model

Moreover, comparison of simplified model with the Shan et al. (2016) analytical model is conducted by use of the same data provided in Table 1. Results of simplified model and the Shan et al. (2016) analytical model are presented in Figure 3. The results of two models are almost the same. The possible reason for this phenomenon is that derivations of the analytical model and the

simplified model were dependent on several same assumptions, but different in derivation way and formula of model. One is analytical, the other is numerical. Comparison between two models indicates that the simplified model is reliable.

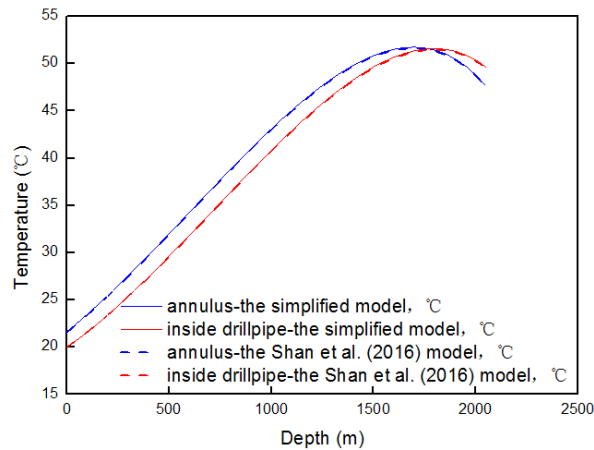


**Figure 3.** The comparison of simplified model with the Shan et al. (2016) analytical model.

#### 4. CONCLUSIONS AND FURTHER RESEARCH

- (1) A simplified model is established in this paper to predict the temperature distribution in wellbore during drilling. The Joule-Thomson cooling effect is considered in the model. In words, the simplified model established in this study is easy to be solved with a high accuracy.
- (2) The calculated results are in good agreement with the measured temperature data. The maximum difference between calculated result and measured data does not exceed 2 °C when circulation is stable. The biggest error between the two does not exceed 7.3% during drilling. In addition, predicted results of the simplified model are in good agreement with results of the analytical model.
- (3) In this paper, the simplified model has only been validated with a single well. Therefore, the simplified model should be validated with more wells later to widen the field application of the model.

#### ACKNOWLEDGMENTS

Project supported by the Key Program of National Natural Science Foundation of China (Project No. 51734010, 51334003).

#### REFERENCES

- [1].Cheng, W. L., Huang, Y. H., Lu, D. T. et al. 2011. A Novel Analytical Transient Heat-Conduction Time Function for Heat Transfer in Steam Injection Wells Considering the Wellbore Heat Capacity. *Energy* 36(7): 4080-4088. [DOI.org/10.1016/j.energy.2011.04.039](https://doi.org/10.1016/j.energy.2011.04.039).
- [2].Davraz, M., Kili arslan,  ., Koru, M. et al. 2015. International Conference on Computational and Experimental Science and Engineering (ICCESN 2015), 14-19 October, 2015 Antalya-Turkey. [DOI: 10.12693/APhysPolA.130.469](https://doi.org/10.12693/APhysPolA.130.469).
- [3].Edwardson, M. J., Girner, H. M., Parkison, H. R. et al. 1962. Calculation of Formation Temperature Disturbances Caused by Mud Circulation. *J Pet Technol* 14 (4): 416-426. SPE-124-PA. [DOI.org/10.2118/124-PA](https://doi.org/10.2118/124-PA).
- [4].Holmes, C.S., Swift S.C. Calculation of Circulating Mud Temperatures. *Journal of Petroleum Technology*, 1970, 22(6): 670-674. [DOI.org/10.2118/2318-PA](https://doi.org/10.2118/2318-PA).



- [5].Kabir C S, Hasan A R, Kouba G E, et al., 1996. Determining circulation fluid temperature in drilling, workover, and well-control operations. SPE Drilling & Completion, 1996, 6:74-79. DOI.org/10.2118/24581-PA.
- [6].Koru, M. and Serçe, O. 2015. International Conference on Computational and Experimental Science and Engineering (ICCESN 2015), 14-19 October, 2015 Antalya-Turkey. DOI: 10.12693/APhysPolA.130.453.
- [7].Kudaykulov, A. and Zhumadillayeva, A. 2015. International Conference on Computational and Experimental Science and Engineering (ICCESN 2015), 14-19 October, 2015 Antalya-Turkey. DOI: 10.12693/APhysPolA.130.335.
- [8].Liu, J et al. 2018. Temperature field analysis on the highly-deviated wellbore in backwashing condition. JOURNAL OF PETROLEUM SCIENCE AND ENGINEERING. 2018, 161:515-529. DOI.org/10.1016/j.petrol.2017.12.018.
- [9].Ramey, H. J. Jr. 1962. Wellbore Heat Transmission. J Pet Technol 14(4):427-435. SPE-96-PA. DOI.org/10.2118/96-PA.
- [10]. Raymond, L. R. 1969. Temperature Distribution in Calculating Drilling Fluid. J Pet Technol 21(3):333-341. SPE-2320-PA. DOI.org/10.2118/2320-PA.
- [11]. Shan, L., Guo, B., and Cai, X. 2016. Development of an Analytical Model for Predicting the Fluid Temperature Profile in Drilling Gas Hydrates Reservoirs. J. Sustain. Energ. Eng. 3(3): 254-269. DOI.org/10.7569/JSEE.2015.629516.
- [12]. Wooley, G. R. 1980. Computing Downhole Temperature in Circulation, Injection and Production Wells. J Pet Technol 32(9): 1509-1522. SPE-8441-PA. DOI.org/10.2118/8441-PA.
- [13]. Wu, B., Zhang, X., Jeffery, R. G. et al. 2012. A Coupled Model For Wellbore/reservoir Temperature Prediction and Stress Analysis During Fluid Circulation. Presented at the 46th US Rock Mechanics/Geomechanics Symposium, Chicago, 24-27 June. ARMA-2012-463.

## Stable Isotope Analysis of Soil Carbon Dioxide for Monitoring CO<sub>2</sub>-EOR and Sequestration in Yanchang Oilfield

Debin Kong<sup>1,2, 3,\*</sup>; Yiqiang Li<sup>1,2</sup>; Shanzhi Xu<sup>1,2</sup>; Hu Guo<sup>4</sup> and Yingfeng Peng<sup>1,2</sup>

<sup>1</sup> State Key Laboratory of Petroleum Resources and Prospecting, Beijing, China

<sup>2</sup> College of Petroleum Engineering, China University of Petroleum-Beijing, Beijing, China

<sup>3</sup> Department of Chemical and Petroleum Engineering, University of Calgary, Calgary, Canada

<sup>4</sup> School of Petroleum Engineering and Environmental Engineering, Yan'an University, Shanxi, China

\* mrdebin@163.com

### ABSTRACT

Monitoring of CO<sub>2</sub> sequestration process has been identified as one of the highest priorities needs to provide safe and secure storage of CO<sub>2</sub>. Soil gas monitoring, as an effective and timely near surface monitoring technique, have been validated by many pilot projects. Periodic monitoring of the soil CO<sub>2</sub> within and around the pilot area can verify any leakage and migration of the injected CO<sub>2</sub> or assess the efficacy of the sequestration process. The <sup>13</sup>C isotopic composition of soil CO<sub>2</sub> was obtained by representative well within and around the pilot area, it indicates no CO<sub>2</sub> leakage and migration to the surface. Moreover, the reservoir tracers verify the reliability of the soil gas monitoring method. The process of CO<sub>2</sub>-EOR and Sequestration in Yanchang Oilfield is deemed robust till now. Periodic monitoring of the reservoir and soil gas should be implemented, and more monitoring method should be used when CO<sub>2</sub> has been injected for several years.

**KEYWORDS** - CO<sub>2</sub>-EOR and Sequestration, Stable Isotope Analysis, Monitoring CO<sub>2</sub>-EOR, CO<sub>2</sub> leakage detection and Sequestration, <sup>13</sup>C isotopic composition

### 1. INTRODUCTION

Carbon capture and storage (CCS) is considered to be one of the promising technologies to achieve greenhouse gas emissions reduction targets. Geological storage method involves mainly injecting CO<sub>2</sub> into underground geological formations, the suitable storage sites mainly include depleted oil and gas field, saline formations, unmineable coal seams, and saline-filled basalt formations. Injecting carbon dioxide into oil and gas fields can not only store CO<sub>2</sub> but also achieve enhanced oil or gas recovery. This geological storage method is attractive than another because of their proven trapping safety and economic potential.

The main purpose and objective of CCS is removing carbon from the atmosphere and storing it safely for long periods of time [1]. Ensuring the storage safety and security of CO<sub>2</sub> in the geological formations is the cornerstone of CCS. It is essential to monitoring and determining the location and state of CO<sub>2</sub> migration in the reservoir. The MVA [2] (monitoring, verification, and accounting) techniques have been applied to several CCS projects, now conducted or have been planned in the worldwide. Soil gas monitoring has been an effective and timely near surface MVA technique to detect CO<sub>2</sub> leakage, which has been included in the MVA plan in several CCS projects [3-7]. The feasibility and efficiency of soil gas monitoring have been validated by many pilot projects. Carbon isotopes – <sup>13</sup>C has been used to distinguish between injected CO<sub>2</sub> and other CO<sub>2</sub> sources [8-10]. It illustrates the baseline surveys of CO<sub>2</sub> sinks and sources should be conducted according to site-specific, and the reliability should be verified combined with more monitoring technologies.

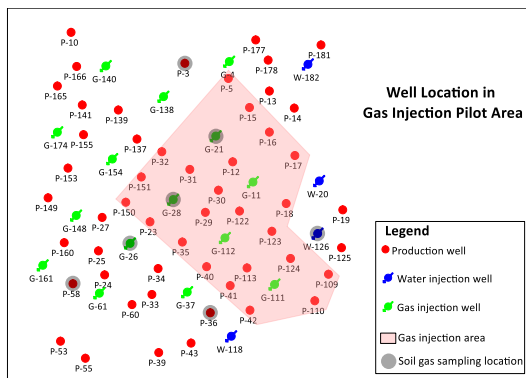


**Figure 1.** Well and sampling location in gas injection pilot area of WQ Oilfield

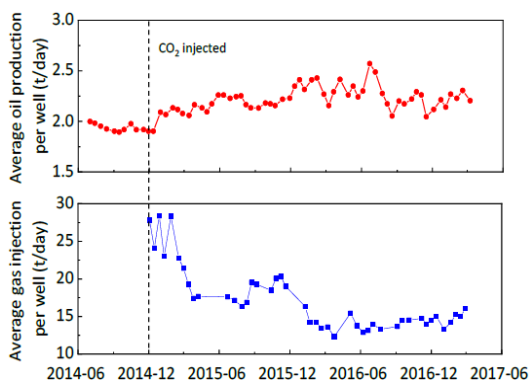


**Figure 2.** Well performance per well per day in the pilot area

Yanchang Oilfield is implementing its first carbon-dioxide enhanced oil recovery (CO<sub>2</sub>-EOR) carbon capture, utilization and storage (CCUS) demonstration project in an extra-low permeability reservoir since 2010. Its slope has a simple structure, stable formation, and less fault developed, which ensures the security and reliability during CO<sub>2</sub> sequestration process. The miscible CO<sub>2</sub>-EOR method was conducted in WQ Oilfield, a waterflood reservoir located in the center of CO<sub>2</sub>-EOR suitable area of Yanchang Oilfield, since December 2014. There are 5 gas injection wells and 18 oil production wells formed 5 well groups of injecting and producing in the pilot area(Figure1). As to the April 2017, the accumulative amount of CO<sub>2</sub> injected is 21400 tonnes with the average injection pressure 9.5 MPa and average injection rate 14.5 tonnes. Figure 2 illustrates that the oil production increase after CO<sub>2</sub> injection 2 months and the average oil production rate is improved by 23.32%.

The study was conducted to demonstrate that the injected CO<sub>2</sub> is securely sequestered in the targeted pilot area and no leakage to the surface. Periodic monitoring of the soil CO<sub>2</sub> within and around the pilot area was conducted before and after CO<sub>2</sub> injection. Meanwhile, the reservoir tracers analyze was used as an additional information source for detecting leaks to verify the reliability of monitoring technology.

## 2. MONITORING METHODS AND PROGRAM

To demonstrate that the injected CO<sub>2</sub> is securely sequestered in the targeted pilot area and no leakage to the surface. The soil gas sampling grid was located as Figure 1 shown, extends beyond

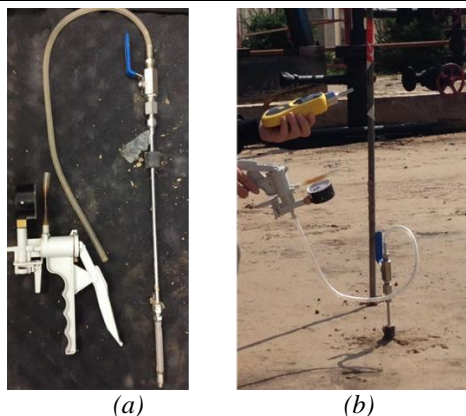


**Figure 3.** Soil gas sampler (a) and on-site sampling process (b)

the pilot area to ensure proactive monitoring of potential leaks beyond areas of interest. The  $\text{CO}_2$  stable isotopes  $^{13}\text{C}$  composition changes are measured to trace the source of  $\text{CO}_2$ . The soil gas is obtained in the shallow (1-2 meter) deep monitoring station holes [12]. As is shown in Figure 3, these are completed with PVC pipe and special soil-gas sampler. The soil gas sampler is perforated across the shallow deep. Afterward, the soil gas is collected and transferred to a Tedlar bag with the special piston-type gas sampler.  $\text{CO}_2$  stable isotopes concentration are measured using GC-IRMS (IsoPrime100) to trace the source of  $\text{CO}_2$ . These stations allow for periodic monitoring of the soil gas within and around the pilot area.

Tracers [2] are used as an additional information source for monitoring. The sulphur Hexafluoride ( $\text{SF}_6$ ) tracers are introduced into the injected  $\text{CO}_2$  to help detect it's migration across the well and verify the reliability of soil gas monitoring technology during  $\text{CO}_2$  storage.

### 3. RESULTS AND DISCUSSION

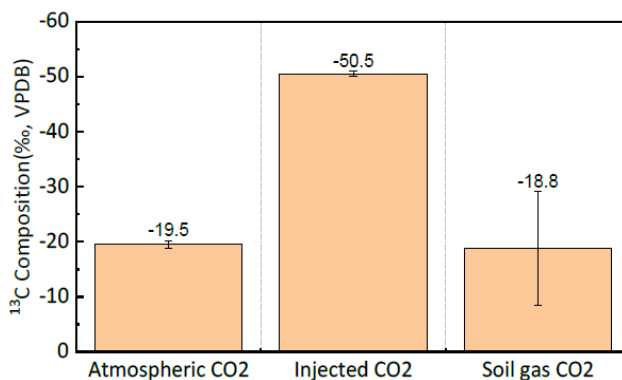


**Figure 4.**  $^{13}\text{C}$  composition of  $\text{CO}_2$  for the pilot project

The baseline sampling was collected from injection  $\text{CO}_2$ , atmospheric  $\text{CO}_2$ , and soil gas  $\text{CO}_2$  before  $\text{CO}_2$  injection in March 2014. The position of sampling soil gas is shown in Figure 1. The carbon isotope compositions of the different  $\text{CO}_2$  sources within the pilot area are shown in Figure 4. The analytical results from different sources show that the  $^{13}\text{C}$  isotopic composition of soil  $\text{CO}_2$  around 7 wells before injection  $\text{CO}_2$  falls between -12.45 and -29.14‰, samples of injection  $\text{CO}_2$  shows a narrow range of the  $^{13}\text{C}$  isotopic composition of  $-50.5 \pm 0.466$ ‰. The relatively large  $^{13}\text{C}$

variation up to the 31.7‰ difference between these two sources, suggests that that carbon isotope is a useful monitoring method for the pilot project.

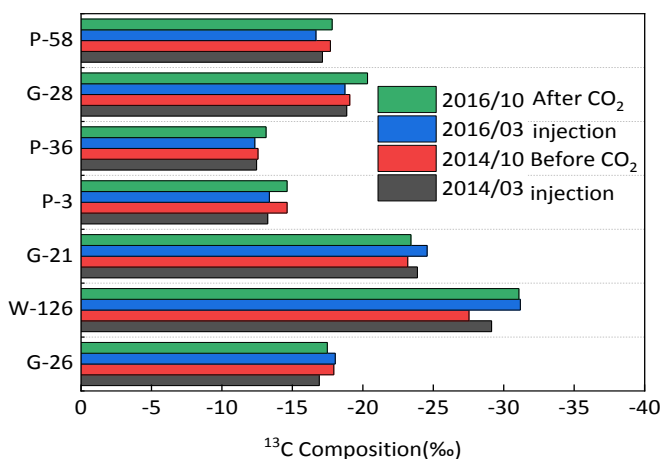


**Figure 5.**  $^{13}\text{C}$  composition of soil  $\text{CO}_2$  around 7 wells in the pilot area

A total of four samplings have been conducted, two before  $\text{CO}_2$  injection and two after  $\text{CO}_2$  injection. The position of sampling soil gas is shown in Figure 1. The analytical results are shown in Figure 5, the  $^{13}\text{C}$  isotopic composition of soil  $\text{CO}_2$  before  $\text{CO}_2$  injection ranges from -12.34‰ of well P-36 to -31.18‰ of well W-126. After  $\text{CO}_2$  injection, the relatively large  $^{13}\text{C}$  isotopic composition variation up to 10.05‰ in March 2016, and up to 9.68‰ of well W-126 in October 2016. It is still in the range of baseline after  $\text{CO}_2$  injection, suggests there is no  $\text{CO}_2$  leakage to the surface. Periodic soil gas sampling and analyses are continuing in the future.

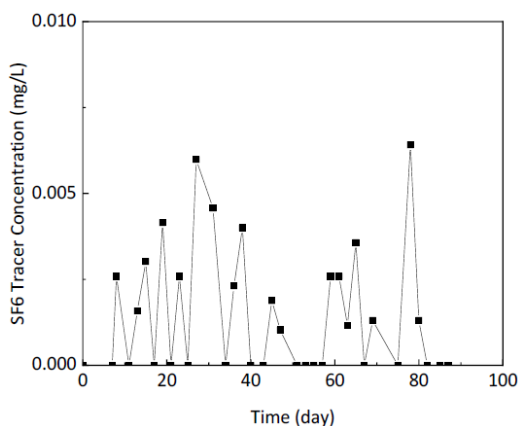


**Figure 6.**  $\text{SF}_6$  trace production concentration curve of well P-31

The sulphur Hexafluoride( $\text{SF}_6$ ) has been used to determine  $\text{CO}_2$  leakage during  $\text{CO}_2$  storage [12]. The  $\text{SF}_6$  concentration of production well was recorded periodically After injected  $0.05\mu\text{g/L}$   $\text{SF}_6$ . Figure 6 shows a narrow range of  $\text{SF}_6$  trace production concentration and lower than  $0.05\mu\text{g/L}$  when it has a breakthrough. It suggests there is no  $\text{CO}_2$  flow across the well and verifies the reliability of soil gas monitoring technology during  $\text{CO}_2$  storage.

#### 4. CONCLUSION

Monitoring is an essential part of any CO<sub>2</sub>-EOR sequestration program. After the injection of CO<sub>2</sub> into the reservoir, the location and state of CO<sub>2</sub> migration in the reservoir need to be determined. The carbon isotope monitoring of CO<sub>2</sub> in the pilot area soil gas is a useful monitoring tool for the pilot project in Yanchang Oilfield. A suite of baseline data has been measured before CO<sub>2</sub> injection, it will be used to interpret future periodic monitor results.

The process of CO<sub>2</sub> Sequestration in the pilot area is deemed robust since large-scale CO<sub>2</sub> is injected. Periodic monitoring of the soil gas should be implemented. More monitoring methods to determine the CO<sub>2</sub> migration and leakage should be introduced when CO<sub>2</sub> has been injected for several years.

#### ACKNOWLEDGMENTS

The authors wish to thank the Shanxi Yanchang oil field for their support. In particular, we wish to express their appreciation for the funding provided by the National Science and Technology Support Program (12BAC26805), the National Science and Technology Major Project of China (No. 2016ZX05010-003-001 and No. 2016ZX05025-003-010) and the China Scholarship Council (201706440109).

#### REFERENCES

- [1]. C. Pawde, R. Parekh, A Discussion of the HSE Aspects of Carbon Dioxide Sequestration. Paper presented at the SPE Asia Pacific Oil and Gas Conference and Exhibition, Jakarta, Indonesia, 2013/10/22/. doi:10.2118/165781-MS.
- [2]. P. Saptharishi, M. Makwana, Technical and Geological review of Carbon dioxide Geo Sequestration along with analysis and study of various Monitoring Techniques. Paper presented at the International Petroleum Technology Conference, Bangkok, Thailand, 2011/1/1/. doi:10.2523/IPTC-15402-MS.
- [3]. N. Zaim, A. Tugrul, H. Atlas, et al., Investigation of Natural Radioactivity of Surface Soil Samples in the Vicinity of Edirne-Turkey, 1 (2016) 64-67. doi:10.12693/APhysPolA.129.64.
- [4]. B.J.A.P.P.A. Çetin, Determination of Natural Radioactivity Concentrations in Surface Soils in the Yeşilirmak River in Amasya, Turkey, 130 (2016) 320-321. doi:10.12693/APhysPolA.130.320.
- [5]. F. Kulalı, İ. Akkurt, N. Özgür, et al., The correlation of the seismic activities and radon concentration in soil gas, Arabian Journal of Geosciences, 11 (2018) 447. doi:10.1007/s12517-018-3743-8.
- [6]. C. Yang, K.D. Romanak, R.C. Reedy, et al., Soil gas dynamics monitoring at a CO<sub>2</sub>-EOR site for leakage detection, Geomechanics and Geophysics for Geo-Energy and Geo-Resources, 3 (2017) 351-364. doi:10.1007/s40948-017-0053-7.
- [7]. C. Yang, K. Jamison, L. Xue, et al., Quantitative assessment of soil CO<sub>2</sub> concentration and stable carbon isotope for leakage detection at geological carbon sequestration sites, Greenhouse Gases: Science and Technology, 7 (2017) 680-691. doi:10.1002/ghg.1679.
- [8]. S. Balasubramanian, M. Sanni, S. Kokal, et al., Geochemical Monitoring Plan for the First CO<sub>2</sub>-EOR and Sequestration Project in Saudi Arabia. Paper presented at the SPE Kingdom of Saudi Arabia Annual Technical Symposium and Exhibition, Dammam, Saudi Arabia, 2016/4/25/. doi:10.2118/182812-MS.
- [9]. G. Johnson, B. Mayer, M. Shevalier, et al., Tracing the movement of CO<sub>2</sub> injected into a mature oilfield using carbon isotope abundance ratios: The example of the Pembina Cardium CO<sub>2</sub> Monitoring project, International Journal of Greenhouse Gas Control, 5 (2011) 933-941. doi:10.1016/j.ijggc.2011.02.003.
- [10]. B. Mayer, M. Shevalier, M. Nightingale, et al., Tracing the movement and the fate of injected CO<sub>2</sub> at the IEA GHG Weyburn-Midale CO<sub>2</sub> Monitoring and Storage project

- (Saskatchewan, Canada) using carbon isotope ratios, *International Journal of Greenhouse Gas Control*, 16 (2013) S177-S184. doi:10.1016/j.ijggc.2013.01.035.
- [11]. A. Yıldız, C. Başaran, M. Bağcı, et al., The measurement of soil gases and shallow temperature for determination of active faults in a geothermal area: a case study from Ömer-Gecek, Afyonkarahisar (West Anatolia), 11 (2018) 175. doi:10.1007/s12517-018-3520-8.
- [12]. L. Stalker, C. Boreham, E. Perkins, A review of tracers in monitoring CO2 breakthrough: properties, uses, case studies, and novel tracers, *Carbon Dioxide Sequestration in Geological Media – State of the Science*, AAPG Studies in Geology, 59 (2009) 595-608. doi:10.1306/13171264St593398.

---

## Precautionary measures of ventilator-associated pneumonia

Katerina Horackova<sup>1\*</sup>, Lenka Škaroupková<sup>1</sup> and Michaela Kalčíková Hisemová<sup>1</sup>

<sup>1</sup> University of Pardubice/Faculty of Health Studies, Pardubice, CZECH REPUBLIC

\* katerina.horackova@upce.cz

### ABSTRACT

The article deals with the occurrence of infectious diseases associated with nursing care focused on ventilator-associated pneumonia in hospitalized patients in intensive care. The emphasis is placed on the issue of ventilator-associated pneumonia, nursing care, and the importance of adhering to guidelines in practice.

The research investigates the incidence of ventilator-associated pneumonia in selected clinical facilities. Based on a quantitative survey, it verifies, through the standardized observation method, the correct procedure for providing nursing care in patients during artificial lung ventilation using a checklist. Partial results pointed out shortcomings in the preventative measures to combat VAP.

**KEYWORDS** - guidelines, nosocomial infections, prevention, ventilator-associated pneumonia (VAP)

### 1. INTRODUCTION

Ventilator-associated pneumonia (VAP) is a specific type of pneumonia in mechanically ventilated patients acquired in ICU. It belongs to a group of hospital-acquired pneumonia – HAPs, respiratory tract infections associated with health care, which are serious illnesses with significant lethality. These infections threaten the quality of health care provided, an operational and economic stability of the healthcare facility, and, in the long run, they are unsustainable even in financial terms. HAPs are especially dangerous for patients because they are often caused by multi-drug resistant microorganisms, thus making the antibiotic therapy more complicated and expensive. [1,2]

Non-medical healthcare staff, especially critical care nurses working in ICU, are significantly involved in preventative measures. Repeated investigative surveys and regular monitoring of adherence to preventative measures to combat VAP, together with targeted training of healthcare personnel, can improve the quality of nursing care provided, reduce the length of hospitalization and reduce the financial cost of health care. [1,2,3]

### 2. OBJECTIVES

1. To evaluate adherence to guidelines in compliance with the standard when suctioning patients with secured airways.
2. To evaluate the observance of the barrier regime as part of the preventative measures to combat VAP.

### 3. METHODS

To achieve the set objectives, a standardized observation method was used, and the observation was recorded in the checklist. For the purposes of objective assessment, criteria for standardized observation (to stand, observe and evaluate as close as possible to the observed person; to set the time for the research and always perform the research at the same time; to observe one subject only; to evaluate objectively and record). [4]

The control checklist provided a total of 16 control criteria that were monitored and evaluated during the survey. To assess the effectiveness of a criterion, a ranking method was established. The individual criteria were assessed in four possible ways (2 points for a match with a performed criterion, 1 point for a partial match, 0 points for a mismatch, and N for not rated). The N assessment was used due to a grave medical condition of a patient on the artificial lung ventilation.



To obtain the result, a percentage calculation was used (see Annexes C, D, E, F), which clearly assessed the outcome of the survey and its successful or unsuccessful execution.

The first survey was conducted at the IP-A clinic (anaesthesiology-resuscitation department) and the second one at the IP-B clinic (Resuscitation Unit of Intensive Care) of the same health facility in the capital of the Czech Republic, Prague. The data obtained were recorded continuously between 9 am and 11 am into a checklist according to the current procedure. This time slot is reserved for personal hygiene in the selected departments, bed-making, treatment of invasive insertions, and general nursing care after pulmonary hygiene for artificial lung ventilation.

The research file consisted of non-medical medical staff at the intensive care clinic A, hereinafter referred to as IP-A, and the intensive care clinic B, hereinafter IP-B, of an anonymous medical facility. A total of 32 nurses for intensive care from the IP-A department and 20 intensive care nurses from the IP-B department participated in the qualitative research.

#### 4. RESULTS

In total, 52 checklists compiled for the research study of a diploma thesis were evaluated. 32 checklists from IP-A and 20 checklists from IP-B were evaluated. Each checklist contained 16 control criteria for assessment.

The results were processed and interpreted by Microsoft Office Excel and displayed in statistical tables by Statistica 12. The authors present only the most significant findings.

**Checklist criterion No. 2.** P Non-medical healthcare staff performs hygienic hand disinfection prior to the procedure.

*Table 1. Hygienic hand disinfection prior to the procedure*

Checklist criterion No. 2	Absolute frequency (n) IP-A	Relative frequency (%) IP-A	Absolute frequency (n) IP-B	Relative frequency (%) IP-B
Match 2 points	19	59	11	55
Partial match 1point	0	0	0	0
Mismatch 0 points	13	41	9	45
Not rated	0	0	0	0
Total	32	100	20	100

**Checklist criterion No. 3** - Proper patient positioning is secured prior to the procedure.

*Table 2. Securing a proper patient positioning prior to suction*

Checklist criterion No. 3	Absolute frequency (n) IP-A	Relative frequency (%) IP-A	Absolute frequency (n) IP-B	Relative frequency (%) IP-B
Match 2 points	21	66	7	35
Partial match 1point	7	22	9	45
Mismatch 0 points	4	12	4	20
Not rated	0	0	0	0
Total	32	100	20	100

**Checklist criterion No. 5** - Non-medical healthcare staff performs suction strictly aseptically

**Table 3. Aseptic suction**

Checklist criterion No. 5	Absolute frequency (n) <b>IP-A</b>	Relative frequency (%) <b>IP-A</b>	Absolute frequency (n) <b>IP-B</b>	Relative frequency (%) <b>IP-B</b>
Match 2 points	32	100	20	100
Partial match 1 point	0	0	0	0
Mismatch 0 points	0	0	0	0
Not rated	0	0	0	0
Total	32	100	20	100

**Checklist criterion No. 9** - The proper technique and duration of suction from airways is respected.

**Table 4. Technique and duration of suction**

Checklist criterion No. 9	Absolute frequency (n) <b>IP-A</b>	Relative frequency (%) <b>IP-A</b>	Absolute frequency (n) <b>IP-B</b>	Relative frequency (%) <b>IP-B</b>
Match 2 points	28	88	20	100
Partial match 1 point	2	6	0	0
Mismatch 0 points	2	6	0	0
Not rated	0	0	0	0
Total	32	100	20	100

**Checklist criterion No. 15** Hygienic hand disinfection is performed after suction.

**Table 5 Hygienic hand disinfection after to the procedure**

Checklist criterion No. 15	Absolute frequency (n) <b>IP-A</b>	Relative frequency (%) <b>IP-A</b>	Absolute frequency (n) <b>IP-B</b>	Relative frequency (%) <b>IP-B</b>
Match 2 points	32	100	20	100
Partial match 1 point	0	0	0	0
Mismatch 0 points	0	0	0	0
Not rated	0	0	0	0
Total	32	100	20	100

## 5. CONCLUSION

The purpose of preventative measures is, above all, to reduce the risk of developing and transmitting infectious agents. The incidence of healthcare-associated infections in patients in a healthcare facility is an indicator of quality and safety in the provision of nursing care.

The results of the research have shown a high level of theoretical knowledge that nurses apply in practice. However, partial results have identified deficiencies in individual steps while adhering to the recommended hospital standard and it is crucial to focus on a remedy. The appendix of the diploma thesis is a case study aimed at pointing out the non-observance of standard procedures that most likely led to the occurrence of ventilator-associated pneumonia detected during the survey.

The obtained partial results showed that both intensive care nurses working both at the IP - A clinic and at the ones working at the IP - B clinic erred in a very high percentage in criteria 2 and 3. Criterion No. 2 was the performance of hygienic hand disinfection prior to the procedure by non-medical healthcare personnel prior to the procedure. Here, alarming results have been found, when non-medical staff practically does not take this step before the suction. From the point of view of prevention of ventilator-associated pneumonia, hygienic hand disinfection prior to the

performance is an important and crucial step. Criterion No. 3 was the proper positioning of the patient prior to the procedure. In this case, the patient's elevation at an angle lower than 30 ° was repeatedly observed. Keeping a patient in Semi-Fowler's position is one of the basic steps in preventing ventilator-associated pneumonia. [2]

Based on the results of the survey, the following measures have been proposed.

1. Focus on hygienic hand disinfection prior to the procedure - suction from patient's airways in a patient on artificial lung ventilation.
2. Use regular audits to verify compliance with guidelines.
3. Continue to update the recommended nursing care standard of the hospital facility, which serves nurses as a methodical instruction, for suction from the airways at regular intervals.
4. Inform medical staff about current preventative measures to combat ventilator-associated pneumonia by regular seminars and attending congresses.
5. Position the bed using the position indicator and check the correct angle. Avoid a subjective evaluation.
6. The recommendation for hospital management stemming from the first objective might be to consider setting the ventilator-associated pneumonia incidence monitor as a quality indicator in all clinics/departments where airway patients depend on artificial lung ventilation. This information would provide comprehensive information on the quality of the guidelines within the preventative measures to combat VAP, assess the risks associated with VAP, and increase the quality of health and nursing care provided to ventilated patients.
7. In view of the previous recommendation, another suggestion is to give priority to the use of a fully enclosed suction system in all clinics where ventilated beds are provided, for more transparent monitoring of the incidence of VAP. [5,6]

## REFERENCES

- [1].European Centre for Disease Prevention and Control. Point prevalence survey of healthcare-associated infections and antimicrobial use in European acute care hospitals: 2011-2012. Stockholm, 2013. ISBN 978-92-9193-485-0.
- [2].Guideline for Prevention of Surgical Site Infection. In: Infection Control and Hospital Epidemiology [online]. 2017, s. 9-31 [cit. 2017-09-06]. <https://www.cdc.gov/nhsn/pdfs/pscmanual/9pscscscurrent.pdf>
- [3].Maďar, R, Podstatová, R, a Řehořová, J. Prevence nozokomiálních nákaz v klinické praxi. 1. vyd. Praha: Grada, 2006, s. 40-56. ISBN 80-247-1673-9.
- [4].Reichel J. Kapitoly metodologie sociálních výzkumů. Praha: Grada, 2009. Sociologie (Grada). ISBN 978-80-247-3006-6.
- [5].Kara, Ü, Kara ,Y., Akkurt, I. Study on Radiation in Operating Room in Suleyman Demirel University , Acta Physica Polonica a 1(2016) 401-403. DOI: 10.12693/APhysPolA.130.401
- [6].World Health Organization, Patient Safety. WHO Guidelines for Safe Surgery 2009: Safe Surgery Saves Lives. 2009. ISBN 978-924-1598-552. [online].: [http://apps.who.int/iris/bitstream/10665/44185/1/9789241598552\\_eng.pdf](http://apps.who.int/iris/bitstream/10665/44185/1/9789241598552_eng.pdf)

---

## Hygiene and Epidemiology Nursing - Student Grant Competition

**Jana Wichsova<sup>1</sup>, Katerina Horackova<sup>1\*</sup> and Barbora Lidakova<sup>1</sup>**

<sup>1</sup> University of Pardubice/Faculty of Health Studies, Pardubice, Czech Republic

\* katerina.horackova@upce.cz

### ABSTRACT

The topic of this presentation is to present a project from the Student Grant Competition of the Faculty of Health Studies, University of Pardubice, Czech Republic. It is related to two areas: nursing, and hygiene and epidemiology. The project generally focuses on the protection and promotion of health, enhancement of life quality and lengthening of human lifetime. The research is partly focused on the occurrence of infections associated with health care. The danger lies in the lengthening of the treatment period, which increases the costs of health care.

To achieve the set targets a combination of several research tools will be used. To map the incidence of the infections associated with health care, retrospective and prospective research survey methods done by means of studying materials have been chosen. The following research methods have been used to detect the most frequent mistakes causing the spread of infections associated with health care and to assess the compliance between the methodical instructions of the chosen medical facility and the real situation: covert observation, checklist audit.

The contribution of the project will be clinical (improvement of the quality of care) and educational.

**KEYWORDS** - *Hygiene, Epidemiology, Nursing, Infection Control*

### 1. INTRODUCTION

The Student Grant Competition is subsidized by the Internal Grant Agency of the University of Pardubice. Students of doctoral and Master's degree study programmes are involved in projects under the guidance of academic staff at the Faculty of Health Studies. In 2017, the following projects were worked on:

- The Quality of Care in Health Facilities in 2016.
- Health Assessment of Patients in Otorhinolaryngology (ENT) and Intensive Care
- Hygiene and Epidemiology in Nursing - Part of Quality Management Care

The last one is related to two areas: nursing, and hygiene and epidemiology. The project generally focuses on the protection and promotion of health, enhancement of life quality and lengthening of human lifetime. The research is partly focused on the occurrence of infections associated with health care, which represents serious problem in contemporary health care, especially in nursing [1,2,3]. The danger lies in the lengthening of the treatment period which increases the costs of health care [4]. That is why the project focuses particularly on the area of anti-epidemic techniques as the main way to prevent infections. Our students are also involved in several projects in other countries, for instance, studies dealing with the risk of radiation [5,6].

### 2. OBJECTIVES

The main aim of the project is to describe current nursing practices in infection control.

The other secondary targets of the project are:

1. To describe the incidence of some Health Care Associated Infections (HCAIs) in certain medical facilities
2. To detect the most common mistakes causing the spread of HCAIs
3. To evaluate the level of compliance with the official instructions at medical facilities in real situations

4. To appraise the knowledge of nurses and other nursing staff relating to prophylaxis of HCAs
5. To prepare study material (university textbook)
6. To make visual supplements to the instruction manual for chosen nursing techniques related to prophylaxis of HCAs

### 3. METHODS

The research will take place in some of the hospitals in the Pardubice Region and some of the other health care facilities in the Czech Republic.

Sample - Respondents were nurses and midwives from these facilities. Also, we have studied patient documentation from these facilities.

To achieve the set targets a combination of several research tools will be used. To map the incidence of the infections associated with health care, retrospective and prospective research survey methods done by means of studying materials have been chosen. This was data collected from the information system of the chosen medical facility and ward based on criteria set in advance – diagnosis, age, sex, etc.

The following research methods have been used to detect the most frequent mistakes causing the spread of infections associated with health care [7,8] and to assess the compliance between the methodical instructions of the chosen medical facility and the real situation: covert observation, checklist audit.

The participants in this project were three academic members of staff, two doctoral students, and seven students from nursing master programs at the Faculty of Health Studies. Two members of staff of Hygiene and Epidemiology Department of Pardubice Hospital also participated in the project as consultants.

The contribution of the project will be clinical (improvement of the quality of care) and educational (scientific publication for students and educational material for paramedical staff).

### 4. RESULTS

The following data presents the first results of our study. This part of the study focused on patients from the gynecology department of one hospital who suffered symptoms of surgical site infection (SSI) [4]. These infections can make recovery from surgery more difficult because they can cause additional complications, stress, and medical costs. It is important that healthcare providers, patients and family members work together to prevent these infections [3].

#### 4.1. The research questions of this study were:

- What is the frequency of patients treated for gynecology with SSI?
- What are the most common risk factors in patients with SSI symptoms?

#### 4.2. Methods used:

- Retrospective study of patient documentation. The sample was 593 respondents.
- Quantitative research.

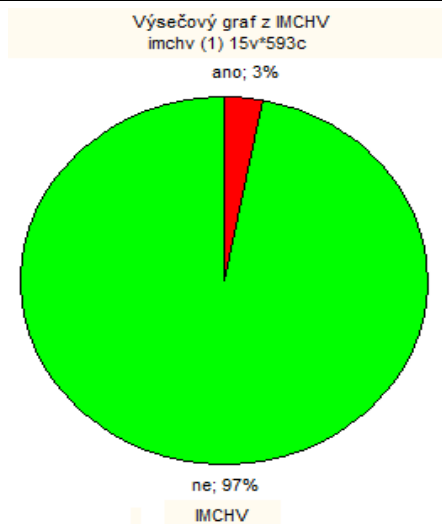


**Figure 1.** Number of SSI

From January to September 2016, 593 patients underwent surgery. The number of patients who suffered SSI was 18 (3%).

The average age of these patients is on Figure 2.

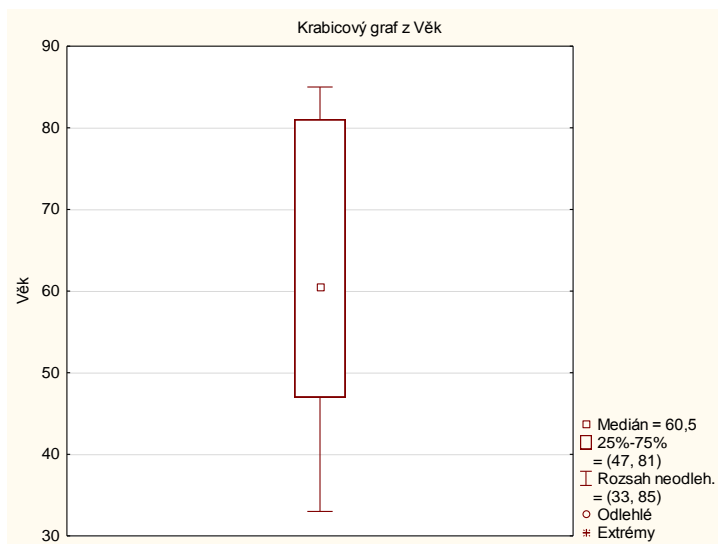


**Figure 2.** Age

The other indicators which were studied were: the length of hospitalization of patients with SSI, the nutritional status, comorbidities (e.g. diabetes, carcinoma), whether the patient was a smoker, and the need for further hospitalization. The average hospital stay was 15,3 days.

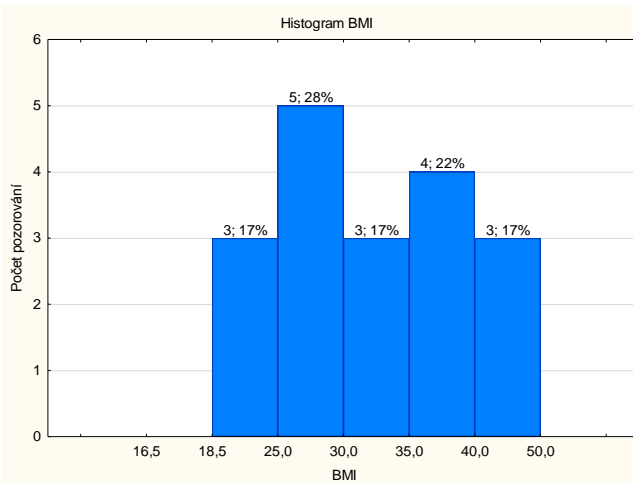


Figure 3. BMI

The number of patients with carcinoma was 72% and 28% with benign diagnosis. The patients suffering from diabetes were 11% and non-diabetic patients were 89%.

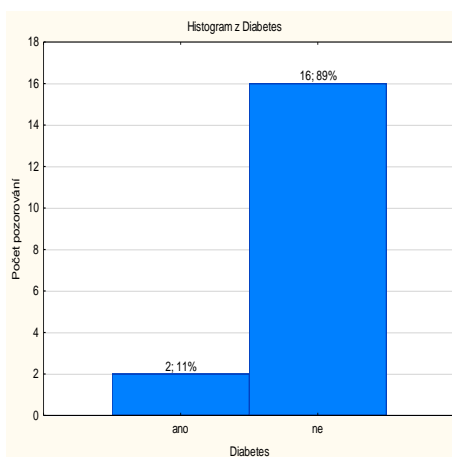


Figure 4. Carcinoma

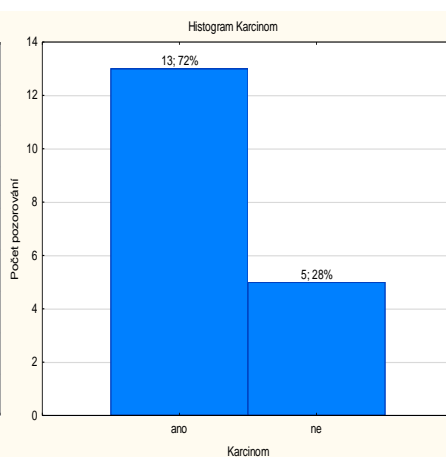


Figure 5. Diabetes

## 5. DISCUSSION

This Student Grant Competition project, which focused on the occurrence of infections associated with health care, could improve conditions of compliance of health care workers in barrier techniques. In particular, the brochure created by our team for students and health care workers could extend knowledge about possibilities of SSI.

According to a study in Obstetrics and Gynecology Survey, nearly 2% of all surgical cases are complicated by an SSI. Each SSI increases the cost of a postoperative hospital stay [1]. We obtained similar results in our sample of 593 patients as there were 18 cases of SSI, which represented 3%. Also, the average hospital stay of these patients with SSI increased to 15,3%.

Patient characteristics and comorbidity play an important role in determining the likelihood of infection after surgery [8]. We also monitored the patients' conditions and these aspects. For instance, in our sample, 17% of patients were smokers, and 83% of patients had obesity levels of

more than 25 BMI). Our finding was that the overweight patients suffer surgical site infection more frequently than the patients with BMI 18,5 - 25.

The results obtained by the students in Student Grant Competition has shown the benefits of engaging students in scientific work.

## 6. CONCLUSION

The paper describes the Student Grant Competition at the Faculty of Health Studies at the University of Pardubice in the Czech Republic. Academic staff and students of doctoral and Master's degrees have participated in this project. The presented study deals with hygiene and epidemiology in nursing practice. The expected results of the project will be clinical (improvement of the quality of care) and educational (scientific publication for students and educational material for paramedical staff).

## REFERENCES

- [1].Rozsypal, H, Michal H, Kosáková, M. Infekční nemoci ve standardní a intenzivní péči. Praha: Karolinum, 2013. ISBN 978-80-246-2197-5.
- [2].Black JD, de Haydu C, Fan L, Sheth SS. Surgical site infections in gynecology. *Obstet Gynecol Surv.* 2014;69(8):501–10.
- [3].European Centre for Disease Prevention and Control. Point prevalence survey of healthcare-associated infections and antimicrobial use in European acute care hospitals: 2011-2012. Stockholm, 2013. ISBN 978-92-9193-485-0.
- [4].Guideline for Prevention of Surgical Site Infection. In: *Infection Control and Hospital Epidemiology* [online]. 2017, s. 9-31 [cit. 2017-09-06]. <https://www.cdc.gov/nhsn/pdfs/pscmanual/9pscscscurrent.pdf>
- [5].Maďar, R, Podstatová, R, Řehořová, J. Prevence nozokomiálních nákaz v klinické praxi. 1. vyd. Praha: Grada, 2006, s. 40-56. ISBN 80-247-1673-9.
- [6].Kara, Ü, Kara,Y., Akkurt, I., Radiation Exposure of Medical Staff in Interventional Radiology, *Acta Physica Polonica a* 1(2016) 404-406. DOI: 10.12693/APhysPolA.130.404
- [7].Kara, Ü, Kara ,Y., Akkurt, I. Study on Radiation in Operating Room in Suleyman Demirel University , *Acta Physica Polonica a* 1(2016) 401-403. DOI: 10.12693/APhysPolA.130.401
- [8].Melicherčíková, V. Sterilizace a dezinfekce v prevenci nozokomiálních nákaz. Praha: Galén, c2007, 57 s. Care. ISBN 978-80-7262-468-3.
- [9].World Health Organization, Patient Safety. WHO Guidelines for Safe Surgery 2009: Safe Surgery Saves Lives. 2009. ISBN 978-924-1598-552. [online].: [http://apps.who.int/iris/bitstream/10665/44185/1/9789241598552\\_eng.pdf](http://apps.who.int/iris/bitstream/10665/44185/1/9789241598552_eng.pdf)



# Numerical investigation of thermal fluid fracturing in low-mobility tight oil reservoirs

Kai Liao<sup>1\*</sup>, Shicheng Zhang<sup>1</sup>, Xinfang Ma and Xun Sun<sup>1</sup>

<sup>1</sup> China University of Petroleum (Beijing) /College of Petroleum Engineering, Beijing, CHINA

\*lzc\_kevin@163.com

## ABSTRACT

For the low-mobility tight oil reservoirs, the production of horizontal wells after multi-stage hydraulic fracturing is not optimistic. With a large amount of cold fracturing fluid injection, the fracturing zone is cooled and the viscosity of crude oil increases, which eventually makes the mobility of oil worse. Thermal fluid fracturing is an effective way to increase production in conventional high condensate reservoirs, but few studies of this technology have been made in unconventional low-mobility reservoirs, which may be the key to figure out the problem.

In this paper, numerical simulation was used to study the imbibition and redistribution of thermal fracturing fluid in fractures and near fractures during injection and well shut-in periods. Firstly, the change regulations of formation temperature field and oil viscosity field were investigated. Secondly, sensitivity analysis was carried out to systematically quantify the impact of injection fluid temperature, fracture complexity, viscosity temperature characteristic and shut-in time on well productivity.

The results indicate that, thermal fluid fracturing can effectively reduce the oil viscosity near the fractures, and solve the problem of cold harmfulness from conventional fracturing. In addition, the higher temperature fluid and more complicated fractures will greatly increase oil production. Moreover, the more sensitive the oil viscosity is to the temperature, the greater impact of fluid temperature on production. Shut-in time has a certain effect on well performance, but its influence is much less than other factors. The study in this paper may help optimize the hydraulic fracturing treatments in low-mobility tight reservoirs.

**KEYWORDS-** Low-mobility, Tight oil, Temperature, Numerical simulation.

## 1. INTRODUCTION

As the development of conventional oil and gas reservoirs has been difficult to meet the global energy demand, unconventional oil and gas resources are expected to have great potential and become a hot issue [1-3]. With the breakthrough of horizontal well and hydraulic fracturing technology in recent years, it is possible for these unconventional reservoirs (e.g. tight oil reservoirs) to realize industrial production. The larger the fracturing scale is, the more complex the fractures are, and the higher the production is [4, 5]. However, for low-mobility tight reservoirs, the crude oil has high viscosity, high solidification point and high wax content, so the cold damage caused by conventional fracturing fluid should not be ignored. In the process of large-scale hydraulic fracturing, a large amount of cold water is injected into the formation, resulting in a series of chain reactions, such as cooling the matrix near the fractures, changing reservoir wettability, increasing oil viscosity and residual oil saturation. Moreover, crude oil solidification and wax precipitation may occur, which will cause low oil recovery [6].

Cold damage caused by water injection is not a new discussion, which is common in conventional heavy oil reservoir development. To solve this problem, injection of thermal fluid is often used to improve oil production. Huang [7] carried out oil-water relative permeability experiment by steady-state and unsteady-state methods, and found that residual oil saturation decreased and irreducible water saturation increased with the increase of temperature. But the result was not significant, the difference of curves was considered to be caused by experimental errors. According to the analysis of rheological and displacement experiments, Li [8] found that the reservoir wettability changes gradually with the increase of displacement phase fluid temperature,

from oil-wet or weak water-wet to water-wet. Jabbari [9] studied the impact of hot water imbibition on wettability in natural fractured reservoirs, whose results further showed that with the increase of injection water temperature, reservoir wettability gradually changed from weak water wet to strong water wet and residual oil saturation decreased. In his work, the impact of temperature change on capillary force was also investigated, but the influence of wetting hysteresis was neglected. Peng [10] established a wellbore temperature field calculation model for conventional low-mobility reservoirs and evaluated the in-situ heat fracturing technique, which relieved sedimentary plugging of oil flow channel near the wellbore by chemical heat generation. Liu [11] chose civilian hot water as the main liquid source of fracturing fluid to reduce the cold damage of reservoirs. In addition, Huang [12] and Wang [13] chose the high-temperature water that was recovered from fractured wells and other thermal fluids for thermal fracturing to improve oil recovery.

Lucaogou Formation in Xinjiang Province was a low-mobility tight reservoir with low porosity, low permeability, high viscosity, high solidification point and high wax content. The development of this type of reservoir was difficult and the oil production was low. Horizontal well with multi-stage fracturing was widely used in tight reservoir stimulation, so thermal fluid fracturing had great potential in avoiding cold damage and improving well productivity. However, it was necessary to evaluate the technology applicability before implementation. Based on numerical simulation method, this paper was organized as follows: Firstly, the description of the method. Next, the temperature field and viscosity field of the formation near the fracture were analyzed, during the process of fracturing fluid injection and well shut-in. Finally, sensitivity analysis was carried out to systematically quantify the impact of various factors. This work might provide guidance for fracturing decision-making of low-mobility tight oil reservoirs.

## 2. METHODOLOGY

In this work, a fit-for-purpose model ( $1/2$  of a single hydraulic fracture stage) was developed excavating the function of a commercial reservoir simulator. Water injection was used to simulate fracturing fluid invasion during hydraulic fracturing, so as to accurately depict water saturation field and temperature field of the formation. Moreover, by combining the thermal influence area and other control variables, sensitivity analysis was carried out.

### 2.1 Model structure and input parameters

A numerical model was established by using the thermal recovery module STARS of commercial reservoir numerical simulation software CMG. The porous media of the model included matrix (M), hydraulic fracture (HF) and opened natural fracture (NF) [14, 15]. Reservoir size is  $1300 \text{ m} \times 300 \text{ m} \times 50 \text{ m}$ , and horizontal well length is  $1200 \text{ m}$  with 17 fracturing stages along the wellbore. In order to balance the huge computation problem, a  $1/2$  fracture model is selected here and its size is  $75 \text{ m} \times 150 \text{ m} \times 50 \text{ m}$ , as shown in Figure 1. The basic parameters of the model input are shown in Table 1 and 2.

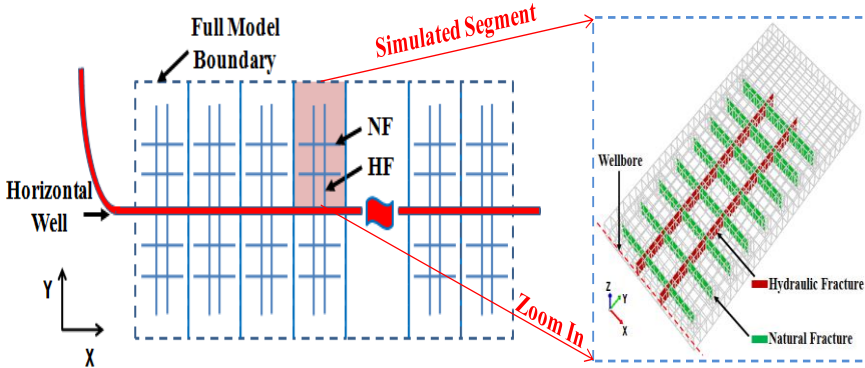


Figure 1 Schematic diagram of the simulation model (zoom scale: Z =0.2 times)

Table 1 Properties for the base case

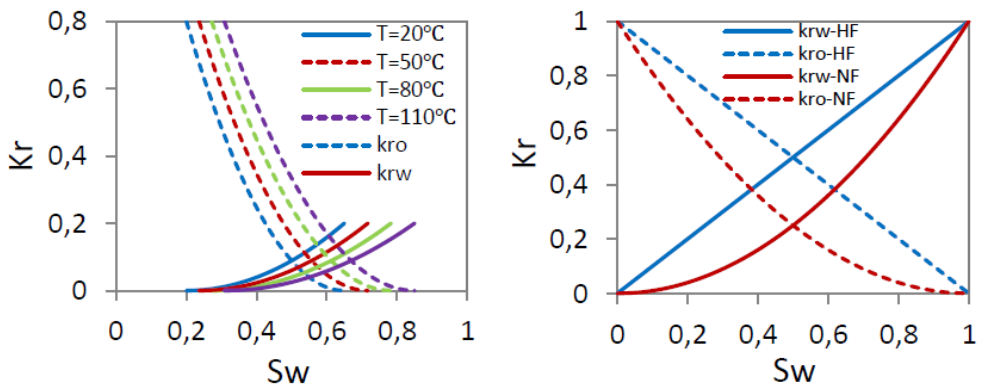
Parameters	Values	Parameters	Values
Reservoir pressure, MPa	37	Matrix initial water saturation	0.2
Reservoir Temperature, °C	80	HF spacing, m	75
Reservoir depth, m	2800	HF half-length, m	120
Reservoir heat conduction, J/(m·day·°C)	$1.5 \times 10^5$	HF conductivity, mD·m	200
Surrounding heat conduction, J/(m·day·°C)	$1.5 \times 10^5$	NF spacing, m	15
Reservoir heat capacity, J/(m <sup>3</sup> ·°C)	$2.4 \times 10^6$	NF length, m	60
Surrounding heat capacity, J/(m <sup>3</sup> ·°C)	$2.4 \times 10^6$	NF conductivity, mD·m	2
Matrix porosity	0.1	HF/NF initial water saturation	0
Matrix permeability, mD	0.1	Single stage injected volume, m <sup>3</sup>	1440

Table 2 Viscosity versus temperature relationship used in the model

Temperature, °C	Viscosity, cp
20	157
30	75
40	44
50	29
80	13
120	5.8

2.2. Relative permeability curves

During the flow of crude oil in matrix, the wettability of rock and the saturation of residual oil change with the change of temperature, as well as the relative permeability [8]. Therefore, the impact of temperature on matrix relative permeability is taken into account in the model, as shown in Figure 2-a. But, the relative permeability curves of HF and NF [14] are assumed to ignore the effect of temperature, as shown in Figure 2-b.



**Figure 2** a. Relative permeability curves for matrix. b. Relative permeability curves for HF and NF

### 2.3. Capillary pressure curves

While water is injected into the tight reservoir, the capillary force of the micro pore and throat in matrix should not be underestimated. Besides the matrix is not always water-wet, capillary force is both the imbibition power and imbibition resistance, which reflects the imbibition hysteresis [16]. In addition, with the increase of temperature, the capillary force decreases with the decrease of oil-water interfacial tension, and the wettability changes from oil-wet to water-wet [9]. The capillary force curves for matrix are showed in Figure 3, for HF and NF are neglected due to their high conductivity.

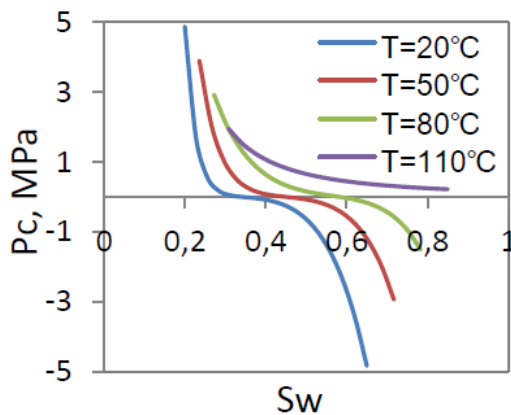


**Figure 3** Matrix capillary pressure curves at different temperatures

### 2.4. Model validation

In order to characterize the temperature field and viscosity field of formation after fracturing, it is necessary to start simulation from the fracturing stage, so as to obtain the accurate distribution of water saturation near the fracture [17]. In this study, water injection is used to simulate the fracturing injection process, and the cumulative injection volume is consistent with the actual fracturing scale. Then the well is produced for one year, so that the curve of water rate normalized pressure (RNP) versus material balance time ( $t_{MB}$ ) can be obtained [18], as shown in Figure 4.

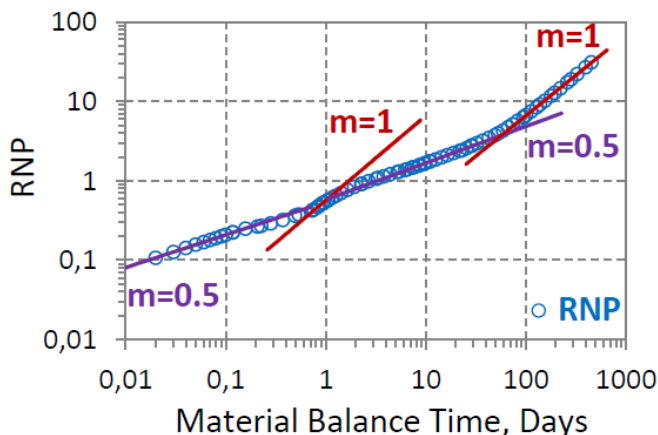


**Figure 4** Water RNP vs.  $t_{MB}$  plot during the one year of production

Figure 4 shows that four possible flow regimes may be identified during production as follows: 1. Transient linear flow in the fractures (half slope) at the early stage of well opening. This flow regime describes fluid flowing from the fracture system to the wellbore perforation. 2. Fractures depletion (unit slope). This flow regime occurs when the pressure response reaches the boundary of the fractures. The duration of this regime is very short here, because the fracture closure is not fully considered in this study and the input compressibility of the fracture is small. 3. Transient linear flow in the matrix (half slope). When the fractures close gradually, the fluid in the matrix begins to flow into the fracture, and the slope begins to deviate from unit. As the matrix linear flow dominates, this flow regime appears. 4. Boundary dominated flow in the matrix (unit slope). This flow regime occurs when the pressure response reaches the base model boundary. The observed flow regions are consistent with the field data and analytical model [19, 20].

At present, the data obtained from the field are generally daily data, but it needs higher frequency data (second data or minute data) for history matching. In addition, the parameters of fractures such as width, conductivity, distribution and compressibility are hard to be measured clearly, which makes matching more difficult. Nevertheless, because of the uncertainty of these data and parameters, it is necessary to establish a mechanism model to explore the performance of thermal fluid fracturing in the development of low-mobility tight oil reservoirs.

### 3. RESULTS

In this section, the distribution of fracturing fluid in the formation is presented, which clarifies the cold damage caused by conventional fracturing in the near-well formation, and also shows the positive effect of thermal fluid fracturing. Then the effects of different factors such as fluid temperature, fracture complexity, viscosity-temperature characteristics and shut-in time on well productivity are analyzed.

#### 3.1. Distribution of the injected fracturing fluid

Based on the model established in the previous section, 20°C and 110°C fracturing fluids are injected into the reservoir respectively, so as to obtain the initial distribution of water saturation, temperature and oil viscosity after fracturing. After shutting down the pump at the end of fracturing, the variation of water saturation, temperature and viscosity field with time in the formation near fractures is obtained as shown in Figure 5.

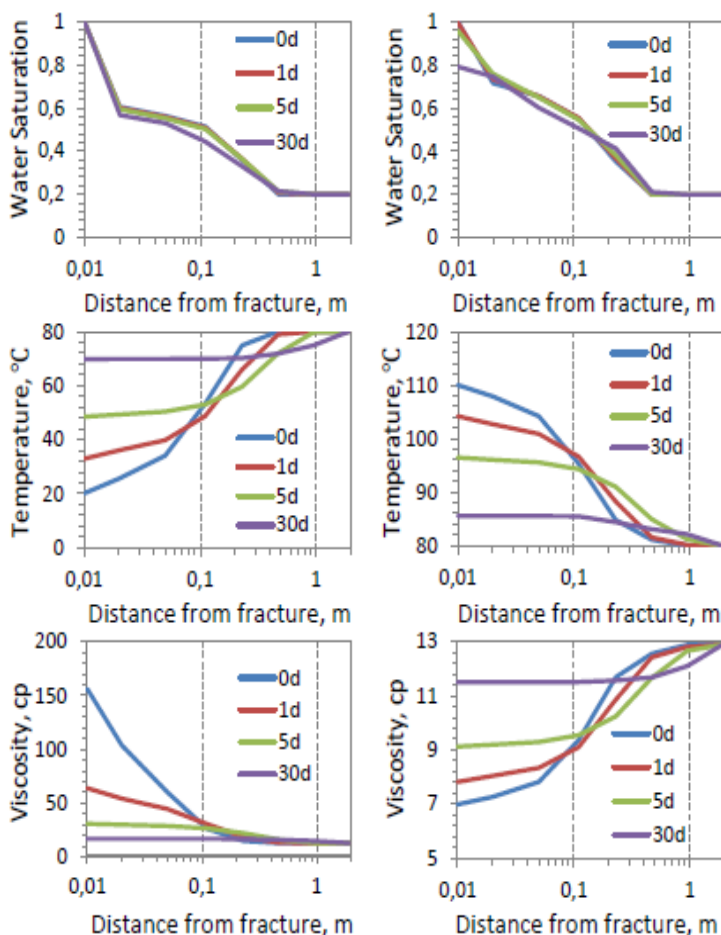


**Figure 5**  $S_w$ , temperature and viscosity distribution from fracture surface to deeper reservoir under different shut-in period: a. 20 °C fracturing fluid. b. 110 °C fracturing fluid

Figure 5-a exhibits that, the cooling area near fractures was about 0.5m after a large amount of cold fluids injected, and the formation temperature dropped below the oil solidification point, which was easy to cause cold damage. In the initial, the oil viscosity near fracture increases greatly, but it recovers quickly with the extension of well shut-in time. It can be seen from Figure 5-b, when thermal fluids are injected, the cold damage is relieved and the oil viscosity near the fracture is decreased. On this basis, the relative permeability of water invasion zone can be adjusted to carry out the next investigation.

### 3.2. Sensitivity analysis

In order to study the practical application significance of thermal fluid fracturing, it is direct and necessary to evaluate it from the perspective of production.

#### 3.2.1. Impact of injection fluid temperature

The most important factor that causes cold damage is the temperature of fracturing fluid. This section investigates the cumulative oil production and flowback rate under different injection temperature which ranges from 20 °C to 50 °C to 80 °C to 110 °C. It can be seen from Figure 6-a

that the oil rate increases gradually at the early stage of production and increases with the increase of temperature, but at the middle and later stages of production, the oil rate decreases with time and the difference between different temperatures also gradually disappears. Figure 6-b shows that with the increase of fluid temperature, the cumulative oil increases, but the increment decreases. While flowback rate is on the contrary, it decreases with increasing temperature.

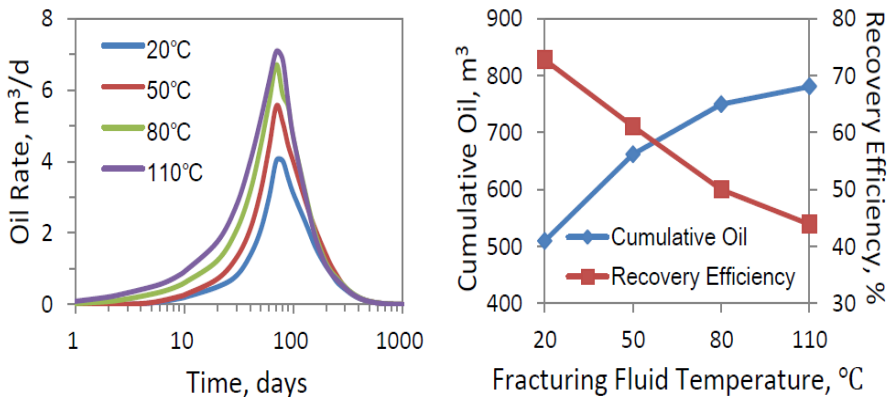


**Figure 6** a. Oil rate graph under different injection fluid temperature. b. The relationship between injection fluid temperature and cumulative oil or recovery efficiency.

### 3.2.2. Impact of fracture complexity

The complexity of fractures is related to the development of natural fractures and the scale of hydraulic fracturing. And the complexity of fractures is also directly related to the contact area between fractures and matrix. This section sets 4 cases from simple fracture structure to complex fracture network, as shown in Table 3. The results show that cumulative oil production increases with the increase of natural fracture number, and the increment increases with the increase of fracturing fluid temperature. On the contrary, the recovery efficiency decreases significantly with the increase of fracture complexity.

**Table 3** The impact of fracture complexities on production performance

Case number	1	2	3	4
Fracture structure diagram				
Cumulative oil – 20°C, m³	344.6	518.8	653.9	763.4
Cumulative oil – 80°C, m³	434.9	738.7	805	857.2
Recovery efficiency – 20°C, %	93.8	76.5	59.3	48.8
Recovery efficiency – 80°C, %	84.1	57.8	45.8	38.5

### 3.2.3. Impact of viscosity-temperature characteristic

For low-mobility oil reservoirs, oil viscosity is very sensitive to temperature changes. This section compares the production performance under different viscosity-temperature characteristics (as shown in Figure 7-a). Figure 7-b shows that the impact of this factor on production is very slight. The reason may be that the volume of injected fluid is relatively small compared with the whole reservoir. It has limited influence on the formation temperature near fractures, and the temperature recovers quickly with time.

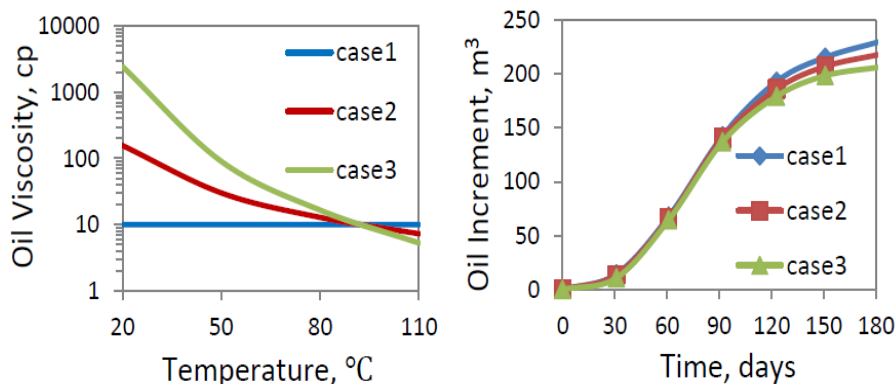


**Fig. 7** a. Viscosity-temperature characteristic profiles for different cases b. Cumulative oil increment profiles under different cases

### 3.2.4. Impact of well shut-in time

The shut-in time after fracturing is related to the recovery of temperature field and viscosity field, and also affects the water imbibition from fracture to matrix. In the relationship curves between cumulative oil and shut-in time (as shown in Figure 8), 20 °C and 80 °C fracturing fluid show different trends. For cold fluid, cumulative oil production slowly increases with the extension of shut-in time. However, for thermal fluid, with the extension of shut-in time, the cumulative oil decreases first and then increases gradually. Because pressure in fractures keeps decreasing and formation temperature near fractures recovers quickly, cumulative oil of short-term shut-in is lower than that produced directly without shut-in. But when the shut-in time is relatively long, the role of capillary spontaneous imbibition is remarkable. The oil near fractures is displaced into the fracture, which makes the production increase.

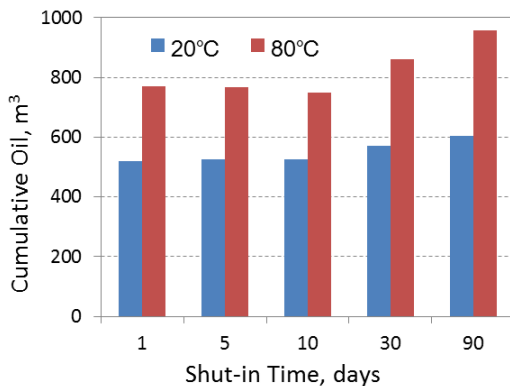


**Fig. 8** The relationship between shut-in time and cumulative oil production under 20 °C and 80 °C water

## 4. CONCLUSIONS

In this work, numerical simulation is mainly used to investigate and analyze the cold damage of low-mobility tight oil reservoir after fracturing. Moreover, the stimulation effect of thermal fluid fracturing in this type of reservoir is evaluated. The conclusions can be summarized as follows:

1. Numerical simulation results demonstrate that during large-scale hydraulic fracturing, reservoir cold damage does occur due to a large amount of cold fluid injected into the formation. When using thermal fluid for fracturing, the problem could be relieved or avoided.



2. The wettability of water invasion zone changes from oil wet to water wet, so water is trapped in the matrix under capillary imbibition and well productivity can be improved obviously. In addition, the more complex the fracture and the longer the shut-in time, are conducive to alleviate reservoir cold damage, as well as able to improve the stimulation effect of thermal fluid fracturing.
3. When the injection fluid temperature was higher than the original reservoir temperature, its promotion effect on oil production significantly weakens. The reason might be that the cumulative injected fluid volume is relatively very small compared with the whole reservoir, and the temperature recovery quickly during the shut-in and flowback process.
4. It could be seen that thermal fluid fracturing is effective in solving the cold damage caused by fracturing in low-mobility tight oil reservoirs. But if we want to further improve the well productivity, other stimulation measures might be more effective, such as injecting thermal fluid huff and puff into fractured horizontal wells, which may be investigated in future work.

## REFERENCES

- [1]. L. Song, Z. Ning, L. Duan. Research on reservoir characteristics of Chang7 tight oil based on nano-CT, Arabian Journal of Geosciences (ICCESN 2017), Antalya-Turkey. <https://doi.org/10.1007/s12517-018-3842-6>
- [2]. W. Zheng, Y. Liu, J. Huang, et al. Study on the optimal development method for offshore buried hill fractured reservoirs, Arabian Journal of Geosciences (ICCESN 2017), Antalya-Turkey. <https://doi.org/10.1007/s12517-018-3965-9>
- [3]. L. Huang, Z. Ning, Q. Wang, et al. Enhanced gas recovery by CO<sub>2</sub> sequestration in marine shale: a molecular view based on realistic kerogen model, Arabian Journal of Geosciences (ICCESN 2017), Antalya-Turkey. <https://doi.org/10.1007/s12517-018-3762-5>
- [4]. S. Huang, Y. Yao, S. Zhang, et al. Pressure transient analysis of multi-fractured horizontal wells in tight oil reservoirs with consideration of stress sensitivity, Arabian Journal of Geosciences (ICCESN 2017), Antalya-Turkey. <https://doi.org/10.1007/s12517-018-3639-7>
- [5]. E. Ghanbari, H. Dehghanpour. The fate of fracturing water: A field and simulation study, Fuel, 2016: 282-294. <https://doi.org/10.1016/j.fuel.2015.09.040>
- [6]. M. Wang, S. Yang, R. Wu, et al. Influencing factors and mechanism of the imbibition production in tight oil reservoirs, Petroleum Geology and Oilfield Development in Daqing, 2018. DOI: 10.19597/J.ISSN.1000-3754.201712016
- [7]. S. Huang, M. Shi, P. Guo, et al. The experimental study of impact on temperature and test method for the relative permeability curves based on the same oil-water viscosity ratio, Journal of Chongqing University of Science and Technology(Natural Sciences Edition), 2013, 15(6): 87-91. DOI: 10.19406/j.cnki.cqkxyxbzkb.2013.06.024
- [8]. K. Li, L. Qu, B. Jiang, et al. The relationship of permeability and porosity at different flooding temperature and its impact on the typical parameters of relative permeability curves, Science Technology and Engineering, 2014, 14(19): 60-63.
- [9]. H. Jabbari, K. Afsari, M. Rabiei, et al. Thermally-induced wettability alteration from hot-water imbibition in naturally fractured reservoirs-Part 1: Numerical model development & 1D models, Fuel, 2017: 682-691. <http://dx.doi.org/10.1016/j.fuel.2017.07.016>
- [10]. X. Peng, S. Liu, C. Cai, et al. Calculation model for well bore temperature profiles in high freezing point oil reservoirs with in-situ heat fracturing treatment, Acta Petrolei Sinica, 2003, 24(4): 69-76.
- [11]. L. Liu, J. Li, S. Qu. Study and field test of large-scale thermal fracturing process for high pour-point oil in Caotai buried hill, Special Oil and Gas Reservoirs, 2008, 15(2): 86-89.

- [12]. S. Huang, M. Cao, Q. Huang, et al. Study on reaction equations of heavy oil aquathermolysis with superheated steam, International Journal of Environmental Science and Technology (ICCESSEN 2017), Antalya-Turkey. <https://doi.org/10.1007/s13762-018-1799-3>
- [13]. Z. Wang, Y. Liao, W. Zhang, et al. Coupled temperature field model of gas-hydrate formation for thermal fluid fracturing, Applied Thermal Engineering, 2018: 160-169. <https://doi.org/10.1016/j.applthermaleng.2018.01.039>
- [14]. T. Zhang, X. Li, J. Li, et al. Numerical investigation of the well shut-in and fracture uncertainty on fluid-loss and production performance in gas-shale reservoirs, Journal of Natural Gas Science and Engineering, 2017: 421-435. <http://dx.doi.org/10.1016/j.jngse.2017.08.024>
- [15]. W. Jurus, C. Whitson, M. Golan. Modeling water flow in hydraulically-fractured shale wells, SPE Annual Technical Conference and Exhibition held in New Orleans, Louisiana, USA, SPE 166439, 30 September-2 October, 2013. <https://doi.org/10.2118/166439-MS>
- [16]. A. Almulhim, N. Alharthy, A. Tutuncu, et al. Impact of imbibition mechanism on flowback behavior: A numerical study, Abu Dhabi International Petroleum Exhibition and Conference held in Abu Dhabi, UAE, SPE 171799, 10-13 November, 2014. <https://doi.org/10.2118/171799-MS>
- [17]. A. Zabgabeg, M. Soroush, J. Williams-Kovacs, et al. Parameters affecting load recovery and oil breakthrough time after hydraulic fracturing in tight oil wells, SPE/CSUR Unconventional Resources Conference held in Calgary, Alberta, Canada, SPE 175941, 20-22 October, 2015. <https://doi.org/10.2118/175941-MS>
- [18]. Y. Fu, H. Dehghanpour, D. Ezulike, et al. Estimating effective fracture pore volume from flowback data and evaluating its relationship to design parameters of multistage-fracture completion, SPE Production & Operations, 2017. <https://doi.org/10.2118/175892-PA>
- [19]. A. Alkouh, S. Mcketta, R. Wattenbarger. Estimation of effective-fracture volume using water-flowback and production data for shale-gas wells, Journal of Canadian Petroleum Technology, 2014, 53(5): 290-303.
- [20]. J. Williams-Kovacs, C. Clarkson. Analysis of multi-well and stage-by-stage flowback from multi-fractured horizontal wells, SPE/CSUR Unconventional Resources Conference held in Calgary, Alberta, Canada, SPE 171591, 30 September-2 October, 2014. <https://doi.org/10.2118/171591-MS>

## Effect of Surfactant Emulsification on High Water-cut Reservoir in Shengli Oilfield

Mingda Dong<sup>1\*</sup>, Xiang'an Yue

<sup>1</sup> China University of Petroleum, Beijing 102249, China

\*475582944@qq.com

### ABSTRACT

It is generally considered that reducing oil-water interfacial tension and emulsification is two key factor to enhance oil recovery by surfactant flooding. In Shengli oilfield, surfactant flooding is usually carried out after profile control, which makes the injected surfactant can enter different regions of the reservoir. Therefore, the selection method for surfactant is different from other oilfields.

Base on the conclusion, Rui Feng surfactant which could reach ultra-low interfacial tension and combination surfactant RZ-JD80 with strong emulsifying property are chosen to do oil displacement and profile control-oil displacement experiment in homogeneous core and heterogeneous core respectively. The results show that in the homogeneous reservoir, the effect of two surfactants on oil recovery in the high swept region is similar, but with the decrease of water saturation, RZ-JD80 has better oil displacement effect. In particular, recovery rate of the surfactant flooding with RZ-JD80 is 14.2% higher than that of the surfactant flooding with Rui Feng, which illustrates that surfactant emulsification has remarkable effect on the displacement efficiency of remaining oil. For heterogeneous core, the surfactant with ultra-low interfacial tension will cause most of the injected liquid to flow along the high permeability zone, and the remaining oil in the low permeability zone can not be swept out. Meanwhile, the recovery rate of the surfactant flooding with RZ-JD80 in heterogeneous core model is as high as 41.5%.

It is proved that surfactant emulsification plays an important role in EOR in high water-cut reservoirs in this study. Also, the results are helpful for engineers to choose appropriate surfactant to enhance the oil recovery in Shengli Oilfield.

**KEYWORDS** - *Surfactant, Profile control, Emulsification.*

### 1. INTRODUCTION

There have been many problems in the development of high water-bearing reservoirs [1-5]. At present, the reserves of medium-high permeability and fault-block reservoirs in Shengli Oilfield are 3.18 billion tons, accounting for 45.8% of the total reserves, and the annual output of oil is about 18.4 million tons, accounting for 42.1% of the total output. It can be seen that the stable production of medium-high permeability and fault-block reservoirs has a great impact on the stability of Shengli Oilfield. However, the medium-high permeability and fault-block reservoirs have entered the development stage of extra-high water content as a whole, with an average comprehensive water content of over 90% and a serious decline in production. In addition, the overall high-infiltration and fault-block reservoirs in Shengli Oilfield have lower recovery rates, and the average waterflood recovery is only about 35%. There is still a potential for significant oil recovery. Due to the severe situation of oilfield exploitation and the huge potential for enhanced oil recovery, the demand for new technologies for enhanced oil recovery in ultra-high water-bearing reservoirs has become very urgent. To this end, Shengli Oilfield Research Institute has carried out research on the development potential and development strategy of oilfields in extra high water cut period.

In the reservoir after long-term water flooding, it can be clearly divided into a strong water washing area (the actual injection of PV is very high), a medium water washing area, a weak water washing area (the actual injection PV is very low) and an unaffected original oil saturation area.

The residual oil saturation in the region is different and the potential for further displacement is different.

Surfactants have a significant impact on the development of high water-cut reservoirs [6-10]. Therefore, taking the ultra-high water-bearing reservoir as the simulation object, a one-dimensional homogeneous core and a two-layer heterogeneous core flooding experiment were designed to determine the oil displacement efficiency of surfactants with different properties in different washing zones. At the same time, the improvement of the recovery ability of surfactants with different properties was compared, and the main way to improve the recovery factor of surfactants in high water-bearing reservoirs was obtained.

## 2. EXPERIMENTAL SECTION

### 2.1. Cores and fluids

Two kinds of artificial cores were used in the experiment to study the influence of surfactant emulsifying on oil recovery. One is heterogeneous core model: model size:  $1.5\text{ cm} \times 5\text{ cm} \times 30\text{ cm}$ ; average permeability:  $800 \times 10^{-3} / 1600 \times 10^{-3} \mu\text{m}^2$ , core average porosity is 32%. Another is one-dimensional homogeneous cylindrical core with a core size of  $2.5\text{ cm} \times 30\text{ cm}$  and average permeability is  $800 \times 10^{-3} \mu\text{m}^2$ . These artificial cores are highly similar to natural cores regarding pore structure and cementation degree. Meanwhile, they can meet the permeability range required by experiments. The exterior of the core samples are shown in Fig. 1. The fluid in the experiment is the crude oil of Shengli oil field and brine whose parameters are highly similar to the formation water in Shengli oil field, which is located in eastern China. The properties of the oil and brine are shown in Table 1 and 2.



(a). homogeneous cylindrical core (b). heterogeneous core

**Figure 1.** The exterior of the core samples.

**Table 1.** Oil properties.

Viscosity, mPa·s	Compression coefficient, $10^{-5}/\text{MPa}$	Specific gravity	Asphaltene content, %
4.41	12.4	0.8658	1.83

**Table 2.** Brine properties.

Ion concentration, mg/L						pH	Total salinity, g/l	Water type
$\text{Na}^+ + \text{K}^+$	$\text{Ca}^{2+}$	$\text{Mg}^{2+}$	$\text{Cl}^-$	$\text{SO}_4^{2-}$	$\text{HCO}_3^-$	5.5	112.32	$\text{CaCl}_2$
16152	18521	352	66485	374	63			

### 2.2. Experimental procedure

The experimental steps are divided into the following four steps.

- (1) Put the core into the core holder, vacuum for 6 hours, saturate the simulated formation water, measure the pore volume, and calculate the porosity of the core as a whole.
- (2) Simulating the average permeability of the homogeneous core in the formation water; for the core of the well-saturated formation water, the simulated oil is saturated at an injection rate of 0.1 mL/min (0.076 m/d) to produce the bound water and aging for 24 hours at normal temperature. .
- (3) Water flooding at an injection rate of 1.2 mL/min (0.91 m/d), and testing changes in the inlet end, outlet end and confining pressure during the flooding process, and measuring the water and oil produced at the outlet end.
- (4) Water flooding the core until water content reached the given value, and water flooding ended. Inject different surfactant slugs and continue water flooding to a moisture content of 98%

### 3. RESULTS AND DISCUSSION

In the actual water reservoir exploitation process, the reservoir can be divided into four parts according to the water saturation, namely high water cut area (water saturation >98%), middle water cut area (50% <water saturation <98%), low water cut area (irreducible water saturation <water saturation <50%) and unswept area (water saturation is irreducible water saturation). Surfactant flooding experiments were carried out for different areas. The results are shown in Figure 2. Surfactant used in the experiments are Rui Feng surfactant which could reach ultra-low interfacial tension and combination surfactant RZ-JD80 with strong emulsifying property.

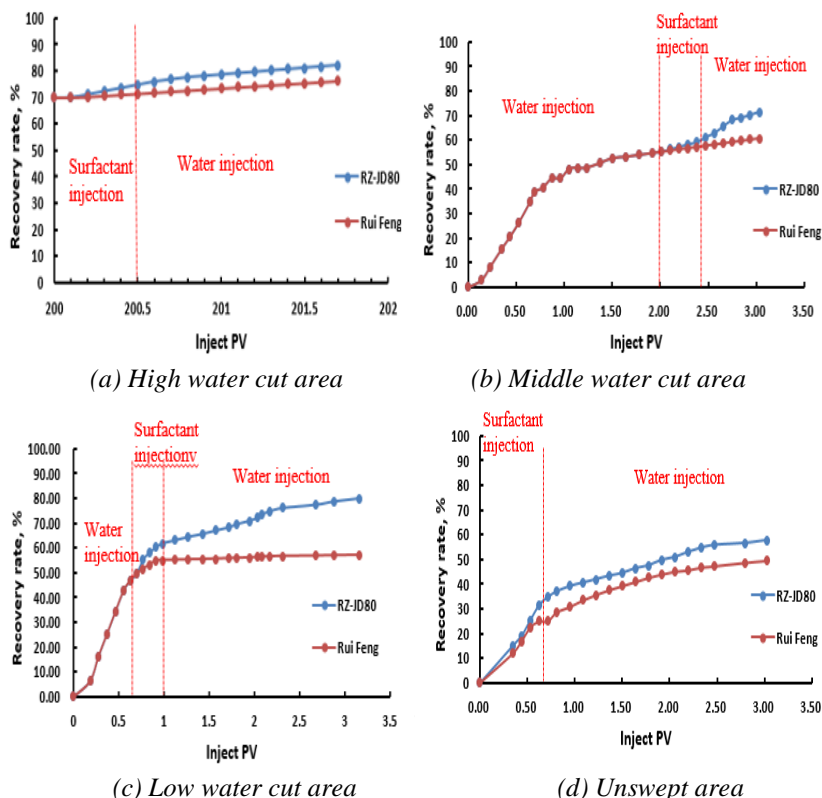


**Figure 2.** Recovery factors of different areas in homogeneous cores.

It can be seen in the figure.2 that in high water cut area, the oil displacement efficiency of two kinds of surfactants after columnar core water flooding 200PV is shown in the figure. It can be seen from the figure that the final recovery rate of RZ-JD80 direct displacement is 76.2%, and the final recovery rate of Rui Feng direct displacement is 72.2. %, the overall improvement of the recovery rate is relatively high. In middle water cut area, it can be seen from the figure that the final recovery rate of RZ-JD80 direct displacement is 72.3%, and the final recovery rate of Rui Feng direct displacement is 67.3 %, the overall improvement of the recovery rate is relatively high. In low water cut area, it can be seen from the figure that the final recovery rate of RZ-JD80 direct displacement is 74.1%, and the final recovery rate of Rui Feng direct displacement is 60 %, the overall improvement of the recovery rate is relatively high. In unswept area, it can be seen from the figure that the final recovery rate of RZ-JD80 direct displacement is 60.11%, and the final recovery rate of Rui Feng direct displacement is 50.44 %, the overall improvement of the recovery rate is relatively high. These results fully demonstrate that the emulsifying properties of surfactants are the main properties of enhanced oil recovery.

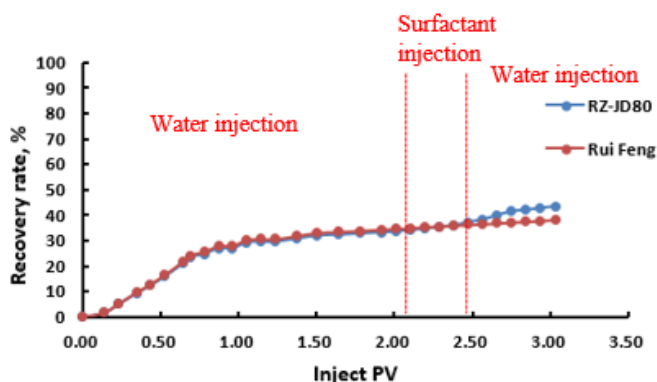


**Figure 3.** Recovery factors of middle water cut area heterogeneous cores.

Surfactant flooding in actual reservoirs is usually carried out under high water conditions, and surfactants can be injected when the water saturation of the heterogeneous reservoir reaches 98%. Fig.3 shows the effect of different surfactants on oil recovery in the heterogeneous reservoir. It can be seen that for heterogeneous core, the surfactant with ultra-low interfacial tension will cause most of the injected liquid to flow along the high permeability zone, and the remaining oil in the low permeability zone can not be swept out. Meanwhile, the recovery rate of the surfactant flooding with RZ-JD80 in heterogeneous core model is as high as 41.5%.

#### 4. CONCLUSION

1. For different water saturation regions, RZ-JD80 has better oil displacement effect than Rui Feng. At the same time, the lower the water saturation, the stronger the oil displacement effect of RZ-JD80 is.
2. For strong heterogeneous cores, enhanced oil recovery ability by only injecting two kinds of surfactant is poor. However, the recovery rate of the surfactant flooding with RZ-JD80 in heterogeneous core model is as high as 41.5%.
3. For Shengli oilfield with high heterogeneity, it is not necessary to pursue ultra-low interfacial tension of surfactant for EOR. In fact, emulsifying properties play a major role, while moderate low interfacial tension can also work effectively for EOR.

#### REFERENCES

- [1]. Li, H., Lin, D., and Cheng, J. 2014. "Remaining Oil Distribution Regularity Study of Complex Small Fault Block Reservoir in Extra-High Water-Cut Period in South Gaoqian Area." *Petroleum Geology and Engineering* 28(4): 74-6.
- [2]. Li, Z., Lin, C., Shi, Q., Li, R., and Peng, X. 2012. "Types of Edge-Water Fault Block Reservoirs and Features of Residual Oil in the Gaoqiannan Area." *Journal of Southwest Petroleum University (Science & Technology (Edition))* 34 (1): 115-20.
- [3]. Well-Spacing Study to Develop Stacked Tight Oil Pay in Midland Basin.
- [4]. Chao, W., Fen, H., and Chao, L. 2004. "Research of Fault-Block Reservoir at High Water-Cut Stage to Enhance Development Efficiency." *Fault-Block Oil & Gas Field* 11 (4): 28-9.
- [5]. Li, Z., Yu, Q., and Peng, P. 1997. "A System of Methods Used for Oilfield Development during High Water-Cut Stage." *Xinjiang Petroleum Geology* 18 (4):363-9.
- [6]. Zhao Junlong et al. Comparison and classification of typical geologic characteristics of typical tight oil in North America. *Lithologic oil and gas reservoirs*, 2015 (01): 44-50.
- [7]. JIA Cheng-zhi et al., China's compact oil evaluation criteria, main types, basic characteristics and resource prospects. *Petroleum Journal*, 2012 (03): 343-350.
- [8]. Du Jinhu, etc., China's lean oil exploration and challenges facing China *Petroleum Exploration*, 2014 (01): 1-9 pages.
- [9]. Yao Jingli et al., Characteristics of Tight Oil in Yanchang Formation of Ordos Basin. *Petroleum Exploration and Development*, 2013 (2): 150-158.
- [10]. Experimental design and Design-Expert, SPSS applications.

# Energy Levels of Hydrogen Like Mendelevium

Güldem Ürer<sup>1\*</sup>

<sup>1</sup> Sakarya University/Physics Department, Sakarya, Türkiye

\*corresponding gurer@sakarya.edu.tr

## ABSTRACT

The studying on hydrogenic ions with high Z is an occasion to understand atomic structure. It also assures us a test of methods used for determination of the atomic structures. Many fields and applications are required for precise atomic data. For this reason, it is performed a hydrogen like study for mendelevium ( $Md^{100+}$ ,  $Z=101$ ). It is calculated the energy levels of  $Md^{100+}$  with both multiconfiguration Hartree-Fock (MCHF) and multiconfiguration Dirac-Fock (MCDF) methods. The calculations have contained Breit-Pauli (BP) relativistic corrections in MCHF calculation and the transverse photon and quantum electrodynamics (QED) effects in MCDF calculation besides electron correlations. It is compared this study results with only and one theoretical works but there is no available experimental data yet for  $Md^{100+}$ .

**KEYWORDS** – Hydrogen Like, Energy Levels, MCHF Method, MCDF Method

## 1. INTRODUCTION

The detailed spectroscopic data needs have increased in the last years. The first stage to precisely describe spectral characteristics is to sensitively calculate the level structure. There are a lot of performed studies for hydrogen like ions with high Z and they are listed NIST atomic database [1]. The studies of  $Md^{100+}$  ( $Z=101$ ) are so sparse. Johnson and Soff [2] and Yerokhin and Shabaev [3] had performed theoretical studies of  $1 \leq Z \leq 110$ . In both studies, there is just  $1s_{1/2}$ ,  $2s_{1/2}$ , and  $2p_{1/2, 3/2}$  states energies. Then Jitrik and Bunge [4, 5] have been performed more comprehensive investigation;  $nl$  (up to  $n=25$ ,  $l=25$ ) for  $1 \leq Z \leq 118$  by using point-nucleus Dirac eigenfunctions. They have presented their results on a web site [6]. To increase the reliability of the theoretical studies, it should be supported with experiments. Unfortunately, it has not performed an experiment yet for  $Md^{100+}$ . Because of their short lifetimes and their radioactivity, it is too hard to experimentally study on actinides especially hydrogen like ions.

## 2. CALCULATION METHODS

There has briefly mentioned the theory of the methods MCHF and MCDF used in the calculation. The details of the methods have been described in [7, 8] and [9-13].

In the MCHF method, the wave function  $\Psi(\gamma LS)$  is expanded as linear combination of configuration state functions (CSFs)  $\Phi(\gamma_i LS)$ ,

$$\Psi(\gamma LS) = \sum_{i=1}^M c_i \Phi(\gamma_i LS), \quad \sum_{i=1}^M c_i^2 = 1. \quad (1)$$

The energy functional based on the non-relativistic Hamiltonian of an atom or ion,

$$H_{NR} = \sum_{j=1}^N \left( \frac{1}{2} \nabla_j^2 - \frac{Z}{r_j} \right) + \sum_{j < k} \frac{1}{r_{jk}}. \quad (2)$$

In fully relativistic MCDF method, the wavefunction Equation 1 is written in the form

$$\Psi_{\alpha}(PJM) = \sum_r^{n_r} c_r(\alpha) |\gamma_r PJM\rangle \quad (3)$$

and energy functional is based on the Dirac-Coulomb Hamiltonian,



$$H_{DC} = \sum_{j=1}^N \left( c\vec{\alpha}_j \cdot \vec{p}_j + (\beta_j - 1)c^2 + V(r_j) \right) + \sum_{j < k} \frac{1}{r_{jk}}. \quad (4)$$

It is clearly seen in equations of wavefunctions and hamiltonians, MCHF method uses *LS*-coupling while MCDF method uses *jj*-coupling. In all calculations, nuclear charge distribution is modeled by the two-component Fermi function. In MCHF method, the relativistic effects are included as a first-order (in order  $\alpha^2$ ) correction to the MCHF approximation by evaluating Breit-Pauli operators (mass correction and Darwin corrections, spin-orbit, spin-other orbit, orbit-orbit, spin-spin contact terms) using CI method. In MCDF, the transverse Breit interaction at the low-frequency limit and the QED corrections (self-energy and vacuum polarization) are considered (in order  $\alpha^2$ ). The both methods include correlation effects.

### 3. RESULTS AND DISCUSSION

On the basis lack of sensitive structure study for  $\text{Md}^{100+}$ , this study has been performed for hydrogen like mendelevium as a part of extensive work about hydrogen helium and lithium like actinides [14-18]. It has been used *nl* ( $n=1-9$ ,  $l=0-4$ ) configurations for both method calculations. The calculations have been performed with widely-used the MCHF atomic structure package [7] and GRASP code [9]. All computed data in this work have been compared as graphically to clarify.

Fig. 1 has represented a comparison between this work methods and other work [6]. Linear correlation coefficient  $R^2$  is 0.994 for MCHF and 1.000 for MCDF. So, both methods have had in an excellent agreement with other work. The average percent error between MCDF method and other works is 0.73% for Jitrik and Bunge [6], 0.19% for Yerokhin and Shabeav [3] and 0.26% for Johnson and Soff's [2]. The average percent error between MCHF method and other works is just a bit great than MCDF comparison; 3.87% for Jitrik and Bunge [6], 2.66% for Yerokhin and Shabaev [3] and 2.65% for Johnson and Soff's [2]. Fig. 2 has also presented MCHF and MCDF methods comparison ( $R^2=0.994$ ). This very small difference has arisen from the fact that both methods involved different contributions (the MCHF has Breit-Pauli and the MCDF has the transverse photon and quantum electrodynamic contributions). The excellent agreement between used in this and other work is a strong evidence for reliability of MCHF and MCDF calculations. In reference [6],  $n_l$  energy values are same  $n(l+1)_j$ . It has been pointed out that MCDF results are more sensible and reliable than reference [6]. Moreover, the presented energy levels data will be useful for the lamb shift studies. On the other hand,  $8g_{7/2, 9/2}$  and  $9g_{7/2, 9/2}$  levels have been determined for the first time.

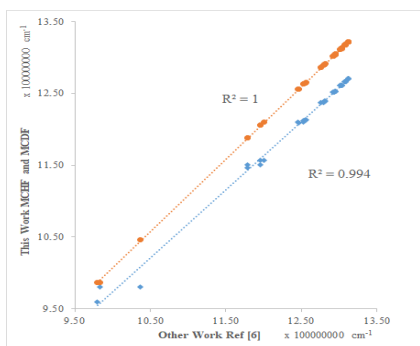


**Figure 1.** The comparison between calculated with MCHF and MCDF methods and other study [6] for  $\text{Md}^{100+}$  energy levels.

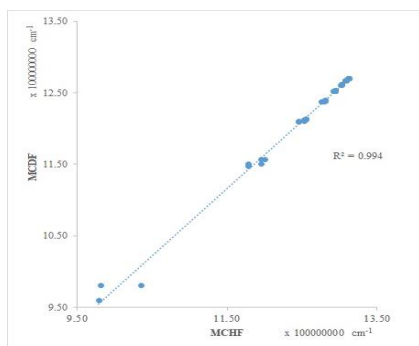


**Figure 2.** The crosscheck of MCHF and MCDF methods of  $\text{Md}^{100+}$  energy levels.

#### 4. CONCLUSION

The paper has aimed to implement the both MCHF and MCDF methods for carrying out the structure of  $\text{Md}^{100+}$ . The excitation energies have investigated in high precision (The given MCHF and MCDF results of  $\text{Md}^{100+}$  have been performed as a part of wide calculation about one, two, and three electron actinide ions with  $Z=89-103$ ). In the calculation, the Breit-Pauli, Breit and QED contributions have surveyed. Thus, it is thought this work is the most precise calculation ever made and some ( $8g_{7/2, 9/2}$  and  $9g_{7/2, 9/2}$ ) levels determined for the first time. It is a hope the present paper will lead to theoretical and experimental studies for  $\text{Md}^{100+}$  and also in the field of technology in future.

#### REFERENCES

- [1]. <https://www.nist.gov/pml/atomic-spectra-database>
- [2]. W. R. Johnson and G. Soff, The lamb shift in hydrogen-like atoms,  $1 \leq Z \leq 110$  At. Data and Nuc. Data Tables 33, 405 (1985).
- [3]. V. A. Yerokhin and V. M. Shabaev, Lamb shift of  $n = 1$  and  $n = 2$  states of hydrogen-like atoms,  $1 \leq Z \leq 110$ , J. Phys. Chem. Data 44 033103 (2015). DOI: 10.1063/1.4927487
- [4]. O. Jitrik and C.F. Bunge, Transition probabilities for hydrogen like atoms, J. Phys. Chem. Ref. Data 33 (2004) 1059. DOI: 10.1063/1.1796671
- [5]. O. Jitrik and C.F. Bunge, Salient features of electric and magnetic multipole transition probabilities of hydrogen-like systems, Phys. Scripta, 69 (2004) 196. DOI: 10.1238/Physica.Regular.069a00196
- [6]. <http://www.fisica.unam.mx/research/tables/spectra/1el/index.shtml>
- [7]. C.F. Fischer, The MCHF atomic-structure package, Com. Phys. Commun., 64 (1991) 369. DOI: 10.1016/0010-4655(91)90133-6
- [8]. C.F. Fischer, T. Brage And P. Jönsson, Computational atomic structure-an MCHF approach, (Bristol and Philadelphia: Institute of Physics Publishing (1997).
- [9]. K. G. Dyall, I. P. Grant, C. T. Johnson, F. A. Parpia And E. P. Plummer, GRASP: A general-purpose relativistic atomic structure program, Comp. Phys. Commun., 55 (1989) 425. DOI: 10.1016/0010-4655(89)90136-7
- [10]. I.P. Grant, Relativistic calculation of atomic structures, Advan. Phys., 19 (1970) 747. DOI: 10.1080/00018737000101191
- [11]. I.P. Grant, Gauge invariance and relativistic radiative transitions, J. Phys. B, 7 (1974) 1458. DOI:
- [12]. I.P. Grant, Computational chemistry (Vol 2) Ed. Wilson S, Plenum, New York, USA (1988).
- [13]. P. Grant, Relativistic quantum theory of atoms and molecules, Springer, New York, USA (2007).
- [14]. G. Ürer, Energies and radiative transitions ( $E1$ ,  $E2$ , and  $M1$ ) for hydrogen-like thorium, Can. J. Phys. 94, (2016) 1138. DOI:10.1139/cjp-2016-0236
- [15]. G. Ürer, Can. J. Phys. (in press). DOI: 10.1139/cjp-2018-0113
- [16]. G.Ürer, A structure calculation for hydrogen like nobelium, Sakarya University Journal of Science, 22 (2018) 970. DOI: 10.16984/sofenbilder.397471
- [17]. G. Ürer, The electric dipole transitions of hydrogen like nobelium, Beykent Üniversitesi Fen ve Mühendislik Bilimleri Dergisi, 11 (2018) 63. DOI: 10.20854/bujse.403031
- [18]. G. Ürer, The lifetimes of hydrogen-like mendelevium, Bilecik Şeyh Edebali Üniversitesi Fen Bilimleri Dergisi, 5 (2018) 18.

# CO<sub>2</sub> Adsorption Capacity of Shale with the Consideration of Adsorption-induced Swelling

Rongrong Qi<sup>1,2\*</sup>, Zhengfu Ning<sup>1,2</sup>, Qing Wang<sup>1,2</sup>, Shuang Zhang<sup>1,2</sup>, Xiaojun Wu<sup>1,2</sup>, Zhilin Cheng<sup>1,2</sup>

<sup>1</sup> State Key Laboratory of Petroleum Resources and Prospecting in China University of Petroleum, Beijing, P. R. CHINA

<sup>2</sup> Ministry of Education Key Laboratory of Petroleum Engineering in China University of Petroleum, Beijing, P. R. CHINA

\*qrr\_cup@163.com

## ABSTRACT

The purpose of this study is to investigate the CO<sub>2</sub> adsorption-induced swelling of shale. This study is of great significance for CO<sub>2</sub> geological sequestration and the improvement of CH<sub>4</sub> recovery.

A theoretical model originally proposed for coal was used in this work to calculate the adsorption-induced swelling of shale, based on the assumption that the surface energy change caused by adsorption was equal to the elastic energy. What the model requires were adsorption isotherms and the mechanical properties of shale. The adsorption isotherm was measured on a shale sample at 80 °C using a volumetric method and the parameters of mechanical properties were obtained from the literature.

Shale samples are mainly composed of organic matter, quartz, feldspar, carbonate, pyrite and clay minerals, of which clay minerals are mainly illite. In calculating the expansion induced by adsorption, only the expansion of organic matter and clay minerals is considered. The calculation results show that the volumetric strain of organic matter is three orders of magnitude higher than that of illite. The adsorption capacity is recalculated at each pressure step by assuming that the void volume is decreased by the expansion amount of the shale samples at that pressure. The results show that under low pressure, the adsorption induced swell has almost no effect on the adsorption amount. With the increase of pressure, the adsorption amount corrected by the expansion of the sample is larger than that of the uncorrected, and the difference increases with the increase of pressure.

**KEYWORDS :** Carbon dioxide, Shale, Adsorption, Swell, Model

## 1. INTRODUCTION

The studies of the adsorption-induced swell have been widely investigated on coal. The main conclusion was that there was a linear relationship between volumetric strain and adsorption at intermediate pressures [1]. However, at high pressures, linear relationship no longer existed, adsorption continued to increase but the swell did not. Further, swelling could be represented by a modified Dubinin–Radushkevich equation [2].

Compared with coal, the test of adsorption-induced swell of shale is challenging, which is reflected in the following aspects: first, the adsorption capacity of shale is one order of magnitude smaller than that of coal; second, shale is stiffer and therefore less prone to swell [3]. Due to the difficulty of shale expansion test, there is almost no experimental study on adsorption-induced swell of shale. In this paper, the adsorption-induced swell model proposed by Pan et al. [4] coupled with the adsorption data carried out by Heller et al. [3] were applied to correct the CO<sub>2</sub> isotherms, and the effect of swelling on adsorption was discussed.

## 2. MODEL

## 2.1. Balance Condition

Basing on the assumption that the surface energy change caused by adsorption was equal to the elastic energy, the linear strain is expressed as follows [4]:

$$\varepsilon = -\frac{\Phi \rho_s}{E_s} f(x, v_s) \quad (1)$$

Where,  $\Phi$  refers to surface potential, J / kg;  $\rho_s$  is the density of the adsorbent, kg / m<sup>3</sup>;  $E_s$  is the elastic modulus of the adsorbent, Pa; term  $f(x, v_s)$  can be expressed as follows:

$$f(x, v_s) = \frac{[2(1-v_s) - (1+v_s)cx][3-5v_s - 4(1-2v_s)cx]}{(3-5v_s)(2-3cx)} \quad (2)$$

Where,  $c=1.2$ ,  $x$  is the ratio of cylinder radius to length in the model [4];  $v_s$  is the Poisson's ratio of the adsorbent.

## 2.2. Surface Potential Energy

The surface potential energy  $\Phi$  was defined as the surface potential energy change caused by adsorption per unit mass of adsorbent [4]. To derive surface potential energy, the adsorption thermodynamics theory proposed by Myers [5] was applied in the study. However, the surface potential energy calculated by Myers can only be applied to incompressible adsorbents. Pan et al. [4] further extended the functions for incompressible solids to compressible solids, and derived the expression of surface potential energy:

$$\Phi = \int_0^P V^a dP - RT \int_0^P \left( \sum_{i=1}^C n_i^a d \ln f_i \right) \quad (3)$$

Where,  $R$  is the gas constant, taking 8.314 J / mol / K;  $T$  is the temperature, K;  $P$  is the pressure, Pa;  $C$  is the number of gaseous adsorbates;  $n$  is adsorption amount, mmol/g;  $f$  is fugacity, which can be simplified as pressure at low pressures;  $V^a$  is the volume change per unit mass of adsorbent, m<sup>3</sup> / kg, expressed as follows [4]:

$$V^a = \frac{3\varepsilon}{\rho_s(1-\phi)} \quad (4)$$

Where,  $\phi$  is the porosity, which can be expressed as following:

$$\phi = 1 - 3\pi x^2(1 - cx) \quad (5)$$

## 3. EXPERIMENTS

The samples applied in this paper were outcrops of black shale from Wufeng-Longmaxi Formation of Sichuan Basin, China. The samples were ground to power less than 100 meshes (0.15 mm), of which 1 – 2 g was used for the total organic matter content (TOC) test, and about 8 g was utilized to measure the mineral composition using X-ray diffraction (XRD) analysis. The high pressure

CO<sub>2</sub> adsorption measurements were conducted basing on a volumetric method. Detailed test procedures for these experiments can be found in our previous work [6].

## 4. RESULTS

### 4.1. The Composition of the Shale Samples

Table 1 shows the composition of shale samples. It can be seen from the table that the shale samples are mainly composed of organic and inorganic matter, among which inorganic materials include quartz, feldspar, carbonates, pyrite and clay minerals. The TOC content is between 2.28 wt. % and 3.61 wt. % with an average of 3.07 wt. %. The total clay mineral content ranges between 15.7 wt. % and 27.4 wt. % with an average of 20.1 wt. %.

**Table 1. The Organic and Inorganic Composition of the Shale Samples.**

Sample	TOC (wt. %)	XRD			Relative content of clay minerals (%)		
		Quartz+feldspar (wt. %)	Carbonates+pyrite (wt. %)	Total clays (wt. %)	Ill <sup>a</sup>	Kln <sup>b</sup>	Chl <sup>c</sup>
1	2.28	72.6		27.4	92	2	6
2	3.31	55.4	27.4	17.2	94		6
3	3.61	41.7	42.6	15.7	100		

<sup>a</sup>Ill=Illite; <sup>b</sup>Kln=Kaolinite; <sup>c</sup>Chl=Chlorite.

### 4.2. Sorption-induced Swell of Shale Samples

The CO<sub>2</sub> gas adsorption experiment was carried out at 80 °C up to 16 MPa. Since the amount of micropores in quartz, feldspar, carbonate and pyrite is small, the adsorption of CO<sub>2</sub> on these components is not considered in the calculation of adsorption expansion. Adsorption data of CO<sub>2</sub> gas on pure carbon and illite in the literature [3] coupled with the sorption-induced swell model described in section 1 were applied to calculate the adsorption expansion of the bulk shale samples. The adsorption data were characterized by Langmuir equation. At low pressures, equation (3) can be turned into:

$$\Phi = \int_0^P V^a dP - RT \int_0^P \left( \sum_{i=1}^C n_i^a d \ln f_i \right) = \int_0^P V^a dP - RT \int_0^P \frac{n_L b}{1 + bP} dP = \int_0^P V^a dP - RT n_L \ln(1 + bP) \quad (6)$$

Where,  $n_L$  is the Langmuir adsorption amount, mmol / g;  $b$  is the Langmuir constant, Pa<sup>-1</sup>. Combining equations (1), (4) and (6) gives the following equation:

$$\varepsilon = RT n_L \ln(1 + bP) \frac{\rho_s}{E_s} f(x, v_s) - \frac{3f(x, v_s)}{(1 - \phi)E_s} \int_0^P \varepsilon dP \quad (7)$$

Where,  $E_s$  and  $v_s$  values for pure carbon and illite are taken from the literature [7].

Figure 1 shows the relationship between volumetric strain and pressure. From the figure we can see that the adsorption swelling strain increases with pressure, and the increasing speed gradually becomes slower. In shape, the relationship curve is similar to the Langmuir type curve. In terms of numerical values, the volumetric strain of organic matter is three orders of magnitude higher than that of illite.

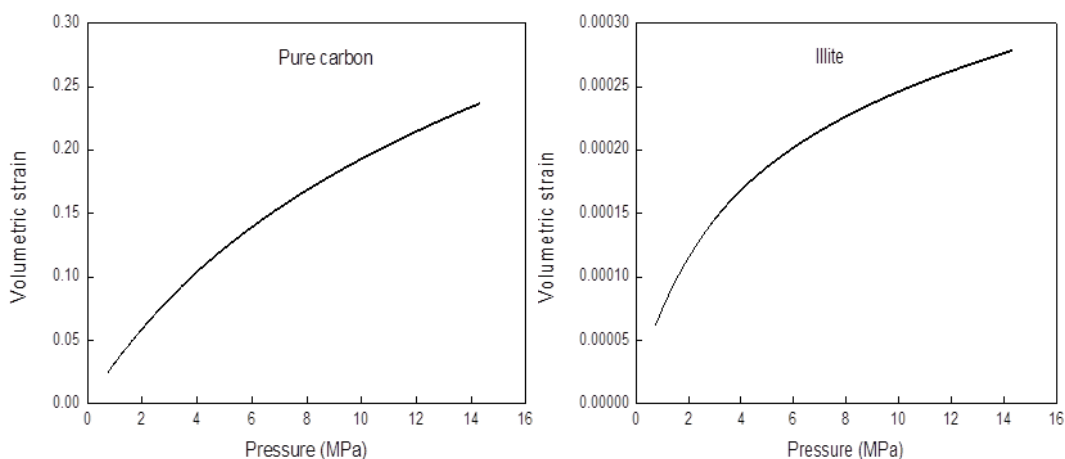
According to the shale mass composition in section 3.1 and the densities of pure carbon (2280 kg / m<sup>3</sup>) and illite (2700 kg / m<sup>3</sup>), the volume of pure carbon and illite in shale samples can be calculated. The expansion volume induced by adsorption at different pressures can be then

obtained basing on the relationship between volume strain and pressure presented in figure 1. The adsorption amount was corrected at each pressure assuming that the void volume was subtracted by the expansion volume at that pressure. Figure 2 shows the excess adsorption of CO<sub>2</sub> gas before and after swelling correction. As can be seen from the figure, under low pressure, the adsorption induced swell has almost no effect on the adsorption amount. With the increase of pressure, the adsorption amount corrected is larger than that of the uncorrected, and the difference increases with pressure. Thus, adsorption induced swelling should be considered in the calculation of CO<sub>2</sub> adsorption on shale, especially at higher pressures.

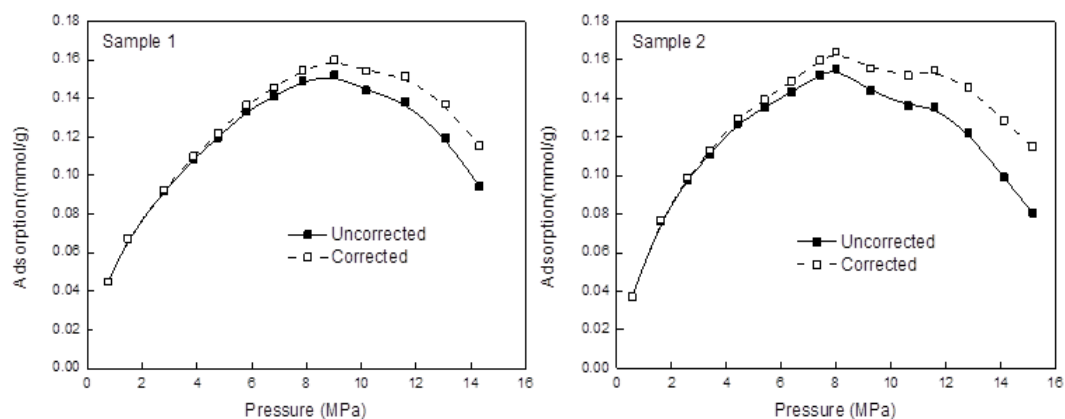
## 5. CONCLUSION

The CO<sub>2</sub> adsorption swelling strain increases with the increase of pressure, and the volumetric strain of pure carbon is three orders of magnitude higher than that of illite.

Swelling has almost no effect on adsorption at low pressures, while at high pressures, swelling will result in underestimation of adsorption. The adsorption amount corrected by swelling is increased by 20 % - 60 % at 16 MPa. Therefore, CO<sub>2</sub> adsorption swelling should be considered in the calculation of adsorption under formation conditions.



**Figure 1.** Volumetric Strain as a Function of Pressure.



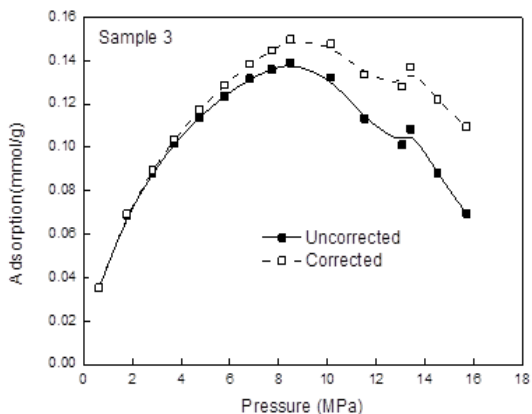


**Figure 2.** Excess Adsorption of CO<sub>2</sub> as a Function of Pressure with the Consideration of Swelling

## REFERENCES

- [1].D. J. K. Ross, R. M. Bustin. The importance of shale composition and pore structure upon gas storage potential of shale gas reservoirs. *Marine & Petroleum Geology* 2009, 26(6), 916-27. DOI: 10.1016/j.marpetgeo.2008.06.004
- [2].S. Day, R. Fry, R. Sakurovs. Swelling of Australian coals in supercritical CO<sub>2</sub>. *International Journal of Coal Geology* 2008, 74(1), 41-52. DOI: 10.1016/j.coal.2007.09.006
- [3].R. Heller, M. Zoback. Adsorption of methane and carbon dioxide on gas shale and pure mineral samples. *Journal of Unconventional Oil & Gas Resources* 2014, 8, 14-24. DOI: 10.1016/j.juogr.2014.06.001
- [4].Z. Pan, L. D. Connell. A theoretical model for gas adsorption-induced coal swelling. *International Journal of Coal Geology* 2007, 69(4), 243-52. DOI: 10.1016/j.coal.2006.04.006
- [5].L. Myers. Thermodynamics of adsorption in porous materials. *Aiche Journal* 2002, 48(1), 145-60. DOI: 10.1002/aic.690480115
- [6].R. Qi, Z. Ning, Q. Wang, et al. Sorption of methane, carbon dioxide, and their mixtures on shales from Sichuan Basin, China. *Energy & Fuels* 2018, 32(3). DOI: 10.1021/acs.energyfuels.7b03429
- [7].G. Mavko. *The rock physics handbook*, 2009. DOI: 10.1017/CBO9780511626753

## Numerical simulation on plugging efficiency of degradable particle based on Fluent software

Wang Jin<sup>1,2</sup>, Zhou Fujian<sup>1,2\*</sup>, Yang Chen<sup>1,2</sup>, Zhang Lufeng<sup>1,2</sup>, Feng Wei<sup>1,2</sup>, Wang Yuechu<sup>1,2</sup>

<sup>1</sup>The Unconventional Natural Gas Institute, China University of Petroleum at Beijing, 102249, CHINA

<sup>2</sup>State Key Laboratory of Petroleum Resource and Prospecting, China University of Petroleum at Beijing, 102249, CHINA

### ABSTRACT

With the development of oil and gas industry, the unconventional resources have become the focus of energy development. Multiple fracturing in heterogeneous reservoir is an indispensable method to achieve enhanced production in unconventional reservoirs. However, the temporary plugging rule of degradable ball in perforation tunnel is still unclear. In this research, a series of numerical simulation were conducted by FLUENT to systemically investigate the effect of injection rate, size of plugging particles, viscosity of carrier fluid on the plugging efficiency. The results showed that the relationship between plugging efficiency and injection rate is clear. It's found that the higher the flow rate in the pipe, the more particles are distributed in the perforation and the maximum flow rate at the outlet is between 16.6 and 17.5m/s. The highest plugging efficiency layer is the lower perforation and the higher the flow velocity at the outlet, the higher the plugging efficiency. Those results would provide an improvement in multiple fracturing technology and instruction of its successful application in unconventional reservoirs.

**KEYWORDS** - Multiple fracturing; Degradable particle, plugging efficiency, FLUENT software.

### 1. INTRODUCTION

With the development of oil and gas fields, the conventional oil and gas resources are running low. Hence, unconventional heterogeneous reservoirs with low permeability has become the focus of development gradually. In order to enhance the production rate of reservoirs, hydraulic fracturing is widely applied in the field. For huge thick layer and long horizontal interval, it's difficult to achieve satisfactory stimulation effect through traditional hydraulic fracturing, resulting in low efficiency, high cost and complicated operation. In addition, traditional hydraulic fracturing doesn't have obvious pertinence, and cannot develop the full potential of reservoir. In response to this, the technology of multiple fracturing was introduced to efficiently stimulate the unconventional reservoir [1-3]. Multiple fracturing in heterogeneous reservoir is an indispensable method to achieve enhanced production in unconventional reservoirs [4-6]. The core of this technology is efficiently plugging the high-permeability perforation, and fracture the low-permeability layer.

At present, two effective methods to execute multiple fracturing are chemical methods and mechanical methods [7]. Mechanical methods include packer multiple fracturing, immovable string multiple fracturing, bridge-plug multiple fracturing, coiled-tubing multiple fracturing. Chemical methods include foam multiple fracturing, gel multiple fracturing, temporary plugging ball multiple fracturing, etc. Compared with mechanical methods which have long operation period, high cost and high risk, chemical methods have become an effective alternative for safe, efficient and economical method of multiple fracturing. Perforation Temporary Plugging by degradable particle, a chemical diverting method, has a promising prospect with low cost and convenient operation. The principle of this method is to pump carrier fluid with temporarily plugging balls or particles into the well, plugging the layer with good physical property, thus increasing the pressure inside the wellbore to open the layer with relatively poor physical property, to achieve the purpose of stimulate multiple layers during one construction. Kastrop first mentioned that the ball sealer can be used to well stimulation in petroleum engineering [8]. Brown



R W studied the performance of the ball sealer in the early stage [6], he studied the inertia force, tension and stabilizing force of the perforation. Erbstoesser performed a series of experiments using balls with different density and found that high-density ball had better plugging efficiency in low speed flow [9-11]. Li built an experiment system that can simulate plugging process in three conditions. He evaluated the influence of injection rate and the number of balls [12-15]. Wang and Desai confirmed the feasibility of plugging by field application [16-19]. According to previous researches, it can be concluded that the application of multiple fracturing by temporary plugging balls was mainly based on experience, and the rule of temporary plugging ball movement needs further study. It's also unclear how plugging is formed in perforation tunnel.

In this study, reservoir condition by controlling the injection rate at the perforation was simulated by the FLUENT software. A series of numerical simulation analysis were performed to investigate the effect of injection rate, the size of plugging particles, the viscosity of carrier fluid on plugging efficiency. This study provided an improvement in optimizing temporary plugging fracturing design.

## 2. MATHEMATICAL MODEL

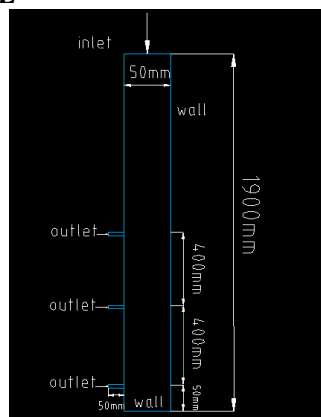


**Figure 1.** Geometrical structure of the wellbore and boundary conditions

In millimeters, The mathematic and grid model were shown in Figure 1 and 2. inflow boundary, outflow boundary and the rest are WALL boundary. According to the calculation needs, the unstructured mesh was established with the Max element was 20 and the volume mesh structure was Tetra/Mixed, setting the boundary layer.

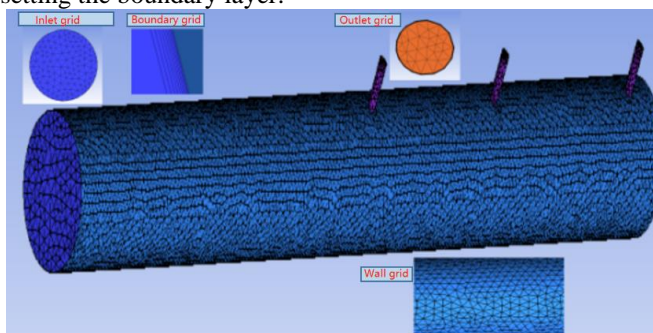


**Figure 2.** Three - dimensional grid model

## 3. RESULTS AND DISCUSSION

### 3.1. Fluid velocity distribution

The magnitude of the velocity can be regarded as the absolute value of each particle and the flow direction can be found from velocity vector in the velocity field. Velocity distribution of water in pipe string was shown in figure 3.

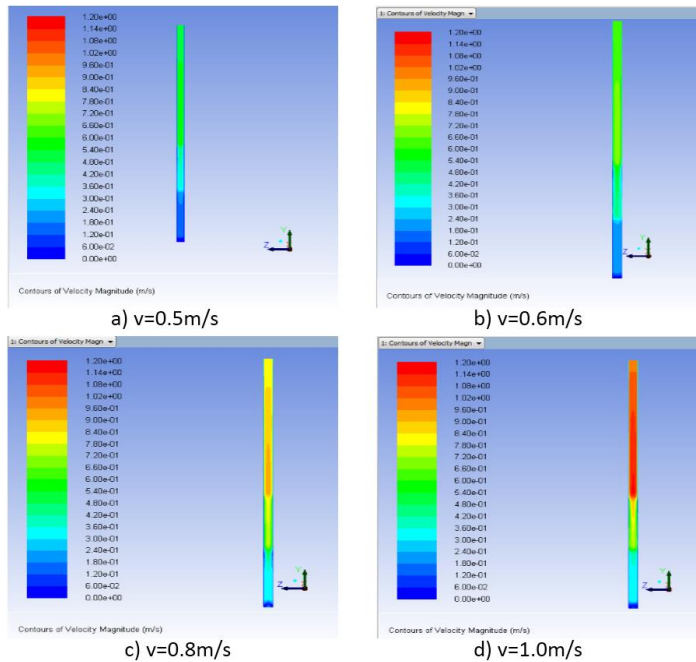


**Figure 3.** The velocity distribution in the column

Velocity distribution:

- a) Inlet liquid velocity is  $0.5\text{m/s}$  (pump displacement  $=0.08\text{ m}^3 / \text{min}$ ),
- b) Inlet liquid velocity is  $0.6\text{m/s}$  (pump displacement  $=0.1\text{ m}^3 / \text{min}$ ),
- c) Inlet liquid velocity is  $0.8\text{m/s}$  (pump displacement  $=0.13\text{ m}^3 / \text{min}$ ),
- d) Inlet liquid velocity is  $1.0\text{m/s}$  (pump displacement  $=0.16\text{ m}^3 / \text{min}$ ).

As shown from the four figures, inlet is not the place where the liquid velocity is highest, and the highest velocity in pipeline appears in the middle position between inlet and the first perforation. The lower the flow rate, the lower the liquid velocity. At the bottom, the flow rate tends to  $0\text{m/s}$ , and an uplifted flow line is generated, which can verify the phenomenon of upwelling backflow in the experiment when small particles are blocked and fall into the bottom of the well, as shown in figure 4.

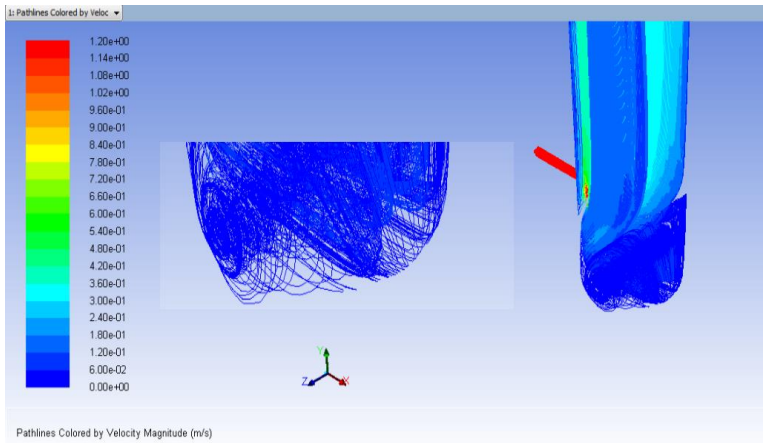


Figure 4. Upwelling backflow at the bottom

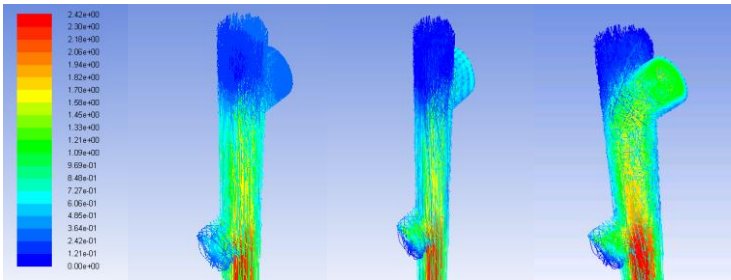
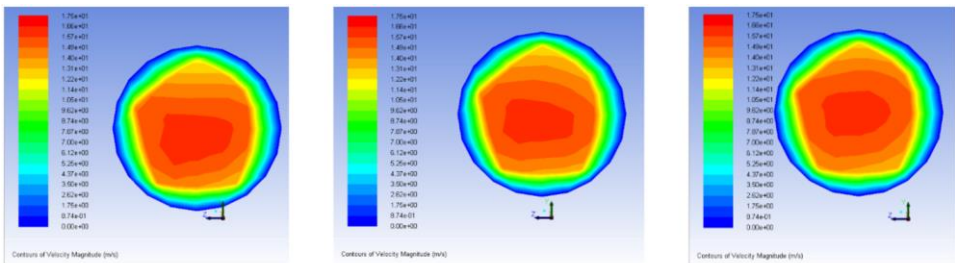


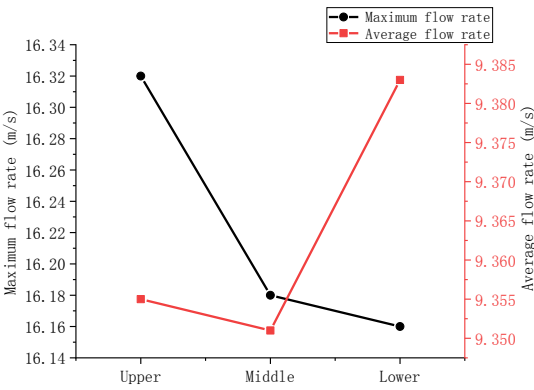
Figure 5. The distribution of velocity particles in different tubes

Figure 5 respectively describe the distribution of particles in case the flow rate in the pipe is 0.2m/s, 0.5m/s and 1m/s, and the higher the flow rate in the pipe, the more particles are distributed in the perforation.



Upper perforation exits      Middle perforation exits      Lower perforation exits  
Figure 6. The flow velocity distribution at the exit of the perforation

The maximum flow rate at the outlet was between 16.6 and 17.5m/s, which was consistent with the measured flow rate, shown in figure 6.



**Figure 7.** The average speed and maximum speed of the three perforated outlets

Shown in figure 7, the maximum velocity of the upper perforation is largest and the average velocity of the lower perforation is largest. This phenomenon is consistent with the experimental result that the plugging efficiency of the upper and lower perforations is higher than that of the middle section during the experiment.

**3.2. Particle migration trajectory**

DPM model was used to simulate particle migration. Figure 8 and 9 showed the migration track of 3mm particles in the model.

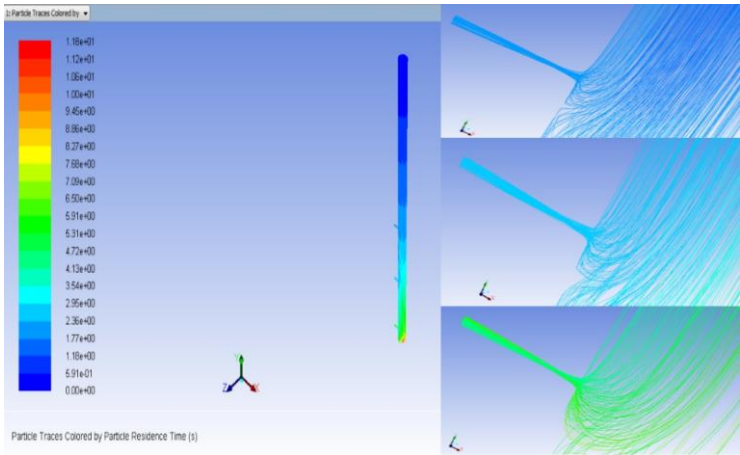


**Figure 8.** 3mm-particles migration path chart( $v=0.5\text{m/s}$ )

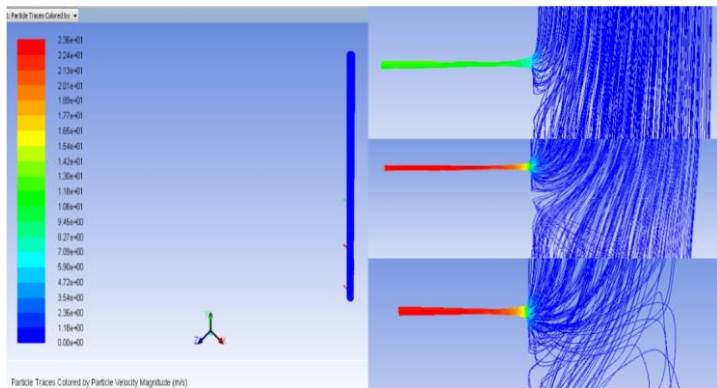


Figure 9. 3mm-particles migration path chart( $v=1\text{m/s}$ )

As shown in figure 8 and figure 9, the migration trajectory and velocity distribution of the 3mm plugging particles at different flow rates. The velocity of carrying fluid has a great influence on particle migration. The faster the fluid velocity, the more concentrated the particles in the perforation.

3.3. Plugging efficiency simulation

Table 1. Number of particles captured at the exit of the perforation

Flow Rate m/s	0.5			0.6			0.8			1		
	3mm	6mm	mixture	3mm	6mm	mixture	3mm	6mm	mixture	3mm	6mm	mixture
Upper	79	30	105	78	30	106	76	30	106	73	30	103
Middle	95	72	167	100	77	183	99	84	183	102	87	189
Lower	119	105	224	122	110	201	127	112	239	128	116	244

Shown in the table 1, no matter what the pump rate is, the highest plugging efficiency layer is the lower perforation, which is consistent with the simulation of multiple-perforation in the experiment. Therefore, the simulation results show that the higher the flow velocity at the outlet, the higher the plugging efficiency.

4. CONCLUSION

In this paper, through the FLUENT software, temporary plugging rule of degradable particle is studied for perforation, and the following conclusions are mainly obtained:

- 1) The inlet is not the place where the liquid velocity is highest, and the highest velocity in the pipeline appears in the middle position between the inlet and the first perforation. The lower the flow rate, the lower the liquid velocity.
- 2) The higher the flow rate in the pipe, the more particles are distributed in the perforation.
- 3) The maximum flow rate at the outlet is between 16.6 and 17.5m/s, which is consistent with the measured flow rate in the experiment.
- 4) The maximum velocity of the upper perforation is largest and the average velocity of the lower perforation is largest. This phenomenon is consistent with the experimental result that the plugging efficiency of the upper and lower perforations is higher than that of the middle section during the experiment.

- 5) The velocity of carrying fluid has a great influence on particle migration. The faster the fluid velocity, the more concentrated the particles in the perforation.
- 6) The highest plugging efficiency layer is the lower perforation and the higher the flow velocity at the outlet, the higher the plugging efficiency.

## ACKNOWLEDGMENTS

This work is financially supported by the Foundation of State Key Laboratory of Petroleum Resources and Prospecting (Grant No. PRP/indep-4-1703), the National Science and Technology Major Projects of China (Grant Nos. 2016ZX05051 and 2017ZX05030), PetroChina Innovation Foundation (2018D-5007-0205), and the Science Foundation of China University of Petroleum at Beijing (Grant No. 2462017YJRC031).

## REFERENCE

- [1]. Wang Z L. Study on underground hydraulic fracturing of low permeability coal seam [Z]. Beijing: China university of mining and technology (Beijing),2015: 1-10
- [2]. Yu H C. Research on reengineering technology of old Wells in Chang 8 reservoir [Z]. Xi 'an: xi 'an university of petroleum, 2013: 3-5.
- [3]. Economides M J, Nolte K G. Reservoir stimulation[J]. Old Tappan, NJ; PrenticeHall Inc., 1989(6): 1-14.
- [4]. Dahi Taleghani, A., & Olson, J. E. (2014) How natural fractures could affect hydraulic-fracture geometry. SPE journal, 19(01), 161-171.
- [5]. ÖÖ. Karaçal. (2016) Computational material analysis of structural and hemodynamic model of coronary stent by cfd/fea in computer aided mechanical engineering approach. Acta Physica Polonica, 130(1), 249-251.
- [6]. Brown R W, Neill G H, Loper R G. Factors Influencing Optimum Ball Sealer Performance[J]. Journal of Petroleum Technology, 1963,15(4): 450-454.
- [7]. Sun H B, Wang W B, Dong Q Q. Analysis and discussion of layered fracturing technology [J]. Chinese petroleum and chemical standards and quality,2012,33(16): 59.
- [8]. Mercado O, Ernesto C. Drill Cuttings-based Methodology to Optimize Multi-stage Hydraulic Fracturing in Horizontal Wells and Unconventional Gas Reservoirs[J]. 2012: 410-420.
- [9]. Erbstoesser S R. Improved Ball Sealer Diversion[J]. Journal of Petroleum Technology, 2013,32(11): 1903-1910.
- [10]. Li S Y, Li Z M. Experimental Study on Ball Sealer Diversion for Lateral Well[J].Advanced Materials Research, 2012,524-527(524-527): 1399-1407.
- [11]. Wang D, Wang X, Liu G, et al. A New Way of Staged Fracturing Using Ball Sealers[J].Spe Production & Operations, 2012,27(3): 278-283.
- [12]. Desai K, Jajal H. (2014) Multi-zone stimulation technology. Journal of Unconventional Oil & Gas Resources, 6(2): 34-38.
- [13]. Economides M J, Nolte K G. Reservoir stimulation[J]. Old Tappan, NJ; Prentice Hall Inc., 1989(6): 1-14.
- [14]. Bale G E. Matrix Acidizing in Saudi Arabia Using Buoyant Ball Sealers[J]. Journal of Petroleum Technology, 1984,36(10): 1748-1752.
- [15]. Nozaki M, Zhu D, Hill A. Experimental and Field Data Analyses of Ball SealerDiversion[J]. Spe Production & Operations, 2013,28(3): 286-295.
- [16]. Zou J, Yue X, Zhang J, et al. Self-assembled microspheres feasibility study for conformance control in high temperature and high salinity reservoirs[J]. Arabian Journal of Geosciences, 2018, 11(9):195.

- [17]. Huang S, Yao Y, Zhang S, et al. Pressure transient analysis of multi-fractured horizontal wells in tight oil reservoirs with consideration of stress sensitivity[J]. *Arabian Journal of Geosciences*, 2018, 11(11):285.
- [18]. Hu Z, Yang J, Liu S, et al. Prediction of sealed annular pressure between dual packers in HPHT deepwater wells[J]. *Arabian Journal of Geosciences*, 2018, 11(17):489.
- [19]. Zheng, W., Liu, Y., Huang, J. et al. *Arab J Geosci* (2018) 11: 640. <https://doi.org/10.1007/s12517-018-3965-9>

## Training on educational uses of ICTs: The disciplinary dimension of learners in the training contents

Yamani Dalila<sup>1\*</sup>, Mouhouche Ali<sup>2</sup> and Ait El Djoudi Amel<sup>3</sup>

<sup>1</sup> ENS of Kouba/Physics Department, Algiers,ALGERIA

<sup>2</sup> ENSA/ Physics Department, Algiers,ALGERIA

<sup>3</sup> ENS of Kouba/Physics Department, Algiers,ALGERIA

\*yamani19@gmail.com

### ABSTRACT

Teacher training in educational ICTs use is an important factor in implementing technologies in classroom. However, there is evidence in literature that several training projects aiming at even professionalization have not fully succeeded. We try by this study to identify variables that have to be taken in designing the training device in ICTs use to teachers integrate efficiently technologies into their practices. We rely on the Acceptance of a Technology Model (Venkatesh & Davis 2000) and the instrumental approach (Rabardel & Samurçay, 2001). We assume that technological, pedagogical and didactic mediatization components of the training device leading to objects learning appropriation enable learners to efficiently integrate ICTs into their teaching practices.

We conducted longitudinal survey of teacher's group at university in Algeria who have received courses in pedagogical ICTs use. Our approach is based on interview before and after the training and the analysis of logbooks written by the participants along the training.

Data analysis reveals difficulties in appropriating learning objects among some participants, and for most, difficulties in transferring the knowledge acquired to the contents taught. The interview conducted one year after training completion allowed us to link non-use of educational technologies in classroom to difficulty of transferring skills acquired by the training to real teaching situations.

**KEYWORDS** - University teacher training, educational ICTs use, Training device.

### 1. INTRODUCTION

The implementation of educational technologies in teaching and learning processes depends on several factors that refer to different dimensions. The authors in [1] cite three important factors among the five identified by Fabry and Higgs in [2]. These three factors concern the human dimension: resistance to change, teacher attitude and professional development. The authors emphasize the professional development and consider it as a key element. The professional development can evolve by continuing training which allows to the learner acquiring professional skills and thus constructing a professional identity [3].

Several training projects aimed to professionalization of teachers for the integration of technologies into teaching and learning practices have been implemented especially at higher education [4]. Algeria has not been left behind and recently has mandated the follow-up of training on educational uses of technologies for newly recruited teachers.

We present in this paper the results of the survey we conducted on a group of newly recruited teachers who have followed a professional training on the integration of ICTs in teaching practices. The objective is to study the impact of such device on the professional practices after the training completion.

### 2. THEORETICAL BACKGROUND

#### 2.1. Utilisation of a technology and ATM model [5]

Davis in 1986 developed the model of acceptance of a technology (ATM) which concerns specifically the prediction of the acceptability of an information system. The model postulates that



the acceptability of an information system is determined by two factors: the perception of utility and the perception of ease of use of this system.

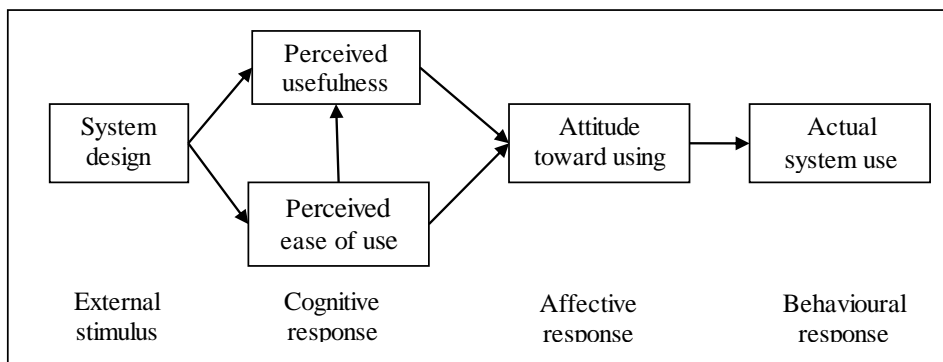


**Figure 2.** A technology acceptance model of Davis (1986)

The perception of utility is defined as the degree in which a person believes that the use of a system improves its performances, while the perception of ease of use refers to the degree in which a person believes that the use of the system will be divested of efforts [5] [6]. In literature, it was largely demonstrated that teacher's knowledge are basically constituted of beliefs about learning, educational approaches, teaching and learning tools including ICTs, and this beliefs represent a important component of teacher's practices [7] [8].

According to Davis, the perception of ease of use would influence significantly the attitude of an individual through two main mechanisms: the auto-efficiency and the instrumentality. In fact, according to the theory of the self-efficacy in [9], more a system is easy to use, more the user will have a feeling of auto-efficiency. Also, the ease of use of a tool would give to the user the sensation to have a control on what he is doing [10]. The auto-efficiency is one of the main factors underlying the intrinsic motivation [9] [10], it is what illustrates the direct link between the perception of the ease of use and the attitude of use.

From the original model, Venkatesh and Davis proposed a model ATM2 (2000) in which they defined the external variables: subjective norms, social and professional image, job relevance, output quality and the result demonstrability.

## 2.2. Instrumental Approach [11]

Rabardel, basing on Vygotski's approach, developed the concept of tool-use where he puts forward two important ideas. First, he conceives the tool as a mixed entity, consisting of an artefact and its utilization schemes [12]. Second, he defines the instrumental genesis, which conceptualizes the different interactions between the user, the tool and the object of his activity [12].

Then according to Rabardel, an artefact as such is not an instrument. It can become an instrument, when the user develops utilization schemes and integrates the instrument into his activity. Schemes constitute the psychological entity of the instrument, if developed by the subject when he uses the artefact in a singular action, they are considered then according to Rabardel as a cognitive invariant, a common framework for equivalent activities. Then, they can be conserved by the subject and used in future actions of the same class.

By this way, the instrument constructed is considered as a mean to capitalize on or crystallize knowledge acquired through experience according to [11]. It can also be considered as a mode to fix the acquisitions of man.

In his model IAS (Instrumented mediated Activity Situations), Rabardel shows the complexity and multiplicity of relations and interactions between the different poles.

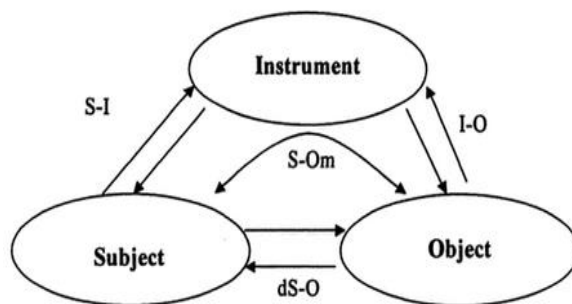


**Figure 2.** The IAS model [11]

In apart from the direct subject-object interaction (dS-O), there are additionally the interactions: those between the subject and the instrument (S-I), those between the instrument and the object (I-O) and those between the subject and the object (S-O).

### 3. METHODOLOGY

The approach consists to question the perceptions of participants, who were following the training, related to the usefulness of ICTs in teaching and learning as well as their ease of use. This was by analyzing the notes that we asked them to write down in logbooks along the training. Notes should be taken for each learning unit and should concern what they have learned, what they believe have mastered, what they think they will mobilize after the training in their teaching practices, the learning objects which were difficult and not understood and of course other elements that they saw important.

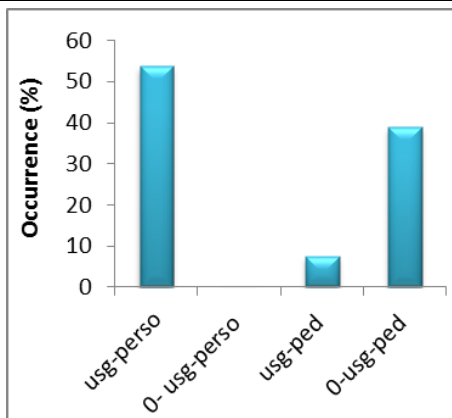
We also conducted two interviews with the participants. The first was before the start of the training. The objective was to define each participant's profile before the training concerning his representations of ICTs, his personal and professional use of ICTs and his ICT's utility and ease of use perceptions. The second was conducted approximately one year after training completion. We wanted by this interview to question the representations of the participants about the ICTs, their perceptions of utility in teaching and learning processes, their perceptions of ease of use, their real pedagogical practices, the possible performances induced to their practices by using ICTs, job relevance, output quality and result demonstrability. Other open questions were also discussed during the interview, giving each participant the opportunity to express his opinion about his training, the difficulties encountered, the factors that he thinks may cause any no appropriation of learning, or at the origin of possible no integration of ICTs in his teaching practices.

The group includes 16 teachers from different specialties: physics, chemistry, mathematics, natural sciences and education sciences. Most of them have already a significant teaching experience.

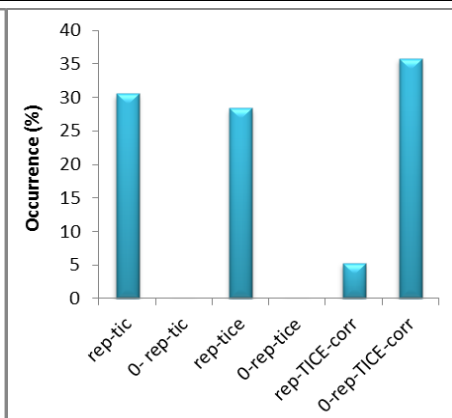
To obtain the data, we proceed to the semantic analysis of the writings on the logbooks collected as well as the answers to the questions of the two interviews. The analyzed expressions were subsequently coded according to the categorical system we defined for our variables.

### 4. RESULTS AND DISCUSSION

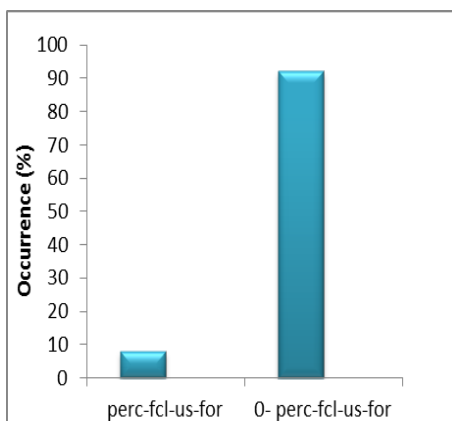
The graphs below show results obtained from analysis of logbooks and interviews for the 16 participants.



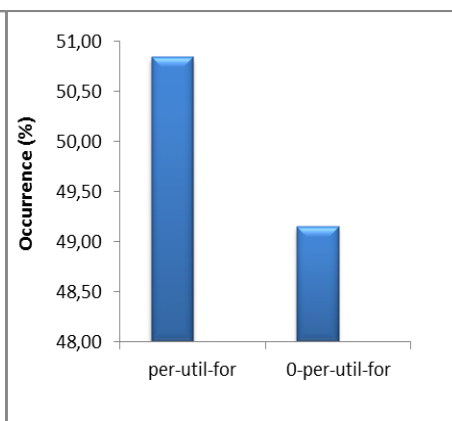
**Graphic 3.** Personal uses of ICTs and pedagogical uses before training



**Graphic 2.** ICT's representations before training

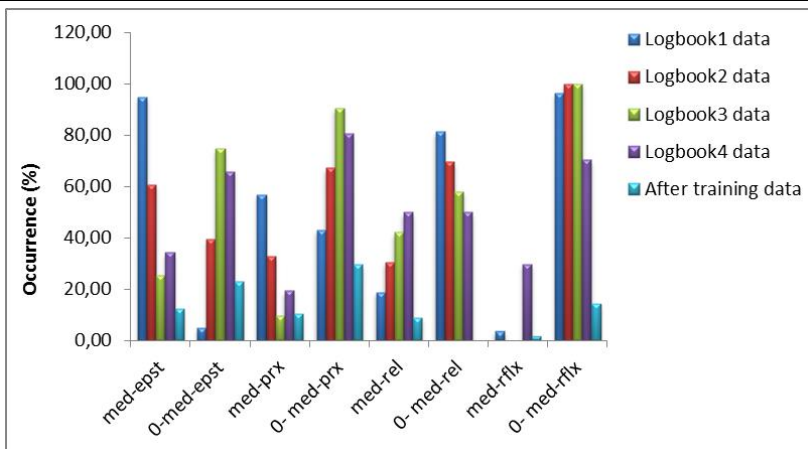


**Graphic 3.** Ease of use perception before training



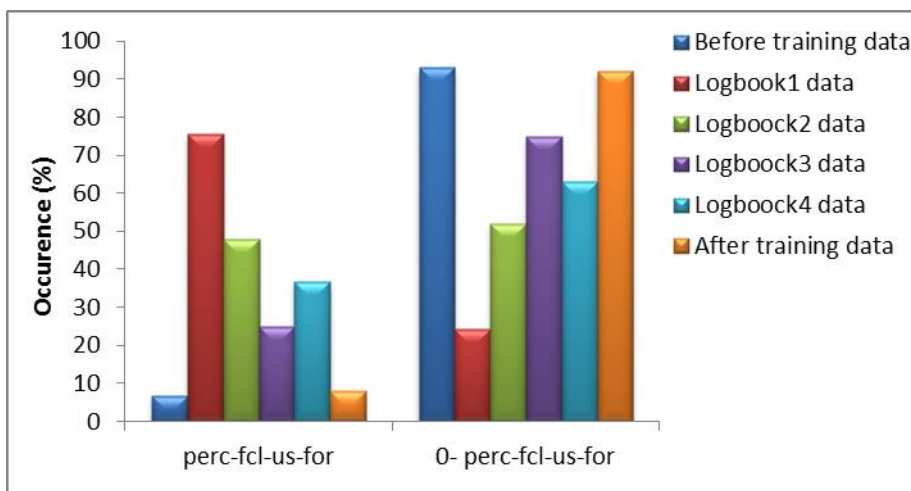
**Graphic 4.** Utility perception of ICTs before training

The four graphics (1, 2, 3 and 4) show the profiles of participants before training. They are characterized by 1) an important personal use of ICT such as email, editing electronic documents (text, slides), information search on internet, 2) a very low pedagogical use of ICTs limited only to slideshow projection in classroom, some videos and some animations for explanation, 3) irrelevant or even false representations of educational use of ICTs, 4) a very low ICTs ease of pedagogical use perception but a significant perception of their usefulness in teaching and learning processes. Graphic 5 shows effects of different mediations mobilized in the training device. We can note that the percentage of occurrences of participant-writings in logbooks that concern positive impact of mediation decreases with time except for the fourth learning unit where it progresses and then relapsed after training.



**Graphic 5.** Effects of mediations mobilized in the training device during and after training

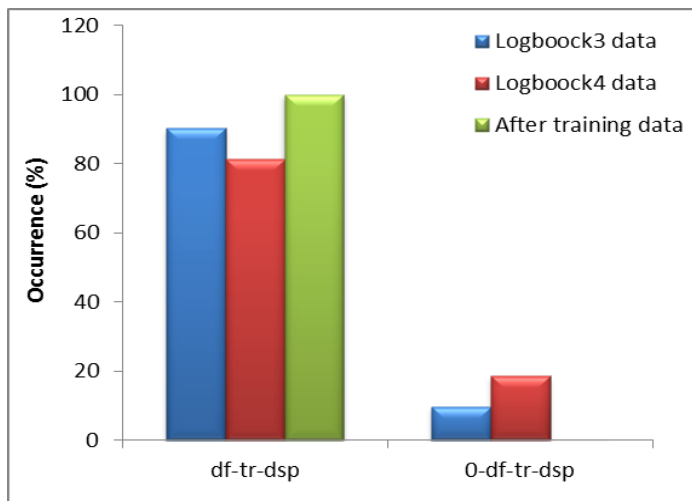
This low impact of the training device mediations on the participant's practices and perceptions is considerably perceived in their answers in the interview after training. It is revealed by an inability's sensation among participants to transfer any knowledge or skills acquired during training to teaching situations. This is confirmed by the whole participants and is approved by their written in logbooks and answers in interview after training concerning "ICTs ease of use perception" as it is shown in graphic 6 and "Difficulties in transferring skills to the subject taught" in graphic 7.



**Graphic 6.** ICTs Ease of use perception before, during and after training

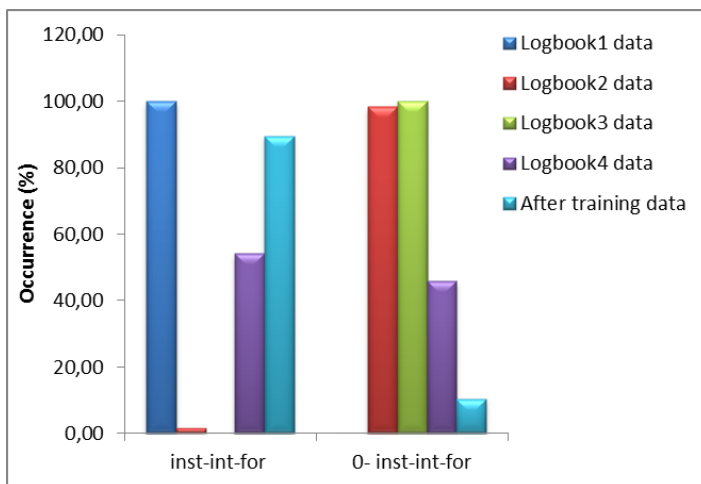
We can see from graphic 6 that before the training a very low percentage of ease of use perception is noted among the majority of participants then a relatively significant percentage of this perception is noted in the first logbook corresponding to the first learning unit (LU) which consists of how to design a conceptual map. The percentage decreases in LU 2 and 3 concerning the design of educational materials with OPALE editor; it increases a little in the fourth logbook corresponding to learn how to design a course in Moodle platform and its implementation on line. In the interview after training, a very low percentage of this perception is noted. The whole of

participants affirm not able to use these tools and in a general way the educational technologies in classroom. They justify this by the lack of material means including the connection to internet among students, insufficient time, but they insist on their inability to transfer what they have learned in training to the specificities of the contents they teach, see graphic 7



**Graphic 7.** Difficulties in transferring skills to the subject taught

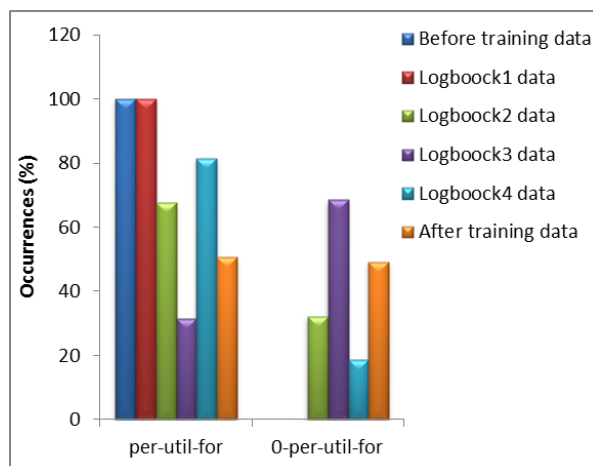
The graphic 8 shows the occurrences of participants writing in logbooks which indicate the constitution of subjective instruments through the training.



**Graphic 8.** Subjective instrument constituted through training

According to our hypothesis, a perception of ICTs ease of use and a perception of their usefulness, resulting of positive mediations effects, must be accompanied by a constitution of subjective instruments by the learner. i.e., the learner appropriates the objects learning as subjective instruments through the processes of instrumentation and instrumentalization according to [11] [13]. In graphic 8, we note the constitution of subjective instruments in the logbooks 1, 4 and in the interview after training. All the participants mentioned an instrument that we believe they have

appropriated which is the forum, and for a few others the conceptual map. We can explain the appropriation of the forum by the fact that it has been used in all learning units as a mean of communication, exchange of ideas and for learning. While the conceptual map, its appropriation could be explained by the sensation of its ease of use which is confirmed in the graphic 6. However, the analysis of their answers in the interview after training shows that this ease of use perception is related only to the technical aspect, i.e. the learning related only to the control of the software used for designing the conceptual map. This can be confirmed by their answers concerning possible future uses of the conceptual maps: they are limited only to the applications seen during the training then we cannot identify any abstraction process in the sense of Piaget.



**Graphic 9.** Utility perception of ICTs before, during and after training

In graphic 9, we note among all participants a high perception of usefulness of ICTs before the training. We can explain this by the fact that these participants had already positive believes about the utility of technologies in teaching and learning. This may be due to their discipline, their personal uses or the effects of socialization, particularly in their professional environment [14].

This positive perception is also noted in writings in logbook 1. The activity consists of designing a conceptual map which should present the module taught by the participant. The application, for educational purposes, seems to be perceived usefulness to all participants. However, we note a decrease in the second and third logbooks, where most of the participants attested to have difficulties in applying the activity to their courses. This is approved by the results shown in graphics 6 and 7 (ease of use perception and difficulties in transferring skills to the subject taught). A significant percentage of a positive perception is also noted after training. We think that it is due to the message conveyed through the training about the importance of using ICTs in teaching and learning and their educational potentials [15].

## 5. CONCLUSION

The study that we carried out allowed us to pursue the evolution of the participants' representations concerning the ICTs and their educational uses, their perceptions of ease of use of these tools and their usefulness in teaching and learning before, during and after training. The study also allowed us to know their actual use of ICTs after a significant duration since completion of the training.

The results obtained show a low perception of ease of use after training and difficulties in transferring the learning objects to the contents taught by participants and not even abstraction processes in the sense of Piaget which means that there was no appropriation of the learning objects by the learners. According to our hypothesis, we refer this non-appropriation to insufficient

mediatization, especially the didactic one. This allows us attesting that content's disciplinary dimension should take an important place in didactic component of the training device in ICT's use.

## REFERENCES

- [1]. T. Karsenti et al., « Intégration des TIC dans la formation des enseignants: le défi du juste équilibre », in Le colloque du Programme pancanadien de recherche en éducation 2002, 2002.
- [2]. Fabry, D.L et Higgs, J.R, « Barriers to the Effective Use of Technology in Education », J. Educ. Comput. Res., vol. 17, no 4, 1997.
- [3]. G. Lefeuve, A. Garcia, et L. Namolovan, « Les indicateurs de développement professionnel », Quest. Vives Rech. En Éducation, no Vol.5 n°11, p. 277-314, janv. 2009.
- [4]. A.Jaillet et C. Depover, « Professionnaliser à distance des enseignants, une utopie moderne ? », Distances Médiations Savoirs Distance Mediat. Knowl., vol. 3, no 12, déc. 2015.
- [5]. Viswanath Venkatesh et Fred D. Davis, « A Theoretical Extension of the Technology Acceptance Model: Four Longitudinal Field Studies », INFORMS, p. 186-204, 2000.
- [6]. F. POYET, « Perception de l'utilité et usages pédagogiques d'environnements numériques de travail par des enseignants du second degré », 2015.
- [7]. M. Crahay, P. Wanlin, É. Issaieva, et I. Laduron, « Fonctions, structuration et évolution des croyances (et connaissances) des enseignants », Rev. Fr. Pédagogie Rech. En Éducation, no 172, p. 85-129, juill. 2010.
- [8]. A.Vause, « L'approche vygotkienne pour aider à comprendre la pensée des enseignants », 2010.
- [9]. Albert Bandura, « Self-efficacy mechanism in human agency », American Psychologist, 37, p. 122-147, 1982.
- [10]. M.R. Lepper, « Microcomputers in education : motivational and social issues », American Psychologist, 40, p. 1-18, 1985.
- [11]. P. Rabardel, Les hommes et les technologies; approche cognitive des instruments contemporains. Université de Paris 8, 1995, 1995.
- [12]. A.Kern, The Use of Key Figures and Its Impact on Activity: The Case of a Hospital. Peter Lang, 2008.
- [13]. E. Duthoit et S. Metz, « Analyse de l'appropriation d'un parcours pédagogique numérique par un formateur: le cas du dispositif Pairform@nce », Pueyo V Zara-Meylan V-Impacts D'outils Gest. Sur Conduite Cult. En, p. 106, 2012.
- [14]. A.Vause, « Le processus de construction de la connaissance ouvragée des enseignants », Cah. Rech. En Éducation Form., vol. 82, p. 1-54, 2010.
- [15]. D. Peraya et al., « Typologie des dispositifs de formation hybrides: configurations et métaphores », p. 10, 2012.

# Saliency Detection with Hybrid Artificial Bee Colony- Firefly Optimization Method

Elif Deniz Yelmenoglu<sup>1\*</sup>, Numan Celebi<sup>2</sup> and Tugrul Taşçı<sup>3</sup>

<sup>1</sup> Isik University, Department of Computer Engineering, Istanbul-TURKEY

<sup>2</sup> Sakarya University, Department of Information Systems Engineering, Sakarya –TURKEY

<sup>3</sup> Sakarya University, Department of Information Systems Engineering, Sakarya -TURKEY

\*deniz.yigitbasi@isikun.edu.tr

## ABSTRACT

Implementation of optimization algorithms in image processing is a quite common area of research. Detecting salient fields in images can be used for problems such as object recognition, image segmentation or video tracking problems. This case makes the determination of saliency an important factor in image processing. The algorithms developed for salient region detection are divided into two approaches as bottom-up and top-down. The bottom-up techniques determine salient regions according to the data, and the top-down techniques discover these regions by the learning of visual information of a certain object. This paper presents an optimization technique for bottom-up saliency detection algorithm based on Hybrid Artificial Bee Colony- Firefly algorithm.

**KEYWORDS** - Saliency detection, Artificial bee colony algorithm, Firefly algorithm.

## 1. INTRODUCTION

Visual saliency has increasingly become very popular topic in the field of computer vision. Detection of salient regions is so important for objects or events in the images can be estimated with the information obtained. The evolved applications of human visual system (HVS) for detecting salient regions can be represented in two main categories [1]: namely top-down and bottom-up. Top-down methods need to use pre-specified information to analyze and process saliency information. Bottom-up methods detect saliency using basic image characteristics such as colour, edge, texture, brightness, etc. In this paper, hybrid ABC-FA optimization by combining Artificial Bee Colony (ABC) Algorithm (Karaboga, 2005) and Firefly Algorithm (FA) (Yang, 2009) will be applied for the determination of the salient regions in the images. Our proposed approach could be classified in Bottom-up region detection methods.

The paper is organized as follows. The basic concepts of Artificial Bee Colony algorithm and Firefly optimization algorithm are defined in Section 2. In Section 3, proposed hybrid approach by combining Artificial Bee Colony (ABC) Algorithm and Firefly Algorithm (FA) is described in detail. Experimental results about detecting saliency are presented in Section 4. Finally, conclusions are presented in Section 5.

## 2. MATERIALS AND METHODS

Optimization is the process of finding the maximum or minimum intended target. In some cases, the search space can be very large, and testing all solutions may require more time than is acceptable. Heuristic optimization algorithms are based on intelligent predictions which lead to the discovery of new solutions. In this work, an optimization technique for bottom-up saliency detection algorithm based on Hybrid Artificial Bee Colony- Firefly algorithm.

### 2.1. Artificial Bee Colony Optimization Algorithm

Artificial Bee Colony (ABC) algorithm was developed by Karaboga (2005) is an optimization algorithm which is modelling the behaviour of foraging bees. In ABC algorithm, an artificial bee colony contains three type of bee. These are employed, onlooker and scout bees. Algorithm has



three control parameters which are the number of food sources (SN), the maximum cycle number and the value of limit.

## 2.2. Firefly Optimization Algorithm

Yang developed Firefly optimization algorithm (FA) (Yang, 2009) which is inspired by the brightness and movement directions of fireflies. Firefly algorithm is applied based on three principles. First, fireflies are considered as unisex and can affect each other without discrimination. Second, the attractiveness of fireflies is proportional to their brightness and the brightest fireflies attract them to the less bright ones. Last principle is that brightness is determined by the value which produces from the functions to be optimized.

## 2.3. Proposed Hybrid ABC-FA Saliency Detection Approach

In this hybrid method, individuals in the population can behave like bees and fireflies. The probabilities of solutions are evaluated according to their fitness values which are calculated by the concept of brightness in the FA algorithm and the search for a better quality resource in the ABC algorithm. In the pre-processing stage, we apply segmentation algorithm to the input image by using ABC-FA optimization technique. Then this technique is also used for generate a saliency map. The steps composing the algorithm are detailed in the following sections.

### 2.3.1. Pre-Processing

In our approach we used ABC-FA optimization technique for a multilevel thresholding step. Before saliency detection, each image must be segmented for the less complexity. Because pixel based identifying can be more difficult. Thus, pixel groups are generated by segmentation process according to their colour and location information. First, we split a colour input image into its three RGB channels. Multilevel thresholding is realized on each one by ABC- FA optimization technique. In this part, three optimal threshold values are found. Than segmentation step generated using these optimal values.

### 2.3.2. Detection of Salient Regions

In this paper, we focus on the bottom-up saliency detection approach based on background information. The border regions of the image have been proved to be good visual cues for background priors in saliency detection [2].

Proposed method can find proposed salient images according to their optimal background value. The framework of saliency detection on images is shown in Figure 1. Fitness values are calculated with the standard deviation of related image. This method is applied on each three segmented images. Than we combine their salient images to achieve final salient image. In FA part of algorithm, probabilities of each source are taken as brightness for adapting FA algorithm. Comparison of the brightness and flying to more bright ones in  $r$  distance takes place at this stage. Checking that whether the failure count values exceed the limit value are handled in ABC part. In ABC-FA, colony size which is defined by  $K$  and varies with  $N$  rows and  $M$  columns of image is equal with the total number of sources. Employed bee number is equal to located source number.

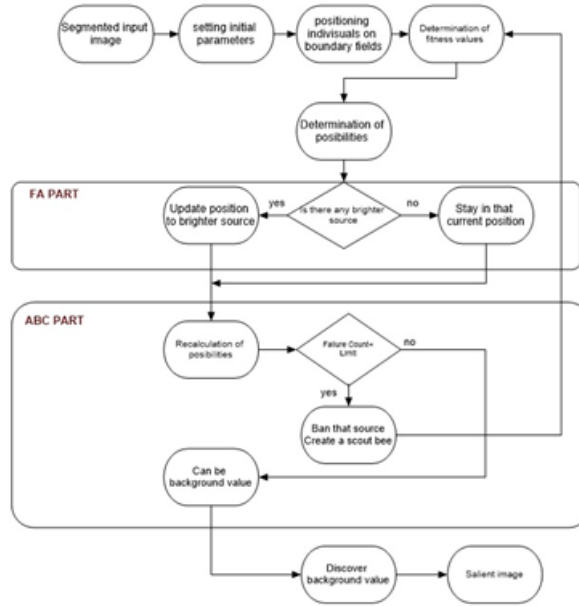


**Figure 1.** Detection of salient regions with ABC-FA technique

### 3. EXPERIMENTAL RESULTS

All the experiments are implemented using MATLAB on Intel i5-8250U CPU (1.8 GHz) workstation having 8GB of RAM. We evaluate the presented algorithm on one of the public datasets: MSRA-1000. The MSRA-1000 dataset [3] contains 1000 images with pixel-wise labelled ground-truth for salient objects. Our method ABCFA is compared against the six methods of IT [4], MZ [5], GB [6], SR [7], IG [3] and AC [8] on 5 images of this dataset as shown in Figure 2.

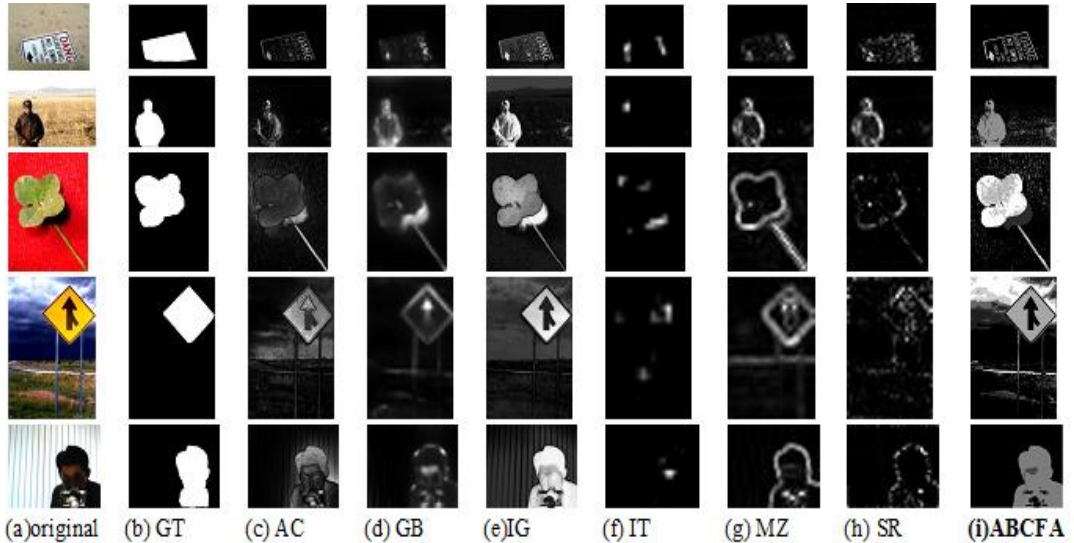


**Figure 2.** Visual comparison of saliency maps. (a) original image, (b) Ground truth images, (c) saliency maps using the method AC, (d) GB, (e) IG, (f) IT (g) MZ, (h) SR and (i) our method

All methods' results are shown in ROC curve as in Figure 3:

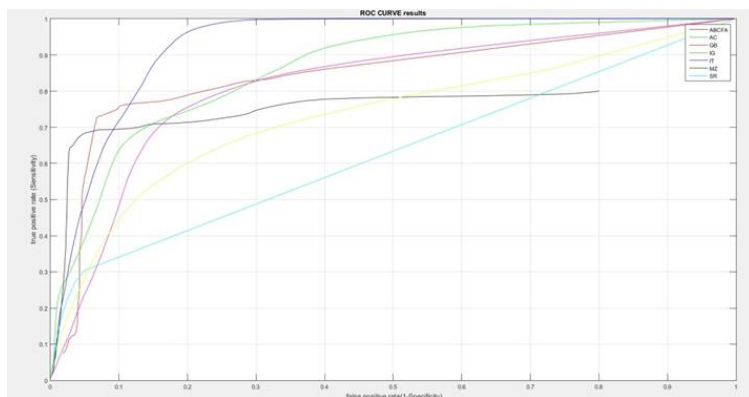


**Figure 3.** ROC curves for AC, GB, IG, IT, MZ, SR and ABCFA.

#### 4. CONCLUSION

This paper presents a saliency detection with hybrid ABC-FA optimization algorithm by combining artificial bee colony (ABC) and firefly (FA) optimization algorithms. We focus on the bottom-up saliency detection approach based on background information. We also performed six state-of-the-art algorithms and compared these results' with our results. Our experiments showed that hybrid ABC-FA algorithm can be use as an alternative method to determine saliency maps.

#### REFERENCES

- [1]. Wei Zhang, QM Jonathan Wu, Guanghui Wang, Haibing Yin, An adaptive computational model for salient object detection, *IEEE Trans. Multimed.* 12 (4) (2010) 300–316
- [2]. Z. Wang, G. Xu, Zhenseng Wang, C. Zhu, “Saliency detection integrating both background and foreground information”, *Neurocomputing*, Vol.216, pp. 468-477, 2016.
- [3]. R. Achanta, S. Hemami, F. Estrada, and S. Susstrunk, “Frequency-tuned salient region detection,” in *Proceedings of the IEEE Conference on Computer Vision and Pattern Recognition (CVPR '09)*, pp. 1597–1604, Miami, Fla, USA, June 2009.
- [4]. L. Itti, C. Koch, and E. Niebur. A model of saliency-based visual attention for rapid scene analysis. *IEEE Transactions on Pattern Analysis and Machine Intelligence*, 20(11):1254–1259, 1998.
- [5]. Y.-F. Ma and H.-J. Zhang. Contrast-based image attention analysis by using fuzzy growing. In *ACM International Conference on Multimedia*, 2003.
- [6]. J. Harel, C. Koch, and P. Perona. Graph-based visual saliency. *Advances in Neural Information Processing Systems*, 19:545–552, 2007.
- [7]. X. Hou and L. Zhang. Saliency detection: A spectral residual approach. *IEEE Conference on Computer Vision and Pattern Recognition*, 2007.
- [8]. R. Achanta, F. Estrada, P. Wils, and S. Susstrunk. Salient region detection and segmentation. *International Conference on Computer Vision Systems*, 2008.
- [9]. A.Aksac, T. Ozyer, R. Alhaji, “Complex networks driven salient object detection based on superpixel segmentation”, *Pattern Recognition*, Vol. 66, pp. 268-279, 2017.
- [10]. N. Pal and S. Pal, “A review on image segmentation techniques,” *Pattern Recognit.*, vol. 26, no. 9, pp. 1277–1294, Sep. 1993.

- [11]. T. Sag and M. Cunkas, "Color image segmentation based on multiobjective artificial bee colony optimization," *Applied Soft Computing.*, vol. 34, pp. 389–401, 2015.
- [12]. Karaboga, D., "An idea based on honey bee swarm for numerical optimization," Tech. Rep. TR06, Erciyes University, Kayseri, Turkey, 2005.
- [13]. E. D. Yelmenoglu, N. Celebi, T. Tasci, "A novel kybrid edge detection technique: ABC-FA", *The Eurasia Proceedings of Science, Technology, Engineering & Mathematics (EPSTEM)*, Volume 1, Pages 193-200, 2017.
- [14]. C.Çiğla and A. A. Alatan, "Efficient super pixel extraction for image segmentation," 2012 20th Signal Processing and Communications Applications Conference (SIU), Mugla, 2012, pp. 1-4.
- [15]. Yang, X.S., Firefly algorithms for multimodal optimization. In: *Proceedings of the 5th International Conference on Stochastic Algorithms Foundations and Applications* vol. 5792 . LNCS Springer : 169 – 178, 2009 .

---

## Cutting Fluids in Machining and Environmental Issues -A Review

**Murat Kiyak<sup>\*</sup>, Orhan Cakır and Ibrahim Sahin**

*Yildiz Technical University/Department of Mechanical Engineering, Istanbul, Turkey*

*\*kiyak@yildiz.edu.tr*

### ABSTRACT

In the last decades the suitability of using cutting fluid to cooling and lubricate machining processes have been heavily discussed. The use of cutting fluid generally causes economy of tools and it becomes easier to keep tight tolerances and to maintain workpiece surface properties without damages. There are various advantages of cutting fluid application as increasing tool life, decreasing machining times and improving surface quality. However, there are some disadvantages of cutting fluid as high costs relating storages, preparation, filtration and recycling, pollution harmful to environment. In the other hand, it brings also some problems, like fluid residuals and human diseases. Because of environmental and health problems, some alternatives have been sought to minimize of cutting fluid in machining operations. Various methods such as spray application, MQL, dry machining and internally cooled cutting tool have been offered in machining processes. However, there are also necessary machining operations where cutting fluid must be used, such as gear making, broaching and honing. Therefore, the application methods of modern cutting fluids and what are new in this area will unavoidably are considered. The results of investigations on the development and use of methods of applying cutting fluids were given in this paper. Moreover environmental issues have been discussed in detail.

**KEYWORDS** - *Cutting Fluid, Machining, Environmental and Health.*

### 1. INTRODUCTION

Machining is a material removal process, in which a sharp cutting tool is generally used to mechanically cut material to produce a desired geometrical part. This manufacturing process provides important advantages in a short time and economically such geometric dimensioning, tolerance and surface quality. In machining, heat is generated at the cutting tool-workpiece interface causing shorter tool life, worst surface roughness and reducing the dimensional accuracy of the workpiece. Thermal damage temperature at the tool-workpiece interface varies depending on the material being processed. In materials that are easy to process this heat is low, while in difficult to process materials [1]. Heat is generated during machining operations as known. Thermal damage and wear on the cutting tool continuously increases and this leads to shorter tool life. Moreover, the wear on cutting tool causes to poor surface quality on workpiece. The rate of tool wear strongly depends on the cutting temperature; therefore, any measures which could be applied to reduce the cutting temperature would reduce the tool wear as well. Fig. 1 shows the parameters that influence the rate of tool wear [2]. The energy dissipated in cutting operations is largely converted into heat, raising the temperature of chip, tool, and workpiece. The cutting fluid, if used, is an excellent heat sink. There are three sources (Fig. 2) for heat development those are plastic deformation of material at primary zone, deformation of chip at secondary zone and friction between cutting tool-chip and cutting tool-workpiece at tertiary zone. [3]. Cutting fluids are employed to minimize influence of heat on cutting tool. There are various advantages of cutting fluids as increasing tool life and improving workpiece surface quality. Besides of these there are some disadvantages as follows, pollution harmful to environment and health problems. Nowadays, many approaches are presented to solve the problems of cutting fluid in cutting process. Various methods such as MQL or internally cooled cutting tools have been offered as alternative methods in machining operations.

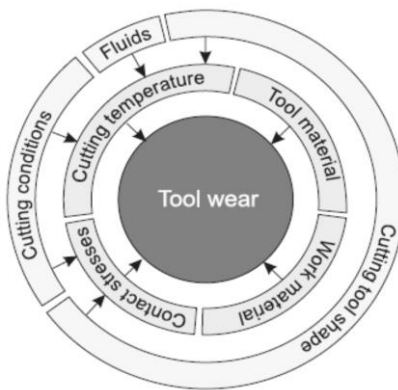


**Figure 1.** Cutting Tool Wear as a Function of Basic Process Parameters

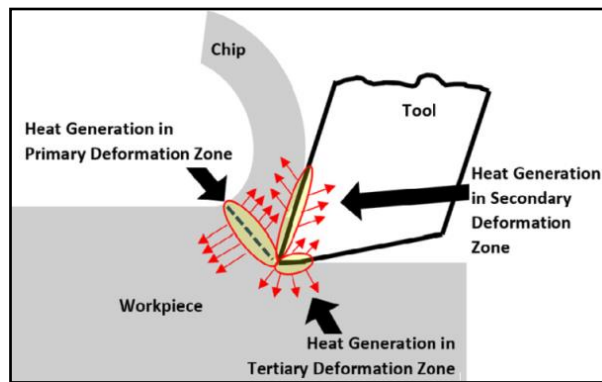


**Figure 2.** Heat Generation in Primary, Secondary and Tertiary Deformation Zones in Orthogonal Machining

## 2. CUTTING FLUIDS

Cutting fluids have been using in machining operations to lubricate the chip-tool and tool-workpiece interfaces, remove heat from the workpiece and cutting zone, flush away chips from the cutting area, and inhibit corrosion [4]. The global lubricant demand was 39.4 million tons in 2015. Cutting fluids represent about 5% of the global lubricant market. Approximately, 85% of the cutting fluids used are mineral based. However, the estimated values deviate significantly because of the processes diversity [5].

## 3. TYPES OF CUTTING FLUID

The modern lubricants are most often the products of the petroleum chemistry. By the physical state, lubricants can be divided into liquids, solids, gaseous and also plastics. Among these, liquid lubricants are the most widely used. Liquid lubricants can be classified based on their origins [6, 7]. Straight oil is made up from entirely mineral oil or vegetable oils and is used primarily for operations where lubrication is required. Although being excellent lubricating oil, their heat transfer capabilities exhibit very low. Mineral oil, which is highly flammable, has low efficiency at high cutting speed and relatively high cost. Soluble oil is a mixture of oil and water and has increased cooling capacity than straight oil and provided rust protection. This type water-based cutting fluids is suitable for turning, milling and grinding process. In addition, water-based cutting

fluids reduce the effect of heat generated by tool wear. Semi-synthetics contains inorganic material or other water-soluble compounds. Adding emulsified oil in synthetic cutting fluid results in semi-synthetic fluids that have properties combined. It is also better than soluble oil, but tarnishes easily when exposed to other machine fluids and can cause dermatitis risk to workers. Synthetic oils are a chemical liquid containing inorganic or other chemical that are soluble in large quantity of water and offer superior cooling performance. Synthetic lubricants were not initially favoured due to their high cost of production. However, as time passes synthetic oils have gained more attention and applications. Synthetic oils can be used for more specific and high performances applications such as operating at extreme temperatures. Synthetic oils include synthetic hydrocarbons such as polyalkylene glycol, various esters and polyalphaolefins. The cutting fluids properties are given in Table 1. Regarding towards to green manufacturing, biodegradable lubricant plays important role.

**Table 1. Cutting fluids properties**

	<b>Straight oils</b>	<b>Emulsions</b>	<b>Semi-synthetic</b>	<b>Synthetic</b>
	Oily	Milky	Translucent	Transparent
Lubricity	Excellent	Good	Good	Poor
Cooling	Poor	Good	Good	Good/ Excellent
Chip removal	Moderate	Moderate	Moderate	Moderate
Corrosion control	Excellent	Poor	Good	Good
Microbial control	Excellent	Poor	Good	Excellent
Fire	Hazard	Non-flammable	Non-flammable	Non-flammable
Other disadvantages	Limited to low-speed operation create mist	Evaporation losses foam tendencies	Hard water influence foam tendencies	Easily contaminated by other processing fluids

Cutting fluids are widely used in machining processes. The advantages and disadvantages of cutting fluids are given in Table 2. The main cutting fluid roles are cooling, reducing friction, removing metal particles, and protecting the workpiece, the tool and the machine tool from corrosion. However, the use of cutting fluids has also associated some disadvantages such as their cost, environmental impact and health hazards to workers. In machining processes, sustainable manufacturing can be addressed for example, by reducing consume of electric energy, improving the tool life and the surface quality of the workpiece. The main alternatives include dry machining, minimum quantity lubrication (MQL), cryogenic cooling, gaseous cooling and nano-fluids [5].

**Table 2. Cutting fluids advantages and disadvantages in machining operations**

<b>Advantages</b>	<b>Disadvantages</b>
Increase tool life	Costs due to purchase, storage, maintenance, waste disposal
Lower cutting forces and power required	Damages on workpiece and machine tool
Higher cutting speeds and feeds rates	Environmental impact
Reduce post-process heat treatments	Worker health hazards
Better workpiece quality	

Cutting fluids reduce the heat, wash away the chips, and protect the machined surface from oxidation. It is a coolant as well as a lubricant. The mechanism of cutting fluid action involves capillary action in which case the fluid should have small molecules and proper wetting of the surface. The cutting fluids are applied in flood or in mist conditions. Flood cooling is applied on gear making, broaching, honing and drilling in generally. Mist cooling is applied in grinding and

turning. Selection of the cutting fluid depends on the workpiece, on the machine tool and on the operator safety [9].

However conventional cutting fluids are growing public health concern worldwide and following this issues, in 2008, Aggarwal et al. [10] have written the following limitations towards conventional cutting fluids:

- Environmental pollution due to chemical dissolution of cutting fluid.
- Biological problems as skin problems and respiratory problems when come in physical contact with the cutting fluid.
- Contamination of water and soil pollution during disposal.
- The need for additional floor space and additional system for pumping, storage, refining, recycling, cooling, etc.
- Increase of the cost of disposal of cutting fluids.

During the machining operations, heat is generated due to plastic deformation of the workpiece and friction. This heat causes the mechanical resistance and abrasion resistance of the cutting tool to fall. Wear and thermal damage can increase during high temperatures, resulting in reduced tool life. In addition, when the wear is increased, the surface quality is reduced. Cutting fluid is used in the conventional way to reduce cutting temperature. The cutting fluid reduces the shear force effect and increases tool life. In addition, the cutting fluid makes it easier to remove the chip from the cutting area.

Problems arising from the use of cutting fluids in the machining process mentioned below [11]:

- storage of fresh cutting fluids
- application in the machining operation
- storage of used cutting fluids
- filtration
- recycling
- water and soil pollution
- gases / fumes generated during the usage

Today, due to increased environmental protection policies and implementing sustainable machining operations, the use of cutting fluids is subject to certain regulations.

Because of the advantages obtained by the use of cutting fluids during machining, different applications have emerged to reduce problems arising from their use. Nowadays, there are different approaches such as the use of minimum quantity lubrication (MQL), solid lubricants and, if possible, dry machining. There is another solution to overcome problems is to employ “internal cooling cutting tools” in machining operations.

#### 4. COOLING TECHNIQUES

Flood (wet) cooling is a technique in which cooling jet aimed at the active zone for cooling, lubricating and get rid of chips produced during machining. This method is suitable for the cutting processes in which excess heat energy is produced. Dry cutting is a process without the use of any cutting fluid during machining. Small quantities of cutting fluid are injected with an air pressure in the form of fine droplets at high velocity (MQL) into the cutting zone. The application types of cutting fluids are given in Fig. 3. Cryogenic cooling is the use of gases in minus temperatures. Liquid nitrogen and carbon dioxide are widely used in cryogenic cooling. Coolant jets are used with very high pressures (High pressure cooling-HPC) which around 100–1000 bar in this system.



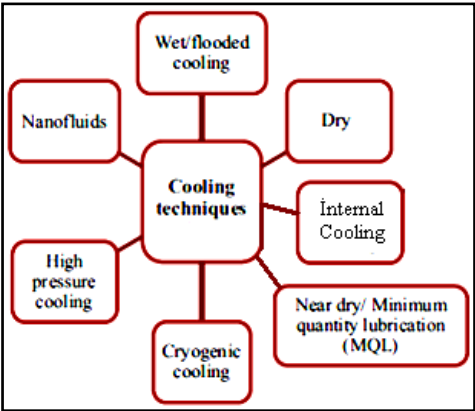


Figure 3. Cooling Techniques

The coolant jet is directed at very high pressure exactly on the rake face of the cutting tool. Nano-fluids are defined as colloidal suspensions of nano-particles in a base fluid and these suspended metallic or nonmetallic nano-particles change the transport properties and heat transfer characteristics of the base fluid. Internal cooling cutting tools (Fig.4) are performed as selected cutting fluid is served through inside of cutting tool by pressurized form into cutting zone in machining operation [11]. This application has been employed since 1940’s and reported results have shown promising advantages. One of the early studies was patented by Taylor in 1947 [7]. This is indeed an indication that work is being carried out even 70 years ago today on environmentally sensitive and harmless manufacturing, which is defined as "sustainable machining" or "green machining".

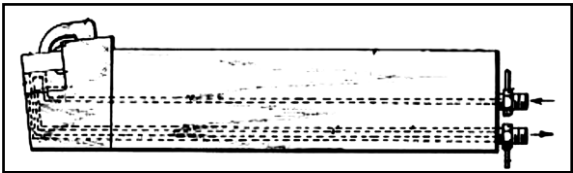


Figure 4. View of the Cooling Fluid Conduit Machined into the Cutting Tool Holder

Table 3. presents qualitative estimation of the environmental impact of various lubricant/cooling systems used in the machining taking into account [5]. As can be noted that, the application of cutting fluids in machining is questionable.

Table 3. Qualitative Estimation of Cooling Environmental Impact

	Residue	Dangerous substances	Mist and emissions	Workers health hazards
Cutting fluid	*****	****	*****	*****
MQL	**	**	***	***
Nanofluids	****	Unknown	****	Unknown
Cryogenic cooling	*	*	**	*
Internal cooling	*	*	*	*
Gaseous cooling	*	*	*	*
Dry Machining (ref)	*	*	*	*

(\*) Very low, (\*\*) Low, (\*\*\*) Medium, (\*\*\*\*) High, (\*\*\*\*\* ) Very high

The purposes of cutting fluid in machining operations are to cool the workpiece and tool, reduce friction and take away the chips. The cutting fluid contributes significantly toward machining cost and also possesses environmental threats. Another environmental impact of the metal cutting sector can be assessed with respect to the fresh water utilization. Although 70% of the earth is filled with water but only 3% of it is usable fresh water [12]. As reported in another reflection that in U.S. more than 20% of total fresh water was utilized by the industrial sector [13]. Several researchers have conducted studies to expose the water footprint involved in the metal cutting operation [14]. A cost based comparison for different cooling and lubrication strategies was reported [15].

There are some attempts to minimize the amount of cutting fluid in machining. The cost effect of different cutting fluids is given in Table 4. The tangible cost factors to be considered include: initial cost per litre, mix cost, production rates, tool life, overheads, part cleaning costs, machining cost per piece, cutting fluid life, scrap caused by rusting, rework costs due to rust, cost of fluid disposal. The intangible cost factors include: cleanliness of machines and the workshop, operator satisfaction and hygiene, smoke problems, work accuracy, ease of handling and viewing parts, adaptability to different jobs, safety, fire hazard, and disposability.

**Table 4. Qualitative Estimation of Cooling System Costs.**

	<b>Fluid consumption</b>	<b>Equipment cost</b>	<b>Cleaning cost</b>	<b>Disposal cost</b>
Cutting fluid	*****	****	*****	*****
Nanofluids	****	****	****	*****
Gaseous cooling	***	****	****	***
Cryogenic cooling	***	*****	*	*
MQL	**	***	**	**
<b>Dry machining (ref.)</b>	*	*	*	*

(\*) Very low, (\*\*) Low, (\*\*\*) Medium, (\*\*\*\*) High, (\*\*\*\*\* Very high

Dry machining refers to the cutting operation without cutting fluid. It is appeared to be the most sustainable option to replace cutting fluids in machining. Dry machining approach also strengthens the sustainability concepts by reducing the machining cost and health hazards also portrayed dry machining as eco-friendly machining approach. The main issue with dry machining is related to high amount of heat generation in the cutting zone [16, 17].

Another study was conducted for the drilling of cast iron using dry, flood (emulsion), minimum quantity lubrication (MQL) and cryogenic cooling/lubrication approaches. Fig. 5 represents the energy consumption, tool cost and total cost with respect to the material removal rate (MRR) for the drilling process for all the mentioned cooling strategies. Dry machining is easy and cost-effective. However, cryogenic and nanofluid applications are difficult and expensive. In the machining process, the application of different cooling systems causes different costs. The cost of the cutting fluid can be up to 14% while the tooling cost is about 4% [19, 20].

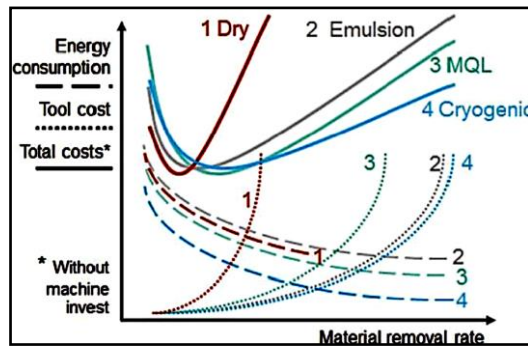


**Figure 5.** Behaviour of Energy Consumption, Tool Cost and Total Cost of Different Cooling Strategies with Respect to Material Removal Rate for Drilling Process

## 5. RESULTS AND CONCLUSIONS

Cutting fluids play an important role on machining operations. However, they use have some drawbacks such as their negative effects over the environment and workers health as by costs associated such as the equipment, fluids purchase and waste fluid treatment. Conventionally, mineral oils were used as cutting fluids. However, the mineral oils cooling capacity is limited and therefore soluble oils were seen as a good alternative. Nevertheless, soluble oils contain water which is susceptible to bacterial attack. Synthetic lubricants are superior in many regards, but cost is higher. The alternative techniques such as MQL, cryogenic, gaseous cooling and nano-fluids have been implementing in some machining processes, even may become more efficient than conventional cooling. Various researchers have carried out studies to reveal the water footprint in the metal cutting process. 70% of the earth filled with water, but only 3% of it is fresh water.

The best environmental alternative is dry machining since completely removes the cutting fluid and ensures a clean atmosphere and workers safety, though it has many application limitations. Another environmental impact of the metal cutting sector can be evaluated in terms of fresh water use. Dry machining is the most sustainable option to replace cutting fluids during processing. Dry machining also strengthens the concepts of sustainability by reducing processing costs and health hazards, and demonstrates dry processing as an environmentally friendly processing approach. However, there are still applications where cutting fluids cannot be ignored in some machining operations like gear making, broaching as well as cutting of difficult-to machine materials.

## REFERENCES

- [1]. Da Silva, M.D., Walbank, J., Lubrication and application method in machining, *Lubrication and Tribology*, 50 (1998), 149-152 DOI: 10.1108/00368799810225082
- [2]. [http://me.emu.edu.tr/me364/ME364\\_cutting\\_wear.pdf](http://me.emu.edu.tr/me364/ME364_cutting_wear.pdf)
- [3]. Pervaiz S., KannanS., Kishawy H.A., An extensive review of the water consumption and cutting fluid based sustainability concerns in the metal cutting sector, *Journal of Cleaner Production*, 197 (2018) 134-153. DOI: 10.1016/j.jclepro.2018.06.190
- [4]. Adler D. P., Hii W.W.S, Michalek D.J., Sutherland J.W., Examining the role of cutting fluids in machining and efforts to address associated environmental/health concerns, *Machining Science and Technology*, 10:1 (2006) 23-58. DOI: 10.1080/10910340500534282
- [5]. Benedicto E., Carou D., Rubio E.M., Technical, Economic and environmental review of the lubrication/cooling systems used in machining processes, *Procedia Engineering* 184 (2017) 99-116. DOI: 10.1016/j.proeng.2017.04.075

- [6]. Osama M., Singh A., Walvekar R., Khalid M., Gupta T.C.S.M., Yin W.W., Recent developments and performance review of metal working fluids, *Tribology International* 114 (2017) 389–401. DOI: 10.1016/j.triboint.2017.04.050
- [7]. Liew P.J., Shaaroni A., Sidik N.A.C., Yan J., An overview of current status of cutting fluids and cooling techniques of turning hard steel, *International Journal of Heat and Mass Transfer* 114 (2017) 380–394. DOI: 10.1016/j.ijheatmasstransfer.2017.06.077
- [8]. Wank Z., The correlation between the penetration force of cutting fluid and machining stability, A Thesis of the Degree of Master of Science, Worcester Polytechnic Institute, May 2010.
- [9]. <http://www.public.iastate.edu/~mebbs/courses/ME322/Machining.html>
- [10]. Aggarwal A., Singh H., Kumar P., Singh M., Optimization of multiple quality characteristics for cnc turning under cryogenic cutting environment using desirability function, *Journal of Materials Processing Technology*, 205 (2008) 42–50. DOI: :10.1016/j.jmatprotec.2007.11.105
- [11]. Murat Kıyak, İbrahim Şahin, Orhan Çakır, Internal cooling cutting tool technology in turning operations, *International Conference on Energy and Thermal Engineering*, 25-28 April 2017, Istanbul ISBN 978-605-9546-04-1.
- [12]. Schneider, S.H., Root, T.L., Mastrandrea, M., Water resources. In: *Encyclopedia of Climate and Weather*, Vol. 2. Oxford University Press, New York, 2011.
- [13]. Zhao, F., Ogaldez, J., Sutherland, J.W., Quantifying the water inventory of machining processes, *CIRP Annals - Manufacturing Technology* 61 (2012) 67-70. DOI: 10.1016/j.cirp.2012.03.027
- [14]. Dahmus, J.B., Gutowski, T.G., An environmental analysis of machining, In: *ASME - International Mechanical Engineering Congress and RD&D Expo*, 2004, 1-10.
- [15]. Lopez de Lacalle, L.N., Angulo C., Lamikiz S. J., Experimental and numerical investigation of the effect of spray cutting fluids in high speed milling, *Journal of Materials Processing. Technology* 172 (2006) 11-15. DOI: 10.1016/j.jmatprotec.2005.08.014
- [16]. Klocke, F., Eisenblatter, G., Dry cutting, *CIRP Annals - Manufacturing Technology* 46/2 (1997) 519-526.
- [17]. Weinert, K., Inasaki, I., Sutherland, J.W., Wakabayashi, T., Dry machining and minimum quantity lubrication, *CIRP Annals - Manufacturing Technology* 53 (2004) 511-537.
- [18]. Neugebauer, R., Drossel, W., Wertheim, R., Hochmuth, C., Dix, M., Resource and energy efficiency in machining using high-performance and hybrid processes, *Procedia CIRP* 1 (2012) 3-16. DOI: 10.1016/j.procir.2012.04.002
- [19]. [http://www.zet-chemie.de/wp-content/uploads/2016/04/1\\_Info\\_Kuehlschmierstoffe\\_in\\_der\\_Metallbearbeitung\\_englisch.pdf](http://www.zet-chemie.de/wp-content/uploads/2016/04/1_Info_Kuehlschmierstoffe_in_der_Metallbearbeitung_englisch.pdf)
- [20]. Astakhov V.P., *Ecological Machining: Near-Dry Machining*, In: Davim JP (ed) *Machining: Fundamentals and Recent Advances*, Springer, London, 2008.

## Experimental and theoretical investigation on proppant embedment of hydraulic fracturing in shales

Ming Chen<sup>1\*</sup>, Shicheng Zhang<sup>1</sup>, Yun Xu<sup>2</sup>, Xinfang Ma<sup>1</sup>, Yushi Zou<sup>1</sup>

<sup>1</sup> State Key Laboratory of Petroleum Resources and Engineering, China University of Petroleum, Beijing, CHINA

<sup>2</sup> Institute of Petroleum Exploration and Development, PetroChina, Beijing, CHINA

\*xmcm0122@126.com

### ABSTRACT

Proppant embedment in hydraulic fracturing is essential to determine hydraulic fracture conductivity and production performance. In this study, a modified uniaxial compression test was established to measure proppant embedment. The contact mechanic model considers the entire deformation regions of proppant embedment into rock fracture surfaces, including elastic, elastoplastic, and plastic deformation. The model was solved by Newton-Raphson method. Sensitivity analysis was conducted based on the new method and the results show that proppant embedment into rocks mainly occurs in the elastoplastic embedment regime. The higher the proppant concentration, the smaller the embedment depth under the monolayer distribution. Under multilayer distribution conditions, increasing the proppant concentration will not change the contact stress and the embedment depth because the proppants coming in contact with the rock have reached the tightest arrangement. The proppant embedment depth increases with the drawdown of fluid pressure in hydraulic fractures during production periods.

**KEYWORDS** – *proppant embedment, uniaxial compression test, contact mechanic.*

### 1. INTRODUCTION

Multistage and multicluster fracturing is a primary technologies for the development of unconventional reservoirs, such as shales, tight sandstones, and coalbeds. During this process, because of the high closure stress exerted on low-concentration proppants, proppants can embed into rock fracture surfaces, especially for soft shales, coals, and unconsolidated rocks [1], which impairs the conductivity of hydraulic fractures. Therefore, predicting the behavior of proppant embedment is of great significance for the design and production evaluation of hydraulic fracturing.

The study on proppant embedment includes experimental investigation, numerical simulation, and theoretical model study. Various experimental studies have been conducted to investigate the mechanisms of proppant embedment. Lacy et al. [2] conducted laboratory studies on weakly consolidated cores and found that proppant embedment was more important when the Young's modulus of the formation rocks was approximately <13 GPa. Alramahi et al. [3] observed that high embedment was associated with high clay contents or low static Young's modulus. Simulation investigation is another important approach to study the behavior of proppant embedment. Cui et al. [4] studied the indentation of proppant into hydraulic fractures using the finite element method. They found that proppant embedment mainly resulted from plastic deformation of the surface of rock fractures.

In this study, we established a modified uniaxial compression test to measure proppant embedment during increasing closure stress. Then, a new theoretical model was proposed to predict proppant embedment. The new model considers the elastic, elastoplastic, and plastic deformation of rock fracture surfaces, thus eliminating the limitation of the elastic model. Moreover, the solution of the embedment depth and the proppant embedment period was obtained by a trial method because the rock deformation contained three regions.

### 2. EXPERIMENTAL STUDY

## 2.1. Experimental setup

A modified uniaxial compression test method is established to measure proppant embedment depth under increasing loads. A standard core ( $\phi 2.54 \times 5$  cm) is cut off from the middle cross section, then a pair of cores is prepared for the test. Proppants of a specific size are evenly laid on the surface of the cut section. A plastic nose with a ring bound is designed to make the loading process on rock samples stable. Figure 1 depicts a photo of the proppant test setup.

The total recorded deformation includes the deformation of the shale sample and proppant embedment depth. Shale deformation was calculated by using Young's modulus and the applied load. Figure 1a shows typical experimental data.

## 2.2. Experiment results and analysis

Typical results of proppant embedment tests are illustrated in Figure 1b. The results show that proppant embedment depth increases with closure stress applied on the rock sample. When the closure stress is less than 10 MPa, the embedment depth increases rapidly with the increase of closure stress. However, the embedment depth increases nearly linearly with closure stress when the closure stress is over 10 MPa.

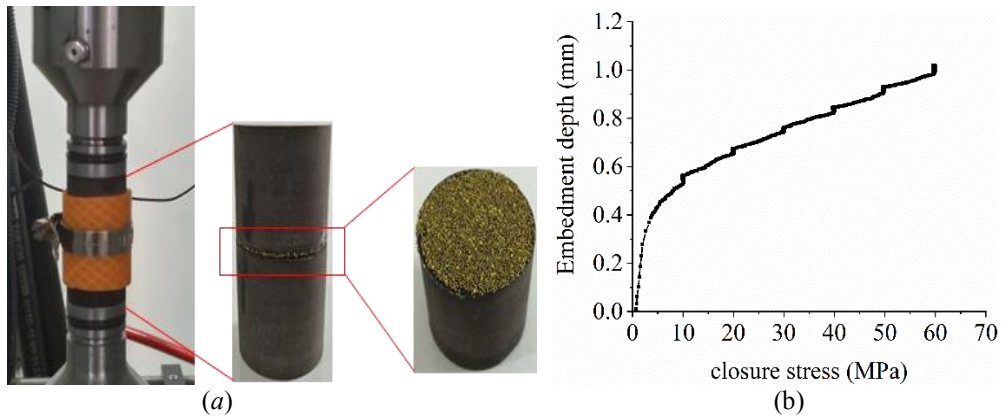


**Figure 1** Experiment setup and typical experimental results of proppant embedment test. (a) Experiment setup (b) typical experimental results of proppant embedment test

## 3. THEORETICAL STUDY

### 3.1. Mathematical model

The average contact stress of a single proppant is

$$\sigma_p = \frac{\sigma_c - (1 - \varepsilon n_t A_{pe}) p_f}{\varepsilon n_t A_{pe}}, \quad (1)$$

where  $n_t$  is the number of proppants that contacted with fracture surface per unit area,  $\sigma_c$  is the closure stress,  $p_f$  is the fluid pressure in the fracture,  $A_{pe}$  is average embedded area of a single proppant.

The embedded area of a single proppant is determined by contact mechanics. With the increase of proppant embedding depth, the local deformation of the contact position between the rock and the proppant exhibits three regions: elastic, elastoplastic, and plastic embedment. The detailed information about the constitutive model for proppant embedment can be found in reference [5].

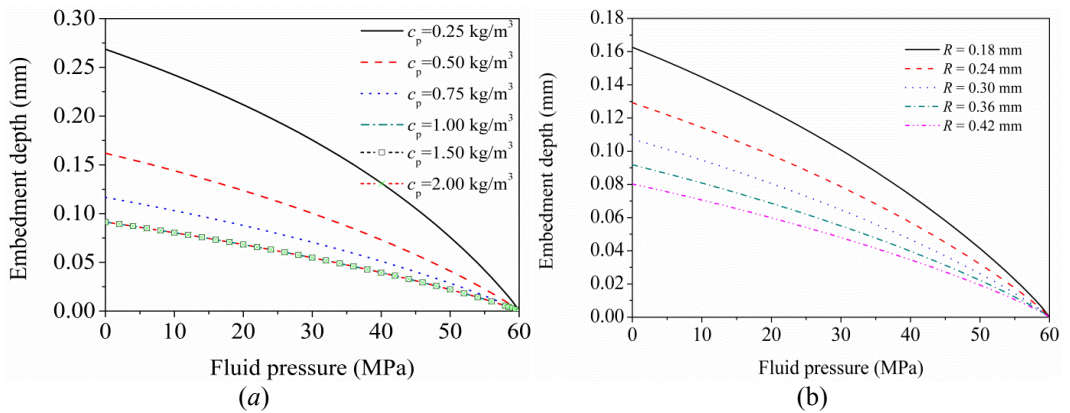


**Figure 2** Proppant embedment depth (a) different proppant concentration (b) different proppant radius

### 3.2. Results and analysis

Figure 2a shows that the proppant embedment depth and the contact stress increase with proppant concentration. However, they both remain constant when the concentration exceeds 1 kg/m<sup>2</sup>, which conforms with the previous analysis. Figure 2(a) shows that the embedment depth at 0.25 kg/m<sup>2</sup> is 2–3 times greater than the embedment depth at 1 kg/m<sup>2</sup>. This finding indicates that the proppant concentration inversely varies with the embedment depth when the proppant is arranged in a monolayer distribution.

Figure 2b shows that the embedment depth increases with decreasing grain diameter under the same parameters. At the fluid pressure of 15 MPa, the embedment depth with 0.18 mm proppant is two times greater than with 0.42 mm proppant.

### 4. CONCLUSION

A modified uniaxial compression test was proposed to measure proppant embedment depth. A new model for calculating the depth of proppant embedment was established in this study based on the stress analysis of the rock–proppant system and the entire deformation region of proppant embedding into rock fracture surfaces. Under the condition of the monolayer distribution, the embedment depth and the contact stress decrease with the increase of the proppant concentration. Proppant embedment depth and contact stress remain constant with the increase of proppant concentration under the multilayer distribution, because the proppants that contact with rock fracture surfaces are densely arranged and remain constant. A small proppant grain diameter means a high embedment depth.

### REFERENCES

- [1].Zou, Y., Ma, X., Zhang, S., Zhou, T., Ehlig-Economides, C., Li, H., 2015. The Origins of Low-Fracture Conductivity in Soft Shale Formations: An Experimental Study. *Energy Technol.* 3, 1233–1242. doi:10.1002/ente.201500188
- [2].Lacy, L.L., Rickards, A.R., Bilden, D.M., 1998. Fracture Width and Embedment Testing in Soft Reservoir Sandstone. *SPE Drill. Complet.* 13, 25–29. doi:10.2118/36421-PA
- [3].Alramahi, B., Sundberg, M.I., 2012. Proppant Embedment And Conductivity of Hydraulic Fractures In Shales. *Int. J. Eng. Sci.* 77, 14–23. doi:10.1016/j.ijengsci.2013.12.005

- [4].Cui, A., Glover, K., and Wust, R.A.J., 2014. Elastic and plastic mechanical properties of liquids-rich unconventional shales and their implications for hydraulic fracturing and proppant embedment : a case study of the Nordegg Member in Alberta , Canada.
- [5].Chen, M., Zhang, S., Liu, M., Xinfang, M. A., Zou, Y., Zhou, T., et al. 2018. Calculation method of proppant embedment depth in hydraulic fracturing. *Petroleum Exploration & Development*, 45(1), 159-166.



# Effects of Socio-demographic Factors on Psychological Conditions of Vocational School Students

Arslan Say<sup>1\*</sup>, Demet Çakır<sup>1</sup>, Arif Ayar<sup>1</sup>

<sup>1</sup>Sabuncuoğlu Şerefeddin Vocational School of Health Services, Amasya University, Amasya-TURKEY

\* arslan.say@amasya.edu.tr

## ABSTRACT

Obsessive Compulsive Disorder (OCD) is a psychological disorder in which unreasonable thoughts and fears (obsessions) force the person to exhibit constant repetitive behaviours. In order to investigate the prevalence of this disease and its effects on socio-demographic characteristics, the data were obtained by using the Maudsley Obsessional-Compulsive Inventory on 409 students attending Sabuncuoğlu Şerefeddin Health Services Vocational School of Amasya University. The results of the research have revealed that the prevalence of discomfort is 3,7%, it is experienced more in females, and obsessions of infection-scepticism and of cleaning (germaphobia) and control are the most common obsessions and compulsions.

**KEYWORDS** - Amasya University, Student, Obsessive Compulsive Disorder, Obsession, Compulsion, Socio-demographic Characteristics

## 1. INTRODUCTION

Obsessive-compulsive disorder (OCD), an anxiety disorder, is a disease that restricts people to the cycle of repeated thoughts and behaviors. People with obsessive-compulsive disorder become restless because of repetitive and stressful thoughts, fears, or images (obsessions) they cannot control. Anxiety caused by these thoughts is caused by the need to perform some rituals or routines urgently (compulsions). Rituals are made by attempting to prevent or avoid obsessive thoughts. Ritual temporarily stops anxiety, and when obsessive thoughts reappear, one must immediately repeat the ritual. This OCD cycle can prevent people from performing their normal daily work by stealing clocks from the day of the person.

People with obsessive-compulsive disorder may be aware that their obsessions and obsessions are unreal or meaningless, but they cannot stop themselves. It is thought that OCD affects 3% of the world's population [1]. Obsessive-Compulsive disorder (OCD) DSM-IV "anxiety disorders" in classification, In the diagnosis classification of the ICD-10 «neurotic, stress related and somatoform disorders» under the headings is a specific diagnostic group classified Individuals with OCD frequently experience additional diagnosable psychiatric disorders over the course of their lifetimes [2]. Disorders reported to occur commonly include tic, 'OCD spectrum', affective, anxiety, substance use and personality disorders [3].

The idea that psychiatric problems such as mood disorders and anxiety will be screened by OCD is gaining popularity. As a result of the increase in the prevalence of OCD, we decided to do this study at Amasya University.

## 2. MATERIAL AND METHOD

He population of our study consisted of 409 students who were learned in Amasya University, Sabuncuoğlu Şerefeddin Vocational School of Health Services. Maudsley obsessional-compulsive inventory was used in our study. Maudsley Obsessive Compulsive Scale This is to investigate the type of OCD symptoms. Scale by Hodgson and Rachman (1977) improved, validity in our country Erol and Savaşır (1988). Scale control, cleaning, slowness, suspicion and rumination [4,5,6]. The scale is applied to people aged 9 and over a subset of 7 questions was added to the study. a new group called rumination has been created. it was used to measure the type and prevalence of obsessive-compulsive symptoms in students. the self-assessment is the scale. it can be applied to healthy subjects and psychiatric patient groups. total 5 subscales and 37 items. accurate / false type

provides measurement by answering. According to the test results 12 points and six areas have the possibility of detecting obsessive compulsive disorder with psychiatric examination but as low, 13-17 points are likely to be diagnosed with obsessive compulsive disorder with psychiatric examinations and areas with 18 points and above the possibility of OCD with psychiatric examination was evaluated as high.

### 3. CONCLUSION

This scale was used to measure the type and prevalence of obsessive-compulsive symptoms in students. The self-assessment is the scale. It can be applied to healthy subjects and psychiatric patient groups. Total 5 subscales and 37 items. Accurate / false type provides measurement by answering. The answers of the students to the demographic questions are as in Table 1.

**Table 1.** The answers of the students to the demographic questions

		<b>n</b>	<b>%</b>
<b>Age</b>	18	65	15,9
	19	115	28,1
	20	127	31,1
	21	46	13,7
	22	23	5,6
	23 age and others	23	5,6
<b>Gender</b>	Female	293	71,6
	Male	116	28,4
<b>Graduated high school</b>	Health vocational high School	123	30,1
	Anatolian High School	152	37,2
	Other	134	32,8
<b>Living place</b>	Family	97	23,7
	Dorm	254	62,1
	Student house	13	3,2
	Friends in a house	45	11
<b>Smoking</b>	Yes	112	27,4
	No	297	72,6
<b>Alcohol</b>	Yes	32	7,8
	No	377	92,2
<b>Chronic Disease</b>	Yes	17	4,2
	No	392	95,8

According to the total score taken from the scale, the score of the students is  $15,3 \pm 6,977$ . According to this result, we can say that "There is a possibility of being diagnosed with obsessive-compulsive disorder by psychiatric examination". The crabbach alpha coefficient of the scale was found to be 0,867. According to this result, we can say that the scale is very safe. Nonparametric tests were used according to normality test. When the obsessions and compulsion distributions of the patients were examined, the control subscale of the male students (70.11%) was higher than the female students (63.02%), and the male students (35.35%) from the cleaning subscale, and female students (41.55%). I can say that it is a little obsessed. In the evaluation of the slow state; male students (43.72%) are slower than female students (51.05%). In the evaluation of doubt subscale; female students (50.46%), male students (47.41%) may be more doubtful.

**Table 2.** Evaluation of the subscales of the Maudsley Obsessive Compulsive Scale

The subscales of the scale	Average scores and standard deviations	
	Control	3,15±2,196
	Cleaning	4,39±2,229
	Slowness	2,21±1,723
	Doubt	3,47±1,467
	Rumination	1,52±1,365

According to the scale sub-group evaluation, it is seen that female students (41.72%) evaluated some thoughts or problems more than a male student (28.87%) with a new perspective. In the female students, the question of the cleaning subscale 'cannot enter toilet bowls' is more dominant than the male students (88,05%), whereas in male students, we can see that the question of ere honesty is more important than anyone else ere (89,65%). ). There was no significant difference between the genders in terms of gender scores ( $p = 0,119$ ;  $p > 0,05$ ).

## REFERENCES

- [1].Nestadt, G., Samuels, J., Riddle, M. A., Liang, K. Y., Bienvenu, O. J., Hoehn-Saric, R., ... & Cullen, B. (2001). The relationship between obsessive–compulsive disorder and anxiety and affective disorders: results from the Johns Hopkins OCD Family Study. *Psychological medicine*, 31(3), 481-487. DOI: 10.1017/S0033291701003579
- [2].Demet, M. M., Deveci, A., Deniz, F., Taşkın, E. O., Şimşek, E., & Yurtsever, F. (2005). Obsesif kompulsif bozuklukta sosyodemografik özellikler ve fenomenoloji. *Anadolu Psikiyatri Dergisi*, 6(3), 133-144.
- [3].Bienvenu, O. J., Samuels, J. F., Riddle, M. A., Hoehn-Saric, R., Liang, K. Y., Cullen, B. A., ... & Nestadt, G. (2000). The relationship of obsessive–compulsive disorder to possible spectrum disorders: results from a family study. *Biological psychiatry*, 48(4), 287-293. DOI:10.1016/S0006-3223(00)00831-3
- [4].Hodgson RJ, Rachman S (1977) Obsessional-compulsive complaints. *Behav Res Ther*, 15:389-395. DOI:10.1016/0005-7967(77)90042-0
- [5].Erol N, Savaşır I (1988) Maudsley Obsesif Kompulsif Soru Listesi. XXIV. Ulusal Psikiyatri ve Nörolojik Bilimler Kongresi Bildiri Kitabı, Ankara, GATA Basımevi, s.107-114.
- [6].Türkbay, T., Doruk, A., Erman, H., & Söhmen, T. (2000). Obsesif kompulsif bozukluğun belirti dağılımının ve komorbiditesinin çocuk ve ergenler ile erişkinler arasında karşılaştırılması. *Klinik Psikiyatri*, 3, 86-91.

---

## Task Planning for Mobile Manipulators Using Backward Climbing

Salim Djezairi<sup>1\*</sup>, Boushaki Zamoum Razika<sup>1</sup>, Bouzouia Brahim<sup>2</sup>, Abahri Ferial<sup>1</sup>

<sup>1</sup> University of M'hamed Bougara of Boumerdes, Institute of Electrical and Electronic Engineering,

Laboratory of Signals and Systems, Avenue de l'indépendance, Boumerdes, Algeria,

<sup>2</sup>Centre de Développement des Technologies Avancées, CDTA, Algeria,

\*salim.djezairi@gmail.com

### ABSTRACT

In recent years, mobile manipulators are being used to replace human operators in factories, warehouses, and even in domestic environments. These robots perform very complex tasks such as part feeding in an assembly line, preparing and serving meals in restaurants or houses, patrolling and guarding. In order to achieve these complex tasks, the robot manipulators must integrate an efficient symbolic planner.

Most state of the art symbolic planners are based on task decomposition or graph search. Task decomposition is not practical in unstructured environments for general tasks because decomposition methods must be specified for each task. Graph search planners can be intractable because the graph size is exponential in the number of instances in the world. Generally, researchers resort to heuristic search in order to find near optimal plans, but completeness and optimality is sacrificed.

This paper introduces an efficient algorithm called backward climbing. The algorithm takes advantage of the fact that mobile manipulators follow some patterns when performing a complex task. These patterns are organized in a layered graph called Layered Task Graph(LTG). The algorithm uses LTG to construct a set of reduced graphs. It then evaluates the simplest graph that contains the goal state, and climbs backward in the graphs hierarchy until reaching the simplest possible graph. This graph has a smaller size than the original graph. It is searched using any graph search algorithm.

The algorithm uses Breadth First Search(BFS) to find solutions in the reduced graphs. It is tested in a simulation environment and the planning is significantly faster than classical graph search (BFS). The algorithm was tested in the Simple Mobile Manipulator Simulator (SMMS) and integrated with a geometric planner for achieving the task of part feeding in an industrial environment.

**KEYWORDS** - Task Planning, Mobile Manipulator, Graph Search, LTG, Backward Climbing.

### 1. INTRODUCTION

Mobile manipulators (MMs) consist of two parts: a mobile platform and a robotic arm. MMs have an extended workspace thanks to their ability to move and can hence execute complex tasks that neither mobile robot nor robotic arms can perform. These tasks include: Fetching and feeding parts in an industrial environment[1], performing household tasks such cleaning and cooking[2], assisting elderly people and nursing [3], performing[4] ...etc.

In order to achieve these tasks, planning is required. The task to be achieved is given to the robot either as a task description or a goal description. The robot has to perform a sequence of primitive actions in order to achieve the goal. The process of finding the sequence of actions that transitions the world from the current state to the goal state is known as task planning. However as tasks become more complex, task planning becomes a challenging problem. The robot has to reason about the symbolic level ( e.g: object is on the table) and the geometric level (e.g path planning[5]).

Most state of the art planners use either task decomposition[6-8] or graph search[9-13]. Task decomposition relies on the knowledge of the world to decompose a high level task into less complex tasks. It has the advantage of being faster than other planner but it lacks flexibility.

Expert knowledge must be provided to the algorithm in order to find proper decomposition of the tasks. The lack of flexibility makes it unsuitable for unstructured or dynamic environments where the task decomposition may change. Graph search is suitable for flexible environment, however it does not scale well in complex environments because the state space becomes large.

This paper introduces an efficient algorithm called Backward Climbing. BC is efficient and scales well in complex environments while keeping flexibility. It uses the MM skills in order to create a set of reduced state spaces. BC efficiently searches the set of state spaces in order to find near optimal solution.

## 2. LAYERED TASK GRAPHS:

In order to effectively reduce the state space, robot skills and task patterns are used. Robot skills are a sequence of primitive actions that the robot can perform, i.e DisplaceObject is not a primitive action, but it is a skill that the robot can perform. Task patterns are sequence of actions that are generally repeated in the planning process. In the remaining of this article, we will refer to both skills and patterns as tasks.

Each task  $t$  represents a node in the LTG, it is connected by arcs to child nodes which represent the sequence it is decomposed to. For example, displacing an object  $O$ , to a Table  $T$  using robot  $R$ ,  $\text{Displace}(R, O, T)$ , is decomposed into  $\text{GraspFrom}(R, O, T')$  and  $\text{PutOn}(R, O, T)$  as shown in fig1. The complete LTG is shown in fig2.

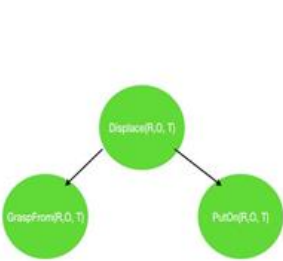


**Figure 1.** Decomposition of Displace action

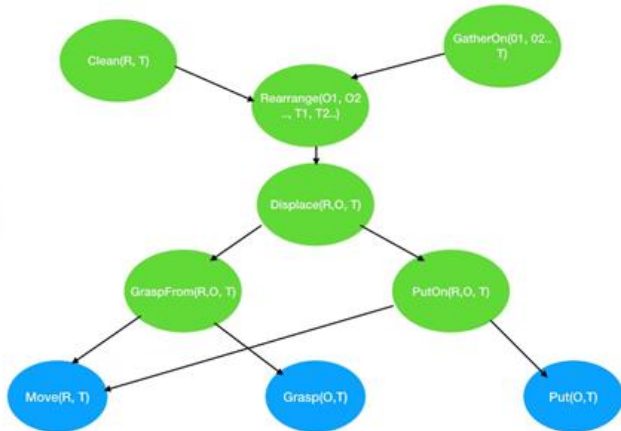


**Figure 1.** Layered Task Graph for a mobile manipulator

## 3. GRAPH REDUCTION:

The State space can be reduced by using the LTG, each layer of the graph results in a reduced state space. The example in figure 3 shows a state space reduction using the tasks show in table 1.

## 4. BACKWARD CLIMBING:

The algorithm 1 efficiently searches the set of state spaces  $S = \{S_0, S_1, \dots, S_n\}$  starting from the goal state  $g$  to the initial state  $s_0$ . It starts by searching the original  $S_0$  from  $g$  to the nearest state in  $S_1$ ,  $s'$ , then it searches  $S_1$  from  $s'$  to the nearest state in  $S_2$ ,  $s''$ . It iteratively searches  $S_i$  to the nearest state in  $S_{i+1}$  until the top level State Space  $S_n$  is reached.  $S_n$  is searched using BFS from  $s_0$  to the last state reached in  $S_{n-1}$ .

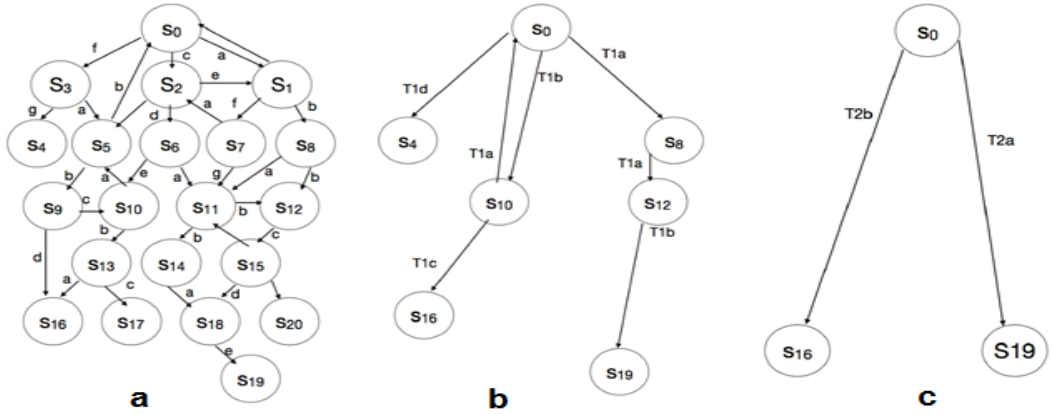


**Table 1.** Task decomposition table, representing an LTG haven 3 layers.

Layer	Tasks
0	a, b, c, d, e, f, g
1	T1a={a,b}, T1b={c,d,e}, T1c={b,a}, T1d={f,g}
2	T2a= {T1a, T1a, T1b}, T2b={T1b, T1c}

- BackwardClimbing()
  - Inputs:
    - s0: initial sate
    - g : Goal State
    - S= {S1,S2, S3 ....Sn} : a Set of State Spaces
    - T: a list of tasks.
  - s'= s0
  - Plan P ={};
  - while( S!=Sn )
    - s = s'
    - Si = S.popFirst(S);
    - s',P=BackwardSearch(s, s' ∈ A) +P;
    - if(p == NULL)
      - Return failure.
  - P=P+BFS(s0, s', Sn).
  - Return P;

## 5. SIMULATION RESULTS:

The algorithm was tested in Simple Mobile Manipulator Simulator (SMMS) where there is a robot, two rooms separated by a door. The first room contains three objects and three tables, the second room contains the machines. The goal is to displace objects to the correct machines. We simulated 3 scenarios and counted the number of explored nodes. The results are shown in table 2.

**Table 2.** The number of explored nodes for 3 scenarios,

Header	BFS	LD	BC
Scenario 1	38	2	2
Scenario 2	21417	600	600
Scenario 3	25477	37825	13453

From the results, it is clear that Backward Climbing (BC) dominates both BFS and LD. BC give similar results to LD when the goal lays in the most reduced state space.

When the goal state is not included in any goal state, LD performs very badly compared to BFS because of the overhead of searching state spaces where the solution is not found, however, BC does not do any unnecessary searches.

Backward climbing is flexible and faster than ordinary graph search methods. It does not have an overhead of unnecessarily searching State Spaces that do not contain the solution. It also preserves the completeness. However, the solutions that are found are not guaranteed to be optimal an its efficiency depends on the choice the tasks in the layered task graph.

## 6. CONCLUSION

The paper presented a task planner for Mobile Manipulators based on Graph reduction. The tasks are grouped into layered graph, called LTG in order to reduce the state space. The paper introduced Backward Climbing that accelerates the graph search by efficiently searching multiple state spaces. The algorithm outperforms classical graph search methods as well as Layered Deepening, while keeping flexibility.

The algorithm was tested in a simulation environment and the obtained results are promising. We plan to implement the algorithm on a real robot and test it in an industrial environment. The algorithm can also be improved by allowing the robot to automatically learn the LTG from experience.

## REFERENCES

- [1]. Mikkel Rath Pedersen, Lazaros Nalpantidis, Rasmus Skovgaard Andersen, Casper Schou, Simon Bogh, Volker Kruger, Ole Madsen, Robot skills for manufacturing: From concept to industrial deployment,, Robotics and Computer-Integrated Manufacturing, 2015.
- [2]. ,Kai Chen, Fangkai Yang, and Xiaoping Chen, Planning with Task-Oriented Knowledge Acquisition for a Service Robot Proceedings of the Twenty-Fifth International Joint Conference on Artificial Intelligence (IJCAI-16), 2016.
- [3]. Daehyung Park, You Keun Kim, Zackory M. Erickson, Charles C. Kemp, Towards Assistive Feeding with a General-Purpose Mobile Manipulator, ICRA2016 workshop on Human-Robot In- terfaces for Enhanced Physical Interactions, 2016.
- [4]. Perez-D'Arpino, Claudia , Agoos, Peter , Zamore, Andrew , R. Gammons, David , Kyritsis, Evie , A. Shah, Julie. (2017). A Theatrical Mobile-Dexterous Robot Directed through Shared Autonomy. 416-416. 10.1145/3029798.3036644.
- [5]. Z. Batik Garip, D. Karayel, S.S. Ozkan, G. Atali, Path Planning for Multiple Mobile Robots Using A\* Algorithm page 685, DOI: 10.12693/APhysPolA.132.685
- [6]. Kutluhan Erol James Hendler Dana S. Nau ,UMCP: A Sound and Complete Procedure for Hierarchical Task-Network Planning, AIPS, 1994.

- [7]. D. Nau, Y. Cao, A. Lotem, H. Munoz-Avila, SHOP: Simple Hierarchical Ordered Planner, 1999,
- [8]. Dana Nau, Tsz-Chiu Au , Okhtay Ilghami, Ugur Kuter, J. William Murdock, Dan Wu, Fusun Yaman, SHOP2: An HTN Planning System, Journal of Artificial Intelligence Research (2003).
- [9]. J. Hoffmann,B. Nebel, The FF Planning System: Fast Plan Generation Through Heuristic Search, Journal of Artificial Intelligence Research, Volume 14, 2001.
- [10]. Bonet, Blai , Geffner, Hector. (2001). Planning as heuristic search. Artificial Intelligence. 129. 5-33. 10.1016/S0004-3702(01)00108-4.
- [11]. Aliakbar Akbari, Muhayyuddin and Jan Rosell, Task Planning Using Physics-based Heuristics on Manipulation Actions, 2016 IEEE 21st International Conference on Emerging Technologies and Factory Automation (ETFA)
- [12]. Nicola Castaman, Elisa Tosello, and Enrico Pagello, Conditional Task and Motion Planning through an Effort-based Approach, CoRR, 2017.
- [13]. T Takahashi, MW Lanighan, RA Gruben, Hybrid Task Planning Grounded in Belief: Constructing Physical Copies of Simple Structures, Proceedings of the 27th International Conference on Automated Planning and Scheduling (ICAPS).



# A Note on the Symmetric Relation for Degenerate Genocchi Polynomials

**Burak Kurt\***

<sup>1</sup> Department of Mathematics, Akdeniz University, Antalya, TURKEY

\*burakkurt@akdeniz.edu.tr

## ABSTRACT

In recent years, many mathematicians studied degenerate Bernoulli, Euler and Genocchi polynomials.

Kim et al. introduced and investigated the degenerate Bernoulli numbers and polynomials and the degenerate Euler numbers and polynomials. Carlitz defined the degenerate Bernoulli numbers and degenerate Euler numbers. Dolgy et al. investigated the modified degenerate Bernoulli polynomials. Lin proved some identities for higher order the degenerate Genocchi polynomials. Young gave a symmetric identity for the degenerate Bernoulli polynomials.

In this paper, we give some differential equation. Also, we prove the symmetric relation for the degenerate Genocchi polynomials.

**KEYWORDS** - Bernoulli, Euler and Genocchi polynomials, Generating function, Degenerate Bernoulli, Degenerate Euler and Degenerate Genocchi polynomials.

## 1. INTRODUCTION

The classical Genocchi polynomials are defined as

$$\sum_{n=0}^{\infty} G_n(x) \frac{t^n}{n!} = \frac{2t}{e^{t+1}} e^{xt}, \quad |t| < \pi. \quad (1.1)$$

When  $x = 0$ ,  $G_n(0) = G_n$  are called the Genocchi numbers.

The classical Bernoulli polynomials and Bernoulli numbers are defined as the following equations in ([1]-[11]) respectively

$$\sum_{n=0}^{\infty} B_n(x) \frac{t^n}{n!} = \frac{t}{e^t - 1} e^{xt}, \quad |t| < 2\pi \quad (1.2)$$

and

$$\sum_{n=0}^{\infty} B_n \frac{t^n}{n!} = \frac{t}{e^t - 1}, \quad |t| < 2\pi \quad (1.3)$$

For  $\lambda \in \mathbb{C}$ , Carlitz [1] defined degenerate Bernoulli polynomials the following generating function

$$\sum_{n=0}^{\infty} B_n(x|\lambda) \frac{t^n}{n!} = \frac{t}{(1+\lambda t)^{\frac{1}{\lambda}} - 1} (1 + \lambda t)^{\frac{x}{\lambda}}, \quad |t| < 2\pi. \quad (1.4)$$

When  $x = 0$ ,  $B_n(\lambda) = B_n(0|\lambda)$  are called the degenerate Bernoulli numbers. Thus, by (1.4), we get

$$B_n(x|\lambda) = \sum_{l=0}^n \binom{n}{l} (x|\lambda)_{n-l} B_l$$

where  $(x|\lambda)_n = x(x - \lambda) \dots (x - \lambda(n - 1))$ .

Degenerate Genocchi polynomials and the higher order degenerate Genocchi numbers are defined by D. Lim [12] as following generating functions respectively;

$$\sum_{n=0}^{\infty} G_n(x|\lambda) \frac{t^n}{n!} = \frac{2t}{(1+\lambda t)^{\frac{1}{\lambda}} + 1} (1 + \lambda t)^{\frac{x}{\lambda}} \quad (1.5)$$

and

$$\sum_{n=0}^{\infty} G_n(0|\lambda) \frac{t^n}{n!} = \frac{2t}{(1+\lambda t)^{\frac{1}{\lambda}+1}}, r \in N. \quad (1.6)$$

Thus, by (1.5), we get

$$\lim_{\lambda \rightarrow 0} G_n(x|\lambda) = G_n(x), \lim_{\lambda \rightarrow 0} G_n(0|\lambda) = G_n, n \geq 0.$$

In this note, we write as  $G_n(x|\lambda) = G_n(x, \lambda)$ .

L. Carlitz introduced and investigated Bernoulli and Euler numbers. T. Kim et al. defined and proved some theorems and gave some recurrence relations. H.-In. Known et al. gave some identities of modified degenerate Euler numbers and degenerate Bernoulli numbers arising from ordinary differential equations. D. Lin proved some theorems for the higher order degenerate Genocchi polynomials in the  $p$ -adic analysis.

In this work, section 2, we give a symmetric relation for the higher order degenerate Genocchi polynomials.

## 2. THE SYMMETRIC RELATION FOR HIGHER-ORDER DEGENERATE GENOCCHI POLYNOMIALS

We will prove the following theorem for the degenerate Genocchi polynomials, which are symmetric in  $a$  and  $b$ .

**Theorem 1.** There is the following symmetric relation for the degenerate Genocchi polynomials

$$\begin{aligned} & b \sum_{l=0}^n \binom{n}{l} \sum_{i=0}^{a-1} (-1)^i G_l^{(m)} \left( \lambda, bx + \frac{bi}{a} \right) G_{n-l}^{(m-1)}(\lambda, ay) b^{n-l} a^l \\ &= a \sum_{l=0}^n \binom{n}{l} \sum_{i=0}^{b-1} (-1)^i G_l^{(m)} \left( \lambda, ay + \frac{ai}{b} \right) G_{n-l}^{(m-1)}(\lambda, by) a^{n-l} b^l. \end{aligned} \quad (2.1)$$

Proof. Let

$$f(t) = \frac{t^{2m-1}(1+\lambda abt)^{x/\lambda}((1+\lambda abt)^{1/\lambda}+1)(1+\lambda abt)^{y/\lambda}}{(1+(1+\lambda a)t/\lambda)^m(1+(1+\lambda b)t/\lambda)^m}.$$

Some calculation, we have

$$= \frac{1}{2^{m-1}a^mb^{m-1}} \sum_{n=0}^{\infty} \sum_{i=0}^{a-1} (-1)^i G_n^{(m)} \left( \lambda, bx + \frac{bi}{a} \right) \frac{(at)^n}{n!} \sum_{r=0}^{\infty} G_r^{(m-1)}(\lambda, ay) \frac{(bt)^r}{r!}$$

by using Cauchy product, we have

$$= \frac{1}{2^{m-1}a^mb^{m-1}} \sum_{n=0}^{\infty} \left\{ \sum_{i=0}^{a-1} (-1)^i \sum_{l=0}^n \binom{n}{l} G_l^{(m)} \left( \lambda, bx + \frac{bi}{a} \right) G_{n-l}^{(m-1)}(\lambda, ay) b^{n-l} a^l \right\} \frac{t^n}{n!}.$$

In a similar manner

$$f(t) = \frac{1}{2^{m-1}b^ma^{m-1}} \sum_{n=0}^{\infty} \left\{ \sum_{i=0}^{b-1} (-1)^i \sum_{l=0}^n \binom{n}{l} G_l^{(m)} \left( \lambda, ay + \frac{ai}{b} \right) G_{n-l}^{(m-1)}(\lambda, bx) a^{n-l} b^l \right\} \frac{t^n}{n!}.$$

Comparing the coefficients of  $\frac{t^n}{n!}$ , we proved Theorem.

## REFERENCES

- [1]. L. Carlitz, Degenerate Stirling Bernoulli and Eulerian numbers, Util. Math. 15 (1979) 51-88.
- [2]. D. V. Dolgy, T. Kim, H.-In Known and J. J. Seo, On the modified degenerate Bernoulli polynomials, Advanced Studies in Contemp. Math. 26 (2016) 203-209.
- [3]. T. Kim, Identities involving Frobenius-Euler polynomials arising from non-linear differential equation, J. Number Theory 132 (2012) 2854-2865.
- [4]. T. Kim and D. S. Kim, Identities involving degenerate Euler numbers and polynomials arising non-linear differential equation, J. of Nonlinear Science and Appl. 9 (2016) 2086-2098.
- [5]. T. Kim, D. S. Kim, H.-In Known and J. J. Seo, Differential equations arising from the generating function of general modified degenerate Euler numbers, Advances in Diff. Equa. (2016) 2016:128, doi:10.1186/s13662-016-0858-7.
- [6]. T. Kim, Y. S. Jang and J. J. Seo, A note on poly-Genocchi numbers and polynomials, App. Math. Sci. 8 (96) (2014) 4775-4781.
- [7]. T. Kim, D. S. Kim and H.-In Known, Some identities relating to degenerate Bernoulli polynomials, Filomat 30.4 (2016) 905-912.
- [8]. T. Kim, D. S. Kim, H.-In Known and J. J. Seo, Differential equations arising from the generating function of general modified degenerate Euler numbers, Advances in Difference Equations, 2016.1 (2016): 129.
- [9]. H.-In Known, T. Kim and J. J. Seo, Some identities for modified degenerate Euler numbers arising from ordinary differential equations, Int. J. of Math. Analysis 10(12) (2016) 565-571.
- [10]. H.-In Known, T. Kim, and J. J. Seo, Some Identities for Modified Degenerate Bernoulli Numbers Arising from Ordinary Differential Equations, Applied Mathematical Sciences, 10.29 (2016): 1441-1447.
- [11]. H.-In Known, T. Kim and J. J. Seo, Modified degenerate Euler polynomials, Advanced Studies in Contemp. Math. 26 (1) (2009) 203-209.
- [12]. D. Lim, Some identities of degenerate Genocchi polynomials, Bull. Korean Math. Soc. 53 (2) (2016) 569-579.
- [13]. V. Kurt, A further symmetric relation on the analogue of the Apostol-Bernoulli and the analogue of the Apostol-Genocchi polynomials, Appl. Math. Sci. 3 (56) (2009) 2757-2764.
- [14]. B. Kurt, A new class of modified degenerate Bernoulli, Euler and Genocchi polynomials, Kuwait J. of Sciences submitted (ICCESSEN2017).
- [15]. Ryoo, C. S. "Nonlinear Differential Equations Associated with Degenerate Tangent Numbers." Applied Mathematical Sciences 11.22 (2017): 1067-1076.

## Evaluation Of The Water Fluoride Exposure In Urban Areas In The Province Of Blida, Algeria

Zouani Amina<sup>1\*</sup>, Guerfi bahdja<sup>2</sup>, Mezroud Fouzia<sup>3</sup>, Kermout Imene<sup>4</sup>, Talailef Assma<sup>5</sup>

1 : University Saad Dahleb. Department of Pharmacy, Laboratory of Toxicology, Blida, Algeria.

2 : University Saad Dahleb. Department of Pharmacy, Laboratory of chemical therapeutic. Blida, Algeria.

\*aminapharmatox@hotmail.fr

### ABSTRACT

**Objective:** Fluorine (F-) is a carioprotector element, but it is toxic in high doses. In Algeria, tooth decay is the most common pathology in schools, on the other hand, the fluorosis problem, affecting many areas of southern and even northern Algeria. Our study focuses on evaluating the water exposure F- in the population of Blida city (in north Algeria near the capital Algiers), based on the determination of F- in network of communal water distribution, in order to predict a possible risk of fluorosis, or orient public health programs related to the fluoride supplementation. **Methods:** 30 water samples were collected during the period from 31 March to 02 April 2014 in three regions of Blida. We performed the assay F- by a colorimetric method (Belcher West) that we validated by SFSTP'92. **Results :** All the contents of F- recovered through Blida (in 2014 ) are below the standard of the World Health Organisation which is from 0.8-1.7 mg/L. The lowest values were observed in the East (L' Arbaa) with 60% of the values <0.05 mg /L, followed by the central region (Blida) with 70% of the values < 0.17 mg / L and finally the Western Region (Elafroune) with 60% of the values <0.17 mg / L. **Conclusion:** Based on these results we can conclude that there is no risk of fluorosis, on the contrary the values found are very low hence the need for the establishment of a fluorine supplementation program.

**Keywords -** Fluorine, water, tooth decay, fluorosis.

### 1. INTRODUCTION AND OBJECTIVES

Fluoride (F-) is a carioprotector element, but it is toxic in high doses. In Algeria, tooth decay is the most common pathology in schools, practically one child on two has, at least, one tooth decay [1]. On the other hand, the fluorosis problem, affecting many areas of southern and even northern Algeria. Our study focuses on evaluating the water fluoride exposure in the population of Blida, based on the determination of fluoride in network of communal water distribution, in order to predict a possible risk of fluorosis, or orient public health programs related to the fluoride supplementation.

### 2. MATERIAL AND METHODS

#### 2.1. Samples :

##### 2.1.1. specimen collection and period

30 samples of communal water distribution, were collected during the period from 31/03/2014 to 02/04/2014 in three municipality of Blida (Larebaa, El-Affroun and Blida city center) (figure 01), by the agents of the Algerian Water Directorate.



**Figure 1.** Administrative division of Blida

### 2.1.2. Conditions

- Let the water flow during few minutes (3-5minutes).
- Rinse water's containers several times with this water before filling them.
- Bottles used are made with polyethylene tetraphthalates (PET).
- Sample's volume is about 300 mL.

### 2.1.3. Conservation

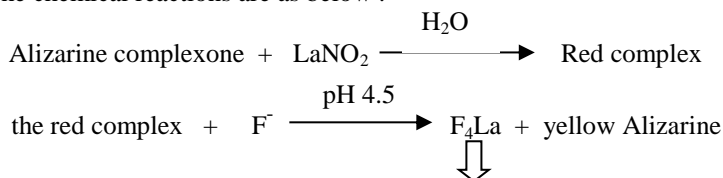
No preservative are used, store at +4°C for a month at most. [2]

## 2.2. Analysis

### 2.2.1. Principle

Colorimetric dosage using the method of Belcher-West modified by Green, Halgue and Riley, which we validated according to the protocol of the French company of technical and pharmaceutical sciences (SFSTP'92) [3].

The chemical reactions are as below :



Blue color : stabilised in presence of acetone

### 2.2.2. Procedure

The procedure of the dosage is described in the table 1 : [3]

**Table 1.** Procedure of the fluorine dosage in water

[illegible]

- Mix the flasks after addition of each reagent.
- Read the absorbance (A) of the different tubes at 618 nm using the blank after 5-10mn.

### 2.3. The analytique validation's procedure:

Application of SFSTP'92 validation's protocole basing on the study of the folowing parameters: specificity, linearity and mesure range, precision and accuracy [4]

Satistic's tests of fidélité were occured by Excel. Linearity tests and accuracy were occured using a software of validation.

## 3. RESULTS

### 3.1. Validation's results :

#### 3.1.1. Specificity :( table 2)

*Table 2. Results of the study of the specificity*

Essay	Concentration in mg/L	Absorbance
Blank standard (in distilled water)	0	0
Blank standard charged	0.1	0.03
Blank matrix (in communal water)	0	0
Blank matrix charged	0.1	0.029

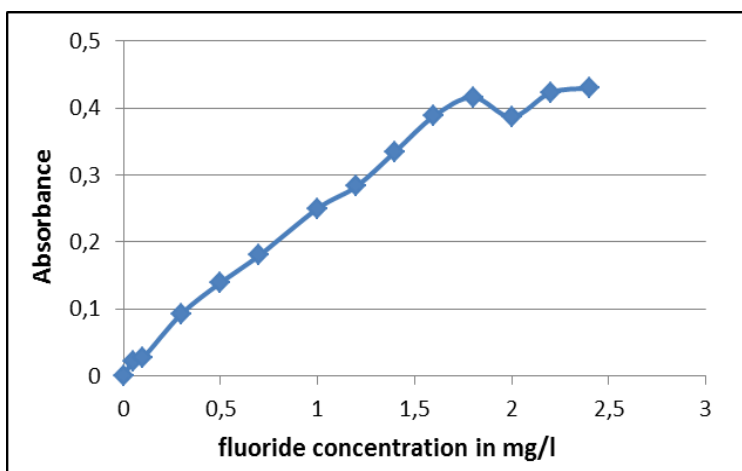
- Standrd blank : were prepared in distilled water.
- Matrix blank : were prepared in normal water but containing 0 mg/l of fluoride.

The blanks standards and matrix are negatif , there is no interference of other water elements on the dosage of fluorine, so the specificity is good .

### 3.1.2. Linearity :

#### 3.1.2.1. range of linearity

The method is linear in the range of concentrations from 0.05-1.8 mg/l (figure 2).



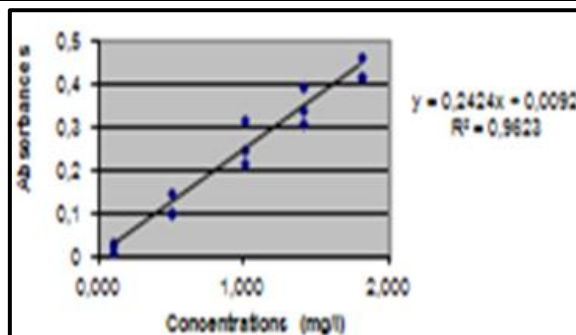


Figure 3. Standard mean curve (fluoride prepared in distilled water)

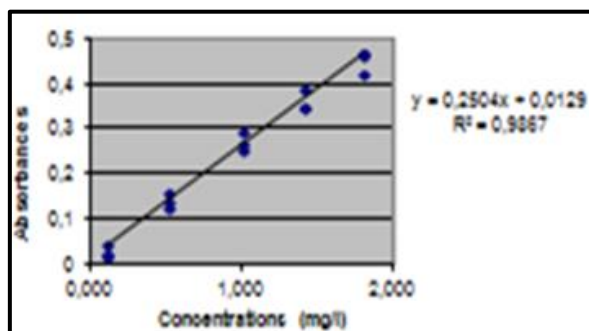


Figure 4. Matrix mean curve

### 3.1.2.2. Determination of means curves(of 3 days of validation) standard and matrix

### 3.1.2.3. Statistical tests of linearity

#### Linearity of standard curves

Table 3. Statistical tests of linearity (standard curve)

Slope (b)					0.2424
intercept (a)					0.0092
Coefficient of regression (r <sup>2</sup> )					0.9623
Comparison of the intercept with the origin(0)					
t <sub>calculated</sub>	t <sub>theorique</sub> 5%	t <sub>theorique</sub> 1%	Condition	Conclusion	
0.61	2.16	3.01	t < t <sub>th</sub>	Valid at a risk of 5%	
Homogeneity of variance					
C <sub>calculated</sub>	C <sub>theorique</sub> 5%	C <sub>theorique</sub> 1%	Condition	Conclusion	
0.44	0.68	0.79	C < C <sub>th</sub>	Valid at a risk of 5%	
Existence of a significant slope					
F <sub>1</sub> calculated	F <sub>theorique</sub> 5%	F <sub>theorique</sub> 1%	Condition	Conclusion	
332.16	4.67	9.07	F <sub>1</sub> > F <sub>th</sub>	Valid at a risk of 1%	
Validity of linear regression					
F <sub>2</sub> calculated	F <sub>theorique</sub> 5%	F <sub>theorique</sub> 1%	Condition	Conclusion	
0.32	3.71	6.55	F <sub>2</sub> < F <sub>th</sub>	Valid at a risk of 5%	

All statistical tests of linearity for the standard curves are valid at risk 5%, so the linearity of the standard curves is good.

### Linearity of the matrix curve:

**Table 4. Statistical tests of linearity (matrix curve)**

Slope (b)					0.2504
intercept (a)					0.0129
Coefficient of regression ( $r^2$ )					0.9867
Comparison of the intercept with the origin(0)					
$t_{calculated}$	$t_{theorique}$ 5%	$t_{theorique}$ 1%	Condition	Conclusion	
1.41	2.16	3.01	$t < t_{th}$	Valid at a risk of 5%	
Homogeneity of variance					
$C_{calculated}$	$C_{theorique}$ 5%	$C_{theorique}$ 1%	Condition	Conclusion	
0.27	0.68	0.79	$C < C_{th}$	Valid at a risk of 5%	
Existence of a significant slope					
$F_1_{calculated}$	$F_{theorique}$ 5%	$F_{theorique}$ 1%	Condition	Conclusion	
962.63	4.67	9.07	$F_1 > F_{th}$	Valid at a risk of 1%	
Validity of linear regression					
$F_2_{calculated}$	$F_{theorique}$ 5%	$F_{theorique}$ 1%	Condition	Conclusion	
0.70	3.71	6.55	$F_2 < F_{th}$	Valid at a risk of 5%	

All statistical tests of linearity for the matrix curves are valid at risk 5%, so the linearity of the matrix curves is good.

### Verification of superposition between the standard and matrix curves :

-Comparison between the intercepts (a<sub>1</sub> and a<sub>2</sub>) , the calcul with Student's test is :

$$t_{exp} = \frac{|a_1 - a_2|}{\sqrt{S a_1^2 + S a_2^2}} < t_{table} \text{ (alpha = 5\%, } N_1 + N_2 - 4 = 2.056)$$

with a<sub>1</sub> = 0.0092, a<sub>2</sub> = 0.0129 and S a<sub>1</sub> = 0.02 S a<sub>2</sub> = 0.01.

t<sub>calculated</sub> = 0.1659 < 2.056 ; so we can conclude that the intercepts of the standard and matrix curves are not significantly different at risk alpha of 5%.

Comparison of the slopes of the adjustment lines , the calcul with student's test:

$$t_{exp} = \frac{|b_1 - b_2|}{\sqrt{S b_1^2 + S b_2^2}} < t_{table} \text{ (alpha = 5\% ; ddl = } N_1 + N_2 - 4 = 2.056)$$

T<sub>exp</sub> = t<sub>calculated</sub> = 0.0457577 < 2.056, so we can conclude that the slopes of standard and matrix curves are not significantly different at risk 5%.

### 3.2. Precision: study of repeatability:



**Table 5. Results of reapeatability**

day	Average (mg/l)	Standard deviation	Coefficient of variation (CV)
Day 1	0.595	0.03317988	5.57
Day 2	0.555	0.00916255	1.65
Day 3	0.467	0.0068903	1.47

**study of intermediate precision:**

**Table 6. Results of intermediate precison**

	Average (mg/l)	Standard deviation	Coefficient of variation (CV)
Standard	0.542	0.0591	10.90

So we can conclude that repeatability of this methode is good and the intermediate precision is accpeted.

### 3.3. Accuracy :

**Table 7. Test of homogeneity of variances:**

<b>S<sup>2</sup>max</b>	1665,3333
<b>Sum of variances</b>	2714,8089
<b>C calculated</b>	0,6134
<b>C theorique 5%</b>	0,68
<b>C theorique 1%</b>	0,79
<b>Conclusion</b>	Valide at risk 5%

**Table 8. Test of means validity.**

	DDL	Sum square	Variance	F <sub>1</sub> calculated	F <sub>1</sub> theorique 5%	F <sub>1</sub> theorique 1%	Conclusion
<b>Totale variation</b>	14	6158,59384	439,89956	0,34	3,48	5,99	Valida t risk 5%
<b>Intra-group variation</b>	10	5429,61770	542,96177				
<b>Intergroup variation</b>	4	728,97613	182,24403				

**Table 9. Estimate of mean revovery**

<b>Average recovery</b>	96,681	
<b>Confidence interval</b>	85,07	108,30

All the tests of accuracy are valid, so we can conclude that this method is accurate.

## 7. RESULTS OF DOSAGE OF FLUORIDE IN WATER :

**Table 10. Fluoride levels in the analysed water samples.**

Concentration (mg/L)	S <sub>1</sub>	S <sub>2</sub>	S <sub>3</sub>	S <sub>4</sub>	S <sub>5</sub>	S <sub>6</sub>	S <sub>7</sub>	S <sub>8</sub>	S <sub>9</sub>	S <sub>10</sub>
Sampling site										
<b>Larebaa</b>	0	0	0	0,0039	0	0,0117	0,1523	0,1132	0,0937	0,1054
<b>EL Affroune</b>	0,1289	0,1289	0,1875	0,3085	0,246	0,2617	0,125	0,125	0,1289	0,1015
<b>Blida city center</b>	0,082	0,0937	0,1484	0,2109	0,2187	0,1562	0,121	0,164	0,0429	0,1015

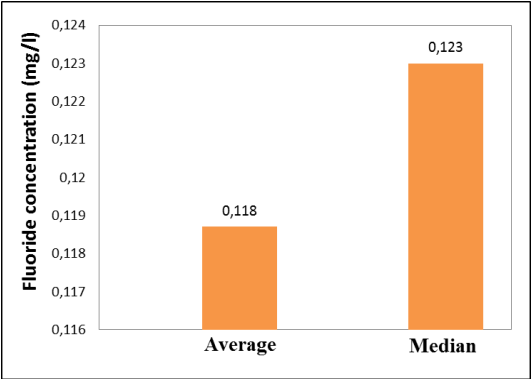


Figure 5. Water fluoride levels in Blida city, mean and median value.

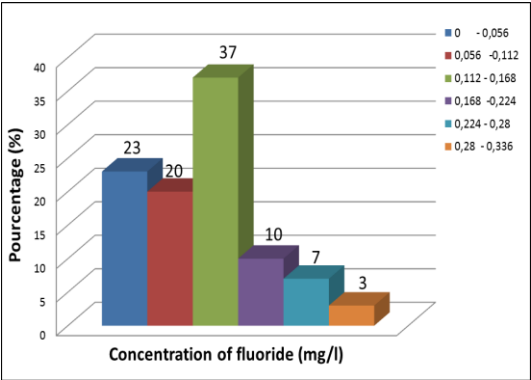


Figure 6. Distribution of water fluoride concentrations found in Blida city

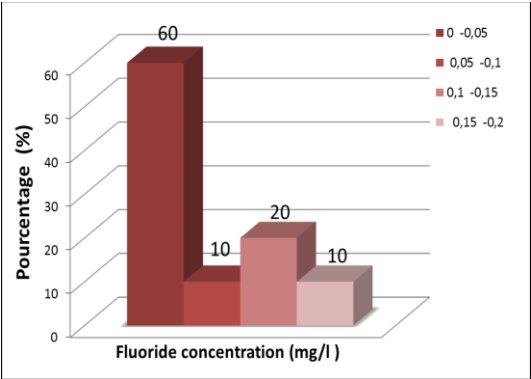
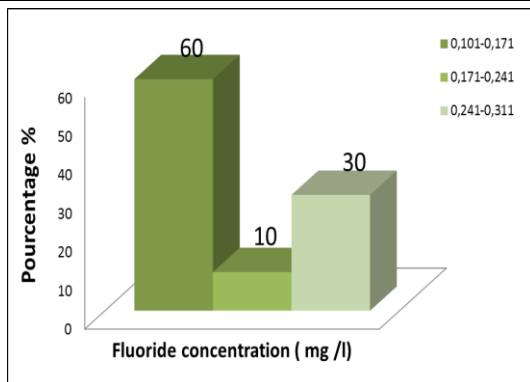
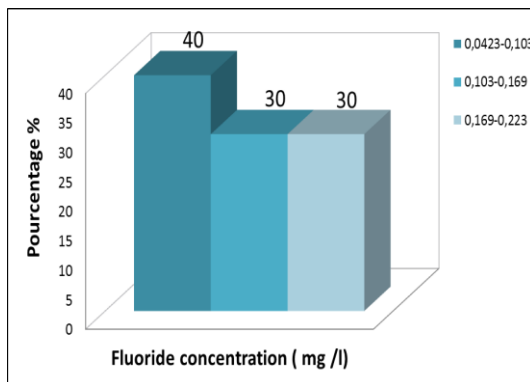


Figure 7. Distribution of water fluoride concentrations found in Larebaa.



**Figure 8.** *Distribution of water fluoride concentrations found in El Affroune.*



**Figure 9.** *Distribution of water fluoride concentrations found in Blida city center*

#### 4. DISCUSSION

The validation results of the method of Belcher-West show that all the statistics tests of the different parameters of validation , required by the SFSTP' 92 protocol , are valid. This results demonstrate the performance and the precision of this method used for the determination of water fluorine levels. ,

All water fluorine levels found in Blida city (average : 0.118 mg/L) are under the algerienne standard of water potability which is 0.5- 2mg/L and under the satndar of the World Health Organisation(WHO) (0.8-1.7 mg/L). These levels are very low throught the different parts of Blida city: east (Larebaa) (0.048 mg/L), center (Blida) (0.13 mg/L) and west (El-Affroun) (0.17 mg/L). In fact these results demonstrate that there is no risk of fluorisis in Blida.

50 % of water fluorine levels are less than 0.123mg/L, the maximal value is 0.308 mg/L. The municipality of Larebaa has the lowest levels with 60 % of the values are < 0.05 mg/L , followed by the municipality of Blida with 70 % of the values <0.17 mg/l and finally the municipality of El-Affroun with 60 % of the values <0.17 mg/L.

We notice that water fluorine levels found in the province of Blida are less than 0.5 mg/L, under this value the Algerian Ministry of Public Health ando Hospital Reform (MPHRH) require a fluorine supplementation in chldren by the administration of sodium fluoride tablets in order to avoid tooth decay.

## 5. CONCLUSION

This study demonstrates that water fluoride exposure in Blida city is very low, in fact all water fluoride concentrations are below the algerian standard for drinking-water and below the WHO's water fluoride standard. So we can conclude that there is no risk of fluorosis in Blida's population, on the contrary these values are very low and they are all below the minimum water fluoride concentration required by the MPHHR from which a fluorine supplementation is necessary.

That is said, further studies are desirable, with more samples to confirm the results of our study in order to recommend to the MPHHR the establishment of a fluorine supplementation program in Blida city as part of prevention of tooth decay in school children.

## REFERENCES :

- [1].Bouchouchi F. Compagne fluor. Ministère de la Santé Public et de la Réforme Hospitalière 2008.
- [2].Rodier J, Legube B, Merlet N et coll. L'analyse de l'eau. 9ème édition.2009.p 9,11
- [3]. Merad R, Reggabi M, Alamir B, Benali S, Abtroun R, Azzouz M, Benaissa D. Travaux pratiques de toxicologie.1992.p 23-26.
- [4]. Bouklouze A, Digua K. Démarche statistique de la validation analytique dans le domaine pharmaceutique (méthodologie et exemple pratique). Les technologies de laboratoires n°1.2006.p 21

# Why the Variable Gradient Drilling Approach Can Better Fit the Complex and Narrow Pressure Window in Ultra-deep Water Drilling?

Hongwei Yang<sup>1\*</sup>, Jun Li<sup>1</sup> and Gonghui Liu<sup>1,2</sup>

<sup>1</sup> China University of Petroleum (Beijing), Beijing, CHINA

<sup>2</sup> Beijing University of Technology, Beijing, CHINA

\* zerotone0205@qq.com

## ABSTRACT

In this paper, a key parameter optimization model in variable gradient drilling (VGD) was established, including optimization objectives, constraints, optimization algorithm, etc., in which the maximum drilling depth under different conditions were the optimization objectives, and the constraint relationships between equivalent circulation density (ECD) and safe density window (SDW) were used as the constraints. The particle swarm optimization (PSO) algorithm was improved to solve this optimization model. Using this optimization method, a case study was conducted to analyze the optimal values of separator position and mud density under a specific safe density window (SDW).

**KEYWORDS** - Variable gradient drilling, Parameter optimization, PSO algorithm.

## 1. INTRODUCTION

With the development of oil and gas developing into deep water and ultra-deep water, there are more and more challenges in the drilling process, i.e., narrow SDW, great difficulty of wellbore pressure control, hydrate blockage, etc. At present, managed pressure drilling is an effective technology to solve these problems, especially the dual-gradient drilling (DGD) technology [1-2]. Li [3] studied the maximum extension limit of horizontal wells under the condition of marine DGD. Stamnes [4] established the model for operational scenarios of DGD and optimized the key operational parameters. However, for deep water area, the above problems still cannot be solved well by DGD. Therefore, we have proposed a technology of VGD [5]. VGD is a new drilling technology, which can better adapt to the SDW of deep water formation.

During the drilling process of VGD, the cyclone separator moves downward together with the drill string, so the density gradient of the annulus fluid changes dynamically. In order to keep the ECD in the SDW, it is necessary to optimize the cyclone separator position and mud density so as to maximize the drilling depth. In this paper, an optimization model for key parameters of VGD was established, and the optimization model was solved based on the PSO algorithm. Using this optimization model and optimization algorithm, the optimal parameters of a specific SDW were studied in order to provide a good theoretical basis for field operation.

## 2. MODEL DEVELOPMENT

The following assumptions were made to simplify the model: (i) ignoring the influence of temperature on physical parameters of mud; (ii) only the case of one cyclone separator on the drill string was considered; (iii) the hollow balls in the drill string was completely separated into annulus by the cyclone separator.

Fig. 1 shows the variation of each parameter during the drilling process of VGD. The maximum depth of the first drilling, starting at the mud line or the casing shoe on the upper casing, is usually determined. Therefore, the drilling depth and mud density of the first drilling were taken as the initial conditions.

## 2.1. Design variables

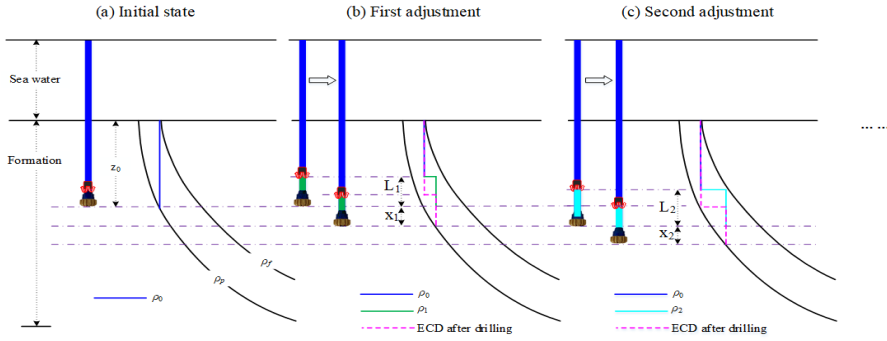


**Fig. 1.** Schematic diagram of key parameters in the process of VGD.

During the subsequent drilling process, the maximum drilling depth and total well depth after each adjustment are:

$$f_i(x) = x_i \quad (1)$$

$$z = z_0 + \sum_{i=1}^N f_i(x) \quad (2)$$

Where,  $x_i$  is the maximum drilling depth after the  $i$ -th adjustment;  $z_0$  and  $z$  are the maximum depth of the first drilling and total well depth, respectively.  $N$  is the number of adjustments.

After  $N$  times of adjustment, the ECD of  $i$ -th adjustment is:

$$\rho_i(z) = \frac{\rho_0 g z_0 + \sum_{j=1}^i [\rho_{Lj} g (z_j - z_{j-1}) + F_f (z_j - z_{j-1})]}{g z_i} \quad (3)$$

Where,  $\rho_0$ ,  $\rho_{Li}$  and  $\rho_i$  are the mud density of the first drilling, the mud density after  $i$ -th adjustment and the ECD, respectively;  $z_i$  is the well depth after  $i$ -th adjustment;  $F_f$  is the annular viscous friction.

In a given area, the SDW of the formation is determined and can generally be obtained by the adjacent well data. It is assumed that the equivalent fracture pressure density (EFPD) and equivalent pore pressure density (EPPD) at a certain depth satisfy the following relationship:

$$\rho_f(z_i) = \rho_{fi} \quad (4)$$

$$\rho_p(z_i) = \rho_{pi} \quad (5)$$

Where the  $\rho_{fi}$  and  $\rho_{pi}$  are the EFPD and EPPD, respectively.

## 2.2. Objective equation

The main purpose of the optimal key parameter design for VGD is to achieve the maximum drilling depth under the condition of the same well configuration, so as to simplify the well configuration and improve the economic effect. Therefore, the optimal objectives are selected as

the maximum drilling depth after each adjustment and the maximum drilling depth under the condition of the same well configuration, i.e.,

$$\text{Max } f_i = f_i(x) \quad (6)$$

$$\text{Max } D = \sum_{i=1}^N f_i(x) \quad (7)$$

Where the  $f_i$  and  $D$  are the maximum drilling depth after each adjustment and the maximum drilling depth under the condition of the same well configuration, respectively.

### 2.3. Optimization parameters

The optimization parameters are the cyclone separator position and mud density, i.e.,

$$X = [L_i, \rho_{Li}] \quad (8)$$

Where  $L_i$  is the distance between the cyclone separator and the drill bit after the  $i$ -th adjustment.

### 2.4. Constraints

As the ECD must meet the relation  $\rho_{pi}(z_i) < \rho_i(z_i) < \rho_{fi}(z_i)$ , the constraints for VGD are defined as:

$$\sum_{m=1}^{i-1} f_m(x) < L_i < z \left( z_0 + \sum_{m=1}^{i-1} f_m(x) \right) - \rho_f^{-1} \left[ \rho_i \left( z_0 + \sum_{m=1}^{i-1} f_m(x) \right) \right] \quad (9)$$

$$\max \{ \rho_p(z), \rho_{i-1}(z) \} < \rho_i(z) < \rho_f \left( z_0 + \sum_{m=1}^{i-1} f_m(x) - L_i \right) \quad (10)$$

$$x_{\min} < x_i < L_i \quad (11)$$

## 3. OPTIMIZATION ALGORITHM

According to the above analysis, the optimization model of VGD is a linear optimization problem. However, considering the large optimization range of parameters, PSO algorithm was adopted to obtain more accurate results and speed up the optimization rate.

Suppose the particle swarm is searched in a space of  $n$ , and the position of the particle in space is  $x_i = (x_{i1}, x_{i2}, \dots, x_{in})$ , the particle velocity is expressed as  $v_i = (v_{i1}, v_{i2}, \dots, v_{in})$ . The model of PSO is [6-7]:

$$v_{id}(k+1) = wv_{id}(k) + c_1 N_{rand1} (S_{idbest}(k) - x_{id}(k)) + c_2 N_{rand2} (S_{idbest}(k) - x_{id}(k)) \quad (12)$$

$$x_{id}(k+1) = x_{id}(k) + v_{id}(k+1) \quad (13)$$

Where,  $x_{id}(k)$  is the position of particle  $i$  on the  $d$  dimension in the  $k$ -th iteration;  $v_{id}(k)$  is the velocity of particle  $i$  on the  $d$  dimension in the  $k$ -th iteration;  $S_{idbest}(k)$  is the optimal position of particle  $i$ ;  $S_{gdbest}(k)$  is the global optimal location of particle swarm;  $c_1$  and  $c_2$  are learning factors;  $N_{rand1}$  and  $N_{rand2}$  are random numbers between 0 and 1;  $w$  and  $k$  are inertia factors and iteration times respectively.

Inertia factors have a significant impact on the optimization and convergence of PSO. The exponential curve inertial factor is used here [8-9], i.e.,

$$w = w_{end} \left( w_{start} / w_{end} \right)^{1/(1+10k/K)} \quad (14)$$

Where the  $w_{start}$  is the maximum inertia factor at the beginning of iteration;  $w_{end}$  is the minimum inertia factor at the end of iteration;  $k$  and  $K$  are the current number of iterations and the total number of iterations, respectively.

4. CASE STUDY

After the above optimization model and optimization algorithm were established, a specific deep water SDW was selected to determine the maximum drilling depth  $D$ , adjustment times  $N$ , and key parameters ( $L_i^{opt}$ ,  $\rho_{Li}^{opt}$ ,  $x_{imax}^{opt}$ ) after each adjustment under the same well configuration. The deep water SDW is shown in Fig. 2. The basic parameters used in the calculation are shown in Table 1.

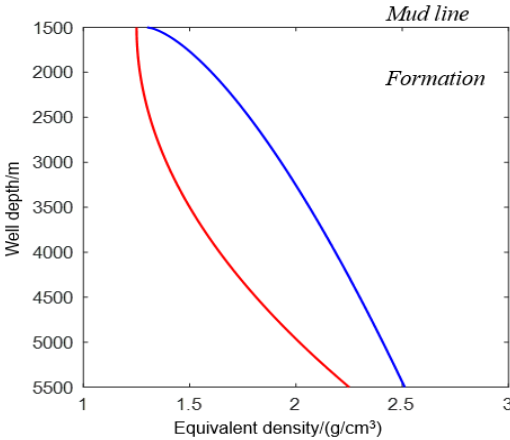


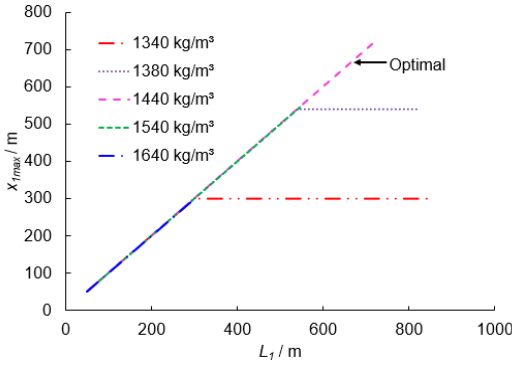
Fig. 2. The deep water SDW

Table 1. Basic parameters of calculation

Variables	Value
Well depth, m	5500
Seawater depth, m	1500
Initial mud density, kg/m3	1300
Initial drilling depth, m	2400
Initial $L_0$	0
Minimum drilling depth, m	50
Learning factor	0.5-2
The maximum number of iterations	1000
Maximum inertia factor at the beginning	0.96
Minimum inertia factor at termination	0.8

The position of cyclone separator and mud density needed to be adjusted several times when drilling to the maximum depth in the same well configuration. The optimization process after each adjustment was the same, and the results after the first adjustment were taken for analysis. Fig. 3 shows the variation of  $x_{imax}$  with  $L_I$  under different  $\rho_{Li}$  conditions. As shown in Fig. 3, with the increase of  $L_I$ ,  $x_{imax}$  increased linearly or increased linearly first and then remained constant. Besides, with the increase of  $L_I$ ,  $x_{imax}$  increased gradually and then decreased gradually. There was an optimal  $L_I$  that made  $x_{imax}$  reach the maximum value, as shown in Fig. 4.





**Fig. 3.** Variation of  $x_{I_{max}}$  with  $L_1$  under different  $\rho_{L1}$  conditions.

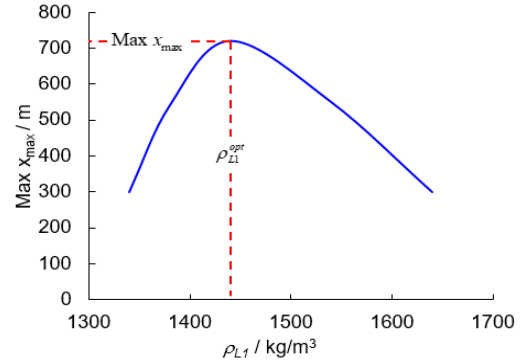


**Fig. 4.** Maximum curve of  $x_{I_{max}}$  under different  $\rho_{L1}$  conditions.

Fig. 5 shows the variation of  $x_{I_{max}}$  with  $\rho_{L1}$  under different  $L_1$  conditions. As shown in Fig. 5, with the increase of  $\rho_{L1}$ ,  $x_{I_{max}}$  increased nonlinearly or first increased nonlinearly and then remained constant. The nonlinear increase of  $x_{I_{max}}$  was caused by the nonlinear EPPD. With the increase of  $L_1$ ,  $x_{I_{max}}$  increased gradually and then decreased gradually. There was an optimal  $L_1$  that made  $x_{I_{max}}$  reach the maximum value, as shown in Fig. 6. In addition, by comparing Fig. 4 and Fig. 6, when  $x_{I_{max}}$  reached its maximum value, it corresponded to the same set of  $[L_1, \rho_{L1}]$ .

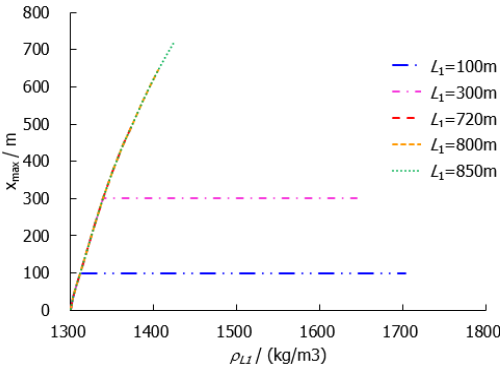


**Fig. 5.** Variation of  $x_{I_{max}}$  with  $\rho_{L1}$  under different  $L_1$  conditions

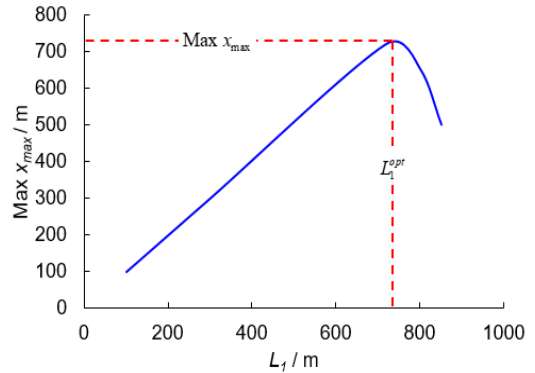


**Fig. 6.** Maximum curve of  $x_{I_{max}}$  under different  $L_1$  conditions

Table 2 shows the final optimization results. As shown in Table 2, after 5 times of adjustment, the drilling depth under the same configuration reached the maximum. As the adjustment number increased, the  $L_i^{opt}$  and  $x_{i_{max}}^{opt}$  decreased gradually while the  $\rho_{Li}^{opt}$  increased gradually.

**Table 2.** The final optimization results.

$N$	$L_i^{opt} / \text{m}$	$\rho_L^{opt} / (\text{kg/m}^3)$	$\text{Max } x_{max} / \text{m}$	$z / \text{m}$
1	720	1420	720	3120
2	510	1546	510	3630
3	300	1638	300	3930
4	190	1692	190	4120
5	80	1722	80	4200

## 5. CONCLUSION

- (1) In this paper, a key parameter optimization model for VGD was established, including optimization objectives and constraints, and the PSO algorithm was adopted to solve the optimization model.
- (2) After each adjustment, there was an optimal set of cyclone separator position and mud density to maximize the single drilling depth.
- (3) The cyclone separator position and mud density needed to be adjusted several times when drilling to the maximum depth under the same well configuration. With the increase of adjustment number, the maximum drilling depth of a single trip decreased gradually, and the distance between the cyclone separator and the drill bit and the mud density increased gradually.

## REFERENCES

- [1].R. Ziegler, P. Ashley, R.F. Malt, R. Stave, K.R. Toftevag, Successful Application of Deepwater Dual Gradient Drilling, IADC/SPE Managed Pressure Drilling and Underbalanced Operations Conference and Exhibition, 17-18 April, 2013 San Antonio, Texas, USA. DOI: <https://doi.org/10.2118/164561-MS>
- [2].J.H. Cohen, R. Stave, E. Hauge, D.O. Molde, Field Trial of Well Control Solutions with a Dual Gradient Drilling System, SPE/IADC Managed Pressure Drilling and Underbalanced Operations Conference & Exhibition, 13-14 April, 2015 Dubai, UAE. DOI: <https://doi.org/10.2118/173822-MS>
- [3].X. Li, D. Gao, Y. Zhou, H. Zhang, A model for extended-reach limit analysis in offshore horizontal drilling based on formation fracture pressure, Journal of Petroleum Science and Engineering 146 (2016): 400-408. DOI: <https://doi.org/10.1016/j.petrol.2016.06.004>
- [4].N.Ø. Stamnes, E. Mjaavatten, and K. Falk. A simplified model for multi-fluid dual gradient drilling operations, IFAC Proceedings Volumes 45 (2012): 211-216. DOI: <https://doi.org/10.3182/20120531-2-NO-4020.00010>
- [5].S. Deng, H. Fan, D. Tian, Y. Liu, Y. Zhou, Z. Wen, W. Ren, Calculation and application of safe mud density window in deepwater shallow layers, Offshore Technology Conference, 2-5 May, 2016 Houston, Texas, USA. DOI: <https://doi.org/10.4043/27063-MS>
- [6].G. Armano, M.R. Farmani, Multiobjective clustering analysis using particle swarm optimization, Expert Systems with Applications 55 (2016): 184-193. DOI: <https://doi.org/10.1016/j.eswa.2016.02.009>
- [7].B. Gürbüz, M. Sezer, Laguerre Polynomial Solutions of a Class of Initial and Boundary Value Problems Arising in Science and Engineering Fields, International Conference on

Computational and Experimental Science and Engineering (ICCESSEN-2015), 14–19 October, 2015 Antalya-Turkey. DOI: 10.12693/APhysPolA.130.382

- [8].A.S. Yüksel, Ş.F. Çankaya, İ.S. Üncü, Design of a Machine Learning Based Predictive Analytics System for Spam Problem, International Conference on Computational and Experimental Science and Engineering (ICCESSEN 2016), 19–24 October, 2016 Antalya-Turkey. DOI: 10.12693/APhysPolA.132.500
- [9].Y. Gür, Digital Fabrication of Mathematical Models via Low-Cost 3D FDM Desktop Printer, International Conference on Computational and Experimental Science and Engineering (ICCESSEN 2014), 25–29 October, 2014 Antalya-Turkey. DOI: 10.12693/APhysPolA.128.B-100

## Investigation of Antiproliferative Effects of AHCC

Arslan Say<sup>1\*</sup>

<sup>1</sup>Amasya University, Sabuncuoğlu Şerefeddin Vocational School of Health Services, Amasya-TURKEY

\*corresponding arslan.say@amasya.edu.tr

### ABSTRACT

An extract of *Lentinula edodes* of the basidiomycete family of fungi, Active Hexose Correlated Compound (AHCC) consists mainly of alpha glucans derived from processed mushroom. The aim of this study is to investigate the antiproliferative effects of AHCC on ovarian cancer, hepatocellular carcinoma (HCC) and human papillomavirus (HPV). Recent studies in animals and humans have suggested that AHCC is a nutritional supplement with significant immunomodulatory effect. It has been observed that AHCC inhibits the proliferation of ovarian cancer cells by inhibiting the suppression of signal transduction and transcription 3 (STAT3) activation, and that AHCC increases survival in liver cancer with systemic and simultaneous chemotherapy. It is claimed that AHCC is good for the cases of persistent HPV even in very recent studies.

**KEYWORDS** - AHCC, Antiproliferative, Ovarian Cancer, Hepatocellular carcinoma, HPV.

### 1. INTRODUCTION

Active Hexose Correlated Compound is a chemical isolated from the Shiitake mushroom. Active Hexose Correlated Compound (AHCC) is an alpha-glucan rich nutritional supplement produced from the mycelia of shiitake (*Lentinula edodes*) of the basidiomycete family of mushrooms. The compound is a subject of research as a potential anti-cancer agent but has not been conclusively found to treat cancer or any other disease, AHCC is a popular alternative medicine in Japan [1,2]. AHCC was first developed in 1987, and has been in use in hospitals, universities, and other institutions around the globe ever since. AHCC modulates the body's innate immunity and supports healthy immune function.

Polysaccharides comprise 40% of the composition of AHCC. These include beta-glucan ( $\beta$ -glucan) and acetylated  $\alpha$ -glucan. Acetylated  $\alpha$ -glucan, produced by culturing the mushroom mycelia, is unique to AHCC. Glucans are polysaccharides and these polysaccharides are known to have immune stimulating effects. In one gram of AHCC, there will be an abundance of saccharides. While saccharides often make one think of sugars such as glucose or sucrose, the type found within AHCC are polysaccharides, such as oligosaccharides, starches, and other combinations of sugar molecules. There are many different types within the polysaccharide group, and their functions within the body vary from type to type. While most mushroom-sourced functional ingredients contain the polysaccharide beta-glucans, AHCC is unique in that it also includes characteristic alpha-glucans [4].

Active Hexose Correlated Compound (AHCC), a member of Phyto-polysaccharide extract, is known to show Biological Response Modifiers (BRM)- like activity. Because Interleukin 12 (IL-12), interferon-  $\gamma$  (IFN- $\gamma$ ) negatively modulate tumor growth we evaluate the possible effect of AHCC on the production of IL-12 and IFN- $\gamma$  as well as NK cell activity which also plays a critical role in cancer immunity [4,5]. Some varieties of polysaccharide are known to have immunomodulatory effects, and AHCC has been shown to modulate the immune system by maintaining optimal NK cell activity, enhancing cytokine production, promoting optimal t-cell and macrophage activity, and increasing the number and activity of dendritic cells. For healthy people AHCC is considered to be useful for health maintenance and helps to prevent infections by aiding in the normal functioning of the immune system. In integrative oncology, research indicates that it may lead to longer post-operative survival, help support patients through chemotherapy, reduce the negative effects of chemotherapy and radiotherapy, and lead to an improvement in quality of life

[6]. AHCC inhibits induction of inflammatory mediators, including inos and TNF-A, in part through inhibition of NF-KB activation in a rat model of liver injury. This findings suggest that AHCC prevents postoperative liver failure after liver resection [8].

A total of 11 RCTs including 6594 patients with AHK were included in the analysis conducted by Niu et al. 1619 patients were treated with placebo and 4975 cases were targeted. The results showed that compared with placebo, sorafenib and ramucirumab, they showed a shorter duration of activity in terms of PR and ORR, and that brivanib was better in ORR. For long-term efficacy, sorafenib and sorafenib + erlotinib treatments show longer OS. Data from the cluster analysis showed that ramucirumab or sorafenib + erlotinib showed relatively better short-term efficacy for the treatment of AHCC [9]. A variety of targeted drug therapies in clinical trials have been proven to be effective for the treatment of hepatocellular carcinoma. In this study, we can observe the short-term and long-term effects of AHCC, one of the different target drugs in the treatment of advanced hepatocellular carcinoma.

In another meta-analysis: clinical trial simulations suggested that, for a patient population with AHCC, axitinib may have a similar efficacy (mOS benefit) to non-SOR AATs, with a low probability of demonstrating superiority to PBO in this phase II trial.

It is observed that AHCC increases median overall survival in patients with hepatocellular carcinoma compared to other drugs [10].

## 2. CONCLUSION

Lentinan is a promising element of chemotherapy that should reduce adverse events during treatment and maintain good quality of life for longer periods of time. In the future, optimal methods of using lentinan should be studied. In addition to academic publications on this subject, many books have been written.

It is certain that AHCC will be available in the years to come to use as a highly effective drug in some cancers.

But nearly all of the research into AHCC has been funded by the manufacturer, which complicates the discussion of currently available results independent research is needed to verify them.

AHCC has been proposed as a treatment for cancer, but research into its effectiveness has produced only uncertain and inconclusive evidence. Detailed research is needed into the pharmacology of AHCC before any recommendation of its use as an adjuvant therapy can be made.

In addition, AHCC has been experimentally proven to be effective in ovarian cancers, even if fully experimental [11,12].

It makes me very sad to hear that very, very serious numbers for this treatment are spent on AHCC extracts.

## REFERENCES

- [1]. AHCC, www.WebMD (Date of access: 01.07.2018)
- [2]. Shah SK, Walker PA, Moore-Olufemi SD, Sundaresan A, Kulkarni AD, Andrassy RJ (2011). "An evidence-based review of a Lentinula edodes mushroom extract as complementary therapy in the surgical oncology patient". JPEN J Parenter Enteral Nutr (Review). 35 (4): 449–58. DOI:10.1177/014860711038068
- [3]. Hyodo I, Amano N, Eguchi K (April 2005). "Nationwide survey on complementary and alternative medicine in cancer patients in Japan". Journal of Clinical Oncology. 23 (12): 2645–54. DOI:10.1200/JCO.2005.04.126
- [4]. Uno, K., Kosuna, K., Sun, B., Fujii, H., Wakame, K., Chikumaru, S., ... & Ueda, Y. (2000). Active hexose correlated compound (AHCC) improves immunological parameters and performance status of patients with solid tumors. BIOTHERAPY-TOKYO-, 14(3), 303-307. DOI:

- [5]. Jiménez-Medina E, Berruguilla E, Romero I, Algarra I, Collado A, Garrido F, Garcia-Lora A. The immunomodulator PSK induces in vitro cytotoxic activity in tumour cell lines via arrest of cell cycle and induction of apoptosis. *BMC Cancer*. 2008;24:8:78. I. Akkurt, private communication, 2014. DOI:10.1186/1471-2407-8-78
- [6]. Oba K, Kobayashi M, Matsui T, Kodera Y, Sakamoto J. Individual patient based meta-analysis of lentinan for unresectable/recurrent gastric cancer. *Anticancer Res*. 2009;29(7):2739-45.
- [7]. Nakatake, R., Tanaka, Y., Ueyama, Y., Miki, H., Ishizaki, M., Matsui, K., ... & Kon, M. (2016). Protective effects of active hexose correlated compound in a rat model of liver injury after hepatectomy. *Functional Foods in Health and Disease*, 6(11), 702-717. DOI: 10.31989 / ffhd.v6i11.305
- [8]. Wakame, K. (1999). Protective effects of active hexose correlated compound (AHCC) on the onset of diabetes induced by streptozotocin in the rat. *BIOMEDICAL RESEARCH-TOKYO*, 20, 145-152.
- [9]. Meng Niu, D. H., Ma, T. C., Chen, X. W., Han, J. H., Sun, J., & Xu, K. (2016). Short-term and long-term efficacy of 7 targeted therapies for the treatment of advanced hepatocellular carcinoma: a network meta-analysis: Efficacy of 7 targeted therapies for AHCC. *Medicine*, 95(49). DOI:10.1097 / MD.0000000000005591
- [10]. Zierhut, M. L., Chen, Y., Pithavala, Y. K., Nickens, D. J., Valota, O., & Amantea, M. A. (2016). Clinical trial simulations from a model-based meta-analysis of studies in patients with advanced hepatocellular carcinoma receiving antiangiogenic therapy. *CPT: Pharmacometrics & Systems Pharmacology*, 5(5), 274-282. DOI:10.1002/psp4.12078
- [11]. Kidd, P. M. (2000). The use of mushroom glucans and proteoglycans in cancer treatment. *Alternative Medicine Review*, 5(1), 4-27.
- [12]. Xu, T., B Beelman, R., & D Lambert, J. (2012). The cancer preventive effects of edible mushrooms. *Anti-Cancer Agents in Medicinal Chemistry (Formerly Current Medicinal Chemistry-Anti-Cancer Agents)*, 12(10), 1255-1263. DOI: 10.2174/187152012803833017

---

## Downhole WOB Measurement Error Owing to Temperature Variation

Chao Wang<sup>1\*</sup>, Gonghui Liu<sup>1,2</sup>, Jun Li<sup>1</sup>, Tao Zhang<sup>3</sup>, Hailong Jiang<sup>1</sup>, Kai Ren<sup>1</sup>

<sup>1</sup> College of Petroleum Engineering, China University of Petroleum (Beijing), Beijing, China

<sup>2</sup> College of Mechanical Engineering and Applied Electronics Technology, Beijing University of Technology, Beijing, China

<sup>3</sup> College of Communication, Beijing Information Science and Technology University, Beijing, China

\* 1062139470@qq.com

### ABSTRACT

The downhole weight on bit (WOB) measurement sensor can produce significant inaccuracies in its readings owing to the effects of temperature variation. To improve the accuracy of downhole WOB measurement, the impacts of temperature variation on WOB measurement were studied via theoretical derivations and simulations. Based on the constitutive equations of thermoelastic materials and the strain theory of strain gauge, the equation of error induced by temperature variation was deduced. Through Matlab simulation, the temperature of the WOB measurement device's inner and outer wall was calculated when drilling. Then the strain of each measuring point was acquired with the help of ANSYS Workbench Simulator. The result showed that the measuring error owing to temperature variation can be ultimately deduced using Wheatstone Bridge. However, the influence of temperature difference between the inner wall and outer wall still could not be removed. The work presented herein can serve as guidance for the downhole WOB measurement.

**KEYWORDS** - Downhole WOB Measurement, Temperature Differential, Wheatstone Bridges, Minimizing Error Method.

### 1. INTRODUCTION

Weight on bit (WOB) is generally recognized as an important parameter in controlling ROP while drilling a well. Properly controlled WOB is necessary to optimize the ROP, which not only reduces the drilling time but also improves bit life. Traditionally, WOB is measured at the surface by comparing the indicated hookload weight to the off-bottom weight of the drill string. However, surface measurement is not always reliable owing to the drag of the drill string on the borehole wall and other factors [1]. Since the 1970s, various systems have been devised for measuring near-bit downhole WOB using strain gauges incorporated into near-bit subs, and transmitting the measured data to the surface in real time [2, 3]. However, the WOB sensor is subjected to significant inaccuracies owing to the effects of temperature [4].

Although temperature increases with depth because of the geothermal gradient, temperature variations may occur within different formations. The annulus temperature and the temperature of the fluid within the drill string are typically different, with the annulus temperature being slightly higher [5]. Considering that the resistance of the strain gauges is dependent not only on the strain but also on the temperature, the change in temperature can lead to inaccuracies in the WOB measurement [6]. To solve the similar problem occurred in the thermal stress determination of thick-wall boiler components, boiler manufacturers determine the thermal stresses based on the temperature measurement in the middle of the wall thickness and near the inner surface of the element. To compensate for the thermal strains induced by temperature variations, Wheatstone bridges are typically employed [2, 7]. This method has achieved significant improvements in the accuracy of down-hole WOB measurement. Temperature sensors are added into the drill collar to further permit temperature compensation [3, 8, 9]. These temperature sensors allow for a steady state temperature correction. But the mechanism and the concrete compensating method are not been elaborated.

Previous compensatory methods have made significant contributions to WOB measurement. To further improve the measurement accuracies, the detailed temperature difference between the inner wall and the outer wall are calculated, and the detailed strain of each measuring point was obtained herein. The proposed methods may be used for achieving improved WOB measurement, and can be significant in improving bit life and ROP.

## 2. IMPACT OF TEMPERATURE VARIATIONS ON WOB MEASUREMENT

### 2.1. Strain errors induced by the change in temperature

The WOB measurement currently is primarily based on the strain theory of strain gauges. Fig. 1a shows the three-dimensional view of the used WOB measuring sub herein. Fig. 1b shows an elevation view into the pocket, with the cap removed, showing the orientation of the strain gauges. Fig. 1c shows an isometric view of the pocket. Owing to temperature variations within different formations, the WOB measuring apparatus and its inside strain gauge temperature varies with the depth of the drill bit.

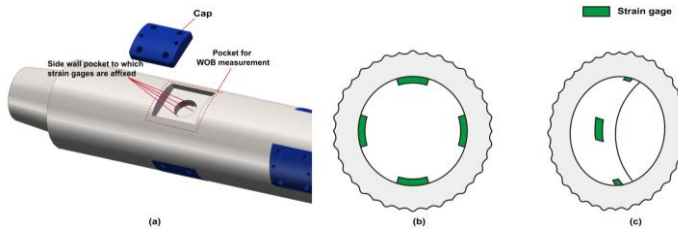


**Fig. 1.** Views of WOB measuring sub and the side wall pocket where strain gauges are affixed

The constitutive equations of thermo-elastic WOB measuring apparatus can be expressed as [10]

$$E = \frac{1}{E} [(1 + \mu)T - \mu\Theta I] + \alpha\Delta T \quad (1)$$

In the cylindrical coordinate system, the expanded formula of Eq. (1) is as follows:

$$\begin{cases} \varepsilon_r = \frac{1}{E} [\sigma_r - \mu(\sigma_z + \sigma_\theta)] + \frac{1}{E} \left[ \frac{E}{1-2\mu} \alpha\Delta T - \mu \left( \frac{E}{1-2\mu} \alpha\Delta T + \frac{E}{1-2\mu} \alpha\Delta T \right) \right] \\ \varepsilon_\theta = \frac{1}{E} [\sigma_\theta - \mu(\sigma_z + \sigma_r)] + \frac{1}{E} \left[ \frac{E}{1-2\mu} \alpha\Delta T - \mu \left( \frac{E}{1-2\mu} \alpha\Delta T + \frac{E}{1-2\mu} \alpha\Delta T \right) \right] \\ \varepsilon_z = \frac{1}{E} [\sigma_z - \mu(\sigma_r + \sigma_\theta)] + \frac{1}{E} \left[ \frac{E}{1-2\mu} \alpha\Delta T - \mu \left( \frac{E}{1-2\mu} \alpha\Delta T + \frac{E}{1-2\mu} \alpha\Delta T \right) \right] \end{cases} \quad (2)$$

From Eq. (2), it can be deduced that the normal strain of each point is equal to the sum of strain caused by external loads (e.g., the apparatus's inner hydraulic pressure, annular pressure, and axial force), and strain caused by temperature differential, which is illustrated in Fig. 2.

Fig. 2a shows the deformation of the pocket under the action of external loads and temperature differential. Fig. 2b is the deformation only under the action of the same external loads. Fig. 2c shows the deformation only under the action of the same temperature differential.



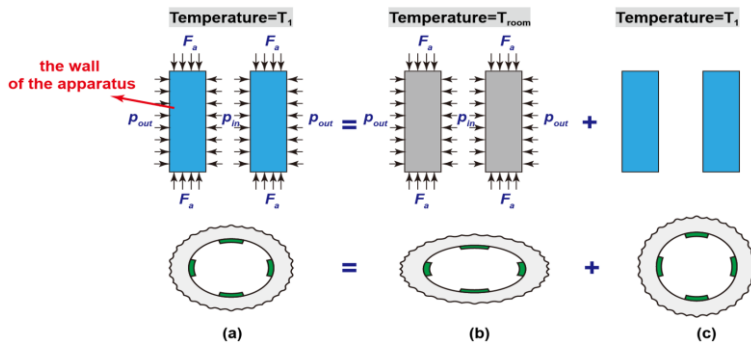


**Fig. 2.** Forces acted on WOB measuring apparatus and deformation of the pocket where strain gauges are affixed

Considering that the relationship between the deformation of the gauge strain and external loads is obtained when the temperature is room temperature ( $T_{room}$ ), it is necessary to eliminate the gauge strain owing to temperature differential, before acquiring the axial force. The apparent strain induced by the variations in temperature can be analyzed as follows.

The resistance of the strain gauge is the function of the gauge strain and temperature, and this function can be expressed as [11]

$$R = f(T_s, l) \quad (3)$$

The gauge strain resistance change rate can be defined as

$$\frac{\Delta R}{R} = \alpha_R \Delta T_s + K \Delta e \quad (4)$$

where  $\alpha_R$  is the resistance temperature coefficient of strain gauge's sensitive grid.  $K$  is the gauge factor.  $\alpha_R$  and  $K$  can be further expressed as

$$\begin{cases} \alpha_R = \frac{\partial R}{\partial T_s} / R \\ K = \frac{\partial R}{\partial e} / R \end{cases} \quad (5)$$

Considering that the strain gauges are attached to the substrate,  $\Delta e$  can be expressed as

$$\Delta e = (\alpha_s - \alpha_g) \Delta T_s + \Delta \varepsilon_\sigma \quad (6)$$

Substituting  $\Delta e$  of Eq. (6) into Eq. (4), the resistance change rate can be further expressed as

$$\frac{\Delta R}{R} = [\alpha_R \Delta T_s + K (\alpha_s - \alpha_g) \Delta T_s] + K \Delta \varepsilon_\sigma \quad (7)$$

From Eq. (7), it can be deduced that the root cause of the measuring error is the generation of  $[\alpha_R \Delta T_s + K (\alpha_s - \alpha_g) \Delta T_s]$ .

2.2. Simulation of temperature and strain

The formation’s temperature is higher than drilling fluid’s temperature with the same well depth. Heat exchange among formation, annulus drilling fluid, drilling tools and inner drilling fluid occurs when drilling. From the heat transfer direction shown in Fig. 3, the annulus drilling fluid temperature is higher than the inner drilling fluid temperature. Thus the outer wall’s temperature of measuring tool is higher than the inner wall’s temperature.

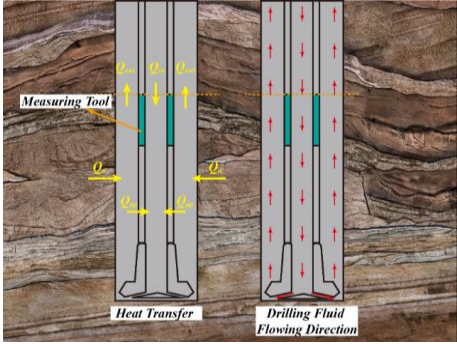


Fig. 3. Heat transfer and drilling fluid flowing direction

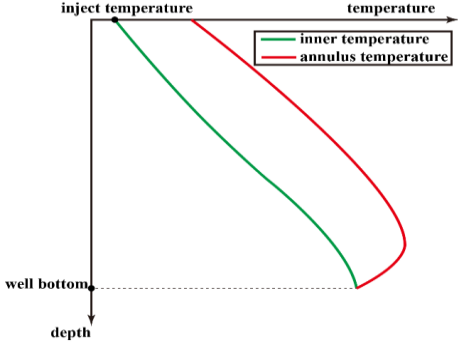


Fig. 4. Typical temperature profile inside the drilling tools and annulus pressure profile

The typical pressure profile inside the drilling tools and annulus pressure profile with the well depth is shown as Fig. 4. The boundary condition at the well bottom can be expressed as

$$T_{annulus} = T_{inner} \tag{8}$$

Considering that the formation’s temperature is higher than the drilling fluid’s temperature, the temperature gap between formation temperature and annulus temperature will shrink and the temperature gap between inner temperature and annulus temperature will widen. However, when the influence of temperature difference between formation and annular is bigger than the influence of temperature difference between inner drilling fluid and annulus fluid, temperature gap between inner temperature and annulus temperature will shrink. So from well bottom to well top, the temperature difference between the inner drilling fluid and annulus drilling fluid firstly increases and then decreases. The measuring tool is usually installed near the bit. The shorter the distance between the measuring tool and bit is, the less temperature difference between the inner drilling fluid and the annulus drilling fluid is.

Now calculate the concrete temperature difference using a well as an example. The well’s detailed information is shown in Table. 1.

Table 1. Well information

Parameter	Value	Parameter	Value
Inlet temperature, °C	30	Specific heat of formation, J/(kg °C)	873
Mud density, kg/m3	1560	Thermal conductivity of formation, W/(m °C)	2.25
Specific heat of mud, J/(kg °C)	2399	Diameter of borehole, mm	215.9
Thermal conductivity of mud, W/(m °C)	14	Well depth, m	5000
Geothermal gradient, °C/100m	3		

The calculated result is shown in Fig. 5.

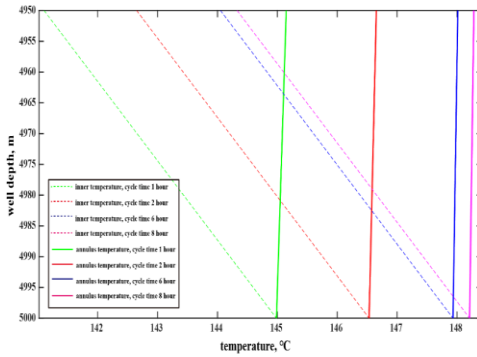


Fig. 5. Temperature profile near bit

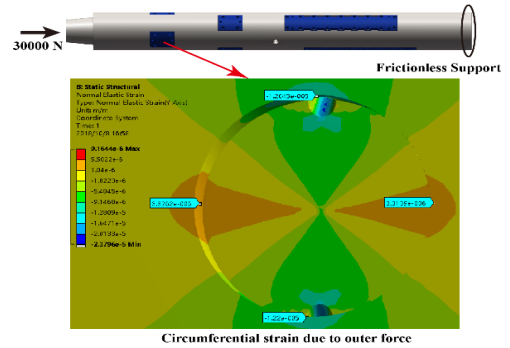


Fig. 6. Group 1 experiment result

If the distance between measuring tool and bit is from 10 m to 50 m, the difference between inner drilling fluid and annulus drilling fluid is 0.8 °C to 4 °C from Fig. 6.

To study temperature's influence to each measuring point, three groups of finite element numerical simulation were carried out using ANSYS Workbench simulator.

Group 1: One end of the measuring tool is fixed and the other end is pressurized with 30000 N. The simulated result is shown as Fig. 6.

Group 2: One end of the measuring tool is fixed. The inner and the outer wall's temperature are 140 °C and 140.8 °C separately. And there is no other force acted on the measuring tool. The simulated result is shown as Fig. 7.

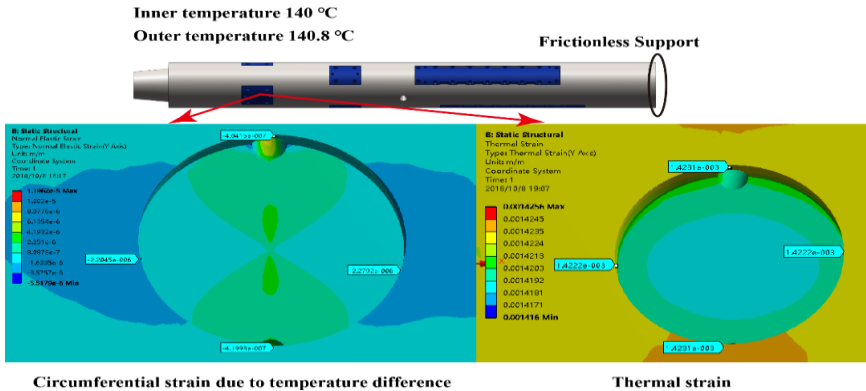


Fig. 7. Group 2 experiment result

**Group 3:** One end of the measuring tool is fixed. The inner and the outer wall's temperature are 140 °C and 144 °C separately. And there is no other force acted on the measuring tool. The simulated result is shown as **Fig. 8**. It is clear that the thermal strain accounts for most of the total strain from Fig. 6 to Fig. 8. Moreover, the circumferential strain due to temperature difference will increase to the same magnitude of circumferential strain due to outer force with the temperature difference increasing. It is necessary to separate the circumferential strain due to temperature difference and thermal strain from the total strain to obtain the outer force.

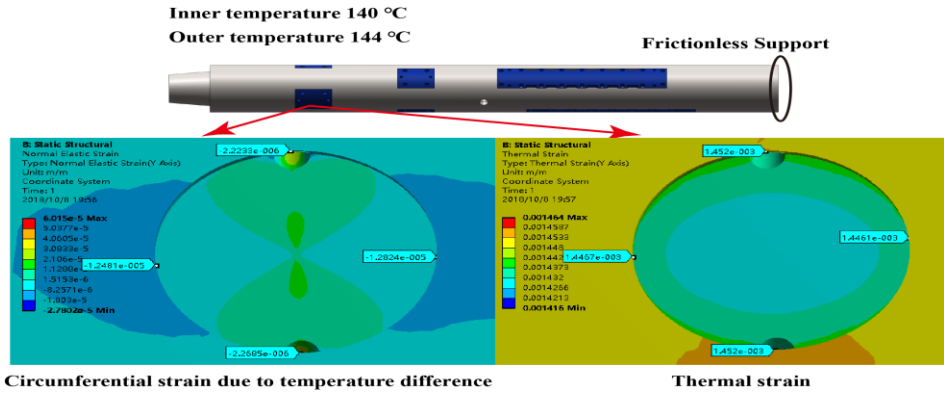


Fig. 8. Group 3 experiment result

### 3. METHOD TO COMPENSATE THERMAL STRAIN

The typical and effective method to compensate for temperature difference is electrically coupling the strain gauges to form a Wheatstone bridge. In the prior works of [3, 7], uniaxial strain gauges were coupled to form the Wheatstone bridge, as shown in Fig. 9.

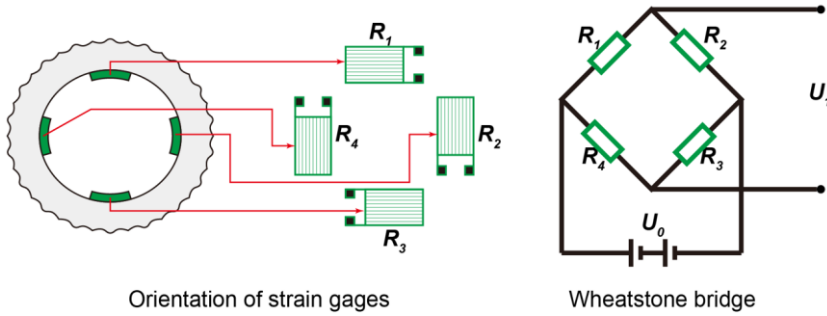


Fig. 9. Uniaxial strain gauges form Wheatstone bridge

The voltage output ( $U_1$ ) of the Wheatstone bridge is

$$U_1 = \frac{U_0}{4} \left( \frac{\Delta R_1}{R_1} - \frac{\Delta R_2}{R_2} + \frac{\Delta R_3}{R_3} - \frac{\Delta R_4}{R_4} \right) \quad (9)$$

where  $R_i$  ( $i=1, 2, 3, 4$ ) is the initial resistance of every strain gauge, and  $R_1=R_2=R_3=R_4$ .  $U_0$  is the input voltage.  $\Delta R_i$  ( $i=1, 2, 3, 4$ ) is the resistance change of the  $i^{\text{th}}$  strain gauge.

Substituting Eq. (7) into Eq. (9) yields

$$U_1 = \frac{U_0}{4} \left\{ \left[ \alpha_R + K(\alpha_s - \alpha_g) \right] \sum_{i=1}^4 (-1)^{i+1} \Delta T_{si} + K \sum_{i=1}^4 (-1)^{i+1} \Delta \varepsilon_{oi} \right\} \quad (10)$$

where  $\Delta T_{si}$  is the temperature change in the  $i^{\text{th}}$  strain gauge.  $\Delta \varepsilon_{oi}$  is the strain of the substrate where the  $i^{\text{th}}$  strain gauge is affixed.

From Eq. (10), it can be deduced that the strain errors caused by the change in temperature can be completely removed if the position of each strain gauge pasted on the substrate surface is the same. However, the temperature of each gauge cannot be the same because of the structure of the measuring apparatus. Moreover, the circumferential strain due to temperature difference between

inner wall and outer wall still could not be eliminated and its magnitude is the same as strain due to outer force.

#### 4. CONCLUSION

We herein deduced the strain errors induced by the change in temperature and calculated the concrete temperature change in measuring tool when drilling. To acquire the detailed strain of each measuring point when temperature changed, we conducted three groups of simulation with the help of ANSYS Workbench Simulator. The results showed that the thermal strain accounts for most of the total strain. Moreover, the circumferential strain due to temperature difference will increase to the same magnitude of circumferential strain due to outer force with the temperature difference increasing. Using Wheastone Bridge can ultimately eliminate the measuring error owing to thermal strain, but the influence of temperature difference between the inner wall and outer wall still could not be removed.

#### REFERENCES

- [1]. Boucher, M.L., A. Schen, et al. Apparatus for weight on bit measurements, and methods of using same. 2005, Google Patents.
- [2]. Das, P.K.,H. Song. Load cells for sensing weight and torque on a drill bit while drilling a well bore. 1995, Google Patents.
- [3]. Wassell, M.E. Apparatus for measuring weight and torque on drill bit operating in a well. 2003, Google Patents.
- [4]. Blanchette, C.,D. Getzlaf. New Downhole Data Clarifies Coiled Tubing Behavior in Horizontal Wells, in SPE/CSUR Unconventional Resources Conference. 2015, Society of Petroleum Engineers: Calgary, Alberta, Canada. DOI: 10.2118/175974-MS
- [5]. Wassell, M.E., M.E. Cobern,C.A. Perry. Apparatus for measuring bending on a drill bit operating in a well. 2013, Google Patents.
- [6]. Hutchinson, M. Apparatus and method for determining axial forces on a drill string during underground drilling. 2014, Google Patents.
- [7]. Tanguy, D.R.,L.J. Leising. Weight-on-bit and torque measuring apparatus. 1982, Google Patents.
- [8]. Wachtler, W.J.,T.M. Yang. MWD tool for measuring weight and torque on bit. 1986, Google Patents.
- [9]. Woloson, S.E.,D.A. Jones. Apparatus for measuring downhole drilling efficiency parameters. 2001, Google Patents.
- [10]. Ugural, A.C.,S.K. Fenster. Advanced mechanics of materials and applied elasticity. 2012: Prentice Hall. 681-681.
- [11]. Richards, W.L. A new correction technique for strain-gage measurements acquired in transient-temperature environments. 1996.

## Use of titanium oxide in phenol degradation of paper

**Dali-Youcef Zohra**

*National polytechnic school, Department of Chemistry, ORAN ALGERIA  
Zohra\_dali2002@yahoo.fr*

### ABSTRACT

With the growth and development of the industrial sector, the problem of pollution remains the subject of interest for many scientists, since it affects several vital sectors. In this context, titanium oxide is used for the degradation of an organic compound phenol.

The experimental study showed that pH and temperature play an important role in the kinetics of photocatalytic degradation of the phenol pollutant by improving the degradation yield. We reach the maximum degradation rate of phenol: 86.84% which is obtained for the pH = 6, thus for an acid reaction medium. The use of titanium oxide alone, chosen as a catalyst, has shown that the rate of phenol degradation increases with the increase in the TiO<sub>2</sub> catalyst mass, the decrease in the volume and the decrease in the initial concentration of solution of the phenol and in the case of an acidic reaction medium.

**KEYWORDS-** *degradation, Titanium dioxide, phenol*

### 1. INTRODUCTION

Waters of surface can introduce an important load of phenols owed to industrial rejections (tannery, refineries, pesticides, industry of pasta, paper and wood etc) giving a characteristic taste in treated water. It is important to reduce their concentration to avoid the training of organo-halogen in general toxic compounds [1-4].

Techniques based on the adsorption come to supplement the course of study of treatment of common waters. The adsorption on porous materials finds its application in several domains, such as extraction, purgation and cleanup. Other techniques such as advanced techniques of oxidation (advanced oxidation process AOP) are nowadays applied for mineralization in aqueous middle of the toxic organic molecules in relation to the man and in environment. They are based on the generation and the use of a very strong oxidizer which is the hydroxyl radical. This last can be produced by different techniques: chemical, photochemical biological, electrochemical, etc [5-7].

In this work, we are interested in a chemical pollutant, phenol, which is used in various synthesis processes and thus its presence in industrial effluents can cause various health problems.

The treatment of a water polluted by phenol is made by titanium oxide TiO<sub>2</sub>, a wastewater treatment process with high levels of toxic compounds and low biodegradability [8-15]. Titanium dioxide is a chemically and biologically inert, non-toxic, inexpensive, and above all insensitive to photochemical corrosion, we have chosen as a catalyst for the degradation of phenol.

The experimental study of phenol degradation has shown that pH and temperature play an important role in the kinetics of photocatalytic degradation of the phenol pollutant by improving the degradation efficiency. The study of the effect of temperature shows a linear relationship between the increase in temperature and the increase in the rate of phenol degradation.

### 2. MATERIAL AND METHOD

#### 2.1. Batch Adsorption Studies

In flasks a mass  $m$  (g) of the catalyst TiO<sub>2</sub> is dispersed in a volume  $V$  (ml) of a solution of phenol of initial concentration  $C_i$  (mg / l). The suspension is kept under constant stirring for a fixed time (min), then centrifuged and the supernatant is analyzed at a wavelength close to 270 nm, using a Perkin Lamda 25 spectrophotometer.

After analysis of the filtrates obtained, the equilibrium concentration ( $C_e$ ) and consequently the corresponding reduction ratio:  $R\% = \frac{C_i - C_e}{C_i} \times 100$  is obtained  $C_e$  (mg / l), the concentration of phenol in the supernatant and  $C_i$ (mg / l) the initial concentration of the phenol solution .

## 2.2. Mass effect of $TiO_2$

To varying masses of  $TiO_2$  catalyst (0.2, 0.5 and 1 g) are added to 100 ml of phenol solution of initial concentration:  $C_i = 300$  mg / L, with stirring for 120 minutes at 500 rpm and at room temperature  $20^\circ C$  . The evolution of the degradation rate of phenol as a function of the  $TiO_2$  mass is given in Figure 1. Figure indicate an increase in the rate of phenol degradation as a function of the increase in  $TiO_2$  catalyst mass. The maximum values of the degradation rate: 66.63% are obtained for a mass of  $TiO_2$  equal to 1g for a maximum of 120 minutes. The quantities of phenol fixed must be consistent with the adsorbent doses in solution to ensure an equivalent number of adsorption sites. The number of adsorption sites increases with the surface of the adsorbent and thus the adsorption rate becomes maximum.

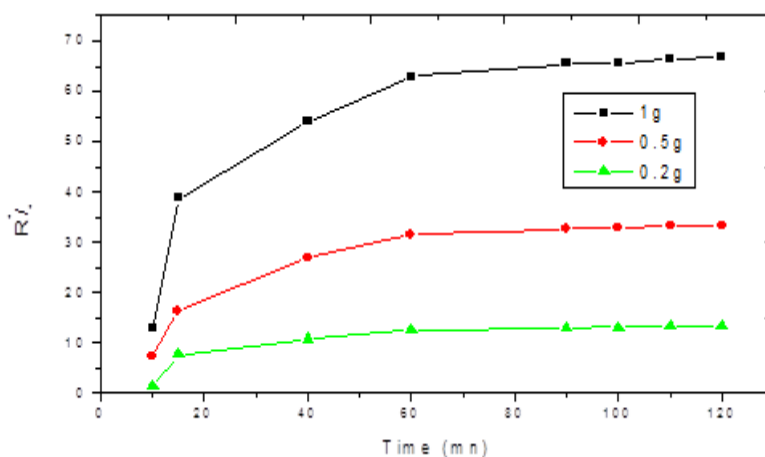


**Figure1.** Evolution of the phenol degradation as a function of the amount of  $TiO_2$ .  $C_i = 300$ mg / L.

## 2.3. Influence of the initial concentration of phenol

100 ml of phenol of different initial concentrations ( $C_i = 0.1, 0.3, 0.4, 0.6, 0.8, 0.9$  and  $1$  g / l) are added to 1 g of titanium oxide at room temperature and with stirring of 500 rpm for a time 120mn. The results of the degradation kinetics of phenol are shown in figure 2. The graph is of type I and corresponds to the microporous materials with the formation of one or two molecular monolayers, due to the steric hindrance effect. The graph indicates that the highest 70.08% phenol degradation rate is obtained for the lowest initial concentration (0.1g / L), which is consistent since the increase in the initial phenol concentration saturates the surface of the catalyst and also decreases its effectiveness.

## 2.4. Influence of pH

In order to verify the effect of the pH on the degradation of the phenol, the following mixtures are prepared: to flasks containing 100 ml of phenol of initial concentration 400 mg / L, is added to 0.2 g of  $TiO_2$  at room temperature and with stirring 500 rpm. The pH of the mixture is adjusted by the addition of a base which is NaOH (1N), in the case of increasing the pH and in the contrary case by the addition of acid,  $H_3PO_4$  (0.5N) (fig.3).

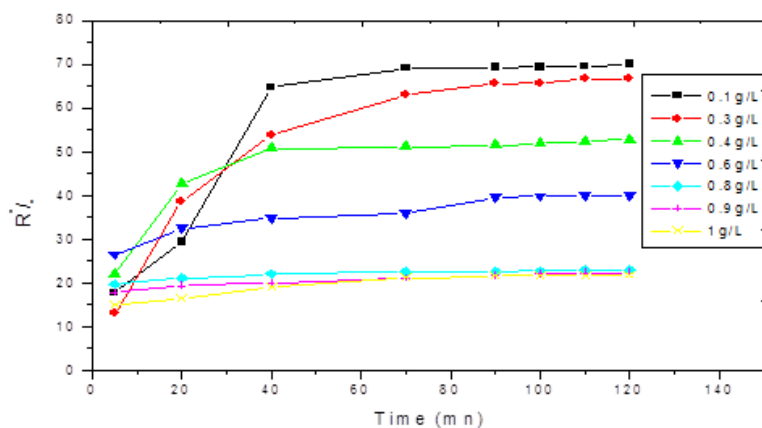


**Figure 2.** Influence of the initial concentration on the rate of phenol removal as a function of time by  $\text{TiO}_2$ .

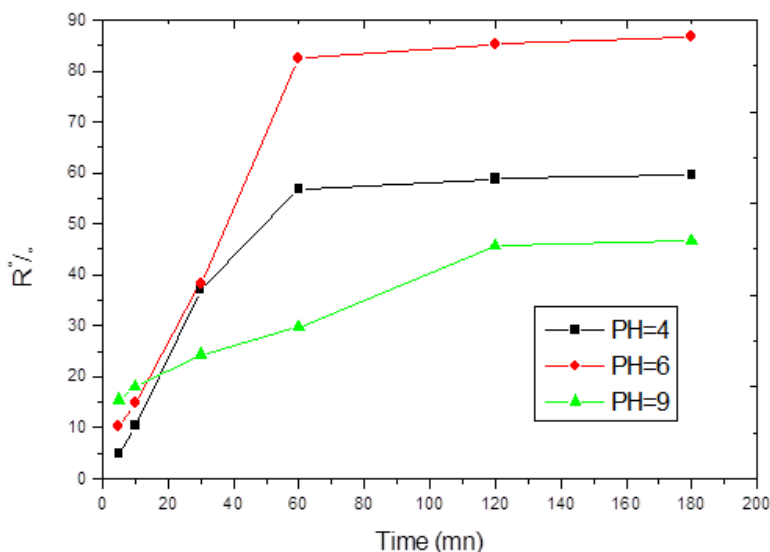


**Figure 3.** Influence of pH in phenol degradation.

Figure 3 indicates rapid phenol degradation from time 60 minutes we reach the maximum degradation rate of phenol: 86.84% is obtained for  $\text{pH} = 6$ , therefore for an acidic reaction medium.

in acidic medium the departure of an electron from the solid to a molecule of  $\text{H}_2\text{O}$ , adsorbed at the interface, leads us to the formation of  $\text{OH}^\cdot$  radicals or  $\text{HO}_2^\cdot$ , leading to oxidation and decomposition of the organic compound, phenol.

## 2.5. Influence of temperature on phenol degradation

0.2 g of  $\text{TiO}_2$  and 5 drops of ethanol are introduced into 250 ml flasks each containing 100 ml of phenol solution of concentration 400 mg / L, the latter being placed in a water bath at the required variable temperatures: 25, 40 and 60 ° C, with constant stirring for 180 minutes. The same



experiment is repeated by adding phosphoric acid to adjust the pH to 6 (fig.4). The graph shows that the rate of degradation increases with increasing temperature. In the case of the addition of phosphoric acid and at 60 °C, the degradation rate becomes 87.16%.

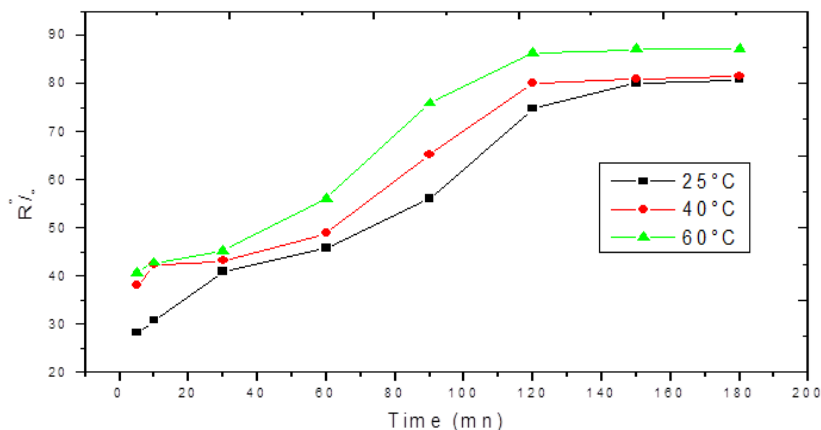


**Figure 4 .** Influence of temperature on the phenol degradation reaction, pH=6.

## 2.6. Adsorption isotherm for phenol

The static adsorption isotherm of phenol was determined in 100 mL of phenol solution (0,1–0,8 mg/L) under 500 tr/mn stirring at 25°C for 120 mn.

To explore the adsorption mechanism, the isotherm results were fitted against the Langmuir and Freundlich models.

The Langmuir monolayer adsorption equation can be expressed as

$$\frac{C_e}{\frac{X}{m}} = \frac{1}{Q_0 \cdot b} + \frac{C_e}{Q_0} \quad (1)$$

C<sub>e</sub>: equilibrium concentration of the solute (mg / l)

X: amount of adsorbed solute (adsorbate) (mg)

m: mass of adsorbent (g)

Q<sub>0</sub> and b: constant

The Freundlich adsorption equation can be expressed as,

$$\log \frac{X}{m} = \log K + \frac{1}{n} \log C_e \quad (2)$$

K and n: constant

Table 1 summarizes the experimental results and reveals that the best description of the adsorption phenomenon is obtained with the Langmuir model which gives the best coefficient of correlation R<sub>2</sub> = 0.9749. The maximum capacity of phenol fixation is 26.759 mg / g.

**Table1.** Values of isothermal parameters of phenol fixation on TiO<sub>2</sub>

Modele	Langmuir			Freundlich		
settings	R <sup>2</sup>	b	Qo (mg/g)	R <sup>2</sup>	n	K
values	0.9914	0.0118	26.925	0.5932	0.4385	0.533

### 3. CONCLUSION

The study showed the enormous potential of titanium oxide TiO<sub>2</sub> for phenol removal found in water and wastewater. The following conclusions are drawn from the above results:

- The equilibrium time for the adsorption of phenol on the adsorbent titanium oxide TiO<sub>2</sub> in the present study from aqueous solutions is found to be 70 minutes.
- The increase in the initial phenol concentration saturates the surface of the catalyst and also decreases its effectiveness.
- the maximum degradation rate of phenol: 86.84% is obtained for pH = 6.
- The rate of degradation increases with increasing temperature, at 60 ° C, the degradation rate becomes 87.16%.
- The adsorption process of phenol can be described by Langmuir and Freundlich isotherm models. However, Langmuir isotherm model shows a better agreement with the equilibrium data.

### REFERENCES

- [1]. F.Belaib, A.H.Menai, M. Bencheikh. Elimination of phenol by adsorption onto mineral/polyaniline. Energy Procedia 18 (2012) 1254 – 1260
- [2]. S.Chraibi, H. Moussout, F. Boukhli, H. Ahla, M. Alami. Utilization of calcined eggshell waste as an adsorbent for the removal of phenol from aqueous solution. Journal of Encapsulation and Adsorption Sciences (2016) 6, 132-146
- [3]. B. Razika, B. Abbes, Ch. Messaoud, K. Souf. Phenol and benzoic acid degradation by Pseudomonas aeruginosa. Journal of Water Resource and Protection (2010) 2, 788-791
- [4]. M. Mohamed, A. Aburas. Removal of phenol using spore Forming Bacillus ABO11 isolated from waste water treatment Plant” Advances in Microbiology (2016) 6, 898-908
- [5]. W. Duan, F. Meng, Y. Lin, G. Wang. Toxicological effects of phenol on four marine microalgae . Environmental Toxicology and Pharmacology (2017) 52, 170-176
- [6]. F. Belaib, A.H. Menai, M. Bencheikh, Lehocine. Elimination of Phenol By Adsorption Onto Mineral / Polyaniline Composite Solid Support (2012) 18, 1254-1260.
- [7]. N. V. Pradeep, S. Anupama, K. Navya, H. N. Shalini, M. Idris” Biological removal of phenol from wastewaters: a mini review” Applied Water Science (2015) 5, 105–112.
- [8]. Q. Zhang, S. Ye, X. Song, S. Luo . Photocatalyst based on TiO<sub>2</sub> nanotube arrays co-decorated with CdS quantum dots and reduced graphene oxide irradiated by γ rays for effective degradation of ethylene. Applied Surface Science (2018) 2, 139-141.
- [9]. S.-y. Ye, S.-w. Shen, L.-m. Ye, X.-l. Song, S.-c. Luo, Enhancement of the photoelectrocatalytic activity of TiO<sub>2</sub>/ACF for ethylene removal by Ag nanoparticles synthesized by γ-ray radiolysis, Materials Science in Semiconductor Processing, (2014) 27, 397-403.

- [10]. Wei Teng, Youmei Wang, Huihui Huang, Xinyong Li, Yubin Tang. Enhanced photoelectrochemical performance of MoS<sub>2</sub> nanobelts-loaded TiO<sub>2</sub> nanotube arrays by photo-assisted electrodeposition. *Applied Surface Science* (2017) 06, .297- 322.
- [11]. W. Wang, F. Li, D. Zhang, D.Y.C. Leung, G. Li.; Photoelectrocatalytic hydrogen generation [12]. and simultaneous degradation of organic pollutant via CdSe/TiO<sub>2</sub> nanotube arrays, *Appl. Surf. Sci.*(2016) 362, 490-497.
- [13]. L. Zheng, S. Han, H. Liu, P. Yu, X. Fang,.; Hierarchical MoS<sub>2</sub> Nanosheet TiO<sub>2</sub> Nanotube [14]. Array Composites with Enhanced Photocatalytic and Photocurrent Performances, *Small, Appl. Surf. Sci.*(2016) 12, 1527-1536.
- [15]. D. Wang, Y. Xu, F. Sun, Q. Zhang, P. Wang, X. Wang,.;Enhanced photocatalytic activity of [16]. TiO<sub>2</sub> under sunlight by MoS<sub>2</sub> nanodots modification, *Appl. Surf. Sci.* (2016) 377, 221-227.
- [17]. C. Liu, L. Wang, Y. Tang, S. Luo, Y. Liu, S. Zhang, Y. Zeng, Y. Xu,.; Vertical single or [18]. few-layer MoS<sub>2</sub> nanosheets rooting into TiO<sub>2</sub> nanofibers for highly efficient photocatalytic [19]. hydrogen evolution, *Appl. Catal.* (2015) 164, 1-9.
- [20]. M. Shen, Z. Yan, L. Yang, P. Du, J. Zhang, B. Xiang,.; MoS<sub>2</sub> nanosheet/TiO<sub>2</sub> nanowire hybrid nanostructures for enhanced visible-light photocatalytic activities, *Chem. Commun.* (2014) 50, 15447-15449.

# A Comprehensive Analysis of Compound Impactor Based on Mixed Flow Impeller Drive

Xiaosong Wen<sup>1</sup>, Gonghui Liu<sup>2\*</sup>, Jun Li<sup>1</sup>, Chunqing Zha<sup>2</sup> and Xueli Guo<sup>1</sup>

<sup>1</sup> China University of Petroleum Beijing, Beijing, CHINA

<sup>2</sup> Beijing University of Technology, Beijing, CHINA

\*Ivan\_cup@163.com

## ABSTRACT

Existing torsion impactor used in the oil field has obvious defects, especially the failure to effectively enhance bit weight. This paper elaborates a brand newly designed compound impactor, in addition, the hydraulic performance of drive unit-the mixed flow impeller is respectively analysed to demonstrate the feasibility of the impactor.

This innovative scheme owns an integrated motion just using one independent mechanical device, resulting in an impact loading on the bit both in the axial and circumferential simultaneously. On the condition of usage of multi-stages turbine, the accessibility of integrated motion has been confirmed by experimental study. Furthermore, numerical simulation is investigated to reveal the relationship between the output torque and relative factors, including the flow rate, rotation velocity, and the incident angle of the guide wheel. Numerical results indicate that a single mixed flow impeller can achieve equivalent output torque with a smaller size in comparison to a four-stage turbine. Compared with earlier single axial vibrator and current torsion impactor driven by a screw or turbine, the tool provides a revolutionary method to prevent stick-slip vibration and realize a high-frequency compound shock on rocks, which is supposed to increase the rock fragmentation efficiency. Moreover, the replacement of multi-stages turbines with a new power device-single mixed flow impeller, leads to the reduction of the tool length and an equivalent output torque.

**KEYWORDS:** *compound impactor, stick-slip vibration, mixed flow impeller, CFD*

## 1. INTRODUCTION

In current exploitation of deep wells, the combination usage of downhole power instruments and polycrystalline diamond compact (PDC) drill bit is widely applied to high-efficiency rock cutting. Due to the considerably complex geological conditions of deep formations, the hardness and abrasive resistance of rocks get an obviously promote, leading to a further limitation to maintaining a stable rate of penetration (ROP), especially in areas which geological cross-sections are extremely heterogeneous. The reasons affecting the rock breaking with a high efficiency in deep formations are primarily attributed to two aspects: the first one is the difficulty in exerting sufficient weight on bit (WOB). With the extension of wellbore, the total stiffness of drilling strings decreases gradually and the friction dissipation between the strings and the wellbore wall increase remarkably. Meanwhile, Gravity accumulation effects are prone to occur in partial strings where the dog leg degree is relatively serious. Besides, drilling strings located in a long horizontal section are more likely to present in a posture of “lying” or “reclining” on the wall along with borehole, resulting in a direct increase of frictional resistance and other derivative problems such as the difficulty of carrying rock fragments from the hole. All the factors mentioned above will inevitably relieve the weight on bit. Secondly, the stick-slip vibration of bit is supposed to prominently restrict the realization of achieving an expected penetration rate, especially in the soft and hard interbedded formation where the bit suffers the most severe impact load. As study and literatures reported, the stick-slip vibration which is an alternate appearance of stick and slip phase on the bit, produces a periodical fluctuation on the torque and weight and ultimately results in an immediate change of torque acting on rocks. Current monitoring data detected by surface logging

system or bottom-hole measurement while drilling (MWD) has confirmed the remarkable change in torque (shown in Fig.1).

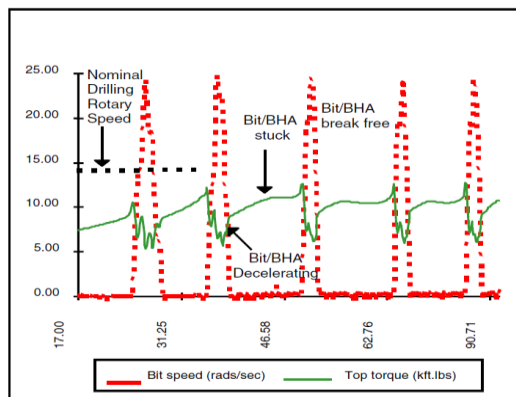


**Fig. 1.** The detected data of stick-slip vibration

In terms of slip phase, the rotational speed of PDC bit has a monotonous deceleration, coupled with a gradual rise on the torque of PDC bit. As the rotation velocity reduce further to the minimum, the torque can accumulate to its maximum magnitude and a sudden stick phase emerges. The nominal torque, required to free the PDC bit again, is approximately equal to the maximum magnitude of accumulation torque but with an opposite direction. Once an active torque exceeded the nominal torque, the subsequent rotation velocity is more about 4-10 times than normal rotational speed. Because of the effect of friction, the torque will drop to the level required to rotate the bit and the slip phenomenon arises again. Also concluded from Fig.1, The data curve between the bit speed and the torque keeps a negative correlation. Numerous literatures have revealed that the danger of stick-slip vibration includes: severe wear of the drill bit, permanent failure of the bottom measurement tool, and poor drilling speed [1-3]. At the same time, stick-slip vibration will also lead to other types of vibration, such as irregular lateral vibration and periodic axial vibration. Therefore, controlling the slip-stick problem and its effects on bit is essentially in modern drilling system.

In response to the above challenges in industry, various optimization strategies and methods [4-10] imposed in actual drilling operations have verified that the most direct and effective method is to add a tool nipple at the position near the bit. The added short tool is hoped to help improve the stress conditions between PDC bit and the rock formation, to alleviate the fluctuation amplitude of WOB or torsion on bit (TOB), to weaken or even eliminate the stick-slip effect and ultimately increase the ROP without changing the essential structure existed in bottom-hole assembly (BHA). All the commercialized tools can be divided into two categories: One is called axial impactor which realizes the reciprocating axial impact on the drill bit and has wildly used in earlier oil field exploration. The other one named torsional impactor which mainly complete the periodic torsional strike on the bit has been gradually arranged for the deep drilling in recent years. However, both these two categories of tools exposed their own obvious deficiencies in the process of application, such as logging signal interface and lower impact energy.

## 2. COMPOUND IMPACT TOOL

Combined with the advantages of axial impactor and torsional impactor, a prototype of compound impact tool was published to fulfil a reciprocating strike movement containing both in axial and circumferential orientation. After that, some preliminary studies were carried out to verify the

possibility. The overall view of this newly brand design could be seen in Fig. 2, and it is mainly consist of three components:

- ① Mixed flow impeller drive unit providing sufficient torque for commutator within a certain frequency.

② Compound strike unit within a compound oscillation cylinder, hydraulic hammer, reverse mechanism, throttle valve, etc.

③ A bit joint to realize the transmitting of drilling torque.

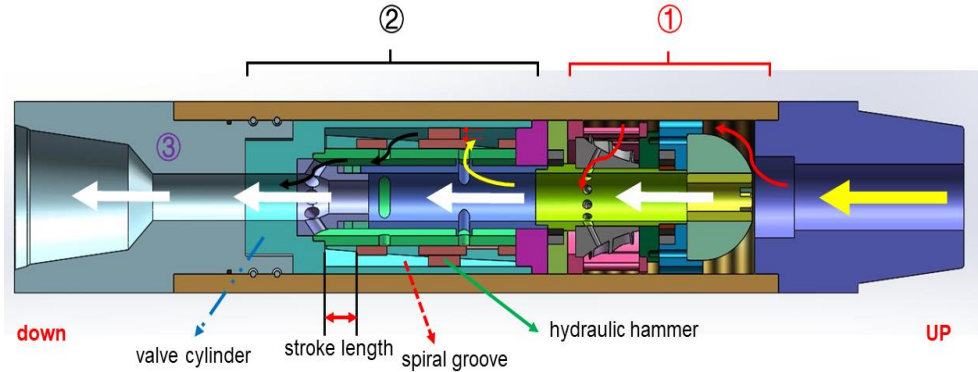


Fig. 2. The section view of compound impactor prototype

2.1. Working principle

The principle of the new composite impact tool is that a demanded proportional hydraulic energy of the drilling fluid was converted into the kinetic energy of the hammer by means of a compound strike. Among all the components, the drilling fluid reversing mechanism producing an alternative high and low hydraulic chamber at a constant frequency plays a crucial role in the performance of the reciprocating motion of the hammer. Also as shown in Fig.2, continuous high pressure drilling fluids (in yellow bold arrows) which flow into the drive unit from the upside of the tool is divided into two parts: partial fluid (in red arrows) flows through the impeller device to active the control shaft to rotate, and the main flow (in white bold arrows) keeps the primary route. Then two parts of flows converge again before entering the next compound strike unit. In the compound strike unit, the higher pressure fluid (in yellow arrows) is assigned to upper chamber, meanwhile, the lower pressure fluid (in black arrows) is extruded into the main flow through an effusion channel. With the dynamically changing hydraulic pressure exerted on the face of hammer, the volume of upper and lower cavity changes linearly. Besides, with the limitation spiral groove, arranged on the inner wall of the valve cylinder, the movement of hydraulic hammer is transformed into the composite impact on the valve cylinder at the end of stroke length. By controlling the rotation velocity of control shaft, the hydraulic chamber was connected to different distribution channel at a required frequency. Moreover, the main specifications of the compound impactor are list on Table 1.

Table 1. The specification of the compound impactor

Parameters	Value
External diameter/mm	203
Length/mm	1193
Working range/ (L/s)	12.5-35
Pressure drop/MPa	1.3-3.2
The frequency of the compound impact/HZ	35-90

2.2. Laboratory test

A Laboratory test (shown in Fig. 3) is conducted to verify the feasibility of the compound impact tool. In this test, all the components are identical with the original plan except for the driven unit using a four-stage turbine. As known from Fig. 4, the total length of a four-stage turbine is over 140mm, while the length of a single mixed flow impeller in the simulation is not exceed 100mm. The recorded data related to this test has proven the amazing availability of the compound strike unit. Another positive information gained from the experiments is that the rotation frequency in the power unit is a key point to obtain a perfect knock in the lower compound strike unit. From the existing empirical cognition, the frequency could not exceed the value of 90, and 60 is regards as the best.



*Fig. 3. The experiment of the compound strike unit*

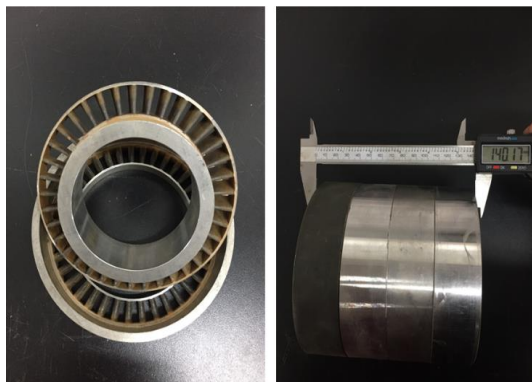


*Fig. 4. The four-stage turbine utilized in the test*

### 3. NUMERICAL PROCEDURE

Even though the initial mixed impeller has largely utilized in hydro-generators currently, it is the first time to apply in drilling instruments. In the simulation, these assumptions are taken into consideration: first of all, all the fluids are thought as continuous phases, i.e. any cross section of the fluid domain complies with the law of conservation of flow. Secondly, the model for numerical calculation (in Fig.5) has removed some insignificant details from the actual physical model for a faster convergence [11-13]. Last but not least, the percentage of fluid entering into the impeller account for 2/3 in a total in this simulation.

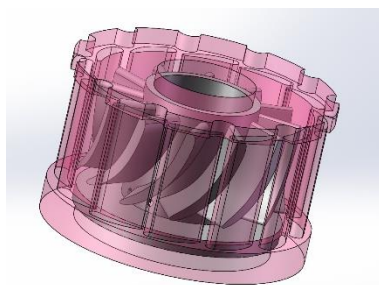


*Fig. 5. The simplified model of the drive unit*

#### 3.1. Analysis Models

All computations are performed using the finite-volume commercial CFD code, CFX 17.0. SIMPLE algorithm is implemented to solve the computations of the pressure-velocity coupling of compressible flow. First-order high resolution scheme is employed to solve the momentum equation. And K- $\epsilon$  model with a 5% turbulence is utilized to simulate the impeller with different

rotation speed [14-17]. The convergent criteria for all calculations are set as the residual which is smaller than  $10^{-4}$  in the control volume for each equation.

### 3.2. Computational domains

ICEM 17.0 mesh-generator is employed to accomplish the meshing. As shown in Fig. 6, computational domains are divided into three parts, and each part is discretized with hexahedron cells in order to control the grid distribution. Progressive mesh is performed to discretize the flow channel-changing region. In this study, the suitable grid density is reached by repeating computations until a satisfactory independent grid is found.

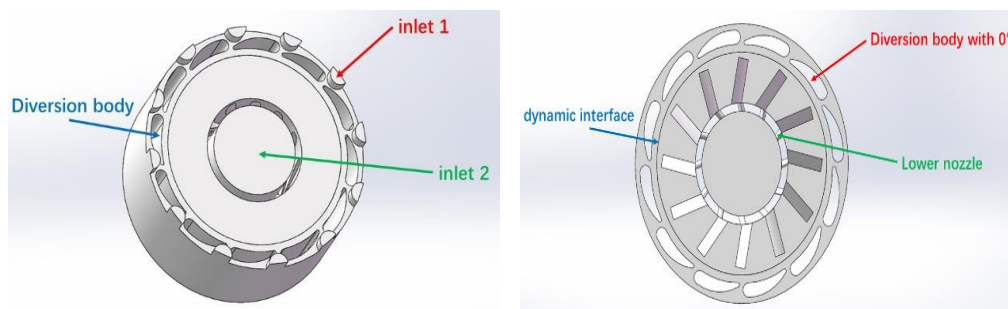


**Fig. 6.** The schematic of the merged solution domains

### 3.3. Boundary conditions

For the purpose of facilitating simulation analysis, the velocity boundary condition of mass flow are set at the inlet and outlet. On the condition of continuity equation, the value of velocity in outlet should be calculated beforehand. The concrete velocity of water in this simulation is defined as Table 2. In order to coincident with the practical environment, the pressure required at outlet is seemed as an atmospheric pressure. No-slip boundary condition is imposed at the wall of the domains.

**Table 2.** Velocity boundary condition

Flow rate (L/S)	Area of Inlet 1(mm <sup>2</sup> )	Inlet 1 (m/s)	Area of Inlet 2 or Outlet(mm <sup>2</sup> )	Inlet 2 (m/s)	Outlet (m/s)
10	906.84	7.352	2922.47	1.141	3.422
15		11.027		1.711	5.133
20		14.703		2.281	6.844
25		18.379		2.851	8.554
30		22.054		3.422	10.265

### 3.4. Grid distributions

The main objective of this simulation is to figure out the exact torque on the rotary wall, so the grid quality severely affects the accuracy of the calculation results. The Unstructured grid of the rotary is shown in Fig.7, with the grid quality higher than 0.48, which is adequately precise to complete the subsequent calculation.



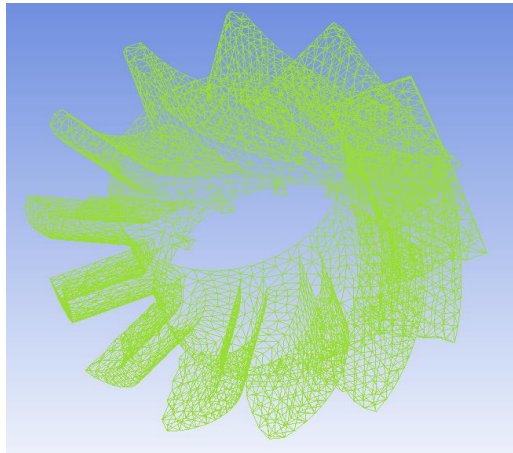


**Fig. 7.** The mesh grid of the compound impeller

## 4. RESULTS AND DISCUSSION

### 4.1. Effect of flow rate and revolution speed

Fig.8 indicate that the torque acting on a blade has a close connection with the revolution speed and flow individually. The quantity of the torque increases notably with the increment of flow. While at the same flow magnitude, the torque will decrease in a small step along with an enhancement in revolution speed. The maximum of torque can achieve about 70 N·m, which is sufficient to drive the commutator though the effect of friction dissipation is considered. However, according to previous research on turbine, the maximum magnitude of torque induced by a four-stage turbine could be achieve nearly 60 N·m.

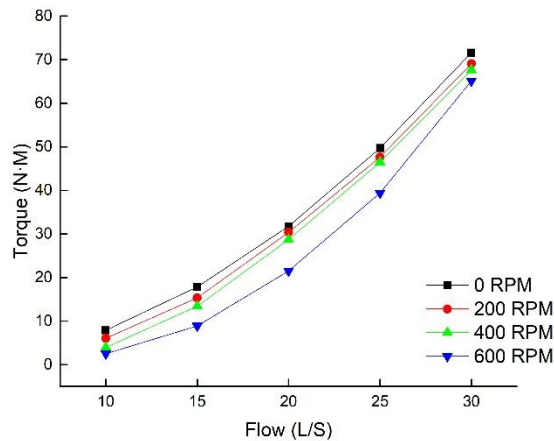


**Fig. 8.** The relationship between output torque and flow rate, revolution speed

### 4.2. Effect of nozzle size

As shown in Fig.9, four types of nozzle diameter are investigated. From the curves of the graphic, we can conclude a conclusion that the torque has an inverse correlation with the size of the nozzle. The more is the flow and the smaller is the nozzle, the torque generated is bigger. When the nozzle closes to 10 mm, the torque is proximately assumed as zero at a flow of 10 L/S.

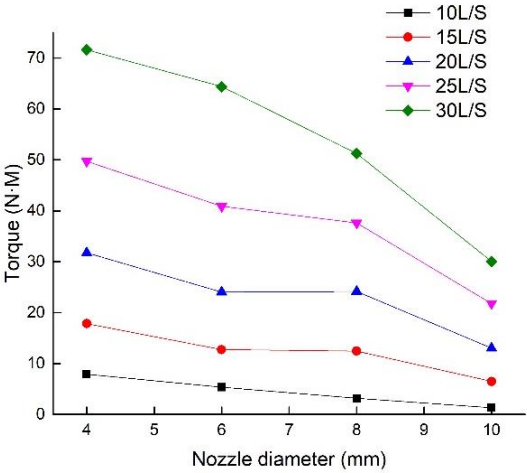


Fig. 9. The relationship between output torque and nozzle diameter

4.3. Effect of diversion angle

Diversion angles are set as  $-7^{\circ}$ ,  $-3.5^{\circ}$ ,  $0^{\circ}$ ,  $3.5^{\circ}$ ,  $7^{\circ}$  separately. A conclusion we can make is that the torque sharply decreases accompanied with the increase of diversion angle. This is very useful during the exact design of a diversion body to make use of the hydraulic energy.

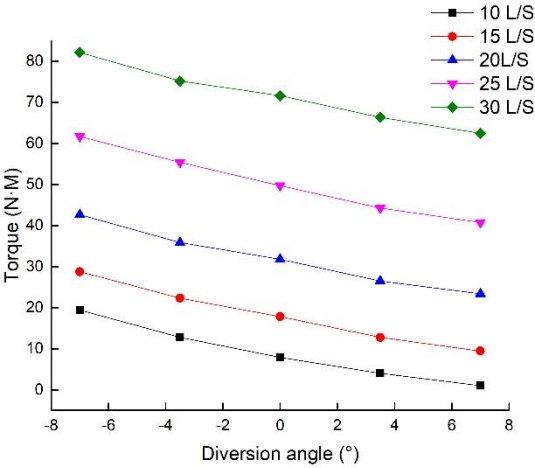


Fig. 10. The relationship between output torque and diversion Angle.

5. CONCLUSIONS

A novel compound impactor was proposed to mitigate the stick-slip oscillation which is significantly suitable for highly mixed and laminated formations. The result of the laboratory experiment shows that the synchronous impact in axial and circumferential direction integrated with each other just utilizing one independent structure was feasible. However, the numerical study offers the convincing evidence that the mixed impeller drive can be an alternative to a turbine or screw with a vital advantage of shorting the overall length in the power unit. All the relative analyses reveal a measurable improvement in the design of compound impactor based on mixed flow impeller drive.

## REFERENCES

- [1]. Yevhen Kovalyshen, Understanding root cause of stick–slip vibrations in deep drilling with drag bits, *International Journal of Non-Linear Mechanics* 67 (2014) 331-341. DOI:10.1016/j.ijnonlinmec.2014.10.019.
- [2]. Fear, M. J., et al. The destruction of PDC bits by severe slip-stick vibration. SPE/IADC Drilling Conference. 4-6 March, 1997 Amsterdam- Netherlands.
- [3]. Richard, T., Detournay, E., Fear, M., Miller, B., Clayton, R., & Matthews, O., Influence Of Bit-Rock Interaction On Stick-Slip Vibrations Of PDC Bits. SPE Annual Technical Conference and Exhibition, 29 September-2 October, 2002 San Antonio, Texas- USA.
- [4]. Kyllingstad, A., & Nessjøen, P. J. A New Stick-Slip Prevention System. SPE/IADC Drilling Conference and Exhibition, 17-19 March, 2000 Amsterdam-Netherlands.
- [5]. Kamatov, K. A. Anti-Stick-Slip Drilling Strategy for Horizontal Wells in Medium-to-Hard Heterogeneous Rocks. SPE Russian Oil and Gas Exploration & Production Technical Conference and Exhibition, 14-16 October, 2014 Moscow-Russia
- [6]. Jones, S., Feddema, C., & Sugiura, J. A New Steady Weight-on-Bit Tool Reduces Torque and RPM Variations and Enhances Drilling Efficiency and Bit/BHA Life, IADC/SPE Drilling Conference and Exhibition, 1-3 March, 2016 Fort Worth, Texas- USA.
- [7]. Dwars, S. Recent Advances in Soft Torque Rotary Systems. SPE/IADC Drilling Conference and Exhibition, 17-19 March, 2015 London, England- UK.
- [8]. Nessjoen, P. J., Kyllingstad, A., Dambrosio, P., Fonseca, I. S., Garcia, A., & Levy, B. Field Experience with an Active Stick-Slip Prevention System. SPE/IADC Drilling Conference and Exhibition, 1-3 March, 2011 Amsterdam-Netherlands.
- [9]. Selnes, K. S., Clemmensen, C. C., & Reimers, N. Drilling Difficult Formations Efficiently With the Use of an Antistall Tool. SPE Drilling & Completion 24 (2009) 513-536. DOI:10.2118/111874-PA
- [10]. Reimers, N. (2012, January 1). Antistall Tool Reduces Risk in Drilling Difficult Formations. *Journal of Petroleum Technology* 64 (2012) 26-29. DOI:10.2118/0112-0026-JPT
- [11]. Hongjun Zhu, Jian Wang, et al. Numerical investigation of flow erosion and flow induced displacement of gas well relief line, *Journal of Loss Prevention in the Process Industries*,37 (2015) 19-32. DOI:10.1016/j.jlp.2015.06.015.
- [12]. Hongjun Zhu, Jian Wang, et al. Numerical analysis of the effects of fluctuations of discharge capacity on transient flow field in gas well relief line, *Journal of Loss Prevention in the Process Industries*, 31 (2014) 105-112. DOI: 10.1016/j.jlp.2014.07.008.
- [13]. Cemil Y, Ufuk D. Wind Turbine Blade Design with Computational Fluid Dynamics Analysis. Conference on Computational and Experimental Science and Engineering (ICCESN 2016), 19-24 October, 2016 Antalya-Turkey
- [14]. M. Günala, A. Ismael. Experimental Investigation of Turbulent Flow Field at Downstream-Facing Round Nosed Pier. 130 (2016) 126-127. DOI:10.12693/APhysPolA.130.126.
- [15]. M. Ozsoya, C. Kurnaz. An Optimization Study of a Hydraulic Gear Pump Cover with Finite Element Method. 132 (2017). DOI: 10.12693/APhysPolA.132.944.
- [16]. Ali SAKİN, İrfan KARAGÖZ. A Computational Comparison of Flow and Pressure Fields in Axial and Reverse Flow Cyclone Separators 3 (2017). DOI: dergipark.ulakbim.gov.tr/ijcesen.
- [17]. Erdem ACAR. Response Surface Based Optimization of Aerodynamic Performance of a Horizontal Axis Wind Turbine. 3 (2017) 7-10. DOI: dergipark.ulakbim.gov.tr/ijcesen.

---

## Power Quality Improvement in Grid-Tied PV System

Saliha Boutora<sup>1\*</sup>, Dhia Elhak Messaoud<sup>2</sup> Hamid Bentarzi<sup>3</sup>

<sup>1</sup> IGEE University M'Hamed Bougara, Boumerdes, Algeria

<sup>2</sup> IGEE University M'Hamed Bougara, Boumerdes, Algeria

\*s.boutora@univ-boumerdes.dz

### ABSTRACT

After entering the grid-tied solar energy conversion systems most of the researches are concentrating on the enhancement of the Power quality, using different strategies on the different parts of the global system. This work presents a grid-tied PV system with two stages starting from the PV panel with MPPT control unit (P&O algorithm), DC-DC Boost converter to be used for lifting the DC voltage, A Five-level Inverter with Space Vector Modulation (SVM) control unit, LC Low pass filter to eliminate harmonics and Finally a current control unit with PI controllers to synchronize the system with the grid. Then, a simulation work is performed using MatLab Simulink, the results are commented.

**KEYWORDS** - Power Quality, Grid-Tied PV system, MPPT (P&O algorithm), Boost Converter, Five Level Inverter, SVM control, Grid synchronization.

### 1. INTRODUCTION

Green and low carbon power is an urgent need today, due to the rising cost of non renewable sources of energy and also because of environmental concerns due to their use. In comparison with other renewable sources of energy such as wind, tidal, etc., solar photovoltaic (SPV) energy conversion systems are gaining momentum due to suitable government policies, falling prices, and increased research in the area. SPV energy conversion systems can be of two types: standalone and grid-interfaced power generating systems. Standalone systems require additional energy storage device for reliable and efficient operation but energy storage devices like batteries increase both capital and maintenance cost of the system. Grid-interfaced solar energy conversion systems do not require storage device. An integration of any renewable energy source to the electric grid has to fulfill standard power quality requirements so that the grid is not polluted due to such interface [1, 2].

Moreover, improving the power quality of the grid-tied SPV is the most recent topic in nowadays and it is taking a large area of researchers interest, especially that the system has different major parts starting from the PV panel till connecting the grid, so improving the quality on any part means improving the quality of the whole system.

Power quality has many factors to be enhanced. Voltage, frequency and signal waveform are all included in the power quality indices, which will, after study, decide whether the power quality has been improved or not.

The proposed system is a two stage three phase grid connected solar photovoltaic system with maximum power point tracking (P&O algorithm) to control the switching pulses of the DC-DC boost converter, The DC-AC converter is a five-level inverter with a space vector pulse width modulation control unit to maintain a good improvement in the AC output signal, an LC low pass filter is to be used as an interface between the inverter output and the grid.

### 2. POWER QUALITY

Despite important papers, articles, and books published in the area of electric power quality, its definition has not been universally agreed upon. However, nearly everybody accepts that it is a very important aspect of power systems and electric machinery with direct impacts on efficiency, security, and reliability. Various sources use the term "power quality" with different meaning. It is

used synonymously with "supply reliability," "service quality," "voltage quality," "current quality," "quality of supply," and "quality of consumption". [3]

### 3. GRID-TIED PV SYSTEM

The main elements that can be included in a system of photovoltaic conversion are Photovoltaic modules, converters, utility grid, loads DC and AC, and Inverters [4].As shown in figure (1).

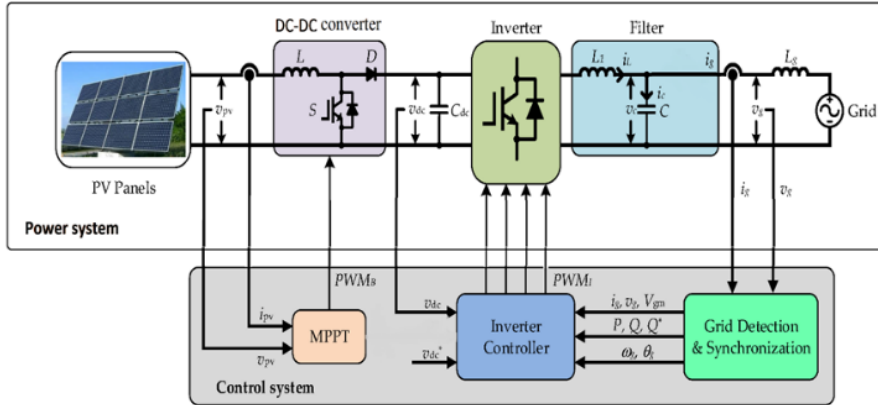


Figure. 1. Grid-tied PV system scheme.

#### 3.1. PV Panels

The solar panel is the power source of all photovoltaic installation. It is the result of a set of photovoltaic cells in series and parallel. PV cell directly converts the solar irradiance into electricity in the form of dc when sunlight interacts with semiconductor materials in the PV cells. [4]

The PV generator starts with one single PV cell up to multiple PV arrays as shown in figure (2).

$$I = N_p * I_{pv} - N_p * I_0 \left[ \exp \left( \frac{V + R_s I}{N_s * a V_t} \right) - 1 \right] \quad (1)$$

Equation (1) shows the mathematical modeling of the PV array based on the single PV cell model. Where  $I$  is the output current,  $I_{pv}$  is the cell produced current,  $I_0$  is the saturation current of the parallel diode,  $V$  is the open circuit voltage,  $a$  is the ideality factor equal to 1,  $V_t$  is the thermal voltage,  $N_p$  and  $N_s$  are parallel and series numbers of the connecting cells.

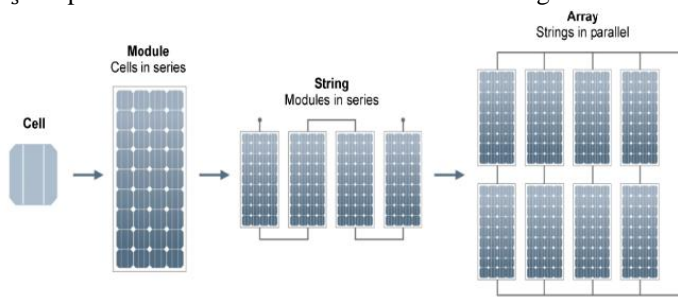
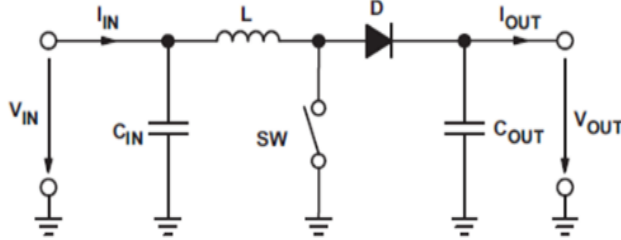


Figure. 2. PV system configuration.

#### 3.2. DC-DC converter

The DC/DC converters are widely used in regulated switch mode DC power supplies. The input of these converters is an unregulated DC voltage, which is obtained by PV array and therefore it will be fluctuated due to changes in radiation and temperature. In these converters the average DC output voltage must be controlled to be equated to the desired value although the input voltage is changing. [5]

There are many types of DC-DC converters, the used one is the Boost converter as shown in figure (3).



**Figure. 3.** Boost converter circuit diagram

Where Sw is the controlled switch, L is the input inductor, C<sub>IN</sub> is the input capacitor, C<sub>OUT</sub> is the output capacitor and D is the diode.

$$D = 1 - \frac{V_{in}}{V_o} \quad (2)$$

Equation (2) shows the output/input voltages ratio that gives D the duty cycle, for the inductor and capacitors they can be obtained using equations (3), (4) and (5).

$$L \geq \frac{V_{in} * (V_{om} - V_{inm})}{\Delta_i * F_{sw} * V_o} \quad (3)$$

$$C_{in} \geq \frac{I_m * D_m^2}{0.02 * (1 - D_m) * V_{inm} * F_{sw}} \quad (4)$$

$$C_{out} \geq \frac{I_m * D_m}{\Delta_v * F_{sw}} \quad (5)$$

Where,  $F_{sw}$ = switching frequency,  $\Delta_v$ = ripple voltage for capacitor,  $I_m$  = output current at maximum output power,  $D_m$ = duty cycle at maximum input power,  $\Delta_i$ = ripple current for inductor,  $V_{in,min}$  = minimum input voltage,  $V_{inm}$  = input voltage at maximum power point,  $V_{om}$ = maximum of output voltage.

### 3.3. Inverter

Inverters are the power electronic circuit, which converts the DC voltage into AC voltage.

Multilevel inverters are more efficient and widely used in nowadays, in this paper the used multilevel inverter is the five-level neutral point clamped diode (NPC) multilevel inverter, it consists of 4 DC link capacitors, 18 diodes and 24 switching devices, the body structure is shown in figure (4), switches positions for each output are shown in figure (5) and the switching states are shown in table (1).

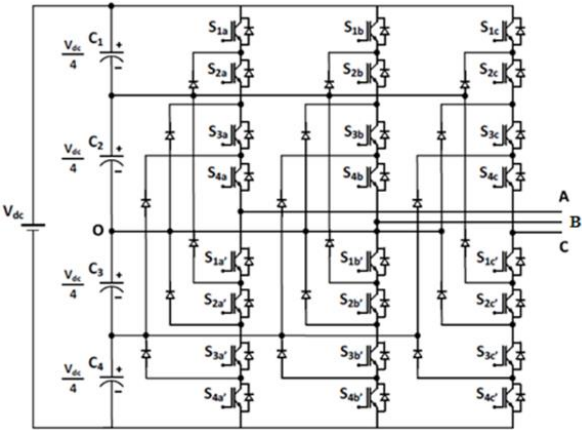


Figure. 4. Five level diode clamped multilevel inverter.

Table. 1. Switching states of each switch

Switching State	$S_{1a}$	$S_{2a}$	$S_{3a}$	$S_{4a}$	$S_{1a'}$	$S_{2a'}$	$S_{3a'}$	$S_{4a'}$	Inverter Terminal Voltage
4	1	1	1	1	0	0	0	0	$\frac{V_{dc}}{2}$
3	0	1	1	1	1	0	0	0	$\frac{V_{dc}}{4}$
2	0	0	1	1	1	1	0	0	0
1	0	0	0	1	1	1	1	0	$-\frac{V_{dc}}{4}$
0	0	0	0	0	1	1	1	1	$-\frac{V_{dc}}{2}$

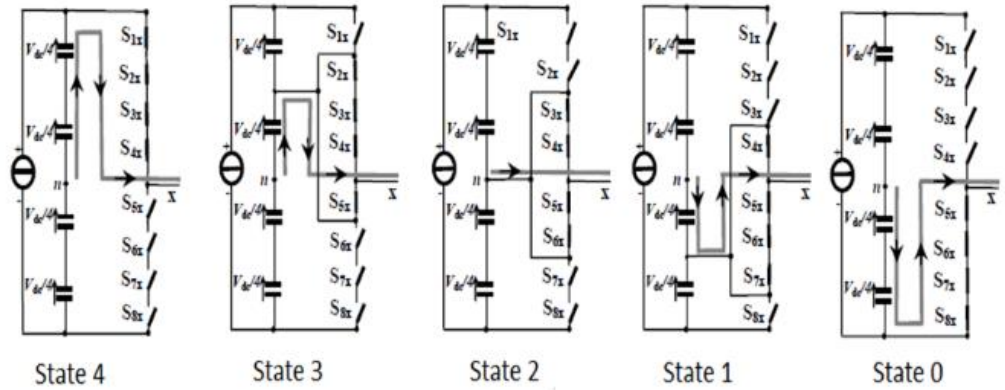


Figure. 5. Switches positions for each state.

3.4. Filter

Electric filter is typically designed to pass certain things and attenuate if not completely block other things. [6]

The LC low pass analog filter is the used one for blocking all harmonics and letting only the fundamental to pass. Equation (7) shows the cutoff frequency.

$$f_c = \frac{1}{2\pi\sqrt{LC}} \quad (7)$$

### 3.5. The grid

An electrical grid is an interconnected network for delivering electricity from suppliers to consumers. It consists of generating stations that produce electrical power, high voltage transmission lines that carry power from distant sources to demand centers and distribution lines that connect individual customers. [7]

## 4. CONTROL SYSTEM

The control system is the brain of the global system which control the power side of the system and it consists of:

### 4.1. MPPT (P&O algorithm)

A typical solar panel converts only 30 to 40 percent of the incident solar irradiation into electrical energy. Maximum power point tracking (MPPT) technique is used to improve the efficiency of the solar panel. According to Maximum Power Transfer theorem, the power output of a circuit is maximum when the Thevenin impedance of the circuit (source impedance) matches with the load impedance. Hence our problem of tracking the maximum power point reduces to an impedance matching problem. [8]

Perturb and Observe (P&O) is the used algorithm, it is based on perturbing the voltage and the current of the PV regularly, and then, in comparing the new power measure with the previous to decide the next variation, the flowchart is shown in figure (7).

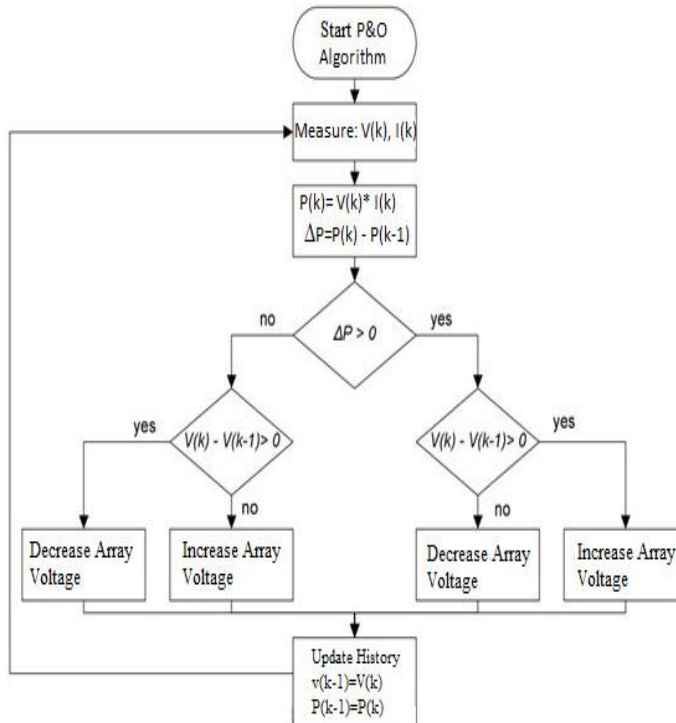


Figure. 7. P&O flowchart.



## 4.2. Inverter Control

To modulate the dc/ac part of the three-level NPC converter, different modulation schemes are available like the carrier-based SPWM method, the space-vector-based space vector modulation (SVM) (or SVPWM) method and the hybrid modulation [9]–[10].

The commonly used modulation strategies for multilevel inverters (MLIs) are the carrier based sinusoidal PWM (SPWM) and the space vector modulation (SVM) schemes. The SVM scheme provides better utilization of the dc link voltage, offers more flexibility in the switching pattern design, reduces the device switching frequency and lends itself easily for digital implementation [11]. As a result, SVM remains a popular choice for industrial applications. The SVM of a two-level VSI is a mature technique [12]. However, the extension of this technique to higher level inverters is not easy, the complications increasing with the increase in the number of levels. The simplification of SVM for multilevel inverters has been widely attempted [13]–[14].

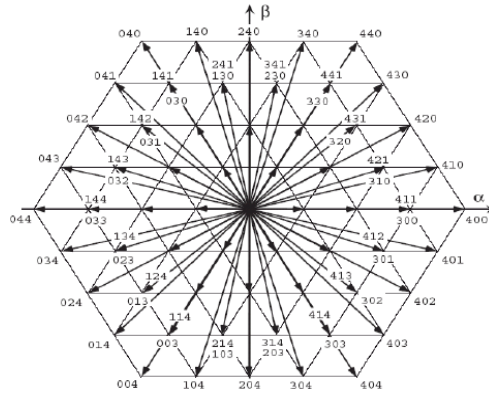


Figure. 8. Space vector diagram for 5-level NPC.

The space vector diagram of the five level NPC inverter is shown in figure (8). The global stages of this method are as listed:

Getting the reference voltage  $V_{ref}$  and the rotating angle  $\theta$  from the phase voltages  $V_a, V_b, V_c$  using Clark transformation equation (8) and using equations (9)–(10)

$$\begin{bmatrix} V_\alpha \\ V_\beta \end{bmatrix} = \frac{2}{3} \begin{bmatrix} 1 & -\frac{1}{2} & -\frac{1}{2} \\ 0 & \frac{\sqrt{3}}{2} & -\frac{\sqrt{3}}{2} \end{bmatrix} \begin{bmatrix} V_a \\ V_b \\ V_c \end{bmatrix} \quad (8)$$

$$|V_{ref}| = \sqrt{V_\alpha^2 + V_\beta^2} \quad (9)$$

$$\theta = \tan^{-1}\left(\frac{V_\alpha}{V_\beta}\right) \quad (10)$$

Decomposing  $V_{ref}$  into  $60^\circ$  plane coordinates (m, n) and getting  $V_{rm}, V_{rn}$  using (11) and (12).

$$V_{rm} = M \sin\left(\frac{\pi}{3} - \theta\right) \quad (11)$$

$$V_{rn} = M \sin(\theta) \quad (12)$$

$$M = \frac{2}{\sqrt{3}} * \frac{V_{ref}}{V_{dc}} \quad (13)$$

M is the modulation index.

Dividing the space diagram (global hexagon) into sectors and regions using  $V_{ref}$ , (m, n) coordinates and  $\theta$  the rotating angle as shown in figure (9).

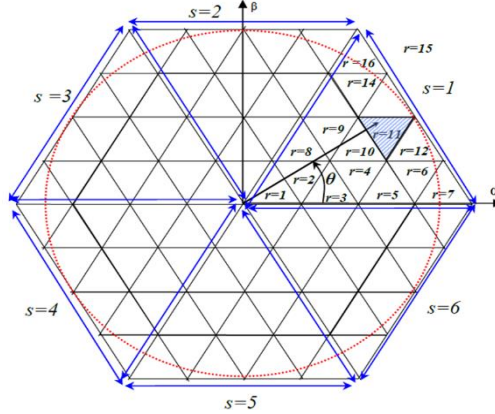


**Figure. 9.** Sectors and regions positions of 5-level NPC inverter.

Dividing each region into X, Y and Z coordinates as shown in figure (10).

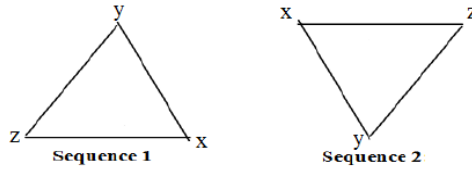


**Figure. 10.** Sequence arrangements of each region.

Calculating the dwelling times  $T_x$ ,  $T_y$ ,  $T_z$  for each region using:

$$V_{ref} = |V_{ref}|e^{j\theta} = \frac{(T_x V_x + T_y V_y + T_z V_z)}{T_s} \quad (14)$$

$$T_s = T_x + T_y + T_z \quad (15)$$

Selecting the switching time by choosing the nearest states to the reference as shown in table (2).

**Table. 2.** Switching time of each switch in region 11.

Phase a	Phase b	Phase c
$S_1 = T_z + \frac{T_x}{2} + \frac{T_y}{2}$	$S_1 = 0$	$S_1 = 0$
$S_2 = T_z + T_x + T_y$	$S_2 = 0$	$S_2 = 0$
$S_3 = T_z + T_x + T_y$	$S_3 = \frac{T_x}{2}$	$S_3 = 2$
$S_4 = T_z + T_x + T_y$	$S_4 = T_z + T_x + \frac{T_y}{2}$	$S_4 = \frac{T_x}{2} + \frac{T_y}{2}$

Grid synchronization

In this section we have to synchronize the inverter output signal with the grid signal. The voltage of the inverter is forced to be constant using a DC bus, the control of the output power (active/reactive) is done using a proportional integrator (PI) current control strategy. [15]

We use also the phase-locked loop (PLL) to get the phase shift  $\theta$  to be used in the d-q transformation block.

In the power DC-AC converters, active and reactive power from the grid-side inverter can be given by:

$$\begin{aligned} P_g &= v_{ga} * i_{ga} + v_{gb} * i_{gb} + v_{gc} * i_{gc} \\ Q_g &= \frac{1}{\sqrt{3}}(v_{gab} * i_{gc} + v_{gbc} * i_{ga} + v_{gca} * i_{gb}) \end{aligned} \quad (16)$$

Where  $v_{ga}, v_{gb}, v_{gc}$  the three-phase voltages at the AC bus  $i_{ga}, i_{gb}, i_{gc}$  are three-phase currents injected into the AC grid. To simplify the work we transfer the equation (16) using park transformation to get

$$\begin{aligned} P_g &= \frac{3}{2}(v_{gd} * i_{gd} + v_{gq} * i_{gq}) \\ Q_g &= \frac{3}{2}(v_{gq} * i_{gd} - v_{gd} * i_{gq}) \end{aligned} \quad (17)$$

Where,  $v_{gd}, v_{gq}$  represent the (d, q) components of the voltage at connection point,  $i_{gd}, i_{gq}$  represent (d, q) components of the line current. For the synchronization to the grid we put,  $v_{gd} = v_g$  and  $v_{gq} = 0$  so:

$$\begin{aligned} P_g &= \frac{3}{2}(v_{gd} * i_{gd}) \\ Q_g &= -\frac{3}{2}(v_{gd} * i_{gq}) \end{aligned} \quad (18)$$

The inverter uses hysteresis switching and controls active power by manipulation of direct-axis current while holding reactive power at 0 VAR.

$$\begin{aligned} i_{gd,ref} &= \left(K_p + \frac{K_i}{s}\right) * (V_{dc,ref} - V_{dc}) \\ i_{gq,ref} &= \left(K_p + \frac{K_i}{s}\right) * (Q_{ref} - Q) \end{aligned} \quad (19)$$

The electrical model presented by three-phase voltages at the AC side of the inverter, is given by:

$$\begin{aligned} v_{ga} &= v_a - \left(L_f * \frac{di_a}{dt} + R_f * i_a\right) \\ v_{gb} &= v_b - \left(L_f * \frac{di_b}{dt} + R_f * i_b\right) \\ v_{gc} &= v_c - \left(L_f * \frac{di_c}{dt} + R_f * i_c\right) \end{aligned} \quad (20)$$

Where,  $v_a, v_b, v_c$  are three-phase voltages at the AC side of the inverter,  $L_f, R_f$  are the grid filter inductance and resistance.

Applying Park transformation, Equation (21) represents the electrical model of the grid side inverter in the (d, q) referential axis.

$$\begin{aligned} v_{gd} &= v_d - \left( L_f * \frac{di_d}{dt} + R_f * i_d \right) + \omega * L_f * i_q \\ v_{gq} &= v_q - \left( L_f * \frac{di_q}{dt} + R_f * i_q \right) - \omega * L_f * i_d \end{aligned} \quad (21)$$

Where,  $\omega$  is the grid frequency.

The current controller still uses PI regulator, described by:

$$\begin{aligned} v_{gd,ref} &= v_d + \left( K'_p * \frac{K'_i}{S} \right) * (i_{d,ref} - i_d) + \omega * L_f * i_q \\ v_{gq,ref} &= v_q + \left( K'_p * \frac{K'_i}{S} \right) * (i_{q,ref} - i_q) + \omega * L_f * i_d \end{aligned} \quad (22)$$

## 5. MATLAB MODELING AND SIMULATION RESULTS

In the simulation work, I simulate the grid-tied PV system using MatLab-Simulink, the PV panel is available in Simscape library, the boost converter, both 3-level and 5-level (SPWM control and SVM control) Inverter cores and the current controller are built using also Simscape library, the SVM control is simulated using MatLab function block, the parameters of each part are:

- PV generator (SUNTECH STP050D)  
 $V_{oc} = 8.8 \text{ v}$ ,  $I_{sc} = 7.68 \text{ A}$ ,  $V_m = 6.85 \text{ v}$ ,  $I_m = 7.1 \text{ A}$   
 $P_m = 48.635 \text{ W}$ ,  $N_s = 40$  ;  $N_p = 55$
- Boost converter  
 $L = 1 \text{ mH}$  with  $R_L = 0.45$ ,  $C = 2 \text{ mF}$
- 5-level Inverter  
 $C = 9 \text{ mF}$  With 400 V, modulation index:  $M = 0.95$
- Filter:  
 $L = 1.5 \text{ mH}$ ,  $C = 7.98 \text{ mF}$ ,  $L_g = 2 \text{ mH}$
- The grid  
 $v_g = 220 \text{ v}$ ,  $f_g = 50 \text{ Hz}$

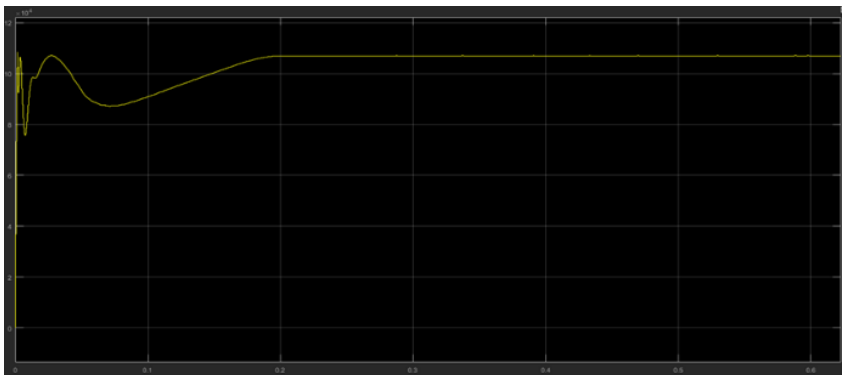


**Figure. 11.** Maximum output power of the PV panel.

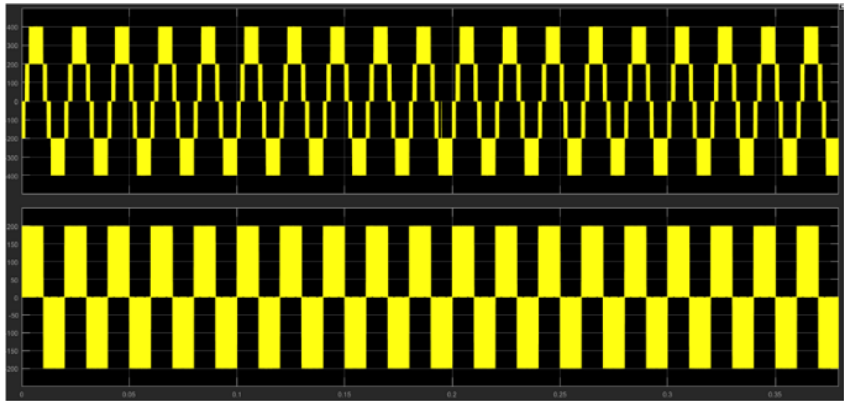


Figure. 12. Three level inverter (SVM control) output without filter ' $V_{l-l}$ ' and ' $i_{ph}$ '.

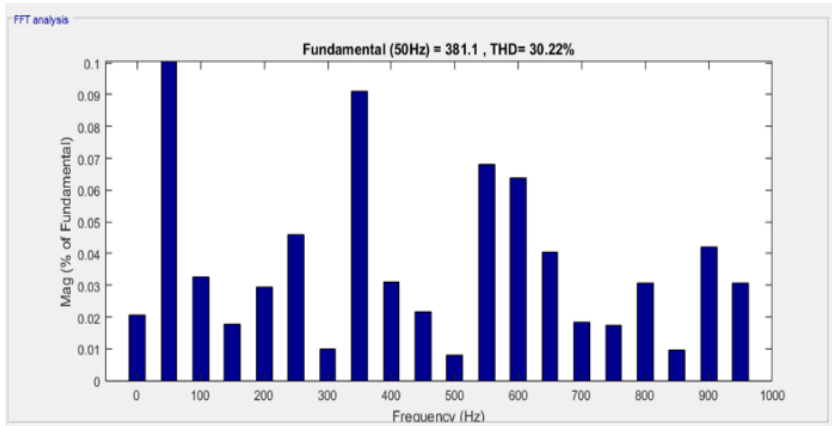


Figure. 13. FFT analysis of the three level inverter (SVM control) unfiltered output signal.

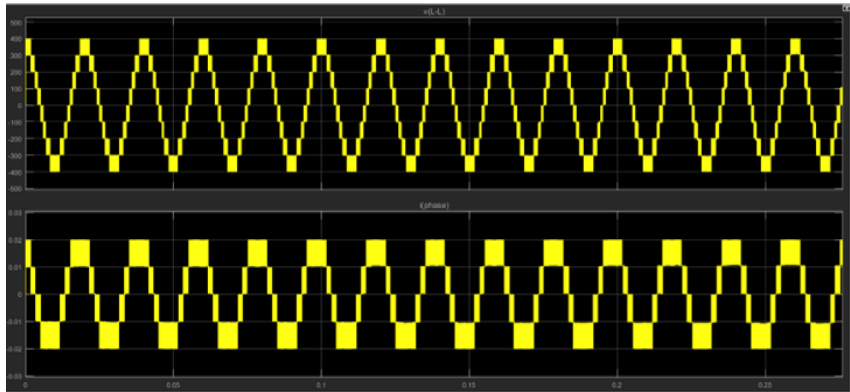


Figure. 14. Three level inverter (SPWM control) output without filter ' $V_{l-l}$ ' and ' $i_{ph}$ '.

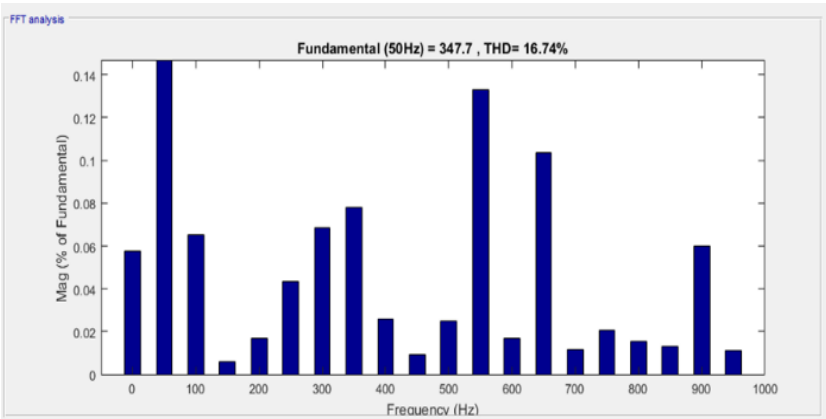


Figure. 15. FFT analysis of the five level inverter (SPWM control) unfiltered output signal.

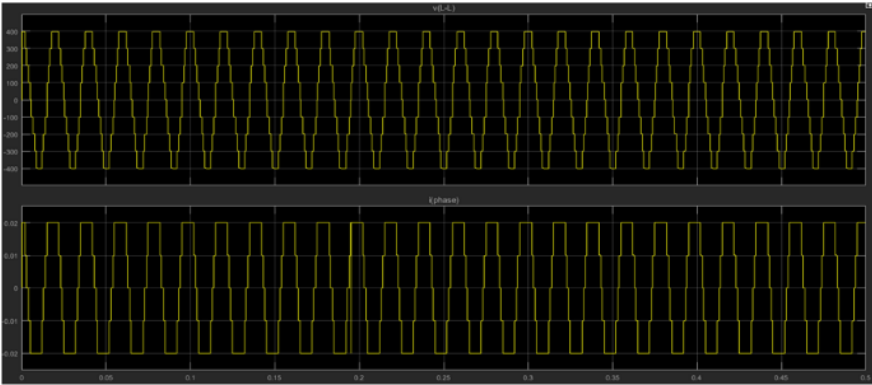


Figure. 16. Five level inverter (SVM control) output without filter ' $V_{l-l}$ ' and ' $i_{ph}$ '.

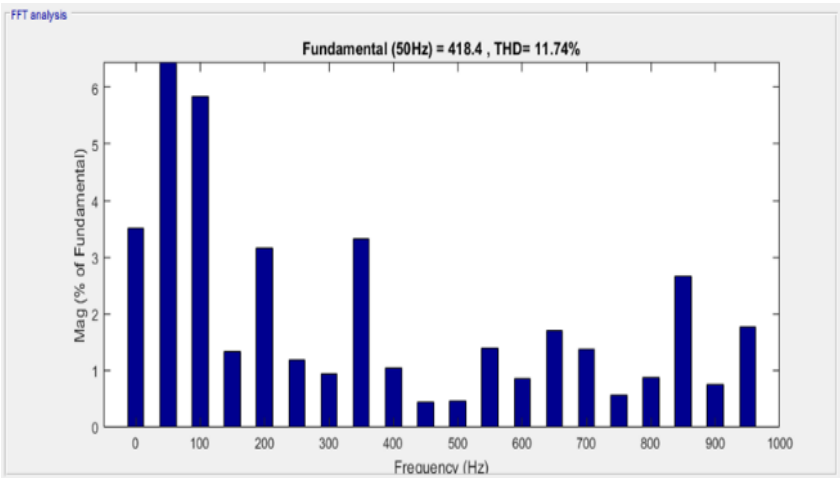
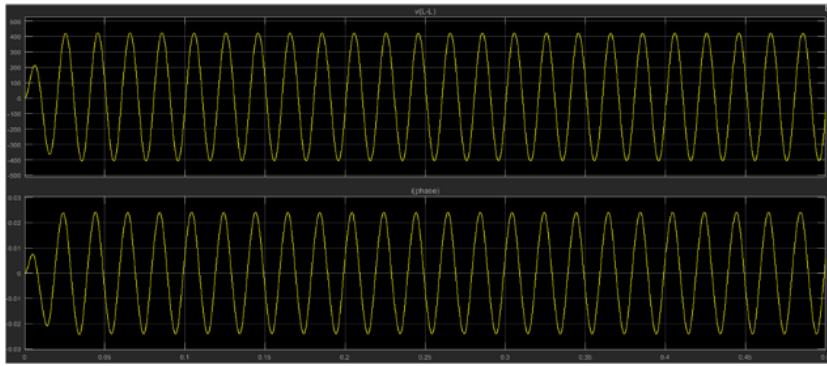
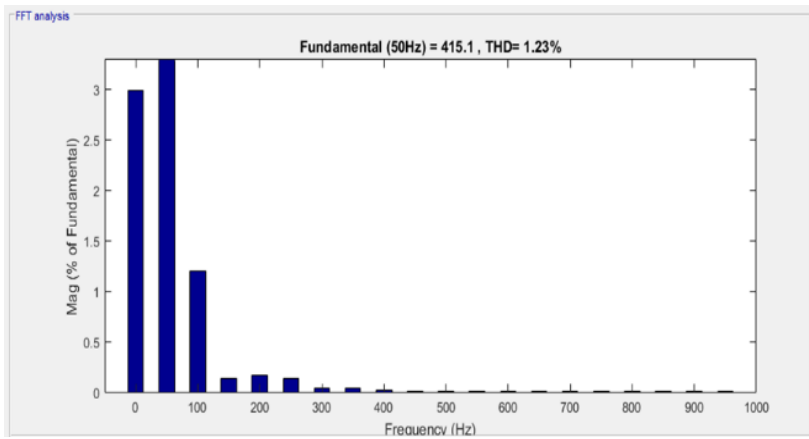


Figure. 17. FFT analysis of the 5 level MLI (SVM control) unfiltered output signal.



**Figure. 18.** Five level inverter (SVM control) output with LC low-pass filter ' $V_{l-l}$ ' and ' $i_{ph}$ '.



**Figure. 19.** FFT analysis of the five level inverter (SVM control) filtered output signal.

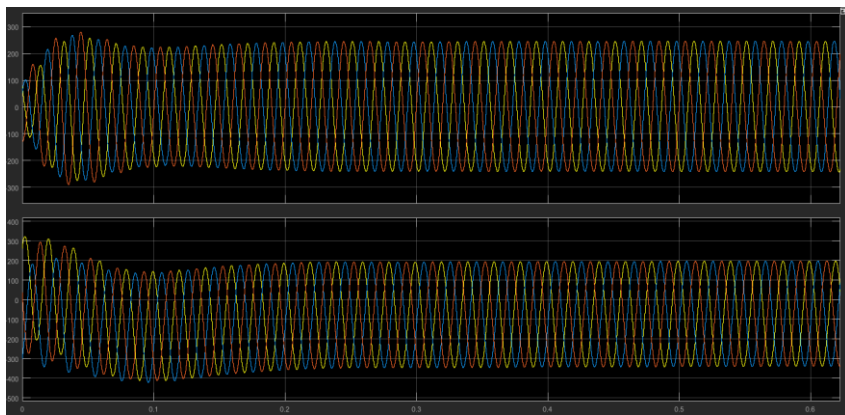


**Figure. 20.** Grid connected PV system output signal (voltage and current).

## Discussion

Figure (11) shows the maximum power point tracking process of the PV panel used; using P&O algorithm, the algorithm worked very well the power curve had a peak value which is, the value of  $V_{oc} * I_{sc}$  and then the MPPT algorithm track the maximum power point which is, the value  $V_m * I_m$ .

Figures (12), (14) and (16) show the phase and line to line voltage output signal of the three level MLI (SVM control), five level MLI (SPWM control) and the five level MLI outputs under a linear load, it is clearly noticeable that the more in levels the more sinusoidal the curve is, also the more in levels the more improved output voltage, these figures show also the good performance of the SVM control comparing with the SPWM control, and it is proved that the output line to line using the SVM control is greater than the output line to line using SPWM by 15% i.e. 13.08%.

Figures (13), (15) and (17) show the FFT analysis of the previous outputs and it is shown that the less in levels the more in THD, the five level MLI using both techniques is better than the three level, but for the more improvement the SVM control technique is the better one with 11.74% THD, which is the nearest one to the pure sinusoidal.

Figures (18) and (19) show the filtered signal of the five level MLI (SVM control) and the FFT analysis of this signal using a simple LC low-pass filter, that gave a THD under the limit 5% i.e. 1.23% to have a pure sinusoidal.

Figure (20) shows the inverter side output in the grid-tied system after the synchronization.

## 6. CONCLUSION

The improvement of the power quality in the grid-tied PV system was the main objective of this presented work, because as we mentioned in the introduction the power quality is the most important topic in the power system.

Using MatLab Simulink, the grid-tied PV system was build starting from the PV module to the synchronization control circuit as presented, both three level and five level MLIs are simulated and the MPPT (P&O), SPWM and SVM control techniques have been simulated and discussed, good results have been obtained, which emphasizes the good performance of the presented work.

Using this work, the power quality was improved in several factors; the cost of the system, the system doesn't use the storage so the storage high costs was removed, with connecting the PV system to the grid; the availability of the power is more certain than the stand-alone PV system, the five-level MLI comparing with the three-level and the simple two level inverters has improved the output power signal by reducing the THD of the signal and simplifying the filter to a simple analog filter.

The SVM control has improved the output voltage (comparing with SPWM) and that's because the good use of the DC link capacitors, this technique also improved the quality by avoiding the use of the additional control circuit for the DC link capacitors which provide more power losses, also no need to use separate sources, consequently, a valuable improvement is achieved on the global system.

## REFERENCES

- [1]. N. Jain, S. N. Singh, and S. C. Srivastava, "A generalized approach for DG planning and viability analysis under market scenario," *IEEE Trans. Ind. Electron.*, vol. 60, no. 11, pp. 5075–5085, Nov. 2013.
- [2]. Byunggyu Yu, M. Matsui, and G. Yu, "A review of current antiislanding methods for photovoltaic power system," *Solar Energy*, vol. 84, pp. 745–754, 2010.
- [3]. Ewald Fuchs, Mohammad A. S.Masoum, "Power\_Quality".
- [4]. J. Singh, "Study and Design of Grid Connected Solar Photovoltaic System at Patiala, Punjab," no. July, 2010.
- [5]. B. M Hasaneen, Adel A. Elbaset Mohammed," DESIGN AND SIMULATION OF DC/DC BOOST CONVERTER",*IEEE*, 978-1-4244-1933-3/08/2008.
- [6]. Steven T. Karris, "Signals and Systems with MATLAB Applications", 2003.
- [7]. U.S.-Canada Power System Outage Task Force, Final Report on the August 14, 2003 Blackout in the United States and Canada: Causes and Recommendations, April 2004, p. 5, <https://reports.energy.gov/BlackoutFinal-Web.pdf>.



- 
- [8]. R. Faranda and S. Leva, "Energy comparison of MPPT techniques for PV Systems", WSEAS Trans. on Power Systems, Vol.3, No.6, June 2008, pp. 446-455.
  - [9]. S. Kouro, M. Malinowski, K. Gopakumar et al., "Recent advances and industrial applications of multilevel converters," IEEE Trans. Ind. Electron., vol. 57, no. 8, pp. 2553–2580, Aug. 2010.
  - [10]. V. Dargahi, A. Khoshkbar Sadigh, M. Abarzadeh, M. R. A. Pahlavani, and A. Shoulaie, "Flying capacitors reduction in an improved double flying capacitor multicell converter controlled by a modified modulation method," IEEE Trans. Power Electron., vol. 27, no. 9, pp. 3875–3887, Sep. 2012.
  - [11]. J. Rodriguez, J.-S. Lai, and F. Z. Peng, "Multilevel inverters: a survey of topologies, controls, and applications," IEEE Trans. Ind. Electron., vol. 49, no. 4, pp. 724- 738, Aug. 2002.
  - [12]. Bin Wu, "High-power converters and ac drives," IEEE Press, 2006.
  - [13]. A. K. Gupta, and A. M. Khambadkone, "A space vector PWM scheme for multilevel inverters based on two-level space vector PWM," IEEE Trans. Ind. Electron., vol. 53, no. 5, pp. 1631-1639, Oct. 2006.
  - [14]. I. Ahmed, and V. B. Borghate, "Simplified space vector modulation technique for seven-level cascaded H-bridge inverter," IET Power Electron., Vol. 7, No. 3, pp. 604-613, Mar. 2014.
  - [15]. E. Benkhelil, A. Gherbi, "Modeling and simulation of grid-connected photovoltaic generation system", 2012.

## Usability of Bentonite and Boron Waste as a Radiation Shielding Materials

Atilla Evcin<sup>1</sup>, Nalan Çiçek Bezir<sup>2</sup>, Iskender Akkurt<sup>2</sup>, Yonca Yahşi Çelen<sup>3</sup>, Kadir Günoğlu<sup>4</sup> and Bahri Ersoy<sup>5</sup>

<sup>1</sup> Afyon Kocatepe University, Faculty of Engineering, Department of Materials Science and Engineering, 03200, Afyon, TURKEY

<sup>2</sup> Süleyman Demirel University, Faculty of Art and Science, Department of Physics, 32000, Isparta, TURKEY

<sup>3</sup> Afyonkarahisar Health Science University, Faculty of Medicine, Department of Dermatology, 03200, Afyon, TURKEY

<sup>4</sup> University of Isparta Applied Sciences, Vocational School of Technical Sciences, 32000, Isparta, TURKEY

<sup>5</sup> Afyon Kocatepe University, Faculty of Engineering, Department of Mining, 03200, Afyon, TURKEY

\*evcin@aku.edu.tr

### ABSTRACT

Bentonite clay, also called Montmorillonite is defined as a naturally occurring clay that is formed mainly of smectite mineral. Chemically, bentonite is described as a hydrous aluminium silicate. Bentonite is generally utilized for bonding, plasticizing, and suspending. Turkey has the biggest reserve of boron minerals. Disposal of this huge amount of boron waste presents a big problem. In this study, usability of bentonite and boron wastes as a radiation shielding materials was investigated. Six mixtures were prepared with various proportions of bentonite and boron waste. Shaped samples were dried and sintered at 1000 °C. Sintered samples were evaluated for density, water absorption, porosity, and gamma ray radiation shielding.

**KEYWORDS** - Boron waste, Bentonite, Radiation, Shielding.

### 1. INTRODUCTION

Bentonite is a native hydrated colloidal aluminium silicate clay material whose major mineralogical component is formed by the smectite group  $[(Na,Ca)(Al,Mg)_6(Si_4O_{10})_3(OH)_6 \cdot nH_2O]$  [1]. It is a type of absorbent clay that is usually refined from volcanic ash. Bentonite has two common types such as calcium bentonite and sodium bentonite [2]. Sodium bentonite is naturally sealant. It is used in many different areas. It also absorbs and removes toxin materials, heavy elements, impurities, and chemicals. Because of this, bentonite clay is a common ingredient in detox and cleansing products [3]. Bentonite clays are a proposed method as an engineered and potential barrier in the geological disposal nuclear waste system. Bentonite is used generally as engineered barrier in the radioactive waste management [4].

The largest boron mineral reserves in the world are located in Turkey. Each year 900,000 tons of boron waste results from boron production. Boron waste is caused big environmental problem in Turkey [5]. In this study, evaluation of bentonite and boron waste was performed to investigate the potential use in shielding materials.

### 2. MATERIALS AND METHOD

Bentonite and Boron wastes were supplied from Karben Chemistry Energy Mining Company in Ankara and EtiBor Boric Acid Factory in Emet/Kütahya respectively. Their chemical compositions were given in Table 1-2. Both powder were mixed to give desired composition in Table 3. Then they were shaped with hydraulic press at 75 bar pressure. Figure 1 shows shaped and sintered samples at 1000 °C for 2 hours.

**Table 1.** Chemical composition of Bentonite

Component	SiO <sub>2</sub>	Al <sub>2</sub> O <sub>3</sub>	Fe <sub>2</sub> O <sub>3</sub>	CaO	Na <sub>2</sub> O	MgO	K <sub>2</sub> O	TiO <sub>2</sub>	P <sub>2</sub> O <sub>5</sub>	SrO
Wt %	59,5	17,9	4,1	3,3	2,4	2,2	1,0	0,4	0,2	0,2

**Table 2.** Chemical composition of Boron waste

Component	SiO <sub>2</sub>	Al <sub>2</sub> O <sub>3</sub>	Fe <sub>2</sub> O <sub>3</sub>	CaO	Na <sub>2</sub> O	MgO	K <sub>2</sub> O	SrO	SO <sub>3</sub>	P <sub>2</sub> O <sub>5</sub>	B <sub>2</sub> O <sub>3</sub>	As <sub>2</sub> O <sub>3</sub>	Lg
Wt %	9.96	1.66	2.64	36.7	0.03	2.33	0.92	2.27	20.5	0.04	1.21	0.68	19.5

Water absorption (W) and porosity % (P) of sintered samples were evaluated as ASTM C 373 standard. Crystal structure of the powders was performed by X-ray diffraction (XRD, Bruker D 8 Advance). XRD patterns are shown in Fig. 2. Experimental and theoretical study of samples has been carried out. Experimental study was performed at Gamma Spectroscopy Lab, at Department of Physics, Faculty of Art and Science, Isparta. The photon attenuation coefficients  $\mu$  of the samples were measured at the photon energies of 662, 1173 and 1332 keV, obtained from <sup>137</sup>Cs and <sup>60</sup>Co  $\gamma$ -ray sources, respectively [6]. The obtained results are summarized in Table 3.



**Figure 1** Shaped samples (75 bar) and Sintered samples (at 1000 °C)

### 3. RESULTS AND DISCUSSION

As can be seen in Fig. 2, boron waste has CaSO<sub>4</sub>·2H<sub>2</sub>O (gypsum) and CaSO<sub>4</sub>·0.15H<sub>2</sub>O (calcium sulphate hydrate) reflections [7,8]. Sintered samples consisting Bentonite & Boron waste has CaSO<sub>4</sub> (anhydride) and Na<sub>0.622</sub>Ca<sub>0.368</sub>Al<sub>1.29</sub>Si<sub>2.71</sub>O<sub>8</sub> (andesine/albite calcian) [9]. In this work, bentonite and boron waste were successfully prepared as a radiation shielding. In the comparison of samples, the highest value of attenuation coefficient has been found for pure bentonite (100%) and the lowest value for bentonite-boron waste (50%). Pure bentonite can provide more efficient  $\gamma$ -ray shielding, when compared to others. The photon attenuation coefficients increase linearly with the increasing bentonite proportion in the mixture [10].

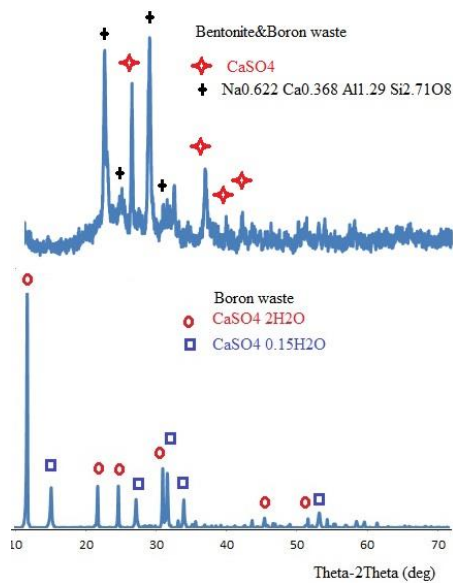


Figure 2 XRD of bentonite and boron waste.

Table 3. Test results of samples

Sample	Bentonite wt %	Boron waste wt%	W %	P %	Attenuation coefficients (1/cm)		
					662 keV	1173	1332 keV
BEN1	100	0	4,55	1,91	0,225678	0,148848	0,142652
BEN2	90	10	4,32	1,80	0,223021	0,145308	0,138751
BEN3	80	20	4,17	1,74	0,220995	0,139959	0,135541
BEN4	70	30	3,96	1,65	0,218013	0,142784	0,136653
BEN5	60	40	3,88	1,62	0,214566	0,137705	0,135438
BEN6	50	50	3,64	1,50	0,213735	0,137233	0,132887

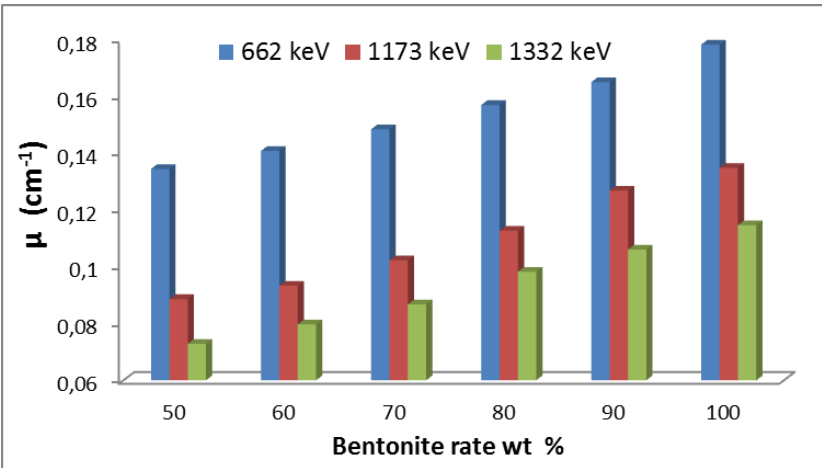


Figure 3. Linear attenuation coefficients as a function of barite rate in composite.

The value of the water absorption and porosity decreases with decreasing bentonite percent in the mixture. The value of the measured linear attenuation coefficient decreases with both increasing photon energy and decreasing bentonite percent in the mixture.

## REFERENCES

- [1]. F. M. Dardir, A. S. Mohamed, M. R. Abukhadra, E. A. Ahmed, M. F. Soliman, Cosmetic and pharmaceutical qualifications of Egyptian bentonite and its suitability as drug carrier for Praziquantel drug, *European Journal of Pharmaceutical Sciences*, Volume 115 (2018) 320-329 DOI: 10.1016/j.ejps.2018.01.041
- [2]. L. Al Attar, B. Safia, B. A. Ghani, Uptake of  $^{137}\text{Cs}$  and  $^{85}\text{Sr}$  onto thermally treated forms of bentonite, *Journal of Environmental Radioactivity Volumes 193–194* (2018) 36-43 DOI: 10.1016/j.jenvrad.2018.08.015
- [3]. B. Tuğrul, S. Erentürk, S. Hacıyakupoğlu, N. Karatepe, N. Altinsoy, N. Baydoğan, F. Baytaş, B. Büyük, E. Demir, S. Gedik, Kinetic and Thermodynamic Behavior of Selenium on Modified Bentonite and Activated Carbon using Radiotracer Technique, *Acta Physica Polonica A*, Vol. 128 (2015) B180-181 DOI: 10.12693/APhysPolA.128.B-180
- [4]. T. Missana, U. Alonso, A. M. Fernández, M. G. Gutiérrez, Colloidal properties of different smectite clays: Significance for the bentonite barrier erosion and radionuclide transport in radioactive waste repositories, *Applied Geochemistry*, Volume 97, (2018) 157-166. DOI: 10.1016/j.apgeochem.2018.08.008
- [5]. İ. Özkan, Utilization of Bigadiç Boron Works Waste Clay in Wall Tile Production, *Acta Physica Polonica A*, Vol. 132 (2017) 427-429 DOI: 10.12693/APhysPolA.132.427
- [6]. E. Al-Sarray, İ. Akkurt, K. Günoğlu, A. Evcin, N.Ç. Bezir, Radiation Shielding Properties of Some Composite Panel, *Acta Physica Polonica A*, Vol. 132 (2017) 490-492 DOI: 10.12693/APhysPolA.132.490
- [7]. İ. Dinçer, *Comprehensive Energy Systems*, Elsevier, 2018
- [8]. C.A. Strydom, D.L. Hudson-Lamb, J.H. Potgieter, E. Dagg The thermal dehydration of synthetic gypsum. *Thermochim Acta* 269–270 (1) (1995) 631–638 DOI: 10.1016/0040-6031(95)02521-9
- [9]. H. S. Dadian, Z. Ramli, N. H. S. N. Abdul Rahman & R. Mehrafarin, X-Ray Diffraction And X-Ray Fluorescence Analysis Of Pottery Shards From New Archaeological Survey In South Region Of Sistan, IRAN, *Mediterranean Archaeology and Archaeometry*, Vol. 15, 3,(2015) 45-56 DOI: 10.5281/zenodo.18357
- [10]. O. Evcin, A. Evcin, N.Ç. Bezir, İ. Akkurt, K. Günoğlu, B. Ersoy, Production of Barite and Boroncarbide Doped Radiation Shielding Polymer Composite Panels, *Acta Physica Polonica A*, Vol. 132 (2017) 1145-1148 DOI: 10.12693/APhysPolA.132.1145

## Effect of Topical Pumpkin Seed Oil Exposure on Morphological Analysis of Hair Fibers on Scanning Electron Microscopy

Nilay Duman<sup>1</sup>, Reşat Duman<sup>2</sup>, Atilla Evcin<sup>3</sup>

<sup>1</sup> Afyonkarahisar Health Science University, Faculty of Medicine, Department of Dermatology, 03200, Afyon, TURKEY

<sup>2</sup> Afyonkarahisar Health Science University, Faculty of Medicine, Department of Dermatology, 03200, Afyon, TURKEY

<sup>3</sup> Afyon Kocatepe University, Faculty of Engineering, Department of Materials Science and Engineering, 03200, Afyon, TURKEY  
\*evcin@aku.edu.tr

### ABSTRACT

In this study we aimed to evaluate the effect of topical pumpkin seed oil (PSO) exposure on morphological analysis of hair fibers using different types of analysis modalities. Gradual morphological changes on the hair fiber surface exposed to PSO at different durations were identified with the help of clinical examination, stereomicroscopic evaluation, light microscopic evaluation, trichoscopic evaluation and the scanning electron microscopy. An exposure time of 10 minutes or 1 hour did not cause a significant change in the hair surface, however, an exposure time of 3 hours lead to both significant coating of PSO on the hair shaft and increased hair thickness. Clinical examination, light microscopic examination, trichoscopic examination and stereomicroscopic examination did not reveal any significant changes. The exposure time of PSO used for hair care is critically important because longer exposure time is associated with a higher coating on the hair surface and as well as a higher potential protective role against hair shaft damage. More research is needed to evaluate the further effect of PSO on hair fibers.

**KEYWORDS** - Hair treatment, Hair growth, Skin physiology/structure.

### 1. INTRODUCTION

In recent years, there is ongoing literature evidence about the stimulatory effect of pumpkin seed oil (PSO) on the hair growth, especially in men with androgenetic alopecia [1]. PSO has also been reported to be effective for treatment of symptomatic benign prostatic hyperplasia [2-4]. These actions have been associated with phytosterols, which are known to inhibit 5 $\alpha$ -reductase [1-4]. Previously effects of various types of oils such as mineral oil, sunflower oil, and coconut oil on the structure of hair fibers have been studied [5, 6], however, there is lack of data about the effect of PSO on hair fiber structure.

It's known that various techniques such as scanning electron microscopy (SEM), light microscopy, trichoscopy and stereomicroscopy may be used to study hair fibers [5, 7-9]. And, this paper presents results of the different types of analysis to evaluate gradual changes in the surface structure of human hair fibers exposed to PSO at the different time of exposures.

### 2. MATERIALS AND METHOD

Untreated black Caucasian dry hair fibers were obtained with approved consent form from a healthy subject who had not performed any procedure including hair treatment, bleaching, coloring or straightening. Hair samples were collected by cutting at a point at least 5 cm both from the root and the distal end. PSO, extracted from seeds of Cucurbita Pepo by mechanical cold pressing method was applied to the hair fibers. 1 ml of the oil was kept for 10 minutes/1 hour or 3 hours in contact with the hair fibers, which were then dried over filter paper at room temperature. And, morphological changes on the hair surface were identified with the help of clinical examination, stereomicroscopic evaluation, light microscopic evaluation, trichoscopic evaluation and the SEM. And comparisons between untreated hair fibers and PSO-treated fibers were performed.

Stereomicroscopic evaluation was done under a commercial stereomicroscope with CMEX-5-WIFI camera attachment (Stereoblue, Euromex Microscopen BV, Netherlands). Light microscopic evaluation was done at  $\times 10$  and  $40$  magnifications with Olympus CX21 microscope (Olympus Corp., Tokyo, Japan). Trichoscopic evaluation was done with the help of Heine Delta 20 plus nonpolarized dermoscope, Heine photo adaptor (Heine Optotechnik, Herrsching, Germany) and Canon EOS 600 D digital camera (Canon USA, Melville, NY).

For electron microscopic analysis longitudinal segments of untreated fibers and fibers treated with PSO were mounted in an aluminum substrate and coated with carbon. The morphological alterations in untreated hair fibers and PSO-treated hair fibers were examined with a digital SEM (Zeiss, Leo 1430 VP, Carl Zeiss, Oberkochen, Germany).

### 3. RESULTS AND DISCUSSION

An exposure time of 10 minutes or 1 hour did not cause significant change in the hair surface, however an exposure time of 3 hours lead to both significant coating of PSO on the hair shaft and increased thickness. Clinical examination, light microscopic examination, trichoscopic examination and stereomicroscopic examination did not reveal any significant changes in any of the samples (Fig. 1).

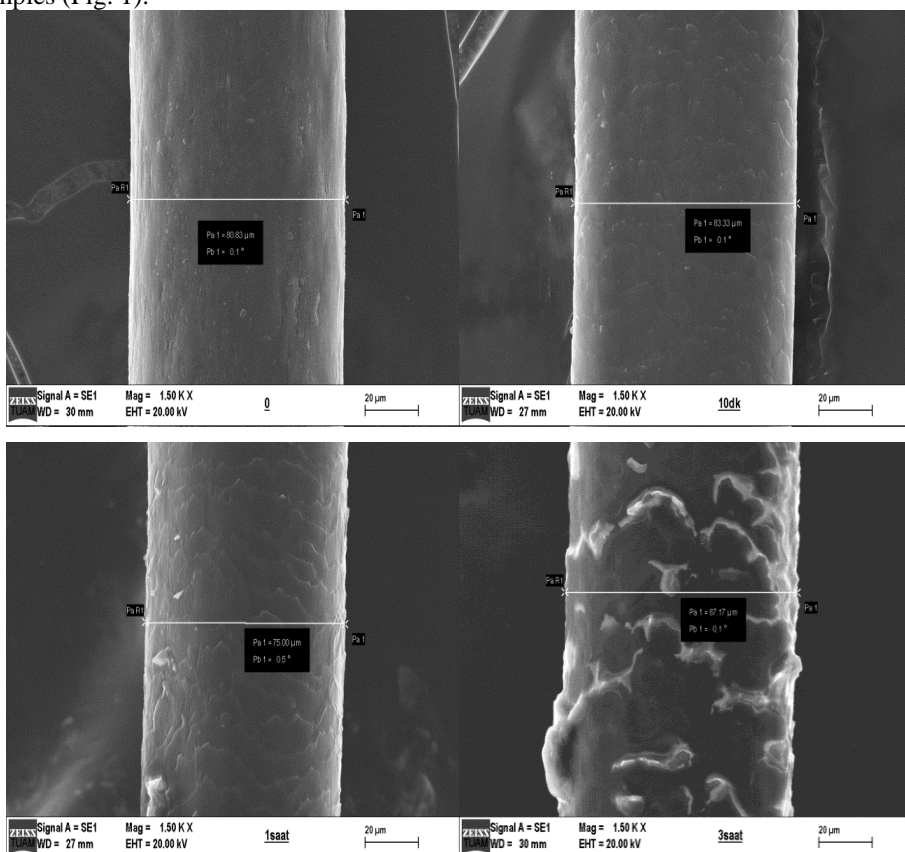


**Figure 1.** The morphological alterations in untreated hair fibers and PSO-treated hair fibers

The cuticle layer is the outer layer of the hair and it is remarkably important, due to its protective role to provide a chemically resistant sheet protecting the internal hair components, such as the hair cortex and the medulla. It is formed by amorphous material and is divided into four subunits

having different chemical compositions: The endocuticle (the most inner layer), the exocuticle, the A-layer, and the epicuticle. The epicuticle is the most external layer and it is hydrophobic and cystine-rich. The cystine groups of the epicuticle are bound to a lipidic layer (18-methyl eicosanoic acid), forming a proteolipidic membrane that covers the cuticle [10]. It's known that factors that can remove the monomolecular layer of fatty acids covalently bound to the cuticle lead to changes in water permeability and hair shaft damage. In addition, factors interacting with the hair surface may increase or decrease the hair surface roughness. Using oils that have high penetrative ability both protect the hair cuticles from damage and nourish them with much-needed nutrients.

Various types of commercial hair oils exist, and it's widely suggested that oiling the hair with oils such as coconut, argan or olive oil might be protective against hair damage by procedures such as hair straightening or bleaching [5, 6, 11]. Rele and Mohile showed the protective effect of coconut oil on hair damage when used as a prewash conditioner as compared to mineral oil and other vegetable oils such as sunflower oil [6]. And they suggested that the ability of coconut oil to penetrate into hair cuticle and cortex seems to be responsible for this effect. In addition, it's suggested that by coating on the hair fiber surface, it can prevent or reduce the amount of water penetrating into the fiber, reduce the lifting and damage of the surface cuticle [6].

The literature data about the effect of the exposure time of hair oils on hair to prevent hair damage is lacking. In this study, we showed that the exposure time of oil on hair shaft is important in the ability of the oil to coat sufficiently on the hair shaft.

In the present study, we also provided literature evidence about the effect of PSO on the morphology of hair fibers by SEM analysis for the first time. In addition, we found that stereomicroscopic, light microscopic, trichoscopic and clinical examination were not able enough to recognize the morphological changes associated with PSO exposure. PSO is a rich source of bioactive compounds such as unsaturated fatty acids (mostly linoleic acid), saturated fatty acids (mostly palmitic acid),  $\alpha$ - and  $\gamma$ -tocopherols, sterols,  $\beta$ -carotene and lutein having positive health effects [12, 13]. In the present study, the significant coating of PSO on hair fiber may be associated with its chemical composition interacting with hydrophobic structure of cuticle and may also reflect its inability to penetrate into the fiber. Sunflower oil, which is also a rich source of linoleic acid similarly to PSO has been reported to not penetrate into the hair fiber [6]. We suggest that significant coating on hair fiber may be important to act as an efficient barrier against hair damage due to external factors such as heat, chemical processing, and UV-exposure. This suggestion needs to be further searched by larger experimental studies. In addition, the ability of an oil to penetrate into the hair shaft means its ability to affect internal structures and increase its potential to stimulate hair growth. Thus, nano techniques to increase the ability of PSO to penetrate into the hair fibers are needed to achieve a stimulatory effect on hair growth in case of topical application.

#### 4. CONCLUSION

The exposure time of PSO used for hair care is critically important because longer exposure time is associated with a higher coating on the hair surface and as well as higher potential protective role against hair shaft damage. More research is needed to evaluate the further effects of PSO on hair fibers.

#### ACKNOWLEDGEMENT

The authors have no conflict of interest and funding source to declare.

#### REFERENCES

- [1]. Cho YH, Lee SY, Jeong DW, Choi EJ, Kim YJ, Lee JG, Yi YH, Cha HS. Effect of pumpkin seed oil on hair growth in men with androgenetic alopecia: a randomized, double-blind,



- placebo-controlled trial. *Evid Based Complement Alternat Med.* (2014), 54972 DOI: 10.1155/2014/549721
- [2]. Hong H, Kim CS, Maeng S. Effects of pumpkin seed oil and saw palmetto oil in Korean men with symptomatic benign prostatic hyperplasia. *Nutr Res Pract.* 3 (2009) 323-327 DOI: 10.4162/nrp.2009.3.4.323
- [3]. Gossell-Williams M, Davis A, O'Connor N. Inhibition of testosterone-induced hyperplasia of the prostate of sprague-dawley rats by pumpkin seed oil. *J Med Food.*9, (2006) 284-286 DOI: 10.1089/jmf.2006.9.284
- [4]. Tsai YS, Tong YC, Cheng JT, Lee CH, Yang FS, Lee HY. Pumpkin seed oil and phytosterol-F can block testosterone/prazosin-induced prostate growth in rats. *Urol Int.*77 (2006) 269-274 DOI: 10.1159/000094821
- [5]. Kaliyadan F, Gosai BB, Al Melhim WN, Feroze K, Qureshi HA, Ibrahim S, Kuruvilla J. Scanning Electron Microscopy Study of Hair Shaft Damage Secondary to Cosmetic Treatments of the Hair. *Int J Trichology.* 8 (2016) 94-98 DOI: 10.4103/0974-7753.188035
- [6]. Rele AS, Mohile RB. Effect of mineral oil, sunflower oil, and coconut oil on prevention of hair damage. *J Cosmet Sci.* 54, (2003) 175-192
- [7]. Kaliyadan F, Gosai BB, Al Melhim WNA, Al Rasasi HM, Kuruvilla PJ. Dermoscopy and scanning electron microscopy in two cases with hair shaft damage secondary to hair straightening. *Indian J Dermatol Venereol Leprol.* 84 (2018) 95-97 DOI: 10.4103/ijdv.IJDVL\_285\_17
- [8]. Mills M, Bonetti J, Brettell T, Quarino L. Differentiation of human hair by colour and diameter using light microscopy, digital imaging and statistical analysis. *J Microsc.*270 (2018) 27-40 DOI: 10.1111/jmi.12646
- [9]. Jimenez FI, Izeta A, Poblet E, Morphometric analysis of the human scalp hair follicle: practical implications for the hair transplant surgeon and hair regeneration studies. *Dermatol Surg.* 37 (2011) 58-64 DOI: 10.1111/j.1524-4725.2010.01809.x
- [10]. Yang FC, Zhang Y, Rheinstädter MC. The structure of people's hair. *PeerJ.* 14 (2014) e619 DOI: 10.7717/peerj.619
- [11]. Faria PM, Camargo LN, Carvalho RS, Paludetti LA, Velasco MVR, da Gama RM. Hair protective effect of Argan oil (*Arganiaspinosa* Kernel Oil) and Cupuassu butter (*Theobroma grandiflorum* seed butter) post treatment with hair dye. *J Cosmet Dermatol Sci Appl.* 3 (2013) 40-4 DOI: 10.4236/jcdsa.2013.33A1006
- [12]. Bardaa S, Ben Halima N, Aloui F, Ben Mansour R, Jabeur H, Bouaziz M, Sahnoun Z. Oil from pumpkin (*Cucurbita pepo* L.) seeds: evaluation of its functional properties on wound healing in rats. *Lipids Health Dis.* 11 (2016) 73 DOI: 10.1186/s12944-016-0237-0
- [13]. Procida G, Stancher B, Cateni F, Zacchigna M. Chemical composition and functional characterisation of commercial pumpkin seed oil. *J Sci Food Agric.* 93(2013) 1035-1041 DOI: 10.1002/jsfa.5843

## Is Video from a Security Footage or Not?

Houssem Memhour<sup>1</sup> and Süleyman Eken<sup>1✉</sup>

<sup>1</sup> Kocaeli University, Department of Computer Engineering, Kocaeli-TURKEY

\*suleyman.eken@kocaeli.edu.tr

### ABSTRACT

The aim of this paper is to implement an efficient program that could determine whether a video is from a security camera or not. To achieve that we rely on the fact that security cameras are stationary, hence their footage should have more similar frames than normal videos. This means that comparing consecutive frames in a video is enough to determine whether it is a security footage or not. As for the algorithm to quantify the similarity between frames, the Structural Similarity Index has been chosen. This algorithm requires more computational resources but it provides more accurate results than the Mean Squared Error. The latter - while simple to implement - is not highly indicative of perceived similarity. Structural similarity aims to address this shortcoming by taking texture into account. Proposed algorithm consists of three steps: (i) preprocessing frames - extracting one frame for each second, converting to grayscale, resizing to 144p (height) maintaining resolution ratio, and splitting frames to 4 groups to feed 4 parallel threads - (ii) thread based computation - comparing each frame with the next 3 frames (3 seconds) and appending the result to a list (ratio) - (iii) decision step according to average ratio.

**KEYWORDS:** *Video classification, Structural similarity index, Multithreading, Security footage, Video surveillance*

### 1. INTRODUCTION

The number of cameras installed around us gives a glimpse on the huge market for video surveillance. The analysis firm IHS Markit estimated the existence of 245 million professionally installed video surveillance cameras in 2014 [1], the same source also predicts a steady growth in this market [2] and that the number will reach 626 million in China alone. It is safe to assume that this trend is not slowing any time soon considering the security threats all around the world.

This situation creates a need for sophisticated methods and algorithms for faster and smarter process and analysis of these. Such methods will allow governments and private corporations to detect, mitigate and even outright prevent security threats before it is too late.

One of the related research topics is video classification in general. The most recent works have shown promising results in achieving this using different architectures of neural networks, such as Convolutional Neural Networks (CNNs).

When it comes to surveillance video specifically, the focus have been on suspicious object or activity detection and face recognition. These problems as well are solvable using a combination of classical image processing and deep learning algorithms. In this work however, we try to answer the following question: is a given video from security footage or not?

### 2. RELATED WORKS ON VIDEO CLASSIFICATION

The recent trend is to rely on Neural Networks (NN) for video classification by extracting what is often called as feature descriptors from frames. Researchers have accomplished this with several methods. In their paper [3], Ng et al. discussed two methods: The first uses CNNs to extract frame-based features through time, and the second treats the video as an ordered sequence of frames fed to a recurrent neural network that uses Long Short-Term Memory (LSTM) cells which are connected to the output of the underlying CNN. However, LSTM are difficult and expensive to train. Graham et al. improved on that by introducing Convolutional Drift Networks for video classification [4], their method relies on combining CNNs and ESNs. A trainable end-to-end architecture that requires no hand-crafted features.

The area of object recognition in surveillance videos also has seen a considerable amount of research. In their paper, Nascimento and Marques [5] compare five different algorithms in this field. Their focus was moving object detection, but these algorithms can be leveraged for non-moving objects as well. More specifically, research on detecting abandoned luggage has shown results as well, either by means of background subtraction [6] or by using CNNs for better results [7]. No work could be found on detecting whether a video is actually from a security surveillance camera or not.

### 3. MSVC: MULTITHREADING SECURITY VIDEO CLASSIFICATION

In this section, the suggested method for detecting security footage is presented. The project was implemented using Python programming language, this choice is mainly due to the ease of use and availability of 3<sup>rd</sup> party libraries to reduce the amount of work needed. This approach relies on comparing consecutive frames from a video to determine a similarity ration between them. Then based on a chosen threshold, any video can be classified as either security footage or not. The whole process follow three steps: pre-processing, computing a similarity ratio, decision

In pre-processing, OpenCV is used to open the video and extract its metadata, namely resolution and Frame Per Second (FPS). FPS is used to determine which frames to use in the comparison because only one frame from each second is taken and then it is converted to gray-scale. While resolution is used to get the aspect ratio which is maintained while resizing the frame to only 144 pixels in height. This pre-processing allows for significantly faster computations and less resources usage in the next step.

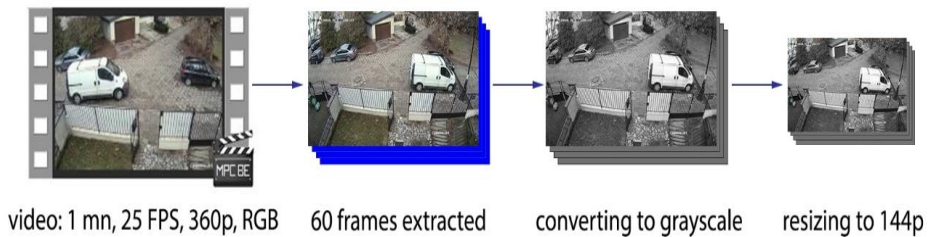


*Figure 1 Pre-processing pipeline*

In the second step, a list of the previously processed frames are passed to a comparison function, where they are split into 4 different groups to allow multithreading computation, each frame in each group is then compared to the next 3 frames, the similarity scores are averaged as one ratio. Finally, this ratio is used to determine whether the video is security footage or not, the threshold can be hand tuned depending on the dataset to achieve better results. As for the method used in the comparison part, two algorithms have been explored: Structural Similarity Index (SSIM) and Mean Squared Error (MSE).

#### 3.1. Mean Squared Error Based Approach

Formally, the mean squared error is defined as

$$MSE = \frac{1}{n} \sum_{i=1}^n (x_i - y_i)^2 \quad (1)$$

where n is the number of pixels in an n-dimensional image vector,  $x_i$  and  $y_i$  are the i-th pixels of the first and second image vectors x and y, respectively. Mathematically, the MSE represents the average squared distance between two vectors, in this case, the distance between two images. It is always non-negative, and values closer to zero signify higher similarity, with 0 being a perfect

match. When comparing images, MSE -while simple to implement and computationally cheap - is not highly indicative of perceived similarity [10].

### 3.2. Structural Similarity Index Based Approach

SSIM was developed by Wang et al [8] and has become a standard for image quality metrics because it solves the drawbacks of MSE [9, 10], by taking texture into account instead of being applied globally. Formally, SSIM is defined as

$$SSIM(x, y) = \frac{(2\mu_x\mu_y + c_1)(2\sigma_{xy} + c_2)}{(\mu_x^2 + \mu_y^2 + c_1)(\sigma_x^2 + \sigma_y^2 + c_2)} \quad (2)$$

where  $\mu_x, \mu_y$  are the average of  $x, y$  respectively,  $\sigma_x^2, \sigma_y^2$  are their variance,  $\sigma_{xy}$  is their covariance,  $c_1 = (k_1L)^2, c_2 = (k_2L)^2$  are two variables to stabilize the division with weak denominator,  $L$  is the dynamic range of the pixel-values ( $2^{bitsperpixel} - 1$ ), and  $k_{1,2} \ll 1$

SSIM value is between 0 and 1, the higher the value the more similar the images. This algorithm comes with Scikit-Image library [11]; hence, there is no need for re-implementation.

### 3.3. Experimental Results

A dataset of 20 videos for a total of 49 minutes of footage was used, and the tests were ran on a system with the following configuration: CPU: Intel i7 7700HQ, RAM: 12 GB DDR4, OS: Ubuntu 16.04 LTS. All results are summarized in the following table:

*Table 1 Test results*

Metric	MSE	SSIM
Running time	45 sec	60 sec
Maximum RAM usage	170 MB	179 MB
Accuracy	95%	100%
Precision	1	1
Recall	0,9	1
F1 Score	0,95	1

## 4. CONCLUSION

While the MSE is faster to compute, the results highlight its shortcomings. On the other hand, SSIM, while slower, is able to perceive the change in structural information of the frames by comparing local regions of the frame instead of globally. Farther work can be done to improve the performance by optimising multithreading for different CPU architectures and/or leveraging GPU acceleration.

## REFERENCES

- [1]. Jenkins, N. (2015, June 11). 245 million video surveillance cameras installed globally in 2014. Retrieved from <https://technology.ihs.com/>
- [2]. Cropley, J. (2018, July 09). Growth in the global professional video surveillance equipment market accelerated in 2017. Retrieved from <https://technology.ihs.com/>
- [3]. Ng, J.Y., Hausknecht, M., Vijayanarasimhan, S., Vinyals, O., Monga, R., Toderici, G. (2015). Beyond Short Snippets: Deep Networks for Video Classification. CVPR, pp. 4694-4702. doi: 10.1109/CVPR.2015.7299101
- [4]. Graham, D., Langroudi, S.H.F., Kanan, C., Kudithipudil, D. (2017). Convolutional Drift Networks for Video Classification; (ICRC), pp. 1-8, doi: 10.1109/ICRC.2017.8123647

- 
- [5]. J.C.Nascimento and J.S.Marques. (2006). Performance evaluation of object detection algorithms for video surveillance. *IEEE Transactions on Multimedia*, vol. 8, no. 4, pp.1-3, doi: 10.1109/TMM.2006.876287
  - [6]. Y.-L. Tian, R. Feris, H. Liu, A. Hampapur, and M.-T. Sun. (2011). Robust detection of abandoned and removed objects in complex surveillance videos, *IEEE Transactions on Systems, Man, and Cybernetics, Part C (Applications and Reviews)*, vol. 41, no. 5, p. 1-2, doi: 10.1109/TSMCC.2010.2065803
  - [7]. Contractor, U., Dixit, C., Mahajan, D. (2018). CNNs for Surveillance Footage Scene Classification. *arXiv preprint arXiv:1809.02766*, 2018 - [arxiv.org](http://arxiv.org)
  - [8]. Wang, Z., & Bovik, A.C. (2002, May). Why is image quality assessment so difficult? *Proc. IEEE Int. Conf. Acoustics, Speech and Signal Processing*, vol. 4, pp. 3313–3316, doi: 10.1109/ICASSP.2002.5745362
  - [9]. Wang, Z., Bovik, A.C., Sheikh, H.R., Simoncelli, E.P. (2014, April). Image quality assessment: From error visibility to structural similarity, *IEEE Transactions on Image Processing*, vol. 13, no. 4, pp. 600-612, doi: 10.1109/TIP.2003.819861
  - [10]. Dosselmann, R. & Yang, X.D. (2011). A comprehensive assessment of the structural similarity index, *X.D. SIViP*, pp. 5-81, doi: 10.1007/s11760-009-0144-1
  - [11]. Scikit-Image, [http://scikit-image.org/docs/dev/auto\\_examples/transform/plot\\_ssim.html](http://scikit-image.org/docs/dev/auto_examples/transform/plot_ssim.html), Accessed: 15 Sept 2018

## A Selective Chemosensor for Lead Divalent Based on Ruthenium-[(E)-2-(((4-(ethoxycarbonyl)phenyl)iminio)-methyl)phenolate] Complex

Amer A. G. Al Abdel Hamid

Department of Chemistry, Yarmouk University, Irbid 21163, JORDAN

\* amerj@yu.edu.jo

### ABSTRACT

The complex Ruthenium [(E)-2-(((4-(ethoxycarbonyl)phenyl)iminio)-methyl)phenolate] has been investigated for its potential in chemosensation. Studying the complex (*utilizing standard analytical and spectroscopic techniques*) with a wide range of metal ions showed that this complex possesses interesting photochemical properties that promotes it to act as a selective detector for Lead(II) ions in aqueous solution. The sensation of the complex for lead ions in aqueous matrix (*employing UV/vis spectroscopy*) was high, with low detection limit. The results presented in this report imply a valuable recruitment of an efficient colorimetric chemosensor for lead ions in aqueous solution.

**KEYWORDS:** Lead: Chemosensor : Detection : Colorimetric : Aqueous : Ruthenium

### 1. INTRODUCTION

Heavy-metals pollution still attracts the attention of the environmental researchers[1-5], this is due to the severely adverse effects on the environment and human health. Lead is one of the three most abundant and hazardous pollutants (including cadmium and mercury) in the environment. For instance, the Centers for Disease Control and Prevention (CDC) set a reference level for the maximum concentration values of lead at 0.1 mg/L (0.5  $\mu$ M or 100 ppb) to evaluate whether the lead levels higher than toxic level [6, 7]. Therefore, monitoring the concentration of Pb(II) ion below the defined toxic level, still a challenge. Toward achieving this goal, many methods of analysis for Pb(II) metal ion have been employed [8-11]. Over the past 10 years, for instance many highly sensitive and selective Pb(II) determination methods have been developed, most of which are primarily based on a several highly sophisticated analytical techniques [12-14]. These techniques usually require complicated instrumentation, delicate sample pretreatment and storage processes. For example and among other recently developed detection methods, researchers have, in many occasions, employed metal nanoparticles for prompt visual detection of Pb(II) ions [15-17]. However, in many circumstances, the color response of the nanoparticle solution was not distinctly visualized, in addition, the absorption spectra of metal nanoparticles were not able to precisely reflect the subtle changes in concentration of Pb(II).

To date, there has been a paucity of studies that can be successfully used for tracking Pb(II) ions in aqueous media [18, 19]. Therefore, exploration of new selective and sensitive probes that can be applied for evaluation of Pb(II) ions in aqueous media (*both biological and environmental applications*) is still demanded. In this study we try to keep up with the ongoing efforts [6] to develop a rapid, reliable and economical technique for on-site determination of Pb(II) ions. In fact, colorimetric probes and their analogues based on small organic functionality now become an indispensable sensing agents for the construction of Pb(II) sensors convenient for aqueous media. Unfortunately, most of these Pb(II) sensitive small organic molecules can only be employed in organic or organic/aqueous mixtures due to their poor water solubility, the fact that might limit their use in aqueous relevant systems.

As such, optimal ratiometric chemosensors (*based on colorimetric spectral changes*) for lead ions that possess fast response at ambient temperature, can selectively detect Pb(II) ions, and can operate in aqueous media are still acquire great attention and highly demanded. Transition metals-Schiff bases complexes are interesting chromophores due to possessing luminescent properties. For examples, Transition metal complexes [20-22] of Schiff bases containing salicylaldehyde and

benzoylacetate have been found to practice a luminescent behavior of good quantum yield in the UV- region [23]. Therefore, assemblies of transition metals-Schiff bases, are anticipated to yield chemical structures that would have the potential to work as chemodetectors, this is when interacted with electron deficient metal center. As a substitute, here, we introduce the complete water soluble Pb(II) sensitive new ruthenium-Schiff base complex (RBL) with the formula  $[\text{Ru}(\text{bpy})_2\text{L}_2]$ , where  $\text{L} = \{(E)\text{-}2\text{-}(((4\text{-}(\text{ethoxycarbonyl})\text{phenyl})\text{iminio})\text{-methyl})\text{phenolate}\}$ . This agent which is aided by the functionality;  $\{(E)\text{-}2\text{-}(((4\text{-}(\text{ethoxycarbonyl})\text{phenyl})\text{iminio})\text{-methyl})\text{phenolate}\}$  can serve as a new sensitive chemodetector that operates quite facilely for lead ions in aqueous medium. The incorporation of Pb(II) cations into this sensor moiety, is expected to influence the absorption properties of RBL core and thus allowing access to a new potential chemosensor based on the chromophore color change as a result of electronic transitions. Interestingly, a few of similar structures that show good solubility in aqueous media would exhibit superior and effectively detection for the Pb(II) traces.

## 2. EXPERIMENTAL

All solvents used throughout this work were of analytical grade and used without any further purification: Salicylaldehyd: (assay > 99, Merck, Schuchardt-Hohenbrunn-Germany), benzocaine (Aldrich, USA),  $\text{Ru}(\text{NO}_3)_3 \cdot 6\text{H}_2\text{O}$  (Aldrich, USA), absolute ethanol (TEDIA), diethyl ether (TEDIA), glacial acetic acid (TEDIA). The ligand;  $((E)\text{-}2\text{-}(((4\text{-}(\text{ethoxycarbonyl})\text{phenyl})\text{iminio})\text{-methyl})\text{phenolate})$  (L) was prepared according to a literature procedure [22, 24]. UV/vis spectra were recorded for water solutions on a Shimadzu UV-1800 spectrophotometer using 1.0-cm quartz cuvettes. Infrared spectra were collected on a Spectrometer ALPHA-Bruker Optics. All IR spectra were recorded as pressed disks of the sample dispersed in KBr powder. Typically, for each spectrum, 100 scans were coadded at  $4\text{cm}^{-1}$  resolution.

Preparation work was started by preparing the complex, *cis*-Ruthenium-bis[2,2'-bipyridine]-dichloride dihydrate,  $\text{Ru}(\text{bpy})_2\text{Cl}_2 \cdot 2\text{H}_2\text{O}$ , which was prepared and characterized as reported, by Sullivan et al[25]. The complex; Ruthenium-bis[2,2'-bipyridine]-bis[ $((E)\text{-}2\text{-}(((4\text{-}(\text{ethoxycarbonyl})\text{phenyl})\text{iminio})\text{-methyl})\text{phenolate})$ ],  $[\text{Ru}(\text{bpy})_2\text{L}_2]$ ,  $\text{L} = ((E)\text{-}2\text{-}(((4\text{-}(\text{ethoxycarbonyl})\text{phenyl})\text{iminio})\text{-methyl})\text{phenolate})$ , (RBL), was prepared by mixing a solution of the Schiff base ligand L (0.50 g, 1.85 mmol, dissolved in 25 mL of ethanol) with a solution of  $\text{Ru}(\text{bpy})_2\text{Cl}_2 \cdot 2\text{H}_2\text{O}$  (0.35 g, 0.67mmol) dissolved in 25 mL of warm water. After mixing, the resulting solution was subjected to reflux overnight. At the end of the reflux time, the mixture was filtered while hot and left to precipitate at room temperature. This lasts for two days, where an orange crystalline product was found to settle down at the bottom of the reaction vessel. The complex (*which is formed in good yield*), was collected, washed with portions of water, ethanol followed by diethyl ether and finally dried in oven under vacuum.

## 3. RESULTS AND DISCUSSION

Interaction of the Schiff base L with the metal ion  $\text{Ru}^{\text{II}}$ , in the form of  $\text{Ru}(\text{bpy})_2\text{Cl}_2 \cdot 2\text{H}_2\text{O}$  has afforded the complex;  $[\text{Ru}(\text{bpy})_2\text{L}_2]$ , (RBL). In this complex, L is expected to coordinate Ru metal ion as a monodentate anionic ligand, where the phenolic protons migrates toward the adjacent uncoordinated imino nitrogens. This kind of interactions is known in literature [24, 26, 27] for transition metal-Schiff bases complexes. The infrared spectrum of the RBL complex, showed three medium intensity bands in the range  $3433\text{-}2939\text{ cm}^{-1}$ . These bands are attributed to the stretching frequency of the O–H, N–H and aliphatic C–H groups, respectively. The characteristic strong two bands at  $1697$  and  $1620\text{ cm}^{-1}$  are assigned for the stretching frequency absorption of C=N and the asymmetric stretching frequency of COO<sup>-</sup> groups.

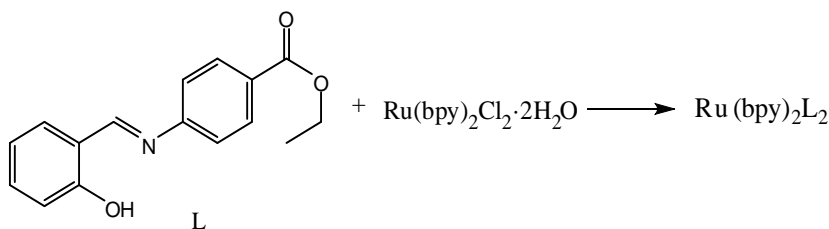


**Figure 1.** Reaction scheme of the ruthenium complex, RBL

The important Ru–O and Ru–N absorption bands appear at 462 and 416  $\text{cm}^{-1}$ , respectively. Other less important bands such as, (asymmetric stretching of CO,  $\text{CO}_2$  at 2360  $\text{cm}^{-1}$ ), (aromatic C=C at 1473  $\text{cm}^{-1}$ ), (aromatic C–O at 1381  $\text{cm}^{-1}$ ) also appear in the spectrum of the RBL complex.

The central  $\text{Ru}^{\text{II}}$  in RBL is six-coordinated [4, 5, 24], this is via the two phenolic oxygens of the two ligands L, and the four nitrogens of the two bipyridine ligands. The two imine nitrogens are not expected to participate in the coordination process with  $\text{Ru}^{\text{II}}$  metal ion, due to their involvement in intramolecular hydrogen bonding with the neighboring hydrogens [24].

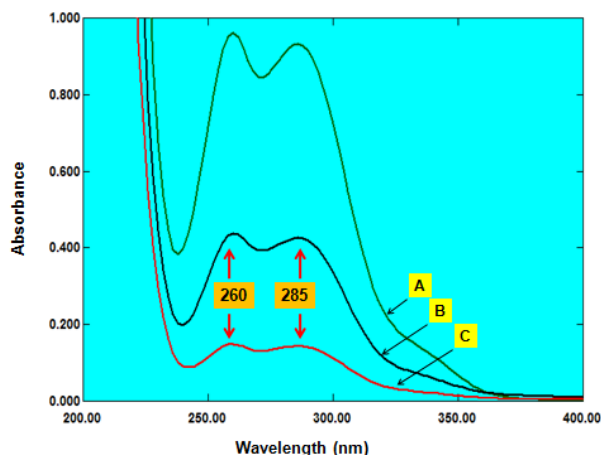


**Figure 2.** Visible absorption spectra of (a) RBL dye (b) RBL treated with 1.5 eq (C) RBL treated with 2.0 eq of  $\text{Pb}^{\text{II}}$  ions

### 3.1. Uv/Visible Spectral Analysis of the RBL Complex

In aqueous solution, the Uv-visible spectra of the complex RBL shows two essential absorption bands: one band is close to the Uv-region and the second band in the visible region, Figure 2a. The Uv-band appears at ~ 260 nm, and the second band appears at ~ 285 nm. Both bands are attributed to the  $\pi \rightarrow \pi^*$  and  $n \rightarrow \pi^*$  electronic transition of the  $-\text{N}=\text{N}-$  group, respectively [28, 29].

### 3.2. Uv/Visible Spectral Analysis of Ru Interacted with Pb(II) Metal Ion

Interaction of RBL with Pb(II) ions in aqueous medium has resulted in a pale yellow colored solution, indicating a reaction between Pb(II) ions and RBL complex. This pale yellow color was observed to develop instantaneously upon mixing the two aqueous solutions of RBL complex and Pb(II). In effect, spectral changes have been facilitated in this solution mixture as a result of the indicated interaction.



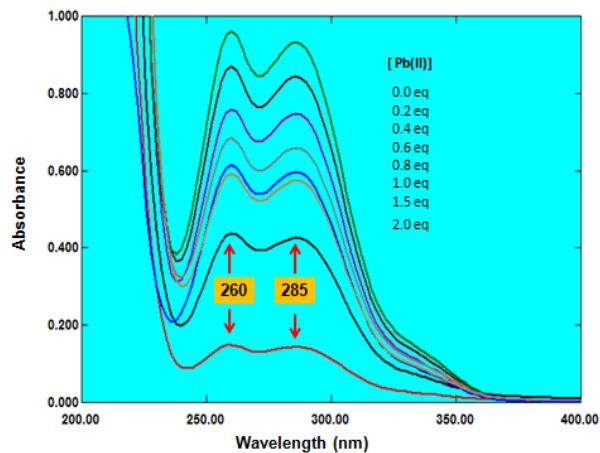


**Figure 3.** Visible absorption spectra of the RBL dye titrated with (2.0 to 0.0) equivalents of  $Pb^{II}$  ions.

A spectroscopic titration of  $Pb(II)$  was conducted with  $1.0 \mu M$  aqueous solution of the RBL complex at pH 7. Upon addition of an increased amount of  $Pb(II)$  ions, the peak areas under both peaks decline, this is shown respectively, in Figure 2, curves b and c. The reaction responsible for these changes was observed to reach completion fast ( $< 2$  min), where the reduction in peak areas was observed to respond to  $Pb(II)$  increments and changes linearly with the added  $Pb(II)$  concentrations, Figure 3. Interestingly, the saturation of RBL complex with  $Pb(II)$  ions was attained beyond the addition of two equivalents of  $Pb(II)$  ions, where, more additions of  $Pb(II)$  ions brought no spectral changes in the absorption profiles, this is shown in Figure 4.

In a control experiment, to test the selectivity of the RBL toward  $Pb(II)$  ions, the proceeded optical measurements were repeated for aqueous solutions of a wide spectrum of cations except  $Pb(II)$  cation. No similar changes in the absorption spectrum of RBL complex was observed upon interaction with the forementioned cations. This demonstrates that RBL complex, neither responding to the other metal cations, nor their accompanied anions. This, in other words means that, RBL complex has enough selectivity toward  $Pb(II)$  ions over other metal ions when co-existed in an aqueous matrix. This was deduced when RBL complex was interacted with an aqueous matrix containing submicromolars of  $Pb(II)$  and micromolars of:  $Ag(I)$ ,  $Zn(II)$ ,  $Cu(II)$ ,  $Hg(II)$ ,  $Cd(II)$ ,  $Ni(II)$ ,  $Co(II)$ ,  $Fe(II)$ ,  $Mn(II)$ ,  $Mg(II)$ ,  $Ca(II)$ ,  $Ba(II)$ ,  $Li(I)$ ,  $K(I)$ ,  $Na(I)$ ,  $Rh(III)$ ,  $Cr(III)$  metal cations.

In additional control experiments, and when other salts of lead were used, similar spectral changes were observed. This reveals that, counter anions accompanying  $Pb(II)$  cation have no effect on the RBL sensation activity. To demonstrate the RBL practical effectiveness as a colorimetric detector for  $Pb(II)$  ions in aqueous medium, the detection limit was evaluated graphically based on the titration profile shown in Figure 4. The plot in the figure, indicates that RBL complex was able to sense  $Pb(II)$  ions in an order of lower than  $0.6$  ppm in aqueous medium. In result, this investigation, has enabled putting hand on a selective and sensitive agent which works efficiently in detecting lead ion in aqueous media. This agent, and as described ahead, shows remarkable sensitivity and selectivity toward  $Pb(II)$  ions in media that mimic the existence of  $Pb(II)$  in contaminated relevant aqueous matrix, where  $Pb(II)$  ions coexists with other interfering ions.

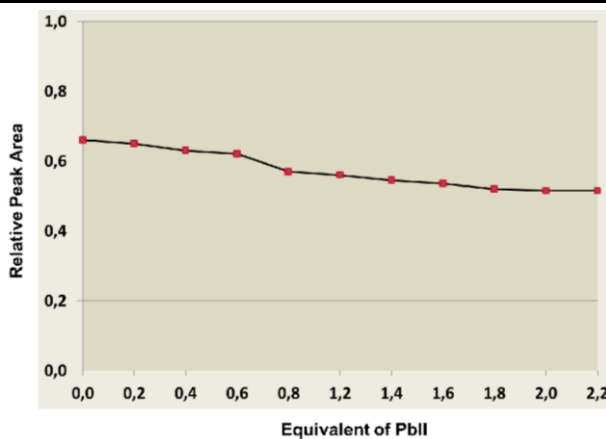


**Figure 4.** Detection limit of the RBL complex toward the  $Pb^{II}$  ions in aqueous solution

#### 4. CONCLUSION

The results presented in this report demonstrate that, RBL complex interaction with  $Pb(II)$  ions was responsible for the observed spectral changes in UV-visible spectrum of the RBL dye. Interestingly, this study has furnished a highly selective and sensitive chemosensor for  $Pb(II)$  ions in aqueous solution even in the presence of relatively high concentrations of potentially competing other metal cations. Furthermore, and based on UV-vis spectroscopy measurements, the limit of detection of the RBL chemosensor, was estimated to be lower than 0.2 eq ( $< 100$  ppm), providing a good chemosensation for  $Pb(II)$  ions.

#### ACKNOWLEDGMENTS

This work was financially supported by the Faculty of Graduate Studies and Scientific Research Yarmouk University, grant number 13/2015.

#### REFERENCES

- [1]. Amer Al Abdel Hamid, et al., Journal of Coordination Chemistry, 2010. 63 (5): . 731–741.
- [2]. Amer Al Abdel Hamid, et al., Jordan Journal of Chemistry, 2016. 11 (1): p. 8.
- [3]. Amer Al Abdel Hamid, et al., Res Chem Intermed 2011. 37: p. 791.
- [4]. Amer A. Hamid, et al., Jordan Journal of Chemistry, 2011. 6(4): p. 393.
- [5]. Amer A. Hamid, et al., International Journal of Inorganic Chemistry, published on line doi 10.1155/2011/843051, 2011.
- [6]. Shih-Yu Kuo, et al., Anal. Chem. , 2015. 87: p. 4765.
- [7]. U.S. Department of Health and Human Services, <https://www.hhs.gov/>
- [8]. Liu J., C. Z., Lu Y. , Chem. Rev., 2009. 109: p. 1948.
- [9]. Tao Li, Erkang Wang, and Shaojun Dong, Anal. Chem., 2010. 82: p. 1515
- [10]. Czarnik A. W., Acc. Chem. Res., 1994. 27: p. 302
- [11]. Prodi L., et al., Coord. Chem. Rev., 2000. 205: p. 59
- [12]. Tahan J. E., Granadillo V. A., and Romero R. A., Anal. Chim. Acta, 1994. 295: p. 187.
- [13]. Badiei H. R., Liu C., and Karanassios V., Microchem. J., 2013. 108: p. 131.
- [14]. Li P. C. and Jiang S. J., Anal. Bioanal. Chem., 2006. 385: p. 1092.
- [15]. Lin S.Y, Wu S. H, and Chen C. H, Angew. Chem. Int. Ed., 2006. 45: p. 4948.
- [16]. Lin Y.W, Huang C. C, and Chang H. T, Analyst 2011. 136: p. 863.
- [17]. Ferhan A. R., et al., Anal. Chem., 2013. 85: p. 4094.
- [18]. He Q, et al., J. Am. Chem.Soc., 2006. 128: p. 9316.

- [19]. Son H., et al., Chem. Eur. J., 2010. 16: p. 11549.
- [20]. Roy Y., Chakraborty A., and M. T. K., Chem. Soc. Rev., 2014. 273: p. 139
- [21]. Binnemans, K., Chem. Rev., 2009. 109: p. 4283
- [22]. El-Nawawy M. A., et al., NY Sci. J., 1996. 4: p.78
- [23]. K., B., Chem. Rev., 2009. 109: p. 4283
- [24]. Abdel Aziz Abu-Yamin, et.al., Journal of Structural Chemistry 2018. in press.
- [25]. B. P. Sullivan, D. J. Salmon, and T. J. Meyer, Inorganic Chemistry, 1978. 17(12): p. 3334
- [26]. Binnemans K., et al., J. Am. Chem. Soc., 2000. 12: p. 4335
- [27]. Binnemans K., et al., Philos. Trans. R. Soc. London A., 1999. 357: p. 3063
- [28]. Wolfgang, K., D. Natasa, and F. Stephanie, J. Molec. Stru., 2003. 656: p. 183
- [29]. Emel, Y. and B. Hamit, Turk. J. Chem., 2002. 26: p. 897

## An Experimental Test for neutron shielding

Sameer Al-Obaidi<sup>1\*</sup>, Kadir Günoglu<sup>2</sup>, Hakan Akyıldırım<sup>1</sup>, Iskender Akkurt<sup>1</sup>

<sup>1</sup>Süleyman Demirel University/Department of physics, Isparta, TURKEY

<sup>2</sup>Isparta Uygulamalı Bilimler Üniversitesi Isparta, TURKEY

\*Sameer\_alobaidi@yahoo.com

### ABSTRACT

The problem of shielding against neutrons has always attracted a great deal of attention. Neutron shielding requires slowing down neutrons and absorbing with a shield material. In this work the neutron shielding properties of different types of shielding materials have been investigated. Where <sup>252</sup>Cf source and many shielding materials were used to obtain neutron total macroscopic cross sections and some shielding parameters by experimentally.

**KEYWORDS** – Neutron, Shielding, total macroscopic cross section.

### 1. INTRODUCTION

Several investigators have contributed to find the shielding properties of concretes and building materials[1].

Concrete is one of the most appropriate and common stuff in composing of neutron shield. There are also various options in using material in producing it that result in composition of concrete material with different densities and compounds for benefiting from proper structural properties [2].

Concrete is a composite construction material composed primarily of aggregate, cement and water. In concrete production the aggregates are very important for durability of the concrete structures. The different aggregates as natural stones or minerals are used in production of concrete [3].

Neutrons have no electrical charge and are not easily stopped by matter because they interact with atoms of matter only via the nuclei. Energetic neutrons are more difficult to shield because absorption cross-section is much lower. Firstly, it is necessary to moderate these neutrons through elastic or inelastic scattering interactions and then slowed neutrons are absorbed with the shielding material. Shielding must be made with appropriate thickness and types of shield materials such as concrete, heavy concrete, and iron[4-6].

Microscopic cross section ( $\sigma$ ) is related to probability of interaction of neutrons with the target material. The sum of the microscopic cross sections of the individual nuclei in the target material per unit volume is called the Macroscopic Cross Section ( $\Sigma$ )

$$\Sigma = N\sigma \quad (1)$$

Where N is the atomic density of the target.

$$\Sigma \text{ (cm}^{-1}\text{)} = \frac{\ln T}{x} \quad (2)$$

Where x is sample thickness [7-9].

### 2. MATERIAL AND METHOD

Our experimental test done on the real shielding container for <sup>252</sup>Cf as neutron source that exist in nuclear laboratory of Physics Department in Suleyman Demirel University. Where the geometry of the <sup>252</sup>Cf neutron source arranged as show in Figure 1. Where we investigated the shielding capability that designed in physics laboratory to attenuate and absorbed the neutron radiation that emitted spontaneously from the <sup>252</sup>Cf source.

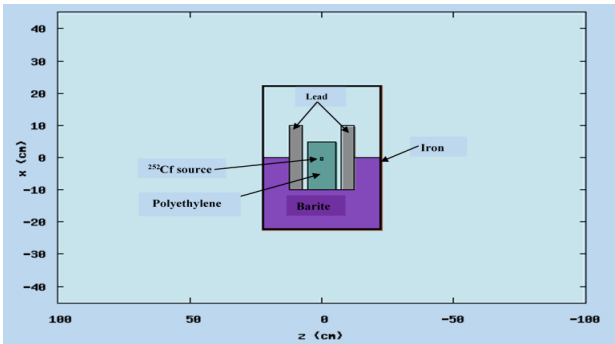


Figure (1): The geometry of neutron <sup>252</sup>Cf source shielding

Also we used three types of concrete where the barite was used in the proportions of 0%, 50% and 100% have been produced and named as BC0, BC50 and BC100. We used the numbers in Table (1) for the three types of concrete BC0, BC50 and BC100 in our experimental test.

The Portland Cement (PC) 42.5 which is obtained from Goltas plant in Isparta, normal aggregate and barite were used to produce concrete. The chemical composition of cement and aggregate has been shown in Table 1. Three different types of concrete where the barite was used in the proportions of 0%, 50% and 100% have been produced and named as BC0, BC50 and BC100, respectively. The water-to-cement ratio was 0.5 for all concrete. In Table 2 the values of mixing proportion of concretes are given.

Table 1. Chemical composition of materials[9].

Chemical compositions	PC I 42.5	BC0 (barite 0%)	BC50 (barite 50%)	BC100 (barite 100%)
CaO	61	39.394	20.269	4.794
MgO	3.56	10.97	4.925	0.648
NaO	0	0.394	0.175	0.027
K2O	0.11	0.045	0.034	0.024
Fe2O3	3.81	0.464	0.394	0.229
P2O5	0	0.003	0.013	0.019
CO2	0	31.463	12.81	0
SiO2	22.56	12.7	7.626	3.29
H2O	0	7.42	6.103	3.909
Al2O3	7.11	1.038	1.353	1.364
SO2	2.7	0.46	0.378	0.205
BaSO4	0	0	46.012	83.046
MgCO3	0	0	0.049	0.09
NaCl	0	0	0.049	0.09
CaCO3	0	0	0.998	1.801
MnO2	0	0	0.099	0.18
NiO	0	0	0.099	0.18

3. RESULTS AND DISCUSSION

The transmission rate of neutron through concretes has been obtained and the results were displayed in Figs. (1-3). It is clear that the transmission rate decreasing with thickness of concrete while increase with increasing the Barite rates and the samples densities in the concrete types (BC 0, BC 50 and BC 100).

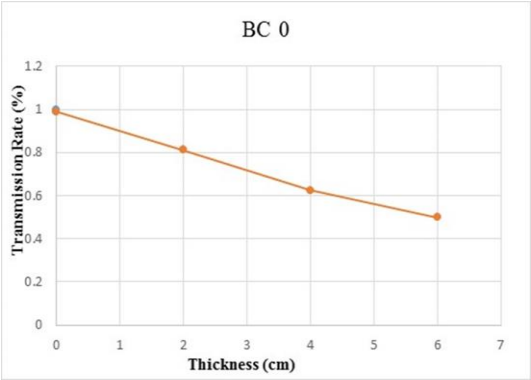


Figure 1. Neutrons Transmission Rate (%) as a function of BC0 Concrete Thickness

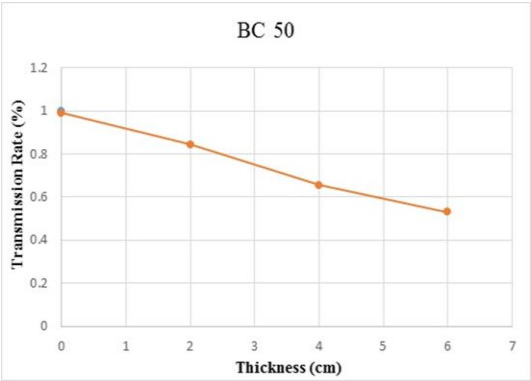


Figure 2. Neutrons Transmission Rate (%) as a function of BC50 Concrete Thickness

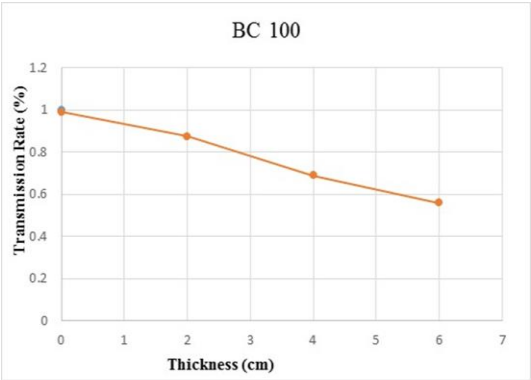
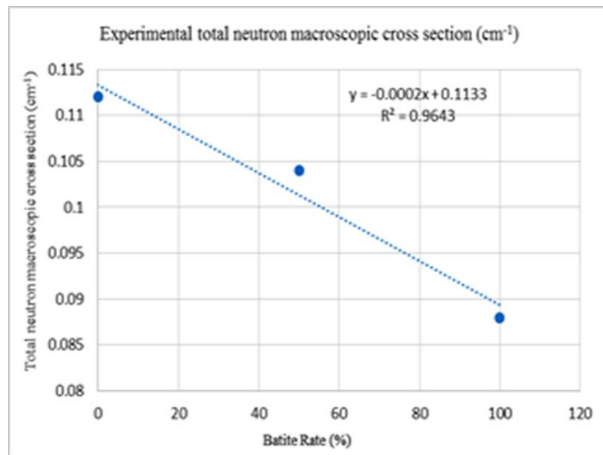
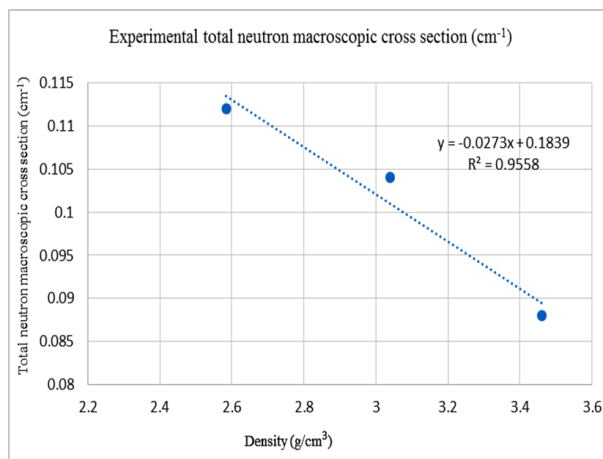


Figure 3. Neutrons Transmission Rate (%) as a function of BC100 Concrete Thickness

The  $\Sigma_t$  ( $\text{cm}^{-1}$ ) total neutron macroscopic cross section as a function of barite proportion in concrete have been displayed in the (Fig. 4). Also it can be seen that the total neutron macroscopic cross section  $\Sigma_t$ , ( $\text{cm}^{-1}$ ) decreased linearly with the increasing barite proportion in the concrete. Concrete density and total neutron macroscopic cross section  $\Sigma_t$ , ( $\text{cm}^{-1}$ ) correlation displayed in the (Fig. 5). It is clearly seen in this figure that the total neutron macroscopic cross section  $\Sigma_t$ , ( $\text{cm}^{-1}$ ) decreased with the increasing concrete density.



**Figure 4.** Variation of total neutron macroscopic cross section  $\Sigma_t$ , ( $\text{cm}^{-1}$ ) versus Barite rate of concrete.



**Figure 5.** Variation of total neutron macroscopic cross section  $\Sigma_t$ , ( $\text{cm}^{-1}$ ) versus Density ( $\text{g/cm}^3$ ) of concrete.

#### 4. CONCLUSION

In this work we calculated several parameters regarding interactions between three types of concrete (BC 0, BC 50 and BC 100)  $^{252}\text{Cf}$  source neutrons. The information on interactions

between neutron and these compositions may be useful in terms of radiation physics. Also we measured neutron total macroscopic cross section.

It can be clearly concluded from this work that the barite not improved concrete shielding properties against neutron radiation. Where the increasing in Barite Rate (%) and density for these types of concrete result in decreasing of total neutron macroscopic cross section  $\Sigma_t$ , ( $\text{cm}^{-1}$ ).

## REFERENCES

- [1].I.Akkurt a, A.M. El-Khayatt, The effect of barite proportion on neutron and gamma-ray shielding Annals of Nuclear Energy 51 (2013) 5–9.
- [2].D. Sariyer, R. Küçer, N. Küçer Neutron Shielding Properties of Concretes Containing Boron Carbide and Ferro – Boron, Procedia - Social and Behavioral Sciences 195 (2015) 1752 – 1756.
- [3].A.M. El-Khayatt, I. Akkurt, Photon interaction, energy absorption and neutron removal cross section of concrete including marble, Annals of Nuclear Energy 60 (2013) 8–14.
- [4].D. Sariyer, R. Küçer, N. Küçer, Neutron Shielding Properties of Concretes Containing Boron Carbide and Ferro – Boron, Procedia - Social and Behavioral Sciences 195 (2015) 1752 – 1756.
- [5].Yousra Mohamed Braima Mohamed, Dr. Nassreldeen Abdelrazig Abdelbari Elsheikh, (2014). Monte Carlo Modeling of Effective Shielding Systems for Fast Neutrons, M.Sc. Thesis in Physics.
- [6].IAEA, (2004). RADIATION, PEOPLE AND THE ENVIRONMENT.
- [7].G.F. Knoll. Radiation Detection and Measurement - 3rd edition, (1999), John Wiley & Sons, Professor of Nuclear Engineering and Radiological Sciences-University of Michigan Ann Arbor, Michigan.
- [8].Erhan GÖRMEZ, Turgay KORKUT, FLUKA MONTE CARLO SIMULATIONS ON NEUTRON INTERACTIONS WITH FeCrP AND FeTiP, Physicochem. Probl. Miner. Process. 49(2), (2013), 453–462.
- [9].Akkurt, I., Akyıldırım, H., Mavi, B., Kilincarslan, S., Basyigit, C., (2010). Photon attenuation coefficients of concrete includes barite in different rate. Ann. Nucl. Energy 37, 910–914



## Model Selection in MARS-Constructed Biological Networks

Gül Bahar Bübül<sup>1</sup>, Vilda Purutçuoglu<sup>2\*</sup>

<sup>1, 2</sup> Middle East Technical University (METU), Department of Statistics, Ankara, TURKEY

\*vpurutcu@metu.edu.tr

### ABSTRACT

In statistical literature, the estimation of high-dimensional graphical models is closely associated with the selection of a regularization parameter. In this study, we suggest model selection criteria, namely, ICOMP, CAIC and CAICF to apply on real microarray datasets, in the high dimensional setting, when selecting an optimal model with the best regularization parameter among a collection of submodels. In the construction of biological networks, we use the loop-based MARS model and compare our results with GCV (MARS's original model selection criterion).

**KEYWORDS** - Model Selection Criteria, Loop-based MARS, Biological Networks.

**Acknowledgement:** The authors thank to the METU research grant (No: BAP-08-11-2017-035) for its support.

### 1. INTRODUCTION

The construction of biological networks can be achieved via different linear and nonlinear modelling approaches, which are corresponding with its specific regression function and are mainly grouped as parametric and nonparametric methods [1]. The ordinary differential equations (ODE), Gaussian graphical model and the generalized additive models (GAM) [4], such as multivariate adaptive regression splines (MARS), random forest (RF) and classification and regression trees (CART), are some of the well-known approaches under this branch. Among these groups, GGM is counted as parametric way to build a biological network as it is based on the multivariate normality assumption of the observations (which is one of the common assumptions in genomic studies), while ODE and majority of methods under GAM are thought as the nonparametric side since they are distribution free and also particularly designed for highly correlated data. In this study, we choose loop-based MARS (LMARS), which has been recently proposed for sparse biological networks [1] and propose new model selection criteria in place of its original criterion, called generalized cross validation (GCV) value. Thereby, in the organization of the paper, we initially describe LMARS, GCV and our proposal LMARS algorithm based our proposal model selection criteria in Section 2. In Section 3, we present the application of all criteria via real networks and in Section 4, we summarize our outcomes.

### 2. LMARS MODEL, GCV AND PROPOSAL MODEL SELECTION CRITERIA

Shortly, MARS [4, 1] is a technique based on a nonlinear model. By combining of two piecewise linear functions, known as linear splines, with a knot, i.e., breaking point, at the value, it can provide a successful approximation of nonlinear structures. In this model, each predictor variable is represented with two basis linear functions and its corresponding knots for each observed value. In this sense, the set of all possible reflected pairs and knots at each observed value, belonging to corresponding predictors, refers to domain when constructing regression model. Thus, to build a MARS regression function, one exploits the collection of basis functions, instead of original predictor variables, which is a preferred way to obtain the classical linear model. On the other hand, LMARS [1] is developed as a special case of MARS where the full model is summarized under merely main effects and for each gene in the system, the interactions with other genes are estimated separately in an iterative way. In the construction of networks, LMARS uses a two-step procedure similar to MARS. These are the forward stage, where we add iteratively the candidate spline functions into the fitted model by controlling whether the term improves the goodness-of-fit

of the fitted model, resulting in the largest model form, and the backward stage, where we eliminate the terms, i.e., splines, from the model by such a way that if a term can be seen as a reason for the least increase on the goodness-of-fit of the model, it is chosen to be discarded from this model. In this greedy model selection strategy, the best model is chosen from the minimum

$GCV(\tau) = \frac{\sum_{i=1}^N (y_i - \hat{f}_\tau(x_i))^2}{(1 - M(\tau)/N)^2}$ , where  $\tau$  indicates the number of terms and  $\hat{f}_\tau$  stands for the best

estimated model.  $\hat{f}_\tau(x_i)$  describes the fitted response vector corresponding with the  $i$ th ( $i = 1, \dots, n$ ) predictor vector  $x_i = (x_{i1}, x_{i2}, \dots, x_{ip})^T$ . So, one aims to obtain the best estimated model with the optimal number of terms, i.e.,  $\tau$ .  $M(\tau)$  refers to the number of effective parameters used in model construction and  $N$  defines the number of the observations. In the high dimensional settings, when constructing a biological network and displaying relationships among its entities, the challenge is selecting an optimal model connected to its penalizing constant. In this study, we propose consistent AIC (CAIC), consistent AIC with inverse Fisher information (CAICF) and information-complexity criterion (ICOMP) [3], to choose the optimal model among a set of submodels of LMARS as the alternative of GCV. Here, we particularly select these criteria since they can measure the complexity without suffering from the multicollinearity problem between system' component. Thereby, in the calculation, we develop the following scheme inserted in LMARS: *i*) Construct model for each gene via LMARS by checking the maximum number of parameters in the backward stage from 2 to  $p$  (total number of genes in the system). *ii*) Compute ICOMP, CAIC, CAICF for each gene under multivariate normal distribution and choose the minimum entries for each criterion to select the optimal submodel. *iii*) Repeat steps (*i-ii*) for every gene in the system.

### 3. APPLICATION

In the evaluation of our proposal criteria, we use 4 real microarray datasets. Dataset 1 is a benchmark data in comparative studies [1] and the rest of datasets is taken from ArrayExpress database with names E-GEOD-9891 (Data 2), E-GEOD-63678 (Data 3), E-GEOD-48926 (Data 4) which are composed of 11 gynecological cancer genes (MAPK2K1, CEBPB, CTNNB1, TFAM, TP53, IMP3, ERBB2, CHD4, MAPK1, PDIA3 and MBD3) [2]. In the following table, we list the accuracy and F-measure of all criteria. Interestingly, the results indicate that, when we convert the estimated covariance matrix which is the model parameters in graphical models [1, 2] and is converted to the binary form under an adjacency matrix to compute the binary accuracy measures (F-measure and accuracy), we obtain exactly the same findings via all approaches as seen in Table 1. Whereas, when we check the estimated regression coefficients for each criterion, individually, we observe that GCV has a tendency to choose the complex models when comparing to our proposal criteria. In other words, GCV tends to generate complex graph with strong strengths, i.e., big regression coefficients for splines, between genes. However, the biological networks are sparse from their natures, hence, they intent to generate hubs, rather than randomly connected genes [1, 2]. On the other hand, the proposal criteria are designed to avoid complex models in the high dimensional setting by taking into interdependence account between components of biological systems. Thereby, they are superior than GCV when handling with sparse structures such as the structures of biological networks. Therefore, when we control the estimated regression coefficients found from CAIC, CAIF and ICOMP, we obtain models which have few regression coefficients with high entries and majority of coefficients with very low entries that can be also taken as "zero" in the binary form of the estimated covariance matrix. But, in this study, we calculate the accuracy measures of binary forms without taking into account the absolute values of regression coefficients and accept all entries as "one" as long as they are different from zero like the original application of LMARS. This outcome shows us that, in fact, the LMARS model may need a decision rule to find the threshold value in the transformation of binary forms since the regression coefficients lie in a wide range in the estimated model. As a result, from the current findings, we see that GCV

mostly indicates models having equally weighted regression coefficients, on the contrary, the proposal criteria always select models owing low regression coefficients for majority of genes and high regression coefficients for only few genes in the detection of optimal model in the given real biological networks which is a more suitable preference for the natures of biological systems.

**Table 1.** The accuracy and F-measure of GCV, CAIC, CAIF and ICOMP for 4 real biological network datasets.

Name of Dataset	Data 1	Data 2	Data 3	Data 4
Accuracy	0.719	0.091	0.091	0.091
F-Measure	0.392	0.162	0.162	0.162

#### 4. CONCLUSION

In this study, we have introduced alternative model selection criteria for LMARS, instead of GCV, for the detection of the optimal model in the construction of biological networks. We have suggested CAIC, CAICF and ICOMP and compared the accuracy of all criteria by real datasets. We have found that the proposal criteria can more successfully select the optimal model.

#### REFERENCES

- [1].E. Ayyıldız, M. Ağraz, V. Purutçuoğlu, MARS as an alternative approach of Gaussian graphical model for biochemical networks, Journal of Applied Statistics 44 (16) (2017), 2858-2876. DOI: 10.1080/02664763.2016.1266465
- [2].B. Bahçivancı, V. Purutçuoğlu, Proc. International Conference on Computational and Experimental Science and Engineering (ICCESSEN 2017), 4-8 October, Antalya-TURKEY.
- [3].H. Bozdoğan, A new class of information complexity criteria with an application to customer profiling and segmentation, Istanbul University Journal of the School of Business Administration 39 (2) (2010) 370-398.
- [4].T. Hastie, R. Tibshirani, Generalized additive models. Statistical Science 1 (3) (1986) 297-318. DOI:10.1214/ss/1177013604

## Evaluation of asynchronous injection alternating production considering boundary layer effect in tight oil with complex fracture networks

Wang Deqiang, Cheng Linsong\*, Cao Renyi, Yin Fuguo

College of Petroleum Engineering, China University of Petroleum, Beijing 102249, China

\* lscheng@cup.edu.cn

### ABSTRACT

The energy dissipation of tight reservoirs is fast. During the asynchronous injection alternating production (AIAP) process, the development can achieve good results. The boundary layer effect existing in the narrow pore throat, which is a non-flow film due to liquid-solid interaction in the nanopore, would reduce the effective flow space and the production. However, very few numerical simulation studies have considered the influence of boundary layer effect on asynchronous injection alternating production under complex seam conditions. In order to describe the distribution of fractures, embedded fracture method (EDFM) has been used. The reduction of effective flow space caused by boundary layer effect (BLE) during AIAP are also considered to evaluate the well performance. In the development of depletion and AIAP, the boundary layer effect will significantly reduce the yield and accelerate the production decreasing, so the evaluation of well performance should consider BLE in the tight oil reservoir. The asynchronous injection alternating production have a longer stable production period, a higher oil recovery and a good application prospect.

**KEYWORDS** - *asynchronous injection alternating production; embedded discrete fracture model; boundary layer; tight reservoir*

### 1. INTRODUCTION

Energy is import for living [1-3] and the development of horizontal fracture wells has become a mainstream technology in the tight oil reservoir. However, tight reservoir recovery is extremely low and production is declining rapidly [4]. Therefore, it is very necessary to supplement the energy when developing the tight reservoirs. Many scholars have reported on the results of laboratory enhanced oil recovery and on-site enhanced oil recovery measures, including water flooding, water huff-n-puff, gas flooding, gas huff-n-puff [5] and depletion. Although the injection ability of gas huff-n-puff and gas flooding are better, but the gas channelling is serious [6]. The traditional water injection development has a higher injection pressure and a relatively low recovery rate [7]. Therefore, asynchronous injection alternating production (AIAP) which has a lower production pressure and a relatively higher recovery rate is a promising way of development [8].

Many scholars have found that the flow characteristics in tiny pores change, and its flow law is no longer the same as the macro flow law [9]. Chiara Neto provided a review of experimental studies regarding the phenomenon of slip of liquids at solid interfaces considering surface roughness and wettability [10]. In the micro-nano pores, due to the fluid-solid interaction force, there is a non-flowing film called Boundary layer effect. Tight reservoir pores are small [11], so BLE is widespread and must be considered. In previous studies, the impact of BLE on production characteristics was less considered in reservoir numerical simulations [12]. In order to accurately characterize the boundary layer effect, this paper deduces the effective permeability expression considering BLE. The EDFM method can carry out numerical simulation research work more accurately [13]. The EDFM method [14] was used for vectorization programming, and the numerical simulation analysis of AIAP was carried out.

## 2. BOUNDARY LAYER EFFECT

In the tight reservoir, the pores and throats radius of the matrix are usually small leading a non-flowing film on the throat due to the fluid-solid interaction [15]. The boundary layer effect, which reduces the effective flow space and the effective permeability of the reservoir leading the production damage, causes the non-flowing thin film on the fluid-solid interface. According to the empirical formula of the boundary layer obtained by Wu [11], the corrected flow expression can be deduced, as shown in Fig.1.

$$Q_a = \frac{k}{\mu} A_a \nabla p = \frac{k_a}{\mu} A_f(r) \nabla p$$

Where

$$h = a r e^{br} (\nabla p)^c \cdot \mu$$

$$f(r) = \int_{-\infty}^{+\infty} \frac{[r-h(r)]^2}{r^2} G(r, r_0) dr = 1 - \frac{2au(\nabla p)^2}{\sqrt{\pi}} e^{\frac{(bs^2+r_0)^2}{2s^2}} + a^2 \mu^2 (\nabla p)^{2c} e^{2r_0b+2b^2s^2}$$

Where  $Q_a$  is modified volumetric flow rate,  $m^3/s$ ,  $k_a$  is modified permeability, md,  $k$  is permeability, md,  $h$  is thickness of the boundary layer,  $\mu m$ ,  $r$  is radius of experimental tube,  $\mu m$ ,  $\mu$  is viscosity of experimental fluid,  $mPa \cdot s$ ,  $p$  is pressure,  $MPa$ ,  $a, b, c$  is the parameters about solid-fluid interaction.

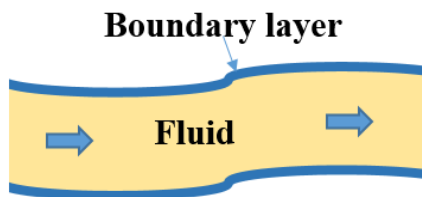


**Figure 1.** Explanation of decreasing the effective flow space because of boundary layer in capillaries model

## 3. METHOD

This paper uses the interflow expression derived from Dr. Fang Sidong's thesis[16]. The Embedded Discrete Crack Method is used to discrete and solve the black oil model.

Describe the similarities and differences between AIAP and depletion by comparing the four phases of Fig.2. First, in the first phase, all AIAP fractured reservoirs are developed using natural energy. In the second stage, the opening and closing of different hydraulic cracks are controlled by a packing device, injecting water from odd cracks and producing fluid from even cracks. In the third stage, the horizontal wells are closed to allow the underground oil-water fluid to be exchanged by osmosis. In the fourth stage, the production well is opened and the fluid is produced. However, for the development of exhaustion, all cracks are always in production until they are abandoned. It can be seen that in the AIAP process, the injection distance between the odd seam and the even seam is short, and the displacement pressure is large, which can overcome the problem of large displacement pressure of tight oil reservoir.

## 4. DISCUSSION

EDFM can simulate the reservoir development process. Many scholars have conducted relevant research and confirmed that EDFM can reflect changes in pressure and saturation during reservoir

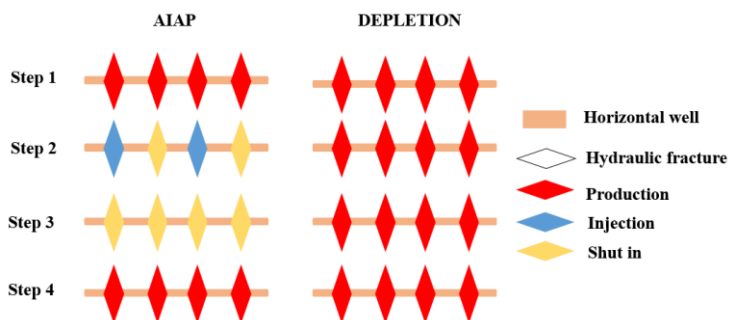


Figure 2. Explanation of AIAP and depletion

development. In the numerical simulation, the set time is 20 years, the hydraulic crack is 10 segments. AIAP and depletion are compared. AIAP is better than depletion. AIAP has low residual oil saturation and a large spread range. The pressure gradient between the water injection crack and the oil production crack is large, which can effectively overcome the difficulty of water injection and high injection pressure in dense reservoir. However, for depletion development, there is a large area of low pressure. It does not form an effective differential pressure displacement. From the quantitative analysis, Fig.3 (a) AIAP is better than exhaustive development under the same geological conditions and two development effects are relatively close within three years of production. However, after three years, the cumulative oil production of AIAP has been increasing, much higher than that of exhaustive development. The reason is that in the AIAP mode, the pressure gradient between the fractures is large, the area of use is large, and the displacement efficiency is high. It can be seen from Fig.3 (b) that the recovery rate of exhaustive development is only 4%, and the recovery of AIAP is 10%.

For typical blocks, it can be seen from Fig. 3(a) (b) that BLE has a large impact on yield. For AIAP, considering BLE, the recovery is reduced from 10% to 8%, which is greatly affected by BLE. However, exhaustion development is less affected by BLE, and whether or not BLE is considered, the recovery is about 4%. Therefore, the development method of using AIAP and other enhanced oil recovery measures should especially consider the impact of BLE.

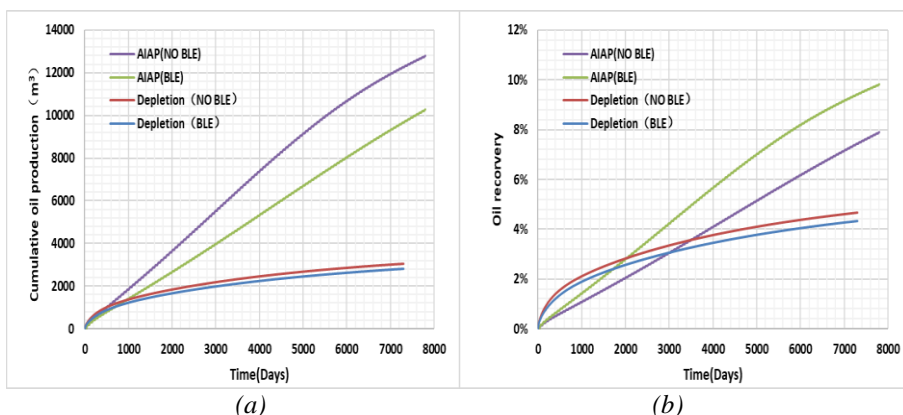


Figure 3. The production comparison of AIAP and depletion

## 5. CONCLUSION

In this paper, the EDFM method is used to simulate the reservoir development process by considering the boundary layer effect, and compares and analyses the pressure and saturation changes of asynchronous injection and failure development in different wells :

1. The BLE can reduce the flow space within the pores and reduce the permeability.
2. In tight reservoirs, AIAP has a wide range of applications, high degree of utilization, and high displacement efficiency.
3. The results show that the ultimate recovery of depletion development is low, only about 4%, AIAP can significantly improve oil recovery, and the recovery can reach 10%.

## REFERENCE

- [1]. I.Akkurt, A. Elkhayat, The Design Steps of a Hybrid Energy System M.E. Şahin, H.İ. Okumuş, 1160, DOI: 10.12693/APhysPolA.132.1160
- [2]. I.Akkurt, Development of a Low Noise and Low Energy Consumption Alpha Spectroscopy Amplifier for 222Rn Gas Detection, DOI: 10.12693/APhysPolA.132.789
- [3]. I.Akkurt, Proc. International Conference on Computational and Experimental Science and Engineering (ICCESN 2014), 24-29 October, 2014 Antalya-Turkey
- [4]. Baker, R., Group, B.R.E., Adj, U.C., Dieva, R., Hughes, B., Jobling, R., Lok, C., 2016. The Myths of Waterfloods, EOR Floods and How to Optimize Real Injection Schemes. Soc. Pet. Eng.
- [5]. Janiga, D., Czarnota, R., Stopa, J., Wojnarowski, P., 2018. Huff and puff process optimization in micro scale by coupling laboratory experiment and numerical simulation. Fuel. <https://doi.org/10.1016/j.fuel.2018.03.085>
- [6]. Sheng, J.J., 2017. Critical review of field EOR projects in shale and tight reservoirs. J. Pet. Sci. Eng. <https://doi.org/10.1016/j.petrol.2017.09.022>
- [7]. Spiteri, E.J., Juanes, R., 2006. Impact of relative permeability hysteresis on the numerical simulation of WAG injection. J. Pet. Sci. Eng. 50, 115–139. <https://doi.org/10.1016/j.petrol.2005.09.004>
- [8]. Yu, Y., Sheng, J.J., 2017. A comparative experimental study of IOR potential in fractured shale reservoirs by cyclic water and nitrogen gas injection. J. Pet. Sci. Eng. <https://doi.org/10.1016/j.petrol.2016.11.034>
- [9]. Zeng, H., Wu, K., Cui, X., Chen, Z., 2017. Wettability effect on nanoconfined water flow: Insights and perspectives. Nano Today 16, 7–8. <https://doi.org/10.1016/j.nantod.2017.05.001>
- [10]. Neto, C., Evans, D.R., Bonaccorso, E., Butt, H.J., Craig, V.S.J., 2005. Boundary slip in Newtonian liquids: A review of experimental studies. Reports Prog. Phys. <https://doi.org/10.1088/0034-4885/68/12/R05>
- [11]. Wu, J.Z., Cheng, L.S., Li, C.L., Cao, R.Y., Chen, C.C., Xu, Z.Y., Ding, G.Y., Cao, M., 2017. A novel characterization of effective permeability of tight reservoir - Based on the flow experiments in microtubes. IOR Norw. 2017 - 19th Eur. Symp. Improv. Oil Recover. Sustain. IOR a Low Oil Price World. <https://doi.org/10.3997/2214-4609.201700299>
- [12]. Sanchez-Rivera, D., Mohanty, K., Balhoff, M., 2015. Reservoir simulation and optimization of Huff-and-Puff operations in the Bakken Shale. Fuel. <https://doi.org/10.1016/j.fuel.2014.12.062>
- [13]. Cheng, L., Fang, S., Wu, Y., Lu, X., Liu, H., 2017. A hybrid semi-analytical model for production from heterogeneous tight oil reservoirs with fractured horizontal well. J. Pet. Sci. Eng. 157, 588–603. <https://doi.org/10.1016/j.petrol.2017.07.008>

- [14]. Li, J., Yu, W., Guerra, D., Wu, K., 2018. Modeling wettability alteration effect on well performance in Permian basin with complex fracture networks. *Fuel*. <https://doi.org/10.1016/j.fuel.2018.03.059>
- [15]. Li, Z., Qu, X., Liu, W., Lei, Q., Sun, H., He, Y., 2015. Development modes of Triassic Yanchang Formation Chang 7 Member tight oil in Ordos Basin, NW China. *Pet. Explor. Dev.* [https://doi.org/10.1016/S1876-3804\(15\)30011-2](https://doi.org/10.1016/S1876-3804(15)30011-2)
- [16]. Fang sidong, Numerical Simulation of Fractured Horizontal Well by Mixed Boundary Element Method. [D]. Beijing: China university of petroleum, 2017.



# A Novel Approach for Production Data Analysis of Fractured Carbonate Wells during Transient Flow Regime

Suran Wang\*, Linsong Cheng, Shijun Huang, Yongchao Xue, Yonghui Wu, Pin Jia and Deqiang Wang

China University of Petroleum, Beijing 102249, CHINA

\*wangsuran1991@163.com

## ABSTRACT

This paper presents an effective method to capture the production performance of fractured carbonate oil wells during the transient flow regime. A comprehensive model for a well in a dual-porosity reservoir is established, and the pseudo-steady state inter-porosity flow is considered in the model. By taking Laplace transform and inverse Laplace transform method, the solution for a well producing at constant bottom-hole pressure is obtained. To make a clear observation of different flow regimes, a series of new type curves are plotted based on the solution of the model. All flow regimes, including transient flow and late boundary dominated flow regimes can be recognized clearly from the new type curves. Furthermore, sensitivity analysis of transient production dynamics for some critical parameters are also analyzed using this new model. Finally, we make a comparison between the results of well test interpretation and the new method. The results show that the interpreted parameters using the proposed model coincide with the well test interpretation.

**KEYWORDS** - Carbonate oil reservoir, Model, Transient flow regime, Type curve, Production performance.

## 1. INTRODUCTION

Advanced decline curve methods are applicable to variable rate production condition and provide well and formation parameter information to reservoir engineers, which have been attracting considerable attention in recent years [1-4]. There is an array of empirical, reservoir simulation, analytical methods that can be used to analyze production data and make forecasts for carbonate oil wells. Arps [5] presented an empirical method that used to conduct history matching and predict future production rates. However, the decline type curves are plotted based on the empirical observation of production decline, which is not grounded in fundamental theory. Although reservoir simulation can take into account complexities, such as reservoir architecture and PVT properties, however, it is time-consuming in gridding and simulating [6]. In recent years, analytical models have gained much attention and been employed to perform production data analysis of black oil wells [7-11]. Fetkovich [7] presented an analytical method for analyzing production data during transient flow and developed a new production decline analysis techniques combined the proposed type curves with Arps type curves. But this method is established based on the assumption that the well is producing at a constant bottom-hole pressure condition. Blasingame and Lee [10] proposed a novel approach for analyzing production data of wells producing at variable bottom-hole pressure and variable production rate conditions. The changing PVT properties could also be considered by introduced the pseudo-pressure equation. Consequently, Blasingame type curves have been widely used for field data analysis of carbonate wells [12]. In fact, when we used the Blasingame type curves to perform production data decline analysis, boundary dominated regime should be observed on the type curves to avoid multi-solution. However, many fractured carbonate oil wells exhibit long transient flow regime and boundary dominated regime could not be observed.

Therefore, the main tasks of this article are (1) to establish and solve a comprehensive analytical model for carbonate oil reservoirs that can be used to analyze production data during transient flow regimes; (2) to make recognition of different flow regimes, including early transient flow regimes

and dominated flow regime from the new type curves; (3) to conduct sensitivity analysis of transient production dynamics; and (4) to perform well test interpretation and rate decline analysis for a real carbonate oil well to verify the validity of the proposed model.

## 2. MATHEMATICAL MODEL

### 2.1. Physical Model Assumptions

The fractured reservoir is structured by matrix system and fracture system. Physical model assumptions are considered as (1) total compressibility, including rock and fluid is a constant; (2) isothermal and Darcy flow is considered in this paper; (3) gravity and capillary forces are ignored; (4) pseudo-steady state inter-porosity flow is considered in the model.

### 2.2. Mathematical Model

For convenience, the mathematical model proposed in this paper is solved in dimensionless form. The dimensionless mathematical model is expressed as [12]:

$$\frac{\partial^2 p_{fD}}{\partial r_D^2} + \frac{1}{r_D} \frac{\partial p_{fD}}{\partial r_D} + \lambda_{mf} e^{-2S} (p_{mD} - p_{fD}) = \omega_f e^{-2S} \frac{\partial p_{fD}}{\partial t_D} \quad (1)$$

$$-\lambda_{mf} e^{-2S} (p_{mD} - p_{fD}) = \omega_m e^{-2S} \frac{\partial p_{mD}}{\partial t_D} \quad (2)$$

Initial condition

$$p_{fD} \Big|_{t_D=0} = p_{mD} \Big|_{t_D=0} \quad (3)$$

The external boundaries is assumed to be closed and given by

$$\frac{\partial p_{fD}}{\partial r_D} \Big|_{r_D=r_{eD}} = 0 \quad (4)$$

The inner boundary condition for a well producing at constant rate production is given as

$$\lim_{r_D \rightarrow 0} (r_D \frac{\partial p_{fD}}{\partial r_D}) = -1 \quad (5)$$

where  $r_D$  is the dimensionless radial distance;  $p_{fD}$  represents the dimensionless pressure of fracture system;  $p_{mD}$  represents the dimensionless pressure of matrix system;  $t_D$  represents the dimensionless production time;  $\lambda_{mf}$  represents the inter-porosity flow factor of matrix system to fracture system, dimensionless;  $\omega_f$  represents the fluid capacitance coefficient of fracture system, dimensionless;  $S$  represents the skin factor, dimensionless.

### 2.3. Solution to Mathematical Model

By using Laplace transform, the solution of the seepage model can be obtained. The dimensionless pressure in Laplace space for constant rate production can be expressed by:

$$\bar{p}_{wD} = \frac{-K_1(\sqrt{f(s)}r_{eD})I_0(\sqrt{f(s)}) - I_1(\sqrt{f(s)}r_{eD})K_0(\sqrt{f(s)})}{s\sqrt{f(s)}[I_1(\sqrt{f(s)})K_1(\sqrt{f(s)}r_{eD}) - I_1(\sqrt{f(s)}r_{eD})K_1(\sqrt{f(s)})]} \quad (6)$$

The dimensionless production rate in Laplace space for a well producing at a constant bottom-hole pressure can be obtained by:

$$\bar{q}_D = \frac{1}{s^2 p_{wD}} \quad (7)$$

### 3. NEW TYPE CURVES FOR DUAL-POROSITY RESERVOIR

In this section, to make a clear observation of different flow regimes, new type curves are plotted based on the solution of the model.

#### 3.1. Flow Regimes Recognition

As shown in Figure 1, four main flow regimes can be observed from the new types, which including the transient flow regime (early radial flow, inter-porosity flow regime), whole radial flow regime and boundary dominated flow regime.

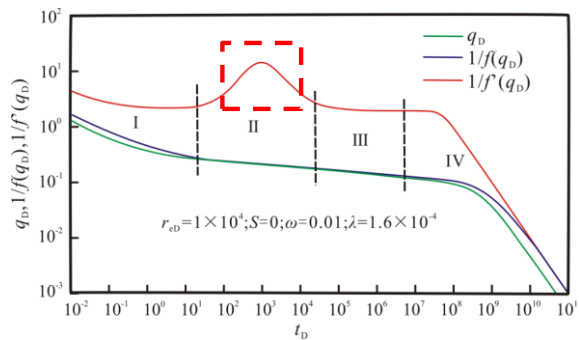


Figure 1. Type curve of production dynamics.

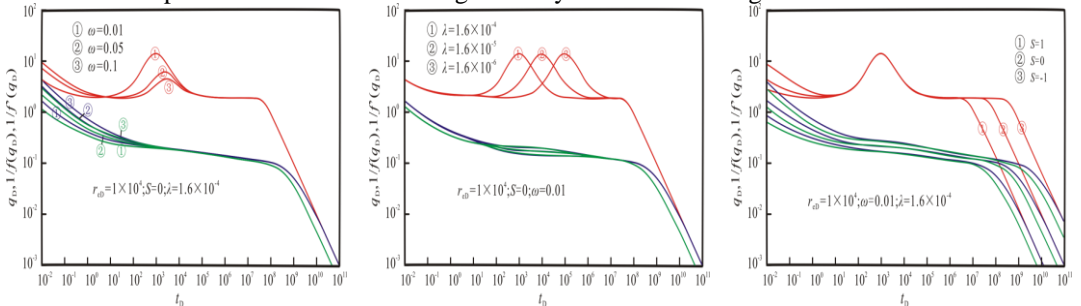
#### 3.2. Characteristics of Transient Production Dynamics

Here, we mainly analyzed the effects of fluid capacitance coefficient of fracture system ( $\omega_f$ ), inter-porosity flow factor ( $\lambda_{mf}$ ) and skin factor ( $S$ ) on production performance.

Figure 2a shows the influence of  $\omega_f$  on type curves. A bigger  $\omega_f$  leads to a lower  $\Lambda$ -shaped hump. The  $\omega_f$  represents the relative capacity of fluid stored in fracture system. A bigger  $\omega_f$  is the response of relative abundant reserves in fracture system.

Figure 2b shows the effect of  $\lambda_{mf}$  on type curves. The  $\lambda_{mf}$  represents the starting time of inter-porosity flow of the matrix system to the fracture system, so the bigger the  $\lambda_{mf}$  is, the earlier the time of inter-porosity is.

Figure 2c shows the effect of  $S$  on type curves. A bigger  $S$  leads to a higher location of dimensionless production rate curve during the early transient flow regime.



(a) Effect of  $\omega_f$  on type curves. (b) Effect of  $\lambda_{mf}$  on type curves. (c) Effect of  $S$  on type curves.

Figure 2. Effects of critical parameters on type curves.

#### 3.3. Model Verification

In this section, the validation of the proposed method is demonstrated in comparison to the results of well test interpretation. Based on buildup test data of a fractured carbonate oil well, we used a well test software to conduct well test interpretation. Then we used the real production data of the same well to perform production decline analysis with the new method. The matching curves are shown in Figure 3. The main interpreted parameters are also shown in Table 1. According to the results shown in Table 1, the interpreted parameters, such as permeability ( $k$ ),  $\omega_f$ ,  $\lambda_{mf}$  and  $S$  using the proposed method is in accordance with the solution of well test interpretation satisfactorily.

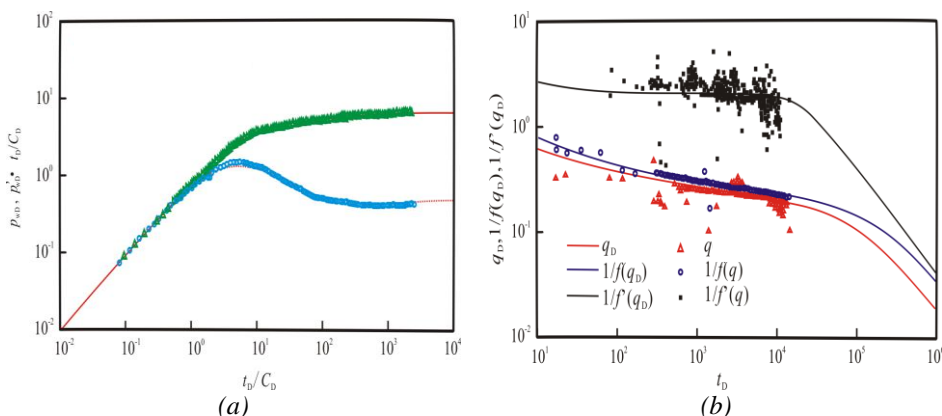


**Figure 3.** Results comparison between well test interpretation and the new method for validation case.

**Table 1.** Main interpreted parameters for validation case.

Interpretation method	$k$ (mD)	$\omega_f$	$\lambda_{mf}$	$S$
Well test	221	0.079	$2.37 \times 10^{-3}$	-2.58
New method	224	0.075	$2.43 \times 10^{-3}$	-2.47

#### 4. CONCLUSION

In this paper, a novel approach for production data analysis of fractured carbonate wells during transient flow regime has been proposed. The following conclusions can be drawn based on the discussions in this paper:

- (1) Four main flow regimes can be observed, including early transition flow regime, inter-porosity flow regime of the matrix system to the fracture system, whole radial flow regime and boundary dominated flow regime.
- (2) The  $\omega_f$ ,  $\lambda_{mf}$  and  $S$  have significant effects on different production regimes.
- (3) The accuracy of the new method is demonstrated through comparison to the well test interpretation.
- (4) Successful field data matching reveals the new method to be valid in performing rate decline analysis of fractured carbonate wells during transient flow regime.

#### REFERENCES

- [1]. H. Jabbari, Z. Zeng, M. Ostadhassan, SPE Annual Technical Conference and Exhibition, October 30 to November 2, 2011 Denver, Colorado, USA. <https://doi.org/10.2118/147008-MS>
- [2]. M.L. Fraim, W.J. Lee, J.M. Gatens, SPE Annual Technical Conference and Exhibition, 5-8 October, 1986 New Orleans, Louisiana. <https://doi.org/10.2118/15524-MS>

- [3]. Fernando Rodriguez, Heber Cinco-Ley, SPE Production Operations Symposium, 21-23 March, 1993 Oklahoma City, Oklahoma. <https://doi.org/10.2118/25480-MS>
- [4]. X. Jia, F. Zhang, SPE Annual Technical Conference and Exhibition, 26-28, September 2016 Dubai, UAE. <https://doi.org/10.2118/181616-MS>
- [5]. J.J. Arps, Analysis of decline curves, Transactions of the AIME 160 (1945) 228-247. <https://doi.org/10.2118/26959-PA>
- [6]. X. Mao, Y. Liu, W. Guan, Experimental and numerical simulation on the influence of anisotropic fracture network deformation to shale gas percolation, Arabian Journal of Geosciences, 11 (2018) 615. <https://doi.org/10.1007/s1251>
- [7]. M.J. Fetkovich, Decline curve analysis using type curves. Journal of Petroleum Technology, 32 (1980) 1065-1077. <https://doi.org/10.2118/4629-PA>
- [8]. L. Song, Z. Ning, L. Duan, Research on reservoir characteristics of Chang7 tight oil based on nano-CT. Arabian Journal of Geosciences, 11 (2018) 472. <https://doi.org/10.1007/s1251>
- [9]. S. Huang, Y. Yao, S. Zhang, Pressure transient analysis of multi-fractured horizontal wells in tight oil reservoirs with consideration of stress sensitivity, Arabian Journal of Geosciences, 11 (2018) 285. <https://doi.org/10.1007/s1251>
- [10]. T.A. Blasingame, T.L. McCray, W.J. Lee, Decline curve analysis for variable pressure drop/variable flowrate systems, SPE Gas Technology Symposium, 22-24 January, 1991 Houston-Texas. <https://doi.org/10.2118/21513-MS>
- [11]. R. Nie, Y. Jia, Y. Meng, Y. Wang, J. Yuan, W. Xu, New type curves for modeling productivity of horizontal well with negative skin factors, SPE Res. Eval. Eng, 15 (2012) 486-497. <https://doi.org/10.2118/163045-PA>
- [12]. P.M. Adrian, SPE Annual Technical Conference and Exhibition, 26-28 September, 2016 Dubai-UAE. <https://doi.org/10.2118/184484-STU>

## Laboratory Investigation of High-speed and High-efficiency Development Mechanism of Sandstone Reservoir

Pin Jia<sup>1\*</sup>, Linsong Cheng<sup>1</sup>, Yongchao Xue<sup>1</sup>, Deqiang Wang<sup>1</sup> and Suran Wang<sup>1</sup>

<sup>1</sup> China University of Petroleum-Beijing/College of Petroleum Engineering, Beijing, China

\*jiapin1990@163.com

### ABSTRACT

The investigation is to research the high-speed and high-efficiency development mechanism from several aspects including flushing efficiency, displacement characteristics and swept volume with methods such as one-dimensional displacement experiments, three-dimensional visualization physical simulation experiments, and numerical simulation. In order to analyse the high-speed and high-efficiency development mechanism from core scale, changes of oil-water relative permeability curve and residual oil saturation are comparatively analysed with one-dimensional displacement experiments at different displacement velocities. At the same time, effects of different production rates' influence are researched from such aspects as displacement characteristics, swept volume by combining three-dimensional visualization physical simulation experiments with numerical simulation tests in the same size. Different methods have shown that high development rate will improve development effect by increasing breakthrough recovery of the sand reservoir while reducing water cut.

**KEYWORDS** – Sandstone reservoir, High-speed development, High-efficiency development, Physical simulation, Swept volume

### 1. INTRODUCTION

Oilfields are usually developed at relative high production rate considering the limitation of development policy and development environment. Sun (2000) mainly focused on the high speed and high efficient development of Shengli Chengdao oilfield, including this field's development policy, history, and its status. Borisov (1971) summarized the development experience of water-flooding in the Soviet Union sandstone reservoirs within 20years, pointing out that increasing pressure difference between producers and injectors, enhancing the injection-production ratio and the injection quantity, will improve the oilfield development. Stosur (1975) and Sorbie (1988) described the relationship between the injection rate and oil displacement efficiency in core scale by displacement experiments. Moore (1995) also indicated that when the displacement rate is relatively high (100ft/day), the Capillarity number will increase, leading to a great improvement of displacement efficiency. Odeh (1985) found that a strong functional relationship remains between oil relative permeability and the displacement rate. Nguyen (2005) used a new dynamic network model to investigate the effects of displacement rate and wettability on imbibition relative permeability. Through the micro-physical model experiments, Sincock (1988) studied the water-flooding process under different displacement rates, and the results indicate that the residual oil saturation decreases with the increasing of the displacement rate. This paper takes Kumkol South Oilfield in Kazakhstan as an example to elaborate the high-speed and high-efficiency development mechanism of sandstone reservoirs from the aspects of flushing efficiency, displacement characteristics and swept volume, using methods of one-dimensional core displacement experiments and three-dimensional visualization physical simulation experiments.

### 2. HIGH-SPEED AND HIGH-EFFICIENCY DEVELOPMENT MECHANISM UNDER ONE-DIMENSIONAL SCALE

Kumkol South Oilfield is a sandy conglomerate reservoir with middle-high-porosity and high-permeability formations. The permeability distribution is  $715 \sim 2690 \times 10^{-3} \mu\text{m}^2$ . The underground

viscosity of crude oil is low (1.15~2mPa•s). In order to explore the high-speed and high-efficiency development mechanism in Kumkol South Oilfield, two cores with similar physical properties are selected to perform one-dimensional core displacement experiments to compare oil-water relative permeability characteristics, changes of residual oil saturation, and the influence on flushing efficiency at different displacement velocities.

## 2.1. Relative permeability characteristics

Figure 1 is relative permeability characteristics of two cores at different displacement velocities. The experiment results show that when the displacement velocity increases, the oil relative permeability and oil phase mobility increase. In addition, as the displacement velocity increases, the residual oil saturation reduce sand flushing efficiency is improved obviously, resulting in better development.

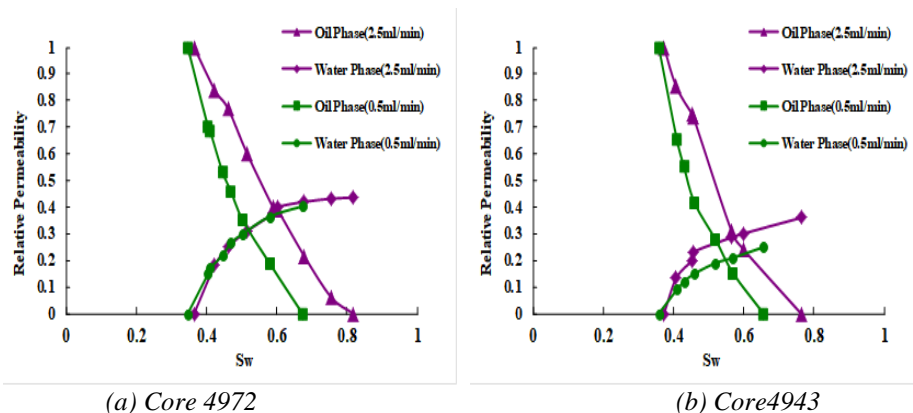


**Figure 4.** Relative permeability curve of core 4972 and core 4943 at different displacement velocities.

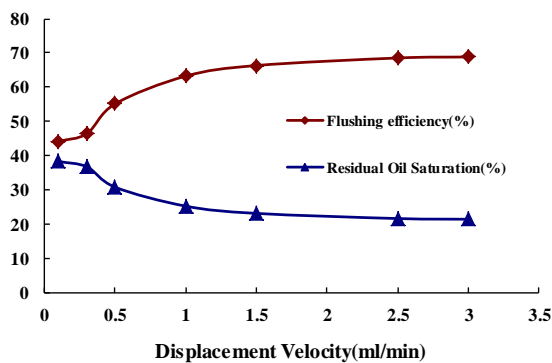


**Figure 2.** Residual oil saturation and displacement efficiency of core 4956 at different displacement velocities.

## 2.2. Influence on residual oil saturation

From the comparison of relative permeability curve characteristics at high and low velocities, it can be seen that displacement velocity has a great influence on core's residual oil saturation. Experiment results show that the displacement pressure increases with the increasing of displacement velocity. The displacement fluid can enter smaller pores and the flushing efficiency

increases. At the same time, residual oil exists in the micro pore throat with columnar, membrane, caecum and island shapes. It can be seen from Figure 2 that after displacement velocity is increased from 0.1mL/min to 3mL/min, the flushing efficiency increases by around 20%. It is the same with the results of core 4972 and 4943.

### 3. HIGH-SPEED AND HIGH-EFFICIENCY DEVELOPMENT MECHANISM UNDER THREE-DIMENSIONAL SCALE

#### 3.1. Experiment equipment

The experiment equipment is three-dimensional low-pressure physical simulation equipment with dimension of 50mm×50mm×3mm. The top and bottom surfaces of this experiment equipment are made of organic glass. Visualization is realized during the experiment process, as is shown in Figure 3.

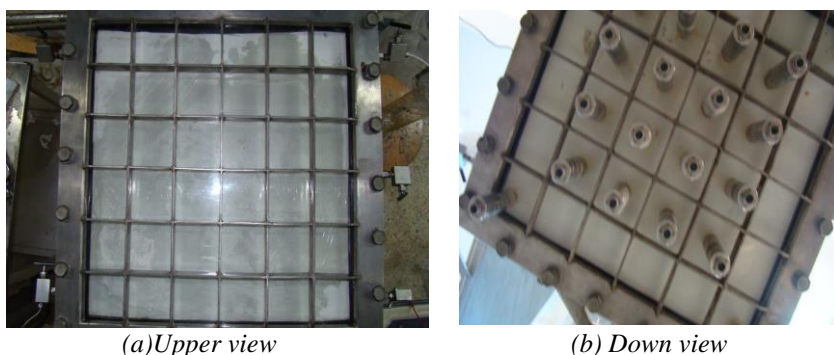


**Figure 3.** Three-dimensional low-pressure physical simulation equipment.

#### 3.2. Physical experiment

Taking inverted nine-spot well pattern as an example to research the influence of different displacement velocities on development effect. Physical simulation is conducted at the water injection rates of 10mL/min, 3.5mL/min, and 0.9mL/min. Displacement characteristics and water swept pattern at different water injection rates are compared after experiments. The displacement characteristics of edge well and corner well at different displacement velocities are analysed, as is shown in Figure 4. The experiment result shows that the water breakthrough time is short when the sandstone reservoir is in high-speed development under the condition of uniform formation, while the water-free recovery factor is high.

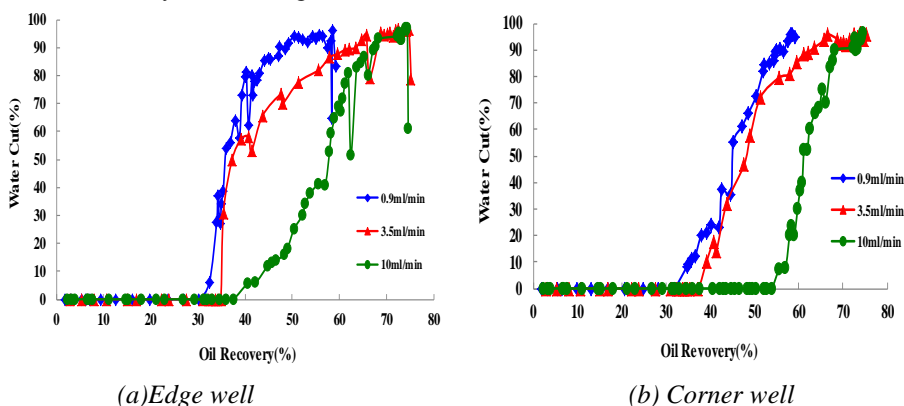
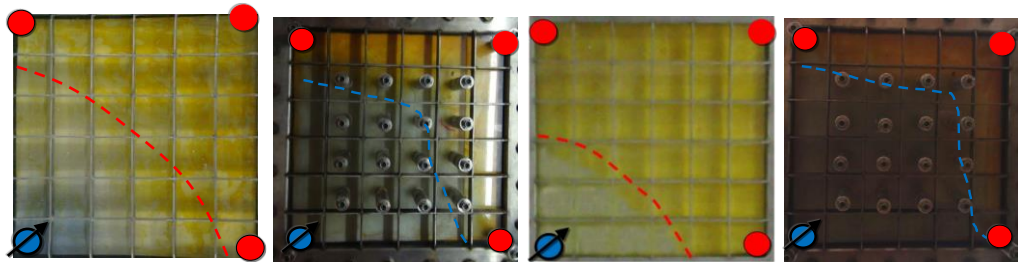


**Figure 4.** Three-dimensional low-pressure physical simulation equipment.



Water swept volume is observed through the visualization window of physical simulation equipment and the mechanism of high-speed development effect is also analyzed. Figure 5 shows the distribution of oil and water on the top surface of model when corner well breakthrough at the water injection rates of 0.9mL/min and 10mL/min. The red color in the figure stands for oil phase, the white one is water phase, the blue lines are front edge on the bottom surface and the read lines are front edge on the top surface.



(a) Top front edge (high) (b) Bottom front edge (high) (c) Top front edge (low) (d) Bottom front edge (low)

**Figure 5.** Water flooding sweep area of single-layer mesh model at different oil recovery rates

#### 4. CONCLUSION

- (1) Change laws of relative saturation curve of oil and water at different displacement velocities are received through one-dimensional displacement experiment of core. The experiment result shows that the relative permeability of oil phase rises at high-speed displacement. Moreover, the residual oil saturation reduces and finally the flushing efficiency is increased.
- (2) As the displacement velocity increases, the injection water can enter more small pores because of the increasing displacement pressure difference and more residual oil are activated. As a result, the residual oil saturation reduces and the final flushing efficiency is increased. When the displacement velocity is increased to a certain degree, the reduction of residual oil saturation slows down and remains almost unchanged.
- (3) Water flooding characteristic curves at different oil recovery rates are obtained through three-dimensional water flooding experiments. As the oil recovery rate increases, water breakthrough time is reduced, but the water-free recovery reserves are relatively high. High-speed development results in higher recovery at the same water cut.

#### REFERENCES

- [1].H. Sun, S. Wang, High-Speed & High-Efficient Development of an Extra-shallow Sea Oilfield. SPE Asia Pacific Oil and Gas Conference and Exhibition, 16-18 October, 2000 Brisbane-Australia. DOI:10.2118/64463-MS
- [2].Y. P. Borisov, Y. P. Zheltov, M. D. Rosenberg, et al. Experience of Oil Field Development in the U.S.S.R. Using Waterflooding Process and the Methods of its Improvement, 8th World Petroleum Congress, 13-18 June, 1971 Moscow-USSR.
- [3].J.J. Stosur, J.J. Taber. Critical Displacement Ratio and Its Effect on Wellbore Measurement of Residual Oil Saturation, Journal of Petroleum Technology 28 (1976) 865-868. DOI: /10.2118/5509-PA
- [4].K.S. Sorbie, D.J. Walker. A Study of the Mechanism of Oil Displacement Using Water and Polymer in Stratified Laboratory Core Systems. SPE Enhanced Oil Recovery Symposium. 16-21 April, 1988 Tulsa-Oklahoma. DOI:10.2118/17397-MS

- 
- [5].T.F. Moore, R.L. Slobod. Displacement of Oil by Water-Effect of Wettability, Rate, and Viscosity on Recovery. Fall Meeting of the Petroleum Branch of AIME. 2-5 October, 1955 New Orleans-Louisiana. *DOI:10.2118/502-G*
  - [6].A.S. Odeh, B.J. Dotson, A Method for Reducing the Rate Effect on Oil and Water Relative Permeabilities Calculated From Dynamic Displacement Data, Journal of Petroleum Technology 37 (1985) 2051-2058. *DOI:10.2118/14417-PA*
  - [7].V.H. Nguyen, A.P. Sheppard, M.A. Knackstedt, et al. The Effects of Displacement Rate and Wettability on Imbibition Relative Permeabilities. SPE Annual Technical Conference and Exhibition. 9-12 October, 2005 Dallas-Texas. *DOI:10.2118/95953-MS*
  - [8].K.J. Sincock, C.J.J Black. Validation of Water/Oil Displacement Scaling Criteria Using Microvisualization Techniques. SPE Annual Technical Conference and Exhibition. 2-5 October, 1988 Houston-Texas. *DOI:10.2118/18294-MS*

## Effect of Descending Viscosity Injection Pattern for Alkali-surfactant-polymer (ASP) Flooding on Enhanced oil Recovery

Dansen Shang<sup>1\*</sup>, Jirui Hou<sup>1</sup>

<sup>1</sup> China University of Petroleum, Beijing, CHINA

\* 765811321@qq.com

### ABSTRACT

The objective of this paper is to study the effect of descending viscosity injection pattern for alkali-surfactant-polymer (ASP) flooding on enhanced oil recovery (EOR). Multilayer heterogeneous core models with and without crossflow were designed and applied. Extensive series of core flooding experiments were conducted using descending viscosity injection pattern in laboratory. Contrast experiments were also conducted using another two injection patterns including constant viscosity injection pattern and ascending viscosity injection pattern. The results indicated that descending viscosity injection pattern had the best performance on mobility modification and EOR among the three injection patterns. The oil recovery could be improved by over 25% using descending viscosity injection pattern, which was higher than that obtained using constant viscosity injection pattern and ascending viscosity injection pattern. Descending viscosity injection pattern had the best sweep efficiency in the middle and low permeability layers. By using descending viscosity injection pattern, the sweep efficiency was dramatically improved. For the descending viscosity injection pattern, fractional flow rate in the middle and low permeability layers would be improved by the high viscosity of the first slug. This paper provided a novel injection pattern for ASP flooding in a multilayer heterogeneous reservoir.

**KEYWORDS** - ASP flooding, Descending viscosity injection, EOR.

### 1. INTRODUCTION

Alkali-surfactant-polymer (ASP) flooding has been identified as a promising chemical enhanced oil recovery (EOR) technique. It is developed out on polymer flooding, surfactant flooding and alkali flooding (Olajire 2014; Sheng 2014). ASP flooding combines the advantages of alkaline, surfactant, and polymer. Polymer can reduce water-oil mobility ratio and improve microscopic displacement efficiency (Wang et al. 2000; Sheng et al. 2015). Alkali can form soaps by reacting with the organic acid in crude oil (Sun et al. 2018). Added surfactant can interact synergistically with soaps to dramatically reduce water-oil interfacial tension (IFT) to ultra-low IFT (Zhao et al. 2015). Thus, ASP flooding can enhance oil recovery by improving mobility ratio, decreasing interfacial tension, increasing capillary number, and increasing both macroscopic sweep efficiency and microscopic displacement efficiency (Thomas & Ali 2001; Denney 2013; Mehranfar & Ghazanfari 2014).

The West Kiehl oilfield first implemented ASP flooding pilot tests in 1987 (Clark et al. 1993). Since then, ASP flooding has been developing rapidly, especially in China. China carries out over 60% of the global ASP flooding pilot tests. In 2014, Daqing oilfield began to implement the commercial production of ASP flooding. China then became the first and the unique country to carry out the ASP flooding industrial application in the world. In 2015, 3.5 million ton of oil which accounts for 9% of the total production was yielded in Daqing oilfield by ASP flooding; by 2016, there were 22 blocks implementing the commercial production of ASP flooding in Daqing oilfield (Guo et al. 2017). The enhanced oil recovery varied in different blocks. For example, it was 18.2% OOIP in Xing II-middle, however it was over 23.5% OOIP in North-I block-east. The average enhanced oil recovery of the 22 blocks was about 20%. The successful pilot tests and commercial production results in Daqing oilfield have proved ASP flooding is a promising EOR technique.

To an industrial application of ASP flooding, the injection pattern is very important. The conventional injection pattern in which the viscosity of the ASP slug remains unchanged can

achieve a satisfactory enhanced oil recovery in homogeneous reservoirs. However, it performed worse in heterogeneous reservoirs due to the severe loss of chemical agents and low sweep efficiency. Most of the major oil layers have reached a super high water cut stage in China. How to exploit the sub-layers effectively has become an urgency matter. In this study, multilayer heterogeneous core models were designed and applied. Flooding experiments were carried out using descending viscosity injection pattern, constant viscosity injection pattern and ascending viscosity injection pattern. The EOR results of three different injection patterns were compared. Effect of descending viscosity injection pattern of ASP flooding on EOR was discussed.

## 2. EXPERIMENTS

### 2.1. Materials

The alkali is sodium hydroxide (NaOH) which is analytical reagent. The polymer is partially hydrolyzed polyacrylamide (HPAM) with an average molecular weight of  $25 \times 10^6$  Da. The surfactant is heavy alkyl benzene sulfonate (HABS) with a content of 50%. The oil for flooding experiments is simulated oil. The oil is obtained by mixing the crude oil from Daqing oilfield and kerosene, and its viscosity is 9.1 mPa·s at 45 °C. The salinity of the brine is 4456 g·L<sup>-1</sup>. The mineral composition of the brine is shown in Table 1.

**Table 1.** Mineral composition of brine

Mineral salt	NaCl	CaCl <sub>2</sub>	MgCl <sub>2</sub> ·6H <sub>2</sub> O	NaHCO <sub>3</sub>	Na <sub>2</sub> SO <sub>4</sub>
Content (g L <sup>-1</sup> )	2.307	0.042	0.172	1.86	0.075

### 2.2. Core models

The core models for flooding experiments include intralayer heterogeneity model and interlayer heterogeneity model. They are positive rhythm models with three layers. The three layers in each model have their own outlet, but they share one inlet. The physical parameters of the models are shown in Table 2.

**Table 2.** The physical parameters of the models.

Model	Size (cm × cm × cm)	Thickness of each layer (cm)	Air permeability of each layer (mD)
Intralayer heterogeneity	30 × 5 × 5	2	800
		2	500
		1	300
Interlayer heterogeneity	30 × 5 × 5	2	800
		2	500
		1	300

### 2.3. Methods

Three different injection patterns are used in this paper. Constant viscosity injection pattern means the viscosity of the ASP slug remains unchanged. Descending viscosity injection pattern means ASP slug is divided into several small slugs and the small slugs are injected into the core model with the viscosity of the small slugs varying from high to low. Ascending viscosity injection pattern means ASP slug is divided into several small slugs and the small slugs are injected into the core model with the viscosity of the small slugs varying from low to high.

Experimental procedure is as follows:

- (1) Vacuum the core model and saturate the model with brine to calculate the pore volume (PV) and porosity.

- (2) Inject oil into the core model until no water is produced at the outlet. The volume of injected oil is recorded to calculate initial oil saturation, and the oil is aged in the model for 10 days.
  - (3) Inject water to flood the model until the water cut reaches 98%.
  - (4) Inject ASP slug after water flooding. The total volume of ASP slug is 0.3 PV for each injection pattern. The concentration of surfactant and alkali for each ASP slug is 0.3 and 1.2 %wt, respectively. Other injection details of the three injection patterns are specified in Table 3.
  - (5) Chase water flooding is performed after ASP flooding until the water cut reaches 98%.
- The flooding experiments are all carried out at 45 °C. The injection rate of each fluid is 0.3 mL·min<sup>-1</sup>.

**Table 3** Injection details of the three injection patterns

Model	Model number	Injection pattern	C <sub>HAPM</sub> (mg·L <sup>-1</sup> )	Viscosity (mPa·s)	Slug size (PV)
Intralayer heterogeneity	AI	Constant viscosity	1250	30.3	0.3
			850	19.7	0.1
	AII	Ascending viscosity	1250	30.3	0.1
			1650	41.9	0.1
			1650	41.9	0.1
	AIII	Descending viscosity	1250	30.3	0.1
			850	19.7	0.1
			850	19.7	0.1
			850	19.7	0.1
Interlayer heterogeneity	BI	Constant viscosity	1250	30.3	0.3
			850	19.7	0.1
	BII	Ascending viscosity	1250	30.3	0.1
			1650	41.9	0.1
			1650	41.9	0.1
	BIII	Descending viscosity	1250	30.3	0.1
			850	19.7	0.1
			850	19.7	0.1
			850	19.7	0.1

## 2.4. Results analysis

Table 4 shows the results of flooding experiments. The oil recovery results are shown in Table 4. In intralayer heterogeneity models, AI, AII and AIII, the oil recovery during water flooding is similar. ASP flooding with constant viscosity injection pattern, ascending viscosity injection pattern and descending viscosity injection pattern can enhance oil recovery by 27.84%, 25.85% and 31.51%, respectively. The results in interlayer heterogeneity models, BI, BII and BIII, are similar to those of intralayer heterogeneity models. ASP flooding with constant viscosity injection pattern, ascending viscosity injection pattern and descending viscosity injection pattern can enhance oil recovery by 24.89%, 21.03% and 28.50%, respectively. By using descending viscosity injection pattern, the oil recovery can be enhanced by over 25%, which is the highest enhanced oil recovery among the three injection patterns. When changing the injection patterns, the oil recovery varies, which means the injection pattern has an impact on sweep efficiency. The results shown in Table 4 indicate that the best sweep efficiency can be obtained by using descending viscosity injection pattern. Thus, descending viscosity injection pattern is recommended as a potential method to improve sweep efficiency for multilayer heterogeneity reservoirs.

**Table 4** Oil recovery of flooding experiments

Model number		Oil recovery (%)		
		Water flooding	ASP flooding	Total
BI	800 mD	40.69	28.94	69.63
	500 mD	36.37	24.59	60.96
	300 mD	8.34	14.43	22.77
	Total	33.73	24.89	58.62
BII	800 mD	41.31	26.48	67.79
	500 mD	36.04	19.18	55.22
	300 mD	8.59	10.34	18.93
	Total	34.01	21.03	55.04
BIII	800 mD	42.12	30.02	72.14
	500 mD	38.77	29.84	68.61
	300 mD	7.09	21.17	28.26
	Total	35.11	28.50	63.61
AI		28.17	27.84	56.01
AII		27.28	25.85	53.13
AIII		28.31	31.51	59.82

## 2.5. Mechanism analysis

As shown in Table 4, there are distinct differences in the permeability. Each layer has its own permeability. Higher permeability means lower flow resistance. At the beginning during ASP flooding, flow resistance in high permeability (800 mD) layer is lower than that in middle permeability (500 mD) layer and low permeability (300 mD) layer. So, most of the injected viscous fluid preferentially penetrated into the high permeability layer, then the middle permeability layer and low permeability layer. With more and more viscous fluid is injected, the flow resistance increases in each layer, and it increases the most in high permeability layer. Fractional flow of the injected ASP slugs in the three layers is determined by flow resistance, and the flow resistance is deeply affected by the viscosity of the first injected ASP slug. Higher viscosity of the first slug will led to higher flow resistance in high permeability layer. The subsequent ASP slugs is tuned to get into the middle and low permeability layers due to the increase of flow resistance. For ascending viscosity injection pattern, the viscosity of the three slug varies from low to high, most of the ASP slugs will flood into the high permeability layers, leading to a low sweep efficiency. For descending viscosity injection pattern, the viscosity of the three slug varies from high to low, the ASP slugs will not only flood into the high permeability layers, but also get into middle and low permeability layers. Due to more fluid gets into middle and low permeability layers, more oils in middle and low permeability layers are recovered, therefore, descending viscosity injection pattern can achieve the best sweep efficiency and the highest enhanced oil recovery compared with descending viscosity injection pattern and constant viscosity injection pattern.

## 3. CONCLUSIONS

- (1) Descending viscosity injection pattern had the best sweep efficiency in the middle and low permeability layers compared with constant viscosity injection pattern and ascending viscosity injection pattern.
- (2) The oil recovery can be improved by over 25% by using descending viscosity injection pattern.
- (3) The enhanced oil recovery is the highest for descending viscosity injection pattern, while it is the lowest for ascending viscosity injection pattern.

## REFERENCES

- [1]. Olajire A. A (2014). Review of ASP EOR (alkaline surfactant polymer enhanced oil recovery) technology in the petroleum industry: Prospects and challenges. *Energy*, 77, 963-982. doi: 10.1016/j.energy.2014.09.005
- [2]. Sheng J. J (2014). A comprehensive review of alkaline-surfactant-polymer (ASP) flooding. *Asia-Pacific Journal of Chemical Engineering*. doi: 10.1002/apj.1824
- [3]. Wang D, Cheng J, Yang Q, Wenchao G, Qun, L, Chen, F (2000). Viscous-elastic polymer can increase microscale displacement efficiency in cores. *Society of Petroleum Engineers*. doi:10.2118/63227-MS
- [4]. Sheng J. J, Leonhardt B, Azri N (2015). Status of polymer-flooding technology. *Society of Petroleum Engineers*. doi:10.2118/174541-PA
- [5]. Sun Z, Kang X, Lu X, Li Q, Jiang W (2018). Effects of crude oil composition on the ASP flooding: A case from Saertu, Xingshugang and Lamadian Oilfield in Daqing. *Colloids and Surfaces A: Physicochemical and Engineering Aspects*, 555, 586-594. doi: 10.1016/j.colsurfa.2018.07.021
- [6]. Zhao F, Ma Y, Hou J, Tang J, Xie D (2015). Feasibility and mechanism of compound flooding of high-temperature reservoirs using organic alkali. *Journal of Petroleum Science & Engineering*, 135, 88-100. doi: 10.1016/j.petrol.2015.08.014
- [7]. Thomas S, Ali S. M. F. (2001). Micellar Flooding and ASP-Chemical Methods for Enhanced Oil Recovery. *Petroleum Society of Canada*. doi:10.2118/01-02-04
- [8]. Denney D (2013). Progress and effects of ASP flooding. *Society of Petroleum Engineers*. doi:10.2118/0113-0077-JPT
- [9]. Mehranfar A, Ghazanfari MH (2014). Investigation of the microscopic displacement mechanisms and macroscopic behavior of alkaline flooding at different wettability conditions in shaly glass micromodels. *Journal of Petroleum Science & Engineering*, 122, 595-615. doi: 10.1016/j.petrol.2014.08.027
- [10]. Clark, S. R., Pitts, M. J., Smith, S. M. (1993). Design and application of an alkaline-surfactant-polymer recovery system to the West Kiehl field. *Society of Petroleum Engineers*. doi:10.2118/17538-PA
- [11]. Guo H, Li Y, Wang F, Yu Z, Chen Z, Wang Y, Gao X. (2017). ASP flooding: theory and practice progress in China. *Journal of Chemistry*, 2017, 1-18. doi: 10.1155/2017/8509563

## A Novel Characterization of Fluid Viscosity in Micro Sized Throats - Based On Micro Flow Experiments

Jiuzhu Wu<sup>1\*</sup>, Deqiang Wang<sup>1</sup>, Changchao Chen<sup>1</sup>, Jing Zhu<sup>1</sup>, Guangtao Chang<sup>2</sup> and Huixian Zhang<sup>3</sup>

<sup>1</sup> China Univesitu of China-Beijing/Petroleum Engineering Department, Beijing, China

<sup>2</sup> Name of Institution/Department, Beijing, China

<sup>2</sup> Natural Gas Business Division, PetroChina Tarim Oilfield Company, Korla, China

<sup>3</sup> Huabei Oil & Gas Branch Company, Sinopec, Zhengzhou, China

\*2015312032@student.cup.edu.cn

### ABSTRACT

As ratio of surface to volume increases sharply, flow in micro throats is affected greatly by solid-fluid interaction. Viscosity of fluid near solid wall increases significantly, which leads to deviating between theoretical value and experimental observation. In this paper, flow experiments were conducted in micro pores with radius of 1.239 $\mu\text{m}$ , 2.346 $\mu\text{m}$  and 4.840 $\mu\text{m}$ . Three main components of crude oil were selected as working fluids: n-hexane, n-octane, and n-hexadecane. The pressure gradient ranged 0.01-42MPa/m. Reynolds number was lower than 1. Experimental flow rate was lower than theoretical value. The deviation was quantitatively characterized. Nonlinear flow was observed and demonstrated theoretically. Based on boundary layer theory, a quasi-solid boundary layer was formed cling to the solid wall due to solid-fluid interaction. Its thickness ranged 200nm-1 $\mu\text{m}$ . Viscosity of boundary layer fluid and bulk fluid was characterized separately, and apparent viscosity of total fluid was a combination of bulk fluid and boundary layer fluid. Three methods were applied to characterize the apparent viscosity of fluids in micro throats, solid-fluid interaction considered: exponential function method, weight function method and three - parameter fitting method. The weights of two kinds of fluid were derived considering the thickness of boundary layer, radius, pressure gradient and original viscosity. Fluid viscosity in micro throat was not homogeneous. Viscosity of boundary layer fluid was higher and decreased with the distance to the wall.

**KEYWORDS** - Micro scale, Boundary layer, Micro tubes, Solid-fluid interaction, Viscosity

### 1. INTRODUCTION

As the development of MEMS (Micro Electronic Mechanic Systems), , researchers show increasing interests in micro flow [1-3]. Researchers conducted flow experiments in tubes made of fused silica with radius of 1-30 $\mu\text{m}$ . Cui [4] noticed that flow resistance for isopropanol and carbon tetrachloride was higher. Xu [5, 6] and Li [7] studied flow of deionized water under high pressure gradient. Nonlinear flow was discovered and investigated. In petroleum engineering, it is widely known as boundary layer. Liu [8] reported that the thickness of boundary layer ranged 80-300nm.

The viscosity change has been seen as an important reason for the deviation between macro and micro flow for a long time. Nonino et al [9], through comparing the result of several numerical simulation methods, demonstrated that in micro scale, the effect of viscosity change was considerable. Wen [10] studied the viscosity change of water and the boundary layer thickness in micro scale. The solid-fluid interaction was considered.

In this paper, flow of three alkanes in micro tubes is investigated. The impact of pressure gradient, fluid properties, and radius on nonlinearity is analyzed. The apparent viscosity of all three working fluids in micro throats is characterized with three different methods.

### 2. EXPERIMENTAL METHODS

The experiment aims to obtain the relationship between flow rate and pressure gradient. Nitrogen container provides pressure (Figure 1.). Nitrogen drives piston in intermediate container. The



piston drives working fluid to flow through micro tube. The micro tube is connected to a metering tube directly. All tubes are made of fused silica, coated with polyimide outside. The inner wall is hydraulic smooth [6]. N-hexane (AR), n-octane (AR) and n-hexadecane (AR) were used, which were abbreviated as C6, C8, C16 respectively.

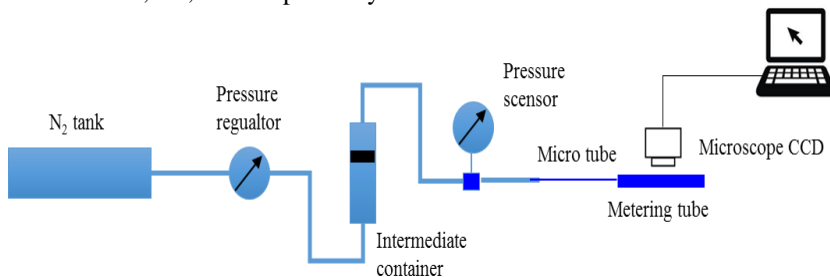


**Figure 1.** Sketch of the experimental device

### 3. EXPERIMENT RESULTS

In micro tubes, experimental flow rate deviated from theoretical value (Figure 2). Poiseuille equation didn't hold to this scale. Both radius and fluid properties affected the flow. The smaller the radius, the larger the deviation (Figure 3). If the flow is linear,  $D$  must be a constant. Inversely, if  $D$  is not constant, the flow is nonlinear. For C6,  $D$  decreased with pressure gradient (Figure 3), revealing the nonlinearity of flow. For C16, no similar trend was found.

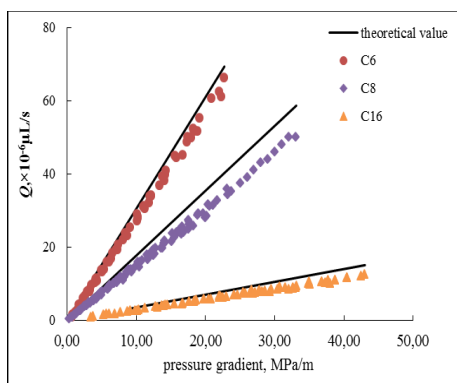


**Figure 2.** The relationship of flow rate and pressure gradient,  $r=1.239\mu\text{m}$

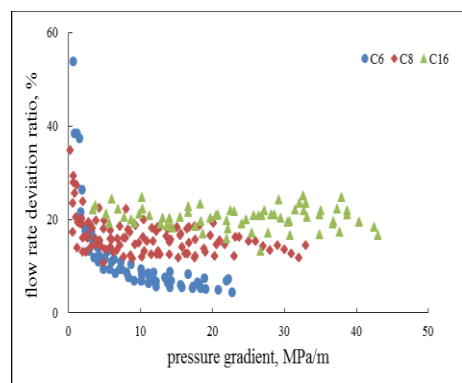


**Figure 3.** The relationship of flow rate deviation ratio and pressure gradient,  $r=1.239\mu\text{m}$

### 4. CHARACTERIZATION OF FLUID VISCOSITY

#### 4.1. Exponential Function Method

Based on experimental studies of the relationship of viscosity versus pressure, Bridgman [11] pointed out that the viscosity of liquids increased with pressure, which can be described as an exponential function. Here we take the pressure gradient as the pressure:

$$\mu = k \exp(\alpha \nabla p) \quad (1)$$

Figure 4 shows the result of exponential function method. For all three fluids used in this paper, the fitting effect was far from ideal when the pressure is high or low. For hexane, which had the lowest viscosity, the deviation was the highest.

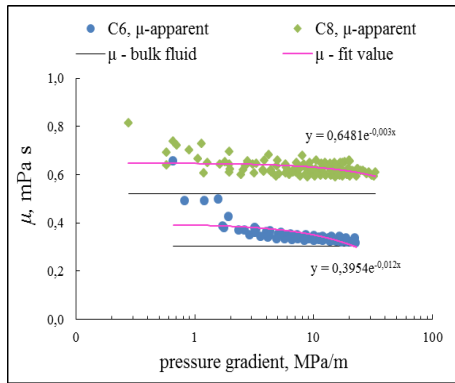


**Figure 4.** The result of exponential function method,  $r = 1.239 \mu\text{m}$

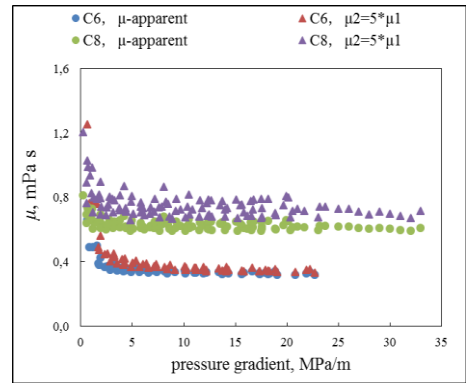


**Figure 5.** The result of weight function method,  $r = 1.239 \mu\text{m}$

## 4.2. Weight Function Method

Huang [12] proposed a method to characterize the apparent viscosity of the whole fluid:

$$\mu = \frac{A_1}{A_1 + A_2} \mu_1 + \frac{A_1}{A_1 + A_2} \mu_2 \quad (2)$$

where  $A_1$  and  $A_2$  are the area of bulk fluid and boundary layer in cross section respectively,  $\mu\text{m}^2$ .  $\mu_1$  and  $\mu_2$  are the viscosity of bulk fluid and boundary layer,  $\text{mPa s}$ . Figure 5 showed the result of calculation of Weight function method. The deviation of the fitting data in Weight function method was greater when the radius was smaller and the original viscosity is higher.

## 4.3. Three - Parameter Fitting Method

In this method, the ratio of deviation between theoretical and experimental data is fitted with a linear function of the reciprocal of the square root of pressure gradient [8]. But for the fluids used in this paper, a quadratic equation, rather than the linear function, was more effective to describe the relationship between  $D$  and the reciprocal of the square root of pressure gradient.

$$\left\{ \begin{array}{l} \mu = \frac{\mu_0}{1-D} \\ D = \frac{a}{(\sqrt{\nabla p})^2} + \frac{b}{\sqrt{\nabla p}} + c \\ A = \frac{0.00125}{r_{\text{micro}}} \\ B = \frac{4 \times 10^{-4}}{r_{\text{micro}}^{1.5}} \end{array} \right.$$

where  $a$ ,  $b$ ,  $c$  were constant. The result was shown in Figure 6. We got better fitting effect than Liu [8]. The result was checked in Figure 7. In order to show the difference between theoretical and experimental data, the ordinate used logarithmic coordinates. The fitting data agreed well with experimental value for all cases. The final expression was:

$$\mu_{C_6} = \frac{\mu_0}{1 - \left[ \frac{43.59}{r^{1.593}} \frac{1}{(\sqrt{\nabla p})^2} + \left( \frac{29.49}{r^{2.389}} - 3 \right) \frac{1}{\sqrt{\nabla p}} + \frac{1.3536}{r^{0.244}} \right]}$$

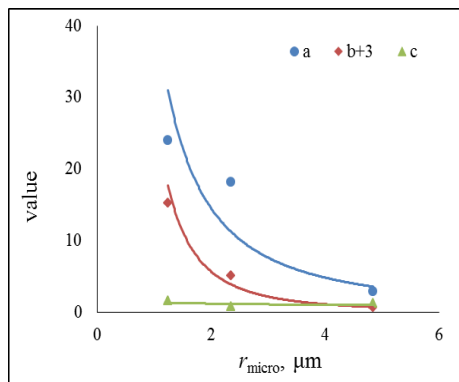


**Figure 6.** The relationship between  $r$  and  $a, b+3$  and  $c, C_6$

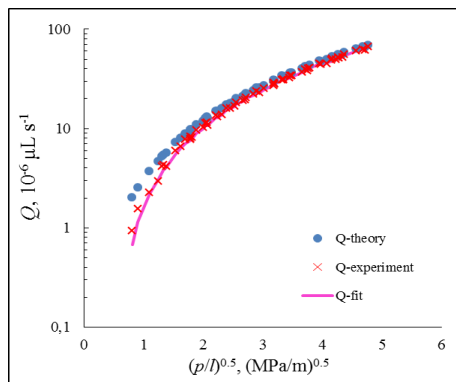


**Figure 7.** The result of weight function method,  $r = 1.239 \mu\text{m}$

## 5. SUMMARY AND CONCLUSIONS

1. Micro flow of liquids shows nonlinear characteristics under low pressure gradient. Nonlinearity is affected by radius, pressure gradient and liquid properties.
2. A stagnant boundary layer is formed cling to the solid wall. This layer thins as the shear force increases, until its thickness reaches a constant value. Boundary layer narrowed down the effective flow space and changes it continuously.
3. The practicability of the index method is poor under low pressure and pressure gradient. Both viscosity of boundary layer fluid and bulk fluid should be considered. The fitting effect is better when more factors were considered. Three-parameter fitting method was the best in characterize the viscosity of the fluids.

## ACKNOWLEDGEMENT

We acknowledge the support for this research provided by Joint Fund for Petroleum and Chemical Industry (A: U1762210), the National Natural Science Foundation of China (Nos. 51574258 and 51674273).

## REFERENCES

- [1]. Huang S, Yao Y, Zhang S Pressure transient analysis of multi-fractured horizontal wells in tight oil reservoirs with consideration of stress sensitivity. ICCESN 2017
- [2]. Song L, Ning Z, Duan L. Research on reservoir characteristics of Chang7 tight oil based on nano-CT. ICCESN 2017
- [3]. Huang L, Ning Z, Wang Q. Enhanced gas recovery by CO2 sequestration in marine shale: a molecular view based on realistic kerogen model. ICCESN 2017
- [4]. Cui H, Li Z, Zhu S, Phys. Fluids 2004, 16(5), 1803-1810. DOI: 10.1063/1.1691457
- [5]. Xu S, Yue X, J. China Univ. Petrol (Nat. Sci. Ed.) 2007, 31(5), 60-63.

- [6]. Xu S, Yue X, J. Hou, Chin. Sci. Bull. 2007, 52(6), 849-854.
- [7]. Li Y, Lei Q, Liu Q, et al. Petroleum Exploration and Development, 2011, 38(3):336-340
- [8]. Liu Z, Pang Y. Acta Mechanica Sinica, 2015, 31(1): 45-52. DOI: 10.1007/s10409-015-0015-7
- [9]. Nonino, C., Del, G., Savino, S. Int. J. Heat Mass Transfer 2006, 49, 4469–4481
- [10]. Wen, S., Theory and Application of Microscale Flow Boundary. Metallurgical Industry Press, Beijing (2002)
- [11]. P. W. Bridgman, The Physics of High Pressure ~G. Bell and Sons, London, 1949
- [12]. Huang Y. Percolation mechanism of low permeability reservoir. Beijing: Petroleum Industry Press, 1998

# A novel embedded discrete fracture model based on GEM of two-set nodes

Xiang Rao<sup>1\*</sup>, Linsong Cheng<sup>1</sup>, Renyi Cao<sup>1</sup>, Pin Jia<sup>1</sup>, Yonghui Wu<sup>1</sup>

<sup>1</sup> China University of Petroleum, Beijing, China

\*raoxiang0103@gmail.com

## ABSTRACT

This paper proposes a novel embedded discrete fracture model (EDFM) base on Green element method (GEM) of two-set of nodes. GEM of two sets of nodes is a modification of previous GEMs, which indeed has a second accuracy and is adaptive to unstructured grid. Compared to original boundary element method (BEM), the GEM can solve nonlinear problems in heterogeneous media. Compared to original EDFMs, the novel EDFM based on Green element method (GEM) of two-set of nodes can handle the interflow between matrix and fracture more accurate due to the application of boundary integral equation. Therefore, the proposed novel model can effectively solve the pressure and flow rate distribution of transient flow in heterogeneous media with some discrete fractures.

**KEYWORDS** - *Embedded discrete fracture model, Green element method of two-set nodes, transient flow, heterogeneous media.*

## 1. INTRODUCTION

Accurate modelling and simulation of Transient flow in fractured reservoirs (NFR) is quite challenging. One of widely-used methods is embedded discrete fracture model (EDFM). The original EDFM was firstly proposed by Li and Lee [1], in which, a structured grid is used to divide the matrix, and fractures are embedded in the structured grid by making clear the geometrical relationship of fractures and matrix. Therefore, it avoids the complex grids division of discrete fracture model (DFM), and can be more convenient to be coupled with the existing numerical simulators which are based on finite volume method (FVM). However, the approximation of the interflow transmissibility between matrix and fracture was only relevant to geometric parameters, which was not conform to actual physical process. BEM may be a good method to approximate the interflow between matrix and fracture, but the reservoir is always heterogeneous, classical BEM can not to handle this problem effectively. Therefore, GEM is a natural idea to replace classical BEM to be used here. The Original GEM was firstly proposed by Taigbenu [2], then Archer [3] used overhauser interpolation functions to reduce the effect of the approximation of the normal flux in original GEM. Pecher et al. [4] and Lorinczi P [5] proposed a flux-vector-based GEM aiming to improve accuracy. Taigbenu [6] proposed a flux-correct GEM, and returned to the original GEM and approximated the interface fluxes in terms of the primary variable [7]. Rao et al. [8-9] proposed a GEM based on two sets of nodes.

This paper proposed a novel EDFM based on the GEM of two-set nodes, which can make the approximation of interflow more accurate and effectively solve transient flow in heterogeneous fractured reservoir.

## 2. MATHEMATICAL FORMULA

In this section, discrete flow formula in reservoir matrix based on GEM of two-set nodes is introduced with specific detail as follows.

It is known that the formula of single-phase flow in porous media is:

$$\nabla \cdot (K \nabla p) = \frac{\partial p}{\partial t} + f \quad (1)$$

where  $K$  is permeability,  $p$  is pressure, and  $f$  is the source or sink term, in matrix cell not containing fractures,  $f$  is generally equal to 0.

Eq. (1) can be rewritten as

$$\nabla^2 p = -\nabla \psi \cdot \nabla p + \sigma \frac{\partial p}{\partial t} + \nu f \quad (2)$$

where  $\psi = \ln K$ ,  $\nu = 1/K$ ,  $\sigma = c\nu$

In GEM of two-set nodes, One set of nodes contains all vertices of the polygonal cells representing the value of pressure, called pressure nodes, the other contains all edge-center points of cells representing the value of normal flux, called flux nodes. We use a triangle cell to illustrate these two sets of nodes, in which the pressure nodes are at the vertices and the flux nodes are at three edge-centers.

Then the boundary integral equation of Eq. (2) is applied to each triangular cell.

$$-\lambda p_i + \int_{\Gamma_e} (p \nabla G \cdot \mathbf{n} + G \frac{q_n}{K}) ds + \iint_{\Lambda_e} G [-\nabla \psi \cdot \nabla p + \sigma \frac{\partial p}{\partial t} + \nu f] dA = 0 \quad (3)$$

At each pressure point, the corresponding base function of the pressure nodes are denoted as  $\phi_1, \phi_2, \phi_3$  respectively. The values of pressure within the cell is approximated by means of weighted mean of the nodal values and base functions. At each flux node, because the normal flux is piecewise continuous, normal flux at one edge is assumed to be a constant, and this is a difference from original GEM of two-set nodes. The local equations within an element is as follows:

$$q_n = M p^{(n+1)} + b \quad (4)$$

$$\text{where } M = -(\theta B^{-1} E + \frac{B^{-1} C}{\Delta t})$$

$$b = \left( -(1-\theta) B^{-1} E + \frac{B^{-1} C}{\Delta t} \right) p^{(n)} - B^{-1} F$$

It can be seen that, there is quantities in above equations need to be specified. In EDFM, the interflow between matrix and fracture is regarded as source or sink term in matrix flow formula of Eq. (1). Therefore, it is a need to know that, in which cell, there is a source or sink term, and this is relevant to the geometric relationship between discrete fractures and matrix. As we know, in EDFM, fractures are divided to multiple segments by lines of matrix cells and intersecting fractures. There is a node in each fracture segment, and the node is set at the midpoint of the fracture segment.

In the matrix cell which contains fracture cells,  $f$  in Eq. (1) is replaced by  $q_{omf}$ , then the equations within the cell are rewritten as

$$-\lambda p_i + \int_{\Gamma_e} (p \nabla G \cdot \mathbf{n} + G \frac{q_n}{K}) ds + \iint_{\Lambda_e} G [-\nabla \psi \cdot \nabla p + \sigma \frac{\partial p}{\partial t} + \nu q_{omf}] dA = 0 \quad (5)$$

where  $q_{omf}$  is the interflow between matrix and fracture.

For fluid flow in discrete fracture networks and into the wellbore, finite difference method (FDM) is used to discretize flow formula in an implicit form shown in Eq. (6), which is similar to the treatment proposed by Jia et al.[10].

$$B'_i p_{f,i-1}^{(n+1)} + \left( C'_i - \frac{F'_i}{\Delta t} \right) p_{f,i}^{(n+1)} + D'_i p_{f,i+1}^{(n+1)} + E'_i q_{omf,i} + E'_i q_{well} + \frac{F'_i}{\Delta t} p_{f,i}^{(n)} = 0 \quad (6)$$

where  $B'_i$ ,  $C'_i$ ,  $D'_i$ ,  $E'_i$  and  $F'_i$  are corresponding coefficients,  $q_{well}$  is the flowrate from the fracture segment to the well. In the fracture segment without a well,  $q_{well} = 0$ . In the fracture segment with a well, may as well assume the well is producing at a constant bottom pressure  $p_{wf}$ , i.e.,  $p_f = p_{wf}$ , the unknowns of this fracture segment is  $q_{omf}$  and  $q_{well}$ , but unknowns of other fracture segments without a well are  $q_{omf}$  and  $p_f$ . Therefore, there are two unknowns in each fracture segments. The conclusion in case of the well is at a constant production rate is similarly obtained.

The whole global equations are over-determined due to the application of GEM based on two-set nodes. Adding the sealed outer boundary condition, the resultant equations may as well be assumed to be written as:

$$(b_i)_{n_e+2n_f} = (M_{ij})_{(n_e+2n_f) \times (n_e+2n_f)} (p_i^{(n+1)})_{n_e+2n_f} \quad (7)$$

According to orthogonal projection theorem in functional analysis, solving this over-determined system is equivalent to the solution in Eq. (8). Then the unknowns can be solved easily.

$$(M^T M) p^{(n+1)} = M^T b \quad (8)$$

### 3. VALIDATION OF PROPOSED MODEL

This example give a validation of proposed model by comparing the computational oil production rate curve with that obtained by LGR. Therefore, the fracture in this example need to be along the direction of grid line such that to be solved by LGR. As shown in Fig. 1, a rectangular reservoir with a length of 1010 meters and a width of 1010 meters is adopted to illustrate specific cell division, and a fracture with a length of 210 meters are embedded in the reservoir. It is worth to state that, although there is a rectangular reservoir illustrated in the example, the proposed novel EDFM is adaptive to reservoirs with complex boundary due to the GEM of two-set nodes is adaptive to unstructured grid. The outer boundary condition is sealed in reservoir simulation, and the initial pressure of the reservoir is 20MPa. The thickness of the reservoir is 10meters, and a horizontal well with a diameter of 0.1 meter crosses the fracture at the point (505,505) in 2-D plane. Values of other physical properties of this example are listed in Table. 1. The sketch of the reservoir and fractures is illustrated in Fig. 2. Oil production rate curves obtained from proposed model and LGR are plotted in Fig. 6. It can be seen that, the results of the novel EDFM based on GEM of two-set of nodes are much consistent with that of LGR, which verifies the validation of proposed model.

**Table 1. Physical properties of the reservoir and fluid**

Properties	Value	Properties	Value
Matrix porosity	0,1	Matrix permeability	1 md
Fracture porosity	0,4	Fracture permeability	20000 md
Fracture aperture	10 mm	Oil coefficient of compressibility	$3.02 \times 10^{-3} \text{ MPa}^{-1}$
Rock coefficient of compressibility	$1.07 \times 10^{-4} \text{ MPa}^{-1}$	Oil viscosity	2 mPa·s

### 4. CONCLUSION

A novel embedded discrete fracture model (EDFM) base on Green element method (GEM) of two-set of nodes is presented to effectively solve single-phase transient flow in fractured heterogeneous reservoir.

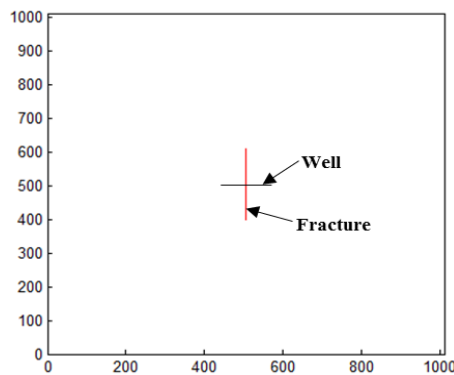


**Figure 1.** Sketch of the reservoir domain in example 1

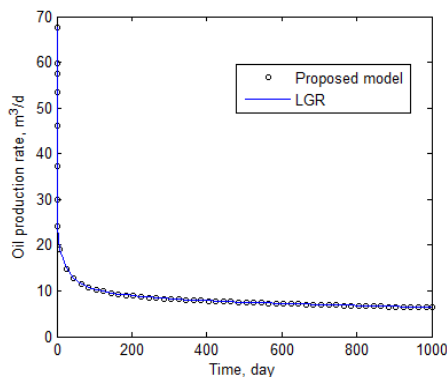


**Figure 2.** Comparison of oil production rates of proposed model and LGR

Due to the application of boundary integral equation in GEM, the proposed novel model can handle the interflow between matrix and fracture more accurately and be adaptive to complex boundary shape because GEM of two-set nodes is adaptive to unstructured grid.

## ACKNOWLEDGEMENT

We acknowledge that this study has been funded by National Postdoctoral Program for Innovative Talents (No. BX20180381), National Natural Science Foundation of China (No. U1762210, No. 51574258 and No. 51674273) and National Science and Technology Major Project of China (No. 2017ZX05013004-003).

## REFERENCES

- [1]. Li, L., Lee, S. H. (2008). Efficient Field-Scale Simulation of Black Oil in a Naturally Fractured Reservoir Through Discrete Fracture Networks and Homogenized Media. SPE Reservoir Evaluation & Engineering, 11(4), 750–758.
- [2]. Taigbenu AE. The Green element method. Int J Numer Meth Engng. 1995, 38, 2241-2263. <https://doi.org/10.1002/nme.1620381307>
- [3]. Archer R. C1 continuous solutions from the Green element method using Overhauser elements. Appl Num Math 2006;56:222–9. <https://doi.org/10.1016/j.apnum.2005.04.001>



- 
- [4]. Pecher R , Harris SD, Knipe RJ, L. Elliott, D.B. Ingham. New formulation of the Green element method to maintain its second-order accuracy in 2D/3D. 2001, 25, 211-219. Eng Anal Boundary Elements 2001;25(3):211-219. [https://doi.org/10.1016/S0955-7997\(01\)00008-X](https://doi.org/10.1016/S0955-7997(01)00008-X)
  - [5]. Lorinczi P, Harris SD, Elliott L. Modified flux-vector-based Green element method for problems in steady-state anisotropic media. Eng Anal Boundary Elements 2009;33:368–87. <https://doi.org/10.1016/j.enganabound.2008.06.004>
  - [6]. Taigbenu AE. The flux-correct Green element formulation for linear, nonlinear heat transport in heterogeneous media. Eng Anal Boundary Elements 2008;32:52–63. <https://doi.org/10.1016/j.enganabound.2007.05.005>
  - [7]. Taigbenu AE. Enhancement of the accuracy of the Green element method: Application to potential problems. Eng Anal Boundary Elements 2012;36:125-136. <https://doi.org/10.1016/j.enganabound.2011.07.005>
  - [8]. Rao, X., Cheng, L., Cao, R., et al. (2018), et al. A novel Green element method based on two sets of nodes. Eng Anal Boundary Elements 2018, 91, 124-31. <https://doi.org/10.1016/j.enganabound.2018.03.017>
  - [9]. Rao, X., Cheng, L., Cao, R., et al. (2018). A novel green element method by mixing the idea of the finite difference method. Eng Anal Boundary Elements 2018, 95, 238–247. <https://doi.org/10.1016/j.enganabound.2018.07.015>
  - [10]. Jia P, Cheng L, Huang S, Liu H. Transient Behavior of Complex Fracture Networks. J Petrol Sci and Eng 2015; 132: 1-17. <https://doi.org/10.1016/j.petrol.2015.04.041>

## Study on the Feasibility and Oil-displacement Mechanisms of Nano-TiO<sub>2</sub> in Low-permeability Reservoirs

Tingting Cheng<sup>123\*</sup>, Jirui Hou<sup>123</sup>, Yulong Yang<sup>123</sup>, Xiaoyu Feng<sup>123</sup>, Haoya Zhai<sup>123</sup>, Ajiao Jiang<sup>123</sup>

*1*China University of Petroleum (Beijing), Institute of unconventional oil and gas science and technology, Beijing-CHINA

*2*Basic Theory Laboratory of Improve Oil Recovery in Low Permeability Oil Field, Tertiary Oil Recovery Key Laboratory, Petro China, Beijing 102249, P R of CHINA ;

*3*Oilfield Development Key Laboratory of MOE, Beijing 102249, P R of CHINA.

\*chengtingting0826@126.com

### ABSTRACT

This study presents titanium dioxide nanoparticles as a displacing agent to improve oil recovery in low-permeability reservoirs. The main objective is to demonstrate the feasibility and oil-displacement mechanisms of TiO<sub>2</sub> nanoparticles by conducting visualization experiments in the delicately designed and fabricated 2D microfluidics. Microfluidics models are designed according to the similarity criteria. The types of residual oil and their distribution characteristics after water flooding are determined in the network-crack microfluidics. Visualization experiments illustrate that the residual oil exists primarily in the form of oil columns after waterflooding. The adsorption of nanoparticles on the solid surface can alter the wettability from oil-wet towards more water-wet, and therefore the oil column is easily cut off, leaving an oil film adhered to the surface. The nanoparticles are distributed in the remaining oil film, and the emulsification effect causes the oil film to become small droplets, which are stripped from the rock surface by the subsequent water injection. Moreover, we conclude that the oil recovery reaches its maximum with the injection of TiO<sub>2</sub> nanoparticles at a concentration of 0.1% and pore volume of 0.3.

**KEYWORDS** - Titanium dioxide nanoparticles, Microfluidics, Oil-displacement mechanisms, Enhanced oil recovery

### 1. INTRODUCTION

Nanotechnology provides a powerful tool to solve various industrial problems [1-5], for example, optical material, dye-based solar cells, biomedical research, organic detection, and oil exploitation. With the demand for global oil supply, the development of low permeability reservoirs is particularly important. Different laboratory studies have shown that nanofluid (also known as "smart fluid") can effectively recover trapped oil from low permeability reservoirs. However, mechanisms of enhanced oil recovery by nanofluids remain unsolved.

The microscopic visualization model is a useful research method for studying the mechanisms and migration characteristics of fluid displacement in porous media. Microfluidics is the most widely used laboratory technology on pore-level chips, offering an effective way to understand the mechanisms of nanofluid flooding and its flow characteristics in low-permeability reservoirs. Javadpour and Fisher [6] developed a micromodel with sapphire windows to study fines migration at pressures exceeding 35 MPa and at a temperature of 150°C. Khezrnejad et al. [7] illustrated that particles were added to the water phase of water alternating gas and injected into waterflood residual oil in two-dimensional glass micromodels to study the effect of the nanoparticles at low pressures. Li and Torsæter [8] conducted a micromodel test to study the effects of different kinds of nanoparticles and different nanoparticle concentrations on EOR. It is demonstrated that as the nanoparticle concentration increases more trapped oil can be produced because of the emulsification effect and the reduction of IFT. Xu [9] developed a microfluidic model to explain how the nanoparticles affect the remobilization of the remaining oil trapped at a pore throat, showing that the NP's effect is very similar to that of surfactant in mobilizing an oil droplet

trapped in the pore–throat structure, i.e., the reduction of IFT plays a key role. Buchgraber [10] designed a dual-porosity micromodel with features and characteristics of a dual-porosity pore system to mimic the multiphase flow in carbonate reservoirs. The authors directly observed the pore-level displacement mechanisms and pore-network characteristics during fluid flow experiments.

In this paper, a two-dimensional network-crack microfluidic chip is used to study the migration characteristics of crude oil, the types of remaining oil in micro-cracks, and the recovering mechanisms of remaining oil by TiO<sub>2</sub> nanofluids. The optimal injection parameters are given to provide theoretical references for the application of nano-displacement technology in unconventional oil reservoirs.

## 2. MATERIALS AND METHODS

### 2.1. Materials

We use kerosene dyed with methyl orange to simulate typical crude oil with density 0.826g/cm<sup>3</sup> and viscosity 2.59~3.87mPa·s in a low permeability reservoir. Nanofluids are prepared with 10nm hydrophilic titanium dioxide nanoparticles in distilled water. The weight percent of nanofluids is 0.1%. The dimensions of a 2D microfluidic chip are given in Table 1.

**Table 1.** Geometric Parameters in the 2D-Microfluidic Device.

Geometric parameters	length(μm)
Pore body depth	20
Throat width	30
Throat depth	20

### 2.2. 2D Microfluidic Experiments

The tests for studying oil displacement mechanisms of nanofluids were performed in a two-dimensional network-crack model chip. Water flooding, nanofluid flooding, and subsequent water flooding were carried out sequentially. Figure 1 compares the residual oil patterns in a section of a 2D glass microfluidic model after plain water injection. It is shown that a significant quantity of remaining oil exists in the form of oil columns.

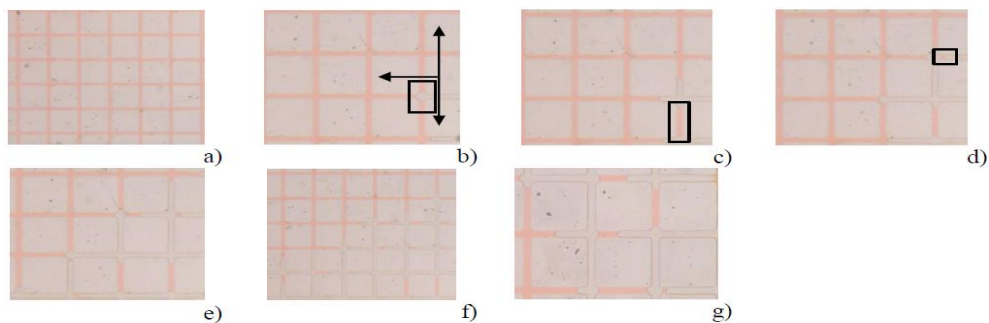


**Figure 5.** Microscopic residual oil distribution after water flooding in 2D microfluidic: a) initial saturated oil (red area); b) water reaches the T-zone and flows in three directions; c) in the adjacent cross zone, the oil is cut off, forming a small oil column; d) smaller oil columns is generated; e) as the water advances, partial residual oils in the form of oil columns are produced in the horizontal and vertical directions; f) microscopic residual oils in the micro-cracks, which exist in the form of small oil columns; g) zoom of flow in the network-crack model chip: the presence of oil columns and the contact angle morphology.

The results of our pore-scale flow visualization experiments revealed that wettability alteration and emulsification are two essential mechanisms by which nanofluid improves waterflood efficiency (see Figure 2). At the early stage of nanofluid injection, we observed the rock surface is oil-wet (see Figure 2a). With the injection of nanofluids for a period, the contact angles at the three-phase boundary of water/oil/solid were modified, and the wettability of rock surface changed from oil-wet to weakly oil-wet (see Figure 2b). As the nanofluid continues to be injected, the oil columns in network cracks were peeled off and turned into small oil droplets, leaving some oil films adhered to the surface and the wettability of rock surface further changed from weakly oil-wet to strong water-wet (see Figure 2c). On the other hand, the emulsification effect can decrease the interfacial tension between water and oil, which causes the oil film to be stretched and released from the pore wall in the form of some tiny droplets (see Figure 2d). When the subsequent water was injected, the remaining oil film and the stripped oil column gradually shrank and deformed, and was finally driven out from the crack (see Figure 2e, 2f). In the visualized micromodels, we clearly observe how the nanofluids initiate the trapped oils and its flow characteristics in network structures.

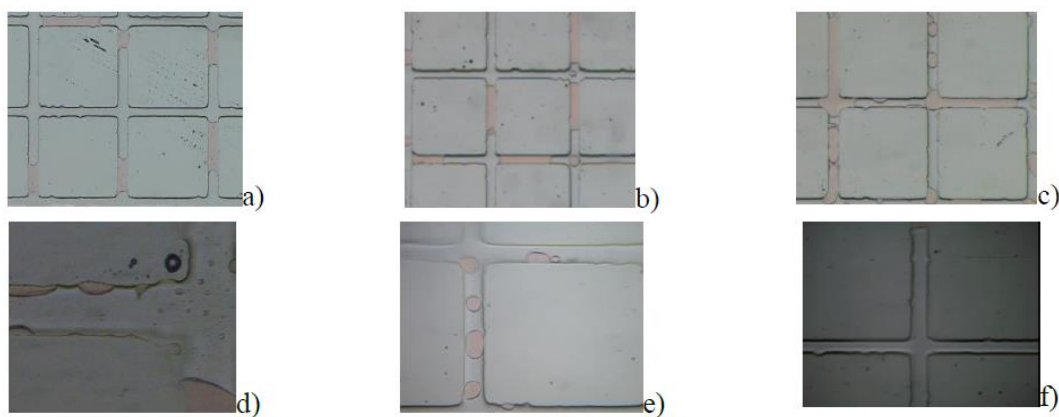


**Figure 2.** Microscopic residual oil distribution after nanofluid flooding in 2D microfluidic: a) patterns of residual oil after plain water flooding (red area). Both ends of an oil column are concave, and the rock surface is oil-wet at this stage; b) after injecting nanofluid for a period of time, the contact angles are modified, and the rock surface changes from oil-wet to weakly oil-wet; c) continue to inject the nanofluid, the oil column is cut into small oil droplets, leaving some oil films adhered to the surface and the rock surface changes from weakly oil-wet to strong water-wet; d) as the nanofluid is continuously injected, the oil film is emulsified into small droplets; e) the remaining oil films and the stripped oil column gradually shrank and deformed; f) the remaining oil films and the stripped oil column in the crack are driven out.

### 2.3. Coreflood Experiment

In this section, we report the result of a coreflood experiment that has been used to optimize the injection parameters of the nanofluid displacement system. The coreflooding test was carried out on a 10mD core. This coreflood experiment was performed to investigate the performance of tertiary nanofluid displacement after establishing the initial water and oil saturation in the core. When the oil recovery by water flood reached to its plateau and no further oil was produced, nanofluid was injected with exactly the same rate of injection (0.1ml/min) as the first waterflood. The experiment shows the oil recovery and pressure in the experiment (see Figure 3). As the concentration of nanoparticles increases, the oil recovery increases. However, when the nanoparticle concentration reaches 0.1%, the oil recovery reaches the optimum value. The oil recovery is 33.75% after waterflooding, and the final oil recovery after 0.3PV of nanofluid

injection reached 51.54%, indicating an enhanced recovery of 17.95%. The pressure increased 1.36MPa during the initial waterflood and reduced to 1MPa during the injection of the nanofluid, and then further declined to 573KPa after the subsequent water flooding, which is less than the initial water injection pressure. The pressure decline after the subsequent water flooding is explained by the alteration of surface wettability from oil-wet to water-wet and the consequent stripping of crude oil. In the subsequent water flooding, the nanofluid further emulsified the residual oil film into small droplets, giving rise to a reduction in the resistance of oil flow.

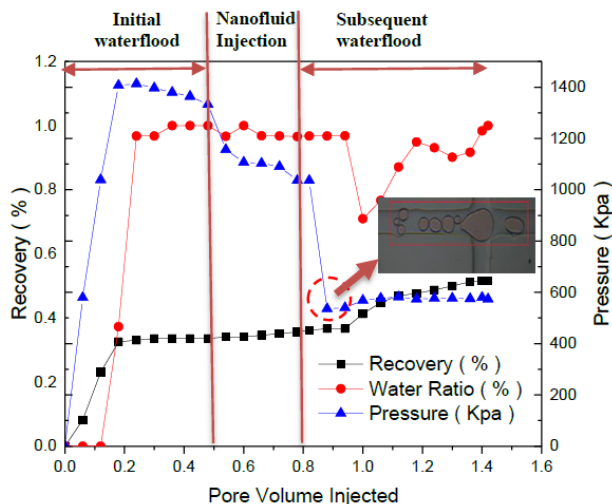


**Figure 3.** The oil recovery and the differential pressure in the experiment with NPs 0.1wr% and 0.3PV

### 3. CONCLUSIONS

We constructed a microfluidics model to investigate the mechanisms of stripping of residual oil trapped in a microfracture structure. A coreflooding experiment was also performed. Our experimental results allow drawing the following conclusions.

The wettability of the rock surface can be altered by TiO<sub>2</sub> nanofluids from oil-wet to more water-wet, causing the detach of oil columns from the rock surface and the adherence of an oil film to the surface. The nanoparticles adsorbed on the interface between the oil film and water phase play a role of emulsifying similar to surfactants.

Nanofluids can significantly reduce injection pressure, which verifies the effectiveness of tertiary nanofluids flooding. The optimized nanofluids injection parameters in our experiments are 0.3PV of nanofluids injection volume and 0.1% of nanoparticles, respectively. The final enhanced oil recovery in the coreflooding test is as high as 17.95%.

### REFERENCES

- [1]. Evcin A, Bezir N Ç, Kayalı R, et al. Characteristic properties of Dy-Eu-Ag co-doped TiO<sub>2</sub> nanoparticles prepared by electrospinning processes[J]. Acta Physica Polonica A, 2015, 128: 303-306. DOI:10.12693/APhysPolA.128.B-303
- [2]. Boran F, Çetinkaya S, Şahin M. Effect of surfactant types on the size of tin oxide nanoparticles[J]. Acta Physica Polonica A, 2017, 132(3): 546-548. DOI:10.1007/s12517-018-3842-6

- [3]. Atici T, Çolak D A. The Healing Effect of Cimin Grape Against Toxic Effects of ZnOTiO<sub>2</sub> Nanocomposite[J]. Acta Physica Polonica A, 2017, 132(3). DOI: 10.12693/APhysPolA.132.919
- [4]. BORAN F, Çetinkaya S. Influence of reaction time on the size of SnO<sub>2</sub> nanospheres and its sensing properties to VOC gases[J]. International Journal of Biological and Medical Science, 2016, 1(2): 1-4.
- [5]. Zou J, Yue X, Zhang J, et al. Self-assembled microspheres feasibility study for conformance control in high temperature and high salinity reservoirs[J]. Arabian Journal of Geosciences, 2018, 11(9): 195. DOI: org/10.1007/s12517-018-3544-0
- [6]. Javadpour F, Fisher D. Nanotechnology-based micromodels and new image analysis to study transport in porous media[J]. Journal of Canadian Petroleum Technology, 2008, 47(02). DOI: 10.2118/08-02-30
- [7]. Khezznejad A, James L A, Johansen T E. Water enhancement using nanoparticles in water alternating gas (WAG) micromodel experiments[C]//SPE Annual Technical Conference and Exhibition. Society of Petroleum Engineers, 2014. DOI: org/10.2118/173484-STU
- [8]. Li S, Torsæter O. An experimental investigation of EOR mechanisms for nanoparticles fluid in glass micromodel[C]//Paper SCA2014-022 was prepared for presentation at the International Symposium of the Society of Core Analysts held in Avignon, France. 2014: 8-11. DOI:10.13140/RG.2.1.4181.3604
- [9]. Xu K, Zhu P, Huh C, et al. Microfluidic investigation of nanoparticles' role in mobilizing trapped oil droplets in porous media[J]. Langmuir, 2015, 31(51): 13673-13679. DOI: 10.1021/acs.langmuir.5b03733
- [10]. Buchgraber M, Al-Dossary M, Ross C M, et al. Creation of a dual-porosity micromodel for pore-level visualization of multiphase flow[J]. Journal of Petroleum Science and Engineering, 2012, 86: 27-38. DOI: org/10.1016/j.petrol.2012.03.012

## Variation of Detector Resolution with the Source-Detector Distance

Faez Waheed<sup>1\*</sup>, Kadir Günoğlu<sup>2</sup>, Hakan Akyıldırım<sup>1</sup>, İskender Akkurt<sup>1</sup>

<sup>1</sup> Physics Department, Suleyman Demirel University, Isparta-TURKEY

<sup>2</sup> Isparta Uygulamalı Bilimler University, Isparta- TURKEY

\*faez\_radiophysics@yahoo.com

### ABSTRACT

Radiation and radioactive material may be of artificial origin started to be used in the many beneficial application of different fields in medicine, industry, agriculture and research as well as for nuclear power as a result of the technology development. This made the radiation measurement equality is important for many proposes, therefore, should be measured carefully. Many different important quality parameters to be considered and should be determined and adopted for such kind of measurements. Furthermore, obtaining these parameters are important for gamma spectroscopy measurement system and can affect the measurement quality.

In this study investigated experimentally some of the important equality parameters such as energy calibration, the energy resolution (R), and the full width at the half of maximum (FWHM) for a 3" x 3" NaI(Tl) detector (Canberra Inc.), furthermore, determinate the distance impact between the detector-source to the quality parameter value. The measurements were performed at different seven axial distances for five energy. Thus, fundamental data for further works with this detector system were obtained.

**KEYWORDS:** Gamma ray , NaI(Tl) , Energy Resolution .

### 1. INTRODUCTION

The radiation was widely used around the world in medical treatments, industrial, as well as the application in thousands of usage throughout developed over the last 50 years [1]. The major sources of radiological dose to the public are natural and medical. Any source of radiation, as with most hospital radiation sources and some industrial processes can be entirely shielded to protect workers and the public [2].

This made radiation measurement is important for radiation protection and other proposes. Because of the higher value of radiation is hazardous for human health. In this case, radiation detection becomes vital and it should be measured carefully [3,4]. Many different parameters to be considered and should be determined and adopted for such kind of measurements. Furthermore, obtaining these parameters are important for gamma spectroscopy measurement system and can affect the measurement quality [5]. The determination some of the quality parameters such as the energy of gamma rays, detector dimensions, source dimensions, geometric, source-detector distance for one detector may not be applied for other measurements [6]. Thus in this work, the main important quality parameters of the gamma spectrometer will be determined.

The measurement of ionizing radiation is sometimes expressed as being the rate of counts per unit time registered by a radiation monitoring instrument, of which counts per minute (cpm) and counts per second (cps) are commonly used. Count means a single detected event registered by a detection system. Count rate measurements are normally associated with the detection of particles [6].

The sodium Iodide energy resolution Typically is 7% to 9% when using Cesium life radioactive source (energy 0.662 MeV). At lower energies, the energy resolution is better (smaller %) and at higher energies it is worse (larger %) (RCT 1.05-SG, 2013). This is an important parameter for a gamma ray spectrometer because it determines how close in energy two gamma rays can be before the instrument gives a single broad peak instead of two distinctly separate peaks. The energy

Resolution is very important when unknown gamma emitters are being recorded since photons differing in energy by less than the energy resolution will not be separately detectable [7].

Furthermore, the non-proportional light response in scintillation detectors makes it essential to carry out a calibration based on peak width, which establishes the conformity between the peak width and energy that corresponds to peak channel, because it is the main source causing the energy resolution. Energy Resolution calibrations are necessary for both the peak-analysis software to separate different gamma ray emissions in a narrow energy range and the Monte Carlo simulations to obtain desired, idealized spectral responses. Because the width of peak is often given by the full energy width at half the intensity maximum (FWHM) of the gamma peak at the gamma energy, this calibration establishes a function to describe the dependence of FWHM values on the gamma ray energy [1], the peak width versus the spectral energy.

Many studies for the determination quality parameters of NaI (Tl) detector were performed experimentally by several authors in the literature. Abbas [8] offers straightforward mathematical expressions to calibrate NaI(Tl) detector. Akkurt, I., et al. [9] detected experimentally the efficiency of NaI(Tl) detector in the range (0.511 – 1.332) MeV.

This work is focused on assessment the energy calibration, full width at the half of maximum, and energy Resolution. The studied NaI(Tl) detector that have great importance in nuclear investigations and in all experimental studies that measure radiation. Moreover, these characteristics of detectors are the most important parameters used to determine the numerical results of a study [6]. The impact of source-to-detector distance and energy on the full energy peak resolution has been also investigated.

### 1.1. Radiation Detection

The radiation detection depends on the nature of the radiation interaction with the sensitive medium of a detector, therefore the radiation instruments basically involve generating electrical signals which result from this interaction. The radiation detection methods are based on the process of excitation or ionization of atoms in the detector medium by the passage of a charged particle inside the sensitive medium. Electromagnetic radiation gives a rise to energetic electrons by one of the three types of processes, namely the Photoelectric effect, Compton scattering and Pair production. All of these interactions provide radiation properties, such as its energy, intensity. Detection efficiency of a detector system depends on different parameters and thus various kinds of energy definition are used to cover those parameters [10]. Absolute efficiency: it is the ratio of the number of or to the number of gamma rays emitted by the source in all direction.

- a. Intrinsic efficiency: it is the ratio of the number of the detector to the number of gamma rays hitting the detector.
- b. Full-energy peak (or photo peak) efficiency: it is the energy peak pulses only, rather than a pulse of any size, for the gamma ray.
- c. Resolution:- the detector characteristic to be able to differentiate between two close radiation energies. The higher the resolution, the closer the radiation energies can be to each other and still be differentiated.

### 1.2. Detector Yield

Sodium Iodide detectors measure radiation as a function of its observed effects, a correlation must be made between the effect and the incident radiation. For example, for all photons that enter a detector, only 25% may create an output pulse. This detector would be said to have a yield of 25%. The less than 100% yield is caused by factors, such as size and shape of the detector; the



characteristics of the detector materials; the energy of the radiation; and the probability of ionization for the radiation in the detector materials. The yield is concerned only with the detector, however, that detector yield is only a factor in overall instrument response to radiation. The position of the detector relative to the source, scatter, and self absorption of the radiation by the source itself are some of the factors involved.

**Table 1.** Data of the radionuclides used for the determination the energy calibration, energy resolution, and the full width at the half of maximum.

Nuclide	Energy (keV)	Emission probability (%)	Channel number	Half-life (year)	Activity (Bq)
Cs-137	661.6	85.1	1808.89	30.08	31515
Na-22	511.0	178.0	825.52	2.6018	5811
	1274.5	99.94	1983.53		
Co-60	1173.2	99.85	2133.05	5.2711	14817
	1332.5	99.9826	2413.15		

For the gamma-ray spectrometry technique the energy calibration, the energy resolution and the full width at the half of maximum are important parameters to be determined. Those parameters are usually done using a function to fit the efficiency at a wide energies range and detector-source distance, as the number of energy peaks obtained from radioactive sources is limited. For these purposes the energy calibration, the energy resolution, and the full width at the half of maximum (FWHM) of the 3" x 3" NaI(Tl) detector have been determined experimentally at 0.511, 0.662, 1.173, 1.275, and 1.332 MeV energy obtained from  $^{22}\text{Na}$ ,  $^{60}\text{Co}$ , and  $^{137}\text{Cs}$  life radioactive sealed sources.

The geometry is used to analysis spectroscopy of these sources have been done for many different axial distances starts from 1 cm until to 15 cm from the detector surface. In order to reduce the background level of the system, the detector is shielded using lead on all sides as illustrate in Figure (1).



**Figure 1.** Photographs of the experimental setup

## 2. EXPERIMENTAL: MATERIAL AND METHODS

In order to calculate the energy calibration, energy resolution, the geometry were tested against gamma-rays using gamma spectrometer in Suleyman Demirel University Physics Department in the summer 2018. The equality parameters were measured for gamma rays of five different energies: 0.511, 0.662, 1.173, 1.275, and 1.332 MeV. The gamma rays for them were obtained from  $^{22}\text{Na}$ ,  $^{137}\text{Cs}$ , and  $^{60}\text{Co}$  sources. For each distance the energy resolution and FWHM were measured depending on the relation between incoming and passing gamma rays through the lead collimator.

## 2.1. Gamma Spectrometer System

The gamma spectrometer was performed to test if the material is radioactive and then find the source of that radioactivity. The gamma spectrometer was also identified the energy of gamma rays of the samples. The gamma spectrometer, however, consists of a detector (NaI (TI) in our case), counting electronic system (high voltage, preamplifier, amplifier 16384-channel Multichannel Analyses (MCA)), and a PC (where software was installed) to record data. In order to reduce the background level of the system, the detector is shielded using lead shielding on all sides. Figure 2 shows a schematic description of this spectrometer that was used in this study.

The measurements were implemented using a low level gamma counting spectrometer including a 3"x3" NaI (TI) detector by ORTEC Inc., connected to a multichannel pulse height analyzer. The necessary power for the detector as well as the acquisition of gamma spectra were achieved by an integrated spectroscopic system. This system was controlled by a personal computer. The control of acquisition parameters and analysis of the collected spectra were carried out with aid of MAESTRO-32 (version 6.06) software package.

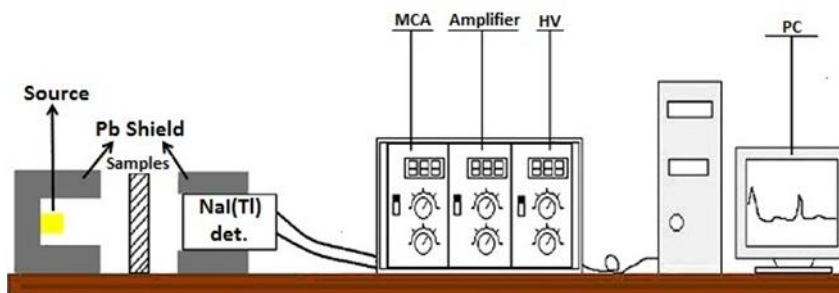


*Figure 2. Schematic view of the experimental system setup*

## 2.2. Energy Calibration

The quality for spectroscopy of gamma energy resolution depending on the calibrating procedure of NaI(Tl) scintillation detectors such as the energy calibration, the energy resolution calibration and the efficiency calibration before usage. These calibrations provide a more accurate assessment; allow correctly identifying the isotopes and determining the activity of the involved ones [1].

The detector system used in this work was calibrated before using in radiation detection in order to convert channel number to energy scale by using  $^{22}\text{Na}$ ,  $^{137}\text{Cs}$ , and  $^{60}\text{Co}$  life radioactive point sealed sources, five different energy peaks, were used to get the certain peak to see channel number. All the sources were counted for 4000 seconds. The energy calibration is the determination of the energy position of the incident photon for each channel [11]. The energy calibration was conducted to appear the relationship between the channel numbers and photon energy, the peak of the standard source was used.

### 2.3. Energy Resolution (R).

The energy resolution, as another important characteristic of a detector system is obtained from the full width of a single peak (at a specific energy) at half its maximum height (FWHM) of a single using the following equation:-

$$R = \frac{FWHM}{E_0} \times 100 \quad (1)$$

Here  $R$  is energy resolution and  $E_0$  is the related energy.

The experimental full energy peak efficiency at energy  $E$  was computed by the equation below:-

$$\varepsilon_{fep}(E) = \frac{N(E)}{A \cdot t \cdot p(E)} \quad (2)$$

Where  $N(E)$  is the number of net counts recorded in the photo peak for that energy,  $A$  is the known activity of radionuclide,  $t$  is the preset counting time (in second) and  $p(E)$  is the gamma ray emission probability for each of applied radionuclides.

The Sodium Iodide Scintillation detector such as NaI has an a good energy resolution for gamma-ray spectroscopy. The energy resolution of a gamma-ray detector is the measurement of the possible variation in the size of the electrical pulses resulting from the complete absorption of a gamma ray of the same energy. A small value of a calculated resolution ( $R$ ), as in equation below means that the detector can distinguish between two gamma-rays with closely energies [12] (Figure 4).

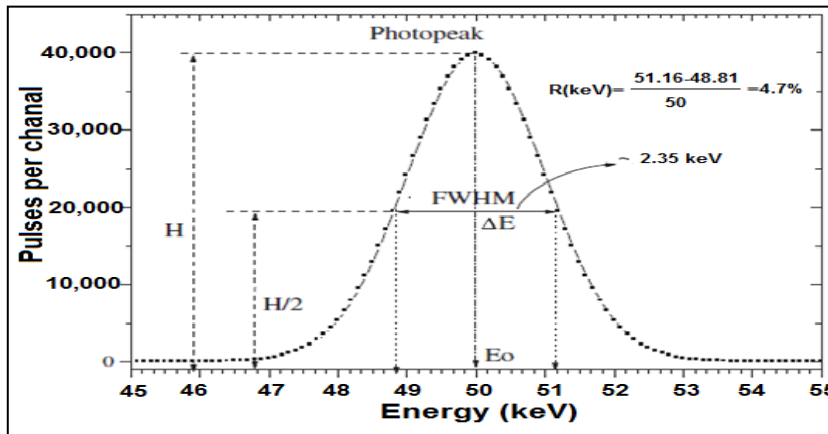


Figure 3. Energy resolution and FWHM procedure calculation for energy peak.

The energy resolution ( $R$ ) of a NaI detector can be calculates as follow [13].

$$R = FWHM \times \left( \frac{\Delta E}{\Delta ch} \right) \times 100 \quad (3)$$

Where:

$R$ :- Energy resolution (keV).

FWHM:- Full width at half maximum (channel).

$\Delta E$ : Difference between two-separated gamma lines (keV).

$\Delta ch$ :- Difference between the photo-peaks of the two gamma lines (channel).

### 3. RESULTS AND DISCUSSION.

The NaI detector equality parameters such as the energy calibration, the energy resolution, and the full width at the half of maximum FWHM have measured for 5 energies gamma ray started from 1 cm up to 15 cm with extension, furthermore, measuring source-detector distance impact to these equality parameters.

#### 3.1. Energy Calibration.

The detector should be calibrated before using in radiation measurements in order to covert channel number to energy scale. This is carried out experimentally under laboratory conditions. Three radioactive point source are used to get certain peak to see channel, this is done using  $^{22}\text{Na}$ ,  $^{137}\text{Cs}$ ,  $^{60}\text{Co}$  radioactive sources as they emitted gamma-ray of 0.511, 0.662, 1.173, 1.275, 1.332 MeV respectively. The gamma-ray spectrum obtained from those sources and related fit has been displayed (In Figure 5).

#### 3.2. The Energy Resolution (R %):-

The energy Resolution (R%) of the NaI(Tl) detector was obtained using gamma-ray energies emitted by the  $^{22}\text{Na}$ ,  $^{137}\text{Cs}$ ,  $^{60}\text{Co}$  life point radioactive sealed sources. The results have been obtained as a function of distance for five gamma-ray energies show in Figures (6 - 7), As can be seen from these Figures, there is a great variety of analytical function that is used to describe the energy Resolution depended on the gamma-ray energy and source-detector distance. It can be seen that the line is the description with the correlation coefficient between the energy Resolution value and variation source-detector distance as a function gamma-ray energies, in general cases is not less than  $R^2 = 0.88$ .

As the energy Resolution of the NaI(Tl) detector can vary with the energy and the distance to the face of the detector, the energy Resolution has been obtained for 7 different distance from the detector. The results are displayed in Figure (6 – 7) for 7 different distances and 5 different energies. It can be seen from these Figures that the energy Resolution has been decreased with the increasing distance from the detector face to the same energy, and also it decreases with increasing the gamma ray energy to the same source-detector distance.

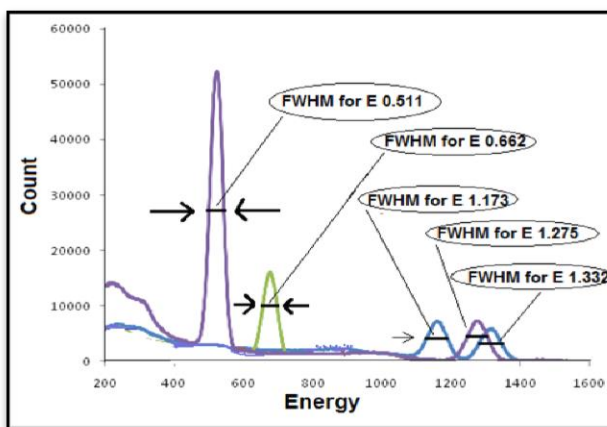


Figure 4. FWHM procedure calculation for energy peak.

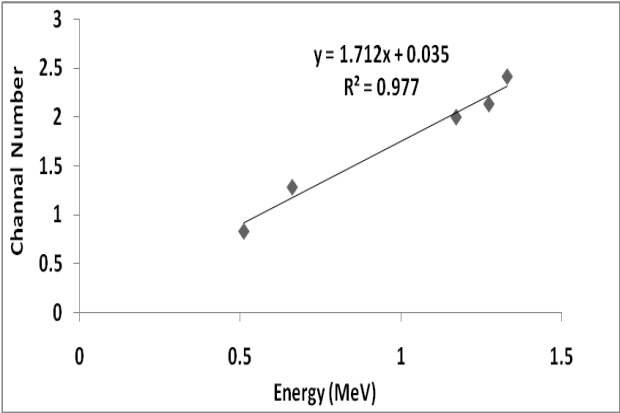


Figure 5. Calibration the energy with the channel number

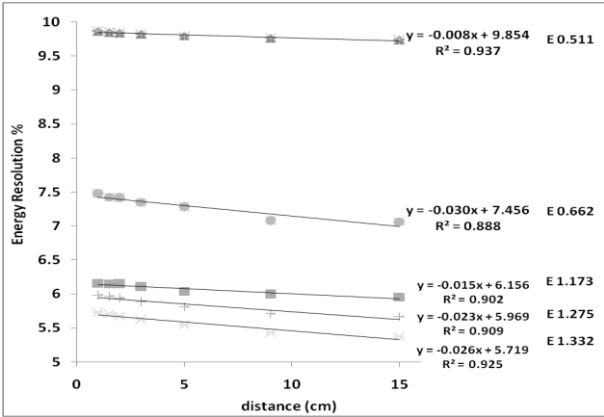


Figure 6. Energy Resolution as a function of distance to the  $^{22}\text{Na}$ ,  $^{137}\text{Cs}$ ,  $^{60}\text{Co}$ .

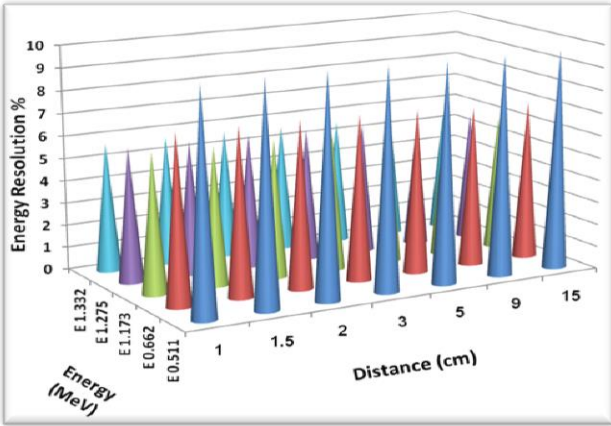


Figure 7. Energy Resolution as a function of distance to the  $^{22}\text{Na}$ ,  $^{137}\text{Cs}$ ,  $^{60}\text{Co}$ .

#### 4. CONCLUSIONS

In this study, Three of most important gamma spectroscopy parameters have been determined experimentally the energy calibration and the energy resolution (R %) for the 3" x 3" NaI(Tl) scintillation detectors. The impact of source-detector distance with the gamma-ray energy to the energy Resolution were also investigated. It was found from this work that the Resolution depend on energy and also source distance to the detector.

#### REFERENCES

- [1] Casanovas, R., Morant, J. J., and Salvado', M. (2012). Energy and resolution calibration of NaI(Tl) and LaBr3(Ce) scintillators and validation of an EGS5 Monte Carlo user code for efficiency calculations. *Nuclear Instruments and Methods in Physics Research A*, 675, 78–83.
- [2] Akkurt, I., Mavi, B., Akkurt, A., Basyigit, C., Kilincarslan, S., Yalim, H., A., 2005. Study on Z-dependence of partial and total mass attenuation coefficients. *J. Quant. Spectrosc. Radiat. Transfer* 94 (3–4), 379–385.
- [3] Alsarray, E., 2016. Investigation of radiation shielding properties of some composite material. MSc thesis Fen Bilimleri Enstitüsü- SDU.
- [4] Waheed, F., Q., 2017. Investigation of buildup factor in gamma ray measurement. MSc. Thesis Fen Bilimleri Enstitüsü- SDU
- [5] Akyildirim, H., Waheed, F., Günoğlu, K., & Akkurt, İ. (2017). Investigation of Buildup Factor in Gamma-Ray Measurement. *Acta Physica Polonica A*, 132(3), 1203-1206.
- [6] Karadeniz, Ö. and Vurmaz, S. (2017). Experimental investigation on the photopeak efficiency of a coaxial High Purity Germanium Detector for different geometries. *Journal of Basic and Clinical Health Sciences*, 1, 18–22.
- [7] Gouda, M. M., Badawi, M. S., El-Khatib, A. M., Mohamed, M. M., Thabet, A. A., & Abbas, M. I. (2015). Calibration of well-type NaI (Tl) detector using a point sources measured out the detector well at different axial distances. *Journal of Instrumentation*, 10(03), P03022.
- [8] Abbas, M. I. (2010). Analytical approach to calculate the efficiency of 4 $\pi$  NaI (Tl) gamma-ray detectors for extended sources. *Nuclear Instruments and Methods in Physics Research Section A: Accelerators, Spectrometers, Detectors and Associated Equipment*, 615(1), 48-52.
- [9] Akkurt, I., Gunoglu, K., & Arda, S. S. (2014). Detection efficiency of NaI (Tl) detector in 511–1332 keV energy range. *Science and Technology of Nuclear Installations*, 2014.
- [10] Ashok, D., & Thomas, F. (2003). *Introduction to nuclear and particle physics*. World Scientific..
- [11] Regguigui Nafaa, Gamma Ray Spectrometry Practical Information, September 2006.
- [12] Jibiri, N. N., & Abiodun, T. H. (2012). Effects of food diet preparation techniques on radionuclide intake and its implications for individual ingestion effective dose in Abeokuta, Southwestern Nigeria. *World Journal of Nuclear Science and Technology*, 2(03), 106.
- [13] Sudarshan, M., & Singh, R. (1991). Effect of fast neutron damage on the performance of a high resolution HPGe coaxial detector. *Measurement Science and Technology*, 2(12), 1192.

## The Importance of of Buildup Factor for NaI(Tl) Detector System

Faez Waheed<sup>1\*</sup>, Hakan Akyıldırım<sup>1</sup>, Kadir Günoğlu<sup>2</sup>, İskender Akkurt<sup>1</sup>

<sup>1</sup> Physics Department, Suleyman Demirel University, Isparta-Turkey

<sup>2</sup> Isparta Uygulamalı Bilimler Üniversitesi, Isparta-Turkey

\* [faez\\_radiophysics@yahoo.com](mailto:faez_radiophysics@yahoo.com)

### ABSTRACT

The knowledge of buildup factor is important in radiation measurement technique and other purposes as a result of the technology development of using radiation and radioactive material. The only way to prevent photons from being scattered is to side and back shield the detector and the source is well collimate. Buildup factors are the shielding material and geometry-dependent parameters which correct the simple attenuation calculations so that they include the contribution of the radiation field produced by the collided part of the beam. Buildup factors have been calculated by experimental for life radioactive gamma-ray sources, through seven source-detector distance geometry design at five energies 0.662 MeV by using Cesium radioactive sealed sources.

**KEYWORDS:** Gamma ray, NaI(Tl), Buildup factor, Collimator, Geometry.

### 1- INTRODUCTION

The gamma-ray measurement technique is critical in nuclear technology as it is mostly used in a wide variety of peaceful purposes in radiation shielding and other purposes [1-3], and it is also important to build radiation protection for human health. Obtaining a good geometry is considering as one of the most important issues in radiation shield measurement to get measurement equality [4, 5]. Buildup factors should be determined and adopted for such kind of measurements. Furthermore, obtaining this factor is an important proper gamma attenuation measurement system and can affect the measurement quality [6, 7]. As photon interaction with attenuator, uncollided photons and collided photons will appear within or beyond the attenuator. Thus, determination one of most important equality parameter such as the buildup factor is being important for measurement technique, buildup factor is the ratio of a quantity at a point due to the total number of particle to that same quantity at that same point due to uncollided particles only [8, 9, 10]. This work is focused on the determination of the buildup factor experimentally. The buildup factor of NaI(Tl) measurement has great importance in nuclear investigations and in all experimental studies that measure radiation.

### 2. EXPERIMENTAL: MATERIAL AND METHODS

As a photon pass through a shielding, an interaction occurs between the photons and matter resulting in energy transfer to the observer. The interaction can result in a large energy transfer or even complete absorption. However, a photon can be scattered rather than absorbed and retain most of the initial energy while only changing direction. The attenuation of a gamma ray photon beam is governed by the decay law given below:-

$$I = I_0 e^{-\mu x} \dots\dots\dots (1)$$

where  $\mu$  represents the linear attenuation coefficient and  $x$  gives the thickness of the attenuator. However, practically, more photons are received at a reference point than what one can calculate using the decay law. The additional number of photons are received due to the buildup factor  $B$  of

the attenuator and the simple mathematical form of the decay law is modified to a new form given in equation (2).

$$I = B \cdot I_0 e^{-\mu x} \dots\dots\dots (2)$$

Equation (1) is valid only in narrow beam geometry when a collimated beam of radiation is used. However, in a broad beam geometry, we must take in to account the buildup factor and hence equation (2) will give us a more correct and precise value. For the gamma-ray spectrometry technique, the buildup factor is an important parameter to be determined. This parameter is usually done using a function to fit the efficiency at a wide energies range and detector-source distance. The geometry is used to analysis spectroscopy of these sources have been done for many different axial distances starts from 1 cm until to 15 cm from the detector surface. In order to reduce the background level of the system, the detector is shielded using lead on all sides as illustrate in Figure 1.

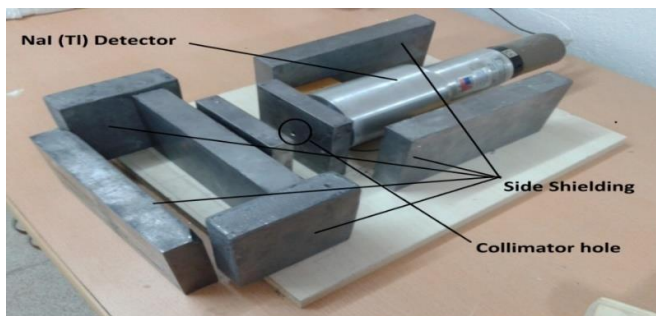


*Figure 1. Buildup Factor Geometry*

### 3. RESULTS AND DISCUSSION.

The energy absorption buildup factor by using 3" x 3" NaI scintillation detector have been measured for 0.662 MeV gamma-ray emitter started from 1 cm up to 15 cm with extension, furthermore, measuring source-detector distance impact to the value of it.

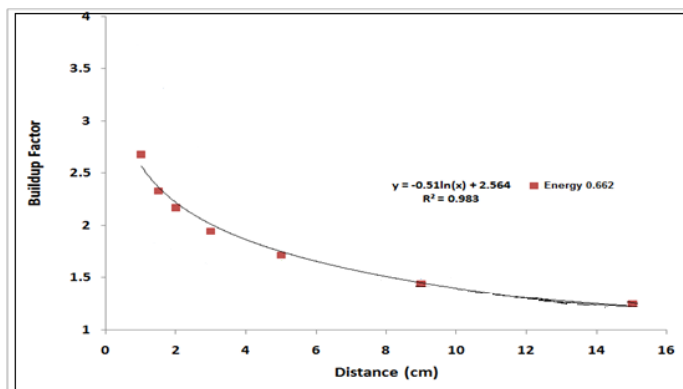


*Figure 2. Buildup factor as a function of distance.*



The results have been obtained as a function of distance and shown in Figures 2. As can be seen from these Figure that the variation of buildup factor as a function of distance. There is a great variety of analytical function that is used to describe the energy absorption buildup factor depended on the source-detector distance. It can be seen that the line is the description with the correlation coefficient between the buildup factor variation as a function of source-detector distance ( $R^2 = 0.98$ ).

### 3. CONCLUSIONS

In this study, Energy absorption Buildup factor parameter has been determined experimentally for the 3" x 3" NaI(Tl) scintillation detectors. The impact of source-detector distance with the energy absorption buildup factor was investigated. It was found from this work that the energy buildup factor depend on source distance to the detector.

### 4. REFERENCES

- [1] Categorization of radioactive source. Revision of IAEA-TECHDOC-1191, international Atomic energy Agency, Vienna (Austria). Available at: [http://www.iaea.org/inis/collection/NCLCollectionStore/\\_public/34/065/34065394.pdf](http://www.iaea.org/inis/collection/NCLCollectionStore/_public/34/065/34065394.pdf)
- [2] KAVAS, E., (2016). Energy absorption exposure factors in polymers by nuclear track detectors, Asian journal of chemistry , Vol. 28, No. 8, 1673-1681.
- [3] Radiological Control Technician, RCT 1.13-SG, 2013. Sandia National- U.S Depart of energy's / National Security Administration DOE-AC04-94AL85000. SAND.NO.2013-0024P.
- [4] BRAR G.S., SIDHUG.S., SINGH P. S., MUDAHAR G.S., 1997. Buildup factor studies of HCO-materials as a function of weight fraction of constituent elements, Radiation Physics and Chemistry: Vol.49,No.8,pp.977-980,1998.
- [5] Kazuo, S., and H. Hirayama. "Calculation of gamma ray buildup factors for two layered shields made of water, concrete and iron and application of approximating formula." *Radia. Phys. Chem* 64 (2001): 583-584.
- [6] SHIRANI A., ALAMATSAZ M. H., 2013. Calculation of exposure Buildup factors for point isotropic gamma ray sources in stratified spherical shields of water surrounded by lead and optimization of water-lead combination, Iranian Journal of Science &Technology, A1: 29-34.
- [7] SINGH B., KUMAR V., DEVI M., SIDHUG., 2013. Investigation of mass attenuation coefficient and energy absorption Buildup factor of some low-Z gamma ray shielding materials, International Journal of Latest Research in Science and Technology: ISSN (Online) : 2278 - 5299, Volume2, Issue5: Page No. 73-77, September - October2013, <http://www.mnkjournals.com/ijlrst.htm>.
- [8] MANOHARA S. R., HANAGODIMATH S. M., GERWARD L., MITTAL K. C., 2010. Exposure Buildup Factors for Heavy Metal Oxide Glass: A Radiation Shield, Journal of the Korean Physical Society, Vol.59, No.2, August 2011, pp.2039~2042.
- [9] SHIMIZU A., HIRAYAMA H., 2003. Calculation of gamma ray Buildup factor up to depths of 100 mfp by the method of invariant embedding (I). J. Nucl. Sci. Tech., Vol. 40, No.4, pp.192-200.
- [10] Singh, B., Kumar, V., Devi, M., Sidhu, G., 2013. Investigation of mass attenuation coefficient and energy absorption Buildup factor of some low-Z gamma ray shielding materials, International Journal of Latest Research in Science and Technology: ISSN (Online):2278-5299, Volume 2, Issue 5: Page No.73-77,September-October 2013. <http://www.mnkjournals.com/ijlrst.htm>

## Hastanelerde Çalışan Ebe Ve Hemşirelerin Hepatit A Ve B Hakkında Bilgi Düzeyleri Ve Aldıkları Önlemlerin Belirlenmesi

Hüseyin Eriş<sup>1\*</sup>, Feray Kabalcıoğlu Bucak<sup>2</sup>

Harran Üniversitesi Sağlık Hizmetleri Meslek Yüksekokulu, Şanlıurfa, TURKEY

Harran Üniversitesi Sağlık Bilimleri Fakültesi Şanlıurfa, TURKEY

\*erisharran@hotmail.com

### ÖZET

Dünyada ve ülkemizde halen önemli bir enfeksiyon hastalığı olan hepatit-B virüsü (HBV) ile hepatit-A virüsü (HAV) sağlık alanında çalışanlar, çalışma ortamında hastalardan ve fizik çevreden bulaşabilecek birçok enfeksiyon hastalığı açısından risk altındadırlar. HBV ve HAV enfeksiyonu ve oluşturduğu sonuçlar önemli halk sağlığı sorunlarından birisidir. Bu çalışma, Şanlıurfa il merkezinde yataklı kurumlarda görev yapan ebe ve hemşirelerin hakkında HBV ve HAV enfeksiyonu bilgi düzeyleri ve aldıkları önlemlerin belirlenmesi amacıyla yapılmıştır. Çalışma tanımlayıcı olarak yapılmış olup, Şanlıurfa ilinde bulunan Harran Üniversitesi Araştırma ve Uygulama Hastanesi (285 Hemşire/ebe) ile Şanlıurfa Kamu Hastaneleri Kurumuna Bağlı 4 hastanede çalışan (823 Hemşire/ebe) kapsamaktadır.

Araştırmanın evrenini bu hastanelerde çalışan ve fiilen görevinde olan toplam 1.108 ebe / hemşire/ sağlık memuru, örneklemini ise ulaşılabilen, soru formunu doldurmaya istekli 550 kişi oluşturmaktadır. Konu ile ilgili literatürler taranarak ve uzman görüşü alınarak soru formu oluşturulmuş ve ön deneme yapıldıktan sonra soru formuna son şekli verilmiştir. Bu formda çalışan hemşirelerin sosyo - demografik özelliklerini, kurumların ve hemşirelerin HBV ve HAV virüslerinden korunmaya yönelik aldıkları önlemleri içeren 36 soru bulunmaktadır. Çalışmaya başlamadan önce kurumlardan ve araştırmaya katılan bireylerden gerekli izin alınarak soru formu 2 Ocak- 31 Mayıs 2016 tarihleri arasında, araştırmacılar tarafından yüz yüze görüşme tekniği ile uygulanmıştır. Araştırmadan elde edilen verilerin istatistiksel değerlendirilmesinde SPSS (22) paket programından yararlanılarak, istatistik analiz programı, sayı, yüzdelik, ortalama, standart sapma değerleri ile değerlendirilmiştir.

**Anahtar Kelimeler:** Sağlık Kurumları, Sağlık Çalışanları, İşçi Sağlığı

## Determining the Knowledge Levels of The Midwives and Nurses Working in the Hospitals About Hepatitis A and B and The precautions They Take

### ABSTRACT

The healthcare professionals working in the health field of hepatitis-B virus (HBV) and hepatitis-A virus (HAV) which are still an important infectious disease in the world and in Turkey are at risk in terms of many infectious diseases that may be infected from the patients and the physical environment in the work environment. HBV and HAV infection and their outcomes are among the important public health issues. This study was conducted to determine the knowledge levels of the nurses and midwives, working in the institutions with beds in city center of Şanlıurfa, about HBV and HCV infections and the precautions they take. This descriptive study included the nurses and midwives working in Harran University Research and Application Hospital (285 Nurses/midwives) and in 4 hospitals (823 Nurses/midwives) affiliated with Şanlıurfa Public Hospitals Institutions in city of Şanlıurfa. While the population of the study consisted of 1.108 midwives/nurses/health officers working and being on duty in these hospitals, the sample consisted of 550 people who could be reached and were voluntary to fill out the questionnaire. A questionnaire was prepared by reviewing the related literature and receiving the expert opinions and the questionnaire form was put in the final form after the preliminary study was performed. In

this form, there are 36 questions including the socio-demographic characteristics of the nurses and the precautions taken by the institutions and the nurses in order to be protected from the HBV and HAV. Before starting the study, the required permissions were taken from the institutions and participants and the questionnaire was applied using the face-to-face interview technique by the researchers between January 2<sup>nd</sup> and May 31<sup>st</sup> 2016. The statistical evaluation of the data obtained in the study was performed by using SPSS (22) packaged software as well as number, percentage, mean, and standard deviation values.

**Keywords:** *Health Institutions, Healthcare Professionals , Occupational Health*

## 1. GİRİŞ

Enfeksiyon hastalıklarının kan yoluyla bulaşanlar grubu, tüm dünyada önemli bir sağlık sorunudur. Sağlık çalışanlarının hepatit B (HBV), hepatit C virüsü'ne (HCV) maruz kalmaları riski tüm dünyada önemli ve önlenabilir bir problemdir (1). HBV ve HCV enfeksiyonları tüm dünyada yaygın olarak görülen, morbidite ve mortalitesi yüksek sağlık sorunlarından (2,3). Daha çok kan materyalleri yoluyla bulaşması olası viral hastalıkların en önemlilerinden birisi Hepatit B virüsü enfeksiyonudur. Hepatit, sağlığı olumsuz etkileyen ve yaşamı tehdit eden, kronik hastalığa yol açan viral enfeksiyonun neden olduğu bir karaciğer inflamasyonu olarak tanımlanır (4-7). Ebe ve hemşireler günlük çalışma ortamında, hastalardan, hastaya kullanılan malzemelerden ve fizik çevreden bulaşabilecek birçok enfeksiyon hastalığı açısından risk altındadır (8-10). Özellikle kan ve kan ürünleri ile bulaşanlar, gerek sıklık gerekse yarattığı uzun süreli olumsuz etkiler nedeni ile ayrı bir öneme sahiptir (11).

Bulaşmış (Kontamine) aletler hem hasta hem de sağlık çalışanı açısından enfeksiyon kaynağıdır. Bu enfekte materyallere maruz kalan sağlık çalışanlarının enfeksiyon hastalıkları meslek hastalığı olarak kabul edilmektedir (12). Özellikle acil servis, ameliyathane, yoğun bakım ve laboratuarda çalışanlar kan ve vücut sıvıları ile temas etmekte, bu da bulaşma riskini artırmaktadır. En sık karşılaşma kontamine iğne batması, kontamine kesici-delici tıbbi aletler, kan ve vücut sıvılarının mukozalara teması şeklinde olmaktadır. Kesici delici aletlerin birçoğunun artık tek kullanımlık olması hastalar için riski azaltmışken mesleki maruziyetle enfeksiyon bulaşı devam etmektedir (13).

Bu çalışmanın amacı, Şanlıurfa il merkezinde yataklı kurumlarda görev yapan ebe ve hemşirelerin HBV, HCV hakkında bilgi düzeyleri ve aldıkları önlemlerin belirlenmesidir.

## 2. GEREÇ VE YÖNTEM

Tanımlayıcı ve kesitsel nitelikte olan bu çalışma; Şanlıurfa il merkezinde bir üniversite hastanesi, dört devlet hastanesi olmak üzere 5 hastanede çalışan 550 ebe ve hemşireye ulaşılmıştır. Örneklem seçimi yapılmamış, çalışma esnasında fiilen görevinde olan araştırma kapsamına alınmıştır. Araştırmanın gerçekleştirildiği kurumlardan yazılı izin, çalışan personelden sözel onam alınarak çalışma yürütülmüştür. Araştırmacılar tarafından literatür taraması sonucunda oluşturulan soru formu yüz yüze görüşme tekniği ile uygulanmıştır. Araştırmadan elde edilen verilerin istatistiksel değerlendirilmesinde SPSS (22) paket programından yararlanılarak, istatistik analiz programı, sayı, yüzdelik, ortalama, standart sapma değerleri ile değerlendirilmiştir.

## 3. BULGULAR

Bu bölümde araştırmaya ait çeşitli bulgular verilmektedir. Araştırmaya katılanların %56,2'si 27 yaş ve altında, %74,4'ünün kadın, %66,2'sinin lisans mezunu, %53,6'nın 0-4 yıl arasında çalıştıkları, 80,2'sinin devlet hastanesinde çalıştıkları, %47,1'nin servislerde çalıştığı, %60,4'ünün servis hemşiresi olduğu ve %68,5'inin ise vardiya usulü ile çalıştığı tespit edilmiştir. Araştırmaya katılan ebe ve hemşirelerin %89,1'i "kan ve vücut sıvılarıyla temasları olduğunu", buna karşın ebe ve hemşirelerin %83,3'ü önlem aldıklarını belirtmişlerdir. Ne tür önlem aldığınız sorusuna ebe ve hemşirelerin sırasıyla %71,4'ü eldiven kullandığını, %24,7'si çift eldiven taktığını ve %20

civarında ise önlük veya maske kullandıklarını belirtmişlerdir. Kan ve vücut sıvısına temas olduğunda ne tür işlem yaptıklarına ise ebe ve hemşirelerin %73,3'ü "Hastada bulaşıcı bir hastalığı olup olmadığını araştırmış", %53,5'i "Hepatit marker sonuçlarına baktırmış", %53,1'i "Yaralanan/temas eden bölgeyi soğuk suyla yıkamış" ve "%52'si ise "Yaralanan/temas eden bölgeyi baticonla yıkadığını" belirtmiştir. Bakım verdiğiniz hastalar Hepatit B için bulaşıcı özellik taşıyor muydu? Sorusuna ebe ve hemşirelerin %41,5'i evet derken, Hepatit C için bulaşıcı özellik taşıyor muydu sorusuna %42,7'si hayır demişlerdir. Ebe ve hemşirelerin yaralanma olaylarının gerçekleşme şekillerine bakıldığında %66'sının eline iğne batması, %52'si enjektör ucunu kapatırken, %37,3'ü göz ve mukozalara kan ve vücut sıvılarının sıçraması sonucu birkaç farklı şekilde yaralandıklarını belirtmişlerdir.

Araştırmaya katılan ebe ve hemşirelerin "Her hastada hepatit enfeksiyonu varmış gibi düşünerek önlemler alarak çalışıyor musunuz? Sorusuna %73,3'ü evet demiştir. Yine ebe ve hemşirelere sorulan Hepatit B virüsü taşıyıp taşımadığının tespiti için bir tetkik yaptırdınız mı? Sorusuna %90,5'i evet demiştir. Hepatit B aşısı yaptıran hemşirelerin oranı %86,7'i iken, hepatiti B aşısını yaptırmaya sayılarına bakıldığında hemşirelerin %56,6'sı 3 kez, %13,2'si 2 kez ve %9,2'si 1 kez yaptırdığını belirtmiştir.

"Aşı sonrası antikor baktırdınız mı?" sorusuna ebe ve hemşireleri %76,9'u evet demiştir. Hepatiti B aşısını yaptırmama nedenlerine gelince, ebe ve hemşirelerin %28,8'i önemsemediği için, %24,7'si risk altında bulunmadığı için, %15,1'i ya fırsat bulamadığı için ya da hepatit B geçirdiği için ve %11'i ise kendini iyi bir şekilde koruduğu için yaptırmamışlardır.

Araştırmaya katılan ebe ve hemşirelere sorulan "Hepatit C virüsü taşıyıp taşımadığının tespiti için bir tetkik yaptırdınız mı?" sorusuna %60,4'ü evet derken, hepatit C tespit edildimi sorusuna ise %96,1'i hayır cevabını vermiştir. En son serolojinize ne zaman baktırdınız sorusuna, araştırmaya katılan ebe ve hemşirelerin %31,5'i 1 yıldan daha uzun süredir baktırmadığını, %9,8'i ise hiç baktırmadığını belirtmiştir. Çalıştığınız kurumda hastane enfeksiyonları kontrol komitesi var mı? sorusuna %97,3'ü evet demiştir. Hepatit B ve C hakkında eğitim aldınız mı? sorusuna ebe ve hemşirelerin %77,5'i evet derken, alınan eğitimin şekli sorusuna %76,3'ü hizmet içi eğitim cevabını vermiştir. Hepatit B ve C konusunda eğitim almak istersiniz sorusuna araştırmaya katılan ebe ve hemşirelerin %78,9'u evet derken, %21,1'i ise hayır demiştir.

#### 4. TARTIŞMA

Hepatit virüsü bulaşıcı bir hastalık olması sebebiyle ülkemizde önlenabilir bir halk sağlığı sorunu olmaya devam etmektedir (14). Dünyada yaklaşık iki milyar kişinin HBV ile enfekte olduğu bildirilmektedir. Her yıl yaklaşık 600.000 kişi HBV'ye bağlı akut ya da kronik olaylar sonucunda hayatını kaybetmektedir. Hasta bakımından birebir sorumlu olan ebe ve hemşireler bu tür hastalara bakım verirken risk altındadırlar. Çalışmamızda katılan ebe ve hemşirelerin %89,1'i "kan ve vücut sıvılarıyla temasları olduğunu", buna karşın ebe ve hemşirelerin %83,3'ü önlem aldıklarını belirtmişlerdir. Çalışmada ebe ve hemşirelerin %90,5 Hepatit B virüsü, %60,4 'ü Hepatit C virüsü tespiti için bir tetkik yaptırdığını bildirmişlerdir. Yurtdışında birinci basamak sağlık hizmeti veren doktor, kadın doğum uzmanı, hemşire ve ebelerle mektup gönderilerek yapılan bir çalışmada HBV testinin %98 oranında, başka bir çalışmada ise %93 oranında istendiği bildirilmektedir (15,16).

Bu testlerin rutin yapılması hastalığın erken dönemde tanınması ve tedavi sürecinin başlaması yönünden önem taşımaktadır. Çalışmada ebe ve hemşirelerin %53,5'i "Hepatit marker sonuçlarına" baktırdığı tespit edilmiştir. Benzer şekilde 2014 yılında Pamukkale Üniversite Hastanesi'nde çalışan hemşire ve teknisyenlerde yapılan çalışmada %67,6'i hepatit markerlarına baktırdığını bildirmiştir. Bu bulgunun yüksekliği hemşire ve teknisyenlerin Hepatit B aşılama programında markırlarına bakılmasını sağlık taraması kapsamında değerlendirilmesinden kaynaklı olduğu düşünülebilir (17).

Çalışmada ebe ve hemşirelerin yaralanma olaylarının gerçekleşme şekillerine bakıldığında %66'sının eline iğne batması, %52'si enjektör ucunu kapatırken, %37,3'ü göz ve mukozalara kan

ve vücut sıvılarının sıçraması sonucu birkaç farklı şekilde yaralandıklarını belirtmişlerdir. Mersin ilinde, bir üniversite hastanesi, iki devlet hastanesi ve 54 sağlık ocağında görev alan sağlık personelinin kapsayan çalışmada, sağlık çalışanlarının % 79,1'inin çalışma hayatında en az bir kez kesici-delici aletle yaralandığı, yaralanmaların % 60,9'unun kanla bulaşmış aletle ve çoğunlukla enjektör iğnesi ile yaşandığı (% 89,2) belirlenmiştir (18).

Yine benzer şekilde Kuruüzüm ve ark. Dokuz Eylül Üniversitesi Tıp Fakültesi Hastanesinde yaptıkları anket çalışmasında yaralanmaların %97'sinin kesici-delici aletle meydana gelen perkütan yaralanmalar olduğunu bildirmiştir (19). Literatür taramalarında hemşireler ile ilgili benzer araştırmalar yapıldığı tespit edilmiştir. Araştırmamızda ebe ve hemşirelerin %77,5'i enfeksiyon riski taşıyan hastalıklara karşı (hepatiti B ve C) hizmet içi eğitim yöntemiyle eğitim aldıklarını ve %79'u tekrar eğitim almak istediklerini ifade etmişlerdir. Uçan ve ark. tarafından (2006) yapılan bir araştırmada da benzer sonuçlar elde edilmiş, hemşirelerin %52,8'inin HBV ve HCV'den korunma konusunda hizmet içi eğitim aldığı ve buna rağmen hemşirelerin %85,2'sinin bu konuda tekrar hizmet içi eğitim almak istediği belirlenmiştir (11).

Araştırmaya katılan ebe ve hemşirelere, bakım verdikleri hastaların hepatit B ve C özellik taşıyıp taşımadıkları sorusuna, hepatit B taşıyordu diyenlerin oranı %41,5 iken; Hepatit C taşıyordu diyenlerin oranı ise %29,3'e geriliyor. Uçan ve Arkadaşları tarafından (2006) yapılan bir araştırmada da benzer sonuçlar elde edilmiştir (11).

Ebe ve hemşirelere kan ve vücut sıvılarıyla temas sırasında önlem alıp almadıklarına büyük çoğunluğu evet derken, ne tür önlemler aldınız sorusuna ise eldiven, çift eldiven, önlük, maske kullanma gibi önlemler aldıklarını belirtmişlerdir. Çalışkan ve Akdur (2001) ile Uçan ve Arkadaşları tarafından (2006) yapılan bir araştırmada da benzer sonuçlar elde edilmiştir (11, 20).

Ebe ve hemşirelere hepatiti virüsü taşıyıp taşımadıklarının tespit edilmesi için tetkik yaptırdıkları sorusuna, araştırmaya katılan hemşirelerin %90,5'i evet demiştir. Ayrıca hemşirelerin büyük bir çoğunluğu Hepatiti B aşısını 3 doz ve rapel yaptırdıklarını belirtmişlerdir. Uçan ve Arkadaşları tarafından (2006) yapılan bir araştırmada da benzer sonuçlar elde edilmiş ve hemşirelerin %83,1'i rutin olarak kan tetkikleri yaptırdıklarını ve hemşirelerin çoğunun 3 doz ve rapel yaptırdıklarını belirtmişlerdir.

## 5. SONUÇ:

Araştırma sonucunda, araştırmaya katılan ebe ve hemşirelerin büyük bir çoğunluğu "kan ve vücut sıvılarıyla temasları olmasına rağmen gerekli önlemleri aldıklarını belirtmişlerdir. Bu önlemler arasında sırasıyla eldiven, çift eldiven, önlük veya maske kullandıklarını belirtmişlerdir. Ebe ve hemşirelerin çoğunluğu, kan ve vücut sıvısı teması olduğunda hastada bulaşıcı bir hastalığı olup olmadığı, hepatit marker sonuçlarına bakma, yaralanan/temas edilen bölgeyi soğuk suyla yıkama ve yaralanan/temas eden bölgeyi baticonla yıkama gibi müdahalelerde bulunduklarını belirtmiştir.

Araştırmaya katılan ebe ve hemşirelerin çoğunluğu her hastada hepatit enfeksiyonu varmış gibi önlemler alarak çalıştıklarını ifade etmişler. Ebe ve hemşirelerin %90,5'i Hepatit B virüsü taşıyıp taşımadıklarını tespit etmek için tetkik yaptırmışlardır. Hepatit B aşısı yaptıran hemşirelerin oranı %86,7'idir. Hepatit B aşısını yaptıran sayılarına bakıldığında ise ebe ve hemşirelerin %56,6'sı 3 kez, %13,2'si 2 kez ve %9,2'si 1 kez yaptırdığını belirtmiştir.

Ebe ve hemşirelerin çoğunluğu aşı sonrası antikor durumuna baktırmışlardır. Hepatit B aşısını yaptırmama nedenlerine gelince, ebe ve hemşirelerin %28,8'i önemsemediği için, %24,7'si risk altında bulunmadığı için, %15,1'i ya fırsat bulamadığı için ya da hepatit B geçirdiği için ve %11'i ise kendini iyi bir şekilde koruduğunu düşündüğü için yaptırmadıklarını ifade etmişlerdir.

Araştırmaya katılan ebe ve hemşirelerin çoğunluğu hepatit C virüsü taşıyıp taşımadıkları için bir tetkik yaptırdıklarını, test sonucunda ise ebe ve hemşirelerin %96,1'inde hepatit C tespit edilmediği belirtilmiştir. Serolojinize ne zaman baktırdınız sorusuna, araştırmaya katılan ebe ve hemşirelerin %31,5'i 1 yıldan daha uzun süredir baktırmadığını, %9,8'i ise hiç baktırmadığını belirtmiştir.

Araştırmaya katılan ebe ve hemşirelerin çoğunluğu, hastanelerinde hizmet içi eğitimle Hepatit B ve C hakkında eğitim aldıklarını belirtmiş olmalarına rağmen Hepatit B ve C konusunda tekrardan eğitim almak istediklerini ifade etmişlerdir.

#### KAYNAKÇA

- [1]. Yoldaş, Ö., Bulut, A., Ertürk, E., Çelik, D., Karakaşoğlu, Ü., Altındış, M. (2014). Sağlık Çalışanlarında Enfekte Kan ve Vücut Sıvılarına Maruziyet Riskinin Belirlenmesi. Kocatepe Tıp Dergisi, 15(3).
- [2]. Smyth C.M, Manning D.S, Byrne M.F et al (2002). Hepatitis C infection in plasmapheresis donors: an overlooked risk factor for transmission? European Journal of Gastroenterology&Hepatology 14: 891-892.
- [3]. Sagmeister M, Renner E.L, Mullhaupt B et al (2002). Simulation of hepatitis C and based on mandatory reporting system. European Journal of Gastroenterology& Hepatology 14: 25-34
- [4]. Lai CL, Ratzu V, Yuen MF, Poynard T. Viral hepatitis B. Lancet. 2003; 362: 2089-2094.
- [5]. Sharma SK, Saini N, Chwla Y. Hepatitis B Virus: Inactive carriers. Virol J. 2005; (82): 1-5.
- [6]. Lavanchy D. Hepatitis B virus epidemiology, disease burden, treatment, and current and emerging prevention and control measure. Journal of Viral Hepatitis. 2004; 11(2): 97-107.
- [7]. Şahin, N. H., Bilgiç, D., Esen, Ü., Çetinkaya, R., & Tozoğlu, Z. (2009). Bayan Kuaförü Çalışanlarının Hepatit B'ye İlişkin Bilgi ve Uygulamalarının Belirlenmesi. TAF Preventive Medicine Bulletin, 8(2).
- [8]. Çan G, Topbaş M , Kapucu M (2003). Karadeniz Teknik Üniversitesi Tıp Fakültesi Öğrencilerinin Kan ve Enfekte Vücut Sıvıları ile İlgili Bilgi ve Tutumları. Sağlık ve Toplum Dergisi. 2: 91-95
- [9]. Karadakovan A (2002). Hepatit B Enfeksiyonu ve Koruyucu Önlemler. Aile ve Toplum Dergisi 2(5):13-19.
- [10]. Berenguer M, Wright T (2002). Viral Hepatitis. Gastrointestinal and Liver Disease Editör: Mark Feldman, Lawrence s.friedman, Marvin H.Sleisenger. 7th Edition. Chapter 68. Volume II. Saunders. 1285-1317.
- [11]. Uçan, Ö., Ovayolu, N., & Torun, S. (2006). Hemşirelerin hepatit b ve c virüslerinden korunmak için aldıkları önlemlerin belirlenmesi. Journal of Anatolia Nursing and Health Sciences, 9(2).
- [12]. Göçgeldi, E., İstanbulluoğlu, H., Türker, T., Güleç, M., Ceylan, S., Koçak, N., & Komutanlığı, T. S. (2011). Tıp fakültesi öğrencilerinin mesleki maruziyetten kaynaklanan sağlık riskleri konusundaki bilgi düzeylerinin karşılaştırılması. Gülhane Tıp Dergisi, 53(3), 195-204.
- [13]. Sarı, N. D., Fincancı, M., Soysal, H. F., Demirkıran, N., Koyuncu, S., & Özgün, Ö. (2014). Delici Kesici Alet Yaralanmalarının Bildirim Sıklığı Neyin Göstergesi. Haseki Tıp Bülteni, 52, 98-102
- [14]. Tosun S. (2013) Viral hepatitlerin ülkemizdeki değişen epidemiyolojisi. ANKEM Dergisi.27(Ek 2):128-134.
- [15]. Weisbord JS, Koumans EH, Toomey KE, Grayson C, Markowitz LE. Sexually transmitted diseases during pregnancy: screening, diagnostic, and treatment practices among prenatal care providers in Georgia. South Med J 2001; 94(1): 47-53.
- [16]. Keane FE, Neale J, Phillips T, Heard L, Jones R, Guttridge B, Bendall R. Offering routine antenatal testing for HIV and hepatitis B in the rural setting of Cornwall. Sex Transm Infect. 2002; 78(2): 133.
- [17]. Erkan S. (2014) Pamukkale Üniversite Hastanesi'nde Çalışan Hemşire Ve Teknisyenlerin Mesleki Risk Algısının Belirlenmesi; Pamukkale Üniversitesi Sağlık Bilimleri Enstitüsü Yüksek Lisans Tezi Halk Sağlığı Hemşireliği Ana Bilim Dalı, Denizli.

- [18]. Altıok M, Kuyurtar F, Karaçorlu S, Ersöz G, Erdoğan S. Sağlık çalışanlarının delici kesici aletlerle yaralanma deneyimleri ve yaralanmaya yönelik alınan önlemler. *Maltepe Üniversitesi Hemşirelik Bilim ve Sanatı Dergisi* 2009;2(3):70-9.
- [19]. Kuruüzüm Z, Elmalı Z, Günay S, Gündüz Ş, Yapan Z. Sağlık çalışanlarında kan ve beden sıvılarıyla oluşan mesleki yaralanmalar: bir anket çalışması. *Mikrobiyoloji Bülteni* 2008;42(1):61-9.
- [20]. Çalışkan. D., Akdur. R., (2001) Ankara Üniversitesi Tıp Fakültesi Hastanesinde Çalışan Hemşirelerin Kendi Bildirimleri İle Karşılaştıkları Mesleki Riskler, *Ankara Üniversitesi Tıp Fakültesi Mecmuası* Cilt 54, Sayı 2

## Calculations of Cross Sections of Zinc Nucleus Induced by Proton to Produce Gallium-66

Susan Shukur Noori<sup>1,3\*</sup>, İskender Akkurt<sup>1</sup>, Nurdan Karpuz Demir<sup>2</sup>

<sup>1</sup> Süleyman Demirel University, Sciences & Arts Faculty, Isparta-TURKEY

<sup>2</sup> Amasya University, Sabuncuoğlu Şerefeddin Vocational School of Health Services, Amasya, TURKEY

<sup>3</sup> Kirkuk University, College of Science, Kirkuk-IRAQ

\*suzan\_nuclear@yahoo.com

### ABSTRACT

Gallium-66 ( $T_{1/2} = 9.49$  h) is an intermediate-lived radionuclide that has potential for positron emission tomography (PET). In order to improve rates of radioisotope production, nuclear interaction data are mainly needed. The cross sections for the production of  $^{66}\text{Ga}$  radionuclide produced by the proton bombardment of a copper and zinc targets for the reactions  $^{66}\text{Zn}(p, n)^{66}\text{Ga}$  has been carried out using nuclear reaction simulation code TALYS 1.6 that based on Monte Carlo. The results are compared with available experimental data from EXFOR library.

**KEYWORDS:** Cross sections; Gallium-66; TALYS 1.6 nuclear reaction simulation code.

### 1. INTRODUCTION

Cross section concept in simple terms, gives information about the probability of the realization of nuclear reaction. The study of nuclear reactions is important for a number of reasons. Progress in the understanding of nuclear reactions has occurred at a faster pace and generally, a higher level of developed has been achieve compared to similar studies of chemical reactions.

The use of gallium radionuclides in nuclear medicine dates back to more than half a century, which used as diagnostic and therapeutic agents in cancer, bone metabolism and disorders of calcium, radiation therapy is a form of cancer treatment that uses radiation to destroy malignant cells [1,2]. Due to the interesting properties for  $^{66}\text{Ga}$  as a positron emitter for tumor imaging and increasing importance of positron emission tomography in modern medicine, we have focused our attention on producing this radioisotope in this study. Our present study includes theoretical calculations of the nuclear reaction cross section for the proton on Cu and Zn nuclei using a Monte Carlo nuclear reaction simulation code TALYS 1.6 and compared with experimental data existing in EXFOR[3] to evaluate the deviation between our theoretical results and experimental data. Using monte carlo methods other several work have been done in this field [4-9].

### 2. MATERIAL AND METHODS

Nuclear reactions is required for the production of radioisotopes. This process of production involves the selection of projectile energy range to increase radioisotope production and reduce impurity. The calculations based on standard models for nuclear reactions can be helpful for determining the precision of various parameters for these models also predestined from experimental measurements [10]. The Cross Sections for production of Ga via proton induced nuclear reactions on Zn has been calculated.

In this study, the cross section of  $^{66}\text{Zn}(p, n)^{66}\text{Ga}$  reactions were calculated theoretically by Monte Carlo simulation computer code TALYS 1.6 program. the based of TALYS 1.6 code on simulation and prediction of nuclear reactions. TALYS calculates the total reaction cross-section and then



distributes its value according to the branching ratio of different reaction channels and different reaction mechanisms. TALYS is a FORTRAN programming language. Runs on Linux operating system.

### 3. RESULTS AND DISCUSSION

The  $^{66}\text{Zn}(p, n)^{66}\text{Ga}$  for proton induced reaction cross sections were theoretically calculated using TALYS 1.6 code. The obtained results have been compared with the experimental results in the literature existing in the EXFOR databases. The excitation functions to obtained  $^{66}\text{Ga}$  radioisotope by proton induced on Zn nucleus were calculated theoretically using nuclear reaction simulation code TALYS 1.6. This calculations has been achieved for some nuclear reactions  $^{66}\text{Zn}(p, n)^{66}\text{Ga}$  the present results were plotted and compared with available experimental data from EXFOR library which displayed in Figures 1.

In general for  $^{66}\text{Zn}(p, n)^{66}\text{Ga}$  nuclear reaction shown in Figure 1 there is a good agreement between our calculated excitation function and the previously experimental data where the ideal match can be seen for the energies lower than 10 MeV and above 30 MeV, excepted in the peak region we notice the experimental data performed [11,12,13] shows 25% higher value than our calculated results. While the data reported by Hermann, et al., [14] shows a lower value than our calculated results which start from 12 MeV.

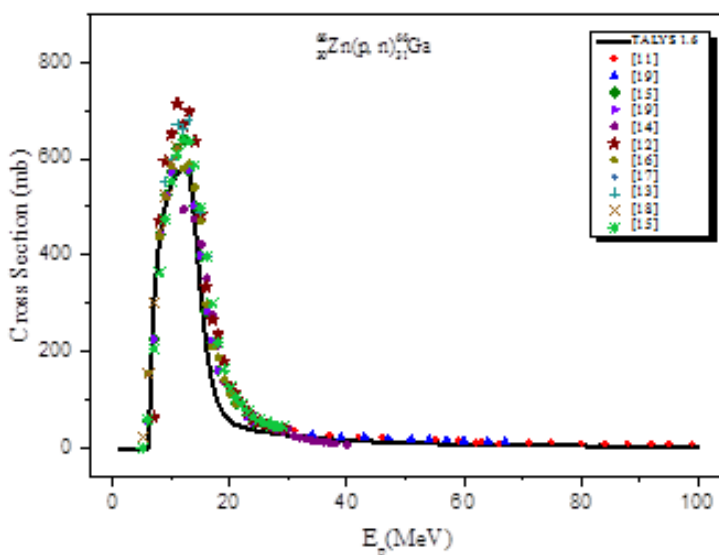


Fig. 1. The calculated cross sections of  $^{66}\text{Zn}(p, n)^{66}\text{Ga}$  reaction

### 4. CONCLUSION

The aim of this study is calculation the excitation functions by induced proton on Cu and Zn target nuclei for different nuclear reactions to produce  $^{66}\text{Ga}$  radioisotope which is an important medical radioisotope for diagnostic in imaging studies by positron emission tomography (PET). A good agreement was see between the theoretical calculated results using TALYS 1.6 code and the experimental data from EXFOR library. When Comparing the our theoretical calculations and the

experimental data, the  $^{66}\text{Ga}$  radioisotopes it can be produced by small sized cyclotrons since the optimum energy ranges are smaller than 38 MeV.

## REFERENCES

- [1] Wong, S. S. M., 1998. Introductory nuclear physics, John Wiley & Sons, Inc., 2nd edition, Weinheim, Germany
- [2] Chitambar, C. R., 2010. Medical applications and toxicities of gallium compounds, International Journal of Environmental Research and Public Health, 7, 2337-2361, DOI:10.3390/ijerph7052337
- [3] EXFOR/CSISRS, Experimental Nuclear Reaction Data File, 2017. Brookhaven National Laboratory, National Nuclear Data Center
- [4] Noori, S. S., Akkurt, İ., Karpuz Demir, N., 2018. Excitation functions of proton induced reactions of some radioisotopes used in medicine, Open Chemistry, 16(1), 810–816 <https://doi.org/10.1515/chem-2018-0085>
- [5] Azizakram, H., Sadeghi, M., Ashtari, P., Zolfagharpour, F., 2018. A Monte Carlo approach to calculate the production prerequisites of  $^{124}\text{I}$  radioisotope towards the activity estimation, Nuclear Technology and Radiation Protection, 33(1), 68-74 <http://doi.org/10.2298/NTRP1801068A>
- [6] Noori, S. S., Akkurt, İ., Karpuz Demir, N., 2017. comparison of excitation functions of longer and shorter lived radionuclides, Acta Physica Polonica A, 132(3-II), 1186-1188 <https://doi.org/10.12693/APhysPolA.132.1186>
- [7] Karpuz Demir, N., Çetin, B., Akkurt, İ., Noori, S.S. 2017. Calculations of double differential cross sections on  $^{56}\text{Fe}$ ,  $^{63}\text{Cu}$  and  $^{90}\text{Zr}$  neutron emission in proton induced reactions, Acta Physica Polonica A, 132(3-II), 1181-1185 <https://doi.org/10.12693/APhysPolA.132.1181>
- [8] Kiliç, F., Karpuz, N., Çetin, B., 2016. Calculation of the (p,n) reaction cross section of radionuclides used for pet applications, Acta physica polonica A, 130(1), 318-319 <https://doi.org/10.12693/APhysPolA.130.318>
- [9] Noori, S. S., Karpuz, N. Akkurt, İ., 2016. Excitation functions of (d,n) reactions on some light nuclei, Acta physica polonica A, 129(1), 484-486 <https://doi.org/10.12693/APhysPolA.129.484>
- [10] Tel E., Sahan, M., Aydin, A., Sahan, H., Ugur E.A. and Kaplan, A., 2011. The newly calculations of production cross sections for some positron emitting and single photon emitting radioisotopes in proton cyclotrons, Radioisotopes - Applications in Physical Sciences, ISBN: 978-953-307-510-5
- [11] Szelecsenyi, F., Steyn, G. F., Kovacs, Z., van der Walt, T. N., Suzuki, K., Okada, K., Mukai, K., 2005. New cross-section data for the  $^{66}\text{Zn}(p,n)^{66}\text{Ga}$ ,  $^{68}\text{Zn}(p,3n)^{66}\text{Ga}$ ,  $^{nat}\text{Zn}(p,x)^{66}\text{Ga}$ ,  $^{68}\text{Zn}(p,2n)^{67}\text{Ga}$  and  $^{nat}\text{Zn}(p,x)^{67}\text{Ga}$  nuclear reactions up to 100 MeV, Nuclear Instruments and Methods in Physics Research Section B: Beam Interactions with Materials and Atoms, 234(4), 375-386 <http://dx.doi.org/10.1016/j.nimb.2005.02.011>
- [12] Levkovski, V. N., 1991. Cross sections of medium mass nuclide activation ( $A=40-100$ ) by medium energy protons and alpha-particles ( $E=10-50$  MeV), (Experiment and Systematics), Inter-Vesti, Moscow.
- [13] Hille, M., Hille, P., Uhl, M., Weisz, W., 1972. Excitation functions of (p,n) and ( $\alpha$ ,n) reactions on Ni, Cu and Zn, Nuclear Physics Section A, 198(2), 625-640 [http://dx.doi.org/10.1016/0375-9474\(72\)90713-0](http://dx.doi.org/10.1016/0375-9474(72)90713-0)
- [14] Hermanne, A., Walravens, N., Cicchelli, O., 1991. Optimization of isotope production by cross section determination, Nuclear Data for Science and Technology, Juelich, 616-618, Germany

- 
- [15] Szelecsenyi, F., Boothe, T. E., Takacs, S., Tarkanyi, F., Tavano, E., 1998. Evaluated cross section and thick target yield data bases of Zn + p processes for practical applications, *Applied Radiation and Isotopes*, 49(8), 1005-1032 [http://dx.doi.org/10.1016/S0969-8043\(97\)10103-8](http://dx.doi.org/10.1016/S0969-8043(97)10103-8)
- [16] Tarkanyi, F., Szelecsenyi, F., Kovacs, Z., Sudar, S., 1990. Excitation functions of proton induced nuclear reactions on enriched  $^{66}\text{Zn}$ ,  $^{67}\text{Zn}$  and  $^{68}\text{Zn}$  production of  $^{67}\text{Ga}$  and  $^{66}\text{Ga}$ , *Radiochimica Acta*, 50(1-2), 19-26 <https://doi.org/10.1524/ract.1990.50.12.19>
- [17] Little, F. E., Lagunas-Solar, M. C., 1983. Cyclotron production of  $^{67}\text{Ga}$  cross sections and thick-target yields for the  $^{67}\text{Zn}(p,n)$  and  $^{68}\text{Zn}(p,2n)$  reactions, *The International Journal of Applied Radiation and Isotopes*, 34(3), 631-637 [https://doi.org/10.1016/0020-708X\(83\)90067-4](https://doi.org/10.1016/0020-708X(83)90067-4)
- [18] Howe, H. A., 1958. (p,n) Cross sections of Copper and Zinc, *Physical Review*, 109(6), 2083 <http://dx.doi.org/10.1103/PhysRev.109.2083>
- [19] Szelecsenyi, F., Kovacs, Z., van der Walt, T. N., Steyn, G. F., Suzuki, K., Okada, K., 2003. Investigation of the  $^{\text{nat}}\text{Zn}(p,x)^{62}\text{Zn}$  nuclear process up to 70MeV: a new  $^{62}\text{Zn}/^{62}\text{Cu}$  generator, *Applied Radiation and Isotopes*, 58(3), 377-384 [http://dx.doi.org/10.1016/S0969-8043\(02\)00345-7](http://dx.doi.org/10.1016/S0969-8043(02)00345-7)

---

## FLUKA calculation of neutron shielding for $^{252}\text{Cf}$ source

Sameer Al-Obaidi<sup>\*</sup>, Hakan AKyıldırım<sup>1</sup>, Kadir Günoğlu<sup>2</sup>, Iskender Akkurt<sup>1</sup>

<sup>1</sup>Süleyman Demirel University/Department of physics, Isparta, TURKEY

<sup>2</sup>Isparta Uygulamalı Bilimler Üniversitesi Isparta, TURKEY

\*Sameer\_alobaidi@yahoo.com

### ABSTRACT

The neutrons are uncharged particles emitted by unstable nuclei, and can also be created through nuclear reactions. They are powerful in terms of penetration into the materials. Neutron is much more dangerous than other types of radiations because it's difficult to detect and control. Thus its shielding property is important and measurements make it difficult to obtain. Different compounds, alloys and composites are usually preferred against neutrons as shielding material.

**KEYWORDS** – FLUKA, Calculation, Neutron Shielding.

### 1. INTRODUCTION

FLUKA is a Monte Carlo simulation package for a variety of models of particle transport and interaction with matter. FLUKA is a general purpose tool for calculations of particle transport and interactions with matter, covering an extended range of applications: from proton and electron accelerator shielding to target design, calorimetry, activation, dosimetry, detector design, Accelerator Driven Systems, cosmic rays, neutrino physics, radiotherapy, etc.[1]. The FLUKA code is one of the most practical simulation tools for many applications in high-energy physics and engineering aspects. FLUKA can simulate the interaction and propagation in matter of more than 60 different particles, such as heavy-ions, electrons, neutrons, photons, neutrinos and muons, in many types of research fields: shielding design, detector response studies, cosmic ray studies, medical physics and dosimetry calculations. In recent years FLUKA has been extensively developed and improved; the newest version introduces many fundamental changes to the implementation of modern physics algorithms, as well as programming upgrades [2].

Neutrons have no electrical charge and are not easily stopped by matter because they interact with atoms of matter only via the nuclei. Energetic neutrons are more difficult to shield because absorption cross-section is much lower. Firstly, it is necessary to moderate these neutrons through elastic or inelastic scattering interactions and then slowed neutrons are absorbed with the shielding material. Shielding must be made with appropriate thickness and types of shield materials such as concrete, heavy concrete, and iron [3,4,5].

### 2. MATERIAL AND METHOD

The simulations were performed with the version 2011.2c of the FLUKA Monte Carlo code. Input files have been prepared to run simulations. There are many options in input files as beam properties, irradiation geometry, material definition, physical settings, score options and primary radiation weight. Each option is represented by an input card and the sequential order of these cards is important. This sequence should be in form beam properties, irradiation geometry, material definition, physical settings, and score options. Simulations have been started for  $10^6$  primary particles and the code was run for 5 cycles. Simulation results have been read from FLUKA output files. USRBIN and USRBDX detectors have been used to obtain the results.

$^{252}\text{Cf}$  as neutron source was used with energy of (2.14 MeV) in this calculation. Detector area and volume values were taken as defaults of the code. Geometry for source shielding is shown in Figure 1. It can be seen that 5 different variation (shielding materials) have been tested as listed below.

- No shielding,
- Polyethylene
- Polyethylene + Lead
- Polyethylene + Lead + Barite
- Polyethylene + Lead + Barite + Iron

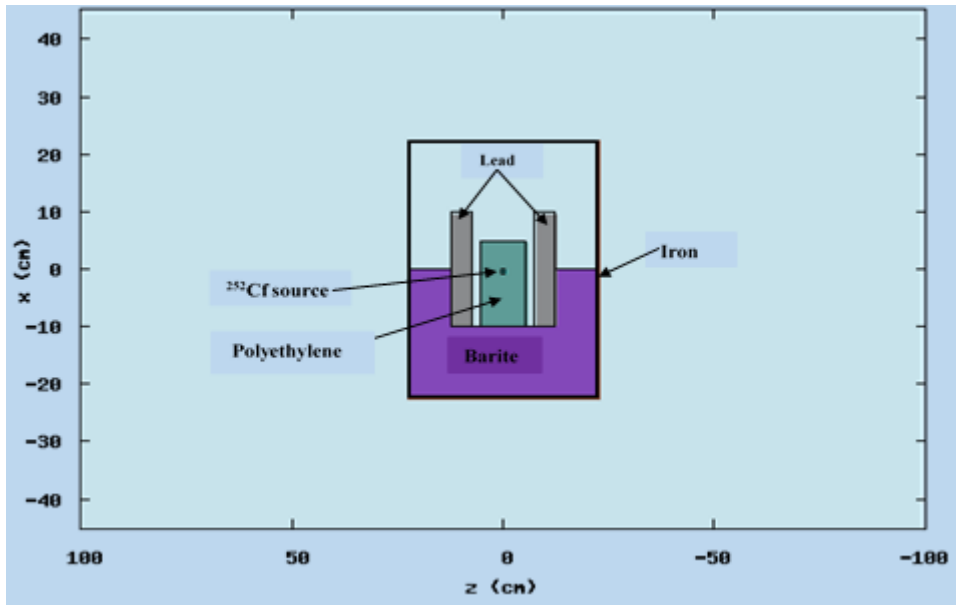


*Figure.1: The geometry of neutron  $^{252}\text{Cf}$  source shielding*

### 3. RESULTS AND DISCUSSION

Shielding properties of  $^{252}\text{Cf}$  source have been investigated and FLUKA calculation done for 5 different material combination. The obtained results have been displayed in Figure 2. It can be seen from this figure that the dose rate in ( $\mu\text{Sv/s}$ ) from  $^{252}\text{Cf}$  source decreased with increasing the shielding material layers.

### 4. REFERENCES

- [1] FERRARI A., SALA P.R., FASSO` A., RANFT J., (2005). FLUKA: a multi-particle transport code.CERN-2005-010, INFN/TC\_05/11, SLAC-R-773

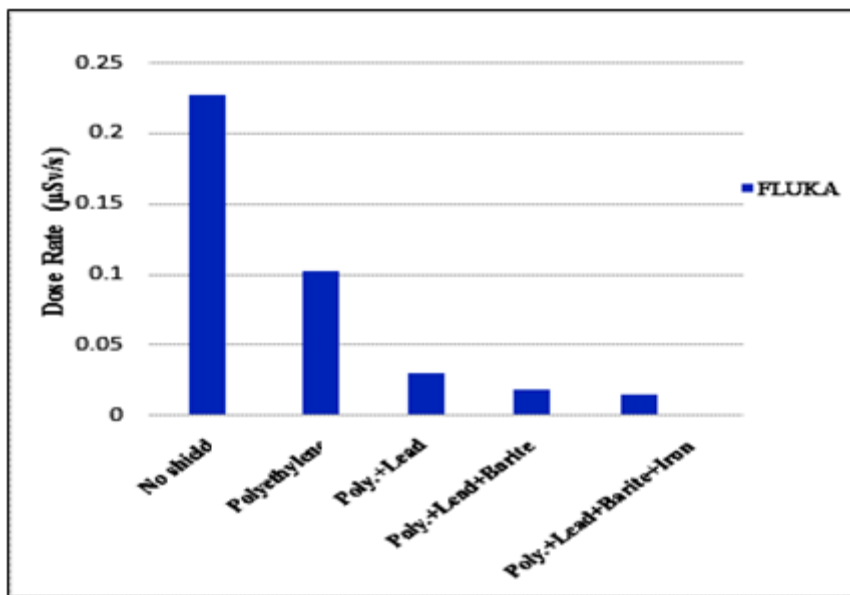


**Figure.2:** Column chart represents dose rate in ( $\mu\text{Sv/s}$ ) as a function of different shielding material layers by FLUKA simulation code.

- [2] Turgay Korkut, Abdulhalik Karabulut, Gokhan Budak, Bunyamin Aygun, Osman Gencel, Aybaba Hancerliogullari,. Investigation of neutron shielding properties depending on number of boron atoms for colemanite, ulexite and tincal ores by experiments and FLUKA Monte Carlo simulations, Applied Radiation and Isotopes 70, (2012), 341–345.
- [3] D. Sariyer, R. Küçer, N. Küçer, , Neutron Shielding Properties of Concretes Containing Boron Carbide and Ferro – Boron, Procedia - Social and Behavioral Sciences 195, (2015), 1752 – 1756.
- [4] Yousra Mohamed Braima Mohamed, Dr. Nassreldeen Abdelrazig Abdelbari Elsheikh, Monte Carlo Modeling of Effective Shielding Systems for Fast Neutrons, M.Sc. Thesis in Physics, (2014).
- [5] IAEA, (2004). RADIATION, PEOPLE AND THE ENVIRONMENT.

## Investigation of Shielding Properties of Recycled Rubber Composite for Gamma Radiation

Abdlhamed Abdlhamed<sup>1\*</sup>, Zeynep Parlar<sup>2</sup>, Iskender Akkurt<sup>3</sup>

<sup>1</sup>Education Ministry, Anbar, IRAQ

<sup>2</sup>Istanbul Technical University, Istanbul, TURKEY

<sup>3</sup>Suleyman Demirel University, Isparta, TURKEY

[ab200515@gmail.com](mailto:ab200515@gmail.com)

### ABSTRACT

Radiation is one of the hazardous factors for human health that found in the environment. Because of the soil, rocks and building materials contain some uranium and its radioactive progenies, radiation exposure inevitable in daily life. Besides that, the artificial radiation sources are involved in with industrial developments and nuclear medicine to human life. Therefore radiation protection technologies are developing rapidly. Researchers are working on producing shielding materials and increasing their attenuation coefficients by using various components. The purpose of this study to produce composites which include one or more ingredient. Fiberglass was used to obtain composites in different combination rates. The prepared composites are exposed by gamma-ray sources <sup>60</sup>Co and <sup>137</sup>Cs in order to investigate their shielding capabilities. It can be concluded that the recycled rubber which used as the main material in the components is suitable to use for radiation protection with appropriate additives.

**KEYWORDS** – Radiation shielding, Composite materials, Recycled Rubber

### 1. INTRODUCTION

The radiation is one of the facts in our life due to the existence since creation of universe. After invention of radiation it started to be used in a variety of different fields and thus its hazardous effect becomes one of the main subject for researcher [1-5]. In environment the occurrence of radioactive materials is natural, carbon-14, potassium-40 and polonium-210 are natural radioactive materials found in our bodies. Interaction of radiation with a matter depends on its energy and each radiation type has different properties. Non-ionizing radiation may shake or move the molecules. Ionizing radiation could break molecular bonds, causing unpredictable chemical reactions. Ionizing radiation has not only energy waves but particles. The exposure to ionizing radiation comes from cosmic rays and some materials are natural. Human exposure to natural radiation is in question for certain numbers of mutations and maybe cancers.

### 2. MATERIAL AND METHOD

In order to shield gamma rays a composite material has been produced. Rubber composite has been produced in adding on it glass and fiber. In the study of linear attenuation coefficient  $\mu$  ( $\text{cm}^{-1}$ ), Rubber as a main material, Glass-Fibre (R-G/F) as additions to composite in (Figure 1). The composite materials were manufactured in Istanbul Technique University's laboratory [6]. The measurements have been done using gamma spectrometer system in Suleyman Demirel University [7].



Figure 1. Rubber used in the composite

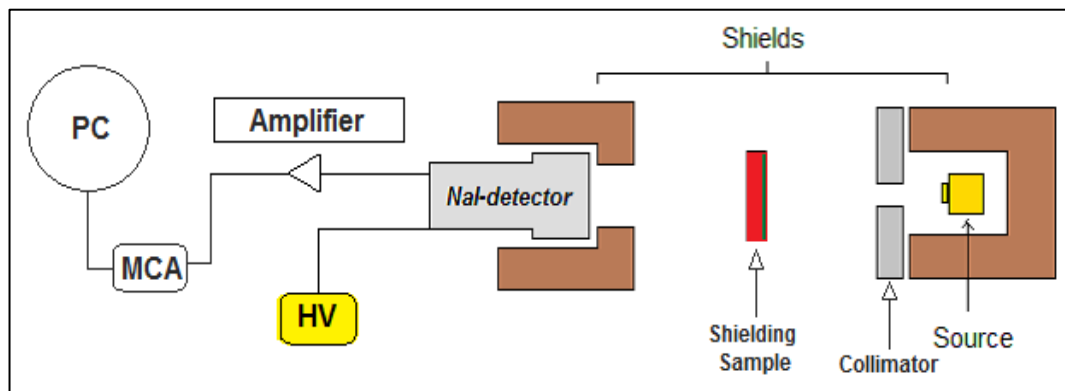


Figure 2. Schematic view of gamma Spectrometer and electronic units

The system consists of a detector which is NaI(Tl), counting electronic system (spectroscopy amplifier, high voltage, Multichannel Analyses MCA) and a personal computer PC (where software was installed is MAESTRO 32) for recording data. In order to reduce the background level of the system, the detector is covered by shield prepared from lead about 6 cm on all side (Figure 2).

### 3. RESULTS AND DISCUSSION

The linear attenuation coefficients of composite material have been measured at the Suleyman Demirel University. The measurement has been performed using  $^{137}\text{Cs}$  and  $^{60}\text{Co}$  gamma sources. Those sources provide 662-1773-1332 keV gamma ray energies. The obtained result has been displayed in Figure 3. It can be seen from this figure that the linear attenuation coefficients decreased with the increasing gamma ray energies.



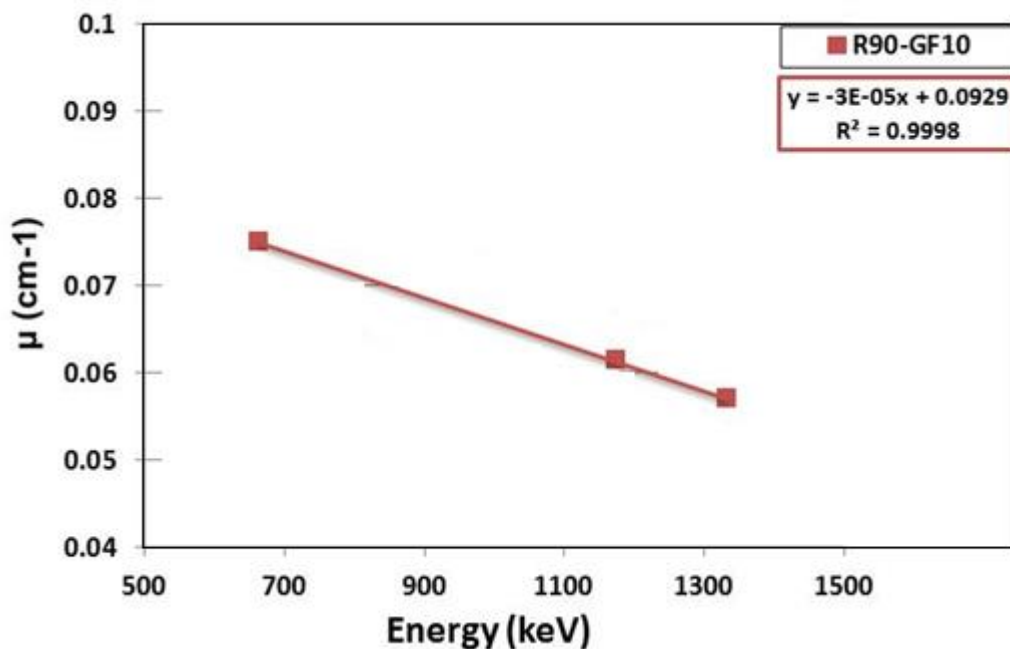


**Figure.3:** The relationship between  $\mu$  (cm<sup>-1</sup>) and energy (keV) for R90-GF10

#### 4. REFERENCES

- [1] Basyigit, C., Akkurt, I., Kilincarslan, S., & Akkurt, A. (2005). Investigation of photon attenuation coefficients for marble. *Journal of Radiological Protection*, 25(2), 189. ISO 690.
- [2] Alsarray, E., (2016). Investigation of radiation shielding properties of some composite material. MSc thesis Fen Bilimleri Enstitüsü- SDU.
- [3] Akkurt, I., Akyıldırım, H., Mavi, B., Kilincarslan, S., & Basyigit, C. (2010). Radiation shielding of concrete containing zeolite. *Radiation Measurements*, 45(7), 827-830.
- [4] Akkurt, I., Altindag, R., Gunoglu, K., & Sarıkaya, H. (2012). Photon attenuation coefficients of concrete including marble aggregates. *Annals of Nuclear Energy*, 43, 56-60.
- [5] Akkurt, I., Kılınçarslan Ş, Basyigit, C. (2004). The Photon Attenuation Coefficients of Barite, Marble And limra, *Annals of Nuclear Energy*. 03/2004; 31 (5): 577-582. DOI: 10.1016 / j.anucene.2003.07.002.
- [6] Parlar, Z., Samankan, S., & Temiz, V. (2015). The Effect of Counter-face Roughness on the Tribological Behavior of Filled and Unfilled PTFE. *Automation*, 609.
- [7] Akkurt, I., Gunoglu, K., & Arda, S. S. (2014). Detection efficiency of NaI (Tl) detector in 511–1332 keV energy range. *Science and Technology of Nuclear Installations*, 2014.

# Application of Analytic Hierarchy Method for Solar Artificial Intelligence Systems

**Zuhal ER**

*<sup>a</sup>Department of Physics Engineering (13b), Faculty of Science and Arts, Istanbul Technical University, Istanbul, Turkey*

*\* [erzuh@itu.edu.tr](mailto:erzuh@itu.edu.tr)*

## ABSTRACT

In recent years, Internet of things (IoT) has become widespread to reach data with technology 4.0 for intelligent facilities. Along with these technological developments, the use of Artificial Intelligence (AI) brings and exhibits new discussions / expertise in the field of solar energy. On the other hand, a large number of maker seeking to acquire technological returns and data may not having the methodological knowledge of which data may be available, which systems have the right criteria, and which mechanisms are available to obtain important data. Hence, to contribute to the issues in the decision criteria of AI systems is the primary motivation of this study, with the novelty. An application of Analytical Hierarchy Method (AHP) that is finding the answer to the choice of the best alternative that fits all the criteria of the decision maker is novelty of the study. This paper targets using AHP in determining the importance of the criteria. Then three categories of information related to managerial levels and the decision managers are investigated in the study. These are named Decision Support System (DSS), Management Information Systems (MIS), Data Processing Systems (DPS). With analysis of the calculated results requiring the use of AHP the objectives, the criteria affecting prioritization, and the alternatives to be prioritized are determined as weights of the positive (p) features, negative (n) features, requirements(r) for efficient solar system. Therefore, the p factor is more important than n with calculated importance of criteria as 0.320, 0.386, 0.294 for weight of 0.047, 0.280, 0.311 respectively.

**KEYWORDS:** Solar energy system, Solar panels, Solar cell efficiency, Solar cell performance, Artificial Intelligence, Internet of Things.

## 1. INTRODUCTION

In the near future, you can expect AI to not only change your rates and the types of tools available to you, but also the types of interactions you have with your smart system and whether you need the best one at all. In the last five years, robots have more managed to produce 10 percent of global GDP (gross domestic product) [1]. In the other words, with the advancement in electronic technology and computer networks, it is possible to access this data quickly. In this context, the innovations via exponential increase in technology and popularity of IoT applications is more widely used with the cheaper products [2].

On the other hand, competitive pressure is apparent in reflecting these technological developments to the systems [3]. The consequences of this pressure: from the commercial point of view, it will be able to provide better results and customized services; according to scientific view, it will also be able to collect fast data, classify and segment data, and help create hypotheses. So, the data itself is worthless. It is knowledge in the direction of our desired aim. The knowledge can also be defined as what is derived from an answer to a question. The knowledge is the scope of information, while information is the act of communicating knowledge. The information is processed for a purpose and it's raw data. Data is not just numbers or letters; data is numbers and letters, and also their meanings. Data is the lifeblood of AI. In fact, it's quite clear it can be a challenge for companies to aggregate data which is crown jewel [4]. Data conversion is called data analysis which allows the systems to look at patterns of the raw data and their relationship to everyday performances and operations. The producing and receiving data are now done with

intelligent objects and machines. Today planet becomes to be "smart planet" with the scientific improvement and technological development under multi-disciplined studies such as applications of artificial intelligence (AI). The data were examined by various methods and are still being examined. On the other hand, data mining includes machine learning, pattern recognition, statistics, and database systems. Meanwhile, it exhibits that scientific accumulations interdisciplinary integrated studies that direct the industrial robot technologies whose role in industry 4.0 / 5.0 is rapidly increasing [5]. These developments include the use of the internet of things (IoT) applications in the solar industry. Objects with all types of monitoring devices, sensors, biochips, or access devices, such as Radio Frequency Identification (RFID)-like sensors and identifiers, produce information on solar energy systems.

A solar energy system has heart equipment that is named PV panel which is used to gain energy from the Sun light with the photovoltaic effect [6]. Furthermore, the core technology in IoT could break down to 3 different areas: connectivity, control and sensor. Additionally, an electrical operator must ensure a precise balance between electricity generation and consumption at any time.

In this point, it is clearly see that the work on the smart technology of PV phenomena has expanded. It is clear that without any deceasing making control, in the environment of large number of choices and criteria, the manufacturer (and or operator) are being forced to production PV panel. Despite of fact that, Analytic Hierarchy Process (AHP) is used to make a proposal for production (and or operation, managing) the PV panel problem. This study is focused on AHP and applications of artificial intelligence (AI) in the solar photovoltaic technology. Therefore, this study emphasizes the importance of decision strategies with analytical hierarchy method for producers who want to make faster business decisions in smart solar production operations and want to manage data abundance efficiently.

## 2. EXPERIMENTAL DETAILS

There are some parameters to be taken into consideration by the ones who want to manufacture a PV panel by using intelligent technologies in their operation and production and also management. Firstly, a strategy is needed to use integrated architecture and intelligent technologies to achieve performance goals. It is particularly important that the panels define the opportunities to use Information Technology (IT) and Operations Technology (OT) to consolidate on a single system using a unified network infrastructure and to use IoT technologies that provide seamless connectivity and information sharing between the others, processes, and objects. The classification of sensors are illustrated in the Table 1. A sensor is a device for sensing, the receiving pulses in the system is converted to signals and generating data by the sensor as given by the Figure1. Data warehouses, nowadays widely used, are intended to store a database of daily used databases that are combined and more suitable for processing as shown in the Figure 2.

## 3. RESULTS AND DISCUSSION

Desired information from the daily databases is selected and stored in the data warehouse after necessary pre-processing. Then, the data is retrieved from the warehouse and converted into a standard form for data mining.

*Table 1. Defined IoT devices in the common usages for a Panel*

<b>Abrivations</b>	<b>IoT sensors</b>
Th	Thermal sensor
Opt	Optic sensor
Mch	Mechanic sensor
Mag	Magnetic sensor

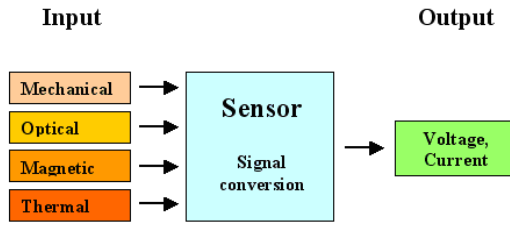


**Figure 1.** Working principle of the sensors

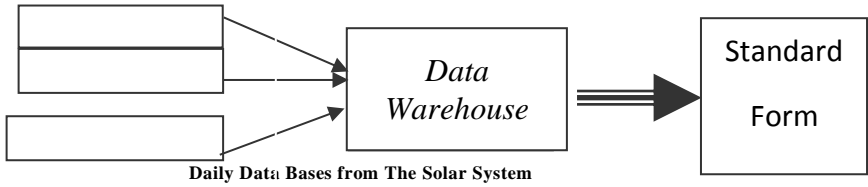


**Figure 2.** Flow diagram of the data mining for the solar system.

After the data is created in the data warehouse, this data can be analyzed by manually or by eye. IoT devices and various programs are used for this purposes. Thus, data mining supported by AI provides the possibility to examine the correlations between data and present the results as graphs or reports. These reports can be classified with respect to four categories as given below:

- Determination of operational strengths and weaknesses
- Analyzing the processes, planning development initiatives
- Design and implement better production systems
- Using performance management systems

The choosing/defining of the IoT for the system control is usually constructed due to several parameters of the system output criteria such as price, weight, size, etc. which are illustrated in the Figure 3. In this point, to achieve these requirements, the analytical hierarchy method (AHP) will be applied for the analysis of relationships and define rules using meaningful and useful data from large quantities of intelligent technologies in the solar energy systems. The data obtained from the intelligent solar systems is a rather complex decision making problem because the evaluation process involves a large number of criteria and requires a compromise between these interrelated criteria. Qualitative factors are of primary importance in AHP, which is one of the multi-criteria decision-making approaches. It is a technique that can combine qualitative and quantitative factors in the detailed evaluation of alternatives. The parameter subject to the decision making problem with the AHP method is divided into its components and examined in a hierarchical structure which is illustrated for a solar system in the Table 2. Bilateral comparisons are the basic building blocks in the AHP method. In making binary comparisons between criteria, the basic comparison chart shown in Table 3 is used. In this context, for the panel prototype which is produced with 2 different technologies equipped with intelligent system, the optimum management of the system has been tried to be examined by comparing it against 3 different criterions. According to expert opinion and classification in the literature, important criteria in parameter selection; temperature, environmental pollution factors, radiation power.

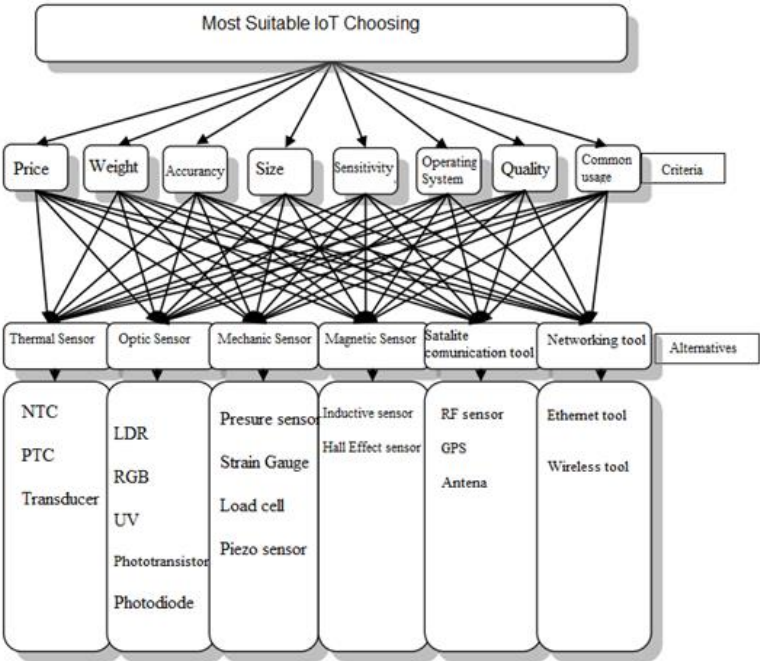


Figure 3. Decision and relationship for the choosing parameter of the IoT in a solar System.

Table 2. The parameters of data due to hierarchical structure

IMPORTANCE LEVEL	DESCRIPTIONS
1	Two Criteria Contribute to Equality
3	A Criterion Contributes Some More to Purpose According to Other
5	A criterion is considerably overpriced due to the other
7	A Criteria Has Too Much Contribution To The Objective By The Other
9	One Criterion is Extremely Important for Others
2,4,6,8	Intermediate values (values between two consecutive judgments to be used when reconciliation is required)

Table 3. Evaluation of Criteria for the Price

Sensors / Tools	Price	Inverse of the price	P
Mechanic sensor	0.5	2	0.047
Thermal sensor	1	1	0.280
Optic sensor	1.5	0.6	0.294
Magnetic sensor	2	0.5	0.311
Satellite tool	2.5	0.4	0.320
Networking tool	3	0.3	0.386
Total	10.5	4.8	1,344

#### 4. CONCLUSION

The results obtained gives a clear idea about the usage of AHP method to choosing criteria for behavior of the smart PV panel system under variation of main parameters like mechanical effects, solar radiation, temperature etc. This study demonstrates the following: It provides a useful contribution in the context of data analysis of decision making by the AH method. Because the sensors for the direct need of the system and the system will know what the operation, with analytical evaluation will provide. The analyst will present the data on the understanding of how the system works better due to the systematic approach with more statistical analysis.

#### 5. REFERENCES

- [1] Z. Er, A Study of Evaluation of Solar Energy Simulation and Modeling Systems, *Acta Physica Polonica A*. Vol. 130, No. 1, 72-77 (2016).
- [2] C. Philibert(Ed.); Solar Energy Perspectives; OECD/IEA; International Energy Agency, France (2011).
- [3] S.B. Kennedy(Ed.); Sustainable Energy for All, Global Tracking Framework; 77889 v.3, ESMAP and the International Energy Agency, World Bank (2013).
- [4] P. Hersch, K. Zweibel(Eds); Basic Photovoltaic Principles and Methods; Solar Energy Research Inst., United States (1982).
- [5] G. Knier; How do Photovoltaics Work?, *National Aeronautics and Space Administration* (NASA), (2002), at solar cell. 1-3.
- [6] Nalan Cicek Bezir, I. A. (2010, October 20). Estimation of Horizontal Solar Radiation in Isparta (Turkey). *Energy Sources Part A Recovery Utilization and Environmental Effects*, 32(6):512-517. Retrieved May 13, 2018, from <https://www.britannica.com/technology/solar-cell>

## The Effect of Interference Force on the Lifecycle of Lip Seals

Vildan Giriřta, İsmail Kaya and Zeynep Parlar

*İstanbul Technical University/Mechanical Engineering İstanbul, Turkey*

*\* parlarze@itu.edu.tr*

### ABSTRACT

Sealing elements play an important role in mechanical design, where breakdown of the sealing elements can lead to crucial operational problems in mechanical systems. Surface roughness, interference, surface machining quality of the shaft and seal affect the sealing behavior of the seals. In this study, a test system is developed in order to determine the influence of the interference force on the lifetime of the sealing element. A series of experiments is performed with radial lip seals with three different diameters varied by the lip tolerance (40, 39.80 and 39.60 mm). EP gear oil is used as the lubricant. In order to determine the lifecycle of the sealing element, the leaking oil is weighed.

**KEYWORDS** - Lip seal, interference, sealing performance, leakage.

### 1. INTRODUCTION

In many mechanical systems, lubricants are used to prevent heating between relative moving surfaces. It is the duty of the sealing elements to ensure that lubricants remain in the system. Failure of the sealing element to perform its function may lead to oil leaks in the mechanical system, which causes high friction, wear and premature life completion of system components. The cost of such a situation is much higher than the cost of the sealing elements. Therefore, determining the lifetime of the sealing element is important to avoid such unexpected damages. The sealing capability and lifetime of the lip seals are affected by contact pressure, lip geometry, material properties, temperature, circumferential speed, lubricant type and interference. By this mean, various studies are present. Tasora investigated the effect of temperature on the contact force. Kerküklü investigated the effect of surface roughness on the sealing characteristics of the rotary lip seals. Lee studied the geometric design parameters of the lip seals and proved that interference has a major effect on wear behaviour and sealing performance. Bulut investigated the effect of interference force on the frictional behaviour of rotary lip seals. By this mean, a similar test procedure is employed. The main purpose of this study is to investigate the effects of the interference on the lifetime and frictional behaviour of lip seals, experimentally.

### 2. EXPERIMENTAL SET-UP AND PROCEDURE

A test system is built to investigate the effects of interference on the life cycle of the lip seals. The shaft is driven by a DC motor. The DC motor is operated at 2400 rpm and linear velocity between the shaft and lip surface of the seal is 5 m/s. The diameter of the shaft is 40mm's. The shaft is machined of stainless steel with HRC30 and  $R_a = 0.5\mu m$ . A series of experiments are performed with radial lip seals with three different inner diameters vary by 0,20 mm lip surface tolerances. Opet Orsa EP gearbox lubricant is used as system lubricant and no pressure is applied during experiments. In order to determine the lifetime of the sealing components, leaking lubricant mass is measured. Before each experiment, a piece of superabsorbent paper is weighed. After 8 hours of operation system is shut down and outer side cheek of the seal is wiped with the superabsorbent paper. The paper is weighed again. The difference is the leaked oil mass. In this study, leakage-exceeding limit is determined as 0.002 g/h where permissible leakage varies according to the application area.

### 3. RESULTS AND DISCUSSION

In Figure, leaking fluid mass versus sliding distance is given. During the initial 200 km sliding distance, 40 mm diameter sealing element had the lowest leaking fluid mass. However, this seal in total had the shortest lifecycle. 39.60 mm diameter seal had the most leaking fluid during its lifetime. Despite this fact, 39.60 mm sample had the longest service life. It is seen that the total amount of leaking fluid mass during the lifecycle is not related to the lifetime of the sealing element.

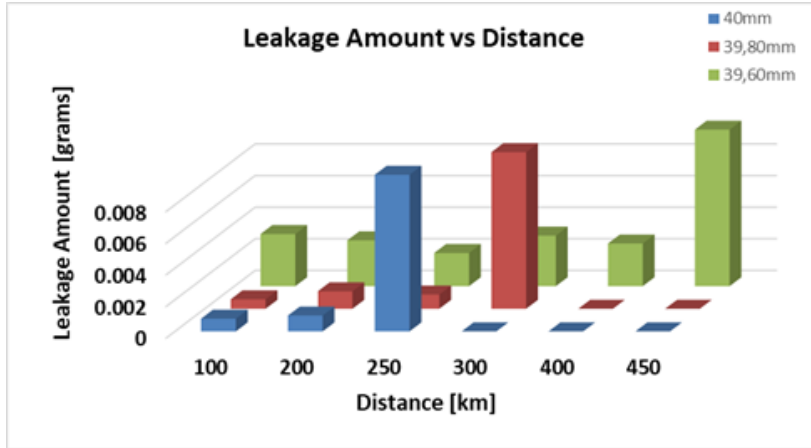


*Fig.1 Leakage amount versus sliding distance.*

As Flitney stated that pumping mechanism is highly dependent on the interference. The lip must touch the shaft but the interference of the flute should not disturb the lip contact. Thus in our study, it can be assumed that radial forces generated by radial interference effected the surface texture and higher leakage is observed during the tests of 39.60 mm sample.

### 4. CONCLUSION

In this study, the effect of interference on the life cycle of the radial lip seals were investigated. Three lip seals with inner diameters of 39.60 mm, 39.80 mm and 40 mm were employed as test specimens. Although 39.60 mm sealing element has leaked more amount of lubricant during experiments, it has longer service life. It was determined that the amount of leaking fluid during operation is not directly related to lifetime of the seal. As a future content, contact surfaces of the sealing elements will be examined and mathematical model will be studied.

### 4. REFERENCES

- [1] A. Tasora, E. Prati, T. Marin, A method for the characterization of static elastomeric lip seal deformation, *Tribology International*, 60, 2013, pp. 119-126.
- [2] D. Bulut, V. Temiz and Z. Parlar, The Effect of Interference on the Friction Torque Characteristics of TPU Based Rotary Lip Seals, *Tribology in Industry* 37, 2015, pp. 346-353.
- [3] K.O. Lee, Y.M. Hur, J.H. Kang, S.S. Kang, Performance estimation of dust wipers for hydraulic cylinders and optimization of geometric design variables, *Journal of Materials Processing Technology*, 2007, pp. 215-219
- [4] R. K. Flitney, *Seals and Sealing Handbook*, 5th ed. Elsevier Science, 2007.
- [5] Y. Kerküklü, *Dönel sızdırmazlık elemanlarının performansına yüzey pürüzlülüğünün etkileri*, Istanbul Technical University, 2008.



---

## Locomotion Control of Soft Robot with Surface Texture

Umut Serdar Çivici, Zeynep Parlar\*

*Istanbul Technical University/Mechanical Engineering İstanbul, Turkey*

*\* parlarze@itu.edu.tr*

### ABSTRACT

Soft robotic actuators, which have ability to perform motions of elongation, crawling, rotation, grasp and manhandling, are created via soft robots produced nowadays. The main aim of the study was to examine the motion mechanism within air propulsion system on three different surface textures and to understand that which surface texture provide the most elongation and crawling movement. Three surface texture types used in this study: half spherical as first surface texture, trapezoidal as second texture were used to differentiate, and pointed texture end towards the direction of motion. It was seen that pointed texture end towards the direction of motion provided more elongation motion, and other surface textures followed these phenomena in an order.

**KEYWORDS** - Soft Robot, Surface Texture, Elongation Performance.

### 1. INTRODUCTION

Soft robotics focus on the application of soft materials to improve human-robot interaction. Soft robots made of flexible materials and biologically natural, are becoming increasingly widespread today, but more pneumatic actuators are needed in the design of movement mechanisms. In this study, a pneumatically driven soft robot with a triangular cross-sectional area was investigated for tribological reasons affecting creep and extension in three surface models with different textures. The surface texturing effect on elongation was investigated by Carmel Majidi [1]. The main purpose of this study is to examine the motion mechanism of the soft robot in three different surface textures and to find out which surface texture the soft robot is performing more elongation and creep. In a study on soft robots at the University of MIT [2], single-actuated soft robots were coated on the surfaces of soft robots with kirigami art to enhance their crawling and creeping abilities. In this study, the soft robot with a triangular cross-sectional area will be pneumatically driven in three different surface textures, and the surface texturing with the greatest extension will be examined by experimentally.

### 2. EXPERIMENTAL SET-UP AND PROCEDURE

#### 2.1 Surface texturing

Plastic plates with PLA material (150 \* 50 mm) with three different surface textures are used in the experiment. Surface textures that soft robot will go on, have been chosen by bio inspired. In Figure 1a, this surface texture has been inspired from pangolin's skin. Second surface texture (Figure 1b) was chosen because of its similarity to cockroach crust. Third one the trapezoidal texture is taken from snake skin (Figure 1c). After designing 3D models of surfaces, they are 3D printed. The soft robot will be placed on each surface separately and moved equally with equal air intake to examine the movement of the surface profiles.

#### 2.2 Soft robot design and fabrication

Casting techniques are commonly used fabrication of soft robots [3-5]. In the design of the soft robot, three different models are primarily considered, the modular PLA material is produced in a three-dimensional printer.

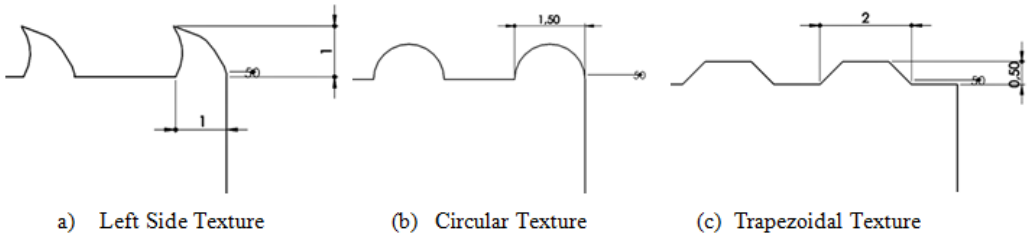


**Figure 1.** View of Surface Textures.

The liquid silicone is manufactured by pouring into a mold cavity using male and female die part. Figure 2 shows that the mold design and production processes of triangular cross-section soft robot. Mold manufacturing is made with a three-dimensional printer and the layer accuracy of the printer is set to 0.2 mm. Eco-flex liquid silicone was used for the soft robot material, the liquid silicone was removed from the mold after four hours from casting.

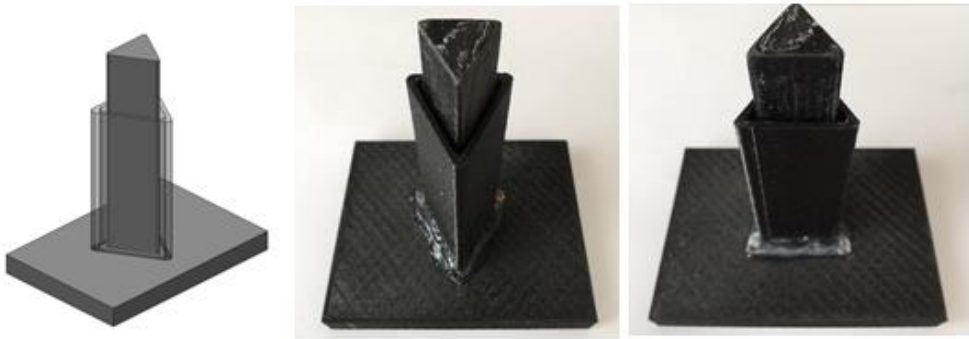


**Figure 2.** Mold Design

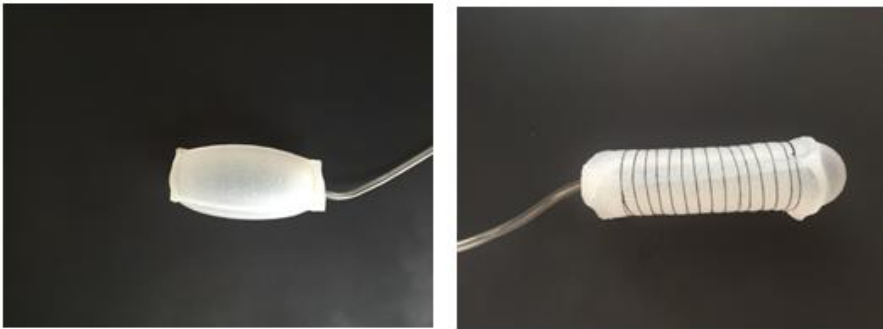


**Figure 3.** Soft Robot: a) radially expanded with air, b) wrapped with a special material

A soft robot is produced and connected to the syringe to provide air flow. In Fig. 3a, the syringe is pneumatically actuated, and the soft robot is radially expanded instead of back-and-forth elongation. To solve this problem, the soft robot is wrapped around a special material to prevent the expansion in the radial direction and to prolong it in the axial direction (Figure 3b). A test system is built to investigate the effects of interference on the life cycle of the lip seals. The shaft is driven by a DC motor. The DC motor is operated at 2400 rpm and linear velocity between the

shaft and lip surface of the seal is 5 m/s. The diameter of the shaft is 40mm's. The shaft is machined of stainless steel with HRC30 and  $Ra=0.5\mu m$ . A series of experiments are performed with radial lip seals with three different inner diameters vary by 0,20 mm lip surface tolerances. Opet Orsa EP gearbox lubricant is used as system lubricant and no pressure is applied during experiments. In order to determine the lifetime of the sealing components, leaking lubricant mass is measured. Before each experiment, a piece of superabsorbent paper is weighed. After 8 hours of operation system is shut down and outer side cheek of the seal is wiped with the superabsorbent paper. The paper is weighed again. The difference is the leaked oil mass. In this study, leakage-exceeding limit is determined as 0.002 g/h where permissible leakage varies according to the application area.

### 3. RESULTS AND DISCUSSION

The soft robot is equal in time to the movement on the textures, and the air stream sent by the robotic robots is kept equal. For three experiments, 20 ml of air flow were sent equally to the soft robot during 40 s with the 1 s time intervals, and the paths taken in the textures at the end of the workout were measured in millimeter. As indicated in Figure 4, texture-1, which is left-side texture (Figure 1a), has better results than other texture types. This is due to the fact that it supports to soft robot through direction of motion and prevents backward movement in accordance with the two-support motion crawling motion. Texture-2, which is circular texture, is not successful enough in backward motion compared to the first texturing, and finally if we look at the performance of third texture, which is called before trapezoidal texture, has the lowest distance value comparing to other textures, reason for that trapezoidal shapes not also blocks soft robot for back movement but also blocks it for further movement.

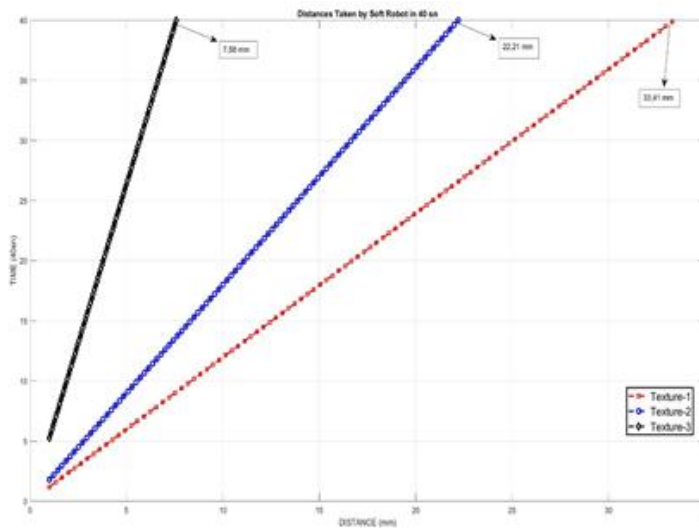


Figure 4. Motion Distances Measured in Textures

### 4. CONCLUSION

In this study, we tried to find out what surface characteristics and tribological factors that have an effect on soft robot motion. It is experimentally observed that these factors together with the robot extension make it difficult to progress in one direction or accelerate the movement. It has been seen that between three surfaces, left side texture has better effect on soft robot locomotion, the reason for this result is; left side texture supports the soft robot for forward direction and helps the robot not to do backward motion when the robot's air is taken away.

## **5. REFERENCES**

- [1] Majidi, C., Shepherd, R.F., Kramer, R.K., Whitesides, G. M., Wood, R. J., Influence of surface traction on soft robot undulation, *The International Journal of Robotics Research*, 32(13), 2013, pp.1577-1584. 2013
- [2] Rafsanjani, A., Bertoldi, K., Rubinstein, S., Locomotion of a kirigami skinned soft crawler, *Science Robotic*, 2018, pp.1-7
- [3] Shepherd, R.F., Ilievski, F., Choi, W., Morin, S. A., Stokes, A. A., Mazzeo, A. D., Chen, X., Wang, M., Whitesides, G.M., Multigait soft robot, *Proceedings of the National Academy of Sciences*, 108, 2011, pp. 20400–20403.
- [4] Cianchetti, M., Arienti, A., Follador, M., Mazzolai, B., Dario, P., Laschi, C., Design concept and validation of a robotic arm inspired by the octopus, *Materials Science and Engineering: C*, 31, 2011, pp. 1230–1239.
- [5] Lin, H.-T., Leisk, G.G., Trimmer, B., GoQBot: a caterpillar-inspired soft-bodied rolling robot, *Bioinspiration & Biomimetics*, 6, 2011, pp. 026007.

## Hastanelerde Algılanan Değer ile Hasta Sadakati Arasındaki İlişki: Bir Üniversite Hastanesi Örneği

Hüseyin ERİŞ<sup>1✉</sup>, Ayça KARAHAN<sup>2</sup>

Harran University Health Services Vocational School erisharran@hotmail.com

Pamukkale University Kale Vocational School akarahan@pau.edu.tr

### ÖZET

Literatür çalışmasında algılanan değeri çok boyutlu ölçekle inceleyen ya da algılanan değer ile hasta sadakati arasındaki ilişkiyi inceleyen sınırlı sayıda araştırmaya rastlanmaktadır. Türkiye’deki tüketicilere yönelik yeterli sayıda çalışma olmamasının yanı sıra, hizmet sektörünün önemli bir kolu olan sağlık hizmetleri sektörü tüketicilerine yönelik de yeterli sayıda çalışma bulunmamaktadır. Bu araştırmanın amacı; sağlık sektöründe algılanan değer ile müşteri sadakati arasındaki ilişkiyi ve bu ilişkide müşteri tatmininin oynadığı rolü incelemektir. Bu araştırma 1-30 haziran 2017 tarihleri arasında Şanlıurfa’da bulunan Harran Üniversitesi Araştırma ve Uygulama hastanesine poliklinik hizmetleri almaya gelen 783 hasta ile anket yöntemi kullanılarak yapılmıştır. 7 alt boyut ve 31 maddeden oluşan Sağlık Sektörü Algılanan Değer (SSAD) Ölçeğinin genel Cronbach alfa katsayısına göre iç tutarlılık anlamındaki güvenilirliği 0,973 olarak bulunmuştur. Hasta memnuniyeti boyutlarının “hasta sadakati” üzerindeki etkisinin doğrusal regresyon aracılığıyla açıklandığı modelin anlamlılığı ANOVA testi ile incelenmiş ve model için düzeltilmiş R-kare katsayısı 0,672 olarak hesaplanmıştır. Bu değer, hasta sadakatindeki değişkenliğin %67,2’sinin doğrusal regresyon modeli aracılığıyla hasta memnuniyeti boyutları tarafından açıklandığını göstermektedir. Ayrıca hasta memnuniyeti boyutlarının “hasta tatmini” üzerindeki etkisinin doğrusal regresyon aracılığıyla açıklandığı modelin anlamlılığı ANOVA testi ile incelenmiş ve model için düzeltilmiş R-kare katsayısı 0,706 olarak hesaplanmıştır. Bu değer, hasta tatminindeki değişkenliğin %70,6’sının doğrusal regresyon modeli aracılığıyla hasta memnuniyeti boyutları tarafından açıklandığını göstermektedir. Sonuç olarak, hasta memnuniyetinin “hasta sadakati” ve “hasta tatmini” üzerinde olumlu etkisi olduğu tespit edilmiştir. Sağlık kurumundan memnun ayrılan hastanın, tedavi gördüğü sağlık kurumuna sadakati artmakta ve hasta olarak ihtiyaçlarını karşılamış olarak ayrılmaktadır. Bu çalışma sınırlı bir alanda yapıldığı için genelleme yapılamaz ve yapılacak yeni araştırmalar için yön gösterici olacaktır.

**ANAHTAR SÖZCÜKLER:** Sağlık Kurumu, Hasta Memnuniyeti, Hasta sadakati, hasta tatmini

### GİRİŞ

Sağlık sektöründe kurumlarının varlığını sürdürmek, kurumlarının pazar payını arttırmak isteyen sağlık kurumları yöneticileri, mevcut müşteriyi elde tutmanın yeni müşteri bulmaktan daha az maliyetli olduğunun bilinciyle sektördeki yoğun rekabetin de baskısıyla hastalarının davranışsal niyetleri üzerinde etkili olabilecek yeni stratejiler geliştirmeye çalışmaktadırlar. Algılanan değerın stratejik yönetimde etkili olan temel faktörlerden biri olmasının fark edilmeye başlanmasıyla konu birçok araştırmacının da dikkatini çekmeye başlamıştır[1]. Algılanan değerin hem müşteri tatmini hem de müşteri sadakati üzerinde etkileri bulunmaktadır [2]. Bu nedenlerle sağlık sektöründe, algılanan değerin hasta tatmini ve hasta sadakati üzerindeki etkilerinin araştırılması gerektiği düşünülmüş ve sağlık sektöründe algılanan değer, hasta tatmini ve hasta sadakati kavramları bu çalışmanın konusu olmuştur.

### KAVRAMSAL ÇERÇEVE

#### Algılanan Değer

Algılanan değer kavramı psikoloji, sosyoloji, ekonomi ve işletme gibi birçok farklı disiplinle bağlantısı olan, multidisipliner bir kavramdır [3]. Zeithaml [4] algılanan değer kavramını da ele aldığı çalışmada, algılanan değer kavramını, müşterilerin algılarına yönelik olarak, bir ürün için neler verdiği (harcanan para, zaman veya çaba) ile karşılığında neler aldığının (miktar, kalite veya uygunluk) kapsamlı bir değerlendirmesi şeklinde tanımlanmıştır. Diğer bir anlatımla müşteri değeri, bir müşterinin bir ürün ya da hizmeti elde etmesi sonucunda sağladığı faydanın, bu fayda karşılığında ödediği maliyetlerden yüksek olması durumunda ortaya çıkmaktadır [5]. Sanchez ve arkadaşları ise [6] hizmete yönelik olarak değeri, müşterilerin algıladıkları yarar ve algıladıkları maliyetler arasındaki karşılaştırma olarak tanımlamışlardır. Ancak özellikle sağlık sektörü dikkate alındığında bu kayıplar sadece parasal olmamakta, kaybedilen zaman, harcanan çaba, yaşanan stres gibi parasal olmayan kayıplar da işin içine girmektedir [7]. Tüm bunlar dikkate alındığında algılanan değer çok boyutlu bir yapı olduğu görülmektedir. Bu nedenlerle bu çalışma kapsamında da algılanan değer kavramı kuruluşun işlevsel değeri, ilgili kişinin profesyonelliğinin işlevsel değeri, hizmetin kalitesinin işlevsel değeri, parasal maliyetlerin işlevsel değeri, parasal olmayan maliyetlerin işlevsel değeri, duygusal değer ve sosyal değer olmak üzere yedi alt boyuttan oluşan çok boyutlu bir yapı olarak ele alınacaktır.

### **Müşteri Tatmini**

Oliver çalışması müşteri tatminini, tüketim sonucunda müşterinin bir ihtiyacının, bir arzusunun veya bir amacının kendisine keyif verici şekilde tamamlanması şeklinde tanımlamaktadır [8]. Sağlık kurumları açısından hasta tatmininin, tatmin olan hastaların sağlık hizmeti aldıkları o sağlık kurumunu başta başkalarına tavsiye etmeleri olmak üzere [9], olumlu kulaktan kulağa iletişim, yüksek kârlılık, doktor tavsiyelerine uyma eğiliminin artması gibi olumlu başka sonuçları da bulunmaktadır. Bu nedenlerle sağlık kurumları yöneticilerinin hasta tatminine önem vermeli, hasta tatminini etkileyen algılanan değer boyutlarını tespit etmelidirler [10].

### **Müşteri Sadakati**

Müşteri sadakati müşterilerin bir markaya, bir mağaza ya da bir tedarikçiye karşı olumlu tutum ve davranış sergilemesi şeklinde açıklanmaktadır [11]. Bazı araştırmacılar [12] müşterilerin bir ürüne sadık olması için öncelikle o üründen tatmin olması gerektiğini savunurken, bazı araştırmacılar [13] ise algılanan değer ile müşteri sadakati arasında direk bir ilişki olduğunu savunmaktadırlar.

## **GEREÇ VE YÖNTEM**

### **Araştırmanın Amacı**

Bu çalışmanın amacı sağlık sektöründe algılanan değer çok boyutlu olarak incelenmesi ve algılanan değer kavramının müşteri tatmini ve müşteri sadakati üzerindeki etkilerinin ortaya konmasıdır.

### **Veri Toplama Aracı**

Araştırmada veri toplama yöntemi olarak anket formu kullanılmıştır. Bu amaç doğrultusunda iki bölümden oluşan veri toplama aracının birinci bölümünde algılanan değer ölçümü için 31 ifade [14], müşteri tatmininin ölçümü için 3 ifade [15] ve müşteri sadakatinin ölçümü için 1 ifade [16] olmak üzere toplam 35 ifadeye; ikinci bölümünde ise hastaların demografik özelliklerini belirlemeye yönelik sorulara yer verilmiştir. Araştırma kapsamında 1-30 Haziran 2017 tarihleri arasında Şanlıurfa'da bulunan Harran Üniversitesi Araştırma ve Uygulama Hastanesi'nde poliklinik hastalarına gerekli izinler alındıktan sonra anket uygulanmıştır. Eksik ve/veya hatalı

olan anketler çıkarıldıktan sonra kalan, 783 tam ve hatasız anket değerlendirmeye alınmıştır. Araştırmada kullanılan ölçekte ifadeler, 5'li Likert tipi ölçek ile değerlendirilmiş olup; “kesinlikle katılmıyorum” (1) ile “kesinlikle katılıyorum” (5) arasında değer almaktadır. Araştırmada Algılanan Değer Ölçeği'ne ilişkin ölçülen Cronbach Alpha güvenilirlik katsayısı 0.973 olarak hesaplanmıştır.

## ANALİZ ve BULGULAR

### Tanımlayıcı Bulgular

Tablo 1’de görüldüğü üzere araştırmaya katılan hastaların %45,8’i kadın, %54,2’si ise erkektir. Hastaların çoğunluğu 31-41 yaş aralığında (%26,1) olup, hastaların %56,1’i hastaneye Şanlıurfa merkezinden gelmektedirler. Hastaların %45,6’sı ilköğretim mezunudur ve %41,3’ünün herhangi bir geliri yoktur. Hastaların üste ikisinin (%67,6) sosyal güvencesi SGK iken, hastaların %23’9’u bu hastaneye ilk defa gelmişlerdir.

### Poliklinik Hastalarının Algıladıkları Değere Yönelik Bulgular

Araştırmaya katılan hastalara ayrıca hasta tatmini ve hasta sadakatine yönelik sorular sorulmuş, algılanan değerin hangi kavram üzerinde daha çok etkisi olduğu ortaya konmaya çalışılmıştır. Aşağıda yer alan Tablo 2’de algılanan değer boyutlarının hasta tatmini üzerine etkisini tespit etmek üzere yapılan regresyon analizinin bulgularına yer verilmiştir. Algılanan değer alt boyutlarının hasta tatmini üzerindeki etkisinin doğrusal regresyon aracılığıyla açıklandığı modelin anlamlılığı ANOVA testi ile incelenmiştir. ANOVA testine göre model istatistiksel olarak anlamlı bulunmuştur. Bunun anlamı; algılanan değer alt boyutlarının, hasta tatmini üzerindeki etkisi doğrusal regresyon modeliyle incelenebilir demektir. Ayrıca model için düzeltilmiş R-kare katsayısı 0,706 olarak hesaplanmıştır. Bu değer, hasta tatminindeki değişkenliğin %70,6’sının doğrusal regresyon modeli aracılığıyla algılanan değer alt boyutları tarafından açıklandığını göstermektedir (Tablo 2). Doğrusal regresyon modelindeki katsayıların tahminlerinin anlamlılığı student-t testi ile incelenmiştir. Elde edilen bulgulara göre ilgili kişinin profesyonelliği, parasal olmayan maliyetler ve sosyal değer değişkenlerinin katsayıları istatistiksel olarak anlamlı, diğer değişkenlerin katsayıları istatistiksel olarak anlamsız bulunmuştur. Katsayısı anlamsız bulunan değişkenler modelden çıkarılarak yeni bir yeni bir regresyon modeli oluşturulmuştur. Üç bağımsız değişken içeren yeni modeli de anlamlı bulunmuştur. Ayrıca model için düzeltilmiş R-kare katsayısı 0,706 olarak hesaplanmıştır. Bu değer, hasta tatminindeki değişkenliğin %70,6’sının doğrusal regresyon modeli aracılığıyla algılanan değer boyutları tarafından açıklandığını göstermektedir (Tablo 3). Elde edilen modele göre değişkenlerin üçünün de hasta tatmini üzerinde pozitif etkisi vardır. Bulgulara göre hasta tatmini Y, ilgili kişinin profesyonelliği X1, parasal olmayan maliyetler X2 ve sosyal değer X3 ile gösterilirse doğrusal regresyon modeli

$$Y = -0,012 + 0,107 \times X1 + 0,100 \times X2 + 0,807 \times X3$$

olarak elde edilmiştir. Ayrıca standart katsayılar göre, ilgili kişinin profesyonelliği değişkenindeki 1 birim artış (bu boyuttaki algılanan değerin 1 birim artması) tatmin değişkeninde 0,090 birim artışa, parasal olmayan maliyetler değişkenindeki 1 birim artış tatmin değişkeninde 0,090 birim artışa ve sosyal değerdeki 1 birim artış hasta tatmininde 0,716 birim artışa sebep olması beklenmektedir. Katsayıların student-t istatistiği değerlerine bakıldığında sosyal değer değişkeninin hasta tatmini üzerinde daha yüksek öneme (etkiye) sahip olduğu yorumu yapılabilir. Algılanan değer boyutlarının hasta sadakati üzerindeki etkisinin doğrusal regresyon aracılığıyla

**Tablo 1 Hastalara Yönelik Tanımlayıcı Bulgular**

<b>DEĞİŞKENLER</b>	<b>f</b>	<b>%</b>
<b>Cinsiyet</b>		
Kadın	359	45,8
Erkek	424	54,2
<b>Yaş Grupları</b>		
17-23 yaş	200	25,5
24-30 yaş	198	25,3
31-41 yaş	204	26,1
42 yaş ve üstü	181	23,1
<b>Geldiği Yer</b>		
Şanlıurfa şehir merkezi	439	56,1
Şanlıurfa ilçeleri	310	39,6
Diğer iller	34	4,3
<b>Eğitim Durumu</b>		
İlköğretim	357	45,6
Lise	256	32,7
Önlisans	99	12,6
Lisans	58	7,4
Lisans üstü	13	1,7
<b>Gelir Durumu</b>		
Gelirim yok	323	41,3
Asgari ücret	290	37,0
1405-3000 TL	130	16,6
3001-4577 TL	36	4,6
4578 TL ve üzeri	4	,5
<b>Sosyal Güvence</b>		
SGK	529	67,6
Sosyal güv. yok	37	4,7
Yeşil kart	176	22,5
Özel sğ. sig.	32	4,1
Diğer	9	1,1
<b>Geliş Sayısı</b>		
1	187	23,9
2	220	28,1
3	176	22,5
4 ve üzeri	200	25,5
<b>Toplam</b>	<b>783</b>	<b>100,0</b>



**Tablo 2:** Algılanan Değer Alt Boyutlarının Hasta Tatmini Üzerine Etkisi İçin Doğrusal Regresyon Bulguları

	Regresyon Katsayıları	Standart Regresyon Katsayıları	t	p
Sabit	0,007		0,067	0,947
Kuruluşun İşlevsel Değeri	-0,030	-0,026	-0,929	0,353
İlgili Kişinin Profesyonelliğinin İşlevsel Değeri	0,118	0,099	2,779	<b>0,006</b>
Hizmet Kalitesinin İşlevsel Değeri	0,054	0,042	0,996	0,319
Parasal Maliyetlerin İşlevsel Değeri	-0,079	-0,070	-1,966	0,050
Parasal Olmayan Maliyetlerin İşlevsel Değeri	0,118	0,107	2,980	<b>0,003</b>
Duygusal Değer	0,037	0,032	0,750	0,454
Sosyal Değer	0,789	0,700	18,075	<b>0,000</b>
<b>R</b>	<b>R kare</b>	<b>Düzeltilmiş R kare</b>	<b>F</b>	<b>p</b>
0,842	0,709	0,706	268,155	,000a

**Tablo 3:** Modelde Katsayısı Anlamsız Bulunan Değişken Çıkarıldıktan Sonra Oluşturulan Doğrusal Regresyon Modelinin Bulguları

	Regresyon Katsayıları	Standart Regresyon Katsayıları	t	p
Sabit	-0,012		-0,121	0,904
İlgili Kişinin Profesyonelliğinin İşlevsel Değeri	0,107	0,090	3,451	0,001
Parasal Olmayan Maliyetlerin İşlevsel Değeri	0,100	0,090	2,958	0,003
Sosyal Değer	0,807	0,716	24,998	0,000
<b>R</b>	<b>R kare</b>	<b>Düzeltilmiş R kare</b>	<b>F</b>	<b>p</b>
0,841	0,707	0,706	625,680	,000a

açıklandığı modelin anlamlılığı ANOVA testi ile incelenmiştir. ANOVA testine göre model istatistiksel olarak anlamlı bulunmuştur. Bunun anlamı; algılanan değer boyutlarının, hasta sadakatı üzerindeki etkisi doğrusal regresyon modeliyle incelenebilir demektir. Ayrıca model için düzeltilmiş R-kare katsayısı 0,672 olarak hesaplanmıştır. Bu değer, hasta sadakatındaki değişkenliğin %67,2'sinin doğrusal regresyon modeli aracılığıyla algılanan değer boyutları tarafından açıklandığını göstermektedir (Tablo 4). Doğrusal regresyon modelindeki katsayıların tahminlerinin anlamlılığı student-t testi ile incelenmiştir. Elde edilen bulgulara göre parasal olmayan maliyetler, duygusal değer ve sosyal değer değişkenlerinin katsayıları istatistiksel olarak anlamlı, diğer değişkenlerin katsayıları istatistiksel olarak anlamsız bulunmuştur. Katsayısı anlamsız bulunan değişkenler modelden çıkarılarak yeni bir yeni bir regresyon modeli

oluşturulmuştur. Üç bağımsız değişken içeren yeni modeli de anlamlı bulunmuştur. Ayrıca model için düzeltilmiş R-kare katsayısı 0,672 olarak hesaplanmıştır Bu değer, müşteri sadakatindeki değişkenliğin %67,2'inin doğrusal regresyon modeli aracılığıyla algılanan hasta değer boyutları tarafından açıklandığını göstermektedir (Tablo 5). Elde edilen modele göre değişkenlerin üçünün de hasta sadakatini üzerinde pozitif etkisi vardır. Bulgulara göre hasta sadakatini Y, parasal olmayan maliyetler X1, duygusal değer X2 ve sosyal değer X3 ile gösterilirse doğrusal regresyon modeli

$$Y = 0,231 + 0,149 \times X1 + 0,120 \times X2 + 0,676 \times X3$$

olarak elde edilir. Ayrıca standart katsayılara göre, parasal olmayan maliyetler değişkenindeki 1 birim artış (bu boyuttaki algılanan değer 1 birim artması) sadakat değişkeninde 0,139 birim

**Tablo 4:** Algılanan Değer Boyutlarının Hasta Sadakatini Üzerine Etkisi İçin Doğrusal Regresyon Bulguları

	Regresyon Katsayıları	Standart Regresyon Katsayıları	t	p
Sabit	0,193		1,826	0,068
Kuruluşun İşlevsel Değeri	-0,026	-0,023	-0,779	0,436
İlgili Kişinin Profesyonelliğinin İşlevsel Değeri	-0,002	-0,002	-0,043	0,966
Hizmet Kalitesinin İşlevsel Değeri	0,083	0,067	1,489	0,137
Parasal Maliyetlerin İşlevsel Değeri	0,014	0,013	0,336	0,737
Parasal Olmayan Maliyetlerin İşlevsel Değeri	0,122	0,114	3,012	<b>0,003</b>
Duygusal Değer	0,114	0,102	2,300	<b>0,022</b>
Sosyal Değer	0,651	0,596	14,680	<b>0,000</b>
<b>R</b>	<b>R kare</b>	<b>Düzeltilmiş R kare</b>	<b>F</b>	<b>p</b>
0,822	0,675	0,672	229,383	,000a

**Tablo 5:** Modelde Katsayısı Anlamsız Bulunan Değişken Çıkarıldıktan Sonra Oluşturulan Doğrusal Regresyon Modelinin Bulguları

	Regresyon Katsayıları	Standart Regresyon Katsayıları	t	p
Sabit	0,231		2,391	0,017
Parasal Olmayan Maliyetlerin İşlevsel Değeri	0,149	0,139	4,265	0,000
Duygusal Değer	0,120	0,107	2,505	0,012
Sosyal Değer	0,676	0,619	15,673	0,000
<b>R</b>	<b>R kare</b>	<b>Düzeltilmiş R kare</b>	<b>F</b>	<b>p</b>
0,821	0,673	0,672	534,717	,000a

artışa, duygusal değerlerdeki 1 birim artış sadakat değişkeninde 0,107 birim artışa ve sosyal değerlerdeki 1 birim artış hasta sadakatinde 0,619 birim artışa sebep olması etmesi beklenmektedir. Katsayıların student-t istatistiği değerlerine bakıldığında sosyal değer değişkeninin hasta sadakati üzerinde daha yüksek öneme (etkiye) sahip olduğu yorumu yapılabilir.

## SONUÇ ve ÖNERİLER

Sağlık kurumlarında hastaların algıladıkları değeri oluşturan parçaların tanımlanması ve sonrasında hastaların algıladıkları değerin artırılması çok önemlidir. Çünkü algılanan değerin arttırmanın bir sonucu olarak hastalarla kurulacak uzun dönemli ilişki beraberinde sağlık kurumuna büyümeyi ve kârlılığı getirecektir [17]. Bunlardan yola çıkarak bu çalışmada algılanan değer, algılanan değerin alt boyutları, hasta tatmini ve hasta sadakati konuları incelenmiştir. Çalışma sonucunda hastaların aldıkları hizmetin değerine yönelik algılarında en çok duygusal değer ve sosyal değer alt boyutlarının etkili olduğu görülmüştür. Buna göre çalışanların hastalara yönelik olumlu tutumları, hastaların kendilerini rahat hissetmeleri, hastanenin toplumdaki yeri ve hastanın çevresindeki kişilerin hastane hakkındaki düşünceleri hastaların değer algılarını önemli şekilde etkilemektedir. Diğer yandan çalışmada hasta tatminini ve hasta sadakatini etkileyen algılanan değer alt boyutları tespit edilmeye çalışılmıştır. Çalışma sonucunda parasal olmayan maliyetlerin işlevsel değeri ve sosyal değer alt boyutlarının hem hasta tatmini hem de hasta sadakati üzerinde etkili oldukları görülmüştür. İlgili kişinin profesyonelliğinin işlevsel değeri alt boyutu hasta atmini üzerinde etkili iken, duygusal değer alt boyutu ise hasta sadakati üzerinde etkilidir. Ettinger'e [7] göre sağlık kurumları yöneticileri öz (core) hastalarının neye değer verdiğini bilmelidirler ve hizmet sunumunu bu değeri yükseltecek şekilde tasarlamalıdır. Çalışmanın sonuçların göre hastaların sadakatini etkileyen en önemli algılanan değer alt boyutlarında parasal olmayan maliyetlerin işlevsel değeri, sosyal değer ve duygusal değer olduğu ortaya çıkmıştır. Buna göre sağlık kurumları yöneticileri sadık hastalarının algıladıkları değeri yükseltmek için özellikle bu üç alt boyutun altında yer alan ifadelerle yönelik iyileştirme çalışmaları yapmalıdırlar. Bu çalışmadan elde edilen sonuçların hem araştırmacılara hem de yöneticilere hastaların değer algılarını etkileyen faktörlerin, algılanan değerin hasta tatmini ve hasta sadakati ile olan etkileşimlerinin anlaşılması açısından yardımcı olacağı düşünülmektedir.

Hastaların farklı ihtiyaçları, farklı tercihleri, farklı değerleri ve farklı finansal durumları olduğu için farklı değer algıları olduğu da unutulmamalıdır [17]. İleride farklı demografik özelliklere sahip hastaların değer algılarına yönelik araştırmalar yapılmasının literatüre katkısı olacağı düşünülmektedir.

Bu araştırma Şanlıurfa İli'nde yer alan Harran Üniversitesi Araştırma ve Uygulama Hastanesi'nin polikliniklerine başvuran 783 hasta ile sınırlı kalmıştır. Bu nedenle, bu araştırmadan elde edilen sonuçlar tüm kurum ve kuruluşlara genellenemeyeceği için, araştırma konusuna yönelik olarak daha sonra yapılacak araştırmaların daha farklı bölgelerde daha geniş popülasyonlarda yapılması önerilmektedir.

## KAYNAKÇA

- [1] Sánchez-Fernández, R., & Iniesta-Bonillo, M. Á. (2007). The concept of perceived value: a systematic review of the research. *Marketing theory*, 7(4), 427-451.
- [2] Yang, Z., & Peterson, R. T. (2004). Customer perceived value, satisfaction, and loyalty: The role of switching costs. *Psychology & Marketing*, 21(10), 799-822.
- [3] Eskiler, E., & Altunışık, R. (2015). Algılanan Değer ve Müşteri Memnuniyetinin Satın Alma Eğilimleri Üzerine Etkisi. III. Rekreasyon Kongresi.
- [4] Zeithaml, V. A. (1988). Consumer perceptions of price, quality, and value: a means-end model

- and synthesis of evidence. *The Journal of marketing*, 2-22.
- [5]Tekin, M., & Çiçek, E. (2005). İşletmelerde Rekabet Üstünlüğü Sağlamada Farklı Bir Yaklaşım: Değer Temelli Pazarlama. V. Ulusal Üretim Araştırmaları Sempozyumu, İstanbul Ticaret Üniversitesi, İstanbul.
- [6]Sánchez, J., Callarisa, LL.J., Rodrı'guez, R.M. and Moliner, M.A. (2006), "Perceived value of the purchase of a tourism product", *Tourism Management*, Vol. 27 No. 4.
- [7]Ettinger Jr, W. H. (1998). Consumer Perceived Value: The Key to a Successful Business Strategy in the Healthcare Marketplace. *Journal of the American Geriatrics Society*, 46(1), 111-113.
- [8]Oliver, R.L. (1997), *Satisfaction: A Behavioral Perspective on the Consumer*. New York: Irwin/McGraw. Ve Müşteri Memnuniyeti (İstanbul Örneği). *Journal of Academic Studies*, 11(43), 85-98.
- [9]Çaha, H., & Bayyurt, N. (2009). Sağlık Hizmetleri Birleştirmesinden Sonra Özel Hastanelerde Hizmet Kalitesi
- [10]Dursun, Y., & Çerçi, U. M. (2004). Algılanan sağlık hizmeti kalitesi, algılanan değer, hasta tatmini ve davranışsal niyet ilişkileri üzerine bir araştırma. *Erciyes Üniversitesi İktisadi ve İdari Bilimler Fakültesi Dergisi*, (23).
- [11]Sheth, J. N., Mittal, B., Newman, B. I., & Sheth, J. N. (2004). Customer behavior: A managerial perspective.
- [12]Oliver, R. L. (1999). Whence consumer loyalty?. *the Journal of Marketing*, 33-44.
- [13]Chahal, H., & Kumari, N. (2011). Consumer Perceived Value and Consumer Loyalty in the Healthcare Sector, *Journal of Relationship Marketing*, 10(2), 88-112.
- [14]Özer, L., Başgöze, P., & Karahan, A. (2017). The association between perceived value and patient loyalty in public university hospitals in Turkey. *Total Quality Management & Business Excellence*, 28(7-8), 782-800.
- [15]Baker, D. A., Crompton, J. L. (2000). Quality, satisfaction and behavioral intentions. *Annals of Tourism Research*, 27(3), 785–804.
- [16]McDougall, G. H., & Levesque, T. (2000). Customer satisfaction with services: Putting perceived value into the equation. *Journal of Services Marketing*, 14(5), 392–410.
- [17]Chahal, H., & Kumari, N. (2012). Consumer perceived value: the development of a multiple item scale in hospitals in the Indian context. *International Journal of Pharmaceutical and Healthcare Marketing*, 6(2), 167-190.